Light-based therapies in Prostate Cancer treatment

Alejandra Martinez de Pinillos Bayona

A thesis submitted to University College London in fulfilment of the degree of Doctor of Philosophy (PhD)

2016

Division of Surgery and Interventional Science

University College London, UCL

I, Alejandra Martinez de Pinillos Bayona, certify that the work presented in this thesis is my own. Where information has been derived from other sources, I confirm that this has been indicated in the thesis.

Abstract

Photodynamic Therapy (PDT) and Photochemical Internalisation (PCI) are both light-based therapies which can be used for the focal treatment of cancer. Both PDT and PCI require the combination of photosensitisers, light and molecular oxygen to induce photooxidative reactions that damage biomolecules. However, while PDT employs a photosensitiser as the sole therapeutic agent, PCI combines low-dose PDT with another therapeutic agent to enable the improved delivery of this agent to its intended subcellular targets. The overall aim of this study was to investigate PDT and PCI for prostate cancer in both *in vitro* and *in vivo* tumour models.

In the PCI procedures, the ribosome inactivating protein type 1 saporin was used as a model chemotherapy agent. We have concluded an enhancement in cell killing in prostate carcinoma cells after PCI compared to PDT in 2-dimensional models, i.e. 80% cell death, compared to 32% killing after PDT. Similar observations resulted from qualitative observations in the 3-dimensional model. Moreover, conjugation of a photosensitiser to cell penetrating peptides (TAT or Antp), resulted in a similar difference in cytotoxicity after PCI and PDT using lower concentrations of the conjugates - 76% and 14% respectively. These data confirm the synergistic effect of drug and photosensitiser in PCI.

Three different clinically relevant photosensitisers were used *in vivo* in a subcutaneous rat model. Vascular-targeted PDT resulted in the most efficient treatment, and photosensitisers targeting a cellular effect, showed a better outcome with shorter drug-light intervals. The analysis of tumour samples through immunohistochemistry and molecular analysis revealed an innate inflammatory response that led to an adaptive immune response. A highly suppressive tumour microenvironment was suggested by the infiltration of regulatory T cells ($FoxP3^{+}$), up-regulation of PD-L1 and down-regulation of cytolytic proteins (i.e. Perforin). Moreover, the beneficial effect of using immunoadjuvants (cyclophosphamide) was investigated.

Light based therapies could play an important role in prostate cancer treatment both eradicating tumours and generating long-term immune protection against secondary tumour deposits.

Table of Contents

List of Figures

List of Tables

List of Abbreviations

Acronym	Definition
2D	2 Dimensional
3D	3 Dimensional
3Rs	Replacement, Reduction, Refinement
5-ALA	5-Aminolevulinic Acid
ABC	ATP-binding cassette
AIF	Apoptosis Inducing Factor
AJCC	American Joint Committee on Cancer
$AlPcS_{2a}$	Aluminium Phtalocyanine
Antp	Antennapaedia, Penetratin
APC	Antigen Presenting Cell
AR	Androgen Receptor
Bcl-2	B Cell Lymphoma-2
Bcl-3	B Cell Lymphoma 3-encoded protein
BCR	B Cell Receptor
BPD-MA	Benzoporphyrin derivative Monoacid – Visudyne
CAF	Cancer Associated Fibroblast
CCD	Charge-Coupled Device
CD	Cluster of Differentiation
cDNA	Complementary DNA
Ce6	Chlorin e6
Ce6-PVP	Chlorin e6 derivative – Fotolon
CNV	Choroidal Neovascularisation
CPP	Cell Penetrating Peptide
CRUK	Cancer Research UK
CTLA-4	Cytotoxic T Lymphocyte-associated Antigen-4
CY	Cyclophosphamide
DAMP	Damage Associated Molecular Pattern
DC	Dendritic Cell
DDS	Drug Delivery System
DLI	Drug-Light Interval
DMSO	Dimethyl Sulfoxide
DVDMS	Sinoporphyrin Sodium
EGFR	Endothelial Growth Factor Receptor
EGP-2	Endothelial Glycoprotein-2

EMT	Epithelial-to-Mesenchymal Transition
EPR	Enhanced Permeability and Retention
ER	Endoplasmic Reticulum
FAS	Tumour Necrosis Factor Receptor Superfamily
FASL	Tumour Necrosis Factor Receptor Superfamily Ligand
FFPE	Formalin Fixed Paraffin Embedded
FLA	Focal Laser Ablation
FoxP3	Forkhead Box P3
GAG	Glycosaminoglycan
GzmA	Granzyme A
HdP	Hematoporphyrin derivative – Photofrin
HER-2	Human Epidermal Growth Factor Receptor-2
HIF-1	Hypoxia Inducible Factor-1
HIFU	High Intensity Focused Ultrasound
HLA	Human Leukocyte-Associated
HMGB-1	High Mobility Group Box-1
HOMO	Highest Occupied Molecular Orbital
HPD	Porfimer Sodium
HSP	Heath Shock Protein
HUVEC	Human Umbilical Vein Endothelial Cell
IHC	Immunohistochemistry
I.P.	Intraperitoneal
I.V.	Intravenous
IACUC	Institutional Animal Care and Use Committee
IC	Infiltrating Cells
ICD	Immunogenic Cell Death
IGF	Insulin Growth Factor
IKK	IκB Kinase
LAMP1	Lysosomal Associated Membrane Protein 1
LD_{50}	Lethal Dose 50
LH	Luteinising Hormone
LOMO	Lowest Occupied Molecular Orbital
LS11/MACE/NPe6	mono-L-asparyl chlorin e6 – Talaporfin
LuTex	Motexafin Lutetium
MAL	Methyl Aminolevulinate
MDR	Multidrug Resistance
MDSC	Myeloid-derived Suppressor Cells
MEM	Minimum Essential Medium
MHC	Major Histocompatibility

MLL	MatLyLu cells
MMP	Metalloproteinase
MSC	Mesenchymal Stem Cell
mTHPC	m-Tetra(hydroxyhenyl)chlorin – Termoporfin, Foscan
NDP	Nanozoomer Digital Pathology
NFkβ	Nuclear Factor kappa β
NFW	Nuclease Free Water
NIH	National Institutes of Health
NK	Natural Killer cell
NLS	Nuclear Localisation Signal
P-gp	P-glycoprotein efflux pump
PACT	Photodynamic Antimicrobial Chemotherapy
PAD	Photoactivated Disinfection
PAMP	Pathogen Associated Molecular Pattern
Pc4	Silicon Phtalocyanine
PCI	Photochemical Internalisation
PCUK	Prostate Cancer UK
PD-L1/PDL1	Programmed Cell Death Ligand-1
PD1	Programmed Cell Death-1 Receptor
PDI	Photodynamic Inactivation
PDT	Photodynamic Therapy
PMO	Phorodiamidate Morpholino Oligomer
PS	Photosensitiser
PSA	Prostate Specific Antigen
PSMA	Prostate Specific Membrane Antigen
qRT-PCR	Quantitative-Real Time Polymerase Chain Reaction
RIP	Ribosome Inactivating Protein
ROI	Region of Interest
ROS	Reactive Oxygen Species
S.C.	Subcutaneous
SEM	Standard Error Mean
SnEt2	Tin ethyl etiopurpurin – Purlytin
TAA	Tumour Associated Antigen
TAM	Tumour Associated Macrophage
TAT	Transactivator of Transcription
Tc	Cytotoxic T cell
TC	Tumour Cell
TCR	T Cell Receptor
TGF-α	Transforming Growth Factor-α

TGF-β	Transforming Growth Factor β
Th	Helper T cell
TKI	Tyrosine Kinase Inhibitor
TLR	Toll Like Receptor
TOOKAD (WST-09)	Padoporfin
TOOKAD (WST-11)	Padeliporfin
$TPCS_{2a}$	Disulfonated Tetraphenyl Chlorin – Amphinex
TPP	Tetraphenyl Porphyrin
$TPPS_{2a}$	Disulfonated Tetraphenyl Porphyrin
TRAIL R	Tumour Necrosis Factor Apoptosis Inducing Ligand Receptor
Treg	Regulatory T cell
UICC	Union International Cancer Control
UKCCCR	United Kingdom Coordinating Committee on Cancer Research
VEGF	Vascular Endothelial Growth Factor
vMIP-II	viral Macrophage Inflammatory Protein-II

Acknowledgements

I would like to start by thanking the Doctorates in Europe programme (“la Caixa” Foundation), Bogue Research Fellowships and the Division of Surgery & Interventional Science (both UCL) for funding this PhD project.

Secondly, I would like to thank my supervisor Prof. Alexander MacRobert for granting me the opportunity to carry out this research project. My sincere gratitude to Dr. Caroline Moore, Dr. Josephine Woodhams and Dr. Rifat Hamoudi for all the trust and support I have received throughout these years not only academically but also personally. Thanks for always backing me. Besides my supervisory team, I would like to say thank you to all my colleagues at the National Medical Laser Centre (NMLC) and the Department of Tissue and Energy. A huge special thanks to Dr. Elnaz Yaghini, Dr. Pilar Acedo, Dr. Hayley Pye, Dr. Derick Adigbli and Dr. Melissa Bovis (my British sister) for their endless guidance and assistance and moreover, their invaluable friendship and hours of fun.

My deepest gratitude to Prof. Michael Hamblin at the Wellman Center for Photomedicine (Boston, USA) for the invaluable advice and expertise provided during my short placement in his group; and his team, specifically Ms. Andrea Brissette, Dr. Yingying Huang, Dr. Yuguang Wang, Dr. Ahmed El-Hussein, Dr. Cleber Ferraresi, Miss Fernanda Freire and Dr. Daniela Vecchio for the amusing long office hours and support in the laboratory.

I would also like to thank Prof. John Masters for providing with cells used in the study; Dr. Ian Eggleston’s team at University of Bath for supplying the targeted photosensitiser conjugates; and Dr. Naomi Guppy at UCL Advanced Diagnostics for conducting immunostaining on tumour samples.

I am extremely grateful to all the friends I counted on before moving to London and those amazing ones I have made along the way (too many to list here, but thanks to one and all); without their infinite support this work would not have been possible. Special thanks to my path companion Mr. (soon Dr.) Xiang Weng, providing me with infinite support and confidence.

Finally, I would like to dedicate this thesis to my family, my exceptional brother Borja, and my extremely loving parents Ana and Alberto, who have been my moral support and pillars throughout my entire education and my life in general.

Chapter 1 Background and Introduction

1.1 Introduction to the prostate

The prostate is a gland in male individuals located above the pelvic floor, below the bladder and in front of the rectum, with the urethra running transversely through its central region (from bladder to penis), see Figure 1. A healthy normal prostate weights 18g approximately and measures 3 cm (length) x 4 cm (width) x 2 cm (depth) (Wein et al., 2012).

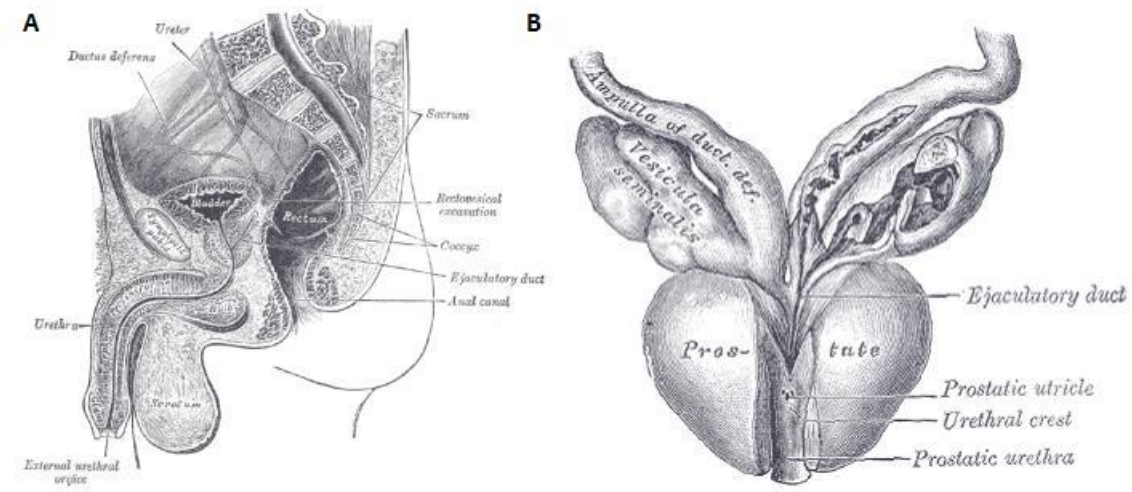

Figure 1. Anatomy of the male urinary system.

(A) Midsagittal section of the male reproductive and urinary system. (B) Detailed representation of the prostate gland and surrounding organs. Images taken from [(Gray, 1918)*]*

The prostate is composed of connective tissue and smooth muscle fibres and can be divided in four clearly defined parts:

- Anterior region: rich in muscle fibres with no glandular structures.
- Peripheral region: main component of the gland, around 70% of the prostate belongs to this region. It is the zone where most cancers are developed.
- Central region: located surrounding the transition region (25% of the entire structure), it is the zone where the ejaculatory duct is found. 10% of the cancers are found in this region.
- Transition region: located in the inner part of the gland, composed of two lobules directly surrounding the urethra between the upper section of this structure and the bladder. This is the smallest part, corresponding to

5% of the whole structure. 25% of prostate cancers will be localised in this region.

The main function of this gland is the production of the fluid component of semen. As such, prostatic gland cells continuously secrete a protein- and mineral- rich thin fluid which is responsible for the maintenance and correct functioning of the sperm. A role in urine flow regulation has also been described for the prostate: its muscle fibres surrounding the urethra are controlled by the involuntary nervous system and therefore regulate the urine flow (Chapple and Steers, 2011).

Several pathological conditions have been described in the prostate, namely prostatitis, benign prostatic hypertrophy and prostate cancer.

Prostatitis can be an acute or chronic condition, sometimes associated with bacteria in the urine (acute or chronic prostatitis) and sometimes not. It can be difficult to diagnose and difficult to treat, and there can be significant overlap with chronic pelvic pain syndrome. On the other hand, benign prostatic hypertrophy is characterised by the abnormal growth of cellular components of the prostate, due to an imbalance between proliferation and apoptosis. It is mostly related to ageing and the presence of androgens.

1.2 Prostate cancer

Prostate cancer is the fourth most common cancer, second most frequent in men and fifth cause of cancer-based deaths worldwide (WHO, 2012).

In 2012, 1.1 million men were diagnosed with this type of cancer, accounting for 15% of the overall cancer diagnosed in men that same year. In 2016 only in the U.S. over 180,000 new cases are estimated (10.7% on the overall cancer diagnosis) (National Cancer Institute, 2016). In the UK, around 330,000 suffer currently from this disease and yearly diagnosis are already above 47,000 new cases, implying 130 diagnoses per day (PCUK, 2016). Moreover, it has been hypothesised that it will be the most common cancer by 2030 (CRUK, 2016). It has also been anticipated that prostate cancer will be diagnosed in 14% men throughout their lifetime. A higher incidence is generally found in developed countries, probably due to the existence of more advanced diagnostic capacities.

Over 307,000 deaths worldwide in 2012 (6.6% deaths in men) and 26,000 in the U.S. in 2016 were documented. Fortunately, prostate cancer survival is high: 94%, 85% and 84%, at year 1, 5 or 10 after diagnosis correspondingly. In fact, in the U.S. 5-year survival involves nowadays 98.9% of the cases (CRUK, 2016; National Cancer Institute, 2016; WHO, 2012)

1.2.1 Aetiology and risk factors

Prostate cancer is a multifactorial disease, much influenced by endocrine, genetic and environmental factors. Incidence is considerably associated with family history, race and age. In addition, androgens play a major role in prostate cancer development and maintenance. Prostate cells are very sensitive to the presence of these hormones (mainly dihydrotestosterone and testosterone).

Age is a key influencer, with 75% of diagnosed cases occurring in patients over 65. Regarding ethnical and geographical distribution, the greatest incidence of prostate cancer has been recorded in African-American men, while China and Japan suffer the least cases, possibly based on lifestyle and genetic factors. Family history also enhances the probability of developing prostate cancer, 1.5 to 5-fold higher likelihood depending on the degree of relatedness and number of family cases. In addition, lifestyle appears to be a secondary factor in the increase of the risk to develop prostate cancer. For instance, while red meat and fat have been associated with an increased risk; the consumption of vegetables, vitamin E, vitamin D, selenium, etc. are thought to be linked to a reduced probability (Castiñeiras Fernandez, 2007; Provencio Pulla, 2011).

1.2.2 PSA and Prostate Cancer diagnosis

Generally, prostate cancer is an asymptomatic disease. Only when tumours reach advanced stages are the symptoms detectable.

Early diagnosis is based on the combination of rectal examination, prostate specific antigen (PSA) levels, imaging studies and eventually the pathological examination of a tissue biopsy. PSA has revolutionised prostate cancer diagnostics and follow-up over the last two decades. It is a glycoprotein belonging to the kallikrein family of proteins

(serine proteases), secreted almost exclusively by the prostatic epithelial cells. It is considered an organ-specific marker, yet not tumour-specific since an increase of this marker has also been noted in several benign conditions. The “normal” cut offs of PSA are much debated with the latest PCUK guidelines suggesting referral of men with a PSA over 2.5 ng/ml. In given radical treatment, the PSA reduces dramatically, and PSA kinetics post intervention of tumours has become a good prognosis indicator (Castiñeiras Fernandez, 2007)

1.2.3 Gleason score

Among all prostate cancer subtypes, adenocarcinomas represent 95% of the total number of cases, most localised in peripheral regions. Other less frequent subtypes can be detected including carcino-sarcoma, transitional carcinoma, or sarcoma amongst others (Grignon, 2004).

Gleason scoring is nowadays the most widely accepted system to conduct histopathology grading of prostate cancer. This system was developed first in 1960-1970s (Gleason, 1992) and modified recently in 2005. It is based on the cellular distribution and architectural patterns within a prostatic tumour.

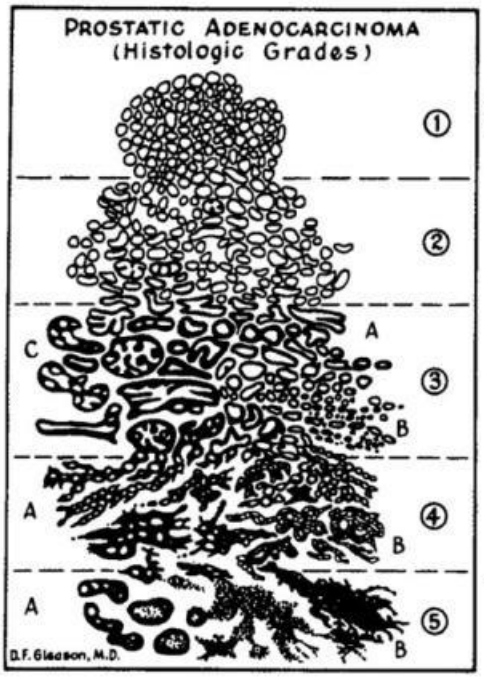

Grade	Description
1	Simple round glands, close-packed in rounded masses with well-defined edges
2	Simple rounded glands, loosely packed in vague, rounded masses with loosely defined edges
3A	Medium sized single glands of irregular shape and irregular spacing with ill-defined infiltrating edges
3B	Very similar to 3A, but small to very small glands, which must not form significant chains or cords
3C	Papillary and cribriform epithelium in smooth, rounded cylinders and masses; no necrosis
4A	Small, medium, or large glands fused into cords, chains, or ragged, infiltrating masses
4B	Very similar to 4A, but with many large clear cells, sometimes resembling “hypernephroma”
5A	Papillary and cribriform epithelium in smooth, rounded masses, more solid than 3C and with central necrosis
5B	Anaplastic adenocarcinoma in ragged sheets

Figure 2. Gleason grading system for Prostate Cancer.

Graphical illustration (left) showing the scoring system (1-5) and description (right) as developed by Dr. Gleason [(Gleason, 1992)*].*

Different patterns are given different values 1-5 and then the two most common Gleason scores are reported providing a Gleason sum or score (see Figure 2 for a detailed description).

- Grade 1: Uniform glands, with reduced stroma. No infiltration observed.
- Grade 2: Similar to grade 1. Glands exhibit slightly larger size and shape disparity, with a greater amount of stroma between cells.
- Grade 3: tumour infiltration within and between non neoplastic glands. Glands exhibit a smaller size than in previous grades.
- Grade 4: stroma infiltration between normal glands. Main difference with grade 3 is the fusion between glands.
- Grade 5: tumour infiltration creating diffuse stages. Glands are no longer noticeable.

New grading system	Gleason score	Histologic definition	Probability of 5-year BCR-free progression after RP (%)
Grade group 1	≤3 + 3 = 6	- Only individual discrete well-formed glands	96
Grade group 2	3 + 4 = 7	- Predominantly well-formed glands with lesser component of poorly formed/fused/cribriform glands	88
Grade group 3	4 + 3 = 7	- Predominantly poorly formed/fused/cribriform glands with lesser component of poorly formed glands[a]	63
Grade group 4	8	- Only poorly formed/fused/cribriform glands - Predominantly well-formed glands and a lesser component lacking glands[b] - Predominantly lacking glands and lesser component of well-formed glands	48
Grade group 5	9–10	Lack of gland formation (or with necrosis) with or without poorly formed/fused/cribriform glands[a]	26

Table 1. New Gleason scoring system and associated prognosis.
Table taken from [(Matoso and Epstein, 2016)*]*

The Gleason grade assigned to a particular prostate cancer case relates to its growth rate and prognosis although the view about this relationship has evolved since its development (Matoso and Epstein, 2016). Accordingly, higher Gleason grade refers to less differentiated, more advanced tumours and worse prognosis. Briefly, nowadays Gleason grade 1 and 2 are considered normal prostate epithelial tissue and have been removed from the scoring system; 6 is the lowest score possible; although tumours presenting Gleason score 3+4 and 4+3 are both treated as 7 in relation to treatment, they differ in their prognosis; a slight improvement in prognosis has been noted in

Gleason 8 cancers compared to 9-10, and there is no substantial difference between 9 and 10. A new grading system using grade groups 1-5 has been proposed, where the lowest grade group (1) corresponds to Gleason 3+3, and grade group 5 encompasses Gleason sum 9 and 10 (Matoso and Epstein, 2016).

1.2.4 TNM staging system

In addition to Gleason scoring, prostate cancer is classified based on the TNM scoring of malignant tumours developed initially by Pierre Denoix (Harmer et al., 1970), and maintained and modified by Union for International Cancer Control (UICC) and the American Joint Committee on Cancer (AJCC). This classification implies an alpha-numerical coding system that described the stages of an initially solid tumour. Accordingly: T – refers to the size of the original tumour and the potential invasion of nearby tissues; N – refers to involved lymph nodes located close by; M – refers to the existence of metastatic tumour deposits. In prostate cancer TNM staging is as follows:

T – Primary Tumour	
TX	Primary tumour cannot be assessed
T0	No evidence of primary tumour
T1	Clinically apparent tumour neither palpable nor visible by imaging
T1a	Tumour incidental histological finding in ≤5% of tissue resected
T1b	Tumour incidental histological finding in ≥5% of tissue resected
T1c	Tumour identified by needle biopsy (e.g. because of elevated PSA)
T2	Tumour confined within prostate
T2a	Tumour involves ≤one-half of one lobe
T2b	Tumour involves >one-half of one lobe
T2c	Tumour involves both lobes
T3	Tumour extends through the prostate capsule
T3a	Extracapsular extension (unilateral or bilateral)
T3b	Tumour invades seminal vesicle(s)
T4	Tumour is fixed or invades adjacent structures other than seminal vesicles such as external sphincter, rectum, bladder, levator muscles, and/or pelvic wall
N – Regional Lymph Nodes	
NX	Regional lymph nodes were not assessed
N0	No regional lymph node metastasis
N1	Metastasis in regional lymph node(s)
M – Distant Metastasis	
M0	No distant metastasis
M1	Distant metastasis
M1a	Non-regional lymph node(s)
M1b	Bone(s)
M1c	Other site(s) with or without bone disease

Table 2. TNM staging of Prostate Cancer.

Table adapted from the 2010 revision of American Joint Committee on Cancer (AJCC) for the classification of prostate cancer tumours [(Cheng et al., 2012)*]*

1.2.5 Currently available treatments for Prostate Cancer

Prostate cancer treatment will vary based on the tumour staging combining Gleason grade, TNM stage and PSA levels. Among the available alternatives, surgical removal of the prostate (prostatectomy), chemotherapy, radiotherapy (both external beam radiotherapy and brachytherapy) and hormonal treatment are the most widely applied therapies (Castiñeiras Fernandez, 2007; Provencio Pulla, 2011).

- Radical prostatectomy involves the complete removal of the prostate and seminal vesicles, being a suitable approach for healthy young patients (below 70) suffering from localised prostate cancer. Frequently, this surgical procedure results in some degree of urinary incontinence and erectile dysfunction. Partial surgical removal of the prostate (exclusively focusing on affected regions) still remains a challenge given the usual peripheral localisation of tumours in the gland. Recently, the partial removal of tumours located in the anterior region of the prostate has been successfully achieved, reducing the above-mentioned side effects, e.g. erectile function was maintained in 83% of the cases 3 months after treatment as opposed to 54-90% measured 12 months after radical prostatectomy (Villers et al., 2016).
- Radiotherapy is a suitable strategy for localised and locally advanced prostate cancer. It can be administered as treatment itself or adjuvant to surgery, should there be affected marginal regions such as seminal vesicles or extracapsular extension. In addition, there seems to be a direct relationship between the efficacy of radiotherapy and the dose of radiation given. Currently administered doses are ≥ 70 Gy over a 6-7 week period. Among side effects, radiotherapy causes urinary and bowel toxicity and sexual dysfunction.
- Low dose brachytherapy consists of the administration of radioactive material seeds within the parenchyma of the prostate, resulting in high radiation doses within the prostate (around 145 Gy doses) while minimising the radiation of surrounding tissues. It is only indicated in patients with a positive prognosis (low Gleason and TNM scoring and PSA levels below 10 ng/ml). Despite the localised application of radioactivity, brachytherapy often results in rectal and genitourinary toxicity.
- Hormone therapy is mainly based on the administration of anti-androgens and blockers of the Luteinising Hormone (LH) to achieve hormone deprivation and consequently inhibit neoplastic cell growth. This approach is generally followed in patients with advanced metastatic lesions as well as adjuvant treatment to high risk patients and post-radiotherapy. Generally, side effects include weight

gain, higher risk of thrombosis, loss of libido, osteoporosis, fluid retention and hot flushes. In addition, tumour response to hormonal treatment is limited to a relatively short period of time (24-36 months), after which tumours progressively develop independence to the absence of hormones, and PSA levels increase continuously, in the end resulting in the deterioration of patients and eventually irreversible death.

- Chemotherapy is the gold standard for metastatic prostate cancer. The most common chemotherapeutics for prostate cancer are docetaxel (Taxotere), cabazitaxel (Jevtana) and mitoxantrone (Novantrone)

1.2.5.1 Focal treatment of prostate cancer and active surveillance

Side effects associated with current prostate cancer treatments (i.e. incontinence, rectal toxicity, sexual dysfunction, etc.) have led to the investigation and development of different strategies to reduce such undesired effects. For example, active surveillance is becoming every day a more frequent alternative for low risk prostate cancer patients, thus avoiding complications related to treatment. Several clinical trials are being conducted these days worldwide, in which some participating men have already surpassed the 10 and 15 year time point, indicating the potential of this strategy in eligible patients (Tosoian et al., 2016). On the other hand, the delay in treatment during active surveillance could result in missing the most adequate therapeutic window, in addition to the concern developed in patients knowing the existence of a non-treated tumour (Lindner et al., 2010).

Focal treatment of prostate cancer is becoming a widely used alternative nowadays. It involves the combination of minimally invasive image-guided systems with ablative techniques directly applied to diseased regions of the prostate while minimising damage to surrounding healthy tissues, reducing adverse side toxicity and systemic effects (Bozzini et al., 2013b). These alternatives have to be deliverable to the prostate and capable of destroying tumour cells. Some of these are (Bozzini et al., 2013b; Lindner et al., 2010):

- Cryotherapy is the direct application of very low temperatures followed by thawing to the prostate. This will cause direct tumour cell death as well as trigger inflammation. Early application of this technique resulted in high

morbidity but it has improved nowadays thanks to the development of transrectal ultrasonography and needles introduced through the perineum which allow the visualisation of the process. Additional improvements involve the use of argon-based cryoprobes (miniature cryoneedles) or probes monitoring temperature throughout the process. An overall analysis of the temperature in the prostate and surroundings would improve tumour destruction and avoid side damage to tissues close by such as nerves or the rectum.

- High-intensity focused ultrasound (HIFU) implies the administration of sound waves at a high frequency (0.8-3.5 MHz) combined with power > 5 W/cm^2. This way tumour will be destroyed in two manners: the focal application of ultrasound will result in heat (>60ºC), denaturising biological molecules such as proteins, then causing necrosis; cavitation in tissue will occur as a result of rarefaction and compression cycles. The procedure is performed using an ultrasound probe inserted into the rectum.

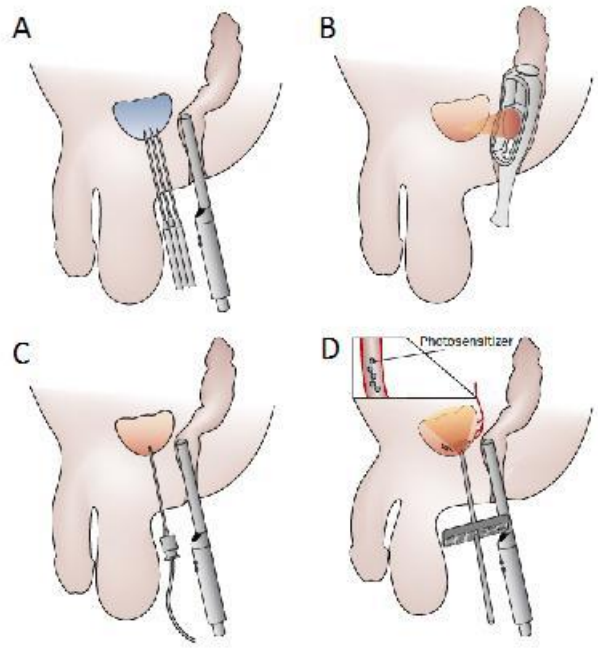

Figure 3. Graphical representation of focal therapies for prostate cancer treatment.
(A) Cryotherapy, (B) High-Intensity Focused Ultrasound – HIFU; (C) Focal Laser Ablation (FLA); (D) Photodynamic Therapy – PDT

- Focal Laser Ablation – FLA consists of the application of a laser fibre through the perineum aided by transrectal ultrasound imaging or in-bore MR imaging, delivering an excess heat directly into the prostate. Prior to the administration of high temperatures, MRI or TRUS will determine the optimum positioning of the laser fibre in the diseased prostatic tissue, and temperature will be monitored

throughout using probes, minimising side damage. FLA has low morbidity in patients: mild haematuria or perineal discomfort in some cases, not affecting urinary tract or sexual functions.

- Photodynamic Therapy, which is a major focus of the present document and will be further reviewed in sections below.

Importantly, during the application of focal therapies for prostate cancer treatment it is crucial to take into consideration that this cancer is usually multifocal, hence the use of these site-specific focalised treatments could be questioned. However, the hypothesised existence of an "index lesion" supports the need for focal therapy even in more advanced, extended prostate cancer cases. "Index lesion" implies that the greatest tumour component in the prostate is responsible for disease progression outside the prostate, and eventually metastatic spreading. This is supported by studies reporting a monoclonal, single-cell origin in other metastatic cancers. Based on this, the identification of the index lesion and treatment concentration around this single-focus origin will control the progression of the remaining diseases foci. Challenges currently reside in developing potent techniques to identify the leading lesion (i.e. biomarkers) (Lindner et al., 2010).

1.3 History of light-based therapy

The use of light in therapeutic applications dates 1400 BC in India, as described in the sacred Hindu text *Atharva Veda* for curative purposes to treat pathologies such as vitiligo combining plant extracts (i.e. *Eclipta prostate, Curcuma longa, Citrullus colocynthis*) and sunlight (Fitzpatrick and Pathak, 1959).

Indeed, medical reports in the 18th century described on several occasions the treatment of different diseases based on energy coming from sunlight (Giese, 1964; Rollier, 1927; Russell and Russell, 1927). Among these, a cancerous mass on the lip was cured with a sunbath in 1735 (Giese, 1964), skin ulcers in 1774 (Russell and Russell, 1927), wound healing and tumour destruction in 1776 (Rollier, 1927), or even non superficial disorders such as rickets (Giese, 1964).

It was not until 1877 that the use of sunlight to kill bacteria was discovered when comparing the turbidity of sugar solutions placed either in the shade or exposed to light (Downes and Blunt, 1877). Not only treatment but also prevention of rickets was already hypothesised with sun baths (Palm, 1890, 1888). Later on, it was speculated

that rays coming from the sun or other light sources such as an electric arc lamp could stimulate tissues. Accordingly, red-light was used to address the treatment of skin conditions such as exanthemata of eruptive diseases, i.e. small-pox (Bie, 1899). Dr. Finsen hypothesised the capacity of light to aggravate pre-existing inflammation lesions. He then took advantage of this for bactericidal applications, as stated in Remarks on Finsen's Phototherapy "*As the "chemical" (blue, violet, and ultraviolet) light are capable of causing an inflammation (erythema of the healthy skin), it might be assumed that they […] equally be capable of aggravating pre-existing inflammations the method consists local superficial bacterial skin diseases by the concentrated chemical rays of light"* (Bie, 1899). Within a short period of time, sunlight was first used in 1902 to heal wounds followed by cavities and foci caused by tuberculosis ("Light treatment in surgery. By Dr. O. Bernhard (St. Moritz). Translated by R. King Brown, B.A., M.D., D.Ph., Medical Officer of Health, Bermondsey: Lecturer in Public Health, Guy's Hospital Medical School. Medium 8vo. Pp. 307, illustrated. 1926. London: E," 1927). Rollier then established an important distinction between "hot-air bath" and "sunbath" and developed a way to irradiate the body with sunlight. The term heliotherapy then started to be used and gained popularity (Rollier, 1927).

In 1900, Photodynamic Therapy (PDT) was discovered by Raab, a medical student who observed that the combination of acridine red and light during a thunderstorm killed the paramecium Infusoria (Raab, 1900). It was initially speculated that this cytotoxicity was due to the transfer of energy from light to the compound in a similar manner to plant photosynthesis. Soon after this, the use of photosensitisers in humans was first reported (Prime, 1900). In his studies, Prime noticed the development of dermatitis in light-exposed skin during the oral treatment of epilepsy using eosin (fluorescein-derived dye). Founded on the above, a combination of topically administered eosin and white light was used clinically for the first time as a therapy for skin tumours (von Tappeiner and Jesionek, 1903). The need for oxygenated conditions was then described (von Tappeiner and Jodlbauer, 1904) and the concept of "photodynamic action" was introduced in 1907 (von Tappeiner and Jodlbauer, 1907). In spite of their great contribution to the development of PDT, J. Dougherty was pioneer in the application of PDT in medicine and thus often considered father of the this therapeutic approach (Dougherty et al., 1979; Weishaupt et al., 1976). The idea of low-level lasers therapy was conceived by Mester during his observations on increased skin healing and hair regrowth (Mester et al., 1971, 1968a, 1968b). PDT was then addressed to treat other skin disorders, such as vitiligo and psoriasis (Parrish et al., 1976, 1974).

1.4 Photodynamic Therapy – *PDT*

Photodynamic Therapy (PDT) involves the administration of photosensitive compounds - photosensitisers (PS) in the presence of light and oxygen. PS exist in a ground stable singlet state in which their electrons are spin paired and found in low-energy orbitals. If these are exposed to light at the specific wavelength where maximal absorption of the PS is found, they absorb photon energy: the electron found in the highest occupied molecular orbital (HOMO) will be excited to the lowest unoccupied molecular orbital (LUMO) (Huang and Hamblin, 2014). When this process occurs, PS reach an unstable excited state (^{1}PS*). In PDT, this high-energy state will rapidly lose energy in the form of heat, light and more importantly, exhibiting “intersystem crossing”: the spin of the excited electron will be reversed and lead to a different excited triplet state (^{3}PS*). This triplet state has lower energy but longer lifetime than the singlet state (Huang and Hamblin, 2014).

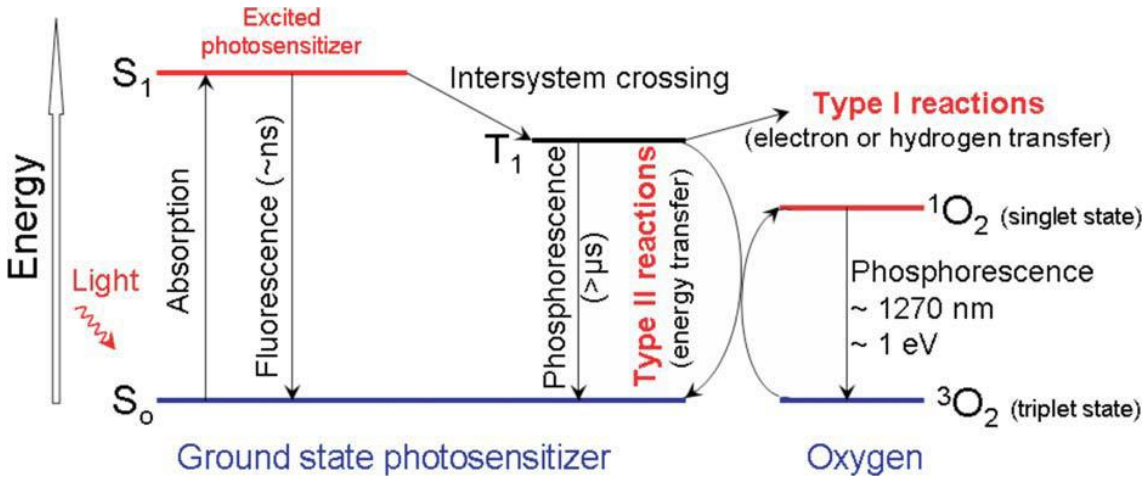

Figure 4. Jablonksi diagram.

Schematic representation of the excitation of photosensitisers, showing the transition between singlet and triple states and the consequent energy transfer and formation of reactive oxygen species (ROS). Figure taken from [(Agostinis et al., 2011)*]*

From this point, the excited electron will slowly correct its spin orientation to then relax back to the initial singlet state, or either reacts with molecules present in the environment through photooxidative reactions. Selection rules determine that interactions between triple-triplet are spin-allowed, while triplet-singlet are not. Consequently, ^{3}PS* will most probably transfer energy via different reactions to molecular oxygen (O_2), since only a minority of environmental molecules are naturally found in a ground triplet (Huang and Hamblin, 2014).

- Type 1 reactions: the excited PS transfers an electron leading to the formation of superoxide anion ($O_2\bullet^-$) then resulting in hydroxyl radical ($\bullet OH$) and hydrogen peroxide (H_2O_2) among other free radicals.
- Type 2 reactions: the excited PS transfers energy to O_2. Environmental oxygen in its ground state is a triplet molecule with its two most external orbitals unpaired and spin parallel. Type 2 processes will alter the spin of one of the furthermost electron and displace it into the orbital of the other unpaired electron. As a consequence, the resulting orbital will contain two electrons of opposite spin. This is a highly reactive species known as singlet oxygen ($^1O_2$); however, it is not a "radical" due to the pairing of all electronic spins. As a result of its electronic instability, $^1O_2$ effect is restricted by its short lifetime (~10-320 ns), thus its diffusion will be limited to around 10-55 nm in cells, only affecting cellular structures located close enough for short periods of time (Agostinis et al., 2011).

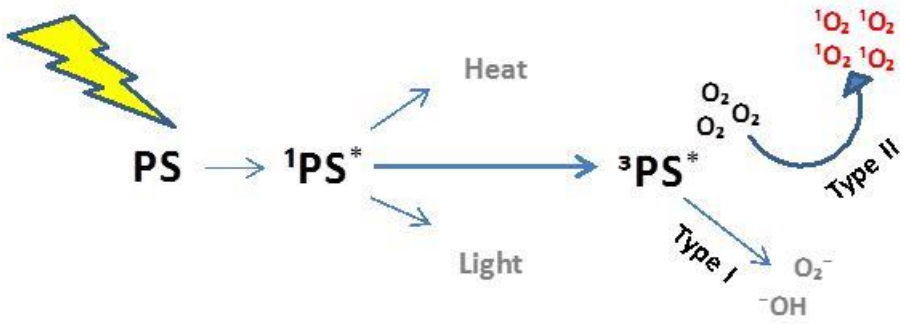

Figure 5. Detail of excitation of photosensitisers.

The excitation of photosensitisers from the ground stable state to the triplet excited state leads to the formation of singlet oxygen ($^1O_2$) during the interaction with molecular oxygen present in the environment.

The generated reactive oxygen species (ROS) cause oxidation of cellular structures compromising their integrity and inducing several molecular changes. Proteins are considered major PDT targets due to their abundance and high rate constants in reactions with singlet oxygen and other ROS released in the process. These are also differences based on the aminoacid composition of each protein and location of these susceptible components, causing distinctive damage to residues in the protein's side chains. The prime targets in protein photooxidative modification are cysteine, methionine, tyrosine, histidine and tryptophan. In addition to modifying aminoacid residues, covalent cross-linking, PS-protein photo-binding may result in the formation of molecular aggregates. Overall, proteins may lose their biological activity (catalytic in

the case of enzymes, cell signalling, etc.) (Benov, 2015). Similarly, lipids are also targets of PDT-induced damage Highly abundant unsaturated fatty acids in biomembranes (i.e. membranous organelles and cellular membrane), make these a target for peroxidation reactions that may even conclude in the formation of radicals capable of initiating free-radical chain reactions which exponentially expand the process, affecting other biological molecules and even altering metabolic and signalling functions. The high solubility of oxygen in lipids makes this damage specially relevant, given the oxygen demand for these oxido-reduction reactions to happen (Benov, 2015). Furthermore, an important PDT-induced cellular damage is DNA oxidation, entailing for instance base modification or DNA nicks. The low ionisation potential of guanine makes this base particularly susceptible, producing guanine cation radical that can then react with residues in proteins such as lysine, serine and arginine causing DNA-protein cross-links. In spite of this, it has not been reported that PDT-based DNA mutation could be the source of additional mutations that will unleash the formation of secondary tumours (Benov, 2015).

1.4.1 Cell death mechanisms after PDT

Extensive studies on programmed cell death mechanisms were conducted by John Sulston, Sydney Brenner, and H. Robert Horvitz during the investigation of the genetic regulation surrounding organogenesis and cell growth in *C. elegans* (Hedgecock et al., 1983; Sulston et al., 1983). Since then, cell death pathways have been further studied on many occasions, for instance in relation to different cancer treatments.

Three main cell death routes are involved in PDT damage: apoptosis, necrosis and autophagy. Apoptosis is generally accepted as an active “programmed cell death”, a series of events resulting in cell-induced suicide through which cells will experience condensation and fragmentation of the nucleus, and cleavage of DNA resulting in internucleosomal fragments and final formation of apoptotic bodies within an intact plasma membrane. These apoptotic cells will be recognised by phagocytic cells, generally avoiding inflammation. Conversely, necrosis is the consequence of an ATP-deficiency which is not compatible with cell endurance. The outcome of this will be cytoplasm vacuolation, membrane disruption as well as release of pro-inflammatory molecules and thus an inflammatory response in the cell environment (Edinger and Thompson, 2004). Finally, autophagy is a survival mechanism followed by cells to degrade and recycle cellular components under certain conditions such as nutrient limitation (Agostinis et al., 2011; Edinger and Thompson, 2004). The engagement of PDT in these three cell death pathways will be commented below.

Apoptosis

Apoptosis was first described by Willey et al (Kerr et al., 1972) and is now accepted as the major cell death pathway acting in PDT. This can occur via permeabilisation of mitochondria outer membrane (MOMP) governed by proteins belonging to the Bcl-2 family and in a p-53 independent manner. MOMP can be triggered by mitochondria-associated PS acting on Bcl proteins bound to the mitochondrial membrane, such as Bcl-227-29; or else leakage of cathepsins from lysosomes owing to lysosomal membrane damage (Agostinis et al., 2011). Thereupon, pro-apoptotic signals and molecules can be released, caspase activators (cytochrome c, Smac/DIABLO), apoptosis-inducing factor (AIF) among others. Blockage of caspase pathway will delay cellular damage by PDT or alternatively result in necrotic damage.

In addition, PDT has been related to an increment in intracellular calcium levels inducing the influx through ion channels, releasing internal storage in mitochondria and the endoplasmic reticulum (ER) or via exchange mechanisms (Castano et al., 2005). This calcium increase could activate proteases such as calpains (calcium-dependent cysteine proteases) which are also involved in phototoxicity propagation (Agostinis et al., 2011).

Necrosis

The basic mechanisms by which necrotic phototoxicity happens are not clear. That said, it is known that the activation of receptor interacting protein 1 kinase, ROS excessive formation, lysosomal damage and Ca^{2+} overburden result in necrotic cell death. In line with this, in the event of mitochondrial permeability transition, caused by a severe damage to their inner membrane, as well as the mentioned Ca^{2+} overburden could shift from apoptotic to necrotic damage (Agostinis et al., 2011).

Furthermore, it has been recently described that signal transduction pathways may be engaged in necrotic cell death. These suppose mechanisms of cells to receive external signals and respond accordingly. Among the most important are the mitogen-activated protein kinase (MAPK) signalling pathways, comprising p38 kinases, ERK 1/2, and c-Jun N-terminal kinases/stress-activated protein kinases (JNK/SAPK). Upon PDT treatment, JNK can be activated via exposure of cells to tumour necrosis factor-α (TNF-α) and interleukin 1 (IL-1) (Castano et al., 2005).

Autophagy

To a lesser extent oxidative stress is known to trigger autophagy. As a matter of fact, PDT damage could act as inducer of the autophagic pathway to secure cell viability (Agostinis et al., 2011). PDT phototoxicity involves several other biological components and processes such as transcription factors, biological structures participating in cell adhesion, cytokines, stress-signalling molecules, hypoxia, angiogenesis, etc. (Castano et al., 2005)

In brief, PDT treatment conditions such as physicochemical properties of PS, subcellular location, PS and oxygen concentration, light wavelength as well as dosage, will be determinant in the occurring cell death pathway (Mroz et al., 2011b). On this basis, there are several probable scenarios. Mitochondria-localised PS will most likely result in apoptosis under certain levels of oxidative stress; whereas lysosome-targeted PS will prevent or at least setback apoptotic cell death in favour of necrotic cell death. Necrosis is likely to emerge as a consequence of endoplasmic reticulum/Golgi membrane targeting. Generally, the amount, site and type of ROS produced will dictate the oxidative damage caused. Overall moderate levels of stress on the cellular membrane will trigger apoptosis; yet if these were extensive necrosis would be unleashed, disrupting its overall integrity (Benov, 2015). Following this same line of argument, sublethal photooxidative stress results in apoptotic cell death; however, if this is severe, ATP production will be impaired and necrotic cell death pathway will be forced. It has been recently suggested that apoptotic cell death may be favoured by very low light fluences, additionally minimising adverse effects, and reducing associated morbidity, yet at the same time improving tumour control and maintaining therapeutic efficacy (Benov, 2015).

1.4.2 Photosensitisers in PDT

Despite initial studies involved dyes such as acridine orange or eosin, PDT studies were greatly propelled with the discovery of porphyrins. These are water-soluble aromatic macrocycles composed of four pyrrole rings (closed structures built with one nitrogen and four carbon atoms) linked through methane groups (−CH=). Featured by a characteristic red-purple colour they can be found within biological structures i.e. protoporphyrin in haemoglobin.

The first PS studied in depth was hematoporphyrin, derived from the acid hydrolysis of haemoglobin, after which iron is removed from the heme group (von Scherer, 1841). Initial examination of hematoporphyrin preparations revealed a rather impure solution which was proved to be more efficient in therapeutic applications than the pure compound itself (hematoporphyrin stereoisomers, hematoporphyrin vinyl deuteroporphyrin isomers, and protoporphyrin – later known as hematoporphyrin derivative, HpD, Photofrin®) (Huang and Hamblin, 2014). Moreover, the interaction of hematoporphyrin with neoplastic tissue was first observed during the studies carried out in 1924 by Policard (Policard, 1924). Dougherty carried out a clinical trial using this PS combined with red light in a wide range of cancers including recurrent colon carcinoma, metastatic prostatic carcinoma, metastatic breast carcinoma, metastatic squamous cell carcinoma of the skin, metastatic angiosarcoma, metastatic endometrial carcinoma and metastatic chondrosarcoma in 1978 (Dougherty et al., 1978), proving HdP-mediated PDT to be an efficient anticancer approach in tumours that did not respond to other treatments.

Photosensitiser	Structure	λ (nm)	Cancer type
Porfimer sodium (HPD)	Porphyrin	630	Lung, oesophagus, bile duct, bladder, brain, ovarian
ALA	Porphyrin precursor	635	Skin, bladder, brain, oesophagus
ALA esters	Porphyrin precursor	635	Skin, bladder
Temoporfin (Foscan, mTHPC)	Chlorin	652	Head and neck, lung, brain, skin, bile duct
Verteporfin	Chlorin	690	Ophthalmic, pancreatic, skin
HPPD	Chlorin	665	Head and neck, oesophagus, lung
SnEt2 (Purlytin)	Chlorin	660	Skin, breast
Talaporfin (LS11, MACE, NPe6)	Chlorin	660	Liver, colon, brain
Ce6-PVP (Fotolon), Ce6 derivatives (Radachlorin, Photodithazine)	Chlorin	660	Nasopharyngeal, sarcoma, brain
Silicon phtalocyanine (Pc4)	Phtalocyanine	675	Cutaneous T-cell lymphoma
Padoporfin (TOOKAD)	Bacteriochlorin	762	Prostate
Motexafin lutetium (Lutex)	Texaphyrin	732	Breast

Table 3. Clinically approved photosensitisers for PDT.
Table adapted from [(Castano et al., 2004)*]*

The discovery of porphyrins as PS together with the principle behind porphyria (disorders that emerge due to the accumulation of natural constituents of porphyrins in the body) sowed the idea of endogenous PS production. In line with this, the combination of exogenous 5-aminolevulinic acid (5-ALA) administration (basic component found in biological porphyrins) and red light, successfully resulted in the synthesis of porphyrin derivatives (uroporphyrin and protoporphyrin IX) (Malik and Lugaci, 1987). Since then several photosensitisers have been approved by medical

regulatory agencies worldwide: Photofrin® (1993 in Canada, 1994 in Japan, 1998 FDA), 5-ALA (1999 FDA), Visudyne (verteporfin formulation – 2000 FDA, more than (Huang and Hamblin, 2014). See summary table below (Table 3).There has always been a great interest in the modification and optimisation of PS (Boyle and Dolphin, 1996), which might be crucial for the future of PDT. Along these lines, second generation PS were designed with the ultimate objective of maximising photooxidative damage to finally eradicate tumour masses whilst minimising side damage caused to surrounding healthy tissues. Such is the case of Pc4 (silicon (iv) phtalocyanine), benzoporphyrins (i.e. Visudyne), porphycenes, chlorins (i.e. Termoporfin) and metalated derivatives. These second generation PS exhibit absorption at longer wavelengths than first generation PS. Moreover, third generation PS are nowadays being developed to be excited well into the red and highly selective.

Most PS used share a basic tetrapyrrole structure and ideally fulfil a series of requirements:

- Purity. Rather than impure mixtures as is the case of Photofrin®, new photosensitisers are designed to be pure solutions of single PS, enabling this way a tight quality control.

- Absorption peak 600-800 nm (red to deep red). The aromatic nature of most PS leads to small energy differences between HOMO and LOMO orbitals, and in most cases visible and near infrared light are used for their excitation (Huang and Hamblin, 2014). Longer wavelengths are less energetic and thus insufficient to excite oxygen from its ground triplet to the excited singlet state in order to produce ROS characteristic of PDT (Agostinis et al., 2011; Juzeniene et al., 2006). Red light is preferred over the more energetic blue “counterpart” due to the greater penetration of this light on the grounds of the optical properties of tissues (“optical window”). Briefly, red light is able to penetrate up to 3 mm into tissue as opposed to blue light, penetrating < 1 mm into tissue (Master et al., 2013). Endogenous chromophores found in biological molecules such as collagen, water, proteins, melanin and haemoglobin will absorb light themselves within the blue region of the spectrum (Figure 6A), leading to light scattering, limiting penetration and thereby affecting photosensitisers’ capacity to induce phototoxicity (Agostinis et al., 2011; Allison and Sibata, 2010; Benov, 2015; Huang and Hamblin, 2014). For the above reasons, chlorins, bacteriochlorins and phthalocyanines are often chosen for PDT in cancer treatment (see Figure 6B).

- Reduced aggregation. Most PS contain aromatic rings within their structures, which limit their solubility in aqueous environments and result in aggregation under physiological conditions. PS should exhibit low aggregation profiles to avoid affecting energy transfer processes occurring during photochemical treatment (quantum yields of ROS production) (Boyle and Dolphin, 1996).

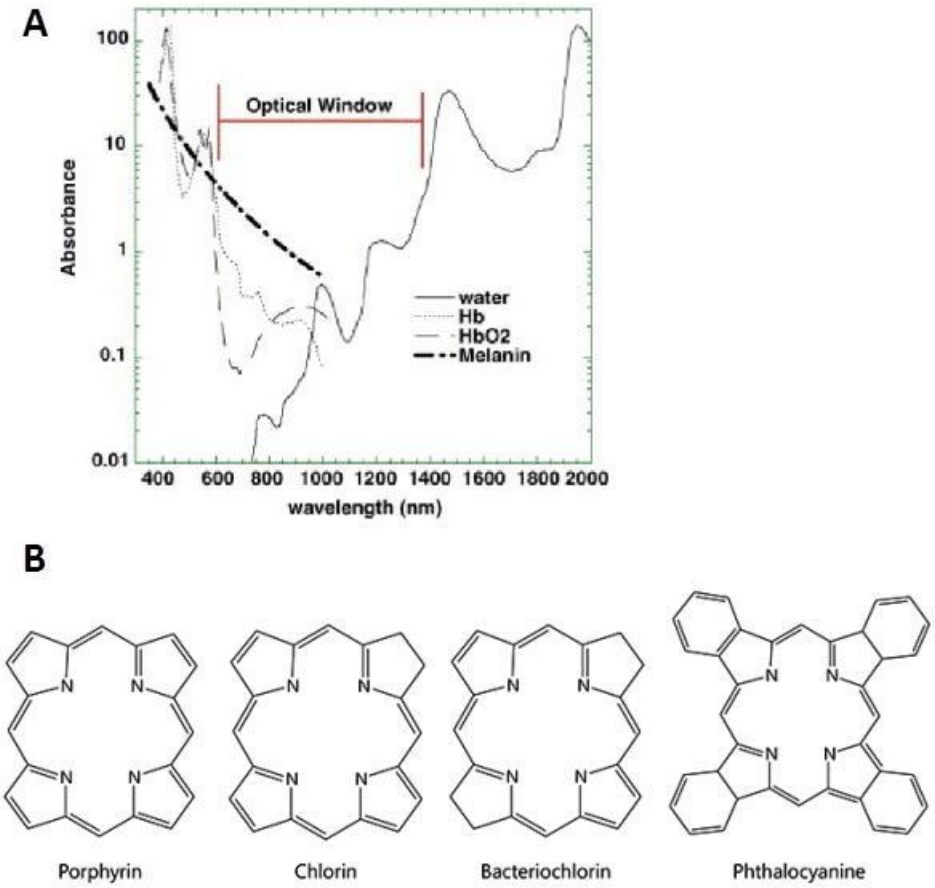

Figure 6. Therapeutic window for clinical use and main groups of photosensitisers used in PDT.

(A) High absorbance of biological molecules is observed at wavelengths under 600 nm (i.e. haemoglobin shown in red) and above 800 nm (i.e. water shown green). Therefore, clinically relevant photosensitisers must exhibit adequate absorption levels 600-800 nm; picture taken from [(Castano et al., 2004)*]. (B) Representation of the most relevant PS used in a clinical setting: porphyrin, chlorin, bacteriochlorin, phtalocyanine; picture taken from [*(Benov, 2015)*].*

- Rapid biodistribution and clearance from the system. Photosensitisers have a major disadvantage: photosensitivity. This was already noticed with the first photosensitiser used for cancer treatment, HdP, remaining within patients for a long time (up to even 8 weeks), who in turn had to avoid sun exposure to avoid skin phototoxicity (Agostinis et al., 2011; Castano et al., 2004). In line with this, PS dark toxicity should be as low as possible (Allison and Sibata, 2010).

Relative fast metabolism and elimination of PS would avoid undesired toxicities. However, a balance is required between the persistence of PS within the body, and the amount of time needed for these to be biodistributed (specifically into tumours). In line with this, drug light intervals (DLI) tend to be long to enable PS diffusion to tissues; yet, the benefit of shorter DLI have been reported due to their effect in vasculature, which will be addressed in the following sections (Agostinis et al., 2011; Castano et al., 2004).

- Preferred accumulation in tumour cells. This is closely related to the above, generally the aim is to reduce presence in the skin in favour of a greater PS burden in the tumour mass. The first demonstration of specific retention of PS by cancer cells dates back to 1924 (Policard, 1924). Since then, this has been observed in many occasions (Agostinis et al., 2011; Penjweini et al., 2014; Zhang et al., 2015). It has been hypothesised that the reason behind this phenomenon is an "enhanced permeability and retention" (EPR) effect (Agostinis et al., 2011). This is based on the combination of two factors: on the one hand a passive extravasation of drugs from the vasculature into the tumour mass due to the leaky nature of recently formed immature blood vessels in tumours; and the poor lymphatic drainage of these on the other hand, which results in the retention of drugs within malignant cells for a longer period of time (Greish, 2010). An increase in the hydrophobic features of PS or else the modification of these to add amphiphilicity can improve tumour selectivity remarkably, reducing levels of PS found in the skin (Jori, 1996). This tumour-selectivity can be further enhanced by designing PS targeted against molecules specifically located or overexpressed in malignant cells. Some of these strategies include binding PS covalently to antibodies, peptides and proteins (EGFR -endothelial growth factor receptor-, insulin, transferrin…), folic acid, carbohydrates, etc. (Agostinis et al., 2011; Pereira et al., 2015). This will be further reviewed later chapters.

- Additional desirable features of PS include low manufacturing costs and stability for mid- to long-term storage (Agostinis et al., 2011).

1.4.3 Therapeutic application of PDT

PDT is considered a minimally invasive treatment with low side effects and good cosmetic outcome. Consequently it is widely used for dermatological purposes both in cancerous and non cancerous lesions. Among these, non-melanoma skin cancer, acne vulgaris, psoriasis vulgaris, cutaneous T-cell lymphoma, disseminated actinic porokeratosis, localised scleroderma, vulvar lichen sclerosus, photorejuvenation, hidradenitis suppurativa. In addition to dermatological applications, there are also non dermatological uses such as anal and vulvar carcinoma, Barrett's oesophagus (Taub, 2007). Due to PDT's major effect on vasculature, it has been used to address choroidal neovascularisation (CNV). Among these, the most relevant is the classic use for age-related macular degeneration treatment; other uses include secondary to pathological myopia, central serous chorioretinopathy and choroidal haemangioma (Battaglia Parodi et al., 2016).

The development of the antimicrobial potential of PDT experienced difficulties with the discovery of antibiotics to treat infections caused by pathogens such as bacteria, fungus, protozoa, helminths, etc. It has slowly taken up from 1970s and is experiencing nowadays a rapid growth due to the rise of antibiotic resistance as an alternative antimicrobial therapy (Kharkwal et al., 2011). In these cases, it can be sometimes known as photodynamic inactivation (PDI), photoactivated disinfection (PAD) or photodynamic antimicrobial chemotherapy (PACT). Multiple clinical applications for infectious purposes involve the administration of 5-ALA topically or else the ALA-methyl ester, methyl aminolevulinate (MAL), in turn resulting in the excess accumulation of PPIX (Protoporphyrin IX) in cells. Other antimicrobial applications of PDT include viral lesions and dentistry and more recently it is being studied in clinical trials for *Helicobacter pylori* infection, brain abscesses and leg ulcers (Kharkwal et al., 2011). Moreover, beyond clinical applications, PDT is being used for water sterilisation and surface disinfection (Benov, 2015).

Despite the variety of applications of PDT, it was initially developed for tumour imaging and treatment, and to day, it remains to be its main application. In line with the above, several PDT-based effects have been described in cancer treatment:

- Direct cytotoxicity, as reported above in 1.4.1 Cell death mechanisms after PDT.
- Vascular shutdown. In addition to a direct effect in cell death, PDT's effect on vasculature (i.e. clinical application in macular degeneration) can be exploited in

cancer treatment. As a matter of fact, tumour growth is largely dependent on the existence of blood supply mechanisms. This has been addressed previously through the use of anti-angiogenic agents blocking the formation of new vessels in tumours; yet the elimination of already existing vasculature remained unaddressed. PDT has demonstrated a great capacity to affect tumour vasculature. In short, PDT-PS can accumulate in endothelial cells or else associate to the walls of blood vessels severely damaging the lumen of blood vessels and triggering physiological processes such as thrombogenesis, aggregation of platelets, constriction of vessels, increasing permeability, etc. Consequently, blood flow is blocked, casing tissue haemorrhage and overall causing ischemic death (Huang et al., 2008). This is supported by several studies, for example complete ischaemia upon irradiation was determined during indocyanine green-based PDT treatment to melanoma tumours (Abels, 2004).

Moreover, PDT has shown potential addressing multidrug resistance (MDR), which has become a major obstacle in cancer treatment nowadays (Gottesman, 2002). MDR can has different origins in each case, although there are two major hypotheses, both of which affect drugs before these can pursue their biological activity. First, the overexpression of energy dependent transporters (P-glycoprotein efflux pumps) mainly belonging to the ATP-binding cassette (ABC) family of proteins. Second, the degradation of drugs in mature lysosomes.

1.4.3.1 PDT in cancer treatment – Preclinical studies

In addition to its application in a clinical context as will be commented below, PDT has been studied for several types of cancers in pre-clinical investigations both *in vitro* and *in vivo*. For instance, breast cancer cell lines (MCF7) and their Adriamycin-resistant counterpart were subjected to Chlorin e6 (Ce6)-mediated PDT (H. Wang et al., 2016). In this study, PDT effectively affected viability of both cell types, also finding a direct relationship between PS/light dose and cytotoxicity. However, Adriamycin-sensitive cells appeared to be more affected by PDT than resistant cells. Interestingly, despite both cell types showed a similar PS intake, sensitive cells exhibited a higher production of ROS, suggesting that the underlying mechanisms which confer resistance to Adriamycin could likewise lead to emerging mechanisms against

oxidative stress. This same study also concluded different cell death mechanisms in both cell lines, specifically apoptosis or autophagy in sensitive and resistant cells respectively (H. Wang et al., 2016). In a different investigation, *in vitro* and *in vivo* breast cancer models looked into the PDT effect of sinoporphyrin sodium (DVDMS) (Xiaobing Wang et al., 2015). Specifically, a significant increase in the production of ROS was observed *in vitro* in a light-dose dependent manner. Moreover, PDT-treated mice did not only show a delay in tumour growth but also an inhibition of the formation of metastatic nodules in the lung, consequently enhancing survival of these animals (Xiaobing Wang et al., 2015).

Osteosarcoma cells have been likewise exposed to ALA-PDT, verifying the accumulation of PpIX 4 hr after the administration of ALA as well as a light-dependent cell death. Even the lowest PS concentration (0.5 mM) led to a substantial reduction of cell viability under 3 J/cm^2 light (White et al., 2016). Similarly, liposomal ALA-PDT was recently investigated for melanoma treatment, concluding a more significant cell death, enhancement in the accumulation of ROS intracellularly and reduction of mitochondrial potential, than free 5-ALA (Lin et al., 2016). This serves as a first glimpse on how the adequate design of PS formulations can enhance therapeutic outcome.

Recent investigations of PDT for prostate cancer involved the use of the photosensitiser Pc413 targeted against prostate-specific membrane antigen (PSMA). *In vitro*, PSMA-expressing PC3 cells showed an increased uptake of the PS conjugate compared to non PSMA expressing cells, which then lead to a greater PDT-induced toxicity. Imaging of *in vivo* samples showed major presence in PSMA$^+$ tumour cells as opposed to other tissues as well as a strong growth delay after a single dose of the targeted conjugate (X. Wang et al., 2016).

1.4.3.2 PDT in cancer treatment – Clinical studies

Skin cancers are common targets for PDT treatment clinically due to the accessibility and easy application of both photosensitisers and light (Huang, 2005). For instance, topical PDT was recently investigated in extramammary Paget's disease using 5-ALA as PS (Gao et al., 2015). In this study, patients were grouped in two cohorts, either treated with PDT alone or a combination of PDT and surgery. In the former group, 4-6 sessions were necessary to achieve complete tumour regression. Among the study's findings, a higher recurrence rate was observed in the PDT group, which was thought

to be due to the limitations in light penetration, possibly not completely eradicating tumour cells located in deeper regions (Gao et al., 2015). In a different trial, patients suffering from facial nodular basal cell carcinomas were subjected methyl aminolaevulinate (MAL)-PDT, comparing conventional PDT to ablative fractional illumination. Overall, despite ablative fractional laser PDT still requires optimisation, resulting in a higher cure rate (100% vs 88%) as well as a delay in recurrence with the new PDT approach under investigation (Haak et al., 2015).

Brain tumours have also been PDT-treated on several occasions (Huang, 2005). Along these lines, 27 patients suffering from parenchymal brain malignant tumours were treated with talaporfin sodium as an adjuvant treatment to surgery. At least 91% progression free survival was observed, even achieving 100% rate when tumours were identified as glioblastoma (Muragaki et al., 2013). On it side, PDT has also shown potential to address breast cancer chest wall progression in patients where previous treatments had been unsuccessful. Although a larger cohort is needed to reach more conclusive findings, at least a partial response was observed in 5/9 patients, additionally verifying apoptotic cell death through histological observation of tumour samples (Morrison et al., 2014).

In addition, PDT treatment of intractable advanced lung cancer has been recently assessed in combination with chemotherapeutics to address airway stenosis. Throughout this study, an improvement in the production of sputum and pneumonia were found as soon as 1 week after light treatment. The early blockage of bleeding post PDT was attributed to the effect of PDT on microvasculature. Moreover, a control on the growth of bronchially localised tumours was concluded after PDT, while systemic chemotherapy had a positive effect in survival of patients (Kimura et al., 2015).

1.4.3.2.1 PDT in Prostate Cancer

Importantly, PDT has also been applied clinically for prostate cancer (see PS used clinically in prostate cancer in Table 4) (Arumainayagam et al., 2010; Moore et al., 2011, 2009).

During the application of PDT in the prostate, it is important to design the arrangement of fibres and source used for light delivery so as to ensure the appropriate illumination of the gland and succeed in the treatment. Accordingly, a feasibility study measuring optical properties (diffusion of different light fluences) prior and post administration of LuTex-PDT to patients was conducted in 2005. Light penetration was confirmed

between 0.1-1.1 cm, which was in fact smaller than determined previously in pre clinical studies in the canine prostate. Importantly, differences between patients suggested prostate-based differences and the need of real-time dosimetry to determine light fluences during specific treatments (Zhu et al., 2005a). Light distribution, oxygenation of tissues and drug concentration were further investigated in the same phase I clinical trial. Briefly, the authors concluded that variation of light fluence, as previously reported, was caused by disparities in the optical properties throughout the prostate tissue (i.e. photosensitiser accumulation, light distribution and oxygenation) (Zhu et al., 2005b).

In 2006 mTHPC was used to treat 6 patients suffering from localised prostate cancer, observing a reduction in PSA as soon as after 8 sessions of light delivery. Moreover, tumour biopsies showed inflammation and fibrotic formation 2 months after treatment. The lack of PDT-induced irreversible necrosis, i.e. to connective tissue, resulted in a positive outcome regarding uretho-fistulas, sexual function or continence. Although co-morbidity was reported by some patients, it resolved spontaneously in almost every case, with the exception of patients previously exposed to radiotherapy. This study also concluded no cumulative toxicity after the repeated sessions (Moore et al., 2006).

Target	Photosensitiser	Drug-light interval
Tissue	Haematoporphyrin derivative	48 hours
	Porfimer sodium (Photofrin)	72 hours
	mTHPC (Temoporfin)	72 hours
	5-ALA	4 hours
Vasculature	Motexafin Lutetium (LuTex)	3/6/24 hours
	Padoporfin (Tookad® WST-09)	10 minutes
	Padeliporfin (Tookad® WST-11)	10 minutes

Table 4. Photosensitisers used clinically in prostate cancer PDT.
Table adapted from [(Arumainayagam et al., 2010)*]*

More recently, TOOKAD® Soluble was used in 85 patients enrolled in a Phase II multicentre study (Azzouzi et al., 2013). 74% of the patients had negative biopsies 6 months after treatment, which was significantly different ($p < 0.0001$) to previously reported studies. As soon as 7 days after, vascular targeted PDT resulted in necrosis in 78% of prostate tissue. Overall, it was concluded that TOOKAD-PDT was safe and tolerated by patients, showing early efficacy for site-specific prostate cancer treatment (Azzouzi et al., 2013). Similar conclusions were drawn from the joint analysis of 3 clinical studies with this same photosensitiser including 117 men. A total of 68.4% of negative biopsies was determined 6 months after PDT and mean 76.5% of prostatic necrosis 7 days after light. Adverse effects (mild to moderate) were noted in almost

every patient, including dysuria, erectile dysfunction, haematuria, perineal pain, mictourinition urgency and urinary retention. Therefore, despite the focal application of PDT, co-morbidity is still detectable (Azzouzi et al., 2015). Recently, a TOOKAD Soluble dose escalation study conducted in the US concluded 4 mg/kg and 200 J/cm are the optimal doses (TOOKAD Soluble and light respectively) to be used clinically (Taneja et al., 2016).

1.4.3.2.2 Clinical limitations of PDT

In spite of the great benefits of PDT as a focal treatment of cancer, several limitations have been identified, some of which have already been briefly mentioned above.

The main disadvantage of PDT is related to the capacity of light to penetrate tissues (Agostinis et al., 2011). As stated previously, penetration of red light is limited to 3 mm, which could result in tissue damage up to 1 cm, restricting the application of PDT to tumours located superficially (i.e. skin) or else easily accessible through laser-fibre illumination (i.e. colorectal, oesophageal). Besides, severe skin photosensitivity, as reported with various photosensitisers, is another major drawback of this therapeutic application, and upon administration of photosensitisers patients need to be protected from a direct exposure to light for several days (Castano et al., 2004; Moore et al., 2006).

Moreover, light dispersion can occur during illumination, damaging surrounding tissues which have been equally exposed to systemically administered PS (Arumainayagam et al., 2010). On the other hand, this site-specificity, will be a limitation for PDT treatment of more advanced metastatic lesions, which nowadays imply a major challenge. More recently, the potential of PDT in the elucidation of an immune response has been reported (Garg et al., 2010), opening the possibilities of PDT as regards metastasis. This will be further reviewed in the following chapters.

As regards PDT in prostate cancer specifically, variability in the positioning of fibres and shape of the prostate between imaging during treatment planning and the treatment itself carried out at a later time point, could result in inefficient light delivery. This could be enhanced by real-time monitoring (Arumainayagam et al., 2010).

1.5 Photochemical Internalisation – PCI

Chemotherapy has become nowadays a gold standard treatment for most types of advanced cancers. However, it is associated with undesirable side effects and resistance to several chemotherapy drugs has been reported during the application of anti-cancer treatments (MDR). Moreover, chemotherapeutics can have difficulties reaching their biological targets: endosomes bearing chemotherapy compounds can fuse with catalytic lysosomes and this will eventually result in the degradation of the chemotherapy drugs before they have exerted their biological activity. (Gottesman, 2002; Zahreddine and Borden, 2013).

On the other hand, a large volume of knowledge has emerged regarding cellular targets for different therapeutic approaches, which together with the improvement of production technologies, have resulted in a great increase of the number of macromolecular drugs available (immunoconjugates, toxins, antibodies, growth factors for targeting, peptides, ribozymes, siRNA, peptide nucleic acids) (Høgset et al., 2004). For instance macromolecular chemotherapy drugs that result in higher specificity than their smaller counterparts. In line with this, there are several macromolecular drugs approved for clinical use currently that exhibit different specificities: CD33-targeted immunoconjugate (Mylotarg), HER2-targeted antibody (Herceptin), (EGFR)-targeted antibody (Cetuximab), IL-2 modified diphtheria toxin fusion protein (Ontak) (Berg et al., 2006).

Albeit this progress, cellular uptake of these therapeutic compounds may be an issue to consider. First, small molecules generally diffuse easily through cellular membranes; however, there are exceptions in which cell membranes may pose a difficulty in terms of internalisation of low molecular weight particles, as noted with hydrophilic molecules (Høgset et al., 2004; Martinez de Pinillos Bayona et al., 2016). Second, larger compounds are internalised by cells through endocytosis, in which the molecule at issue interacts with the external cell membrane and is engulfed, leading to the formation of cytosolic vesicles or endosomes. Moreover, there are several lipid membranes drugs will encounter and need to go through: the external cell membrane, endolysosomal membranes or even the nuclear membrane in the case of nuclear agents acting in the nucleus. Thus, physicochemical properties are a limiting factor for the different compounds to exert their cytotoxic effect within tumour cells (Adigbli and MacRobert, 2012; Norum et al., 2009d). Even if a particular drug is very efficient in a cell-free environment, its capacity to exert toxicity within a cellular system can be

limited. Consequently, despite many compounds could potentially become therapeutic agents, it may not occur when used alone.

Based on all the above, several different drug delivery systems (DDS), for example Photochemical Internalisation (PCI), are being studied to enhance drugs' cytotoxicity, assisting the delivery of biologically active agents to their intracellular targets and in the end enhance the therapeutic outcome. Importantly, the lack of toxicity in the absence of a suitable DDS and provided that cytotoxicity is triggered only where required, results in site-specific treatments (Berg et al., 1999; Høgset et al., 2004; Martinez de Pinillos Bayona et al., 2016).

PCI was developed by Berg & co-workers in 1999 (Berg et al., 1999), emerging as a further development of PDT. Despite the shared features between PDT and PCI, these two treatments differ in key aspects. Unlike PDT, PCI is a site-specific DDS based on the use of low dose PDT in combination with therapeutic agents where PS are not a therapeutic compound on their own (Adigbli and MacRobert, 2012; Martinez de Pinillos Bayona et al., 2016; Wang et al., 2013). In this respect, there are a wide range of compounds and molecules with different nature and size, susceptive of PCI-based delivery (DNA, peptides, oligonucleotides, genes, immunoconjugates…), turning PCI into a very versatile tool.

PCI requires the administration of sub-lethal doses of light and PS, limiting the PDT effect and being the delivered therapeutic agent the main responsible for the curative outcome. Specifically, during a standard PCI approach, the photosensitiser and the therapeutic compound at issue are administered and desirably uptaken by cells through endocytosis. PS designed for PCI are amphiphilic molecules whose hydrophobic domains remain within the endosomal or lysosomal lipid membranes during internalisation, while their hydrophilic motifs face the matrix of the vesicles and impede the complete penetration through cellular membranes (Arentsen et al., 2014). On the other hand, drugs in PCI should locate inside these endocytic vesicles, featuring hydrophilic properties, hence being trapped inside the matrix (Martinez de Pinillos Bayona et al., 2016). Upon illumination, excitation of PS located in the endo/lysosomal membranes, far from affecting the external cell membrane and inducing cell death, they will lead to the disruption of cytosolic vesicles carrying the therapeutic molecules, and consequently enable their transport to cellular targets. A crucial requisite in PCI is therefore the localisation of PS in endo/lysosomal membranes (Martinez de Pinillos Bayona et al., 2016; Selbo et al., 2010), ensuring photochemical damage on these rather than on the cell membrane.

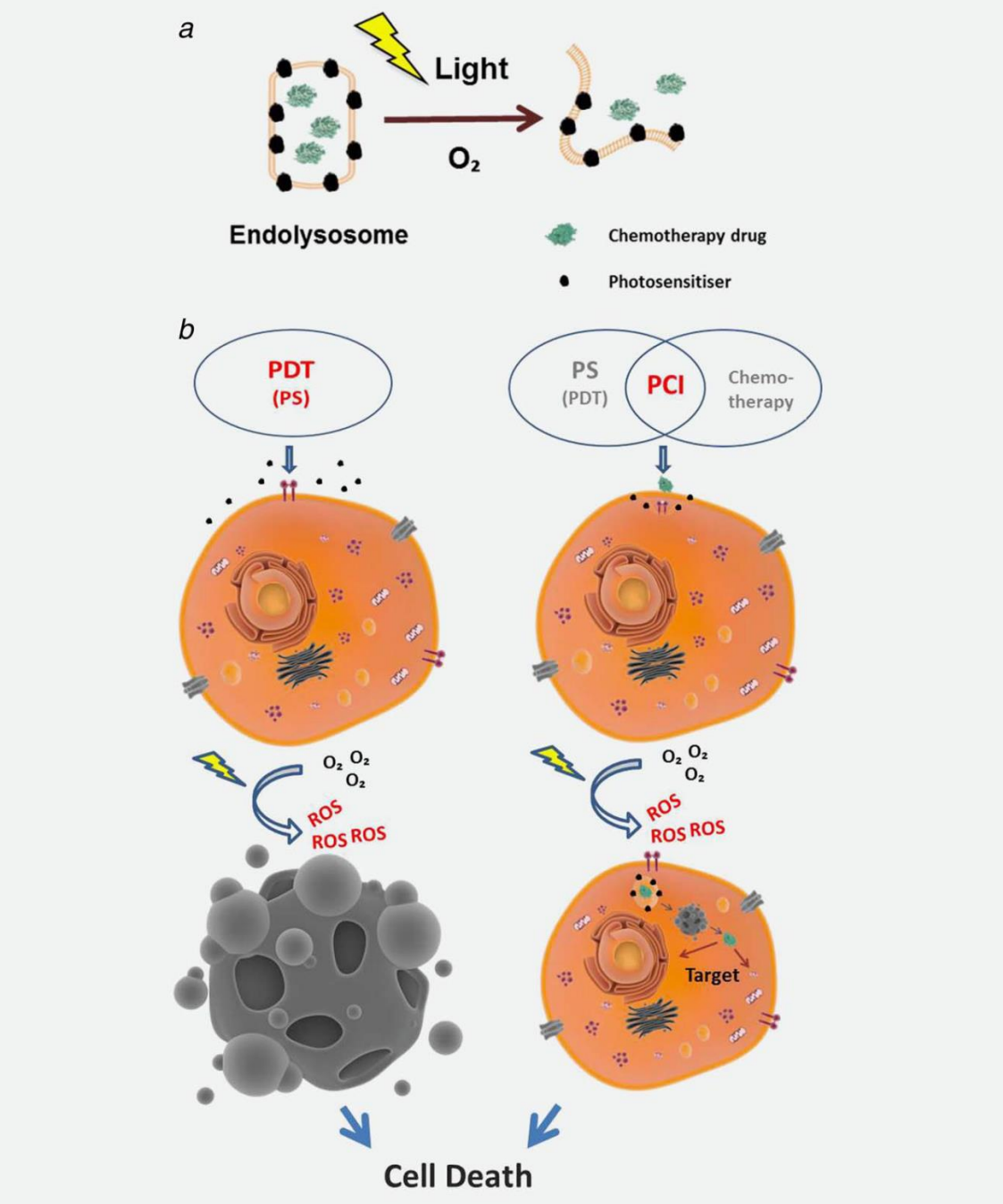

Figure 7. Schematic representation of PDT vs. PCI.

(A) Detail of endolysosomal disruption during light exposure. (B) Graphic display of the underlying differences between PDT and PCI. Image taken from [(Martinez de Pinillos Bayona et al., 2016)*]*

Initially, PCI was developed to enhance the delivery of macromolecular drugs which, due to their high molecular weight, had difficulties traversing cellular membranes and escaping from endocytic vesicles, as is the case of some chemotherapy drugs (Berg et al., 2006). However, PCI has also achieved an efficient intracellular delivery of low-molecular weight compounds, such as Bleomycin (MW 1400), which is unable to

penetrate cellular membranes efficiently, thereby accumulating in endosomes. Therefore, both large and low molecular weight molecules could be eligible for PCI-based delivery (Berg et al., 2006).

1.5.1 Photosensitisers in PCI

The above-stated requirements of PS used in PDT can be equally applied to PCI. One important distinctive feature is the prerequisite for the localisation of these in membranes within endosomes or lysosomes. (Lim et al., 2012). This can be achieved by the presence of a limited number of carboxyl-groups in photosensitisers, which due to their high pK_a enable cell membrane penetration. Otherwise, these could be replaced with sulfonate groups. Yet, in this case, more than one group is necessary to avoid penetration through cell membrane due to the low pK_a of these groups, which impedes protonation even in the acid environment of lysosomes. This pair of sulfonate groups will be responsible for the adsorptive endocytosis of photosensitisers. In addition, cellular membranes act in a protective manner with ROS, rendering longer lifetime and thereby greater toxicity (Berg et al., 2011)

As with PDT, when facing clinical application, PS in PCI should not cause dark toxicity in the host and exhibit desirable pharmacokinetics such as being rapidly uptaken mainly by tumour tissues and a fast clearance from the body (Berg et al., 1999; Bozzini et al., 2012; Cunderlíková et al., 2001; Dietze et al., 2003; Friberg et al., 2003; Pass, 1993; Prasmickaite et al., 2002; Sibata et al., 2001; Weyergang et al., 2011, 2006). Likewise, tissue penetration is also a major issue to consider when performing photochemical treatment.

$AlPcS_{2a}$ (aluminium phthalocyanine) has been widely used for *in vivo* PCI due to structural reasons: a main porphyrin macrocycle enhancing the absorption in the far-red region of the spectrum (peak at 670 nm), together with two sulfonate groups conferring amphiphilicity (Berg and Moan, 1994; Selbo et al., 2002). Recently, $TPCS_{2a}$ (sulfonated chlorin-based photosensitiser - Amphinex®) was developed (Berg et al., 2011). It is featured by the more efficient and reliable production compared to $AlPcS_{2a}$.

$TPCS_{2a}$ has optimal photobiological and photophysical features for PCI (Wang et al., 2013). For example, the enhanced photobleaching rate would benefit patients by reducing skin toxicity (Berg et al., 2011). Moreover, due to the above-mentioned reproducibility and purity during the manufacturing process as well as the high

absorption of this PS within the therapeutic window (600-800 nm), $TPCS_{2a}$ was proposed in 2011 for the first time, as a clinically suitable PS. Importantly, $TPCS_{2a}$ has been recently used in the first-in-man dose-escalating phase I/II study of PCI in combination with the antibiotic bleomycin for the treatment of cutaneous and subcutaneous malignancies either local recurrent, metastatic or advance for patients who had no success with other forms of treatments –ClinicalTrials.gov, NCT00993512 (Sultan et al., 2016). The successful outcome of this study has led to a larger phase II trial among several European centres. $TPCS_{2a}$ has also been combined with gemcitabine for the treatment of inoperable advanced cholangiocarcinomas – ClinicalTrials.gov identifier: NCT01900158 (Martinez de Pinillos Bayona et al., 2016).

In vitro, light absorption by PS will remain unaffected, thus compounds with low absorption in the optical window such as porphyrins can be used. Accordingly, $TPPS_{2a}$ (meso-tetraphenylporphin disulfonate), has been proved extensively to be efficient as a photosensitiser *in vitro* (Berg and Moan, 1994; Fretz et al., 2007; Lilletvedt et al., 2011).

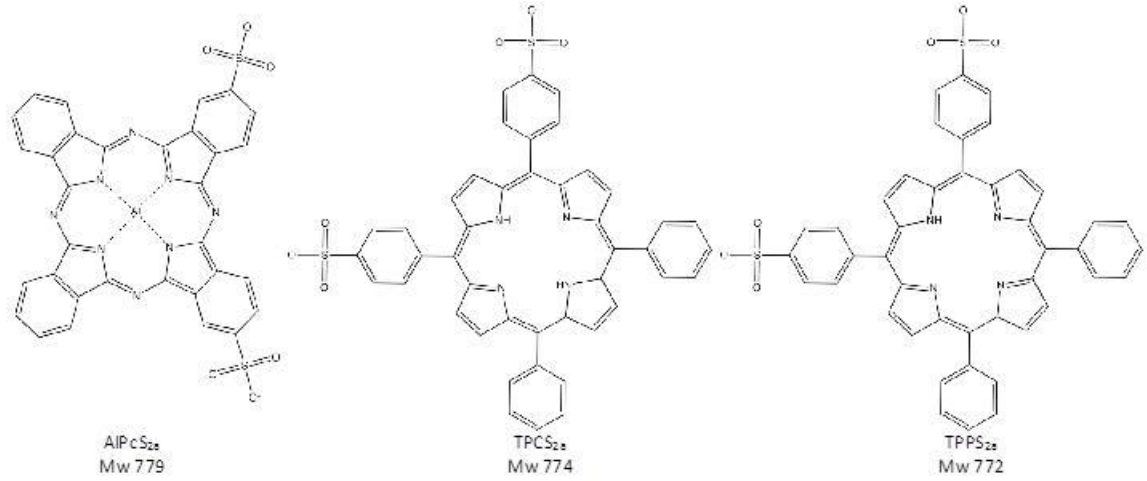

Figure 8. Photosensitisers used in PCI.
$AlPcS_{2a}$, $TPCS_{2a}$ (Amphinex®) and $TPPS_{2a}$ are three photosensitisers commonly used for PCI.

1.5.2 PCI modalities

The PCI procedure previously described corresponds to the traditional “light after” treatment. More recently, “light before” PCI has been described (Prasmickaite et al., 2002). Briefly, as opposed to “light-after” PCI, during a “light before” approach, light is applied before the administration of the therapeutic agent.

- *Light after.* Both photosensitiser and therapeutic drug are administered before illumination. They will both be endocytosed and localised in the endolysosomal membrane or matrix respectively. When excitation of PS occurs, the endolysosome will be disrupted and its content will be discharged into the cytosol, enabling the access to its target (see Figure 9A)
- *Light before*. Light-activation of PS will be triggered prior to the administration of the drug at issue. It has been hypothesised that after PS incorporation within endosomes and illumination, cytosolic vesicles present in the cell are disrupted (Prasmickaite et al., 2002), so that upon administration of the second therapeutic agent, newly formed endosomes containing the drugs will fuse with already disrupted endosomes, releasing the drug content (see Figure 9B). Further study of this more novel PCI proposal needs to be conducted to better determine the adequacy of either.

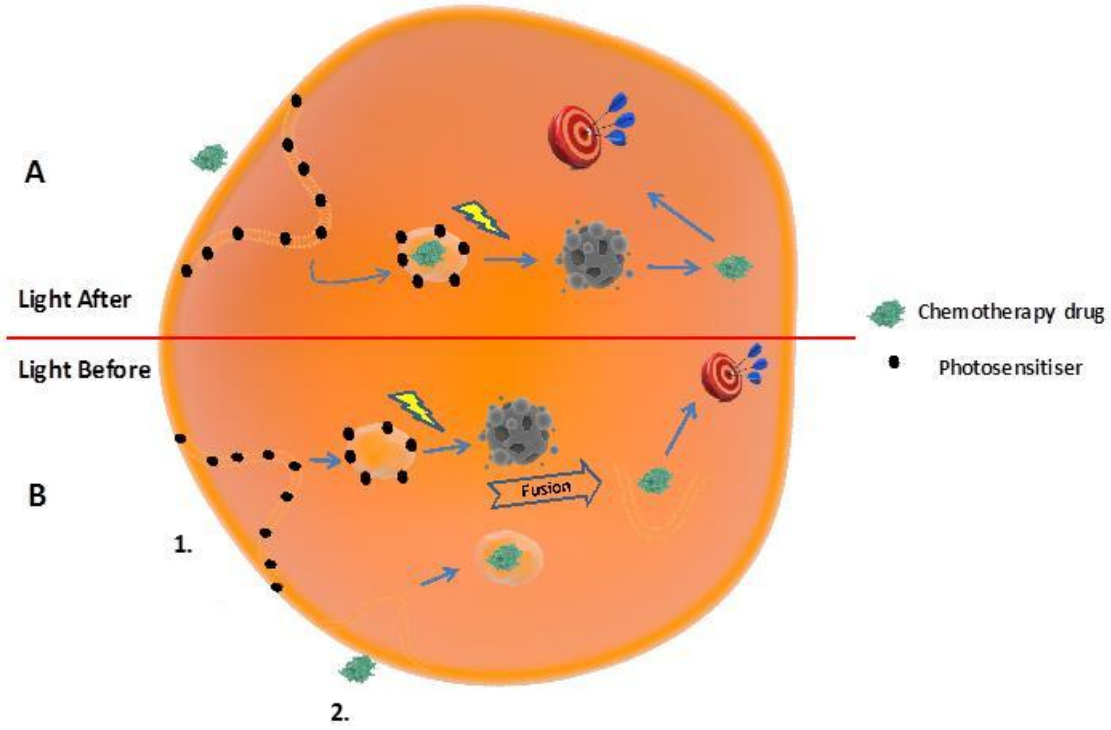

Figure 9. Schematic representation of the different PCI strategies: Light-After vs. Light-Before.

(A)Light-after PCI: light delivery occurs after co-administration of the chemotherapeutic drug and the photosensitiser. (B)Light-before PCI: the administration of photosensitiser is followed by the application of light and prior to the administration of the chemotherapeutic drug.

The higher efficiency of either approach seems to be dependent on the particular nature of the therapeutic compound that will be delivered, its sensitivity to PS-induced

photochemical toxicity (Prasmickaite et al., 2002; Weyergang et al., 2011). It is therefore likely that molecules and compounds less resistant to ROS species will suffer more damage when administered before PS light excitation, especially when located close enough to be affected by $^1O_2$. This could be applied to oligonucleotides, genes and other DNA sequences (Prasmickaite et al., 2002). Additionally, light before PCI has also been successful *in vivo*, i.e. for the treatment of subcutaneous colon adenocarcinoma tumours combining $AlPcS_{2a}$ and gelonin (Berg et al., 2006). From a clinical setting, light-before may also be an advantage, since light treatment could be performed at the same time as drug administration (Prasmickaite et al., 2002). Additional examples will be given in the following sections.

1.5.3 Therapeutic application of PCI

The use of PCI has been mainly investigated for cancer treatment with different macromolecules, nanoformulations, etc. However, as a DDS, it has is also an effective system to delivery several nucleic acids. Most of these are uptaken by cells through endocytosis, after which the release from cytosolic endosomes into the cytoplasm or else transport into the nuclear compartment, where these will perform their activity, remains to be a major challenge (Selbo et al., 2010).

For example, PCI has been previously used in combination with oligonucleotides (i.e. ribozymes, antisense DNA, peptide nucleic acids, siRNA). Along these lines, phorodiamidate morpholino oligomers (therapeutic oligonucleotide) were recently used in PCI bound to Ce6 and combined with dendrimer structures. Despite the previously described difficulties in endosomal escape of PMO, after PCI PMO resulted in an 20% cell death. Moreover, when compared to the widely used transfection agent Lipofectamine, PCI induced a greater expression of eGFP, concluding an effective release from endosomes and entry into the nucleus of the PMO of interest (Yuan et al., 2015). In a different study, PCI together with tetraglucosylated polyethilenimine were used to transfer p53 into pharynx carcinoma cells exhibiting a mutated version of p53. PCI did not only increase the efficiency of transfection but was also able to maintain the expression of the transgene in 10% cells for 144 hr after delivery. In the end, an increased cell death (up to 50%) induced by p53 was observed in these mutant cells (Ndoye et al., 2004).

1.5.3.1 PCI advantages over PDT

Despite the shared features between PDT and PCI, we believe that an optimised PCI strategy has several advantages over PDT. In the first place, the lower dose of both photosensitiser and light fluence used in PCI will potentially reduce skin sensitivity and side phototoxicity as reported for PDT.

Additional advantages of the former are:

- Greater effect in tumour vasculature:

Vascular shutdown has been often described as an important event occurring post PDT (Pizova et al., 2012; Selbo et al., 2010; Weyergang et al., 2011). Likewise, PCI is equally capable of affecting vascular structures. For example, a vascular shutdown was observed at a later timepoint for PCI, hypothesising that the combination of PS and bleomycin in this case resulted in a more subtle damage to endothelial cells possibly due to the lower light fluence employed (Norum et al., 2009b). Moreover, tumour oxygenation needed for singlet oxygen formation would have occurred for a longer period of time during PCI, resulting overall in greater tumour eradication (Norum et al., 2009b). Endothelial cells as such, namely fibrosarcoma and human umbilical vein endothelial cells (HUVECs), were further considered as direct targets of PCI in the studies conducted by Vikdal et al. combining saporin with either $TPPS_{2a}$ or $AlPcS_{2a}$ (Vikdal et al., 2013). A more efficient uptake of PS was confirmed in HUVEC cells, being localised in endosomal organelles. Interestingly, a higher dose of saporin was required to achieve a comparable PCI effect between endothelial and cancer cells (100 nM and 10 nM respectively) and a higher efficiency of the PS was likewise shown in cancer cells. The authors of the study hypothesised that disparities in traffic pathways between cell types were the cause of the above observations (Vikdal et al., 2013). Overall, this sheds light to the importance of endothelial cells during light-based therapies and potential vascular shut down within the context of tumours *in vivo*.

- Enhanced damage to the tumour periphery:

Distinct areas within a tumour are involved differently in tumour growth and development. More specifically, cells exhibiting slower proliferative capacity are more common in the central region of tumours, while peripheral cells usually proliferate at a higher pace. This was observed for example in the study carried out on a human glioma *in vitro* model (Mathews et al., 2012). Through cell monolayer and spheroid

toxicity observations, not only was PCI capable of inducing synergy between PDT and bleomycin, but also whereas PDT had a major effect in the tumour's central region, PCI exerted a major effect in the quickly proliferating periphery. This led not only to the temporary delay in tumour's growth but their complete eradication (Mathews et al., 2012). Similar results were obtained when combining PCI of bleomycin with other treatments such as external-beam radiotherapy (Norum et al., 2009a) or marginal surgery (Norum et al., 2009c). In the former, PCI treatment before ionizing radiation, led to a 13-day further delay of tumour growth opposite to radiation on its own (Norum et al., 2009a). Hence, the major destruction of tumours post-PCI could be explained by the combination of radiation - acting on the inner tumour mass, and PCI - affecting a large region of the tumour periphery. In addition, this enabled the reduction of the overall dose of radiation applied. Furthermore, during PCI delivery of bleomycin to the existing tumour bed after tumour resection in a fibrosarcoma *in vivo,* PCI resulted in up to a 17-day delay of tumour growth. However, PDT on its own did not improve the results observed after resection. Moreover, recurrence took 3 times longer after PCI compared to PDT when surgery had not been completely successful (Norum et al., 2009c). In a different study, the same group confirmed higher efficacy of PCI towards periphery cells through magnetic resonance imaging (MRI) measuring perfusion based on vascular shutdown. In this case, two hours after either PDT or PCI, the access of MRI agents to the centre of the tumour was blocked, whereas high levels of perfusion were observed in the periphery revealing a smaller area of viable peripheral tumour tissue post-PCI on the treated animals through histological observation (Norum et al., 2009b). Importantly, the greater cell killing in this highly proliferating area was associated to the delivery of bleomycin in the tumour parenchyma. Dietze et al. determined deeper necrosis after PCI than PDT: up to 7 mm and 4 mm from the skin surface respectively (Dietze et al., 2005). Importantly, achieving a greater depth penetration is particularly relevant in solid tumours.

- Overcoming MDR:

In several cases PCI been able to overcome resistance to several chemotherapy agents, enhancing the biological effect of these to an even greater extent in resistant subclones than parental sensitive cells. This has been successfully performed with doxorubicin- and mitoxantrone- resistant cells for instance. Both of these drugs are weak bases which are unable to penetrate membranes in their protonated form: diffusion of these into lysosomes results in their protonation and sequestration, hence causing drug resistance. Moreover, highly acidic organelles have been reported in cells exhibiting a drug resistance phenotype (Altan et al., 1998). In 2006, Lou et al. proved

the possibility of overcoming doxorubicin resistance caused by endosomal entrapment of the drug in MCF-7 breast cancer cell lines, promoting transport of the drug to cell nuclei, where it is expected to exert its cytotoxic effect (Lou et al., 2006). Cell viability measured on MCF-7 parental cells after PCI showed additive effects between photosensitiser-based photooxidative damage and chemotherapy-based damage; yet, synergistic effects were seen in the doxorubicin-resistant counterpart together with an 8-fold decrease in LD_{50} (>20 M to 2.5 μM). Based on doxorubicin's delivery "light-before" and "light-after", PCI was more efficient when drug accumulation in cytosolic vesicles was avoided as opposed to relocation after accumulation (Lou et al., 2006). Similarly, PCI was also capable of triggering cell killing in mitoxantrone-resistant cells in a dose-dependent manner, i.e. combining the PS hypericin and mitoxantrone as shown by Adigbli et al. on both breast and bladder cancer cells (Adigbli et al., 2007). Again, up to 13% higher reduction in cell viability was seen in resistant cells compared to parental sensitive. Also, this enhanced cell killing after PCI was not due to changes in P-glycoprotein (Pgp, drug-excreting efflux pump) expression in resistant cells. Surprisingly, when breast cancer cells were exposed to PDT using low doses of PS, some proliferation was seen, possibly due to activation of cell pathways under cell stress which are able to propagate cell proliferation (Adigbli et al., 2007). This recurrence was not observed in the bladder cancer model used, suggesting the induction of proliferative signals after PDT could happen at a later time, correlating with the described recurrence in bladder cancer patients after a primary PDT procedure (Yavari et al., 2011). More recently, Olsen et al. (Elisabeth Olsen et al., 2013) concluded based on studies performed on uterine sarcoma cells, that upon doxorubicin's integration in the DNA structure it can induce ROS formation as well as expression of ROS scavengers as a consequence of cellular adaptation to the environment (Elisabeth Olsen et al., 2013). It is suggested that the release of chemotherapeutic drugs located in cytosolic vesicles after exposure to light in PCI, occurs before their capture by ROS scavengers. ROS scavenger overexpression, together with the attenuation of p-38 death signal in the MES/Dx5 resistant cell line, clarifies the origin of PDT ($TPPS_{2a}$ used as photosensitiser) and doxorubicin resistance. P-gps were also studied as a consequence of their participation in drug resistance (Gottesman, 2002); however, high PS uptake was seen even under exposure to P-gp inhibitors (Elisabeth Olsen et al., 2013).

Aims of the thesis

Based on the potential PDT has shown already clinically as a focal therapy, the main aim of this thesis is to evaluate the potential of light-based therapies (PDT and PCI) for prostate cancer, specifically advanced, aggressive, and highly metastatic.

Despite the success PDT has shown in tumour eradication in clinical trials for prostate cancer treatment, there are still some limitations as regards co-morbidity induced by side phototoxicity. Therefore, in addition to the investigation of PDT, we will also examine the capacities of the PDT-derived drug delivery system PCI as therapy for prostate cancer. Both these therapies are difficult to optimise due to the number of influencing variables, especially PCI. Taking this into consideration, we hypothesise that should a PCI approach be optimally designed, it could result in an improvement over PDT regarding both therapeutic outcome and adverse side effects.

During this project, we aimed to conduct experiments *in vitro* which could serve as a basis for further investigations *in vivo*. Several goals were established, each of which is covered in a different chapter of the present thesis.

The first objective was to investigate both PDT and PCI in our prostate cancer model *in vitro*. This involved rat cells (MatLyLu) as basis for later *in vivo* studies, and a human cell line (PC3) to compare and assess translation to human disease. Moreover, we aimed to evaluate the effect of different photosensitisers, differing in their nature, hence physico-chemical properties: $AlPcS_{2a}$, $TPPS_{2a}$, $TPCS_{2a}$, BPD-MA. These studies aimed to investigate the cytotoxicity exerted by each treatment as well as the underlying mechanism behind both therapies. In addition, founded on the false positive rate frequently noted when drug testing in 2-dimensional studies, we aimed to additionally conduct equivalent studies in 3-dimensions to validate 2D observations and potentially reduce the number of animal experiments required in future PDT/PCI work.

The second objective was to evaluate the benefits of targeted PDT and PCI strategies could provide regarding site-specificity and further reduction of side phototoxicity, with important implications in a clinical setting (i.e. decreased skin sensitivity). To conduct this study, conjugates composed of the photosensitiser TPP covalently bound to different cell penetrating peptides (TAT, Antp) were tested *in vitro* against human prostate cancer cells. Additionally, CXCR4 - highly expressed receptor in prostate cancer, was the subject of a more specific targeting of these compounds via the vMIP-II moiety.

The third objective was to transfer *in vitro* findings to experiments conducted in Copenhagen rats. So as to determine the most suitable DLI in these subjects as well as bioavailability of the PS drug, a pharmacokinetic analysis was conducted before initiating light-based treatment on tumours. For the performance of light-treatments, different PS exhibiting a varied suitability for PDT and PCI were used. For instance, hydrophobic BPD-MA was used following a vascular targeted PDT approach, while amphiphilic $TPCS_{2a}$ and $AlPcS_{2a}$ were either used for PDT or combined with saporin in PCI. The overall aim of these studies was to evaluate therapeutic outcome, which we carried out through tumour growth monitoring, tumour cell death and survival of animal subjects.

The final objective of this thesis was to determine whether PDT and PCI were eliciting an immune response in our advanced prostate cancer model. In line with this, we rechallenged previously cured rats with a second injection of tumour cells, observing whether these individuals were capable of rejecting the rechallenge. In addition, to further measure the effect of these treatments at a molecular level, we have analysed the expression of different genes involved related to the immune system and have also pursued IHC stains to perform a similar evaluation at the protein level.

Chapter 2 *In vitro* studies of PDT and PCI in Prostate Cancer

2.1 Introduction

Both photodynamic therapy and photochemical internalisation have been successfully applied in multiple *in vitro* cancer studies as already discussed in Background and Introduction. Most published PCI studies in cancer treatment focus on the delivery of macromolecular agents although some other smaller drugs have also been assayed (Martinez de Pinillos Bayona et al., 2016). These could be grouped into the following categories: glycopeptide antibiotics and anthracyclines, macromolecular drug delivery vehicles and macromolecular toxins (Martinez de Pinillos Bayona et al., 2016).

Bleomycin is a hydrophilic glycopeptide (1.4 kDa) that has been widely reported in published PCI studies and is currently subject of PCI clinical trials as commented previously. This drug's potential to induce pneumonitis has been demonstrated, eventually resulting in lung fibrosis (Berg et al., 2005). Consequently, there is a need to reduce drug dosage as well as the number of repeated administrations without compromising the efficacy, all of which could be potentially overcome by PCI. For instance, an efficient delivery of bleomycin resulted in complete tumour eradication in 60% of the animals used in the study carried out by Berg et al. in 2005 in combination with $AlPcS_{2a}$ for the treatment of colorectal adenocarcinoma (Berg et al., 2005). In a more recent publication by the same group, Amphinex-based bleomycin delivery (combination currently used in clinical trials), was able to delay tumour growth further than that seen in the PDT group using m-THPC (Foscan®), even at the lowest light fluence tested (Berg et al., 2011). Bleomycin has also shown potential in several human and non human cancer models *in vitro;* in bladder cancer for instance, at least an additive effect between the PS and the drug was seen (Arentsen et al., 2014). It was also compared to other chemotherapeutic agents not as cytotoxic, suggesting bleomycin's physico-chemical features are ideal for PCI.

Despite the fact that large molecules are more commonly used in PCI, anthracycline drugs of smaller size such as doxorubicin (0.5 kDa) and mitoxantrone (0.4 kDa) have also been used in several PCI studies (Adigbli et al., 2007; Lai et al., 2007; Lou et al., 2006). The former acts intercalating DNA and is associated to deadly cardiac damage; the latter was developed as a doxorubicin analogue in an attempt to reduce side cardiotoxicity. Some studies with both of these drugs have been reported in the Background and Introduction.

As noted in above, PCI is a multifactorial process whose optimisation is not straight forward and involves the consideration of several entangled variables. There are no available publications addressing this matter as such, given the additional role the diverse biological systems play in the process as well. Therefore, different variables will be evaluated in our prostate cancer model *in vitro* in the following sections.

2.1.1 Photochemical Internalisation of Ribosome Inactivating Proteins

Ribosome inactivating proteins (RIPs), are enzymatic toxins widely distributed among plants with N-glycosidase activity (EC 3.2.2.22). RIPs cleave a specific adenine residue located in tetranycleotide G(A^{4324})GA within a sequence in the rRNA in the 28S ribosomal subunit part of the 60S subunit of the rat ribosome. This will irreversibly affect the interaction between ribosomes and the elongation factor 2 during translation of mRNA in protein synthesis resulting in cell death (Polito et al., 2013). This rRNA sequence is considered to be universally conserved throughout eukaryotic species (Puri et al., 2012; Schrot et al., 2015; Walsh et al., 2013). Additionally, some RIPs can act on other substrates such as mRNA, tRNA, DNA and poly(A), or even poly(ADP-ribosyl)ated proteins (Polito et al., 2013). A guanine cleavage has also been sometimes reported and thus, these proteins are sometimes considered polynucleotide adenosine glycosidases i.e. PAP from *Phytolacca americana*, which can also cleave guanine on *Escherichia coli* rRNA (Schrot et al., 2015).

Two main types of RIPs have been described:

- Type 1: composed of a single chain A responsible for the enzymatic activity of these protein toxins.
- Type 2: consisting of 2 polypeptide chains A and B linked by a disulphide bridge. The latter is a lectin peptide capable of binding to galactosyl residue found on the surface of animal cells, therefore enabling the entry of chain A inside the cytosol and hence acting on their target organelles.
- Type 3: only described in maize (b-32) and barley (JIP60), these consist of a N-terminal domain with catalytic activity and a C-terminal with unknown function. They are synthesised as ProRIPs that undergo processing to form an active toxin (Schrot et al., 2015).

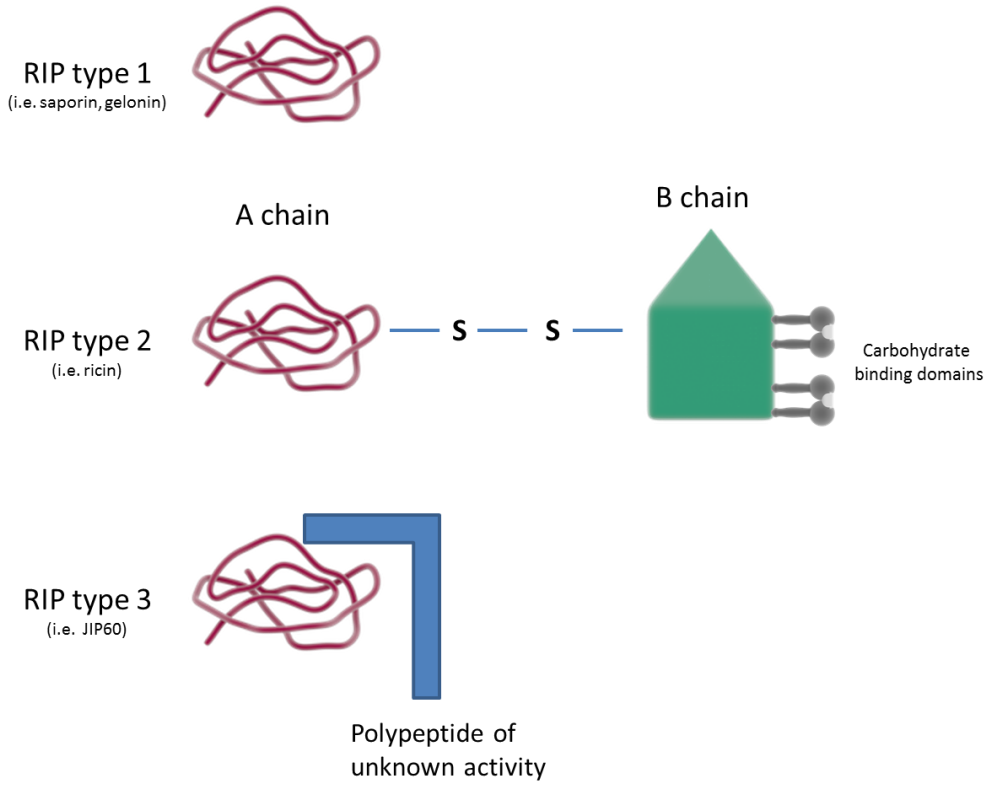

Figure 10. Structural differences between Ribosome Inactivating Proteins (RIPs).

RIP type 1 are composed of a single A chain responsible for the enzymatic activity. RIP type 2 are composed of two peptides: chain A and chain B. This last peptide is a lectin-type protein assisting the entry of proteins into cells.

Structural differences between RIPs type 1 and 2 explain the differences in toxicity exerted by both. On the one hand, RIPs type 2 are very potent toxins (the best known is ricin). On the other hand, the lack of lectin-type B chain renders RIPs type 1 less toxic within a cellular environment, despite the great efficiency these have demonstrated in cell-free systems or when modified via conjugation to cell-binding molecules. Ricin has been reported to enter mammalian cells through endocytosis and reach the endoplasmic reticulum (ER) via retrograde transport through the Golgi complex. It will then reach its subcellular target exploiting ER-associated degradation route (Vago et al., 2005).

Due to cell uptake-associated difficulties, PCI has been used on several occasions as a delivery vehicle for RIPs. For instance, RIPs type 1 such as gelonin and saporin, have been combined with photosensitisers in different cell lines and cancer models (Berg et al., 1999; Dietze et al., 2005, 2003; Prasmickaite et al., 2002; Selbo et al., 2000a). In its early stages, PCI studies were carried out in cervical carcinoma cells combining gelonin and $TPPS_{2a}$ or $AlPcS_{2a}$, observing a greater 200-fold increase in cell death

after PCI as opposed to either treatment on its own as well as synergy between PS and the toxin (Berg et al., 1999). It is important to take into account the integrity of the therapeutic agent, which could be compromised by the PCI protocol followed as already mentioned. It was seen in the study conducted by Selbo et al. that gelonin could be affected by the acidic lysosomal environment if PCI was delayed and upon illumination the drug was released from these organelles rather than earlier endosomes, consequently eliciting a reduction in cell death (Selbo et al., 2000a). This was further confirmed by the significant enhancement in cytotoxicity when delivering light before administering gelonin. It seems that vesicle disruption prior to gelonin administration avoids damage to the toxin in the endocytic environment, hence result in a faster delivery time (Prasmickaite et al., 2002).

In a different study, Dietze et al. (Dietze et al., 2003) selected different cells derived from human synovial sarcoma tumours as a model for their study. Again, photochemically delivered gelonin was more efficient than PDT regardless of the differences of uptake rates or traffic pathways between cell lines, being able to reduce light dose four times the amount required to reduce cell viability by 80% (Dietze et al., 2003). In a later study (Dietze et al., 2005), the same group completely eradicated sarcoma induced in mice in 50% of PCI treated animals, and showed tumour regrowth after 20 days in the remaining 50% significantly delaying the end point of the study compared to PDT or non-treated groups (Dietze et al., 2005).

Saporin is a monomeric protein belonging to RIPs type 1 family of proteins which has been as well subjected to PCI and is focus of the present thesis in different prostate cancer models. It is a multigene family of proteins comprising more than 9 isoforms which differ in biological and chemico-physical properties. Yet, all of them have a similar molecular weight around 30 kDa, being saporin-S6 the most representative (Polito et al., 2013). Its mechanism of entry into cells has not been clearly elucidated to date. In a similar way to other RIPs type 1, passive entry of saporin through mechanisms such as pinocytosis was initially proposed, its uptake was suggested to happen in a non-specific manner. However, the existence of specific receptors emerged due to resistance to saporin found in some cell lines together with the higher sensitivity found in some organs. There is discrepancy between studies claiming uptake of saporin occurs through receptor-mediated endocytosis through the α_2-macroglobulin receptor (low-density lipoprotein receptor-related protein, LRP) or either mechanisms independent of specific binding sites i.e. non-coated vesicles (Polito et al., 2013). Upon cell endocytosis of biologically active saporin, it needs to reach cytosolic ribosomes. Several pathways have been described in different cell lines, concluding

that saporin could reach various intracellular compartments, even possibly by more than one pathway (Polito et al., 2013). Cytotoxicity induced by saporin has been evaluated both *in vitro* and *in vivo*. In the latter, necrotic damage in spleen, liver and kidney has been found. As for *in vitro* studies, saporin-based cytotoxicity has been related in the first place to protein synthesis inhibition; besides, nucleic acid depurination has also been reported. There is evidence of apoptotic death based on fragmentation of chromatin, formation of apoptotic bodies, cellular hypodiploicity and caspase activation in cells exposed to saporin. Other cell death pathways have been described, i.e. autophagy or necrosis. In fact, triggering of autophagy could result in cell death due to atrophy or else activate necrosis or apoptosis. Saporin has sometimes been found in the nucleus, indicating possible DNA damage in addition to its RIP function. Overall, apoptosis appears to be the major cell death route but cell fate may vary in different cell lines (Polito et al., 2013).

2.1.2 Three Dimensional (3D) tumour models

Efficiency and reliability of studies performed in two dimensions is being increasingly questioned, since culturing cells in a monolayer environment is far from resembling the natural 3D environment of cell growth. Publications throughout the literature have already proven three dimensional culture to improve the outcome of several studies, more accurately mimicking the natural setting (Antoni et al., 2015). Cells growing in monolayers will lack contact with other cells in most of their dimensions, being only connected to other “neighbour” cells in the edges, as opposed to conforming multi-dimensional structures similar to the biological environment. This will eliminate naturally existing communication and intercellular contact, affecting different aspects of cell behaviour: metabolism, physiology or even phenotypical features. Overall, this may affect the outcome of research based on 2D cell culture, leading to misinterpretation, misleading results or unreal conclusions, as has been reviewed previously (Nyga et al., 2011).

Within organisms, cells undergo a series of interactions, communication, transport and signals between them as well as with elements present in the extracellular matrix surrounding them. Therefore, it is essential that cell culture environments preserve this spatial distribution and cell polarisation so as to enhance cellular performance (viability, proliferation, response to the surrounding environment, metabolism, morphology, phenotype maintenance, communication with neighbour cells, protein and gene expression, etc.). There is evidence of 3D culturing of cells resulting in an improvement

on several cell functions, including the above (Bono et al., 2016; Li et al., 2010; Toivonen et al., 2016). Furthermore, they will have greater lifespan due to the longer periods of time required to reach confluence, which enables conducting longer studies important in longer-term drug effect. In line with this, is has been reported that 2D studies may overestimate toxicity exerted by drugs *in vitro* which then result ineffective *in vivo* (Antoni et al., 2015).

Moreover, there is a growing interest nowadays to develop new platforms towards the Replacement, Reduction, and Refinement (3Rs). The use of biomimetic 3D culturing may permit more reliable drug screening thereby reducing the need for animal experimentation, at the same time maintaining the cellular model needed to study the mechanism of PDT and PCI.

In a cancer setting, growth rate and metabolic profile are altered in monolayer cultures, also showing greater sensitivity to therapeutic approaches than in the 3D counterpart. The latter would more accurately recreate lower growth rates, nutrient and supply, waste removal, etc., which in the end result in a genotype and protein expression which more closely resemble to naturally occurring.

2.2 Aims

The main aims of the present chapter are as follows:

- Compare the outcome resulting from PDT and PCI *in vitro*
- Establish optimal parameters for maximal tumour kill during PCI in prostate cancer *in vitro*
- Elucidate the mechanistic processes underlying PCI in prostate cancer

A significant part of the present thesis involved the observation of the therapeutic effect using cell viability assays. Accordingly, the first few sections reported below will look into the optimisation of PCI treatment, while also comparing the outcome to that of PDT. Different experimental settings were examined, assessing the influence of different variables participating in photochemical internalisation such as light dose, drug light interval, photosensitiser and drug dosage.

Both rat and human prostate cancer cells have been exposed to PDT and PCI *in vitro*. A number of different photosensitisers ($TPPS_{2a}$, $TPCS_{2a}$, BPD-MA, $AlPcS_{2a}$) were investigated for either PDT or else combined with saporin when undergoing PCI. Both light-based treatments were performed in conventional two dimensional and more novel and biologically relevant three dimensional models as a more definitive confirmation of the therapeutic effect these treatments would have in biological systems. Investigations performed in both platforms will be detailed below. Experiments performed in the rat prostate cancer model (MatLyLu cells) will serve as basis for later on described *in vivo* experiments; while the human counterpart (PC3 cells) will shed light into the applicability of light treatments, PCI in particular, for its clinical application.

The last sections of the present chapter will investigate the underlying mechanism behind PDT and PCI. Photosensitiser and saporin subcellular localisation were examined before and after exposure of light, tailored to each particular photosensitiser.

2.3 Materials & Methods

Cell work

Both PDT and PCI-based experiments were performed on two prostate cancer cell lines, PC3 and MatLyLu (MLL) of human and rat origin respectively.

PC3 cells, kindly donated by Professor John Masters (Prostate Cancer Research Centre, UCL), are a widely used prostate cancer model for studies *in vitro*. They were originally derived from bone metastases of a prostatic grade IV adenocarcinoma in a 62-year old male Caucasian. They do not express androgen receptor (AR) nor prostate-specific antigen (PSA), and thus are featured as androgen independent cells as well as an aggressive form of prostate cancer. With frequency, they are employed to depict castration-resistant tumours.

MLL cells, purchased from ECACC (catalogue no. 94101454), were derived from a rat adult malignant prostate carcinoma, initially obtained from a 22-month old Copenhagen rat. Development of this cell line was carried out growing it in gradually increasing doxorubicin doses, justifying the multidrug resistance phenotype reported in the literature. They are anaplastic and androgen independant, also highly aggressive and with potentially causing metastases in the lung (Kager et al., 1992; Wenger et al., 1984).

Both cell lines were growth in RPMI 1640 medium containing L-glutamine (Gibco, Invitrogen), further supplemented with 1% penicillin-streptomycin (5,000 U/ml, Invitrogen) and 10% fetal bovine serum (Life Technologies). In the case of MLL, media was additionally supplemented with 250 nM Dexamethasone (suitable for cell culture, Sigma-Aldrich). Cells were kept in culture at 37°C in a 5% CO_2 humidified atmosphere. Media was changed two times a week and cells were subcultured when reaching confluence (usually twice a week) using 1X trypsin (0.5% trypsin-EDTA, Gibco®, Invitrogen). PC3 cells were used at passage 25-45, MatLyLu cells were used at passage 6-15.

Chemicals and photosensitisers

Saporin was purchased from Sigma Aldrich (S9896). Lyophilized powder was dissolved in PBS and stored at 4°C, experimental concentrations were obtained diluting a 1 µM solution in cell media to obtain desirable concentrations.

Saporin-Alexa-Fluor488® conjugate was obtained following a modified protocol from a Molecular probes labelling kit. A saporin solution (Sigma Aldrich, S9896) was eluted with a pH 9.24 carbonate buffer (9 ml 0.1 M $NaHCO_3$ + 1 ml 0.1 M Na_2CO_3) to a 2.5 mg/ml final concentration. Parallel, an Alexa-Fluor488® (ThermoFisher Scientific) solution was prepared in DMSO to a final 4.29 mg/ml concentration. 2 ml of the saporin solution were combined with 222 µL of the dye solution and kept for 1 hr on overhead rotation. This solution was finally eluted in a PD10 column (GE Healthcare) which had been previously equilibrated with PBS, and 2.5 ml were recovered. The concentration of this solution was determined by UV-visible absorbance measurements.

$TPPS_{2a}$, meso-tetraphenyl porphyrin disulphonate, was purchased from Frontier Scientific. The stock solution was prepared by dissolving the powder in DMSO, then diluted in PBS and the the resulting aliquots were stored at -20°C. Working $TPPS_{2a}$ solutions were kept at 4°C and experimental concentrations were obtained diluting a 10 µg/ml solution in cell media to reach desirable concentrations.

$TPCS_{2a}$, meso-tetraphenyl chlorin disulphonate (Amphinex®) was kindly donated by PCI Biotech AS, Oslo, Norway. The 30 mg/ml stock was initially diluted in PBS, storing the resulting aliquots at -20°C. Working Amphinex® solutions were kept at 4°C and experimental concentrations were obtained diluting a 10 µg/ml solution in cell media to reach desirable concentrations.

BPD-MA, benzoporphyrin derivative monoacid ring A (Visudyne®, verteporfin for injection) was purchased from Novartis. 15 mg of lyophilised were dissolved in 1 ml 5% dextrose and keep stored at -80°C. Working BPD solutions were kept at 4°C and experimental concentrations were obtained diluting a 10 µg/ml solution in cell media to obtain desirable concentrations.

$AlPcS_{2a}$, aluminium phthalocyanine disulfonate, was purchased from Frontier Scientific. The stock solution was prepared by dissolving powder in sodium hydroxide, and neutralising with 0.1 M hydrochloric acid to a 1-2 mg/ml final concentration. Working $AlPcS_{2a}$ solutions were kept at 4°C and experimental concentrations were obtained diluting a 10 µg/ml solution in cell media to reach desirable concentrations.

Light source

Different devices were used to tailor light treatment to each photosensitiser:

- LumiSource® (PCI Biotech, Norway) was used to excite cells exposed to $TPPS_{2a}$ and $TPCS_{2a}$ *in vitro*. It consists of four fluorescence tubes emitting light uniformly in the spectral region 375-450 nm at a constant power of 7 mW/cm^2.

- LumaCare™ lamp LC-122 (LumaCare, USA) was used to excite cells exposed to $AlPcS_{2a}$ *in vitro*. A fibreoptic probe was attached to the lamp emitting in the spectra region 660-710 nm, power around 7.96 mW/cm^2

- Omnilux Clear-U™ LED device was used to excite cells exposed to BPD-MA *in vitro*, emitting in the spectra region 400-440 nm at, power around 12.7 mW/cm^2.

LumiSource®

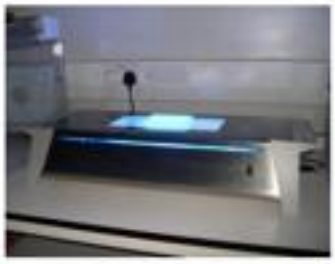

LumaCare™

Omnilux Clear-U™

PS spectral measurements

Different photosensitiser solutions were prepared in methanol to a final concentration ranging 1-15 µM. Absorption spectra were measured using a spectrophotometer (Lambda 5, Perkin-Elmer, Beaconsfield, UK) with 1 cm pathlength quartz cuvettes. Fluorescence emission spectra were measured using a LS50B Perkin-Elmer spectrofluorimeter (Perkin-Elmer, Beaconsfield, UK). Setting absorption at 420 nm for $TPPS_{2a}$, $TPCS_{2a}$, BPD-MA; or 600 nm for $AlPcS_{2a}$.

TPPS2a / $TPCS_{2a}$ (Amphinex®) uptake

PC3 and MLL cells were seeded on 96-well plates at 10000 cells/well or 1000 cells/well respectively. Cells were allowed to grow for 24 hr before administering increasing doses of either photosensitiser solutions prepared in cell media during 24 hr. Plates were then washed once with PBS and replaced with fresh RPMI no-phenol red. Fluorescence emission was immediately measured using a LS50B Perkin-Elmer spectrofluorimeter (Perkin-Elmer, Beaconsfield, UK), with excitation and emission at 420 nm and 650 nm respectively (10 nm bandwidths) and a 515 nm longpass filter to remove any scattered excitation light.

$AlPcS_{2a}$ / BPD-MA (Visudyne ®) uptake

MLL cells were seeded on 24-well plates at 3000 cells/well. Cells were allowed to grow for 24 hr before administering 0.4 μg/ml of either BPD-MA or $AlPcS_{2a}$ prepared in cell media during 8 hr and 24 hr. Plates were then washed once with PBS and replaced with fresh RPMI no-phenol red. A BD FACSAria 1 (Becton Dickinson, USA) flow cytometer was used to quantify fluorescence emission. BPD-MA was excited using a 407 nm laser and emission was measured 530/30 nm; $AlPcS_{2a}$ was excited using a 633 nm laser and emission was set at 660/20 nm.

Drug-dose response curves

PC3 and MLL cells were seeded on 96-well plates at densities ranging from 5000-10000-cells/well or 600-1000 cells/well respectively depending on when cell viability measurements were conducted (24 to 48/96 hr after hypothetical performance of light treatment). These values were selected based on optimal cell count in control groups within MTT detection limits. Cells were allowed to grow for 24 hr before exposing them to increasing doses of either photosensitiser or saporin solutions prepared in cell media during 24 hr. Plates were then washed once with PBS and fresh media was added. After a 4 hr-cell recovery period (chase period), plates involving treatment with photosensitisers belonging to “light” groups, were illuminated. This chase period also enables translocation of PS from the external cellular membrane to a subcellular level. Cell viability was measured at different time points. In those wells where viability was measured later than 48 hr after light treatment, culture medium was replaced once more to avoid starvation-based cell death. Plates were kept in a 37°C humidified atmosphere containing 5% CO_2 at all times, those involving photosensitisers were wrapped in foil and corresponding experimental procedures were carried out protected from light to avoid unintended excitation of photosensitisers.

PDT & PCI (combination) experiments

PC3 and MLL cells were seeded onto 96-well plates at densities ranging from 5000-10000 cells/well or 600-1000 cells/well respectively depending on when cell viability measurements were conducted (24 to 48/96 hr after light treatment). Cells were allowed to grow for 24 hr before undergoing either "light-after" or "light-before" PCI procedures:

a) *"Light-after" PCI*. Cells were exposed to sublethal doses of photosensitisers alone or in combination with saporin prepared in cell media during 24 hr. Plates were then washed once with PBS and fresh media was added. After a 4 hr-cell recovery period (chase period), plates belonging to "light" groups were illuminated.

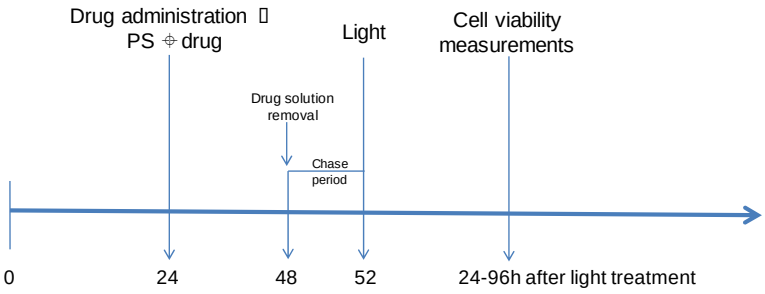

b) *"Light-before" PCI*. Cells were exposed to sublethal doses of photosensitisers alone during 24 hr. Plates were then washed once with PBS and fresh media was added. After a 4 hr-cell recovery period (chase period), plates belonging to "light" groups were illuminated and saporin was administered immediately after light. 24 hr after administration of saporin, drug was washed off once with PBS, and fresh media was added.

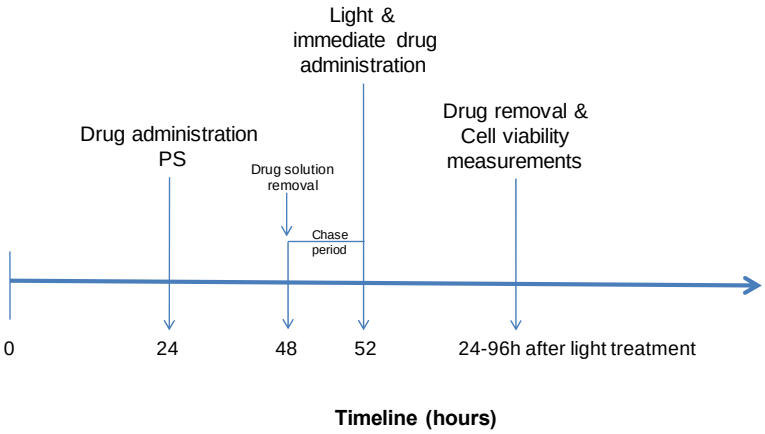

Hereafter cell viability was measured at different time points. In those wells were viability was measured later than 48 hr after hypothetical performance of light

treatment, culture media was replaced on an additional occasion to avoid starvation-based cell death. Plates were kept in a 37°C humidified atmosphere containing 5% CO_2 at all times, wrapped in aluminium foil and experimental procedures were carried out protected from light to avoid unintended excitation of photosensitisers.

Analysis of cell viability in two dimensional models

MTT was used to observe cytotoxicity in 2D experiments. MTT assay [3-(4, 5-dimethylthiazolyl-2)-2, 5-diphenyltetrazolium bromide)] directly assesses cellular metabolic activity and is very frequently used as an indirect measurement of cell number or viability. MTT is a yellow tetrazolium salt that can be reduced by dehydrogenase enzymatic activity present in metabolically active cells, generating NADH and NADPH. This results in the formation of purple formazan intracellular crystals which can be solubilised with organics solvents such as dimethyl sulfoxide (DMSO); subsequent solution that can be spectrophotometrically quantified. Background absorbance levels of this reagent are negligible in the absence of cells.

When performing the MTT assay, cell media was removed from the wells and replaced with 100 µl of a 1 mg/ml MTT (Sigma-Aldrich) solution prepared in cell media. Plates were then placed at 37°C in a 5% CO2 humidified atmosphere during 1 hr 30 min. After this incubation period, the content was removed from the wells and replaced with 100 µl DMSO (Sigma-Aldrich) to dissolve the purple crystals. An ELX800 absorbance plate reader (BioTek Instruments, Inc., Bedfordshire, UK) was then used to measure the absorbance of each well at 570 nm.

Subcellular localisation of $TPPS_{2a}$ and $TPCS_{2a}$

PC3 and MLL cells were seeded onto glass bottom dishes FluoroDish™ (World Precision Instruments, Inc.) at 9000 cell/dish and 2000 cell/dish respectively. Cells were allowed to grow for 24 hr before administering photosensitiser solutions in cell media (0.4 µg/ml). 24 hr post administration, dishes were washed once with PBS and fresh no phenol red RPMI 1640 Media, (Gibco®, Invitrogen) was added. After a 4 hr-cell recovery period, dishes were excited “on-stage”. Intracellular localisation before and after excitation, and light-based redistribution of photosensitisers were assessed using an Olympus IMT-2 epi-fluorescence microscope with a low power (2 mW) 405 nm blue diode laser coupled to a liquid light guide. A PIXIS 512 charge-coupled device (CCD) camera (Princeton Instruments) was attached to the microscope, using 20X magnification objective and 250 x 250-micron scale. A 660 nm bandpass detection filter

was used. Pre-excitation fluorescence images were recorded with 1 s exposure, insufficient time to activate $TPPS_{2a}$ or $TPCS_{2a}$. Later images were taken at different times through additional illumination. Image analysis was performed Image J software.

Plates were kept in a 37°C humidified atmosphere containing 5% CO_2 at all times, wrapped in aluminium foil and experimental procedures were carried out protected from light to avoid unintended excitation of photosensitisers.

Subcellular localisation of BPD-MA and $AlPcS_{2a}$ and cell death assessment after light

MLL cells were seeded onto glass bottom dishes at 4000 cell/dish. Cells were allowed to grow for 24 hr before administering photosensitiser solutions in cell media (2 μg/ml). 24 hr post administration, dishes were washed once with PBS and fresh media was added. After a 4 hr-cell recovery period, dishes underwent light treatment at 1 J fluence rate. Subcellular localisation of photosensitisers was observed using an inverted Olympus Fluoview 1000 confocal laser-scanning microscope (40X magnification objective) 2 hr, 24 hr and 48 hr after light treatment. Images were obtained setting BPD-MA excitation at 405 nm and emission 655-755 nm; $AlPcS_{2a}$ was excited using a 635 nm laser and emission was set at 668 nm. Additionally, cell death was evaluated using propidium iodide (PI, Sigma-Aldrich) 1 mg/ml in PBS. PI is a fluorescent stain for nucleic acids, excluded from viable cells due to cell membrane integrity (excitation 559 nm, emission 612 nm). Prior to imaging cell dishes, cell media was replaced with a 1:100 PI solution and incubated during 15 minutes before washing 3 times in PBS, then replacing it with fresh phenol-free RPMI 1640 media. Image analysis was performed with Fluoview FV1000 (Olympus).

Plates were kept in a 37°C humidified atmosphere containing 5% CO_2 at all times, wrapped in aluminium foil and experimental procedures were carried out protected from light to avoid unintended excitation of photosensitisers.

Subcellular localisation of saporin-Alexa-Fluor488® conjugate

PC3 and MLL cells were seeded onto glass bottom dishes FluoroDish™ (World Precision Instruments, Inc.) at 9000 cell/dish and 2000 cell/dish respectively. Cells were allowed to grow for 24 hr before co-administering $TPPS_{2a}$ or $TPCS_{2a}$ (0.4 μg/ml) with saporin-Alexa-Fluor488® (400 nM) in solutions prepared in cell media. 24 hr post administration, dishes were washed once with PBS and fresh no phenol red RPMI 1640 Media, (Gibco®, Invitrogen) was added. Additionally, cells were incubated with 75

nM LysoTracker® Red DND-99 (ThermoFisher Scientific) prepared in no phenol red media during 30 minutes and then washed once in PBS immediately before imaging. After a 4 hr-cell recovery period, images of subcellular localisation of the conjugate saporin-Alexa-Fluor488® and LysoTracker® Red DND-99 were taken using an inverted Olympus Fluoview 1000 confocal laser-scanning microscope, using 488 nm and 559 nm lasers respectively. Fluorescence images were recorded prior to irradiating with a 405 nm laser, known to activate $TPPS_{2a}$ or $TPCS_{2a}$, during 10 seconds; later images were taken at different times through "on-stage" excitation of photosensitisers. Image analysis was performed with Fluoview FV1000 (Olympus). Cells were kept in a 37°C humidified atmosphere containing 5% CO_2 at all times, wrapped in aluminium foil and experimental procedures were carried out protected from light to avoid unintended excitation of photosensitisers.

Fabrication of 3D collagen hydrogels

Type I rat tail collagen (2 mg/ml in 0.6% acetic acid; First Link, UK) was the basic component of the 3D hydrogels. 80% v/v collagen was mixed with 10% v/v Minimum Essential Medium (MEM) 10X (Sigma-Aldrich). Soluble collagen polymerises when pH reaches values above 7; therefore, commercially available collagen is sold as acid solutions and has to be neutralised prior to seeding cells. To neutralise the collagen prepared mixture, 1:10 and 1:100 dilutions of a 46-51% v/v sodium hydroxide solution (Fisher Chemical) were used. In parallel, a PC3 10% v/v cell suspension containing 4000 cells/100 μl gel solution was prepared. Finally, the neutralised mixture was added to the cell suspension. 100 μl of the final solution was added to single wells in a 96-well plate. Plates were kept in a 37°C humidified atmosphere containing 5% CO_2 for 5 minutes until solidification of collagen gels before adding cell media into the wells and re placing the plates in a 37°C humidified atmosphere containing 5% CO_2.

Analysis of cell viability in three dimensional models

Dead/Live staining was performed through the LIVE/DEAD® Cell Imaging Kit (488/570, Thermofisher Scientific) on 3D hydrogels. The kit is based on two fluorescent dyes: on the one hand, calcein AM, which can be converted by intracellular esterases present in viable cells into an intensely green fluorescent calcein. On the other hand, the impairment of dead cells' membrane enables the entry of the red fluorescent component propidium iodide-based.

To perform this dead/live assay, cell media was removed from the wells and gels were incubated with the dead/live dyes for 15 minutes, then washed three times in PBS and imaged using an Olympus Fluoview 1000 confocal laser-scanning microscope. The nature of collagen gels resulted in entrapment of the red fluorescent dye in spite of the washing steps, causing high background in the images. In addition, there was overlapping in the excitation and emission of fluorescence of PI and PS ($TPPS_{2a}$ and $TPCS_{2a}$ employed), hampering the distinction of both compounds. Therefore, only the calcein green channel was imaged (excitation 495 nm, emission 515 nm), which was combined with transmitted light to evaluate cell viability. Image analysis was performed with Fluoview FV1000 (Olympus).

Statistical analysis

Statistical analysis was performed using GraphPad prism 6. Two-way ANOVA followed by Bonferroni *post hoc* multiple comparison was used. Data is displayed as mean with error bars +/- SEM; significance level of $p < 0.05$ (*p = 0.05 to 0.01; **p = 0.01 to 0.001; ***p = 0.001 to 0.0001)

All experiments were carried out in triplicate. Specifically, in MTT cell viability assays, each data point was the result of experiments carried out in triplicate and each of these repeats was the average of 8-16 wells.

2.4 Results

2.4.1 Photosensitiser spectra

In order to tailor light treatments to specifically excite each photosensitiser, solutions of all the compounds used throughout the project were prepared in methanol and both absorption and emission spectra were measured.

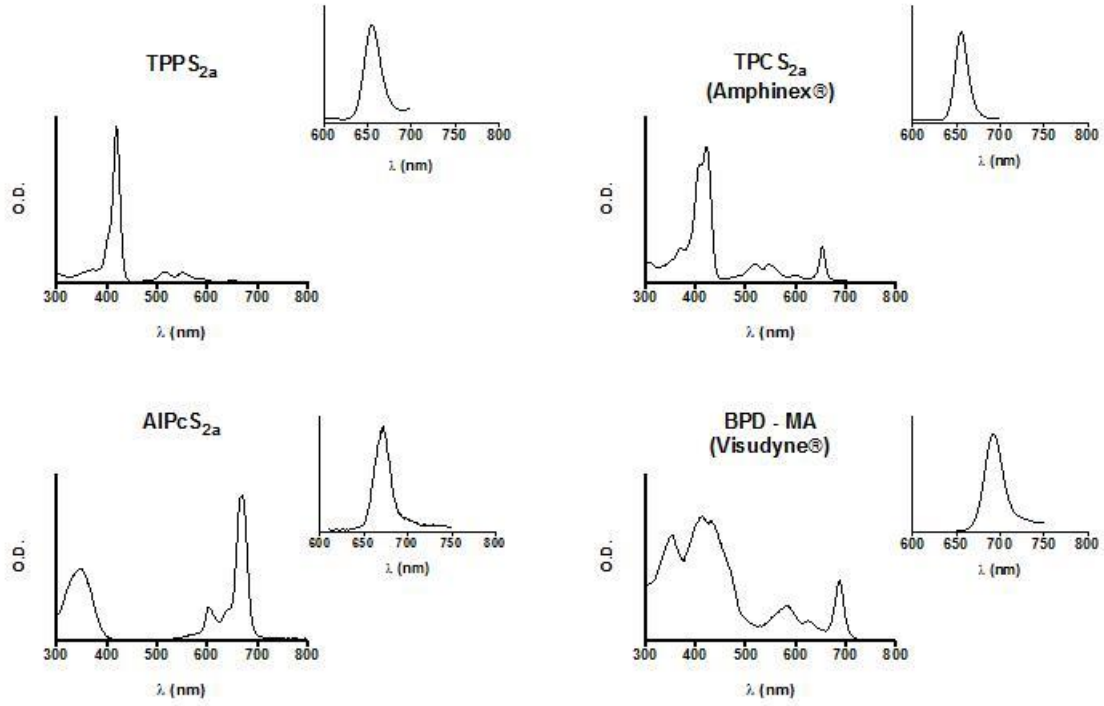

Figure 11. Absorption and emission spectra of $TPPS_{2a}$, $TPCS_{2a}$, BPD-MA, $AlPcS_{2a}$ in methanol (1-15 μM).

Emission spectra were taken exciting $TPPS_{2a}$, $TPCS_{2a}$ and BPD-MA at 420 nm and $AlPcS_{2a}$ at 600 nm; cut-off filters set at 515 nm. Graphs in the right corner of each PS correspond to the emission peaks in the red.

Both the porphyrin- ($TPPS_{2a}$ and BPD-MA) and chlorin- ($TPCS_{2a}$) based photosensitisers showed an absorption peak at around 420 nm, corresponding to the peak of the Soret absorption band. Absorption in the red region of the spectra were also found in all of the above, being particularly noticeable in $TPCS_{2a}$ (Amphinex®) and BPD-MA at 650 nm and 690 nm respectively. Conversely, the phtalocyanine-based photosensitiser ($AlPcS_{2a}$) showed an absorption peak at around 670 nm as well as an additional prominent peak in the ultraviolet region of the spectrum, approximately at

350 nm. All four $TPPS_{2a}$, $TPCS_{2a}$, BPD-MA and $AlPcS_{2a}$ exhibited fluorescence emission peaks in the red spectra. $TPPS_{2a}$, $TPCS_{2a}$, BPD-MA showed emission peaks at 654 nm, 655 nm and 672 nm when exciting at 420 nm; while $AlPcS_{2a}$'s emission peak was found at 692 nm exciting at a higher wavelength, 600 nm (Figure 11).

2.4.2 $TPPS_{2a}$ and TPCS2a uptake in prostate cancer cells

The uptake of $TPPS_{2a}$ and $TPCS_{2a}$ was measured in both rat and human prostate cancer cell lines (MatLyLu and PC3 respectively), related to the overall emission of fluorescence by PS. Specifically, solutions of both photosensitisers were prepared at different concentrations ranging 0.2 – 0.8 μg/ml and following a 24 hr incubation, uptake was measured. Figure 2 shows a comparison of the uptake of both photosensitisers at the different concentrations in PC3 and MatLyLu.

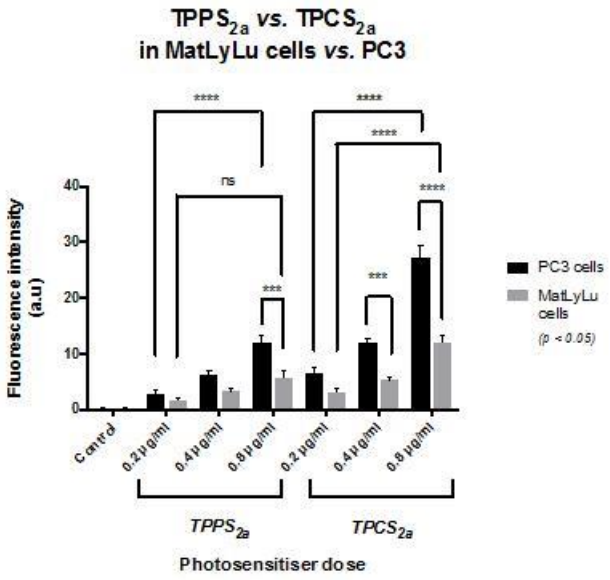

Figure 12. Uptake of $TPPS_{2a}$ and $TPCS_{2a}$ in rat and human prostate cancer cells (MatLyLu and PC3 respectively).

Cells were incubated for 24 hr with 0.2, 0.4 and 0.8 μg/ml photosensitiser solutions, then washed and media was replaced with no phenol red media. Uptake was related to photosensitiser fluorescence intensity. Data is displayed as mean with error bars +/- SEM; two-way ANOVA followed by Bonferroni post hoc multiple comparison was used, significance level of $p < 0.05$.

In both cell lines a concentration dependency was seen, being retention higher in PC3 cells in all cases. A significant increase ($p < 0.001$) in the uptake of both $TPPS_{2a}$ and $TPCS_{2a}$ in PC3 cells was found between 0.2 μg/ml and 0.8 μg/ml, which was also seen in MatLyLu cells when measuring uptake of Amphinex. This photosensitiser also

exhibited the greatest differences between both cell lines. Fluorescence of Amphinex was nearly 2-fold higher than $TPPS_{2a}$ in both cell lines at 0.8 μg/ml (Figure 12).

2.4.3 Saporin dose-response curves

As discussed previously, PCI aims to enhance the delivery of drugs, which will translate in an improvement of drug-based cytotoxicity. Therefore, in order to determine the optimal doses required for PCI combination experiments, it is essential to first determine the most adequate dosage of each drug independently (both photosensitiser and drug to be delivered). To accomplish this, a range of saporin, $TPPS_{2a}$ and $TPCS_{2a}$ doses were assayed in both PC3 and MLL cells to establish subthreshold values of all independently (see section below for photosensitiser dose response study).

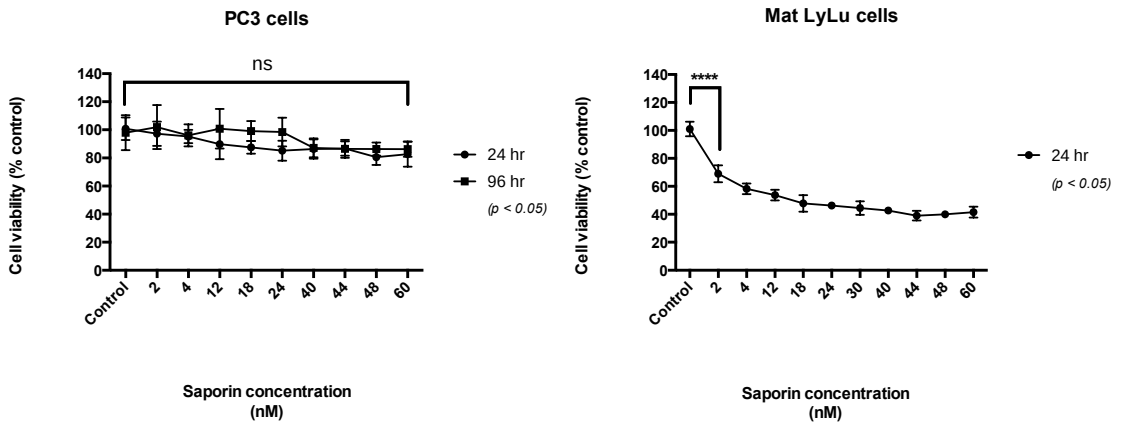

Figure 13. Saporin cytotoxicity in PC3 and MatLyLu cells.

Both cell lines were incubated with saporin solutions ranging 0-60 nM during 24 hr, drugs were then washed off and cell viability was measured 24 hr and 96 hr after light treatment in later PCI combination experiments. Data is displayed as mean with error bars +/- SEM; two-way ANOVA followed by Bonferroni post hoc multiple comparison was used, significance level of $p < 0.05$.

Saporin did not result in significant cytotoxicity in the 0-60 nM range assayed in PC3 cells compared to the control group. Unlike the human prostate cancer model, the rat counterpart exhibited higher sensitivity to the RIP type 1. Even the lowest dose tested (2 nM) measured only 24 hr after drug removal, resulted in 25% cell death. There was a direct dependency between drug dose and cytotoxicity observing a plateau when cell viability was reduced to 40% of control cells (Figure 13).

These saporin drug-response curves served as basis to establish drug doses required in PCI combination experiments. Founded on the higher sensitivity seen in MatLyLu

cells when measuring cell viability just 24 hr after the "hypothetical" performance of light treatment, even the lowest dose assayed (2 nM) would result in higher cell death than the required threshold. Conversely, the human counterpart seemed to be more robust and not affected as much by the RIP type 1 toxin, regardless of the dose used. Therefore, 20 pM and 2 nM were the chosen doses to combine with photosensitisers in PCI in MatLyLu (further reduced from the lowest 2 nM dose examined in Figure 13 to achieve subthreshold toxicity) and PC3 cells respectively.

2.4.4 PDT effect in dose-response curves

Photosensitiser dosage was also evaluated in rat and human cells incubating these with different solutions of $TPPS_{2a}$ and $TPCS_{2a}$, and then exposing the system to light to establish an adequate "low-dose" PDT effect (see Figure 14 and Figure 15). A 3-minute illumination (1.26 J light fluence rate using the Lumisource lamp) was chosen as a start point based on previous studies carried out within the research group.

A direct relationship between photosensitiser dose and cytotoxicity was observed with both compounds under investigation in human prostate cancer cells (PC3 cells, Figure 14), which further increased when cell viability was measured at a later time point after light (Figure 14B, Figure 14D). 24 hr after light, significant cell killing was found only at the highest $TPCS_{2a}$ dose tested (0.8 μg/ml), where only 41% +/- 8 cells would remain viable (Figure 14C). Under these same circumstances, 68% +/- 8 cells remained viable when exposed to $TPPS_{2a}$-based PDT (Figure 14A). If measured 96 hr after light treatment, these cell viability values decreased to 55% +/- 11 and 21% +/- 13 for $TPPS_{2a}$- and $TPCS_{2a}$- PDT respectively (Figure 14B, Figure 14D).

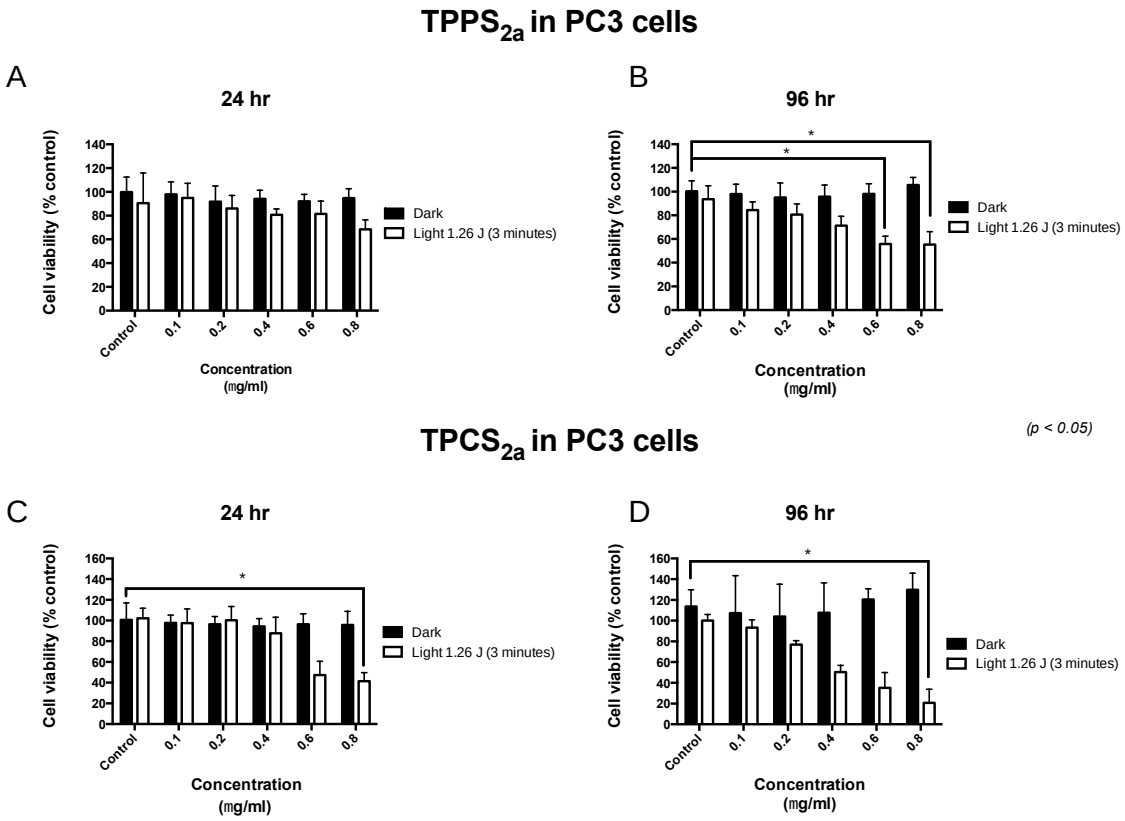

Figure 14. Evaluation of PDT effect in PC3 cells.

Cells were incubated with either $TPPS_{2a}$ (A, B) or $TPCS_{2a}$ (C, D) solutions ranging 0-0.8 μg/ml during 24 hr, drugs were then washed off and a 4 hr chase period was allowed before illumination. Cell viability was measured 24 hr and 96 hr after light treatment. Data is displayed as mean with error bars +/- SEM; two-way ANOVA followed by Bonferroni post hoc multiple comparison was used, differences between dark control and light groups are shown; significance level of $p < 0.05$.

A correlation between photosensitiser doses and cell death was also found in rat prostate cancer cells (MatLyLu cells, Figure 15). Similar to the saporin dose-response curves, these cells appeared to be more sensitive to PDT than the human counterpart. A significant reduction in cell viability was found from 0.2 μg/ml $TPPS_{2a}$, which resulted in 55% +/- 8 viable cells only 24 hr after light (Figure 15A); viability values for $TPCS_{2a}$-PDT at this point were 83% ± 13 (Figure 15B).

No dark toxicity was found regardless of the photosensitiser dose neither in the human nor rat model.

PCI aims to benefit from low dose PDT. In line with this, and based on the above results, 0.2 and 0.4 μg/ml were the subthreshold doses chosen (resulting in below 50% cell death when exposed to PDT alone) for both photosensitisers in later experiments combining photosensitisers with saporin (PCI).

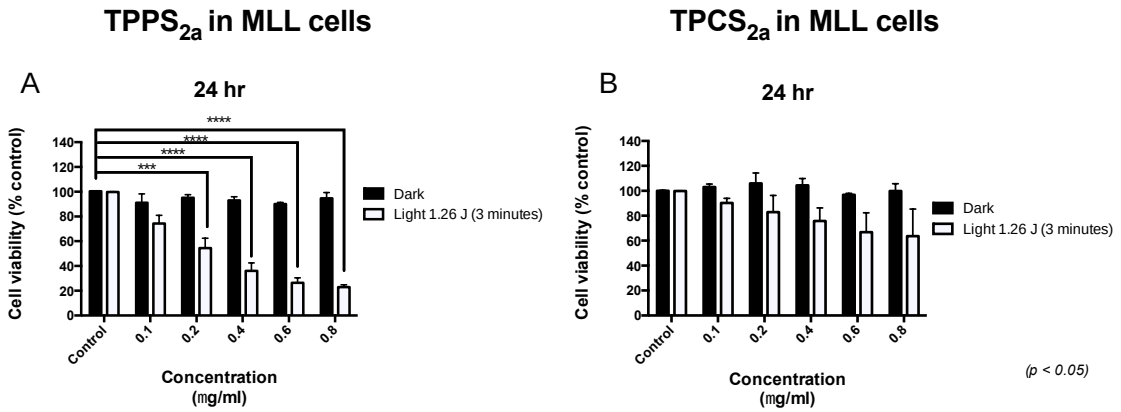

Figure 15. Evaluation of PDT effect in MatLyLu cells.

Cells were incubated with either $TPPS_{2a}$ (A) or $TPCS_{2a}$ (B) solutions ranging 0-0.8 μg/ml during 24 hr, drugs were then washed off and a 4 hr chase period was allowed before illumination. Cell viability was measured 24 hr after light treatment. Data is displayed as mean with error bars +/- SEM; two-way ANOVA followed by Bonferroni post hoc multiple comparison was used, differences between dark control and light groups are shown; significance level of $p < 0.05$.

2.4.5 PCI combination experiments

Successful performance of PCI requires a challenging optimisation of the treatment due to the amount of variables influencing and involved in the therapeutic outcome. Several experimental conditions were assayed using PC3 and MatLyLu cells to establish he optimal PCI procedure, which would result in maximal cell kill. Some of the variables that will be reported below are illumination (fluence rate), interval between drug removal and light-excitation (drug light interval, DLI) or performance of a "light-before" approach.

2.4.5.1 Light dose

Taking 1.26 J (equivalent to 3 minutes of light, using the Lumisource lamp) as a starting illumination time, different light doses were tested in PCI experiments. A clear PCI effect was found 24 hr after exposure to light being this nearly 2-fold more cytotoxic that PDT in PC3 cells (Figure 16A, Figure 16C). Briefly, cell viability was further reduced 29% and 9% combining $TPPS_{2a}$ (0.2 and 0.4 μg/ml respectively) with saporin (Figure 16A). As for Amphinex ($TPCS_{2a}$), combination with saporin resulted in a further 35% and 31% reduction in cell viability (0.2 and 0.4 μg/ml $TPCS_{2a}$ doses

respectively) (Figure 16C). Overall, a maximum 1.6-fold greater cytotoxicity was seen after PCI.

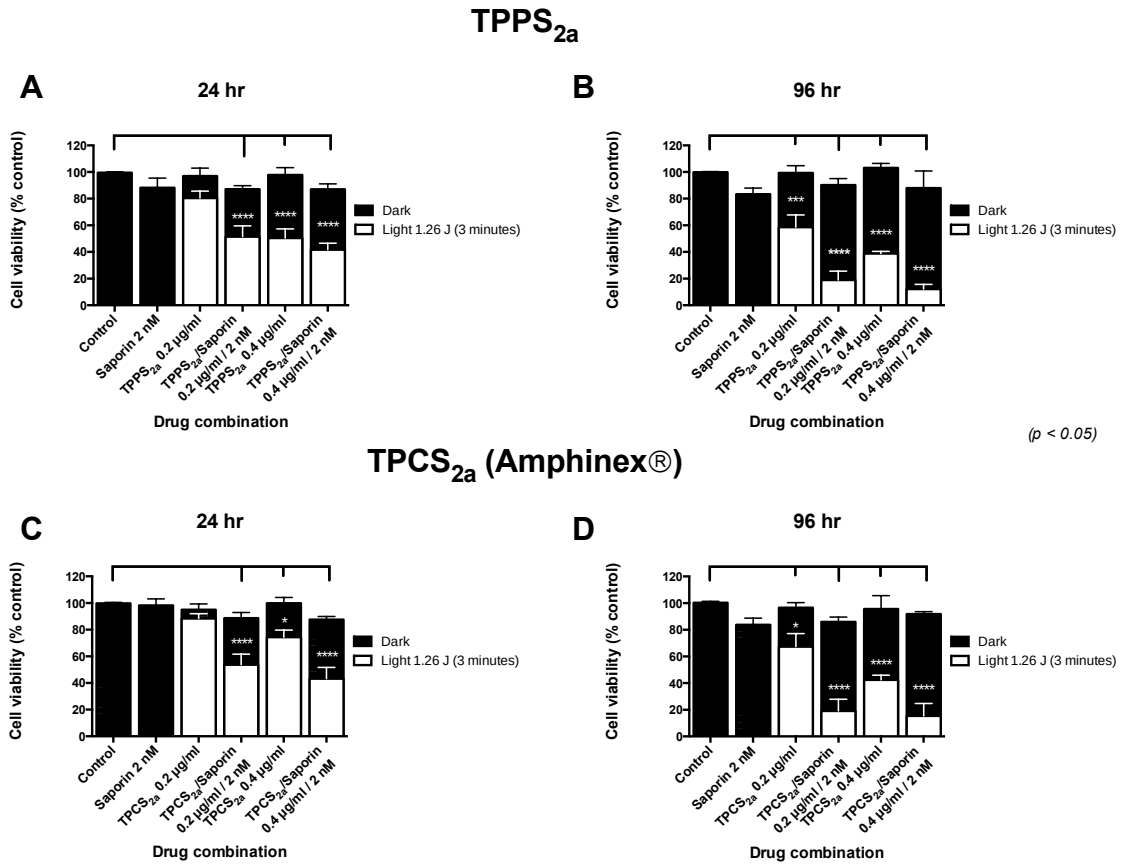

Figure 16. Assessment of PDT/PCI effect in PC3 cells after light (1.26 J, 3 minutes).

Cells were incubated with either 0.2 or 0.4 μg/ml solutions of $TPPS_{2a}$ (A, B) or $TPCS_{2a}$ (C, D), alone or in combination with saporin 2 nM for 24 hr. Drugs were then washed off and a 4 hr chase period was allowed before illumination. Cell viability was measured 24 hr and 96 hr after light treatment. Data is displayed as mean with error bars +/- SEM; two-way ANOVA followed by Bonferroni post hoc multiple comparison was used, differences between dark control and light groups are shown; significance level of $p < 0.05$.

The latest time point tested after light (96 hr) for cell death of PC3 cells, showed the greatest PCI effect in both photosensitisers. $TPPS_{2a}$-PCI resulted in at least 3-fold higher cell killing than the PDT equivalent at both 0.2 and 0.4 μg/ml photosentiser doses (Figure 16B). This was slightly higher for $TPCS_{2a}$-PCI (compared to $TPPS_{2a}$), which resulted in a 3.5-fold higher cell death for the lowest photosensitiser dose (0.2 μg/ml) (Figure 16D). The mean viability after PDT was 67% and after $TPCS_{2a}$-PCI (96 hr and 0.2 μg/ml) was 19%, corresponding to a ratio of 3.5 increase in cell killing with PCI *vs* PDT. As indicated in Figure 13 and Table 5, saporin had a negligible effect on this ratio, since cytotoxicity induced by saporin alone was less than 10%. Hence, cell death in PCI did not correspond to a mere addition, but *synergy* between saporin and

PDT. If the PCI effect had been merely additive (i.e. PDT + addition of saporin), then then the observed ratio between PDT and PCI would have been close to 1.

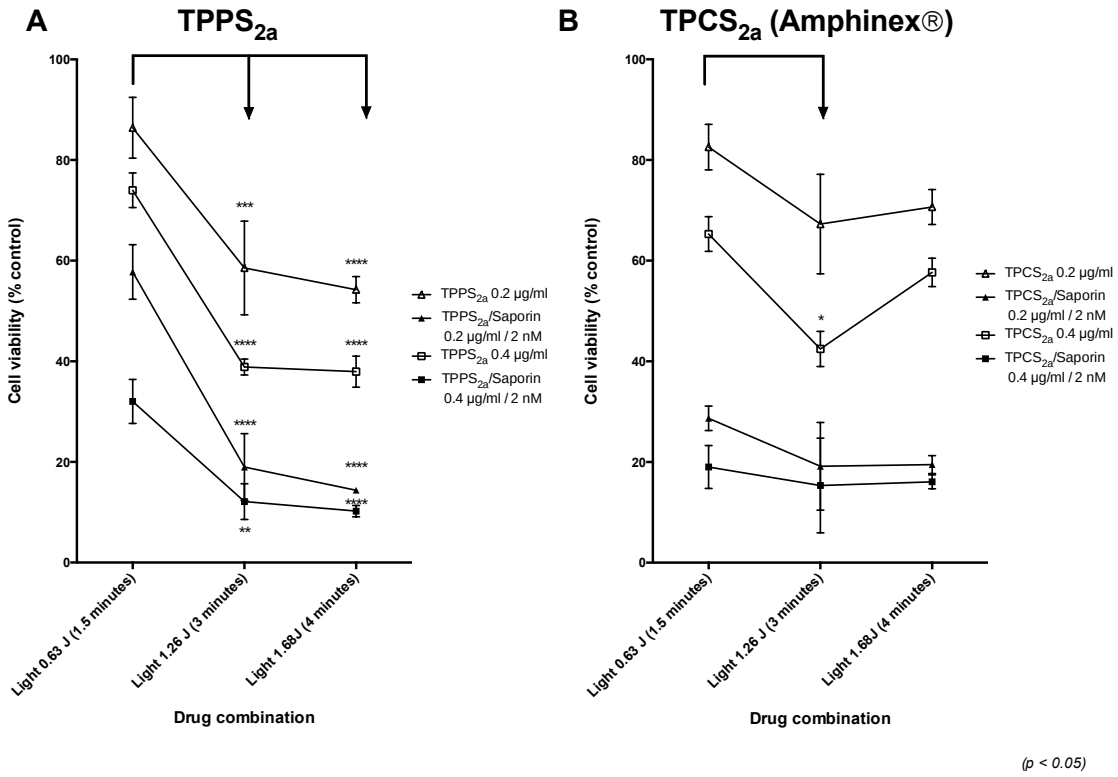

Figure 17. PDT/PCI effect in PC3 cells 96 hr after different light doses.

Cells were incubated with either 0.2 or 0.4 µg/ml solutions of $TPPS_{2a}$ (A) or $TPCS_{2a}$ (B), alone or in combination with saporin 2 nM for 24 hr. Drugs were then washed off and a 4 hr chase period was allowed before illumination. Cell viability was measured 96 hr after light treatment. Data is displayed as mean with error bars +/- SEM; two-way ANOVA followed by Bonferroni post hoc multiple comparison was used, differences between light groups are shown; significance level of p < 0.05.

Figure 17 displays a comparison of PDT and PCI effect in PC3 cells 96 hr after three different light doses (0.63 J, 1.26 J and 1.68 J). A significant increase in cell death was found when light fluence was doubled from 0.63 to 1.26 J in all $TPPS_{2a}$ cases (Figure 17A). However, a substantial difference was only found using $TPCS_{2a}$ as photosensitiser in the 0.4 µg/ml PDT group. In addition, light doses higher than 1.26 J did not seem to significantly affect cell viability of PC3 cells at the doses and experimental conditions tested.

Likewise, a comparison of cell viability of MatLyLu cells after PDT and PCI using different light doses was performed (Figure 18). Given the relevance of Amphinex® in the *in vivo* studies (see Chapter 4), $TPPS_{2a}$ was not further investigated *in vitro* in the rat prostate cancer model (MatLyLu).

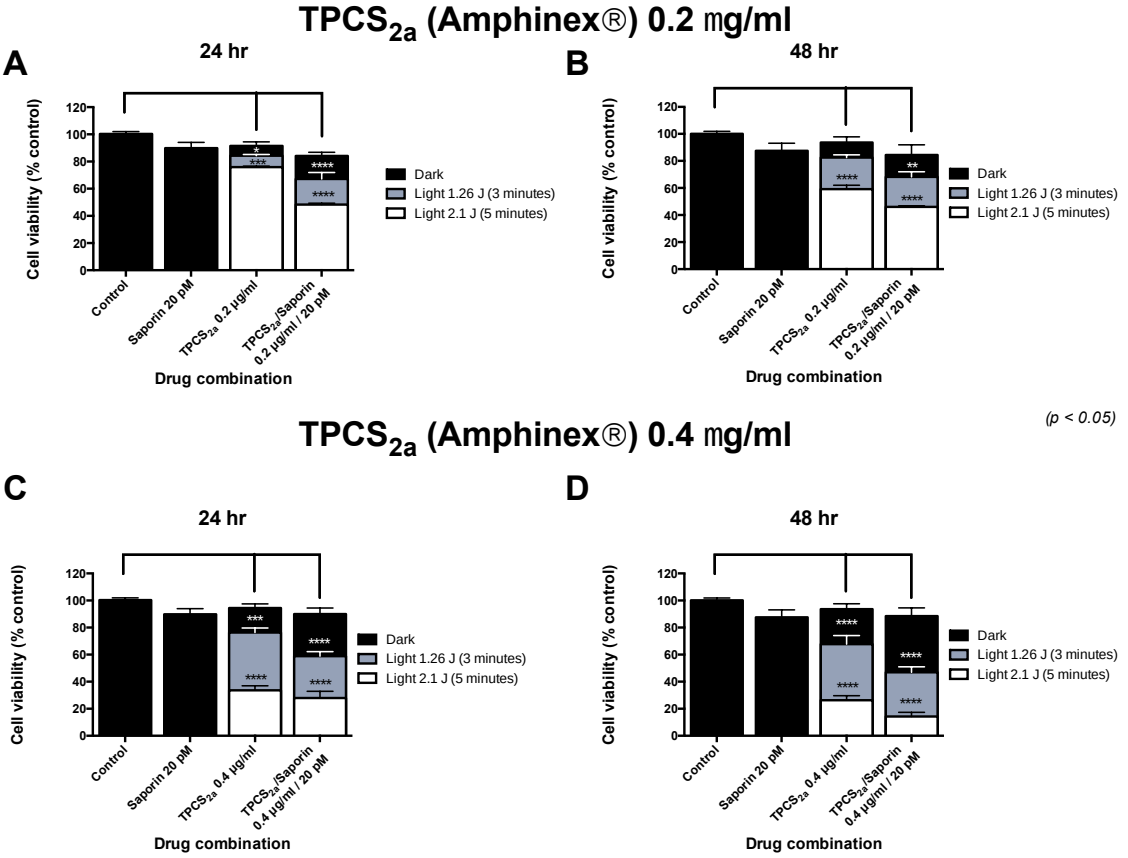

Figure 18. PDT/PCI effect in MatLyLu cells 24 hr and 48 hr after different light doses.

Cells were incubated with either a 0.2 μg/ml (A, B) or 0.4 μg/ml (C, D) solution of $TPCS_{2a}$, alone or in combination with saporin 20 pM for 24 hr. Drugs were then washed off and a 4 hr chase period was allowed before illumination. Cell viability was measured 24 hr or 48 hr after light treatment. Data is displayed as mean with error bars +/- SEM; two-way ANOVA followed by Bonferroni post hoc multiple comparison was used, differences between dark control and light groups are shown; significance level of $p < 0.05$.

This study carried out on MatLyLu cells also showed an enhancement in cell death after PCI in all cases (Figure 18). The highest light dose tested (2.1 J) led to the smallest differences in cell death after PDT and PCI in nearly all cases: 6% (24 hr after light for 0.4 μg/ml), 13% and 12% (48 hr after light for 0.2 μg/ml and 0.4 μg/ml respectively). Yet, 28% resulted from the 24 hr measurements using 0.2 μg/ml $TPCS_{2a}$ (Figure 19A). A relatively similar cell killing efficacy was observed in cells treated with 1.26 J at both photosensitiser doses: 17% and 18% (24 hr after light for 0.2 μg/ml and 0.4 μg/ml respectively), or else 14% and 21% (48 hr after light for 0.2 μg/ml and 0.4 μg/ml respectively) reduction in viable cells. The lowest % of viable cells was seen after 48 hr combining $TPCS_{2a}$ 0.4 μg/ml and saporin 20 pM following a PCI approach, treatment which led to 86% cell death (Figure 18D, Figure 19B)

The direct comparison of cell killing between both light treatment groups revealed significant differences between the lowest and highest dose tested for both PDT and PCI and both 24 hr and 48 hr after light in MatLyLu cells (Figure 19). Cell viability measurements after the highest light dose led to the greatest therapeutic outcome of light treatments, especially at the later time point, 48 hr after light. (Figure 19B)

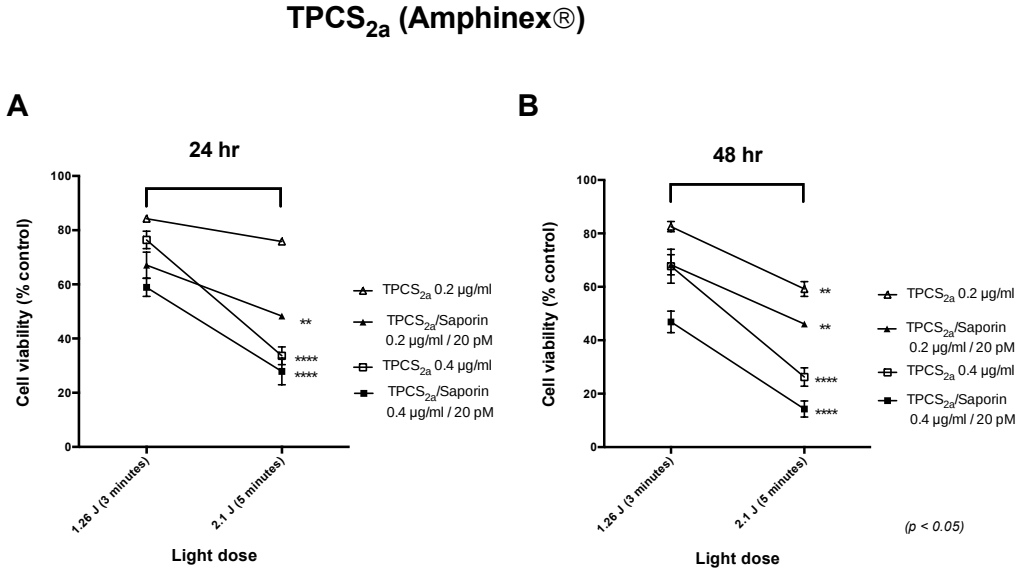

Figure 19. Comparison of light groups after PDT/PCI in MatLyLu cells.

Cells were incubated with either a 0.2 µg/ml or 0.4 µg/ml solution of $TPCS_{2a}$, alone or in combination with saporin 20 pM for 24 hr. Drugs were then washed off and a 4 hr chase period was allowed before illumination. Cell viability was measured 24 hr (A) or 48 hr (B) after light treatment. Data is displayed as mean with error bars +/- SEM; two-way ANOVA followed by Bonferroni post hoc multiple comparison was used, differences between light doses are shown; significance level of $p < 0.05$.

2.4.5.2 Drug-light interval (DLI)

The time window allowed between drug removal and light (DLI) is thought to be particularly important *in vitro* after PCI (indicated as chase period throughout the present chapter). During this time, internalisation of photosensitisers from the external cell membrane into cytosolic endo/lysosomal membranes is enabled in order to achieve a photo-oxidative effect at a subcellular level. Founded on this, the therapeutic effect resulting from different DLIs was evaluated in PC3 (Figure 20, Figure 21) and MatLyLu (Figure 22) cells and results are subsequently reported below.

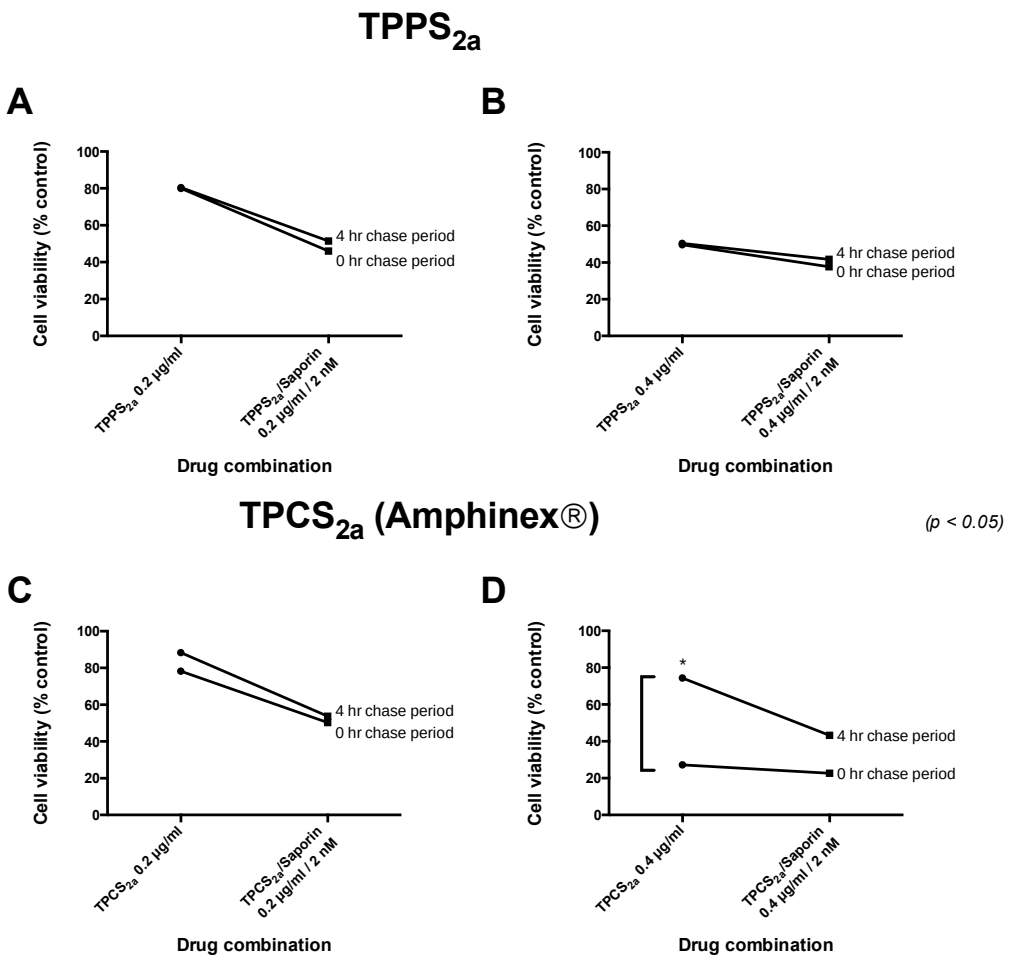

Figure 20. Comparison in PDT/PCI effect with/without chase period before light in PC3 cells.

Cells were incubated with either 0.2 or 0.4 μg/ml solutions of $TPPS_{2a}$ (A, B) or $TPCS_{2a}$ (C, D), alone or in combination with saporin 2 nM for 24 hr. Drugs were then washed off and either a 0 hr or 4 hr chase period was allowed before illumination (1.26J). Cell viability was measured 24 hr after light treatment. Data is displayed as mean; two-way ANOVA followed by Bonferroni post hoc multiple comparison was used, differences between drug light interval groups are shown; significance level of $p < 0.05$.

As shown in Figure 20, the performance of light treatment immediately after drug removal (0 hr chase/drug light interval) resulted in no differences in cell viability compared to the 4 hr DLI in PC3 cells except for $TPCS_{2a}$ 0.4 μg/ml (Figure 20D). In this case, the combination of photosensitiser and saporin did not further enhance cell death and PCI effect was not different to that of PDT 24 hr after light in the 0 hr DLI group.

Further investigation of this in PC3 cells 72 hr after light is shown in Figure 21. In both cases, similar cell viability resulted from 0.4 μg/ml of either photosensitiser after PDT and PCI (see Figure 21A for $TPPS_{2a}$, Figure 21B for $TPCS_{2a}$). Briefly, 29% +/- 13 and 6% +/- 6 cells were viable after $TPPS_{2a}$ (PDT and PCI respectively); while 12% +/- 8 and 10% +/- 6 were the viability values for $TPCS_{2a}$ (PDT and PCI respectively). In the

lowest photosensitiser dose (0.2 μg/ml), an enhancement in cell viability was found with PCI.

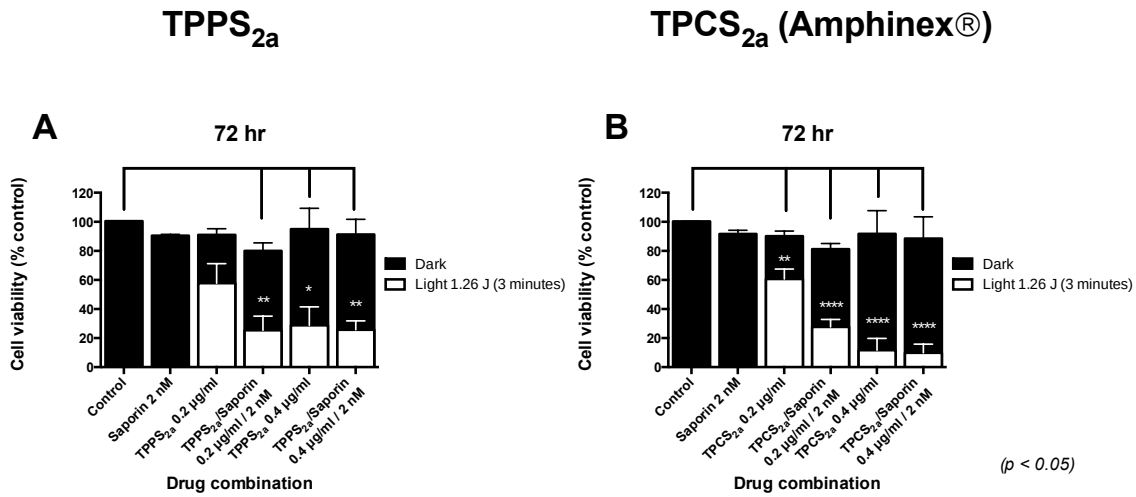

Figure 21. Comparison in PDT/PCI effect without chase period before light in PC3 cells.

Cells were incubated with either 0.2 or 0.4 μg/ml solutions of $TPPS_{2a}$ (A) or $TPCS_{2a}$ (B), alone or in combination with saporin 2 nM for 24 hr. Drugs were then washed off and immediately subject to light treatment (1.26 J). Cell viability was measured 72 hr after light treatment. Data is displayed as mean with error bars +/- SEM; two-way ANOVA followed by Bonferroni post hoc multiple comparison was used, differences between dark control and light groups are shown; significance level of p < 0.05.

On their side, despite the fact that no significant differences between DLI groups were seen in MatLyLu cells, there was a general trend to reduce cell death when increasing the length of the chase period; being cytotoxicity more noteworthy post PCI than PDT of $TPCS_{2a}$ (Figure 22).

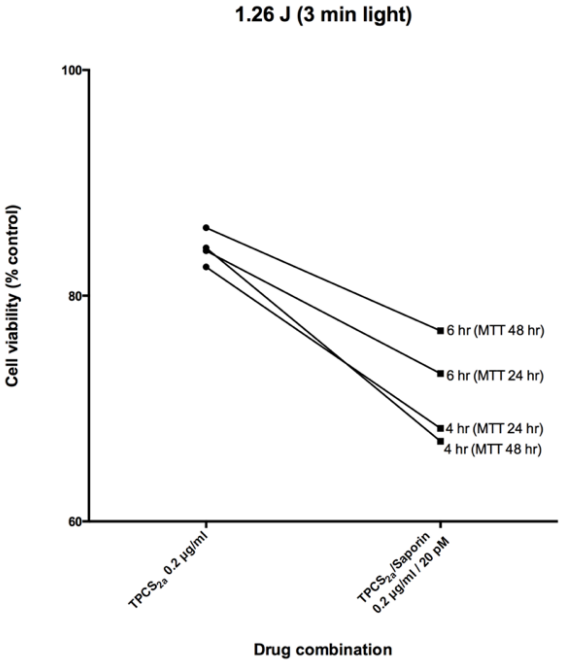

Figure 22. Comparison in PDT/PCI effect after 4 hr or 6 hr chase period in MatLyLu cells.

Cells were incubated with either 0.2 μg/ml solutions of $TPCS_{2a}$ alone or in combination with saporin 20 pM for 24 hr. Drugs were then washed off and either a 4 hr or 6 hr chase period was allowed before illumination (1.26 J). Cell viability was measured 24 hr and 48 hr after light treatment. Data is displayed as mean; two-way ANOVA followed by Bonferroni post hoc multiple comparison was used; significance level of p < 0.05.

2.4.5.3 Light-before PCI

A brief study into the "light-before" PCI procedure was performed on PC3 cells, as shown in Figure 23.

Differences in cell death after "light-before" PCI resulted in 3% - 11% between PDT and PCI. In these cases, PCI did not result in a significant enhancement of the therapeutic outcome, not even when cell viability was measured 96 hr after light. In addition, in the best case, cell viability was reduced to 67% (Figure 23D), and in all groups investigated, cell death remained within 13% (for $TPCS_{2a}$, PDT 24 hr after light – Figure 23C) and 34% (for $TPCS_{2a}$, PCI 96 hr after light – Figure 23D), which was only slightly over 1-fold greater post PCI than PDT (Figure 23). PDT only resulted in significant cell death 24 hr after light in cells treated with $TPPS_{2a}$ (Figure 23A); while cell killing was still significant in all PCI light groups.

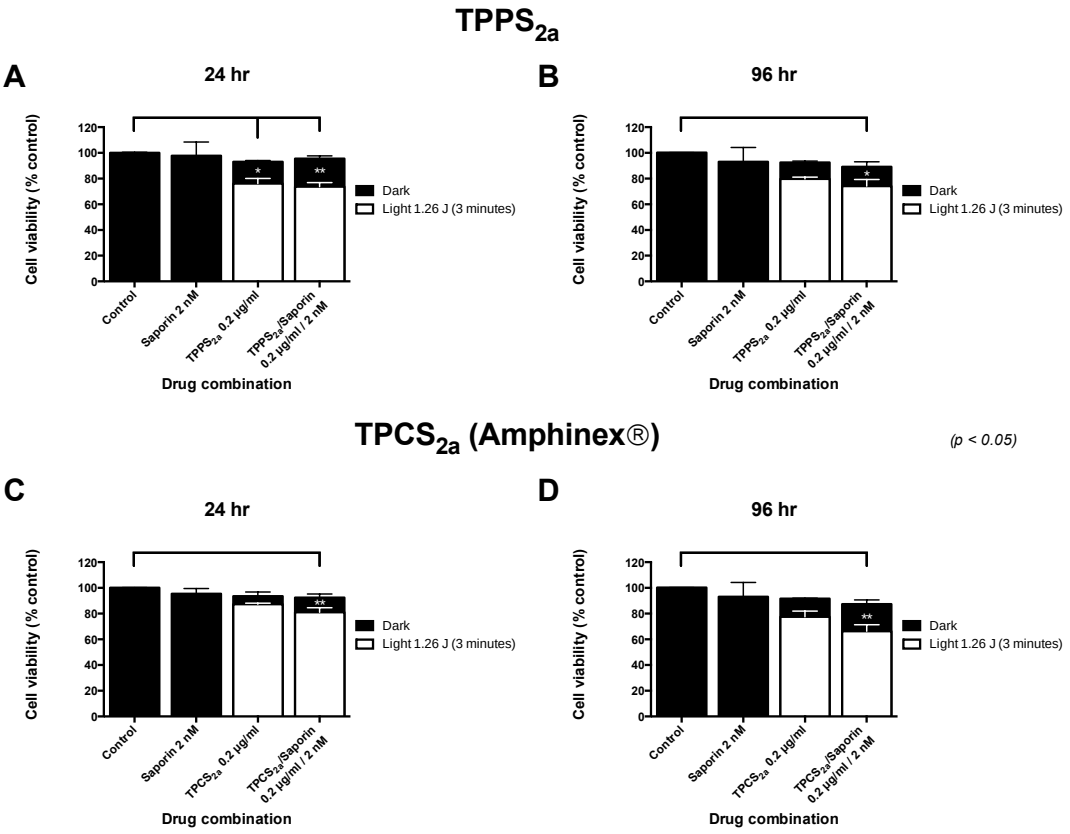

Figure 23. "Light-before" PDT/PCI effect in PC3 cells.

Cells were incubated with 0.2 µg/ml solutions of either $TPPS_{2a}$ (A) or $TPCS_{2a}$ (B) during 24 hr. Photosensitiser solutions were then washed off and a 4 hr chase period was allowed before illumination. A solution of saporin 2 nM was administered immediately after illumination for 24 hr. After this period, drug solutions were removed and cell viability was measured 24 hr and 96 hr after light treatment (1.26 J). Data is displayed as mean with error bars +/- SEM; two-way ANOVA followed by Bonferroni post hoc multiple comparison was used, differences between dark control and light groups are shown; significance level of $p < 0.05$

TPPS2a in PC3 cells

LIGHT AFTER - Cell viability values shown as media ± SEM

		24 hr						72 hr			96 hr		
		NO CHASE		4hr chase				NO CHASE			4hr chase		
		Dark	1.26 J (3minutes)	Dark	0.63 J (1.5 minutes)	1.26 J (3minutes)	1.68 J (4minutes)	Dark	1.26 J (3minutes)	Dark	0.63 J (1.5 minutes)	1.26 J (3minutes)	1.68 J (4minutes)
	Control	99.8 ± 0.4		99.6 ± 0.6				100.4 ± 0.2			99.8 ± 0.6		
	Saporin 2 nM	101.6 ± 4.4		88.3 ± 7.2				90.5 ± 0.9			83.4 ± 4.6		
PDT	$TPPS_{2a}$ 0.2 µg/ml	93.6 ± 4.4	80.2 ± 9.4	97.1 ± 6	82.57 ± 4.16	80.4 ± 5.3	83.2 ± 3	91 ± 4.3	57.8 ± 13.4	99.3 ± 5.4	86.4 ± 6.1	58.6 ± 9.3	54.2 ± 2.6
PCI	$TPPS_{2a}$ / Saporin 0.2 µg/ml / 2 nM	82.4 ± 4	46.2 ± 0.7	87.2 ± 2.7	63.45 ± 2.6	51.4 ± 8.2	48.8 ± 1.3	80 ± 5.5	25.3 ± 9.7	90.1 ± 4.9	57.8 ± 5.4	19 ± 6.7	14.4 ± 0.6
PDT	$TPPS_{2a}$ 0.4 µg/ml	97.2 ± 13.3	49.6 ± 11.4	97.9 ± 5.5	75 ± 4.1	50.4 ± 7	64.8 ± 3.8	95± 14.3	28.8 ± 12.7	103.1 ± 3.4	74 ± 3.5	39 ± 1.6	37.9 ± 3.1
PCI	$TPPS_{2a}$ / Saporin 0.4 µg/ml / 2 nM	92.3 ± 8.8	37.7 ± 5	87.1 ±4	56.4 ± 3.1	41.7 ± 4.9	46.6 ± 1.7	91.3 ±10.5	25.8 ± 6	87.9 ± 12.8	32 ± 4.4	12.1 ± 3.6	10.2 ± 1.1

TPCS2a in PC3 cells

LIGHT AFTER - Cell viability values shown as media ± SEM

		24 hr						72 hr			96 hr		
		NO CHASE		4hr chase				NO CHASE			4hr chase		
		Dark	1.26 J (3minutes)	Dark	0.63 J (1.5 minutes)	1.26 J (3minutes)	1.68 J (4minutes)	Dark	1.26 J (3minutes)	Dark	0.63 J (1.5 minutes)	1.26 J (3minutes)	1.68 J (4minutes)
	Control	100.2 ± 0.1		99.7 ± 0.7				100.2 ± 0.1			100.2 ± 1.2		
	Saporin 2 nM	99.4 ± 1.3		98.2 ± 4.9				91.6 ± 2.5			83.8 ± 5		
PDT	$TPCS_{2a}$ 0.2 µg/ml	94.5 ± 3.9	78.3 ± 3.3	94.9 ± 4.4	86.1 ± 6.7	88.4 ± 3.6	90 ± 1.9	90 ± 3.6	60.8 ± 6.8	96.5 ± 3.8	82.6 ± 4.52	67.3 ± 9.9	70.7 ± 3.5
PCI	$TPCS_{2a}$ / Saporin 0.2 µg/ml / 2 nM	84.8 ± 2.4	50.4 ± 7.9	88.7 ± 4.3	68.6 ± 2.7	53.7 ± 7.9	52.8 ± 5.6	81.3 ± 3.9	27.7 ± 5.2	85.9 ± 3.7	28.7 ± 2.4	19.2 ± 8.7	19.5 ± 1.8
PDT	$TPCS_{2a}$ 0.4 µg/ml	93.2 ± 17	27.2 ± 14.1	99.8 ± 4.4	81.7 ± 5.2	74.4 ± 5.4	79.2 ± 2.6	91.8 ± 15.9	11.7 ± 8	95.6 ± 10.1	65.3 ± 3.5	42.5 ± 3.5	57.7 ± 2.8
PCI	$TPCS_{2a}$ / Saporin 0.4 µg/ml / 2 nM	86.2 ± 8.4	22.6 ± 7.8	87.6 ± 2.3	62.5 ± 4.1	43.2 ± 8.4	50.5 ± 1.5	88.4 ± 15	9.9 ± 5.9	91.8 ± 1.9	10 ± 4.3	15.4 ± 9.4	16.1 ± 1.4

TPPS2a and TPCS2a in PC3 cells

LIGHT BEFORE

Cell viability values shown as media ± SEM

		24 hr		96 hr	
		4hr chase		4hr chase	
		Dark	1.26 J (3minutes)	Dark	1.26 J (3minutes)
	Control	100 ± 0.4		100.2 ± 0.07	
	Saporin 2 nM	97.8 ± 10.7		93.07 ± 11.2	
PDT	$TPPS_{2a}$ 0.2 µg/ml	93 ± 1	76.1 ± 4	92.6 ± 1.1	79.7 ± 1.4
PCI	$TPPS_{2a}$ / Saporin 0.2 µg/ml / 2 nM	95.5 ± 2.2	73.7 ± 3.1	89.1 ± 3.8	74.1 ± 5.2
PDT	$TPCS_{2a}$ 0.2 µg/ml	93.6 ± 3.3	87.3 ± 0.8	91.6 ± 0.4	77.4 ± 4.5
PCI	$TPCS_{2a}$ / Saporin 0.2 µg/ml / 2 nM	92.5 ± 2.8	81 ± 3.6	87.3 ± 3.3	66.3 ± 5

Table 5. Summary of cell viability after PDT/PCI in PC3 cells.

$TPCS_{2a}$- and $TPPS_{2a}$- based PDT and PCI 24 hr and 96 hr after delivery of light. Shown both light after and light before results under different drug-light interval and light conditions.

TPCS2a in MaLyLu cells

LIGHT AFTER - Cell viability values shown as media ± SEM

		24hr						48hr					
		Dark	4 hr chase 1.26 J (3minutes)	2.1 J (5minutes)	Dark	6hr chase 1.26 J (3minutes)	2.1 J (5minutes)	Dark	4 hr chase 1.26 J (3minutes)	2.1 J (5minutes)	Dark	6hr chase 1.26 J (3minutes)	2.1 J (5minutes)
	Control		100.3 ± 1.7			99.9 ± 0.6			100.1 ± 1.8			101.1 ± 2.2	
	Saporin 20 Pm		89.9 ± 4.2			90.6 ± 2.6			87.5 ± 5.6			87.3 ± 2.9	
PDT	TPCS$_{2a}$ 0.2 µg/ml	91.5 ± 3	84.2 ± 1	75.8 ± 0.7	96.4 ± 5.1	84 ± 4.3	75.5 ± 4	93.7 ± 4.1	82.6 ± 1.9	59.2 ± 2.8	90.7 ± 1.4	86 ± 3.1	71.4 ± 4.6
PCI	TPCS$_{2a}$ / Saporin 0.2 µg/ml / 20 pM	84.1 ± 2.7	67.1 ± 4.8	48.3 ± 1	88.6 ± 4.1	73.1 ± 1	60.3 ± 3.3	84.4 ± 7.5	68.3 ± 3.8	46.1 ± 0.8	81.4 ± 2.5	76.9 ± 2.6	72.3 ± 0.1
PDT	TPCS$_{2a}$ 0.4 µg/ml	94.4 ± 3.1	76.4 ± 3.3	55.65 ± 3.3	86.4 ± 5.3	68.2 ± 0.4	45.4 ± 3.4	93.7 ± 3.9	67.7 ± 6.4	26.2 ± 3.4	91.4 ± 3.1	69.9 ± 3.8	47.6 ± 4.4
PCI	TPCS$_{2a}$ / Saporin 0.4 µg/ml / 20 pM	90 ± 4.5	58.9 ± 3.4	27.9 ± 5	93.7 ± 4.4	52.3 ± 0.6	44.6 ± 6.3	88.5 ± 6.1	46.9 ± 4	14.3 ± 3	78.7 ± 3.7	50.1 ± 3	35.8 ± 4.3

BPD-MA in MaTLyLu cells

LIGHT AFTER

Cell viability values shown as media ± SEM

24 hr

			4hr chase		
		Dark	0.25 J	0.5 J	1 J
	Control		97.9 ± 8.1		
	Saporin 20 pM		93.6 ± 7.9		
PDT	BPD-MA 0.4 µg/ml	96.4 ± 5.1	70.3 ± 10.2	41.2 ± 10.2	28 ± 4.1
PCI	BPD-MA / Saporin 0.4 µg/ml / 20 pM	88.6 ± 4.1	49.2 ± 7.1	32.7 ± 7.5	24.8 ± 3.7

AlPcS2a in MatLyLu cells

LIGHT AFTER

Cell viability values shown as media ± SEM

24 hr

			4hr chase		
		Dark	0.25 J	0.5 J	1 J
	Control		92.9 ± 5.2		
	Saporin 20 pM		84.2 ± 6.9		
PDT	AlPcS$_{2a}$ 0.4 µg/ml	94.7 ± 6.9	77 ± +6.1	38.3 ± 6.6	16.3 ± 5.9
PCI	AlPcS$_{2a}$ / Saporin 0.4 µg/ml / 20 pM	86.5 ± 3.6	30.4 ± 6.3	20.4 ± 1.7	13.3 ± 2.4

Table 6. Summary of cell viability after PDT/PCI in MatLyLu cells. TPCS$_{2a}$-, BPD-MA-, and AlPcS$_{2a}$- based PDT and PCI 24 hr and 48 hr after delivery of light.

Shown light after results under different drug-light interval and light conditions.

2.4.6 Subcellular localisation of $TPPS_{2a}$ and $TPCS_{2a}$ in PC3 and MatLyLu cells before and after light treatment

An efficient PCI procedure has the following basic requirements:

1. Endolysosomal localisation of photosensitisers and the therapeutic agent to be delivered. Fluorescent properties of photosensitisers enable this observation. However, a much higher resolution is needed to prove specific localisation within the membranes.
2. Light-induced release from these endolysosomes: consistent with endolysosomal disintegration due to photooxidative damage which then releases the drug content. Again, intrinsic fluorescence of photosensitisers can show this with dispersion of fluorescence into the cytosol upon light exposure.

In our study, in order to observe the subcellular localisation of photosentisers at the moment of exposure to light and better comprehend the occurring PDT effect, cells were incubated with photosensitiser solutions following the same protocol as performed for cell viability measurements reported in the previous sections. Observations of initial localisation of $TPPS_{2a}$ and $TPCS_{2a}$ were achieved through illumination for short periods of time (1 second) which are insufficient to excite the compounds and trigger the characteristic photo-oxidative reactions (as displayed in Figure 24A for $TPCS_{2a}$ in MatLyLu cells and Figure 24B for $TPPS_{2a}$ in PC3 cells). Specifically, at this initial stage of illumination, both photosensitisers were seen conforming discrete granules in the cytoplasm (highlighted with red arrows in Figure 24A, Figure 24B). As cells were being illuminated, these cytosolic granules started fading in a time dependent manner. 10 minutes after light treatment, fluorescence had been redistributed throughout the whole cellular structure, as shown in Figure 24C, Figure 24D. Changes in cell morphology after light were also seen; these were evident in PC3 cells, which seemed to have adopted a rounded morphology as light treatment was performed (Figure 24D).

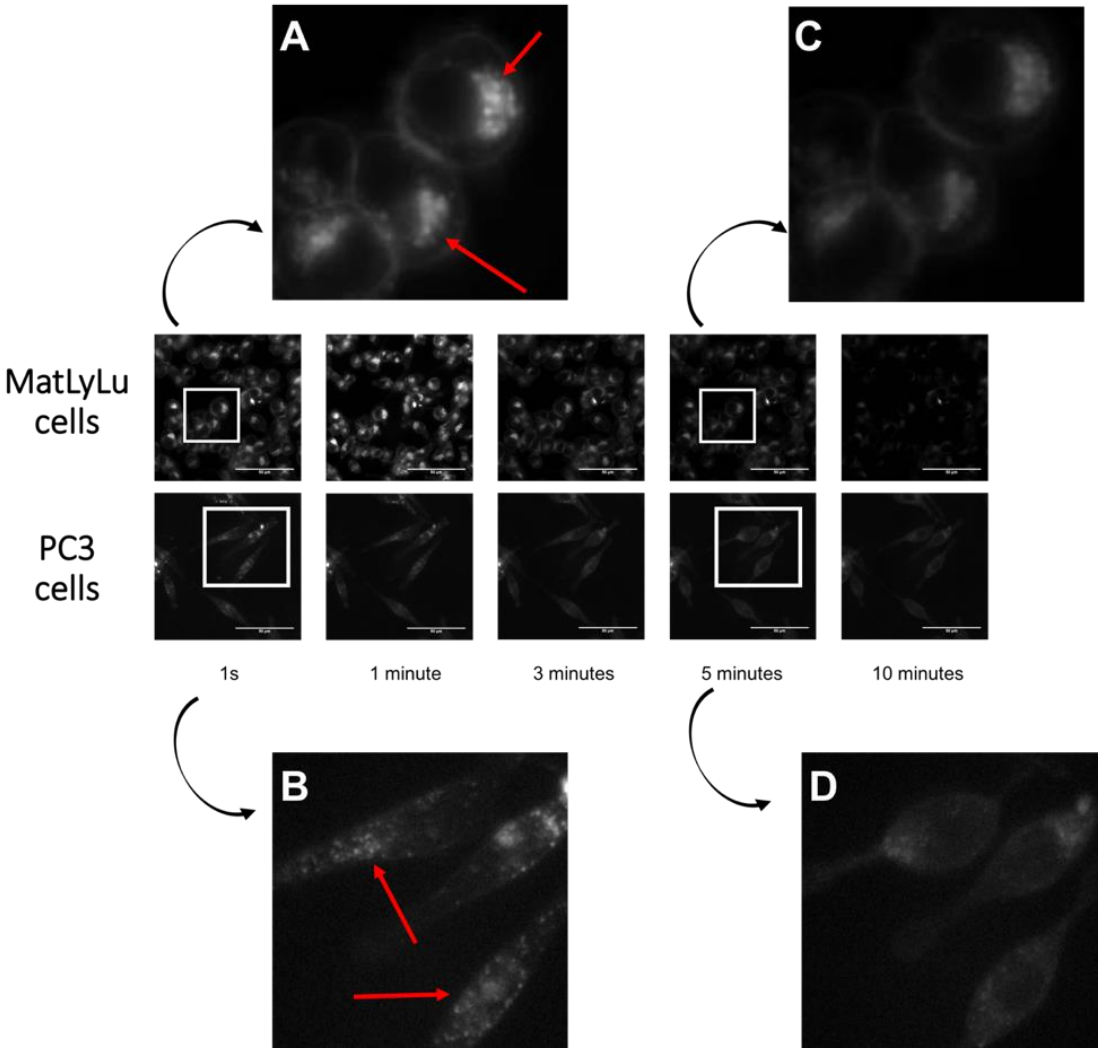

Figure 24. $TPCS_{2a}$ and $TPPS_{2a}$ localisation and redistribution after light treatment in MatLylu and PC3 cells respectively.

Cells were incubated with 0.4 μg/ml solutions of either $TPCS_{2a}$ (MatLyLu cells) or $TPPS_{2a}$ (PC3 cells) during 24 hr. Photosensitiser solutions were then washed off and a 4 hr chase period was allowed before illumination "on stage" using a low power (2 mW) 405 nm blue diode laser coupled to a liquid light guide. Micrographs were taken at a different time during exposure to light. Red arrows indicate PS cytosolic granules. Scale bars shown as 50 μm.

2.4.7 Subcellular localisation of the conjugate saporin-Alexa-Fluor488® before and after excitation of photosensitisers

So as to better understand the subcellular mechanism of PCI in the prostate cancer cells used in the study, we aimed to determine the location of saporin-Alexa-Fluor488® at a subcellular level, as performed with $TPCS_{2a}$ and $TPPS_{2a}$.

Alike above-reported for photosensitisers, saporin appeared in both the human (PC3) and rat (MatLyLu) cell lines as discrete cytosolic granules. Moreover, incubation with

lysotracker red (specific lysosomal dye), resulted in colocalisation with the saporin conjugate (Figure 25).

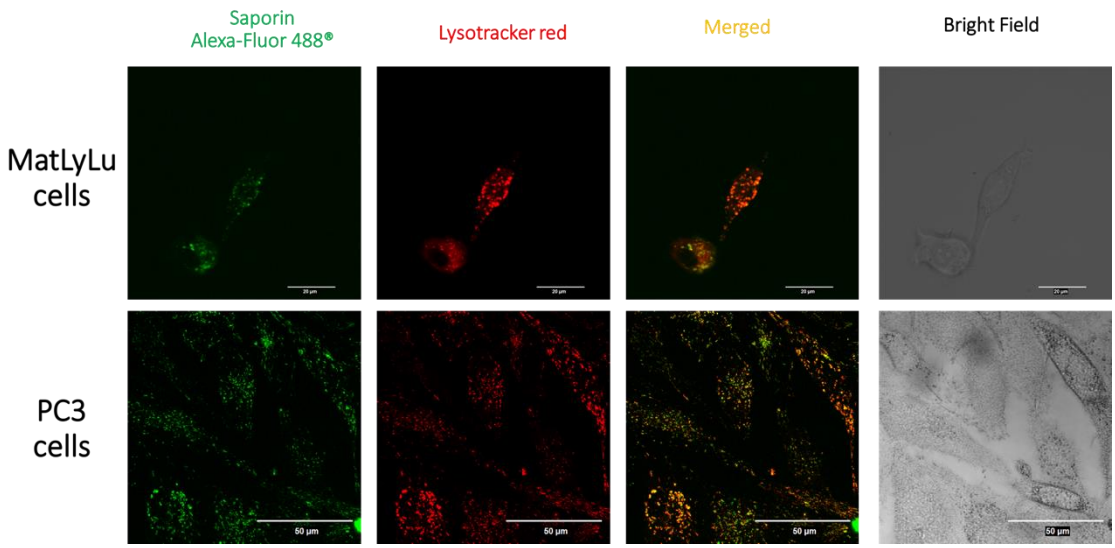

Figure 25. Saporin-Alexa-Fluor488® conjugate localisation in MatLyLu and PC3 cells respectively.

Cells were incubated with a solution of Saporin-Alexa-Fluor488® (400 nM) during 24 hr, then washed, allowing cells to recover for 4 hours. Additionally, cells were incubated with a 75 nM solution of LysoTracker® Red DND-99. Imaging was performed using a 488 nm (for saporin-Alexa-Fluor488®) and 559 nm laser (for lysotracker red). Scale bars shown as 20 µm (MatLyLu cells) and 50 µm (PC3 cells).

$TPPS_{2a}$ and $TPCS_{2a}$ absorb light at 405 nm (see spectra in Figure 11), thus exposure of both compounds to light of this wavelength would result in their excitation. Subcellular distribution of saporin-Alexa-Fluor488® remained unaltered in PC3 cells if these were exposed to a 405 nm laser followed by micrograph capturing, as displayed in Figure 26.

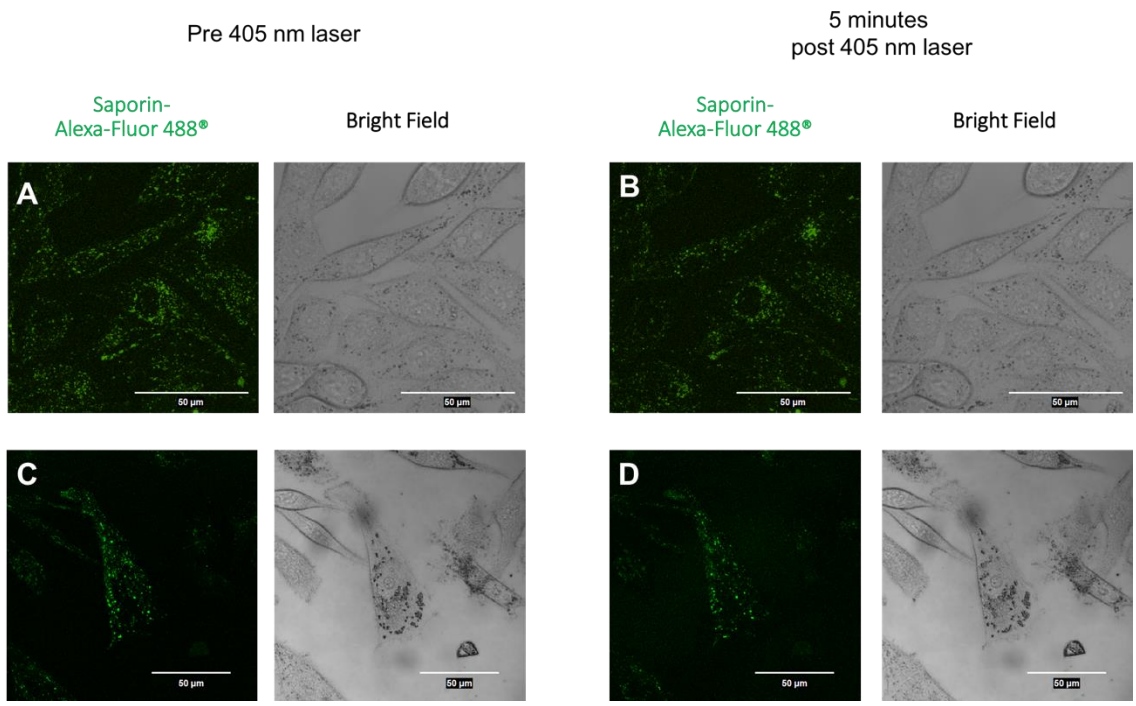

Figure 26. Saporin-Alexa-Fluor488® conjugate in PC3 cells before and after illumination with a 405 nm laser.

Cells were incubated with a solution of Saporin-Alexa-Fluor488® (400 nM) during 24 hr, then washed, allowing cells to recover for 4 hours. Imaging was performed using a 488 nm laser before (A, C) and 5 minutes after (B, D) a 10 seconds "on-stage" excitation with a 405 nm laser. Scale bars shown as 50 µm.

We then aimed to investigate possible changes in subcellular localisation of saporin occurring during PCI. Therefore, saporin-Alexa-Fluor488® and photosensitiser solutions were co-administered in PC3 (Figure 27 and Figure 28) and MatLyLu (Figure 29) cells following the same protocol as for the above cell viability assays. Accordingly, if PC3 cells were imaged before illuminating the cells with a 405 nm blue laser, saporin remained forming green fluorescent cytosolic granules (Figure 27A) as was shown in Figure 26 in the absence of PS. Yet, if cells were imaged after illumination with 405 nm light, the cytosolic vesicles in which saporin was initially located, were dispersed throughout the cytosol (Figure 27B, Figure 27C) similarly to the fading of photosensitiser's fluorescence after illumination shown previously (Figure 24). As highlighted with red arrows in a single cell in Figure 27, overall fluorescence "glow" (B, C) remained after dispersion of the initial discrete fluorescent granules (A).

This same fluorescence dispersion and cytosolic redistribution of the conjugate is represented in a single cell in Figure 28.

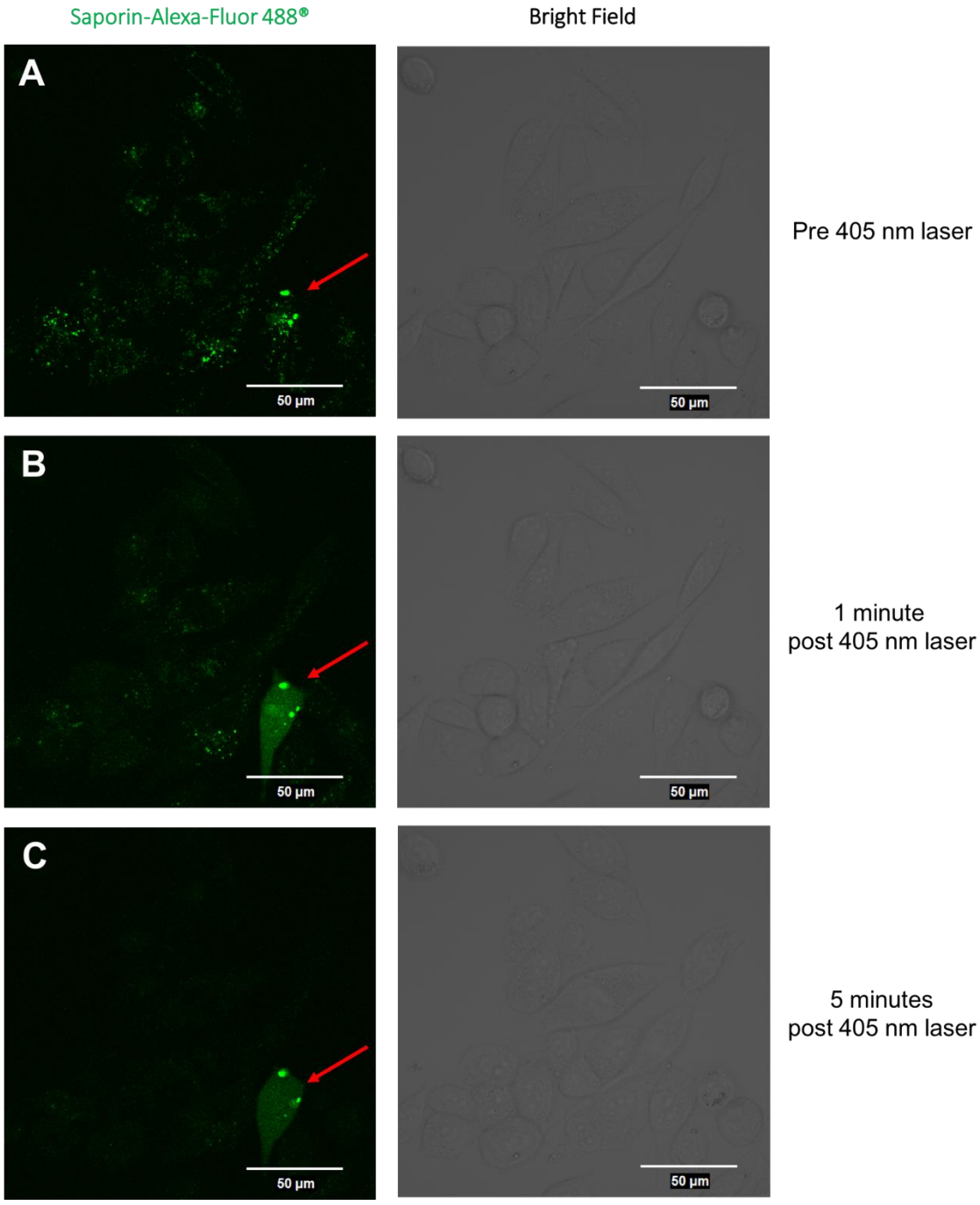

Figure 27. Saporin-Alexa-Fluor488® conjugate in PC3 cells co-administered with $TPPS_{2a}$ before and after illumination with a 405 nm laser.

Cells were incubated with Saporin-Alexa-Fluor488® (400 nM) and $TPPS_{2a}$ (0.4 µg/ml) during 24 hr, then washed and allowed to recover for 4 hours. Imaging was performed using a 488 nm laser before (A), 1 minute after (B) and 5 minute after (C) a 10-seconds "on-stage" excitation with a 405 nm laser. Red arrows indicate Saporin-Alexa-Fluor488® cytosolic granules. Scale bars shown as 50 µm.

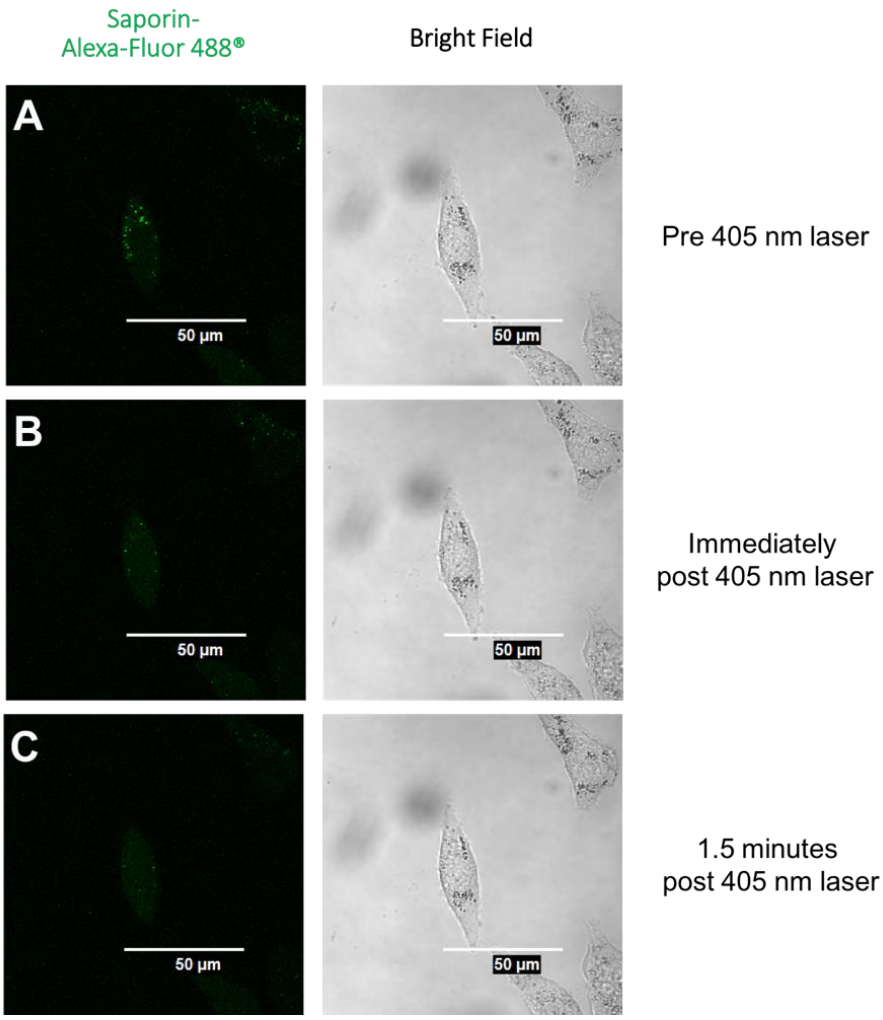

Figure 28. Saporin-Alexa-Fluor488® conjugate in PC3 cells (single cell detail) co-administered with $TPPS_{2a}$ before and after illumination with a 405 nm laser.

Cells were incubated with Saporin-Alexa-Fluor488® (400 nM) and $TPPS_{2a}$ (0.4 µg/ml) during 24 hr, then washed and allowed to recover for 4 hours. Imaging was performed using a 488 nm laser before (A), immediately after (B) and 1.5 minute after (C) a 10-seconds "on-stage" excitation with a 405 nm laser. Scale bars shown as 50 µm.

Similar experiments were performed in rat prostate cancer cells (MatLyLu) exposed to a combination of saporin-Alexa-Fluor488® and $TPCS_{2a}$ following the same drug-combination PCI protocol performed in the human counterpart (Figure 27 and Figure 28). As shown in Figure 29, emission of green fluorescence by saporin-Alexa-Fluor488® was also subject to a time dependant dispersion and redistribution (Figure 29B, Figure 29C). However, this was evident longer after illumination was initiated in this cell line, as shown 10 minutes after 405 nm light irradiation (Figure 29C) opposite to 1.5- (Figure 28C) and 5- minutes after 405 nm light irradiation in PC3 cells (Figure 27C).

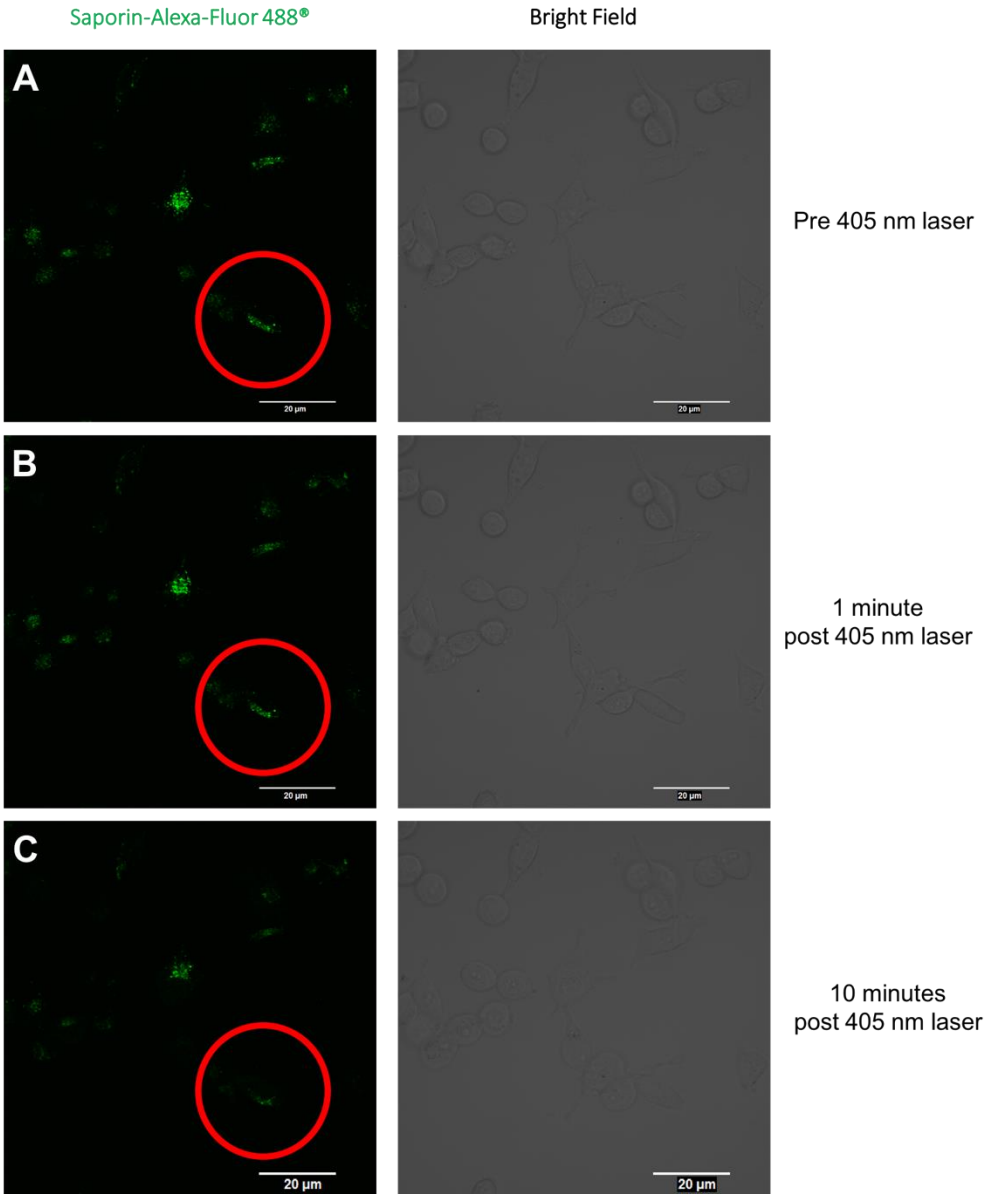

Figure 29. Saporin-Alexa-Fluor488® conjugate in MatLyLu cells co-administered with TPCS2a before and after illumination with a 405 nm laser.

Cells were incubated with Saporin-Alexa-Fluor488® (400 nM) and $TPCS_{2a}$ (0.4 µg/ml) during 24 hr, then washed and allowed to recover for 4 hours. Imaging was performed using a 488 nm laser before (A), 1 minute after (B) and 10 minute after (C) a 10-seconds "on-stage" excitation with a 405 nm laser. Red circle indicates Saporin-Alexa-Fluor488® cytosolic granules. Scale bars shown as 20 µm.

2.4.8 PDT and PCI in 3D collagen hydrogels using $TPPS_{2a}$ as photosensitiser

The above shown images and viability assays were performed in traditional 2D platforms such as cell culture plastic plates and dishes.

Following the 3Rs principle (Refinement, Reduction, Replacement), aiming to mimic more closely the natural environment cells are found in, and thus gain reliability of our results, we performed light treatment (both PDT and PCI) to PC3 cells seeded into collagen hydrogels.

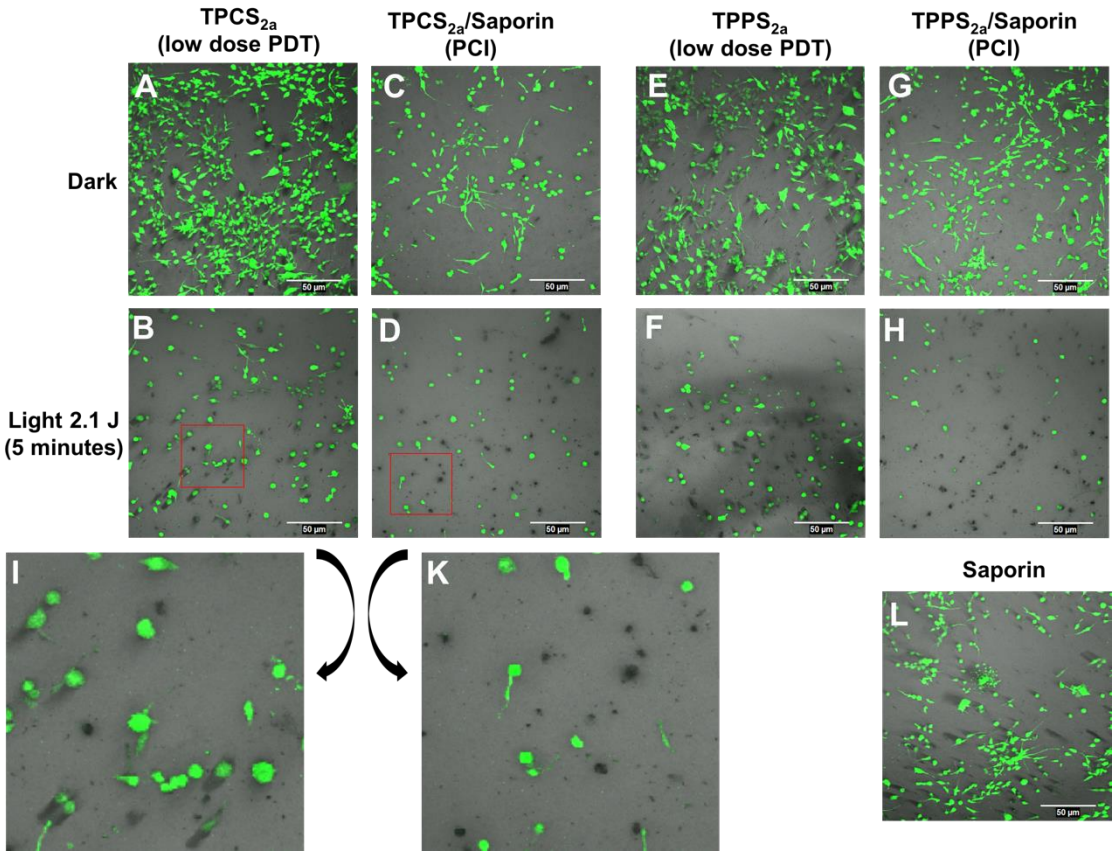

Figure 30. PDT/PCI in PC3 cells seeded onto 3D collagen gels.

Images showing fluorescence of calcein in viable cells. Cells were incubated with either 0.2 µg/ml solutions of $TPCS_{2a}$ (A, B, C, D, I, K) or $TPPS_{2a}$ (E, F, G, H) alone, in combination with saporin 2 nM (C, D, I, K, G, H), or exposed to saporin alone (L) for 24 hr. Drugs were then washed off and a 4 hr chase period was allowed before illumination. Micrographs were taken 96 hr after light treatment. (I) and (K) are zoomed images of (B) and (D) respectively. Scale bars shown as 50 µm.

Cell viability of PC3 cells was affected by both light treatments PCI and PDT 96 hours after light with both photosensitisers ($TPCS_{2a}$ and $TPPS_{2a}$). This was reflected by the lower cell density of these groups after 5 minutes light (Figure 30B, Figure 30D, Figure 30F, Figure 30H) compared to dark (Figure 30A, Figure 30C, Figure 30E, Figure 30G). Combination of photosensitisers with saporin appeared to result in a lower cell density even under dark conditions (Fig. 20C, 20G) in comparison to cells exposed to photosensitisers alone in the dark (Figure 30A, Figure 30E). Like cell viability measurements reported above, cytotoxicity in 3D gels after PCI (Figure 30D, Figure 30H) seemed to be greater that exerted by PDT (Figure 30B, 20F). In addition, PC3 cells were morphologically affected after both PDT and PCI (see details Figure 30I,

Figure 30K), were they adopted a more "round" shape as opposed to their characteristic elongated phenotype.

2.4.9 BPD-MA & $AlPcS_{2a}$ in MatLyLu cells

Due to the relevance for *in vivo* studies reported in Chapter 4, a brief investigation into PDT and PCI effect in MatLyLu using BPD-MA and $AlPcS_{2a}$ as photosensitisers was performed (prior step to *in vivo* experiments). Based on optimal photosensitiser doses established in previously-commented experiments, a single 0.4 μg/ml concentration of either BPD-MA and $AlPcS_{2a}$ was investigated in the sections described below.

2.4.9.1 BPD-MA and $AlPcS_{2a}$ uptake in rat prostate cancer cells (MatLyLu cells)

As reported above with $TPPS_{2a}$ and $TPCS_{2a}$, an initial experiment involved measuring photosensitiser uptake in rat prostate cancer cells. Both BPD-MA and $AlPcS_{2a}$ were administered to MatLyLu cells to measure uptake of these after two different incubation periods (8 hr and 24 hr). In this case, a direct relationship was found between uptake and length of incubation with both photosensitisers with significant differences between time points (see Figure 31). Higher uptake of $AlPcS_{2a}$ than BPD-MA was seen both after 8 hr and 24 hr incubation.

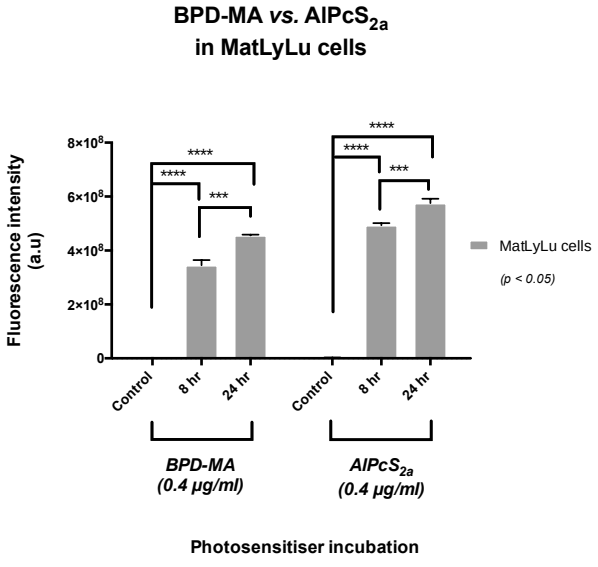

Figure 31. Uptake of BPD-MA and $AlPcS_{2a}$ in rat prostate cancer cells (MatLyLu).

Cells were incubated for 8 hr and 24 hr to photosensitiser solutions at 0.4 μg/ml, then washed and media was replaced with no phenol red media. Uptake was related to photosensitiser fluorescence intensity. Data is displayed as mean with error bars +/- SEM; two-way ANOVA followed by Bonferroni post hoc multiple comparison was used, significance level of $p < 0.05$.

2.4.9.2 Assessment of cell viability after light treatment and subcellular localisation of BPD-MA and $AlPcS_{2a}$ in MatLyLu cells

Different light doses were investigated to establish the optimal *in vitro* treatment of these cells with both compounds. Cell viability 24 hr after light was measured, as displayed in Figure 32.

A direct correlation was confirmed once more between light dose and reduction in cell death for both PDT and PCI in the compounds here discussed, exhibiting significant differences in cell viability compared to the non-treated group. The lowest light fluence tested [0.25 J and 0.5 J with BPD-MA (Omnilux Clear-U™ light source) and $AlPcS_{2a}$ (LumaCare™ light source) respectively] rendered the greatest difference in cell viability between PDT and PCI for both photosensitisers, 21% and 50% for BPD-MA (Figure 32A) and $AlPcS_{2a}$ (Figure 32B); this was even more pronounced in the phtalocyanine-based photosensitiser (Figure 32B). Cytotoxicity after 1 J light was similar in both light treatments and photosensitisers exhibited the greatest cell killing, 87% - 73%. As with the previously tested photosensitisers, no dark toxicity was found in any case.

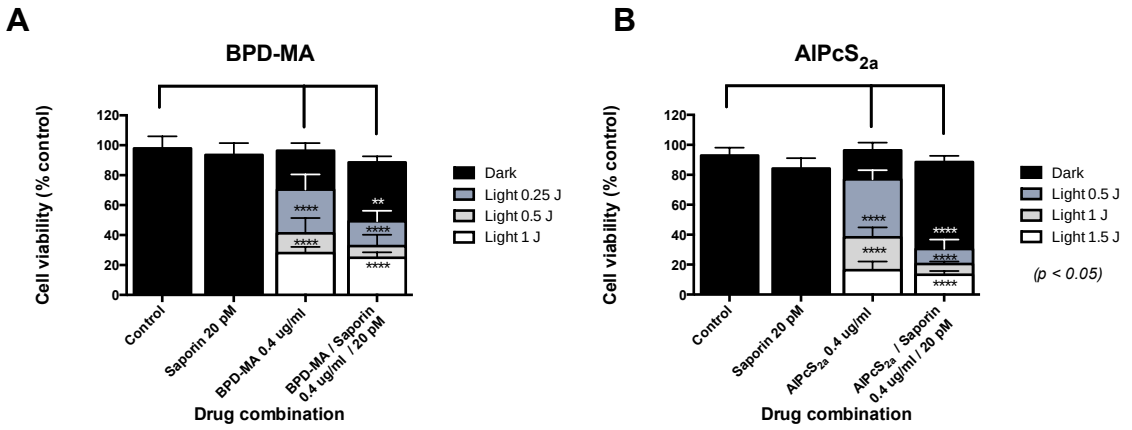

Figure 32. PDT/PCI effect in MatLyLu cells 24 hr after different light doses.

Cells were incubated with either 0.4 μg/ml solution of BPD-MA (A) or $AlPcS_{2a}$ (B), alone or in combination with saporin 20 pM for 24 hr. Drugs were then washed off and a 4 hr chase period was allowed before illumination. Cell viability was measured 24 hr after light treatment. Data is displayed as mean with error bars +/- SEM; two-way ANOVA followed by Bonferroni post hoc multiple comparison was used, differences between dark control and light groups are shown; significance level of $p < 0.05$.

BPD and $AlPcS_{2a}$ cytotoxicity after PDT-light treatment was further evaluated through fluorescence imaging after exposure to light and staining with propidium iodide (membrane impermeant fluorescent dye which is only able to stain cells with an

impaired cellular membrane). As displayed in the red channel (BPD-MA), the photosensitiser was initially located in the cell cytosol (Figure 33A) and was progressively dispersed throughout the whole cell, entering the nucleus by 48 hr after light (Figure 33C). Cell death and more specifically, its time-dependency were confirmed (Figure 33D, Figure 33E). 24 hr after light, PI staining of cells was already detected; yet it significantly increased, resulting in very bright fluorescence 48 hr after light (Figure 33E). In addition, cellular damage was evident as soon as 2 hr after light, detailed in Figure 33H.

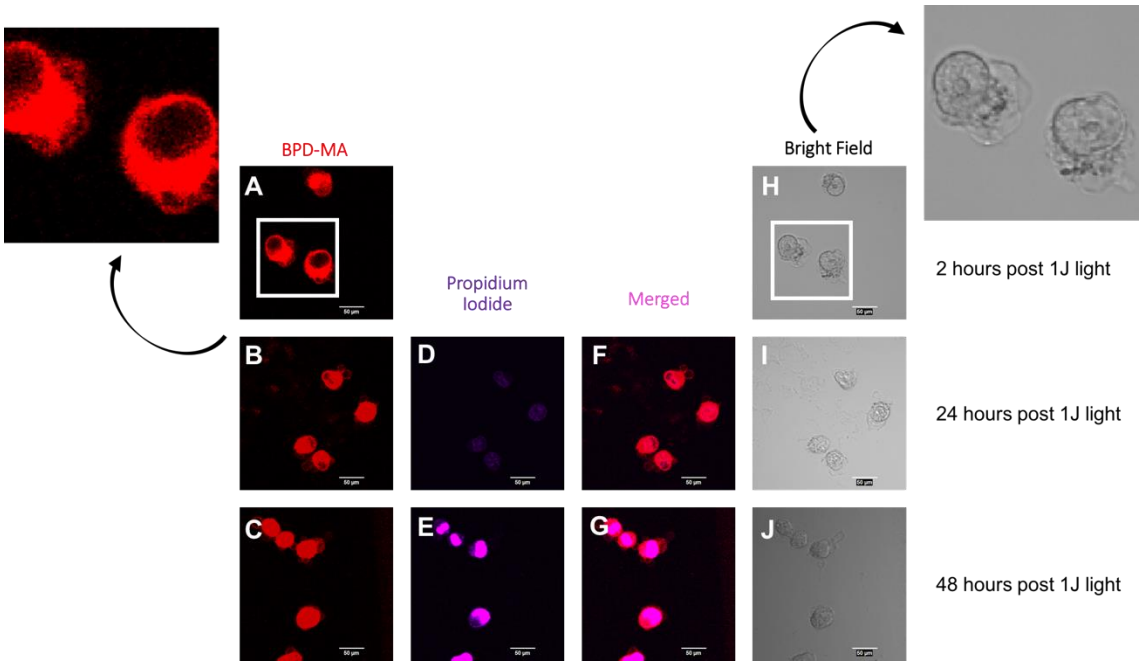

Figure 33. BPD-MA localisation and cytotoxicity in MatLylu cells.

Cells were incubated with 0.4 μg/ml BPD-MA during 24 hr, solutions were then washed off and a 4 hr chase period was allowed before illumination. Additionally, cells were incubated with a 1:100 solution of propidium iodide prior to imaging. Micrographs were taken 2 hr, 24 hr and 48 hr after light using a 405 nm (for BPD-MA) and 559 nm laser (for propidium iodide). Scale bars shown as 50 μm.

As for the assessment of fluorescence after $AlPcS_{2a}$-based PDT in rat prostate cancer (Figure 34), contrary to the subcellular more disperse pattern seen with BPD-MA (Figure 33A), $AlPcS_{2a}$ distributed in a similar way to the above-shown $TPPS_{2a}$ and $TPCS_{2a}$ (Figure 24). Discrete granules were found throughout the cytosol (Figure 34A). PI staining was not as clear as seen above with BPD-MA PDT, cells seemed to be gradually affected when imaged at later time points (Figure 34D, Figure 34E). Cell integrity was maintained even 48 hr after light as opposed to BPD-MA PDT (Figure 33H)

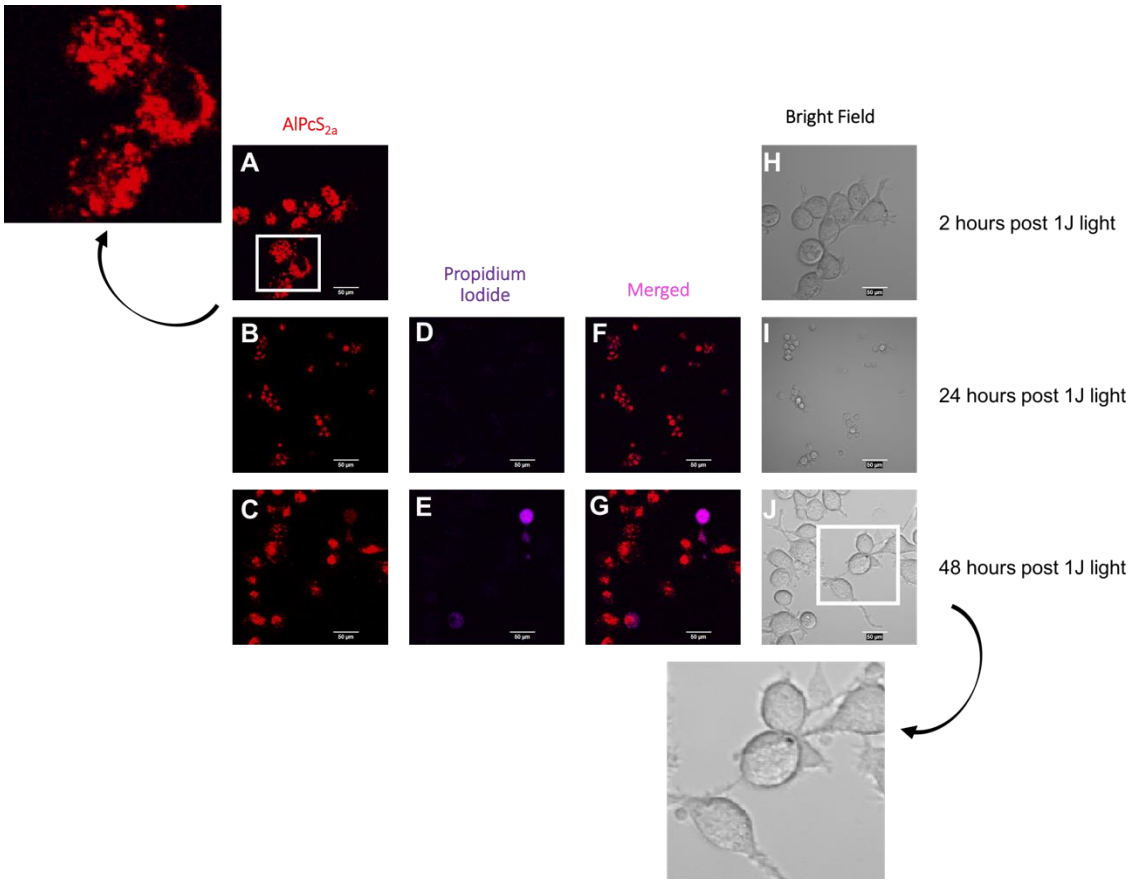

Figure 34. AlPcS2a localisation and cytotoxicity in MatLylu cells.

Cells were incubated with 0.4 μg/ml $AlPcS_{2a}$ during 24 hr, solutions were then washed off and a 4 hr chase period was allowed before illumination. Additionally, cells were incubated with 1:100 solution of propidium iodide prior to imaging. Micrographs were taken 2 hr, 24 hr and 48 hr after light using a 405 nm (for $AlPcS_{2a}$) and 559 nm laser (for propidium iodide). Scale bars shown as 50 μm.

2.5 Discussion

Briefly, the aims of this first chapter were to assess PDT and PCI *in vitro* as potential prostate cancer treatments and compare the therapeutic outcome resulting from each of these light-based therapies.

The absorbance of light (photons) and consequent dissipation of different forms of energy (heat, light, chemical energy) is the foundation of both therapies investigated in the present thesis. Hence, an initial verification of the absorbance and fluorescence emission of each of the photosensitisers used was measured, as shown in the spectra displayed in Figure 11. These proved the eligibility of $TPPS_{2a}$, $TPCS_{2a}$, BPD-MA and $AlPcS_{2a}$ as photosensitive compounds, and thus we moved onto measuring the likelihood of having a positive therapeutic outcome in prostate cancer eradication.

The prostate cancer cell models used throughout the study, PC3 for human and MatLyLu as the rat counterpart, share common features such as androgen independency or metastatic potential, characteristics of advanced human prostate cancer. Despite their similarities, they both exhibited differences such as growth rate and pattern. In line with this, MatLyLu's doubling rate has been previously described as substantially faster that other models (Isaacs et al., 1981). This was confirmed in our experiments, observing a significantly faster growth of these than PC3 cells, which could also be the reflection of a faster metabolic rate.

Moreover, Kouvroukoglou et al. hypothesised the production of autocrine factors by MatLyLu cells. In their studies, they observed growth of these cells in the absence of serum, or a modification in their metabolism as an adjustment to inhibition of glycolysis or mitochondrial respiration (Kouvroukoglou et al., 1998). The differences in growth between cell lines were the reason for the use of different cell seeding densities of each during the experiments. Moreover, rat prostate cancer cells tended to grow forming clumps of cells at low confluence (possibly related to their high metastatic potential), which was not observed in the human prostate cancer model.

Photosensitiser uptake in PC3 and MatLyLu was directly related to emission of fluorescence in cells previously incubated with photosensitiser solutions. No fluorescence was detected in control cells, showing that autofluorescence was negligible. Based on the observations, a direct correlation between photosensitiser dosage and uptake, or between duration of incubation with photosensitisers and uptake

(displayed in Figure 12 and Figure 31 respectively) was demonstrated for $TPPS_{2a}$, $TPCS_{2a}$, BPD-MA and $AlPcS_{2a}$ in the above prostate cancer cells (the two last compounds were evaluated as a direct basis for *in vivo* experiments). In addition, the lack of any sign of saturation (i.e. tending towards a plateau) in the curves suggests non-receptor mediated uptake of the compounds under our experimental conditions. The 2-fold greater fluorescence emission of $TPCS_{2a}$ compared to the porphyrin analogue at the most (Figure 12), could be the result of a higher uptake of this PS in both cell lines. However as discussed previously, differences in fluorescence quantum yields between both photosensitisers (Lilletvedt et al., 2011, 2010; Wang et al., 2013), could be responsible for the differences found; therefore, a higher uptake of this photosensitiser cannot be concluded neither in PC3 nor MatLyLu cells. Likewise, no conclusion can be drawn in spite of the greater fluorescence emission in MatLyLu incubated with $AlPcS_{2a}$ than BPD-MA (Figure 31). The comparison of different photosensitisers would require chemical extraction measurements. Moreover, differences in cell number at the time of PS uptake measurement may also explain the significant differences found in the uptake of $TPPS_{2a}$ and $TPCS_{2a}$ between cancer cell lines (Figure 12). The aim of the PS uptake studies was to verify the internalisation of PS in PC3 and MatLyLu cells under relevant experimental conditions (as established for later experiments).

We proceeded next to determine suitable drug doses (of both photosensitisers and saporin), which would result in under 50% cytotoxicity when administered alone. As a principle, PCI uses low dose PDT directed against organelles at a subcellular level and aims to deliver drugs and enhance the therapeutic outcome exerted by PDT- or drug- alone. Therefore, the objective is to combine subthreshold cytotoxicity levels of both treatments when administered independently.

The lack of cytotoxicity observed in PC3 cells upon exposure to saporin (Figure 13), even at the highest dose tested (60 nM), confirmed the inability of this RIP type 1 to reach cytosolic ribosomes because of the lack of the chain B reported in the literature (Polito et al., 2013). On the other hand, the higher sensitivity to saporin seen in MatLyLu cells even when assaying 2 nM (25% cell death as shown in Figure 13), could be explained by the combination of several internalisation mechanisms involved in these cells together with a higher metabolic rate (suggested by their greater growth rate). Due to this greater toxicity caused by saporin in the rat model, PCI combination experiments performed in these cells required lower saporin doses (20 pM). Uptake of saporin in MatLyLu could occur independently to the type B chain, involved in the entry of RIP type II, i.e. ricin.

No general internalisation mechanism has been defined for saporin yet and it is still not clear how this RIP is uptaken by different cell types or even organs. Different cellular uptake mechanisms and traffic pathways have been described (Polito et al., 2013). For instance, pinocytosis was suggested in human trophoblasts due to the high sensitivity these presented (Battelli et al., 1992); receptor mediated endocytosis via an α2-macrogloblin receptor (low-density lipoprotein receptor) was the most likely hypothesis in lymphoma cells (Cavallaro et al., 1995), yet this was rejected in CHO cells (Bagga et al., 2003); non-receptor mediated endocytosis and localisation in non-coated vesicles in HeLa cells (Bolognesi et al., 2012).

As for PDT effect (described in Figure 14 and Figure 15), 0.2 and 0.4 μg/ml were selected as optimal doses for later PCI experiments in both cell lines based on the large cell death resulting from illumination of cells exposed to the highest PS doses (0.6 and 0.8 μg/ml) and light, which was even further accentuated when measurement of cell viability was performed at a later time point (96 hr for PC3 cells). This greater PDT effect found at higher PS doses is related to the non-saturation in the uptake of PS determined in initial uptake experiments. A greater PDT effect was observed with $TPCS_{2a}$ in PC3 cells. However, $TPPS_{2a}$ was the PS in MatLyLu cells causing greater cytotoxicity (Figure 14).

Both PS could be following different metabolic pathways within MatLyLu and PC3 cells and thus result in different photooxidative rates causing greater or lesser PDT-based killing of these. Different cancer cells show different susceptibility to ROS-based damage. Along these lines, cells develop different mechanisms to coordinate and balance their redox, i.e. varying local concentration of these oxidative species or expressing ROS scavenging proteins as a protection mechanism (Liou and Storz, 2010). As could be expected, mitochondria has been reported to have an important role in ROS balance, being a key organelle in ATP production (Okon and Zou, 2015). Taking all the above into consideration, differences between both cancer cell lines and PSs employed throughout the chapter could be caused by disparities in antioxidant enzymes levels, mitochondrial activity (this can also be directly related to metabolic rates).

As mentioned in Background and Introduction, light absorption by PS will not be affected *in vitro*, unlike *in vivo* where haemoglobin and other chromophores are present, and compounds with low absorption in the red region of the spectra are still active using blue light excitation. Conversely, this is a critical requisite for PS *in vivo*, since 600-800 nm is the optical window considered suitable for tissue light penetration.

On this basis, and regardless of the better outcome exhibited by $TPPS_{2a}$, subsequent experiments in MatLyLu cells (basis for the *in vivo* model reported in Chapter 4) were only performed using photosensitisers more suitable for *in vivo* experiments. These must have relatively intense absorption peaks in the red, such as $TPCS_{2a}$, $AlPcS_{2a}$ and BPD-MA. Experiments with $TPPS_{2a}$ were also performed in PC3 cells as a model compound and a proof of concept of both PDT and PCI in prostate cancer.

The successful performance of PCI faces a challenging optimisation process due to the delicate balance between PDT and PCI. Photosensitiser dose, drug dose, light dose, drug light interval, measurement of cell viability time points are variables involved in tilting this balance towards one treatment or another. Accordingly, taking the pre-determined subthreshold doses of PS and saporin as the starting point, different experimental conditions were assayed.

The first PCI combination experiments displayed in Figure 16 served as initial proof of the higher efficiency that could be achieved with PCI over low dose PDT (1.26 J for both treatment groups) in human prostate cancer cells (PC3): up to 3.5-fold higher cell death was observed 96 hr after light treatment combining $TPCS_{2a}$ 0.2 μg/ml and saporin 2 nM (Figure 16 D). Differences in PDT effect were found between both PS doses tested, with greater cell death at the highest dose (as seen in PS dose response curves, Figure 14 and Figure 15). Despite PDT differences, negligible differences were found in PCI-based toxicity between 0.2 μg/ml and 0.4 μg/ml when comparing each time point (24 hr and 96 hr) independently. This indicates that after PCI, the therapeutic effect relies to a large extent on the drug being delivered (saporin in the present case), giving less weight to photooxidative damage itself.

In addition, the effect was enhanced even more when cell death was measured 96 hr after light as opposed to 24 hr (2.8-fold larger). This could indicate slower cell death pathways post PCI, possibly requiring time-dependant intracellular signalling. Perhaps, saporin could have been transported from cell to cell through communication channels directly into the cytosol of adjacent cells, affecting those that had not been directly affected by either PS or saporin. Transport between tumour cells comprising cell-cell or cell-stroma interaction via gap junctions, integrins, cadherins, etc. has been studied in several occasions (Brücher and Jamall, 2014), aiming to exploit these in the development of anti-tumour treatments. A recently discovered example of intercellular traffic structures are tunnelling nanotubes (membrane bridges), which were detected in several cancer cell types and whose function was to ease the transfer of organelles and material of varied nature between tumour cells (Burtey et al., 2015).

As for MatLyLu cells, viability was only measured up to 48 hr after light exposure. This was due to the rapid growth of this prostate cancer model: viability levels in control groups were found outside MTT's reliable detection limits and the cytotoxic effect of treatments performed could have been masked by regrowth of unaffected cells. Looking at the results after the same light dose (1.26 J) discussed above for PC3 human cells, a PCI effect was also confirmed in the rat counterpart (Figure 18), although not as noteworthy. It is possible that PCI using $TPPS_{2a}$ as PS would have led to a greater enhancement in cell viability than PDT, yet it will not be relevant in the translation to an *in vivo* environment as discussed. As regards $TPCS_{2a}$, outcome of the treatment was relative to the dosage contrary to PC3, where the same PCI effect was seen regardless of PS dose, hence the similarities in cell viability differences between PDT and PCI in MatLyLu (Figure 18).

Further investigation into light dose, positions it as a driving factor in the outcome of PDT and PCI (results displayed in Figure 16, Figure 17, Figure 18, Figure 19, Figure 32). Accordingly, significant differences in cell death were found between the above discussed irradiating light at 1.26 J and lower light doses in PC3 cells (see results after 0.63 J in Figure 17) in both PDT and PCI. However, no benefits in the therapeutic outcome were demonstrated in PC3 cells if the light dose was increased to 1.68 J, for either light treatment neither using $TPPS_{2a}$ nor $TPCS_{2a}$ (Figure 17). In this regard, viability values after PCI could have been restricted by the MTT's detection limits, since these were already below 20% (96 hr after light). Regarding PDT, cell death might have reached a plateau (within the range of light doses tested), being necessary to further increase light fluence in order to reflect changes in cell viability. This was not relevant to the objectives set for the present chapter and thus was not further investigated.

A similar effect was noted in MatLyLu cells when boosting the light dose to 2.1 J (Figure 18 and Figure 19 - light groups' detail). Although cell viability was significantly reduced in all light groups compared to the control cells (i.e. 86% cell death seen after $TPPS_{2a}$ 0.4 μg/ml and saporin 20 pM), in most cases the smallest differences between PDT and PCI were observed at 2.1 J (Figure 18), especially at the higher PS dose (0.4 μg/ml). Nonetheless, statistically significant differences were detected between both light doses at the latest cell viability measurement (48 hr post light), possibly because cell killing at 24 hr did not yet reach values below MTT's detection limits (as reported in PC3 cells) and reductions could be further noted.

Similar studies carried out on HN5, squamous cell carcinoma cells also concluded a significant enhancement in cell killing upon photochemical delivery of saporin using the same light source specified for the present study (Wang et al., 2012). Specifically, cell death was increased at least by a factor of 7.3 compared to saporin-alone or PDT after a 3-minute illumination. Yet, saporin dose used then was at least 500-fold higher.

The last important variable we took into consideration in our "light-after" PCI experiments was the interval allowed between drug removal and illumination (DLI). A 4 hr DLI (chase period) has been reported in traditional PCI *in vitro* approaches (Selbo et al., 2000a; Wang et al., 2012; Weyergang et al., 2006). This has been described to be essential to achieve subcellular photooxidation required for PCI rather than a mainly a PDT effect, stemming from cell membrane damage. Nonetheless, we wanted to observe its relevance during PCI treatment of prostate cancer cells and the effect of different DLI (Figure 20, Figure 21, Figure 22). 24 hr after light, $TPPS_{2a}$-PDT in PC3 cells did not seem to be affected by the 4 hr DLI, and non-significant differences were observed in PCI groups (Figure 20A, Figure 20B). This could suggest a little contribution of PDT. In addition, greater differences might be expected if measured at later time points (i.e. 96 hr after light) based on the gradual and delayed death seen after PCI. On the other hand, DLI could be dependent on the specific PS used, i.e. a more prominent PCI effect using $TPPS_{2a}$ might have been obtained as early as 24 hr after light using longer DLI in order to minimise PDT-based cell death. As for the chlorin-based PS 24 hr after light treatment, only at the higher $TPCS_{2a}$ dose assayed, were significant differences found in the PDT group when allowing a chase period rather than illuminating immediately after drug removal (Figure 20D). In this particular case, PCI effect was similar to PDT in the no-DLI group: it is likely that the high PDT effect was responsible in this case for all cell killing. Viability measurements carried out 72 hr after light (Figure 21) revealed differences between PDT and PCI for both PS used at 0.2 μg/ml, being the outcome similar with the higher PS dose (again, the increase of PS concentration at this time point is weighted too heavily towards PDT). With respect to $TPPS_{2a}$, this serves as an additional confirmation of the delayed death post PCI whilst limiting PDT at acceptable levels.

The large PDT-induced toxicity and smaller differences between PDT and PCI seen 48 hr after treatment in MatLyLu (Figure 18) compared to 96 hr in PC3 cells (Figure 16), took us to investigate whether an increase in DLI in this model would enhance the outcome of PCI treatment (Figure 22). An extension of DLI from 4 hr to 6 hr did not only not enhance PCI, but in fact bridged the gap in cell death resulting from both light treatments. Contrary to what would have been expected initially, longer DLI may result

in the greater breakdown of PS, rendering less active molecules available to be subject to the photooxidative process.

Overall, we conclude that when it comes to DLI, the elected combination of PS dose and DLI will determine the balance between PDT and PCI induced cell death. Higher doses will require longer DLI to internalise PS molecules and avoid tilting the balance towards PDT; yet, this PDT effect using lower PS doses might already be sub lethal and negligible even when no chase period is allowed. Consequently, PCI would be responsible for the effect observed.

Some authors have demonstrated an enhancement of PCI following "light-before" approaches, particularly, when delivering drugs or agents with higher sensitivity to ROS species. For instance, Prasmickaite et al. substantially enhanced gelonin´s cytotoxicity using "light-before" PCI compared to that observed in the "light-after" approach (Prasmickaite et al., 2002). In their study, the most probable mechanism behind "light-before" was discussed: a direct entry into the cell cytosol was rejected based on the participation of endosomal vesicles; passive diffusion was also rejected due to the fast pace at which events occurred. Thereupon, it was hypothesised that endosomal vesicles partially damaged by the activation of the photosensitisers, yet still intact, -then fused with intact vesicles formed post-light treatment which had more recently endocytosed the drug molecules, thus rapidly releasing these into the cell cytosol (Prasmickaite et al., 2002) (see schematic representation of "light-before" PCI in Figure 9). Following this line of thought, and based on the similar nature of saporin to gelonin (RIPs type 1), we looked into the delivery of saporin in PC3 cells following a "light-before" PCI protocol. In these experiments, only a modest increase in cell killing after PCI was achieved regardless of the PS used or the time point at which cell viability was measured (Figure 23). Based on our observations, we hypothesise that the endocytic transport in PC3 cells is different to the malignant melanoma cells (THX) used in other "light-before" PCI studies (Prasmickaite et al., 2002). A slower fusion of PS-disrupted endosomal vesicles with newly formed saporin-containing endosomes could be involved, hence if the latter vesicles were not ruptured and saporin-containing endosomes matured to lysosomes, this RIP type 1 would trapped in the endo/lysosomes and in the end degraded. In the present thesis, the "light-after" strategy resulted in significant enhancement of cell death and "light-before" was rejected as an alternative approach.

Based on all the experimental conditions above-discussed, we concluded 1.26 J as the optimal light dose for the mentioned PS and saporin doses in PC3 cells,

reaching maximal therapeutic effect 96 hr after light, potentially resulting in 100% tumour-cell death. A similar conclusion could be drawn for MatLyLu cells. Given the trend in the increase of cell death overtime after PCI, we hypothesise that had it been possible to extended viability experiments to 96 hr after light, no differences would have been found between 1.26 J and the highest 2.1 J light dose assayed, keeping PDT effect at subthreshold levels in favour of a PCI effect. DLI is dependent on both PS employed and light dose. However, as a general rule we could consider that the same cytotoxicity could result from higher PS doses with longer DLI with and vice versa; yet, specific norms apply to different cell lines (i.e. PC3 *vs.* MatLyLu). A progressive cell killing has been verified after PCI, therefore, there should be not need to increase PS or light dose in order to maximise cell death, and the same therapeutic effect could be observed over time using subthreshold dosages.

Finally, the use of a “light-before” protocol did not result in any beneficial effect over the more conventional “light-after” PCI for our PS and saporin, thus it was not further considered.

These optimal conditions were additionally assayed in PC3 cells seeded onto three dimensional collagen gels and cell death was assessed qualitatively 96 hr after light (Figure 30). A live/dead assay was used to measure cell viability in these experiments: as described above in the materials & methods section, but only the calcein channel was imaged reliably owing to the high background signal affecting the propidium iodide channel. Cell density was affected after all light treatments (PDT/PCI using $TPPS_{2a}$ or $TPCS_{2a}$), showing a strong phototoxicity effect after both PDT (Figure 30B, Figure 30F) and PCI (Figure 30D, Figure 30H), in a similar manner to findings from 2D viability assays. Although differences between PDT and PCI could be detected, they were not as clear as concluded in 2D upon 1.26 J light exposure (Figure 16). Further work would have been required using Alamar Blue for example, had time permitted. Given the greater complexity of 3D gels, a higher light dose was used in these experiments to ensure light delivery throughout the whole structure, which might have weighted the results towards a bigger PDT effect. A recent evaluation of light dosimetry in 3D spheroid ovarian cancer models after PDT (Rizvi et al., 2013), found maximal tumour cell killing when using BPD and high light fluence.

Similarly to our 2D study, no dark toxicity was found (Figure 30A, Figure 30C, Figure 30E, Figure 30G). Not only dead cells were observed after treating with both PS tested, but those cells that remained viable had acquired round morphology, losing their characteristic elongated shape (shown in details Figure 30I, Figure 30K post PDT and

PCI respectively). This could be an indicative of cell detachment prior to death or else due to impact caused to existing interactions between cells and the collagen matrix, or even disruption of collagen hydrogels' structure. However, the consistency of collagen hydrogels remained constant throughout, which leads to think this last hypothesis is not very likely. Against 2D assays findings, a lower number of cells was seen in saporin-treated groups both alone (Figure 30L) as well as combined with PS under no light (Figure 30C, Figure 30G). The comparison of micrographs of the mentioned saporin-affected gels, and those subject to PCI, suggest that this RIP has a cytostatic effect in PC3 cells unless photochemically delivered, where cytotoxicity is demonstrated. Throughout our study, similar conclusions were drawn in 2D and 3D platforms but for the cytostatic effect exerted by saporin found in PC3 cells in the 3D models. The spatial distribution of cells in the latter might maximise the contact area between PC3 and the RIP type 1 concerned, consequently increasing uptake of the drug. Potentially, an increase in the available amount of saporin in the environment could lead to an increase in the number of molecules of saporin being released from endosomes into the cell cytosol. Furthermore, we did not conclude an overestimation of the therapeutic effect in 2D viability assays as compared to 3D as stated by other authors previously (Antoni et al., 2015).

Towards the second half of the results sections (3.4.7., 3.4.8., 3.4.9.) we reported the investigation of the subcellular mechanisms behind PDT and PCI. Figures 14, 23 and 24 serve as an additional visual confirmation of the uptake of $TPPS_{2a}$ and $TPCS_{2a}$ (Fig. 14), BPD-MA (Figure 33) and $AlPcS_{2a}$ (Figure 34). The existence of adjacent disulphonate groups in $TPPS_{2a}$, $TPCS_{2a}$, $AlPcS_{2a}$ confers amphiphilicity to these compounds, thus making them more suitable for PCI experiments; in contrast, BPD-MA is a traditional PDT PS, mainly inducing a vascular PDT effect (Fingar et al., 1999; Kim et al., 2014). Structural differences of used PSs could explain the different distribution patterns within cells found in initial fluorescence images: discrete cytosolic granules for $TPPS_{2a}$, $TPCS_{2a}$, $AlPcS_{2a}$ (Figure 24, Figure 34), *vs.* cytosolic dispersion for BPD-MA (Figure 33). These subcellular localisation and redistribution findings below-discussed are supported by previous studies such as the ones carried out by Wang et al. using $TPCS_{2a}$ in head and neck cancer cells (Wang et al., 2013), $AlPcS_{2a}$ and $TPPS_{2a}$ in HUVECs and HT1080 cells (Vikdal et al., 2013) or in BL2-G-E6 cells (Berg et al., 1999).

In PC3 and MatLyLu cells, $TPPS_{2a}$ and $TPCS_{2a}$ granules redistribute and relocate throughout the cytosol overtime (Figure 24). This suggests initial localisation of PSs in cellular membranes within cytosolic endo/lysosomes (Figure 24A, Figure 24B); yet, the

exposure to light of an adequate wavelength (405 nm) excites the compounds, disrupting the endolysosomal membranes they are docked in, consequently dispersing fluorescence (Figure 24C, Figure 24D). As for $AlPcS_{2a}$, 1 J light was insufficient to observe fluorescence redistribution, but some PDT-based cell death was confirmed with the entry of PI in cells from 48 hr (Figure 34). Similar observations resulted from the incubation of rat prostate cancer cells with BPD-MA (Figure 33), although PI suggested cell death from 24 hr images this was even more significantly noted 48 hr after light. Moreover, the cell structure was affected as early as 2 hr after PDT (Figure 33H). The smaller impact in cell viability found in cells after $AlPcS_{2a}$ alone as opposed to BPD-MA confirms the greater suitability of BPD-MA to PDT; while a reduced PDT effect (PCI feature) was observed with $AlPcS_{2a}$.

Localisation of the conjugate saporin-Alexa-Fluor488® within cells was also studied due to the relevance of saporin in the PCI combination experiments (Figure 25, Figure 26, Figure 27, Figure 28, Figure 29). Colocalisation with lysotracker red in both human and rat prostate cancer cells indicates uptake through endocytosis. Correlation of this observation with saporin's limited toxicity when administered to PC3 cells in 2D experiments confirms the hypothesis of its entrapment in cytosolic vesicles, thus being unable to reach cytosolic ribosomes. However, saporin was able to affect MatLyLu cells in 2D as well as PC3 cells in 3D assays to some extent. In these cases, some molecules of saporin might experience a different entry into the cells, possibly passive diffusion. Confocal images of MatLyLu cells in Figure 15 showed some scattered cytosolic fluorescence on top of the granular pattern, which could be a possible verification of the above mentioned. Illumination of cells treated only with the conjugate saporin-Alexa-Fluor488® during 10 seconds using a 405 nm laser did not affect the granular pattern of green fluorescence as concluded when comparing images taken before and after light (Figure 26). Yet, when PC3 and MatLyLu cells had been initially incubated with a combination of the conjugate saporin-Alexa-Fluor488® and photosensitiser ($TPPS_{2a}$ and $TPCS_{2a}$ respectively) and illuminated with the same 405 nm laser during 10 seconds, the pattern of fluorescence before and after light was affected (Figure 27, Figure 28, Figure 29). This can be interpreted as a disruption of the vesicles containing the fluorescent conjugate caused by the excitation of photosensitisers after light of an adequate wavelength, which concludes with the dispersion of fluorescent granules throughout the cell cytoplasm (Figure 27C, Figure 28C, Figure 29C), as reported by Wang et al. (Wang et al., 2013). A similar redistribution of gelonin was found combined with $AlPcS_{2a}$ (Selbo et al., 2000a).

Moreover, cell integrity seemed to be compromised in the bright field images taken 5 (Figure 27C) and 10 (Figure 29C) minutes after illumination of PC3 or MatLyLu cells respectively, indicated by the adoption of a round shape probably due to cell detachment from plates. The faster effect observed in human than rat prostate cancer cells could correlate with the more relevant enhancement of cell death post PCI measured in viability assays (Figure 16 and Figure 18).

Extrapolating these *in vitro* observations to an *in vivo* context, the performed investigation serves as proof of principle that PCI can result in a positive therapeutic outcome, which can exceed that of PDT, being developed for prostate cancer clinically (Azzouzi et al., 2013, 2015; Kawczyk-Krupka et al., 2015b; Moore et al., 2009). PCI should therefore be capable of causing more efficient tumour eradication, with a lower PS dose thereby minimising side phototoxicity.

In summary, 0.2 µg/ml of either $TPCS_{2a}$ or $TPPS_{2a}$ combined with saporin 10 nM and exposed to 1.26 J light, resulted in an optimal therapeutic effect in PC3 cells. On their side, MatLyLu light-based treatments exhibited a fine performance combining a 0.4 µg/ml photosentitiser solution and saporin 20 pM during a 1.26 J illumination.

Based on the above presented results, we conclude the need to tailor treatments to specific cancer types based on differences seen in therapeutic outcome after light treatments in the different cell lines use.

Chapter 3 Enhancement of PDT and PCI using targeted strategies

3.1 Introduction

One of the main advantages of photodynamic therapy and consequently photochemical internalisation, is the minimal toxicity associated with photosensitisers unless exposed to light. Generally, PS are hydrophobic molecules, and therefore it is challenging to select deliverable formulations of these. Some of the ones used currently consist of organic (i.e. dextrose) or lipid-based (i.e. Cremophor) excipients which can in turn cause an unpredictable biodistribution of the compounds. Even if PSs accumulate in healthy tissues, side toxicity is minimised (this occurs in most cancer treatments, i.e. chemotherapy), since no therapeutic effect will be achieved unless PSs are excited with a particular wavelength of light (see schematic PDT in Figure 35). Hence, great specificity can be reached and more importantly, even if repeated treatments are needed (Master et al., 2013).

Founded on the two basic components involved in PDT (light and PS), it is possible to enhance selectivity of treatments in a dual manner: enhancing accumulation of PS in tumour tissue or else improving irradiation-specificity. Nowadays there is constant development and improvement of fibre-optic laser technology to enhance the focalised delivery of light; yet, side phototoxicity is still currently reported. For instance, although optical fibres were used, genitourinary side effects were found in motexafin lutetium-based PDT for the treatment of locally recurrent prostate cancer (Verigos et al., 2006).

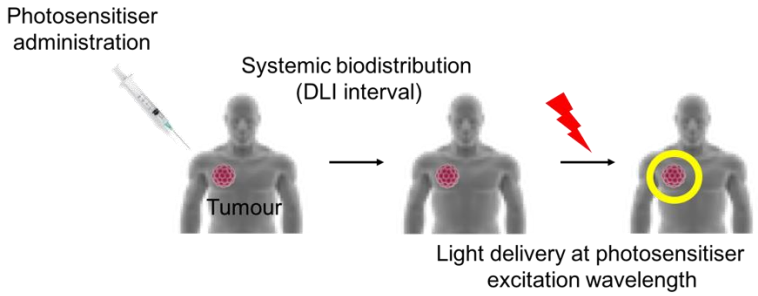

Figure 35. Schematic representation of PDT for cancer treatment.

During a PDT approach, systemic administration and distribution of PSs is followed by the application of light of a specific wavelength known to excite the PS used.

Passive tumour targeting of PS has been explained through “EPR effect”, as stated in Background and Introduction. Whilst passive targeting is non-specific, active targeting of treatment to tumours can be achieved. Ideally, molecular targets to direct treatments against tumours should play differential roles in cancer and healthy cells. Some of the

most relevant changes in malignant cells include transformations at a genetic level and related pathways. However, a more frequent approach to develop targeted strategies implies phenotypic disparities between cancer and normal cells, some of which might correlate with underlying genetic transformations. Some of these are for example changes in protein expression levels (Andrews et al., 2010). In line with this, moieties used in targeted strategies generally bind molecules that are exclusively expressed or whose expression has been significantly increased in diseased cells, in some occasions even combined in multiple targeting strategies, some of which will be reported down below (Huang and Oliff, 2001).

The most commonly used approaches involve the use of antibody-antigen- and receptor-mediated- targeting. The use of monoclonal antibodies can ease drug uptake; yet, it can also result in a decreased biological activity, reduction of stability of the compounds or internalisation difficulties due to the associated increase in size. As for receptor-mediated approaches, low-density lipoproteins, growth factors (i.e. insulin-like growth factor –IGF–, transferrin, endothelial growth factor –EGF–, folate), albumin or nuclear localisation signals (NLSs) among others have shown great affinity for corresponding receptors in cancer cells. This strategy can be hampered if receptors are not just expressed in tumours but also unwanted locations (e.g. metabolically active tissues express EGFR, receptor that is highly expressed in tumours). In this case, the receptor expression ratio between tumour and normal cells will determine the effectiveness of the targeting.

In line with the biodistribution and localisation of PS in target tissues, it is largely important to consider the correlation between the physicochemical properties, structural features of the photosensitiser compounds and their bioavailability (Boyle and Dolphin, 1996). For instance, hydrophobic PS need to be administered in an adequate vehicle due to lack of solubility in water, whose nature will determine the interaction with biological proteins and significantly affect the concentration of PS in tumour tissue. In line with this, the aggregation of hydrophobic photosensitisers within the lipidic tumour microenvironment exerts a major effect. On the other hand, hydrophilic PS generally lack a delivery vehicle and in this case, PS design will play a major role (i.e. charged PS tend to have a greater interaction with tissues in a pH-independent manner) (Boyle and Dolphin, 1996).

3.1.1 Targeted PDT and PCI

The most successful approaches in targeted PDT involve physical conjugation of photosensitisers to antigens or receptors found on tumour surfaces. As regards targeted strategies in PCI, additional targeting subjects arise from the combination of two different therapeutic agents: both targeted PS-conjugates and biologically active drugs-conjugates can be designed. As a matter of fact, since its development, PCI has been used to enable the delivery of large macromolecular drugs that experience difficulties penetrating cellular membranes due to their large size, i.e. immunotoxins, which have an important role in targeted strategies.

An important consideration in these approaches involves the contemplation of tumour-specific molecules not only in the parenchyma but also in the stromal tissue. In line with this, a more effective targeted therapeutic strategy might involve the previous molecular characterisation of the tumour structure under investigation. This would enable a major focus on the former, identifying markers with a more important role in the aggressiveness of a tumours mass (Hamoudi et al., 2010).

Following the above, several targeted PDT and PCI studies have been performed to date *in vivo* and *in vitro,* some of which will be reviewed below.

Folate receptor

One upregulated molecule on many human malignancies is folate receptor (glycosylphosphatidylinositol anchored cell surface receptor). Its expression is limited in healthy tissues and it is frequently associated to highly aggressive types of cancers. In particular, folate receptor's up-regulation has been verified in 90% of ovarian tumours as well as other cancer types including kidney, endometrial, mesothelioma, breast, brain and myeloid leukaemia (Parker et al., 2005). Yet, cancers of the prostate, bladder, liver, lymphomas and sarcomas present normal levels of folate receptor. Expression of this receptor happens in normal tissues within lungs, choroid plexus, kidneys and placenta and is restricted to the apical surface of polarised epithelia (Zwicke et al., 2012). Folic acid is a small, non-immunogenic ligand, stable over a broad range of temperatures and pHs, capable of recognising the folate receptor. For all the above, it is broadly used in targeted strategies. It has been used in several occasions in PDT in combination with albumin as a carrier vehicle. Albumin is subject to EPR effect owing to its size and can be metabolised by activated cells as a source of amino acids and energy, which is increased in malignant cells due to their high

proliferative activity (Neumann et al., 2010). In the recent study carried out by Butzbach et al. using polar β-carboline derivatives bound to folate-tagged albumin as photosensitisers, the phototoxicity caused by the conjugates was demonstrated. It required cellular uptake of the conjugates and was lysosomal dependent. It was concluded that PS coupling to folate-albumin could become a new strategy to avoid undesired side phototoxicity to cells lacking active folate endocytosis (Butzbach et al., 2016).

Transferrin receptor

Transferrin receptors are iron binding proteins found ubiquitously expressed in most human tissues at low levels but several fold highly overexpressed in tumour cells, and whose levels can also be related to tumour stage and progression. They are located in cell membranes and uptake occurs in a clathrin/dynamin dependent manner (Daniels et al., 2012). Based on the need of iron in cancer cell proliferation, transferrin is another frequently employed molecule for targeted treatments, PDT among others. Specifically, transferrin-haematoporphyrin (Tf-Hp) resulted in at least 6-fold higher phototoxicity compared to the untargeted counterpart, observing different sensitivity in the different cell lines assayed. This was probably due to dissimilarities between lipid bilayers in cell membranes, which could have influenced penetration and binding of Hp. In addition, a faster cell death was found with targeted compounds in addition to the enhanced specificity (Laptev et al., 2006). In a different study, no improvement was found in intracellular uptake or phototoxicity using transferrin-bound PEGylated Foscan-loaded liposomes for PDT treatment of oesophageal cancer cells *in vitro*. It was hypothesised that membrane destabilisation could have resulted in Foscan leakage from the Tf-vehicles (Paszko et al., 2013), indicating the importance of the optimal preparation of formulations.

EGFR receptor

Epidermal growth factor receptors (EGFR) are cell surface molecules belonging to the tyrosine kinase family of proteins with abnormal expression in malignant cells. Like the molecules reported above, EGFR is associated to survival and prognosis. Targeting EGFR has been achieved using both monoclonal antibodies (mAbs) and tyrosine kinase inhibitors (TKIs). Cetuximab and panitumumab are the two most advanced mAbs recognising the extracellular domain of EGFR molecules. On their side, TKIs act on the intracellular domains of the receptor inhibiting signalling cascades initiated by tyrosine kinase (Yewale et al., 2013). EGFR plays an essential role in regulation of

proliferation, differentiation and survival, hence its up-regulation in malignant cells. Besides, several ligands can bind to the receptor such as: endothelial growth factor (EGF), transforming growth factor alpha (TGF-α), heparin-binding EGF, epigen, betacellulin, amphiregulin, epiregulin, neuregulin-2β, etc., expanding the possibilities to target this receptor. Recently, the second generation PS phtalocyanine Pc4 was formulated within micelles and bound to the GE11 ligand (known to bind to the receptor) so as to target EGFR (Master et al., 2012). An enhanced uptake of the modified PS was observed in human epidermoid carcinoma cells within just 2 hours. Dispersion of fluorescence was also observed overtime appearing in a punctuated manner at the 6 hr time point and being homogeneously spread throughout the cytosol at 24 hr Non targeted micelles were also able to enter the cell cytosol, yet, this was time and concentration dependant, suggesting receptor-mediated endocytosis occurs at an earlier time point. Regarding PDT effect induced by targeted formulation of PS, significant differences in cell death were observed at the lowest PS concentrations, while no differences were detected at the highest doses. This is indicative that lower doses could be employed for targeted-PS (Master et al., 2012). A recent study performed *in vivo* PDT using nanobody-conjugated PS specifically recognising EGFR. This conjugate was the only one assayed causing necrosis in 90% of the tumours, confirming its potential in PDT for head and neck cancer treatment (van Driel et al., 2016).

EGFR has also been targeted in PCI approaches on several occasions. For instance, very high cytotoxicity was observed combining EGF-saporin with $TPCS_{2a}$, using drug doses as low as 1 pM in a $EGFR^{+}/ABCG2^{+}$ population of human breast cancer cells. ABCG2 is an efflux pump largely responsible for multidrug resistance in malignant cells. Accordingly, it was concluded that PCI photosensitisers could escape recognition by such pumps and overcome the multidrug resistance shown in numerous cancer treatments (Selbo et al., 2012). Comparatively, EGF-saporin was able to induce cytotoxicity at 2pM in ovarian cancer cells, while no cell killing was observed up to 10pM in a breast cancer model. No differences were found after PCI on uterus sarcoma and breast cancer $EGFR^{-}$ control cells between targeted and non-targeted saporin (Weyergang et al., 2006). A similar therapeutic outcome resulted from the conjugation of saporin to Cetuximab®. Negligible cytotoxicity resulted from untargeted saporin as opposed to the enhanced cell killing exhibited by the targeted conjugate in colorectal and prostate cancer cell lines. Minor effects observed were considered to be due to non-mediated receptor endocytosis of the drug (Yip et al., 2006).

Human Epidermal Growth Factor receptor (HER2)

HER2 (Erb2, c-erbB2, HER2/neu) belongs to the family of epidermal growth factor receptors, but due to its relevant role among other proteins of ErbB family, its participation in targeted strategies will be independently reviewed. HER2 is involved in cell growth, differentiation, survival; and its overexpression and up-regulation have been associated with the malignant transformation of cells, being directly related to a poor prognosis in ovarian, gastric, prostate and breast cancer among others (Tai et al., 2010). The anti-HER2 antibody clinically available Herceptin® (trastuzumab) led to a major advance in breast cancer treatment. Conjugation of saporin with this antibody resulted in an enhanced PCI effect when approaching with a light-after procedure (see Chapter 2 for a detailed description of light –before/–after PCI). On the other hand, light-before altered the integrity of the receptor and consequently reduced cytotoxicity (Berstad et al., 2012). In a study performed with gelonin targeting HER2 in cell lines with varied HER2 expression, it was concluded that sensitivity of malignant cells to drugs has to be taken into consideration in addition to toxin uptake levels (Bull-Hansen et al., 2014). Recently, a photosensitiser was also modified to target HER-2 oesophageal carcinoma cells (Pye et al., 2016). Specifically, a fragment of trastuzumab was covalently bound to a near infrared dye and chlorin (main photosensitive component). This structure was investigated as a theranostic platform used for both fluorescence cell-labelling of HER-2 tumour cells and PDT, concluding a successful binding to the target cells in addition to an effective PDT effect (Pye et al., 2016).

Endothelial glycoprotein-2

EGP-2, also known as Ep-CAM, is an epithelium specific marker highly expressed in human carcinomas (McLaughlin et al., 2004). Epitopes in EGP-2 molecules can be recognised by monoclonal antibodies such as MOC-31, then endocytosed by target cells. This specificity has been exploited in PCI studies, i.e. designing MOC31-gelonin immunotoxins and combining it with different photosensitisers. The same effect was observed with both targeted and untargeted toxin in cells exhibiting low EGP2 expression; yet, EGP-2^{+} small cell lung carcinoma cells were significantly more affected by MOC31-gelonin than free toxin (Selbo et al., 2000b). *In vivo,* promising results were observed in mice bearing human colorectal tumours treated with MOC31-gelonin and $AlPcS_{2a}$. Tumours were completely eradicated in 6 out of 9 animals (Selbo et al., 2001).

CD133

There is growing interest nowadays in directing treatments against progenitor cells in cancer, which are thought to sustain proliferation and survival of tumour masses. In line with this, CD133 is a surface molecule described in cancer stem cells, indicator of aggressive tumours with high proliferative and tumour-formation capacity, highly resistant to treatments, in turn resulting in low prognosis (Ren et al., 2013).

Targeting CD133 in PCI has enabled the reduction of drug doses very notably. For instance, CD133-saporin nearly completely eliminated colorectal cells (highly expressing CD133) *in vitro* using femtomolar drug doses. In this case, saporin alone resulted in similar cell death to that of PDT. Moreover, viability of PDT-resistant pancreatic cancer cells with lower expression of CD133 than the colorectal cell line in the same study was reduced to 10% after PCI (Bostad et al., 2013).

3.1.2 CXCR4 receptor and cancer: focus on prostate tumours

CXCR4 is a chemokine receptor belonging to the G-protein-coupled family of receptors, with an important role in haematopoiesis, immunity and organogenesis among others. Changes in its expression have been observed in diseases including cancer. Specifically, dysregulation of this receptor has been observed in metastasis, resulting in enhanced signalling. An additional role as correceptor for the entry of HIV has been confirmed. Stromal cell-derived factor 1 (SDF-1) also known as C-X-X motif chemokine 12 (CXCL12) selectively binds to CXCR4 (Furusato et al., 2010). The expression of CXCR4 in normal healthy tissues is uncommon and its expression in cancer could be hypoxia-induced: hypoxia during tumour progression triggers the production of hypoxia-inducible factor 1 (HIF-1) which is associated to the expression of CXCR4 among others. Vascular endothelial growth factor (VEGF) or nuclear factor kappa β (NFKβ) could also be participants in the increased expression of CXCR4.

The stem cell origin of cancer has been demonstrated in different types of cancer, including prostate tumours. In line with this, surface markers CD133 and CD44 have been recognised as stem cell markers and have been identified in cell populations within the prostate gland epithelia. These cells exhibit a highly upregulated expression of CXCR4, as shown in the stem cell subset isolated from the human prostate cancer cell lines PC3 and DU145 (Dubrovska et al., 2012). CXCR4 is also expressed in

normal stem cells in the prostate and it is hypothesised that cancer stem cells might derive from prostatic stem cells (Dubrovska et al., 2012; Singh et al., 2004).

Participation of SDF-1 in stem cell homing has been reported; consequently, expression of CXCR4 in cancer suggests a participation in metastasis to organs with SDF-1 expression such as lymph nodes, lungs, liver and bones. In addition, bone metastases which is a characteristic in prostate cancer patients, might occur in an organ-specific manner founded on the CXCR4-SDF-1 axis reported above. In greater detail, tumours require host cells to ensure survival and proliferation, participating in the creation of niches within tumour masses that protect cancer stem cells from various external stresses. These participating cells might also be involved in the generation of distant premetastatic niches that will in the end ease tumour migration. Among these cells, mesenchymal stem cells (MSCs) were recently identified as an implicated cell type, recruited by different cytokines. MSCs can differentiate into cancer-associated fibroblasts (CAF), in charge of creating cytokine networks necessary for migration and progression of cancer. Prostate tumours recruit MSCs; precisely, within tumours, CXCL16 interacts with CXCR6 expressed by MSCs, which later differentiate into CFAs and secrete CXC12, responsible for the promotion of the epithelial-to-mesenchymal transition (EMT) of malignant cells (Jung et al., 2013). The interaction between CXCR4 and CXC12 induces the activation and signalling of tumour-associated integrin, which enhances adhesion in circulating cells; besides, it also triggers the expression of metalloproteinases (i.e. MMP-2) involved in degradation of cell invasion barriers as is the case of the extracellular matrix (Singh et al., 2004; Zhang et al., 2008).

Expression of CXCR4 has been verified in PC3 human prostate cancer cells on several occasions (Dubrovska et al., 2012; Hatse et al., 2002; Singh et al., 2004; Zhang et al., 2008).

3.1.2.1 vMIP-II selectively binds CXCR4

vMIP-II (viral macrophage inflammatory protein II), also known as vCCL2 (viral CC motif chemokine) is a chemokine expressed by human herpesvirus 8, that alters the chemokine network in the host to successfully carry out the infection cycle and escape from the protection conferred by the immune system (Szpakowska and Chevigne, 2016). A high affinity interaction between vMIP-II and CC and CXC chemokine receptors has been described: these host chemokine receptors are used by HIV-1 as

coreceptors to enter cells, the most relevant being CXCR4 and CCR5. Specifically, the N-terminal of this protein is thought to be responsible for such interaction (LiWang et al., 1999). In human target cells, viral entry is in fact inhibited by chemokines binding to CXCR4 such as SDF-1α.

Since its discovery, vMIP-II has been modified to promote receptor-selectivity. Following these lines, a peptide derived from the N-terminal of the protein was developed, confirming its interaction with CXCR4 but not CCR5. The relevance of the chosen fraction of vMIP-II protein has been confirmed, clarifying existing differences in binding between vMIP-II and CCR5 or CXCR4. Critical residues within the sequence of the vMIP-II peptide have also been identified, most of which are positively charged (Luo et al., 2000).

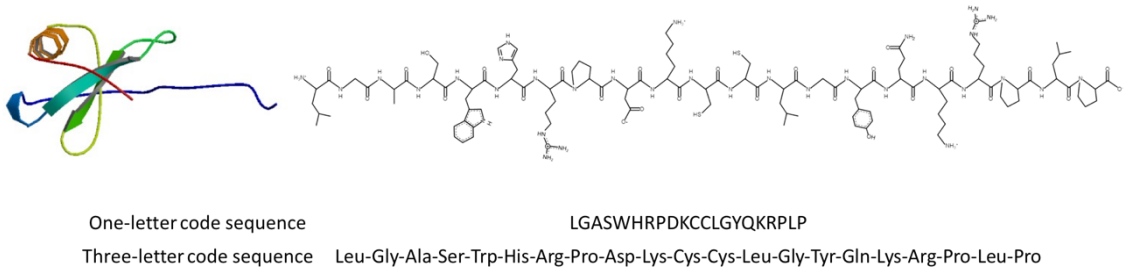

Figure 36. HIV vMIP-II.

NMR structure of the anti-HIV chemokine vMIP-II and sequence of aminoacids 1-21 binding CXCR4. Image adapted from the Protein Data Bank.

3.1.2.2 AMD3100 as CXCR4 inhibitor

AMD3100 (Plerixafor) is a bicyclam, non-peptide antagonist of CXCR4, originally designed as an anti-HIV molecule through inhibition of viral replication. In this context, although gp120 glycoprotein (located in the viral envelope) seemed to be its target of action, this was only an indirect target; while CXCR4 coreceptor was found to be a direct target. Initial trials carried out with plerixafor unexpectedly increased the levels of $CD34^+$ cells (hematopoietic stem cells) in peripheral blood: blockage of the interaction CXCR4-SDF-1 mobilised these stem cells, preventing their homing in the bone marrow.

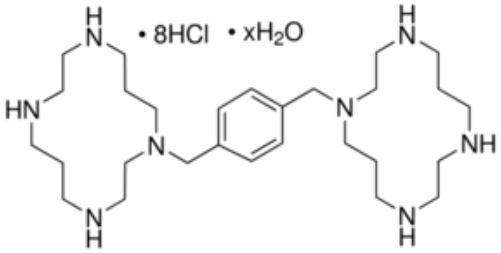

Figure 37. AMD3100, octahydrochloride hydrate.
Structure of AMD3100 (Plerixafor), CXCR4-selective inhibitor.

As for the inhibition now concerning (AMD3100-CXCR4), binding to CXCR4 receptor has been reported to be highly specific and concentration dependent, showing no interaction with other chemokine receptors such as CXCRX1, CXCR2, CXCR3, CCR1, CCR2, CCR3, CCR4, CCR5, CCR6, CCR7, CCR8, CCR9 (Hatse et al., 2002). Agonistic effects of AMD3100 were rejected based on the lack of cell migration and intracellular calcium mobilisation induced in the same study. In a different study, AMD3100 displayed an inhibitory effect on the interaction between a derivative of the vMIP-II protein above reported and CXCR4 (Yang et al., 2014).

3.1.3 Cell-penetrating peptides

In addition to the above reported specificity conferred by proteins and molecules present in tumours at higher levels, or even exclusively expressed in malignant cells, a very common targeting strategy nowadays involves the use of cell penetrating peptides, which have proven to significantly enhance intracellular delivery.

The hydrophobic nature of the external cell membrane protects cells from the surrounding environment, limiting access to the cellular interior to molecules of small size. However, available drugs are increasingly large these days, posing major limitations to their entry into cells. Cell-penetrating peptides (CPPs) have been frequently used as delivery vehicles for large molecular weight drugs (Madani et al., 2011).

CPPs, also known as Trojan peptides, membrane translocating sequences or protein transduction domains, are short peptide sequences (< 40 amino acids long), partially hydrophobic, water-soluble and characterised by the presence of positively charged residues at physiological pH (necessary to interact with negatively charged residues

within the lipid bilayer). CPPs are capable of penetrating cellular membranes while also carrying a wide range of biologically active cargoes efficiently (i.e. polymers, liposomes, low molecular weight drugs, nucleic acids, nanoparticles, etc.). They can successfully achieve this even at low micromolar concentrations (transport is generally dose-dependent) and in the absence of chiral receptors, while maintaining the integrity of cell membranes. The sequence and structure of these CPPs can be modified in order to enhance the delivery of biologically active drugs. For instance, replacement of lysine residues with ornithine confers protection to cellular degradation, modification of the peptides to cyclic peptides or dendrimers improves the delivery efficiency (Copolovici et al., 2014).

CPP-mediated delivery is generally non-specific and thus cell-specific peptides can be included to increase specificity. The mechanisms behind membrane penetration have not been completely elucidated, yet, there is supporting evidence of it occurring via energy-independent processes or endocytosis. This last mechanism seems to be the most likely for low-CPP concentrations (Madani et al., 2011; Schwarze et al., 2000).

Among all CPPs discovered to date, HIV-1 TAT and penetratin (Antp) exhibit the greatest protein-transduction efficiency.

3.1.3.1 TAT peptide

Discovered in 1988, HIV TAT transactivating factor served as a basis to develop CPPs. TAT peptide currently used as CPP is the truncated version of a protein found in human HIV-1 virus, and is essential in viral replication (Bayer et al., 1995; Watson and Edwards, 1999).

TAT peptide has been used on numerous occasions to enhance the outcome of PDT studies. For instance, TAT-conjugated gold nanostars showed significantly increased accumulation and photosensitisation in breast cancer cells *in vitro*, whereas no therapeutic benefit was observed with the non targeted counterpart (Fales et al., 2013). In a different study, no presence of the PS $AlPcS_{2a}$ was demonstrated in KB and HeLa cells unless targeted with TAT. In addition, experiments carried out at 4°C showed some uptake in both cell lines, which was significantly increased when higher temperatures were used. This indicates that despite passive diffusion is responsible for some of the PS-TAT conjugate's uptake, most of it occurs through endocytosis (Zhao

et al., 2011). Initial *in vitro* experiments in PC3 cells and later *in vivo* biodistribution studies confirmed higher tumour-selectivity of porphyrin-TAT compounds in a prostate cancer mouse model as opposed to non targeted mTHPC and hematoporphyrin derivative. Significant phototoxicity was also verified, and dark toxicity was minimised using the targeted conjugate (Sehgal et al., 2008).

Furthermore, TAT peptide has also been employed in a targeted-PCI study (Wang et al., 2012). In this case, TAT-TPP did not only exhibit an enhanced uptake and light-toxicity (even at low concentrations) in head and neck cancer cells compared to free $TPPS_{2a}$, but restriction of subcellular localisation to endo/lysosomal compartments was concluded (key requisite in PCI approaches). This was confirmed in fluorescence microscopy as well as spectroscopic analysis of the compounds, where a red shift in the emission of fluorescence was attributed to binding of the compound to lysosomal membranes (Wang et al., 2012).

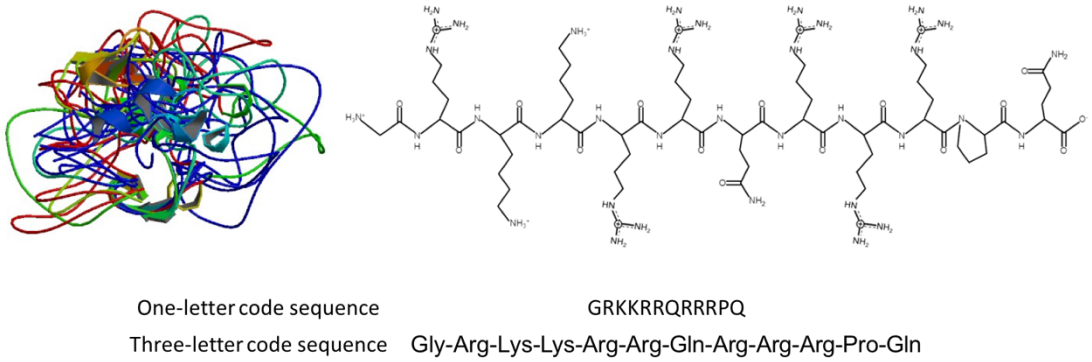

Figure 38. HIV-1 TAT protein.

NMR structure of HIV-1 TAT protein and sequence of aminoacids of TAT peptide used as CPP. Image adapted from the Protein Data Bank.

3.1.3.2 Penetratin peptide

Homeoproteins are trans-activating factors with the intrinsic capacity to bind DNA through their homeodomain. Homeodomains are highly conserved across species and consist of three α-helices, the third of which is particularly relevant in target DNA sequence recognition. Penetratin is a peptide of the homeodomain found in the third helix of *Drosophila* Antennapaedia transcription factor (Dupont et al., 2011).

Alike TAT peptide, membrane penetration of penetratin is not completely inhibited at low temperatures, confirming endocytosis plays a major role but internalisation can also follow an energy-independent route (Derossi et al., 1994; Dixon et al., 2007). Additionally, this internalisation is not completely unspecific, as confirmed by the lack of internalisation exhibited by truncated versions of the peptide (Derossi et al., 1994).

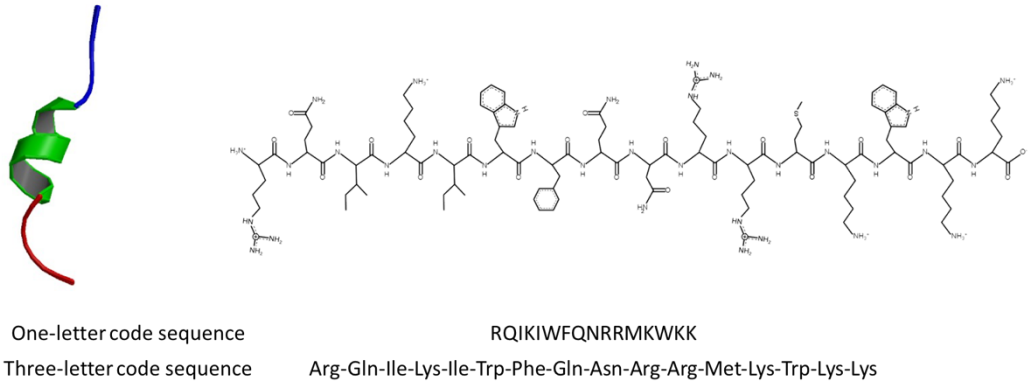

Figure 39. Antennapedia Penetratin.

NMR structure of the third helix of Antennapedia homeodomain and sequence of aminoacids of Antp peptide used as CPP. Image adapted from the Protein Data Bank.

3.2 Aims

Chapter 3 focuses on the potential enhancement of PDT and PCI in prostate cancer following targeted approaches *in vitro*. Therefore, the main aim of the present chapter was to compare therapeutic outcomes resulting from targeted and non targeted light-based therapies.

In order to enhance light-treatments in our prostate cancer model, three different photosensitiser conjugates were examined. All of these consist of a main photosensitive component (TPP-) bound to either cell penetrating peptides alone (TAT, Antp) or conforming a targeting chimaera (vMIP-II-TAT).

Following a similar outline as Chapter 2, the first couple of sections reported assessed the potential benefit targeting strategies offer through measurement of cell viability after PDT and PCI treatments. The optimal parameters determined in Chapter 2 served as basis for the experimental procedures carried out in the present chapter. PCI procedures require the initial determination of PS-conjugate doses yielding subthreshold PDT. These assessments of cell viability were followed by the observation of the biological mechanisms behind targeted PS-derivatives in PDT and PCI through the observation of their subcellular localisation.

Should CPP-derived strategies produce better results, we hypothesise that side phototoxicity after PDT and, hence, PCI, could be significantly reduced or even avoided by using lower drug doses (photosensitiser or a combination of photosensitiser and biologically active drug), whilst maintaining the tumour-eradication capacity of both PDT and PCI treatments.

3.3 Materials & Methods

Cell work

Both targeted- PDT and PCI experiments were performed on PC3 human cancer cells (see detailed description in Chapter 2, Materials & Methods section).

Synthesis of TAT-TPP, Antp-TPP, vMIP-II-TAT-TPP conjugates

Synthesis of targeted conjugates was carried out by Dr. Ruggero Dondi from the Department of Pharmacy and Pharmacology, University of Bath. Three different TPP (tetraphenylporphyrin)-based compounds were conjugated via click chemistry. Targeting peptides were previously prepared through solid phase peptide synthesis according to the Fmoc strategy (see Appendix for detailed description of the synthesis of conjugates)

Three conjugates were designed: TAT- (48-57) and Antp- derivatives as well as a vMIP-II-TAT (48-57) chimaera (CPP and CXCR4 targeted). The structure of TPP-derivatives is displayed in Figure 40. TAT-TPP consists of the TAT protein (residues 48-57) linked to tetraphenylporphyrin through a linker, attaching one of the porphyrin's phenyl ring to TAT peptide (Figure 40A). Antp-TPP is composed of penetratin peptide linked to one of the tetraphenylporphyrin's phenyl rings (Figure 40B). Finally, vMIP-II-TAT is a chimaeric conjugate combining two distinct targeting moieties: N-terminal sequence of vMIP-II peptide directly linked to TAT protein (residues 48-57), which is bound to one of the tetraphenylporphyrin's phenyl rings (Figure 40C).

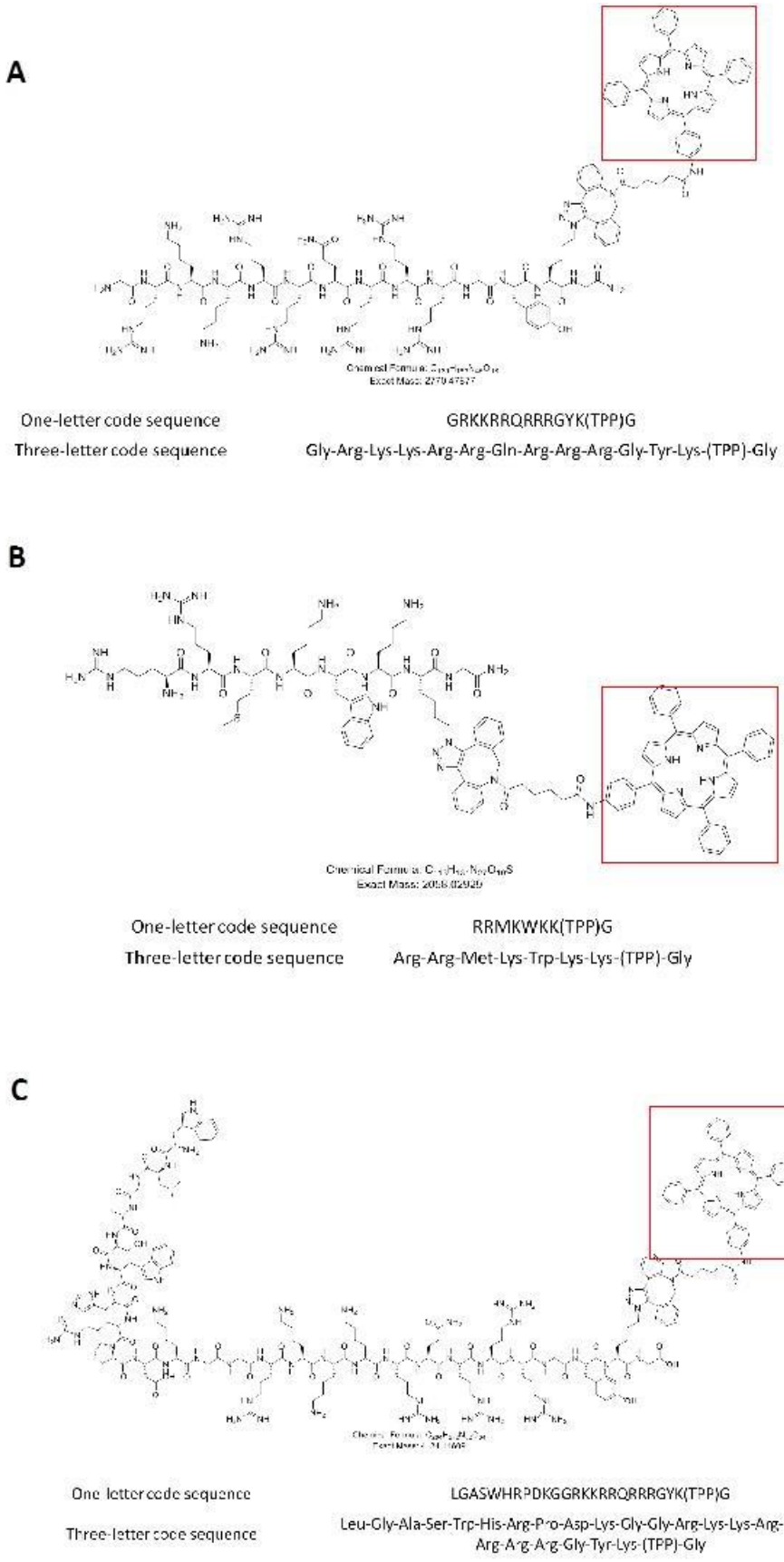

Figure 40. Structure of TAT-TPP (A), Antp-TPP (B), vMIP-II-TAT-TPP (C) conjugates.

Molecular weight 2770.47877, 2058.02929, 4134.14609 (g/mol) respectively. The red box indicates TPP in the compounds.

Chemicals and photosensitisers solutions

Saporin (see detailed description in Chapter 2, Materials & Methods section).

Saporin-Alexa-Fluor488® conjugate (see detailed description in Chapter 2, Materials & Methods section).

$TPPS_{2a}$ (see detailed description in Chapter 2, Materials & Methods section).

TPP-conjugates were dissolved in water, storing the aliquots at 4°C. Experimental concentrations were obtained diluting a 10 nM solution in cell media to reach desirable concentrations.

AMD3100 was purchased from Sigma (A5602). The stock solution was prepared by dissolving the powder in distilled water at 10 mg/ml. Dilutions were then prepared in PBS and the resulting aliquots were stored at 4°C. Experimental solutions were obtained further diluting in cell media to reach desirable concentrations.

Light source

LumiSource® (PCI Biotech, Norway) was used to excite cells exposed to TPP-conjugates and $TPPS_{2a}$ *in vitro* (see detailed description in Chapter 2, Materials & Methods section).

PS spectral measurements

Different photosensitiser solutions were prepared in methanol to a final 8 μM concentration. The same procedure reported in Chapter 2 was then followed (see detailed description in Chapter 2, Materials & Methods section).

TPP-conjugates uptake

The same procedure reported in Chapter 2 for $TPPS_{2a}$ / $TPCS_{2a}$ uptake in PC3 cells was followed (see detailed description in Chapter 2, Materials & Methods section).

PDT-dose response curves

The same procedure reported in Chapter 2 for PS dose-response curves in PC3 cells was followed (see detailed description in Chapter 2, Materials & Methods section).

PDT & PCI (combination) experiments

The same procedure reported in Chapter 2 for "light-after" PCI was followed combining saporin and TPP-conjugates in PC3 cells (see detailed description in Chapter 2, Materials & Methods section).

AMD3100 inhibition experiments

PC3 cells were seeded on 96-well plates at 8000 cells/well. Cells were allowed to grow for 24 hr before administering solutions of AMD3100 ranging 0.01 – 25 μg/ml prepared in cell media. Different procedures were then followed:

- 1 hr after incubation with AMD3100 plates were washed once with PBS and solutions combining TPP-conjugates 12 – 200 nM and AMD3100 at 25 and 50 μg/ml prepared in cell media were administered, incubating cells for 24 hr.
- 1 hr after incubation with AMD3100 plates were washed once with PBS and solutions combining TPP-conjugates at 50 nM and AMD3100 at 0.01 – 25 μg/ml prepared in cell media were administered, incubating cells for 24 hr.
- 24 hr after incubation with AMD3100 plates were washed once with PBS and solutions combining TPP-conjugates at 50 nM and AMD3100 at 0.01 – 25 μg/ml prepared in cell media were administered, incubating cells for 24 hr.

Hereafter, plates were washed once with PBS and wells were replaced with fresh media. After a 4 hr-cell recovery period, plates belonging to "light" groups were illuminated. Cell viability was measured 48 hr after light treatment. Plates were kept in a 37°C humidified atmosphere containing 5% CO_2 at all times, those involving photosensitisers were wrapped in foil and corresponding experimental procedures were carried out protected from light to avoid unintended excitation of photosensitisers.

Analysis of cell viability in two dimensional models

MTT was used to observe cytotoxicity in 2D experiments (see detailed description in Chapter 2, Materials & Methods section)

Subcellular localisation of TAT-TPP, Antp-TPP, vMIP-II-TAT-TPP

The same procedure reported in Chapter 2 for subcellular localisation of $TPPS_{2a}$ / $TPCS_{2a}$ in PC3 cells was followed (see detailed description in Chapter 2, Materials &

Methods section). In this case, a 400 nM solution of the TPP-conjugates was administered to PC3 cells. The same excitation wavelength and imaging settings described in Chapter 2 were used to acquire micrographs of the conjugates under study.

Subcellular localisation of saporin-Alexa-Fluor488® conjugate

The same procedure reported in Chapter 2 for subcellular localisation of saporin-Alexa-Fluor488® in PC3 cells was followed (see detailed description in Chapter 2, Materials & Methods section). In this case, a 100 nM solution of the TAT-TPP was co-administered to PC3 cells. The same excitation wavelength and imaging settings described in Chapter 2 were used to acquire micrographs of the conjugates under study.

Statistical analysis

Statistical analysis was performed using GraphPad prism 6. Two-way ANOVA followed by Bonferroni *post hoc* multiple comparison was used. Data is displayed as mean with error bars +/- SEM; significance level of $p < 0.05$ (*p = 0.05 to 0.01; **p = 0.01 to 0.001; ***p = 0.001 to 0.0001)

In MTT cell viability assays, each data point was the result of experiments carried out in triplicate and each of these repeats was the average of 8-16 wells. All experiments were carried out in triplicate but for AMD3100 inhibition pilot study, where data points are a single average of 8-16 wells.

3.4 Results

3.4.1 Photosensitiser spectra

Every PDT and PCI treatment requires an initial spectroscopic study of PS to determine the optimal excitation wavelength and maximise photooxidation. Following these lines, as performed with the photosensitisers reported in Chapter 2, absorption and emission spectra of all the TPP conjugates were measured (Figure 41).

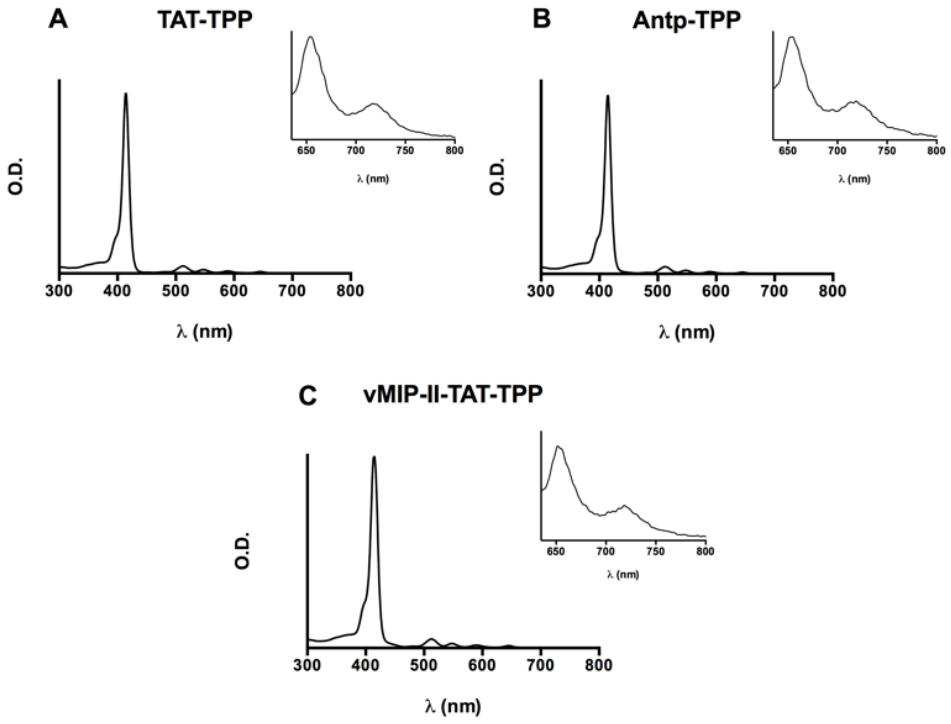

Figure 41. Absorption and emission spectra of TAT-TPP (A), Antp-TPP (B) and vMIP-II-TAT-TAPP (C) in methanol (8 μM).

Emission spectra were taken exciting the TPP-conjugates at 420 nm, cut-off filter set at 515 nm.

All TPP-conjugates exhibited a similar spectrum, showing an absorption peak at around 414 nm. A weaker absorption around 520 nm was also found in all three conjugates. All fluorescence emission peaks were found in the red region of the spectra (around 650 nm).

3.4.2 TPP-conjugate uptake in prostate cancer cells

Again, as performed with photosensitisers in Chapter 2, emission of fluorescence in PC3 cells was measured after incubating these with increasing concentrations of the TPP-derived photosensitisers (12-80 nM), then related to the cellular uptake of the conjugates. A linear relationship between intensity of fluorescence and PS dose was found in all three compounds. Moreover, no plateau was seen (see Fig. 8).

Uptake of TPP bound to Antp (represented by green squares) was significantly higher compared to that exhibited by vMIP-II-TAT (represented by red triangles) at the highest dose tested (800 nM).

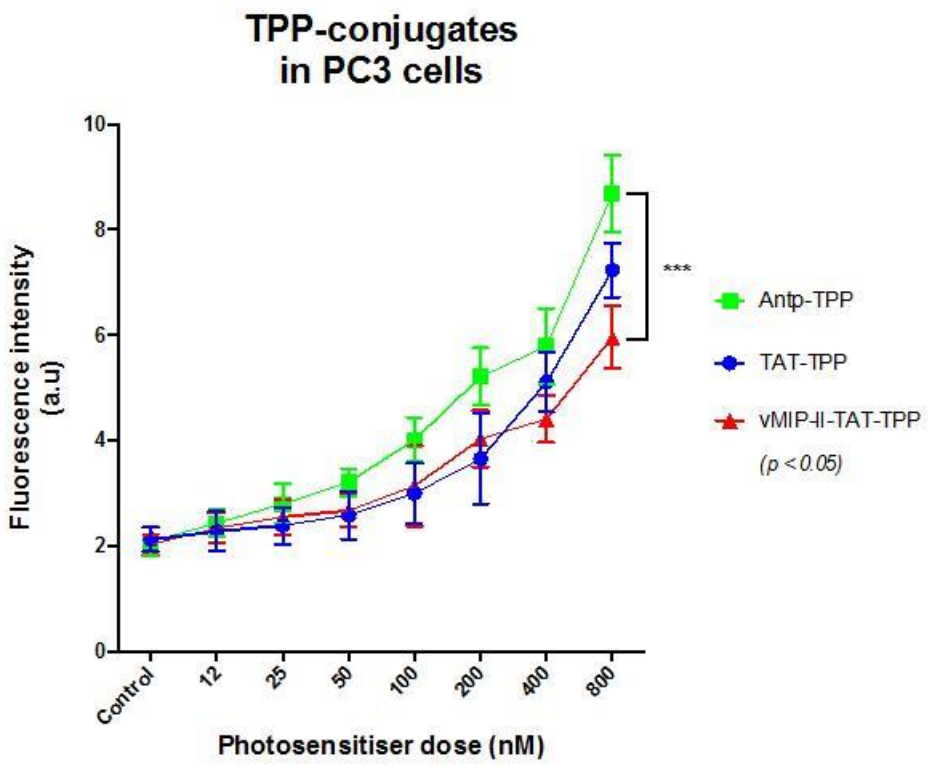

Figure 42. Uptake of TAT-TPP, Antp-TPP and vMIP-II-TAT-TPP in PC3 cells.

Cells were incubated for 24 hr with PS solutions ranging 12-800 nM, then washed and media was replaced with no phenol red media. Uptake was related to PS fluorescence intensity. Data is displayed as mean with error bars +/- SEM; two-way ANOVA followed by Bonferroni post hoc multiple comparison was used, significance level of p<0.05

Despite differences in uptake were not significant in the rest of the cases, the greatest fluorescence was exhibited by cells incubated with Antp-TPP followed by TAT-TPP and vMIP-II-TAT-TPP.

3.4.3 PDT effect in dose-response curves

Based on the optimal conditions established in Chapter 2 which resulted in maximal cell killing following 1.26 J (3 minutes) and 24 hr DLI light treatment, human prostate cancer cells were incubated with increasing doses of the TPP-based photosensitisers to determine the most suitable doses of the new PS conjugates.

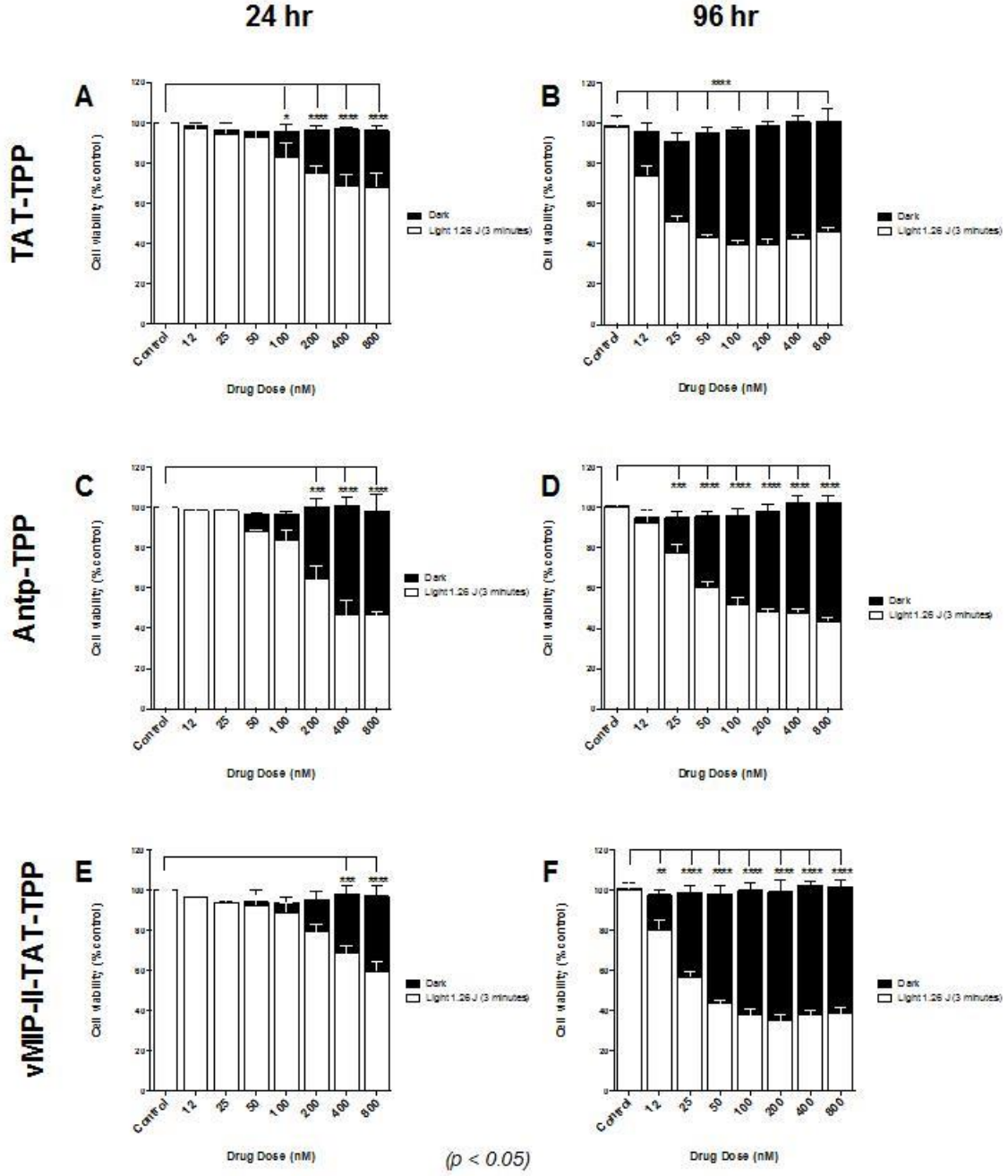

Figure 43. Evaluation of TPP-based PS PDT effect in PC3 cells.

Cells were incubated with either TAT-TPP (A, B), Antp-TPP (C, D) or vMIP-II-TAT-TPP (E, F) solutions ranging 12-800 nM during 24 hr, drugs were then washed off and a 4 hr chase period was allowed before illumination. Cell viability was measured 24 hr and 96 hr after light treatment. Data is displayed as mean with error bars +/- SEM; two-way ANOVA followed by Bonferroni post hoc multiple comparison was used, differences between dark control and light groups are shown; significance level of $p < 0.05$.

The aim of PCI experiments reported in the following sections was to enhance cell death by combining treatments (PDT and a biologically active drug, saporin in this case) that would otherwise result in a subthreshold outcome when administered alone, hence, different doses of the PS-conjugates were assayed in PDT approaches to determine the optimal doses for later PCI experiments.

Measurements 24 hr after light showed a gradual increase in cell death as doses increased and a significant effect was only found at higher doses, from 100 nM for TAT-TPP, 200 nM for Antp-TPP and 400 nM for the vMIP-II-TAT-TPP chimaera. Specifically, 32% was the highest cell death found after PDT with TAT-TPP (Figure 43A), 54% when using Antp-TPP (Figure 43B), and 41% with vMIP-II-TAT-TPP (Figure 43C). All doses assayed for all three PS compounds resulted in significant cell killing 96 hr after light and a plateau in cell death was found from 100 nM under the assayed conditions (Figure 43B, Figure 43D, Figure 43F). This plateau resulted in 40%-50% viable cells with TAT-TPP (Figure 43B) or Antp-TPP (Figure 43 D) and around 60% when using vMIP-II-TAT-TPP (Figure 43F). In addition, no dark toxicity was noted at the assayed concentrations of PS.

On this basis, given the high PDT effect observed at the later time point (96 hr) with the higher doses chosen, 12 nM, 25 nM and 50 nM were selected to be combined with 2 nM saporin in PCI experiments, as will be displayed in the sections below.

3.4.4 PCI combination experiments

Following the main aim of the present chapter, to evaluate the possible enhancement in therapeutic outcome arising from the use of CPP-based PS, viability of PC3 cells was measured when PDT- and PCI- treated with $TPPS_{2a}$ or CPP-derivatives, alone or in combination with saporin respectively.

Viability of PC3 cells was significantly affected by nearly all combinations of TPP-conjugates or $TPPS_{2a}$ and saporin (PCI), regardless of the compound and time point of assessment of cell death (Figure 44). Yet, viability had to be measured 96 hr after light to observe a significant therapeutic outcome after PDT (Figure 44B, Figure 44D, Figure 44F, Figure 44H).

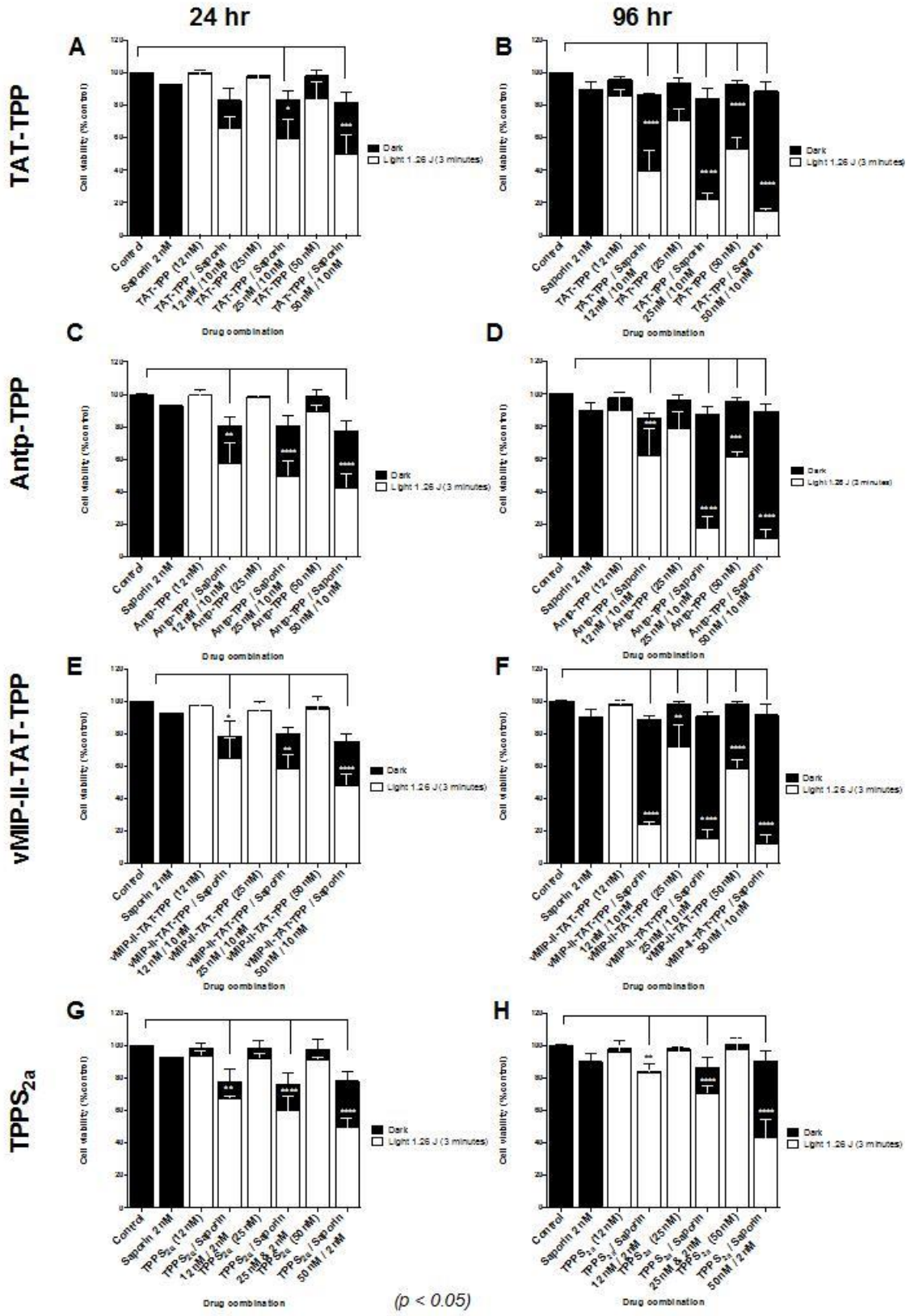

Figure 44. Assessment of PDT/PCI effect of TPP-conjugates in PC3 cells.

Cells were incubated with either 12, 25 or 50 nM solutions of TAT-TPP (A, B), Antp-TPP (C, D), vMIP-II-TAT-TPP (E, F) or $TPPS_{2a}$ (G, H), alone or in combination with saporin 2 nM for 24 hr. Drugs were then washed off and a 4 hr chase period was allowed before illumination. Cell viability was measured 24 hr and 96 hr after light treatment. Data is displayed as mean with error bars +/- SEM; two-way ANOVA followed by Bonferroni post hoc multiple comparison was used, differences between dark control and light groups are shown; significance level of $p < 0.05$.

A similar effect was found 24 hr after both light treatments with all PS (Figure 44A, Figure 44C, Figure 44E, Figure 44G), regardless of the presence of CPP or targeting moieties in TAT-TPP, Antp-TPP and vMIP-II-TAT-TPP. Briefly, in these cases, cell death after PDT remained between 0.71% (12 nM Antp-TPP, Figure 44C) and 16.16% (50 nM TAT-TPP, Figure 44A); while PCI resulted in ranges of cell death between 32.81% (12 nM $TPPS_{2a}$, Figure 44G) and 57.57% (50 nM Antp-TPP, Figure 44D). Yet, differences between compounds became more pronounced over time post illumination. For instance, while the largest PCI effect increased cell killing up to 85.09% (TAT-TPP, Figure 44B), 88.86% (Antp-TPP, Figure 44D) and 87.41% (vMIP-II-TAT-TPP, Figure 44F) for the TPP-conjugates, 57.22% was the greatest cell death when PCI-treating prostate cancer cells *in vitro* with $TPPS_{2a}$ at the same concentration (50 nM in all PS cases). When comparing the outcome after PDT and PCI in these same scenario (96 hr post light), 2.27-fold, 3.55-fold, 4.65-fold and 5.5-fold greater efficiency in cell death were found post PCI for $TPPS_{2a}$, TAT-TPP, vMIP-II-TAT-TPP and Antp-TPP respectively. Light groups 96 hr after illumination are shown in Figure 45, revealing significant differences in cell death between PCI treatment of cells with TPP-conjugates or $TPPS_{2a}$.

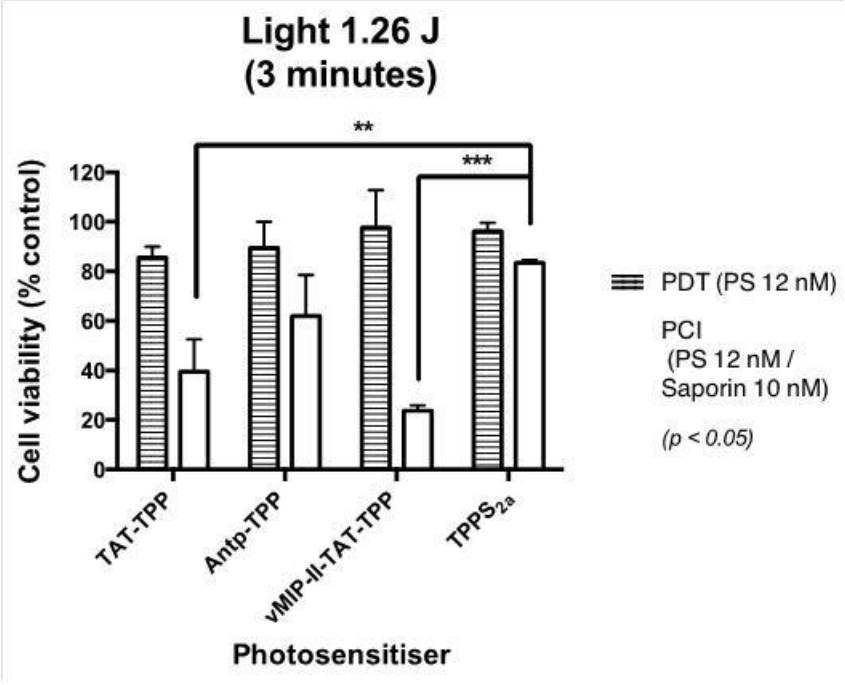

***Figure 45. Comparison of light groups 96 hr**.*

after PDT/PCI effect of TPP-conjugates and $TPPS_{2a}$ in PC3 cells. Cells were incubated with 12 nM solutions of TAT-TPP, Antp-TPP, vMIP-II-TAT-TPP or $TPPS_{2a}$ alone or in combination with saporin 2 nM for 24 hr. Drugs were then washed off and a 4 hr chase period was allowed before illumination. Cell viability was measured 96 hr after light treatment. Data is displayed as mean with error bars +/- SEM; two-way ANOVA followed by Bonferroni post hoc multiple comparison was used, differences between PDT and PCI groups are shown; significance level of $p < 0.05$.

LIGHT AFTER - Cell viability values shown as media ± SEM

			24 hr 4hr chase		96 hr 4hr chase	
			Dark	1.26 J (3minutes)	Dark	1.26 J (3minutes)
	Control		99.9 ± 0.1		100.1 ± 0.3	
	Saporin 2 nM		93 ± 0.1		90 ± 4.7	
TAT-TPP	PDT	TAT-TPP 12 nM	100 ± 1.8	98.9 ± 1.7	95.9 ± 1.8	85.5 ± 4.5
	PCI	TAT-TPP / Saporin 12 nM / 2 nM	83.2 ± 7.5	65.7 ± 7.6	86.4 ± 1.4	39.5 ± 13.1
	PDT	TAT-TPP 25 nM	98.3 ± 2.2	96.6 ± 3.3	94.1 ± 2.7	70.4 ± 7
	PCI	TAT-TPP / Saporin 25 nM / 2 nM	83.6 ± 5.6	59.2 ± 12.3	84.5 ± 6.3	21.9 ± 4.1
	PDT	TAT-TPP 50 nM	98.3 ± 3.3	83.9 ± 10.8	92.5 ± 3	53 ± 7.2
	PCI	TAT-TPP / Saporin 50 nM / 2 nM	81.7 ± 6.3	49.6 ± 12.3	88.7 ± 6.1	14.9 ± 1.7

LIGHT AFTER - Cell viability values shown as media ± SEM

			24 hr 4hr chase		96 hr 4hr chase	
			Dark	1.26 J (3minutes)	Dark	1.26 J (3minutes)
	Control		99.9 ± 0.1		100.1 ± 0.3	
	Saporin 2 nM		93 ± 0.1		90 ± 4.7	
Antp-TPP	PDT	Antp-TPP 12 nM	99.4 ± 4	99.3 ± 2	97.7 ± 3.1	89.5 ± 10.5
	PCI	Antp-TPP / Saporin 12 nM / 2 nM	80.7 ± 5.1	57.5 ± 12.3	85 ± 3.6	62 ± 16.6
	PDT	Antp-TPP 25 nM	98.6 ± 3.8	98.4 ±4.6	96.2 ± 3.4	78.4 ± 10.8
	PCI	Antp-TPP / Saporin 25 nM / 2 nM	80.84± 5.8	49.7 ± 9	87.5 ± 4.8	17.3 ± 7.5
	PDT	Antp-TPP 50 nM	98.5 ± 4	89.5 ± 4	95.5 ± 2.4	61.5 ± 2.6
	PCI	Antp-TPP / Saporin 50 nM / 2 nM	77.6 ± 6.3	42.4 ± 8.1	89.2 ± 4.5	11.1 ± 5.5

LIGHT AFTER - Cell viability values shown as media ± SEM

			24 hr		96 hr	
	Control		99.9 ± 0.1		100.1 ± 0.3	
	Saporin 2 nM		93 ± 0.1		90 ± 4.7	
vMIP-II-TAT-TPP	PDT	vMIP-II-TAT-TPP 12 nM	97.1 ± 3.5	97 ± 3.6	98.1 ± 2.4	97.7 ± 15.2
	PCI	vMIP-II-TAT-TPP / Saporin 12 nM / 2 nM	78.4 ± 9.2	64.8 ± 12.4	88.7 ± 2.6	23.7 ± 2.2
	PDT	vMIP-II-TAT-TPP 25 nM	94.6 ± 5.6	94.1 ± 4.4	97.9 ± 2.3	71.5 ± 14
	PCI	vMIP-II-TAT-TPP / Saporin 25 nM / 2 nM	80.2 ± 3.7	58.7 ± 8.1	90.7 ± 2.4	15.7 ± 5.1
	PDT	vMIP-II-TAT-TPP 50 nM	96.3 ± 6.8	94.7 ± 5.1	98.3 ± 1.8	58.6 ± 5.4
	PCI	vMIP-II-TAT-TPP / Saporin 50 nM / 2 nM	75.4 ± 4.8	48.4 ± 6.6	91.6 ± 6.9	12.6 ± 5.1

LIGHT AFTER - Cell viability values shown as media ± SEM

			24 hr		96 hr	
	Control		99.9 ± 0.1		100.1 ± 0.3	
	Saporin 2 nM		93 ± 0.1		90 ± 4.7	
$TPPS_{2a}$	PDT	$TPPS_{2a}$ 12 nM (0.01 µg/ml)	98.3 ± 3.6	93.8 ± 3	98.1 ± 5.2	96.3 ± 3.4
	PCI	$TPPS_{2a}$ / Saporin 12 nM (0.01 µg/ml) / 2 nM	77.8 ± 7.6	67.2 ± 1.7	84.2 ± 4.9	83.4 ± 1.2
	PDT	$TPPS_{2a}$ 25 nM (0.02 µg/ml)	98.6 ± 4.4	92.2 ± 3.3	98 ± 0.9	96.4 ± 3.3
	PCI	$TPPS_{2a}$ / Saporin 25 nM (0.02 µg/ml) / 2 nM	76 ± 7.4	60 ± 9.1	86.3 ± 6.1	70.3 ± 4.6
	PDT	$TPPS_{2a}$ 50 nM (0.04 µg/ml)	97.8 ± 5.8	90.7 ± 1.7	100.8 ± 3.9	97.2 ± 9.1
	PCI	$TPPS_{2a}$ / Saporin 50 nM (0.04 µg/ml) / 2 nM	78.2 ± 5.5	49.3 ± 6	90.6 ± 6.2	42.8 ± 11.3

Table 7. Summary of cell viability after targeted-PDT/PCI in PC3 cells.

TAT-TPP, vMIP-II-TAT-TPP, Antp-TPP and $TPPS_{2a}$ based PDT and PCI 24 hr and 96 hr after delivery of light. Shown light after results under different drug-light interval and light conditions.

3.4.5 AMD3100 inhibition pilot study

Prior to assessing the inhibitory effect of AMD3100, we evaluated the capacity of the inhibitor itself to affect cell viability when using doses known to cause effective blockage of CXCR4 receptor, as reported in the literature (Hatse et al., 2002; Rosenkilde et al., 2004). As displayed in Figure 46, AMD3100 alone caused no significant killing to PC3 cells at neither of the two concentrations tested.

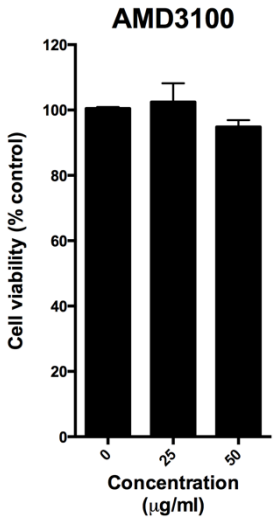

Figure 46. AMD3100 effect in PC3 cells.

Cells were incubated with solutions of AMD3100 at 25 and 50 μg/ml prepared in cell media during 24 hr. Plates were then washed once with PBS and cell viability was measured 48 hr after. Data is displayed as mean with error bars +/- SEM; two-way ANOVA followed by Bonferroni post hoc multiple comparison was used.

Based on the combination of vMIP-II and TAT in the vMIP-II-TAT-TPP chimaera and founded on the specific CXCR4-inhibition reported by AMD3100 in the literature, we hypothesised that the use of this inhibitor with vMIP-II-TAT-TPP would prevent vMIP-II from recognising CXCR4. Blockage of the vMIP-II component would result in a similar effect to that of TAT-TPP after light treatment. Following this line of thought, we aimed to compare the effect of AMD3100 on TAT-TPP and vMIP-II-TAT-TPP. PC3 cells were incubated during 1 hour with AMD3100 solutions at 25 and 50 μg/ml, which were replaced with solutions combining PS and AMD3100, then carrying out light treatment like reported in 3.4.3 and 3.4.4. In this case, cell killing 48 hr after light was only significantly affected with 50 μg/ml AMD3100 and a high concentration of vMIP-II-TAT-TPP (100 nM), as displayed in Figure 47B. On the other hand, a significant reduction in cell viability was noted in all TAT-TPP cases when combined with the highest AMD3100 dose assayed (Figure 47A).

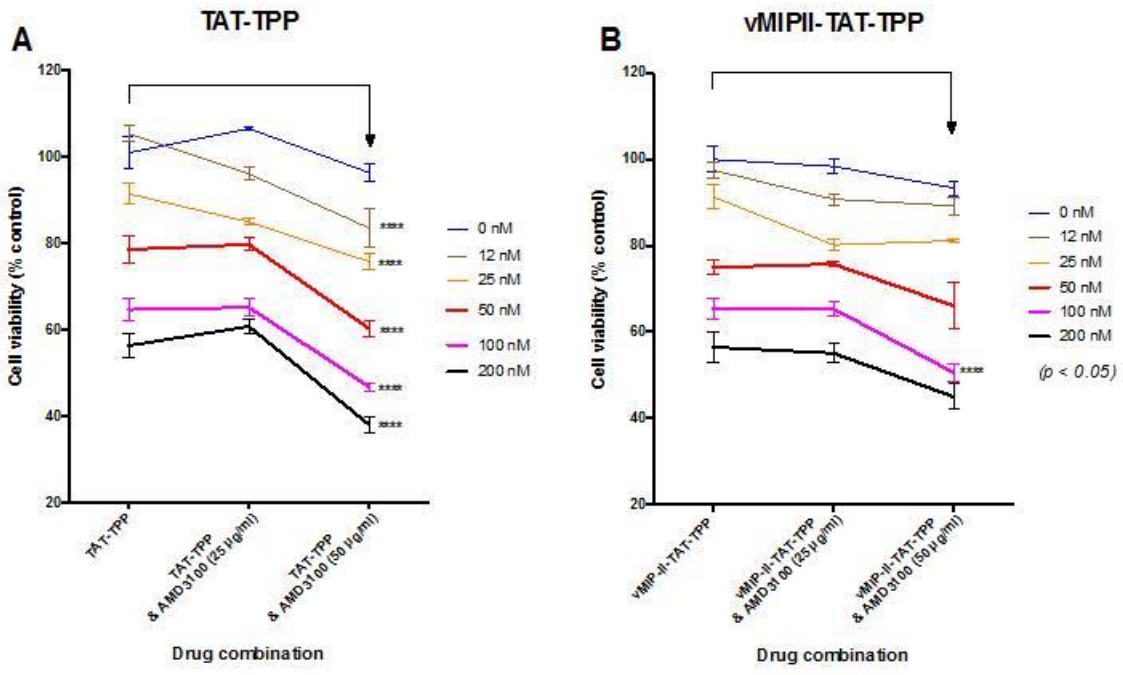

Figure 47. Comparison of PDT effect of TAT-TPP or vMIP-II-TAT-TPP with AMD3100 in PC3 cells (2.1 J, 5 minutes light).

Cells were incubated with solutions of AMD3100 at 25 and 50 µg/ml prepared in cell media. After a 1-hr incubation plates were washed with PBS and solutions combining AMD3100 and TAT-TPP (A) or vMIP-II-TAT-TPP (B) ranging 12-200 nM were administered for 24 hr. Drugs were then washed off and a 4 hr chase period was allowed before illumination (2.1 J, 5 minutes). Cell viability was measured 48 hr after light treatment. Data is displayed as mean with error bars +/- SEM; two-way ANOVA followed by Bonferroni post hoc multiple comparison was used, differences between groups w/wo AMD3100 are shown; significance level of $p < 0.05$.

Due to the effect seen on TAT-TPP-treated cells previously incubated with AMD3100, all three TPP-conjugates were next assessed in PC3 cells to evaluate how the resulting PDT effect would be affected when pre-exposed to AMD3100. Based on the above shown results, we considered that 50 nM was a high enough PS dose to cause noticeable cell death 48 hr after light (time point chosen for the present study). In this specific scenario, no variations were found in the presence or absence of AMD3100 at any dose examined with neither of the TPP-conjugates (see Figure 48).

We next considered whether cell death after light had not been large enough to reveal differences in viability upon exposure to AMD3100 and whether a possible inhibition was being masked. Therefore, in order to maximise potential differences resulting from the use of the inhibitory compound, a 5-minute illumination was performed. In addition, incubation with AMD3100 was increased from 1 hour to 24 hour following the same logic.

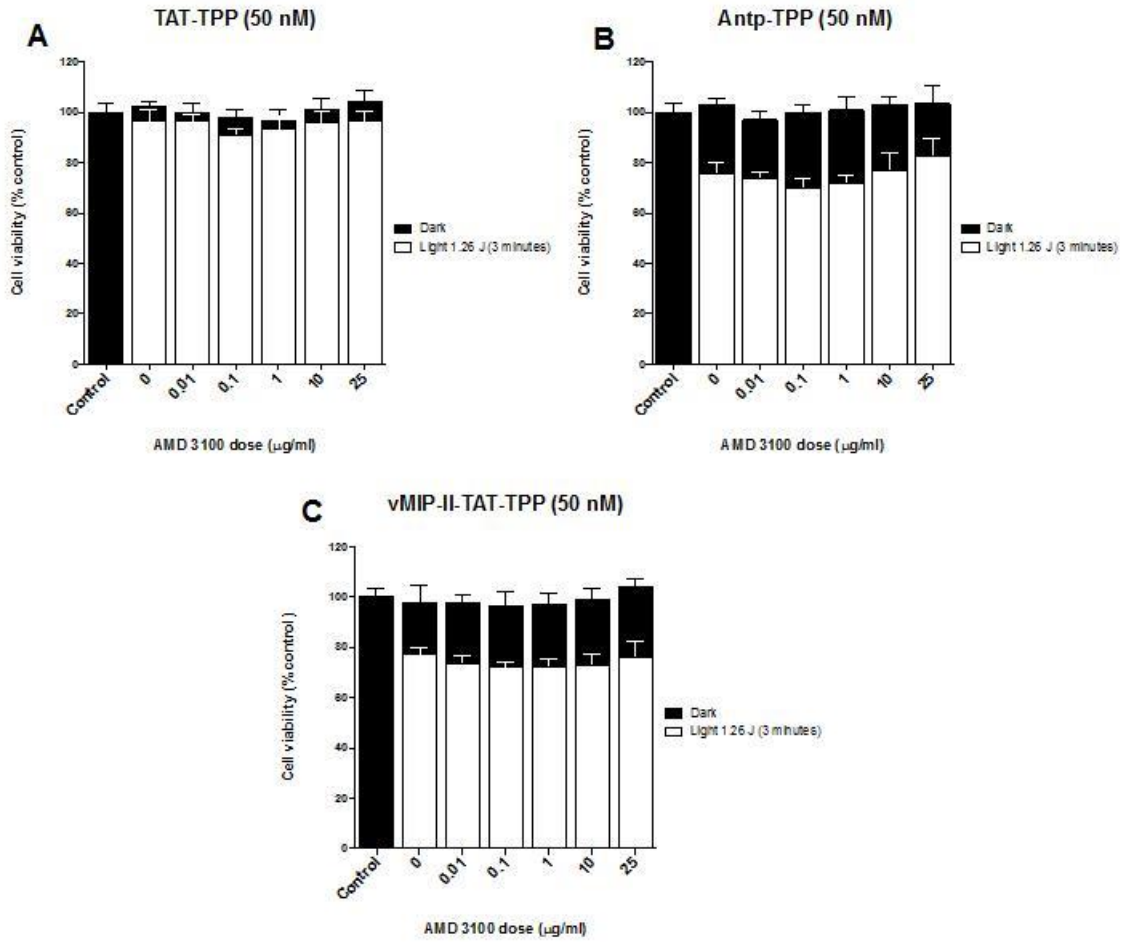

Figure 48. Comparison of PDT effect of TPP-conjugates with AMD3100 in PC3 cells (1.26 J, 3 minutes light).

Cells were incubated with solutions of AMD3100 ranging 0.01 – 25 μg/ml prepared in cell media. After 1 hr incubation, plates were washed with PBS and solutions of TAT-TPP (A), Antp-TPP (B) or vMIP-II-TAT-TPP (C) at 50 nM were administered for 24 hr. Drugs were then washed off and a 4 hr chase period was allowed before illumination (1.26 J, 3 minutes). Cell viability was measured 48 hr after light treatment. Data is displayed as mean with error bars +/- SEM; two-way ANOVA followed by Bonferroni post hoc multiple comparison was used.

Cell death was also assessed in cells pre-incubated with AMD3100 during 24 hr, then exposed to TPP-conjugates and illuminated for 5 minutes (Figure 49). Under these conditions, a significant reduction in cell viability was found up to 10 μg/ml in the TAT-TPP and Antp-TPP groups (Figure 49D and Figure 49E respectively), and up to 1 μg/ml in the vMIP-II-TAT-TPP treated cells (Figure 49F). Hereafter, there seemed to be a trend to increase cell viability at higher AMD3100 doses although no significant differences were seen.

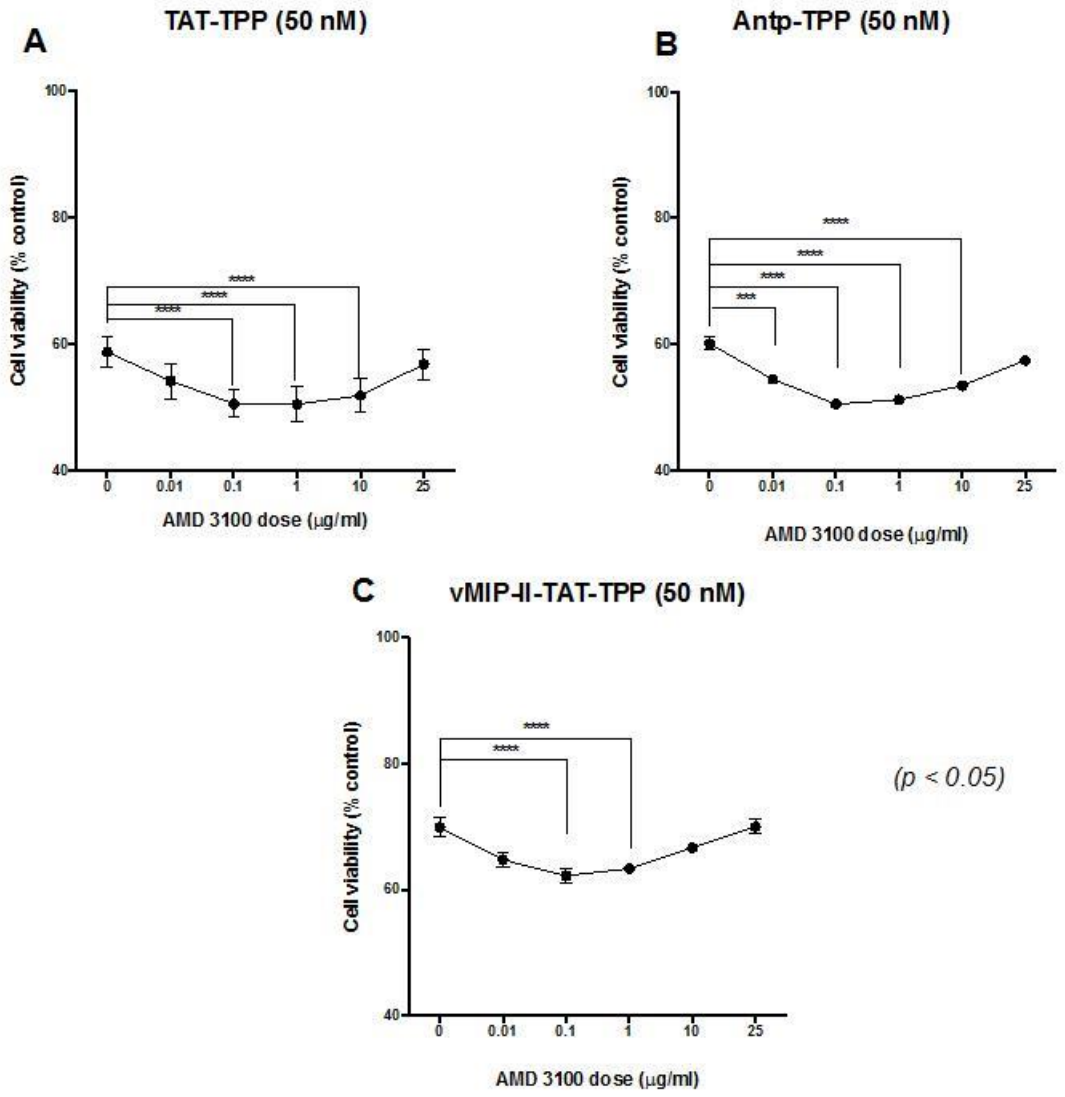

Figure 49. Comparison of PDT effect of TPP-conjugates with AMD3100 in PC3 cells (2.1 J, 5 minutes light).

Cells were incubated with solutions of AMD3100 ranging 0.01 – 25 μg/ml prepared in cell media. After a 24-hr incubation plates were washed with PBS and solutions combining AMD3100 and either TAT-TPP (A), Antp-TPP (B) or vMIP-II-TAT-TPP (C) at 50 nM were administered for 24 hr. Drugs were then washed off and a 4 hr chase period was allowed before illumination (2.1 J, 5 minutes). Cell viability was measured 48 hr after light treatment. Data is displayed as mean with error bars +/- SEM; two-way ANOVA followed by Bonferroni post hoc multiple comparison was used, differences between groups w/wo AMD3100 are shown; significance level of $p < 0.05$.

3.4.6 Subcellular localisation of TAT-TPP, Antp-TPP and vMIP-II-TAT-TPP in PC3 cells before and after light treatment

So as to observe the intracellular localisation of the TPP-conjugates and determine the suitability for PCI, fluorescence micrographs of PC3 cells incubated with PS solutions were taken, like reported in Chapter 2 for $TPPS_{2a}$ and $TPCS_{2a}$.

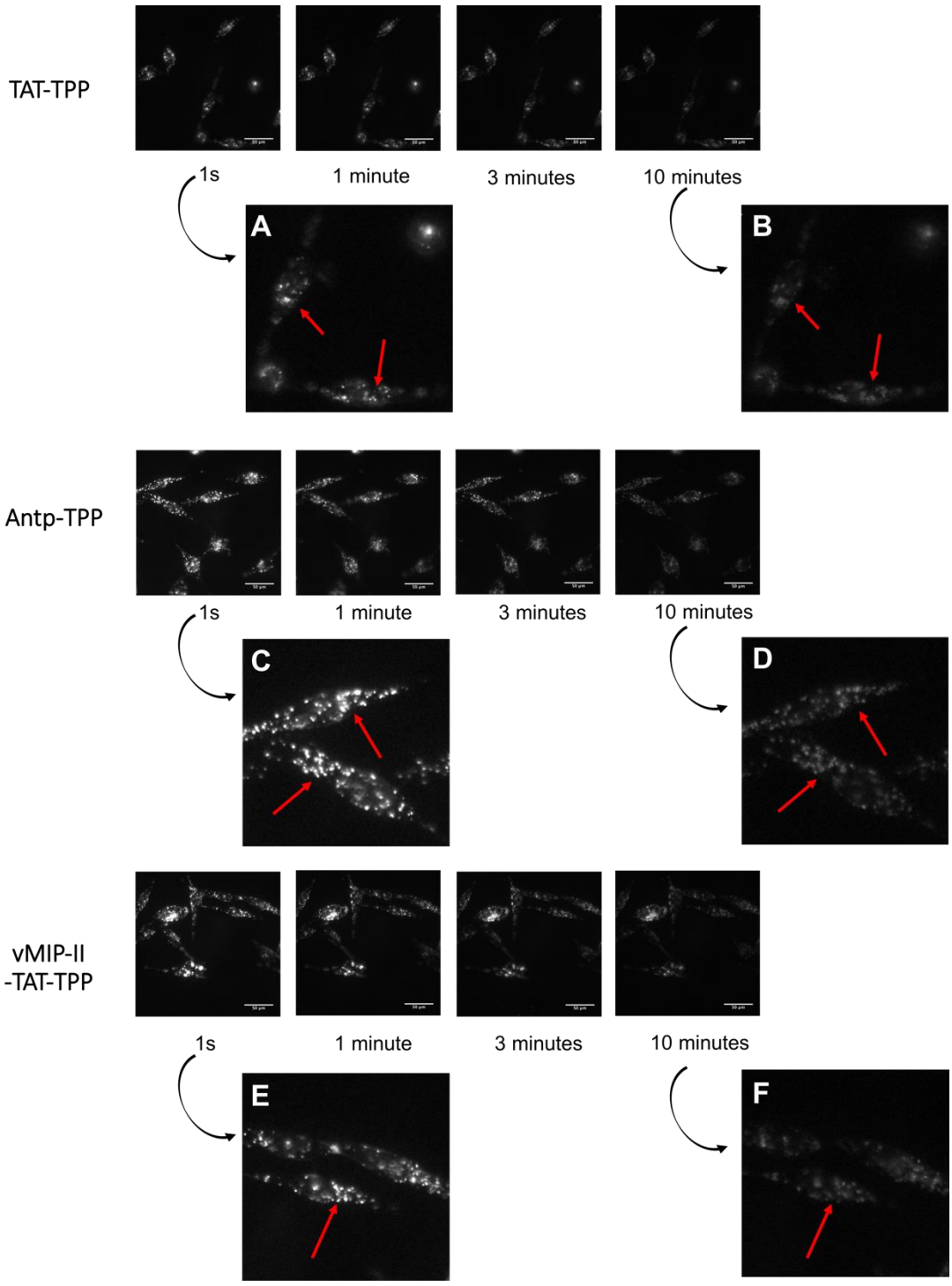

Figure 50. Localisation and redistribution of TPP-conjugates after light treatment in PC3 cells.

Cells were incubated with 400 nM solutions of either TAT-TPP, Antp-TPP, vMIP-II-TAT-TPP during 24 hr. Photosensitiser solutions were then washed off and a 4 hr chase period was allowed before illumination "on stage" using a low power (2 mW) 405 nm blue diode laser coupled to a liquid light guide. Micrographs were taken at a different time during exposure to light. Scale bars shown as 50 μm.

All three TAT-TPP, Antp-TPP and vMIP-II-TAT-TPP exhibited a granular intracellular distribution before light excitation of the compounds, as detailed with red arrows in Figure 50A, Figure 50C, Figure 50E for each conjugate respectively. Cytosolic vesicles in which TPP-based photosensitisers appeared initially were dispersed overtime after

illumination of cells, as shown in micrographs taken at 1, 3 and 10 minutes (see detail in Figure 50B, Figure 50D, Figure 50F).

No apparent changes in cell morphology could be seen, even at the latest time point imaged (10 minutes), with neither of the compounds assayed under the specific experimental conditions (Figure 50B, Figure 50D, Figure 50F).

3.4.7 Subcellular localisation of the conjugate saporin-Alexa-Fluor488® before and after light excitation of TAT-TPP

Interaction of the TPP-conjugates with saporin in the presence of light is decisive during PCI. Hence, fluorescence-based observations were performed in PC3 cells where TPP-based photosensitisers had been previously coadministered with saporin-Alexa-Fluor488® to determine the localisation of the conjugate in the presence of light – similarly to above-noted in 2.4.7 Subcellular localisation of the conjugate saporin-Alexa-Fluor488® before and after excitation of photosensitisers.

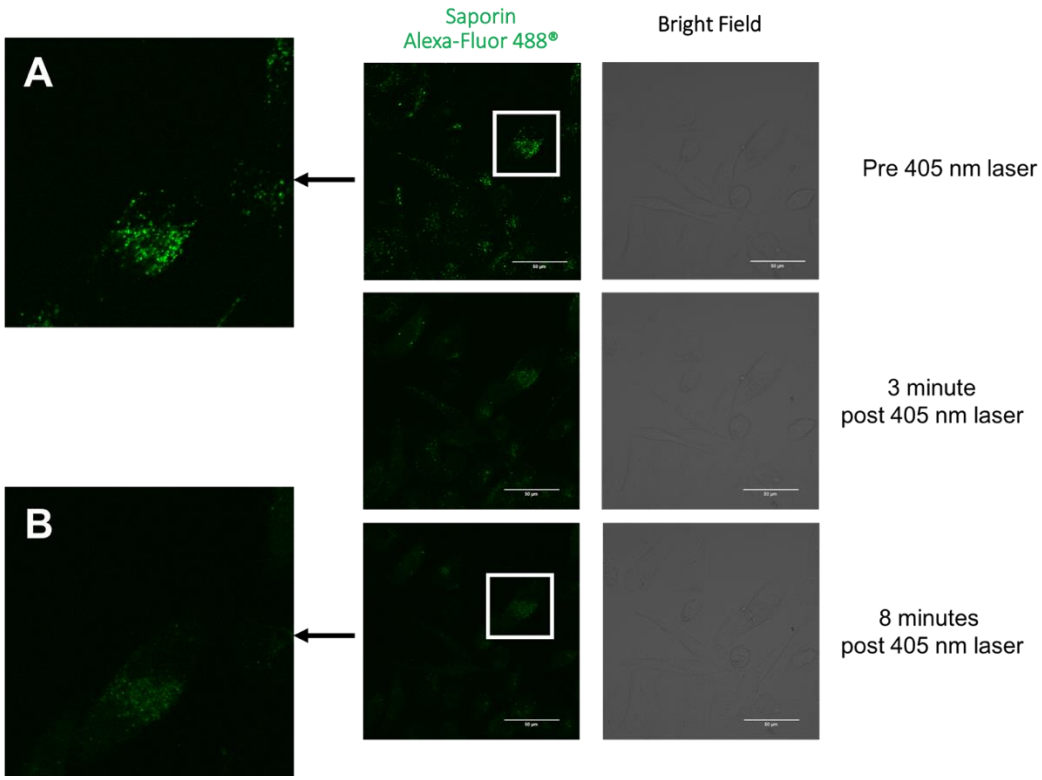

Figure 51. Saporin-Alexa-Fluor488® conjugate in PC3 cells co-administered with TAT-TPP before and after illumination with a 405 nm laser.

Cells were incubated with a solution of Saporin-Alexa-Fluor488® (400 nM) during 24 hr, then washed, allowing cells to recover for 4 hours. Imaging was performed using a 488 nm laser before (A), and 3 and 8 minutes after (B) a 10 seconds "on-stage" excitation with a 405 nm laser. Scale bars shown as 50 μm.

In this case, a 405 nm laser resulted in the excitation of the compounds; concluded by the spectroscopic study of the compounds described in section 3.4.1. As displayed in Figure 51 (see detail A), saporin was initially located conforming cytosolic granules and experimented dispersion, as suggested by the scattering of green fluorescence over time after illumination with the 405 nm laser (Figure 51B). Moreover, no qualitatively noticeable changes in cell morphology were detected.

3.5 Discussion

Based on the reported benefits of CPPs, three different conjugates TAT-TPP, Antp-TPP and vMIP-II-TAT-TPP have been considered in the present thesis to enhance the uptake of tetraphenyl porphyrin (TPP), and in turn its photooxidative-toxicity in prostate cancer treatment. Some of the most common targeting strategies have been reviewed in the introduction, which have also been applied in PDT and PCI. CXCR4 receptor was the molecule targeted in the investigations reported in the present chapter due to its known expression in PC3 cells used throughout the thesis, and specifically its relation to cancer stem cells and metastasis. The experiments reported in the above sections were designed to evaluate the benefits targeted strategies would have in PDT and PCI for prostate cancer treatment and were only performed on the human prostate cancer model (PC3).

The first steps followed with the CPP-based photosensitisers studied in the present chapter involved their spectroscopic evaluation. TPP is the photosensitive component of the conjugates used in our study. It is a porphyrin based photosensitiser, nature which was reflected in the intense Soret band (420 nm) followed by the lower intensity four Q bands (500-650 nm) shown in the absorption spectra in Figure 41 (Kempa et al., 2015). No absorption resulted from illumination at longer wavelengths, i.e. in the red region of the electromagnetic spectra coinciding with the therapeutic window. For this reason, TPP is not a clinically applied photosensitiser in the photodynamic therapy field, yet, it is widely used as standard to determine optimal properties of photosensitive compounds (Kempa et al., 2015). All CPP-conjugates displayed identical absorption and emission, which suggests the the CPP and vMIP-II domains are not affecting the physicochemical properties of these and should then lead to at least an equally efficient photooxidation of the compounds during PDT. In relation to this, previous studies have reported in the literature that the presence of TAT- does not affect TPP's singlet oxygen yield in methanol (Tanielian and Wolff, 1995; Wang et al., 2012). Moreover, the common nature of both TPP and $TPPS_{2a}$, justifies the correlation between the spectra shown in Figure 41 and the one described for $TPPS_{2a}$ displayed in Chapter 2. For this same reason, we would not expect significant variations between singlet oxygen yield of $TPPS_{2a}$ and TPP; thus we consider differences described between PS compounds will be dependent on the presence of CPPs.

We next analysed uptake of the compounds after a 24-hour incubation in PC3 cells. As shown in Figure 42, a dose-related increase in drug uptake was observed in all three compounds. In order to compare uptake rates of the three conjugates, we assumed that the presence of one or another CPP moiety would not alter the spectroscopic properties of these compounds, hence, all conjugates would be identical in their physicochemical properties. Taking this as basis, Antp resulted in the greatest uptake among the TPP-based PSs, which was significantly different to that exhibited by vMIP-II-TAT-TPP by nearly 1.5-fold at the highest 800 nM dose tested. This might indicate that the presence of vMIP-II could be competing with TAT to enter cells or else increasing specificity in the uptake, thus limiting passive entry or non receptor mediated endocytosis and consequently reducing the overall internalisation. Antp seemed to be more efficient in enhancing the delivery of TPP inside cells than the TAT counterpart, although non significant differences were found. Duchardt et al. evaluated different endocytic pathways for CPPs, suggesting differences in the fractions of arginine side chains between TAT and Antp explained differences in delivery efficiency. The authors described a greater uptake of Antp below a critical concentration threshold (10 µM) from which TAT followed non-endocytic pathways, and thus increasing its uptake very significantly (Duchardt et al., 2007). This concentration is 12.5-fold higher than the highest concentration assayed in our investigations (800 nM). In a different study, a TAT-TPP conjugate was investigated in human squamous carcinoma cells (Wang et al., 2012). A dose and time dependent enhancement in the uptake of PS was observed when conjugating molecules to TAT. Additionally, the implication of the endocytic route during the internalisation of the TAT conjugate was confirmed in the experiments carried out at 4°C, which significantly reduced uptake of PS, also correlating to the observations found with $TPPS_{2a}$ (Wang et al., 2012) .

Correlation was found between uptake experiments and PDT 24 hr after illumination. For instance, focusing on the largest PS dose tested (800 nM) and a 3-minute illumination as shown in Figure 43, Antp-TPP showed the greatest therapeutic effect upon PDT treatment, rendering 46.68% viable cells (Figure 43C), notably larger than the other two compounds. A 66.22% (Figure 43A) and 59.69% (Figure 43E) cell viability resulted from TAT-TPP and vMIP-II-TAT-TPP respectively. This supports the hypothesis that either an increase in the specificity of TPP-conjugates or competition between moieties during receptor recognition (which vMIP-II is responsible for), would affect uptake and thus limit PDT's photooxidative effect. If cell viability was measured at a later time point, i.e. 96 hr post illumination as shown in Figure 43B, Figure 43D and Figure 43F, concentrations above 100 nM did not seem to result in any further enhancement of cell death with any of the conjugates. This suggests that the entry of

all three compounds (CPP-mediated) in PC3 cells would happen in a receptor-mediated manner, hence a large concentration of the conjugates leads to saturation and limits the therapeutic effect. A similar saturation plateau has been described in previous studies involving CPP-delivery (Hällbrink et al., 2001).

When compared to free photosensitiser used in Chapter 2, initial doses selected for CPP-TPP were reduced from 0.1-0.8 μg/ml (assayed with $TPPS_{2a}$ and $TPCS_{2a}$, as displayed in Figure 16 and Figure 17) down to 12-800 nM (equivalent to 0.01-0.64 μg/ml) shown in Figure 43. The lowest concentration tested in the former, 0.1 μg/ml did not result in significant reduction of cell viability in neither of the models previously commented (MatLyLu or PC3 cells) neither with $TPPS_{2a}$ nor $TPCS_{2a}$ alone 24 hr after exposure to light treatment in PDT; whereas noticeable cell damage was observed with TPP-conjugates at 100 nM, which is equivalent to 0.08 μg/ml $TPPS_{2a}$. In addition, the plateau earlier described for PDT at the higher doses of CPP-PS, was not detected 96 hr after light treatment using 10-fold larger concentrations of the non CPP-PS (0.8 μg/ml) in Chapter 2. This indicated that despite the enhancement of therapeutic outcome post PDT at low doses, cell death could be limited at larger concentrations, potentially due to a receptor-mediated internalisation of the compounds which CPPs are responsible for. A similar enhancement in phototoxicity was shown conjugating the fluorophore carboxytetramethylrhodamine (TMR) to TAT, compared to the lack of cytotoxicity was exerted by it alone (Srinivasan et al., 2011). This was explained through the interaction of the CPP-PS with cellular membranes and consequent disruption of endosomes upon irradiation.

As performed in Chapter 2, based on the PDT observations, the lower concentrations of the range tested (only resulting in subthreshold toxicity) were combined with saporin to enhance the delivery of this type 1 RIP through PCI. 24 hr after light, viability measurements correlated with uptake (Figure 42) and PDT dose-response assays (Figure 43): Antp-TPP resulted in a more noticeable cell death after PCI from 12 nM compared to killing exerted by TAT-TPP and vMIP-II-TAT-TPP. Yet, all three conjugates tested in PCI combination experiments successfully enhanced delivery of saporin and thus enabled its biological activity at concentrations which did not cause PDT effect when using PS alone as displayed in Figure 44A, Figure 44C and Figure 44E. This effect was even more pronounced 96 hr after light (Figure 44B, Figure 44D and Figure 44F), like reported for $TPPS_{2a}$ and $TPCS_{2a}$ in Chapter 2. Interestingly, PCI results of cell death 96 hr after light combining CPP-conjugates at 12 nM and saporin were inversely proportional to previously reported cytotoxicity levels: vMIP-II-TAT-TPP was the one exhibiting the most substantial cell killing (76.27% death),

followed by TAT-TPP (60.5%) and Antp-TPP (38%). Based on this, vMIP-II might be involved in an additional manner in the cytosolic delivery of saporin, for instance interacting with the RIP type I differently to the other two conjugates assayed, in turn favouring its biological activity further. Perhaps, endocytosis of saporin in PC3 cells occurs via a specific receptor to some extent, explaining the greater efficacy of vMIP-II-TAT-TPP in this case. This higher efficiency of vMIP-II-TAT-TPP was not seen however at higher concentrations of the PS-conjugates. In these circumstances, cell viability was reduced to maximal levels (close to MTT detection limits), overcoming the saturation of receptors involved in the uptake of PS-conjugates, which restricts PDT-based cell death at high CPP-PS dose. Along these lines, 50 nM CPP-PS and saporin resulted in cell viability values as low as 14.91% ± 1.69, 11.14% ± 5.47 and 12.59% ± 5.08 for TAT-TPP, Antp-TPP and vMIP-II-TAT-TPP respectively when combined with saporin. Consequently, differences between photosensitisers might be imperceptible.

As for the comparison between CPP-compounds and free PS in PCI, observations 24 hours after light were similar in all cases (Figure 44A, Figure 44C, Figure 44E *vs* Figure 44G). Measurements 96 hr after light showed minor variations in the free PS compared to the results 24 hr after light (Figure 44H), while significant differences in phototoxicity from 24 hr to 96 hr originated from the CPP-compounds (Figure 44B, Figure 44D, Figure 44F). At this last time point, cell death was up to 3.8-fold greater in CPP-conjugates than free PS (50 nM). As could be concluded from the light-only groups shown in Figure 45, the presence of the CPP components in PS used in PCI could result in a significant enhancement in therapeutic outcome while keeping both PS and biologically active drug at subthreshold levels. Overall, we concluded the CPP component of the PS-conjugates did not impede PCI-delivery of saporin, but in fact promoted it, further enhancing phototoxicity of that resulting from free photosensitisers as shown *in vitro*. A similar enhancement in cell killing was observed by Wang et al. in HN5 cells combining TAT-TPP and the same RIP reported in our studies as opposed to TAT-TPP alone, which served as verification of the potential of TAT-TPP conjugates for PCI (Wang et al., 2012).

This was followed by the evaluation of the interaction between vMIP-II and CXCR4 receptor through the use of the inhibitor AMD3100, founded on the previously stated specific inhibition of such receptor (Hatse et al., 2002). It was first demonstrated that AMD3100 on its own and under the same experimental conditions described for PDT and PCI experiments, did not affect viability of PC3 cells at doses where inhibition had been described (see Figure 46). Previous studies on PC3 cells had confirmed the expression of CXCR4 in the surface of the cell membrane and its relevance in the

maintenance of tumour progenitor cells, tumorigenicity and migratory capacity (Dubrovska et al., 2012; Zhang et al., 2008). Founded on the above, blockage of the interaction between vMIP-II and CXCR4 in PC3 cells would impede the entry of the conjugate into these in a vMIP-II-mediated manner. Accordingly, the resulting PDT effect would occur independently to vMIP-II, altering the cytotoxic outcome.

With the working hypothesis being that vMIP-II interacts with CXCR4, initial inhibition experiments involved the incubation of cells with AMD3100 alone during 1 hr followed by the combination of both inhibitor and vMIP-II-TAT-TPP or TAT-TPP. The latter was used based on the shared TAT-TPP structure. The initial incubation of cells with AMD3100 alone was intended to ensure blockage of the specific receptor prior to enabling recognition of CXCR4 by vMIP-II, hence ensuring inhibition. Opposite to what was expected, differences in phototoxicity were more noticeable with the TAT-TPP compound than vMIP-II-TAT-TPP 48 hr after a 5-minute illumination, suggesting AMD3100 was also affecting the shared TAT-TPP components. In the former, a significant reduction of cell viability resulted from a first incubation with AMD3100 (50 μg/ml) compared to lower concentrations or absence AMD3100 at all PS doses tested (Figure 47A). As for the vMIP-II-TAT-TPP groups, variations in cell death were only found combining the inhibitor at 50 μg/ml with 100 nM of the TPP-conjugate (Figure 47B).

A structural analysis of CXCR4 has previously revealed strong negative charges in its N-terminal, and the interaction with its natural ligand (i.e. CXCL12) has been explained mostly through electrostatic interactions between these and positively charged side chains (Xu et al., 2013). In our investigations, based on the positively charged residues in the CPP peptides, an interaction between TAT and the receptor might also have occurred, as suggested by earlier studies in which a chemokine-like region was described (Xiao et al., 2000). This would justify the differences above-described in the TAT-TPP-treated cells when pre-incubated with AMD3100. In line with this, rather than inhibiting the uptake of PS, AMD3100 at high doses could be sensitising PC3 cells to photooxidation by the conjugates. In relation to this, a strong binding to CXCR4 has been reported for both AMD3100 (Rosenkilde et al., 2004) and vMIP-II (LiWang et al., 1999; Szpakowska and Chevigne, 2016; Zhou et al., 2000). It is possible therefore that the competition between vMIP-II and AMD3100, could be alleviating the sensitisation instigated by the inhibitor, explaining the lesser significant effect. Likewise, prostate cancer cells have been sensitised to docexatel treatment with this same inhibitory compound (Domanska et al., 2012).

In order to evaluate how all three conjugates would be affected and determine whether the AMD3100-inhibition could be enhanced, a study was carried out pre-incubating cells with the inhibitory molecule alone during 24 hr (as opposed to 1 hr), prior to the coadministration of AMD3100 and all three TPP-conjugates. PS were tested at 50 nM based on the consideration that this dose would cause noticeable cell death 48 hr after light (previously observed in Figure 43 and Figure 44); thus, an effect caused by AMD3100 would result in detectable differences in cell viability. Furthermore, light dose was reduced to 3 minutes, in case an excessive PDT effect had masked AMD3100's effect after the longer 5-minute illumination. Moreover, a range of AMD3100 concentrations (0.01-25 μg/ml) were assayed in Figure 48 to investigate a broader scope of experimental conditions. Nonetheless, no remarkable effects on cell viability were found in any case (Figure 48).

One last experiment was carried out in the inhibition pilot study currently discussed, which involved a 24 hr incubation with AMD3100 alone (0.01-25 μg/ml) prior to exposure to PS at 50 nM and AMD3100 followed by a 5-minute illumination. In all cases observed, there was a general trend to reduce cell viability at lower inhibitor concentrations, which then recovered to initial values as AMD3100 concentrations increased. Again, in the presence of AMD3100, cell killing was increased, as shown in Figure 47. Larger differences resulted from longer incubations (24 hr), which suggested AMD3100 effect is time- and dose- dependent, regardless of the CPP-conjugate evaluated. Specifically, increasing the pre-exposure to the inhibitor from 1 hr (Figure 47) to 24 hr (Figure 49) reduced the concentrations required to observe significant differences (10 μg/ml as opposed to 50 μg/ml).

In conclusion, we hypothesise the following possible scenarios:

- Low concentrations of AMD3100 (below 25 μg/ml) could be competing with CPPs during receptor recognition but were insufficient to inhibit the entry of PS. In fact, despite AMD3100 alone does not exert cytotoxicity, PS-conjugates could be interacting with the inhibitor, triggering AMD3100-induced cell death (i.e. assisting uptake by cells in a similar process to PCI).
- High concentrations of AMD3100 (25 μg/ml) could surpass the competition with CPPs to bind CXCR4, resulting in an increase in cell viability as a consequence of the inhibitory outcome. Conversely, the recovery of cell viability could be due to an adaptation of cells to the inhibitor AMD3100, which would then lose the potential to cause cell death.

- Concentrations of AMD3100 over a critical threshold (above 50 μg/ml) could sensitise cells to PDT effect, hence maximising cytotoxicity.
- The association of TPP with vMIP-II-TAT could be causing steric hindrance that would impede a more specific interaction between vMIP-II and the CXCR4 receptor. Therefore, AMD3100 would not cause any additional significant effect during CXCR4 recognition compared to the other PS conjugates.

The last sections of the present chapter (3.4.6, 3.4.7) describe studies carried out to determine the subcellular localisation of all CPP-compounds, similarly to the studies reported in Chapter 2 with $TPPS_{2a}$ and $TPCS_{2a}$. All three compounds TAT-TPP, Antp-TPP and vMIP-II-TAT-TPP resulted in a similar cytosolic pattern to that of the previously assayed PS as shown in the fluorescence micrographs in Figure 50 (Figure 24). Again, this indicated that these PS would be initially found in cytosolic vesicles, very likely docked in endolysosomal membranes, as described in the study carried out by Wang et al. where colocalisation with lysosomal dyes confirmed the above-statement (Wang et al., 2012). As opposed to $TPPS_{2a}$ and $TPCS_{2a}$, TPP lacks the two adjacent sulphonate groups which confer amphiphilic properties, hence making the PS more adequate for PCI (Wang et al., 2013). However, the presence of CPPs could be compensating this lack, resulting in a similar outcome. In addition, exposure to light of a specific wavelength as determined in the initial absorption spectra (Figure 41), resulted in dispersion throughout the cytosol (10 minutes after light, displayed in Figure 50B, Figure 50D, Figure 50F) of the granular fluorescence pattern described after 1 s illumination (Figure 50A, Figure 50C, Figure 50E). This served as an additional visual confirmation that CPP components were not interfering with the photooxidative potential of TPP, which acquired an excited state and disrupted endo/lysosomal vesicles during PCI procedures. The equivalent study described in Chapter 2 revealed morphologic changes in cells after light treatment. In the present study, no significant changes were found despite the fact that the photooxidative effect represented by dispersion of fluorescence would in turn lead to a reduction of cell viability as displayed in Figure 43 and Figure 44. We think this was due to a more discrete and subtle photooxidative damage exerted in this case, affecting cells at a subcellular level rather than having a whole-cell effect. This could be justified by the slightly higher PS concentration used in Chapter 2: 516 nM (equivalent of 0.4 μg/ml) $TPPS_{2a}$/$TPCS_{2a}$ compared to 400 nM CPP-PS used for the experiments now concerning.

Considering that both fluorescence yield and CPP : TPP ratio were the same in all three CPP-TPP conjugates, we qualitatively compared the uptake of PS through the observation of the fluorescence intensity in Figure 50. Accordingly, the greatest

fluorescence resulted from Antp-TPP-exposed PC3 cells, which correlated with the uptake graphs shown in Figure 42. No major variations were found between the other two TPP-conjugates in the fluorescence images (Figure 50).

As for the assessment of the interaction of the CPP-conjugates with saporin to determine suitability of the compounds in PCI (shown in Figure 51), a similar behaviour to that described for $TPPS_{2a}$ and $TPCS_{2a}$ in Chapter 2 was revealed. The fluorescent conjugate saporin-Alexa-Fluor488® formed cytosolic granules prior to illumination with the 405 nm laser, noted as endo/lysosomes in Chapter 2 (Figure 26). Combination of fluorescently labelled saporin with TAT-TPP under the specific light conditions resulted in cytoplasmic dispersion of green fluorescence. This observation together with the earlier described granular pattern of fluorescence of the conjugates alone supports the hypothesis that the CPP-conjugates under investigation were located in endo/lysosomal-membranes and would release their content (labelled saporin in this case) when photochemically disrupted. Likewise, this served as verification of the mechanics behind the commented viability assays after PCI delivery of saporin using the present CPP-TPP combinations and supports conclusions drawn in Chapter 2. Despite this last experiment was only performed on TAT-TPP, the same observations could be extended to Antp-TPP due to the common structure and nature of the compounds. Overall, there is no reason to conclude vMIP-II would alter the process and result in different findings to that of TAT-TPP and Antp-TPP.

To conclude, we hypothesise that under our experimental conditions, TAT and Antp bound to the PS cargo were internalised by PC3 cells through endocytosis (receptor-mediated at several levels depending on the conjugate used), and were capable of releasing drugs also endocytosed but trapped in endosomes (i.e. saporin). Therefore, we conclude these compounds are suitable candidates for PCI treatment. We have verified that the use of CPP and targeting moieties enhance the previously reported outcome of PCI, widening the gap already existing between PDT and PCI. Moreover, PS whose physicochemical features are not as appropriate for PCI as they are for PDT (i.e. not amphipathic), could be used for both irrespectively if conjugated to CPPs. In addition, we conclude that it needs to be predetermined whether maximal cell death or specificity are preferentially pursued, since the further increase of specificity via additional targeting moieties such as vMIP-II might have a detrimental effect on cell killing due to a lower amount of drugs being internalised, especially if there is competition between moieties. As for the use of vMIP-II to target PC3 cells in PDT/PCI, we cannot conclude an exclusive interaction with CXCR4, as suggested by the findings of our study. In addition, observations upon administration of the inhibitor AMD3100

supported previous reports indicating that CPPs with positively charged residues may be responsible for targeted delivery to some extent (binding to receptors present in tumour cells) in addition to their intrinsic capacity to act as delivery agents.

Chapter 4 *In vivo* studies of PDT and PCI in Prostate Cancer

4.1 Introduction

In vivo studies enable a more realistic evaluation of treatment and drug development than the *in vitro* counterpart. Specifically, in cancer treatment as in any other disease, cell lines do not recapitulate every aspect involved in the different disorders nor living organisms. There is a major systemic component missed *in vitro* and this is particularly important in cancer i.e. regarding cellular interactions during the metastatic and oncogenic progression (Cunningham and You, 2015).

Mice models are the most widespread *in vivo* model currently due to the large genetic knowledge available, the rather inexpensive cost compared to other models, as well as the easy generation of disease models with specifically tailored features. In prostate cancer however, rat and canine models have led to important discoveries on prostatic lesions. In addition, the larger size of these species facilitates the performance of experiments on an organ of reduced size as is the prostate's case. However, the development of prostate cancer models still faces a major challenge: the lack of an animal model capable of reproducing the characteristic metastasis to bone experienced by prostate cancer patients (Cunningham and You, 2015).

4.1.1 Dunning R3337 prostate adenocarcinoma model

Androgenic hormones have a major role in prostate and prostatic tumours' growth. This is an important feature of the model chosen in our study of prostate cancer treatment, whose use *in vitro* has been commented in Chapter 2 and will be studied *in vivo* in the present chapter.

The dunning R3327 adenocarcinoma of the prostate initially originated in 1961 from the dorsal prostatic lobe of a 22-month old Copenhagen rat, and its later serial transplantation into hybrid offspring from female Fischer and male Copenhagen rats enabled the characterisation of different related sublines, sharing several common features with human prostate cancer (Isaacs et al., 1978). The R3327-H subline was the first one to be developed from this model. It took several months to develop androgen insensitivity and in the end, these cells were indifferent to hormone-specific endocrine treatment. This led to the generation of additional cell lines such as R3327-HI, R3327-AT and R3327-G (Isaacs et al., 1978; Kager et al., 1992). All cell lines

generated from the original R3327 Dunning model are described in Figure 52 and Table 8. This prostate cancer model covers a range of the different ways in which prostate cancer can appear in humans, for instance both androgen -dependent or -independent. Its potential use both *in vitro* and *in vivo* makes it especially useful for prostate cancer investigations. *In vivo* models based on the implantation of cells or xenografts have an additional advantage over chemically or genetically generated tumour animal models: the greater controllability of tumour growth and hence reproducibility between individuals.

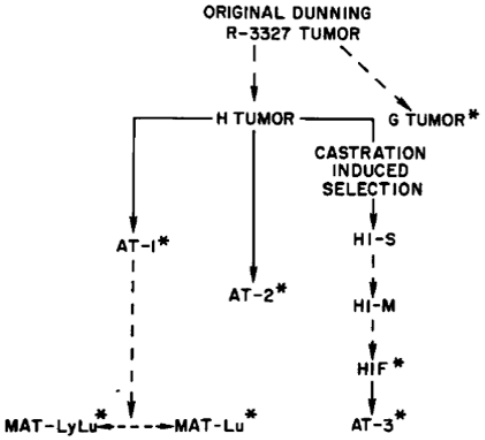

Figure 52. Dunning R3327-derived prostate adenocarcinoma sublines.

Schematic representation of different cell lines obtained from the initial R3327 rat prostate adenocarcinoma. [(Isaacs et al., 1986)*]*

Furthermore, Dunning R3327-derived cell lines have also been used previously for PDT strategies in prostate cancer investigations (Bozzini et al., 2013a; Momma et al., 1998). For instance, R3327-AT2 was used to evaluate the use of 5-ALA PDT in hypoxic tumours following continuous or fractionated illumination. In their study, a sub-optimal PDT was concluded, observing no reproducibility between light treatments. The authors suggested these hypoxic conditions in the tumour were responsible for the outcome of the treatment, given the essential oxygen requirements during PDT (Bozzini et al., 2013a). Momma et al. reported for the first time in 1998 the combination of PDT and surgery in the treatment of orthotopic prostatic tumours (Momma et al., 1998). In this specific study, MatLyLu cells were used to generate tumours in Copenhagen rat's prostate and BPD-MA was used as photosensitiser to treat the tumour bed upon surgical removal of tumours. An improvement in the rate of local recurrence and metastasis was concluded in this study combining prostatectomy and adjuvant PDT (Momma et al., 1998). In a different study R3327-AT6 tumours were treated with interstitially applied light and haematoporphyrin esters, showing consistent

damage of the structure of tumours, also finding a direct relationship between PDT damage and light dose (Lee et al., 1996). The authors of this study additionally confirmed an exclusive PDT effect, being the therapeutic outcome completely independent to hyperthermia, which is frequently associated to PDT treatment.

Subline name	*Properties*
R3327-H	• Well differentiated • Heterogeneous: combination of both androgen-dependent and independent cells • Slow growing: tumour volume doubling time around 20 days
R3327-HI-S	• Generated growing R3327-H in castrated male rats • Androgen-independent
R3327-AT-1	• Generated passaging R3327-H in intact male rats • Fast growing • Anaplastic • Rarely metastatic
MAT-LyLu	• Generated after serial passages of R3327-AT-1 • Fast growing • Anaplastic • Highly metastatic to lungs and lymph nodes
MAT-Lu	• Generated after serial passages of R3327-AT-1 • Fast growing • Anaplastic • Highly metastatic to lungs
R3327-AT-2	• Generated passaging R3327-H • Fast growing • Anaplastic • Low rate of distant metastasis
R3327-HI-M	• Generated by continuous passaging of R3327-HI-S in castrated male rats • Faster growth than precursor sub line • Less degree of differentiation
R3327-HI-F	• Generated by continuous passaging of R3327-HI-M • Faster growth than precursor sub line • Less degree of differentiation • Histologically it is not completely anaplastic
R3327-AT3	• Generated by a specific passage of R3327-HI-F • Completely anaplastic
R3327-AT6	• Longer doubling time: this enables good vascularisation and limits self necrosis

Table 8. Summary of cell lines established from the Dunning R3327 prostate adenocarcinoma model.

Highlighted in bold are MatLyLu cells, chosen for our study (Glowa et al., 2013; Isaacs et al., 1986)

4.1.2 BPD-MA as photosensitiser

Verteporfin (BPD-MA) was originally developed as photosensitiser against age-related macular degeneration. However, its success as a photosensitiser has resulted in further use in a wide range of studies, cancer treatment among others (Ayaru et al., 2007; Fingar et al., 1999; Momma et al., 1998; Schmidt et al., 1999).

In vivo, BPD-MA has been successfully used in "vascular-targeted PDT", a novel concept which is featured by short drug light intervals ranging 0-30 minutes after administration of the photosensitiser, ensuring the compound is located in vascular structures. This intends to affect fundamentally microvasculature with the subsequent increase in permeability and constriction of vessels. In the end, a dramatic damage to tissues and vascular collapse is pursued (Kawczyk-Krupka et al., 2015a).

For instance, BPD-MA has been used in PDT applications for glioma treatment. The selectivity of this photosensitiser for tumour was confirmed in tumour-bearing mice, despite showing differences in tumours directly implanted in the brain or subcutaneously. Encapsulation of BPD in liposomes enhances tumour-delivery, yet, the existence of a blood-brain barrier poses a major hurdle and could protect from the accumulation of photosensitiser in normal brain tissue, while still being present in the intracerebral tumour (Schmidt et al., 1999). This study also carried out both BPD and LED-light dose escalation in a dog model, confirming neurotoxicity above 150J/cm^2, which even led to one PDT-related death due to haemorrhagic necrosis and severe oedema in the brain stem (Schmidt et al., 1999). In pancreatic cancer studies, BPD-MA was rapidly cleared from circulation as well as completely eliminated from animal subjects (within 5-6 hr). In this same investigation, a 15-min drug light interval successfully caused necrosis to all tissues examined. Specifically, around 3-mm of pancreatic tumour tissue was affected upon exposure to light. Importantly, these investigations established suitable settings to achieve necrosis in pancreas at safe levels.

More recently BPD-MA has been subject of several combinatorial therapeutic studies. Along these lines, an enhancement in the outcome of PDT exerted by BPD-MA was found when animal subjects bearing non-small cell lung carcinomas were pretreated with erlotinib (EGFR inhibitor), in spite of the lack of effect when only exposed to this small-molecule inhibitor (Gallagher-Colombo et al., 2015). In fact, the authors concluded a synergistic effect rather than additive. Moreover, the reinforcement of PDT-based vascular damage was hypothesised, possibly caused by endothelial

damage: inhibition of EGFR could reduce proliferation as well as favour apoptosis of endothelial cells. In addition, this pre-treatment with elotinib could potentiate uptake of BPD-MA by tumour cells (Gallagher-Colombo et al., 2015). In a different study, BPD-MA was encapsulated in liposomes together with an anti-VEGF antibody (bevacizumab) for pancreatic cancer treatment. The surface of these liposomes had been in addition functionalised with positively charged molecules which can interact with negatively charged molecules that are frequently overexpressed in the surface of tumour cells such as glycosaminoglycans (GAG) or heparin sulphate. An extensive necrosis of tumours was found 3-4 days after light treatment, leading to complete cure of 33% of the animals (Tangutoori et al., 2016).

4.1.3 $TPCS_{2a}$ as photosensitiser

As described in the Background and Introduction, $TPCS_{2a}$ (Amphinex®) is a recently developed photosensitiser highly suitable for PCI due to the presence of two adjacent sulfonate groups, which confer amphiphilicity to the photosensitive compound. As briefly stated previously, this PS exhibits improved properties to previously reported PCI-based photosensitisers: the preparation of the former does not result in the formation of unwanted sulfonated isomers as occurring with the phtalocyanine-based $AlPcS_{2a}$, thereby avoiding an additional purification step (Wang et al., 2013).

$TPCS_{2a}$ combined with the antibiotic bleomycin was used in a PCI study aiming to assess the therapeutic outcome of an aggressive colon carcinoma tumour model (Berg et al., 2011). Results concluded an important delay in tumour growth, which was also similar to that seen in tumours treated with $AlPcS_{2a}$ and bleomycin (at least 11 days). Moreover, the delay seen after $TPCS_{2a}$ alone following PDT (72-hr DLI) was only 1.9 days. An interesting observation was concluded using this PS: a minimum light dose (10 J/cm^2) was required to observe tumour growth delay, and there was a direct correlation between light dose and growth delay. This suggested PCI might require a minimum light threshold (Berg et al., 2011).

In the first-in-man PCI study with $TPCS_{2a}$ and bleomycin (Sultan et al., 2016), patients were grouped in 3-patient cohorts receiving either 0.25 mg/kg, 0.5 mg/kg, 1 mg/kg or 1.5 mg/kg. Based on previous investigations in animal models, 4 days was the chosen drug light interval in this specific study before illuminating the tumour area with a 652 nm laser. No treatment-related deaths occurred throughout the study and all PCI-based adverse effects were either systemic related to skin photosensitivity or else localised

due to inflammation. Different measures have been determined to control the former, such as sunlight protection during a 3-month period followed by a progressive exposure to sun and gradual exposure to normal day light 2-3 days after $TPCS_{2a}$ administration. Through this dose-escalating study, 1 mg/kg was established as maximum tolerated dose, based on adversities reported in patients who had been administered with the highest dose (1.5 mg/kg). Surprisingly, even the lowest dose (0.25 mg/kg) resulted in a promising treatment response in tumours, observing no dose response effect above this dose and concluding a better therapeutic effect. The success of PCI treatment was described by the authors of the study as a combination of greater therapeutic depth in tumours and complete response outcome (38 mm tumour depth). In addition, this PS exhibited selectivity towards tumour tissue as opposed to healthy surroundings. As for bleomycin, its single administration limits the side effects associated to this antibiotic, described in Chapter 2. Moreover, the fact that it acts on highly proliferating cells might enhance the effect in cancerous cells. This preliminary clinical study has served as a basis for further PCI approaches and additional clinical trials in cancer treatment are being carried out, mentioned briefly in Background and Introduction.

4.1.4 $AlPcS_{2a}$ as photosensitiser

As with the above photosensitiser, the amphiphilic nature of $AlPcS_{2a}$'s structure which favours uptake by adsorptive endocytosis, explains the PS's suitability to cause photooxidative damage not just in PDT, but also for PCI.

$AlPcS_{2a}$-PDT was compared to 5-ALA in the evaluation of the resulting oedema following light and ultimately its capacity to open the blood-brain-barrier (BBB). Different PS concentrations and light fluences were used, demonstrating a higher potency of $AlPcS_{2a}$ based on the higher mortality rates and oedema formed. A 4/5-hr or 18 hr DLI were followed for 5-ALA or $AlPcS_{2a}$ light treatment respectively. It was indicated by the authors that due to the photosensitiser's amphiphilicity, it accumulated in the membrane of endothelial cells present in the BBB and was capable of directly affecting this structure (Mathews et al., 2011).

In a different study, $AlPcS_{2a}$ was combined with bleomycin to treat human colorectal and sarcoma tumour xenografts implanted in mice (Berg et al., 2005). The authors of the study confirmed the complete eradication of 60% of tumours 200 days after light treatment in PCI-treated animals, while only 10% of PDT-treated mice were cured by

this time. A 2-day DLI was used in this study. Importantly, no pneumonitis or fibrosis (characteristic effects of bleomycin) were found upon histological analysis of the samples and loss weight observed in the animal subjects after administration of the drug was recovered soon after treatment (Berg et al., 2005).

4.2 Aims

The present chapter focuses on the application of the minimally invasive focal light-based therapies PDT and PCI in the treatment of prostate cancer tumours *in vivo*.

Copenhagen rats were used as the *in vivo* model from the present chapter of the thesis onwards. Specifically, among the above-described Dunning cell lines, MatLyLu were selected based on their similarities with advanced hormone-independent human prostate cancer and their commercial availability. Tumours were initially grown subcutaneously and all light treatments were performed on heterotopic tumours. However, an orthotopic tumour model has also been developed and will be additionally reported. Different photosensitisers ($TPCS_{2a}$ –Amphinex–, BPD-MA –Visudyne– or $AlPcS_{2a}$) were independently used to evaluate the potential of light-based therapies to treat highly aggressive prostate cancer tumours, as is the case of our chosen model. BPD-MA is a PDT photosensitiser, while $TPCS_{2a}$ and $AlPcS_{2a}$ have been selected primarily due to their application for PCI, although $TPCS_{2a}$ could only be used at UCL owing to a prearranged material transfer agreement between PCI biotech A.S., as the owner of the drug, and UCL. As performed *in vitro* in Chapter 2 and Chapter 3, early studies *in vivo* involve PDT procedures as a starting point to establish the optimal conditions for an effective light-based treatment. Hereafter, we also briefly performed a preliminary investigation combining PS and the chemotherapy agent saporin, following PCI in tumour-bearing rats.

Due to the greater complexity of *in vivo* models, administration of therapeutic agents systemically follows a more intricate “journey” until these reach diseased areas, where there is a continuous interplay between drugs and biological systems. Therefore, *in vivo* experiments require a more thorough consideration as opposed to cells in a laboratory plate *in vitro*. On this basis, before performing light treatments, biodistribution and pharmacokinetic studies of photosensitisers were also evaluated in the above-mentioned rat model.

Overall, the therapeutic outcome of PDT and PCI was assessed and reported in the present chapter through the observation of tumour samples and survival curves. We directly relate the length of time required to reach a pre-established endpoint, to the delay of tumour growth after light treatment. Additionally, the mechanisms behind cell death in light-based treatments were evaluated through immunohistochemistry staining.

4.3 Materials & Methods

Animals and tumour models

Experiments were carried out using a subcutaneous syngeneic rat prostate adenocarcinoma tumour model (MatLyLu subline - Dunning R3327, purchased from ECACC Cat. 94101454). Copenhagen rats were used throughout (100-300 g). All animal experiments were performed in compliance with UKCCCR guidelines (under the authority of both project (70/7666) and personal licences (IC01B2571) granted by the Home Office) or the subcommittee on Research Animal Care (IACUC) of Massachusetts General Hospital in accordance with NIH guidelines (2015N000120).

- Subcutaneous model

10^6 or $4x10^5$ MatLyLu cells prepared in 100 µl RPMI 1640 media were implanted subcutaneously into the right flank of syngeneic Copenhagen rats (approximately 100 g), previously shaved. A state of general anaesthesia was maintained using inhaled isoflurane throughout the procedure.

- *Orthotopic tumour model*

Under general anaesthesia, Copenhagen rats (approximately 250 g, n=4) were shaved in their abdominal region and a 2 cm longitudinal incision was performed from the pubic bone in a cranial direction. The prostate was exposed upon retraction of the bladder. 10^4, $2x10^4$, $2.5x10^4$ or $5x10^4$ MatLyLu cells prepared in 100 µl RPMI 1640 media were injected into the stroma of the ventral lobe of the prostate. PBS was used with frequency to avoid dehydration during surgery. A solution of 10% povidone-iodine was used towards the end of the procedure to irrigate the surgical field in order to avoid growth of tumour cells which could have been unintentionally spilled in the surrounding areas. A 6-0 absorbable (Polyglactin 910) suture was used to repair the muscle layers and a 4-0 suture was used to close the incision in the skin. A state of general anaesthesia was maintained using inhaled isoflurane throughout the procedure. A combination of analgesics, Vetergesic (0.05-0.1 mg/kg) and Rimadyl (5 mg/kg) were administered subcutaneously 30 minutes prior to the procedure and in days following if the animals were found in pain or distress.

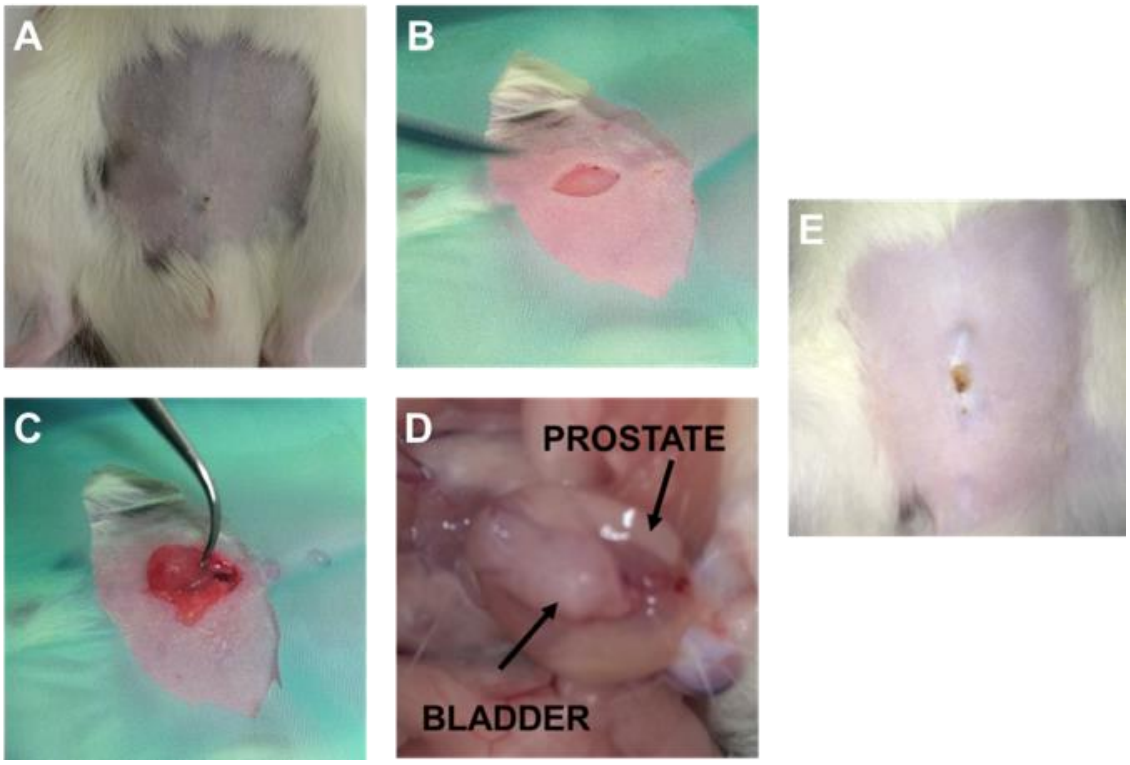

Figure 53. Orthotopic tumour implant procedure.

Copenhagen rats were shaved in their abdominal region (A) and a 2 cm longitudinal incision was performed from the pubic bone in a cranial direction (B). The prostate was exposed upon retraction of the bladder (C). 10^4, $2x10^4$, $2.5x10^4$ or $5x10^4$ MatLyLu cells were injected into the stroma of the ventral lobe of the prostate (D). Incision 3 days after surgery (E)

Chemicals and photosensitisers

$TPCS_{2a}$ (Amphinex®) was kindly donated by PCI Biotech AS, Oslo, Norway. The 30 mg/ml stock in Cremophor was diluted in PBS to a final concentration of 0.25-2.5 mg/ml for intravenous (i.v.) injection, sterile filtered and kept at 4ºC.

BPD-MA (Visudyne®) was purchased from Novartis. 15 mg of lyophilised powder were dissolved in 1 ml 5% dextrose and stored at -80ºC. Working solutions were prepared at 0.5 mg/ml and kept at 4ºC.

$AlPcS_{2a}$ was purchased from Frontier Scientific Inc., U.S. The stock solution was prepared by dissolving powder in sodium hydroxide, and neutralising with 0.1 M hydrochloric acid to a 1-2 mg/ml final concentration. Working $AlPcS_{2a}$ solutions were kept at 4°C and experimental concentrations were obtained diluting a 1-2 mg/ml solution in cell media to reach desirable concentrations.

Saporin (Sigma Aldrich, S9896) was dissolved in PBS to a final concentration of 0.25 mg/ml for intravenous (i.v.) injection and kept at 4ºC.

Qualitative biodistribution of $TPCS_{2a}$ using fluorescence microscopy

2.5 mg/ml $TPCS_{2a}$ was administered intravenously to 15 Copenhagen rats via tail vein. Liver, spleen, skin, tumour, distal colon, prostate, urethra and bladder samples were collected 6 hr, 24 hr, 48 hr and 72 hr after administration and 3 animals were used per group, including control group. Fresh tissue samples were snap-cooled in isopentane for 10 s upon removal. Excess liquid was dried placing the specimen on paper tissue and these were then immersed in liquid nitrogen and kept frozen at -80ºC after collection until sectioning.

OCT Embedding Medium (Raymond A. Lamb, UK) was used to mount samples for cryosectioning. Samples were sectioned at 10 µm and collected on polylysine-coated slides and kept in -20 ºC after collection until imaging. Minimal environmental light was used during sectioning to avoid bleaching of $TPCS_{2a}$.

Fluorescence emission of $TPCS_{2a}$ in tissues was imaged using an Olympus IMT-2 epi-fluorescence microscope with a low power (2 mW) 405 nm blue diode laser coupled to a liquid light guide. A PIXIS 521 charge-coupled device (CCD) camera (Princeton Instruments) was attached to the microscope, using a 10X magnification objective giving 500 x 500 – micron scale images. A 660 nm bandpass detection filter was used. Image analysis was performed using Image J software. Control animal samples without $TPCS_{2a}$, showed insignificant levels of autofluorescence, yet, these were taken into consideration and subtracted when examining the samples under investigation. Accordingly, a baseline for $TPCS_{2a}$-based fluorescence was obtained. After imaging, sections were stained following a standard haematoxylin eosin (H&E) protocol and examined on a Hamamatsu Nanozoomer Digital Pathology (NDP) scanner (Hamamatsu Photonics K.K., UK), which recorded whole sections producing high resolution images.

Quantitative biodistribution of $TPCS_{2a}$ using chemical extraction

2.5 mg/ml $TPCS_{2a}$ was administered intravenously to 15 Copenhagen rats via tail vein. Liver, blood, spleen, skin, tumour and distal colon samples were collected 6 hr, 24 hr, 48 hr and 72 hr after administration and 3 animals were used per group, including control subjects. Tissue samples were kept frozen at -80 ºC after collection.

Solvable™, was purchased from PerkinElmer to perform chemical extraction. Prior to use, samples were completely defrosted and 0.1 g (in triplicate) were cut from each organ sample and immersed in tubes containing 2 ml of Solvable™. Due to expected

higher fluorescence in blood samples, 3 ml Solvable™ were used. Tubes were then placed in a shaking water bath at 50ºC during 2 hours until the samples had completely dissolved. 0.15 ml of these tissue solutions were diluted in 3 ml Solvable™ prior to measurement of fluorescence, again, performed in triplicate. Right before measuring fluorescence, samples were cooled to room temperature and each solution was plated in 4 wells of a black 96-well plate.

Standard curves of $TPCS_{2a}$ were obtained for each organ by making up a $TPCS_{2a}$ series of known concentrations of control tissue and solvable mixtures. Fluorescence was measured at 652 nm, and hereafter used to calculate unknown concentrations in the different groups. The displacement factor of each organ in solvable was taken into account.

Qualitative biodistribution of BPD-MA and $AlPcS_{2a}$ using a fluorescent in vivo imaging system (IVIS)

1 mg/ml BPD-MA or 2 mg/ml $AlPcS_{2a}$ were administered intravenously to Copenhagen rats via tail vein. Images were taken immediately, 15 min or 6 hr (for BPD-MA and $AlPcS_{2a}$ respectively) and 24 hr after administration.

Fluorescence emission of both photosenstisers was imaged using an IVIS® Lumina Series III (PerkinElmer, Inc., Waltham, MA, USA). Before imaging, a state of general anaesthesia was induced using inhaled isoflurane in the subjects. Rats were then placed in the imaging chamber on an adjustable stage. Optimal excitation/emission filters for the phtalocyanine-based PS ($AlPcs_{2a}$) were not available in the existing IVIS equipment. Therefore, for both BPD-MA and $AlPcs_{2a}$, fluorescence emission was measured at 670 nm, setting excitation at 420 nm.

Light sources

Different devices were used to tailor light treatment to each photosensitiser:

- A diode laser emitting at 652 nm was used for Amphinex® treatment groups (Diomed Ltd., UK)
- A LumaCare™ lamp LC-122 (LumaCare, USA) was used for BPD-MA and $AlPcS_{2a}$ treatment groups. A fibreoptic probe was attached to the lamp emitting in the spectral region 670-700 and 635-670 nm for each photosensitiser respectively.

$TPCS_{2a}$ - PDT treatment on subcutaneously grown tumours

For PDT treatments with $TPCS_{2a}$, a 0.25 mg/ml solution was injected 24 hr prior to light delivery via a tail vein administering different PS dosages: 0.5, 1 or 2.5 mg/kg. Before light treatment, the skin above subcutaneously growing tumours was shaved and a small incision was made, exposing these tumours. Two different light treatments were performed hereafter. At least 3 animals were used per combination of PS and light (PDT group - n≥3)

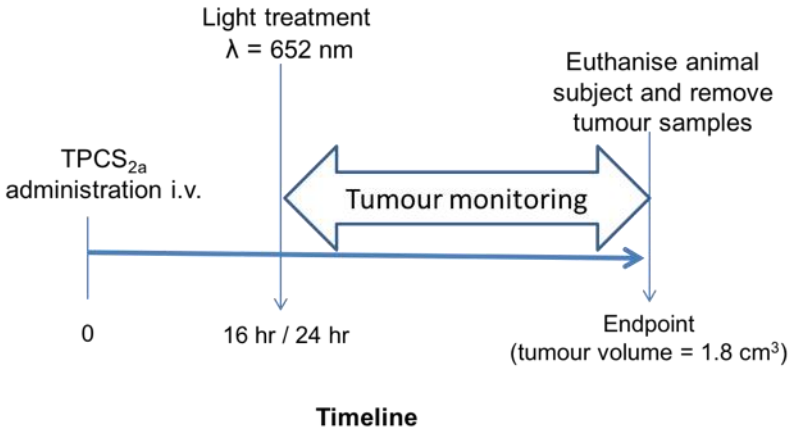

Figure 54. Timeline for $TPCS_{2a}$ treatments in vivo.

$TPCS_{2a}$ solutions were administered i.v. via tail vein, allowing either a 16 hr or 24 hr DLI. After light treatment, animals were monitored regularly and sacrificed when tumour volume reached a humane end point (volume = 1.8 cm^3).

- *Interstitial illumination*

A 400 µm laser fibre was used to deliver light interstitially. The bare cleaved tip of the fibre was used to penetrate the tumour capsule, inserting it perpendicular to the tumour surface (see Figure 55). Laser power was set to 0.1 W at a light irradiance of 10 J or 20 J.

Figure 55. Interstitial illumination of previously exposed subcutaneous tumours.

The area of skin above the growing tumour was shaved and a small incision was made to expose the tumours (0.6-1 cm diameter 7 days after implantation - depending on the cell number injected). A cleaved tip 400 µm laser fibre was used to penetrate the tumour capsule and deliver light in a perpendicular manner into the top of the tumour.

- *Surface illumination*

A 400 µm microlens fibre was placed above the tumour, generating a 2 cm uniform spot of light. Laser power was set to 0.1 W/cm^2 at a light irradiance of 75 J/cm^2. To avoid undesired skin toxicity, the area surrounding the tumour was covered in previously sterilised opaque thick drapes during light delivery as shown in Figure 56.

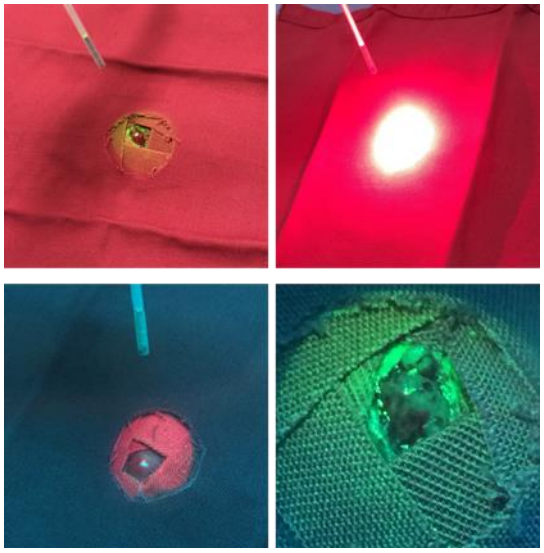

Figure 56. Surface illumination of previously exposed subcutaneous tumours.
The area of skin above the growing tumour was shaved and a small incision was made to expose the tumours (0.6-1 cm diameter 7 days after implantation - depending on the cell number injected). A microlens fibre was used to deliver a 2cm spot of light on top of the exposed tumour surface.

During light treatments a state of general anaesthesia was maintained using inhaled isoflurane throughout the procedure. A combination of analgesics - Vetergesic (0.05-0.1 mg/kg) and Rimadyl (5 mg/kg), was administered subcutaneously 30 minutes prior to the procedure and the days following if the animals were found in pain or distress. Animals were monitored regularly and sacrificed when tumour volume reached a humane end point (volume = 1.8 cm^3). Tumour samples were cleaned in PBS and immersed in formalin for 24 hr – 48 hr based on their size. These were then processed and stained following a standard H&E protocol.

BPD-MA PDT treatment on subcutaneously grown tumours

1 mg/kg of BPD-MA was injected i.v. via tail vein 15 minutes before light treatment. No surgical procedure was carried out during BPD-MA PDT procedures. The fibreoptic attached to the lamp was placed above the skin covering the tumour, which had been previously shaved. Laser power was set to 0.1 W/cm^2 at a light irradiance of 120 J/cm^2. During light treatments a state of general anaesthesia was maintained using inhaled isoflurane throughout the procedure. Buprenex (0.05-0.1 mg/kg) was administered

subcutaneously prior to the procedure and the days following if the animals were found in pain or distress. At least 3 animals were used per combination of PS and light (PDT group - n≥3)

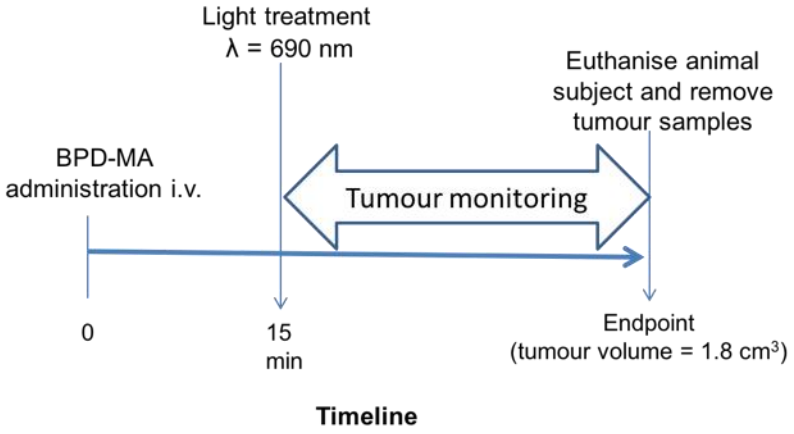

Figure 57. Timeline for BPD-MA PDT treatments in vivo.

BPD-MA solutions were administered i.v. via tail vein, allowing a 15-minute DLI. After light treatment, animals were monitored regularly and euthanised when tumour volume reached a humane end point (volume = 1.8 cm³).

AlPcS$_{2a}$ PDT and PCI treatments on subcutaneously grown tumours

2 mg/kg of AlPcS$_{2a}$ was injected i.v. via tail vein 6 or 24 hr before light treatment. No surgical procedure was carried out during AlPcS$_{2a}$ PDT or PCI procedures. The fibreoptic attached to the lamp was placed above the skin covering the tumour, which had been previously shaved. Laser power was set to 0.1 W/cm^2 at a light irradiance of 100 J/cm^2. During light treatments a state of general anaesthesia was maintained using inhaled isoflurane throughout the procedure. Buprenex (0.05-0.1 mg/kg) was administered subcutaneously prior to the procedure and the days following if the animals were found in pain or distress. In animals belonging to PCI groups, 250 µg/kg saporin was administered 1 hr prior to light. As reviewed previously, photooxidative damage has a vascular effect *in vivo*. Founded on this, saporin was administered before light: this would ensure the systemic delivery of saporin, i.e. tumour area, in the event of a later vascular shut down. At least 3 animals were used per combination of PS and light (PDT group) or PS, light and saporin (PCI group) (n≥3).

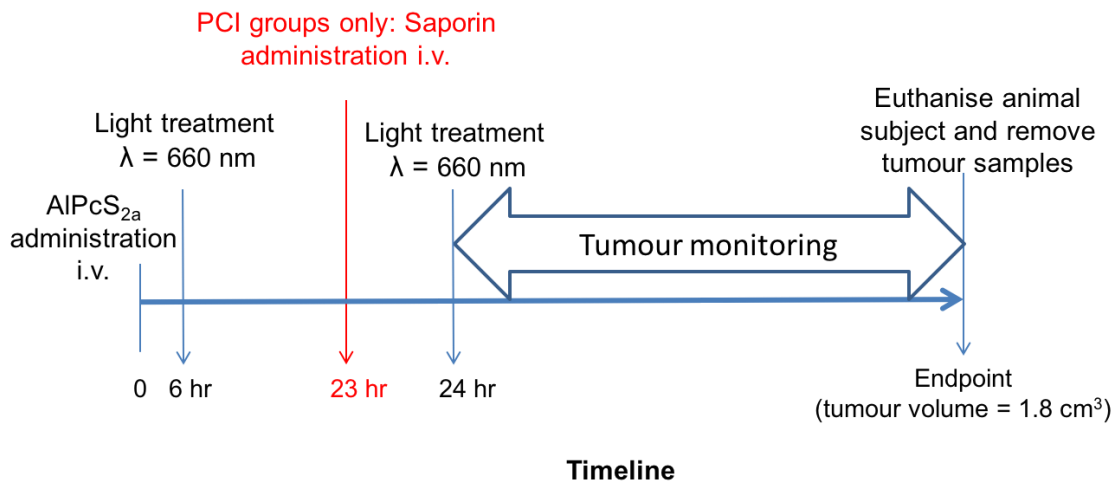

Figure 58. Timeline for $AlPcS_{2a}$ PDT/PCI treatments in vivo.

$AlPcS_{2a}$ solutions were administered i.v. via tail vein, allowing either a 6 hr or 24 hr DLI. 1 hr before light treatment, 250 µg/kg saporin was administered i.v. via tail vein to animal subjects belonging to the PCI group. After light treatment, animals were monitored regularly and euthanised when tumour volume reached a humane end point (volume = 1.8 cm^3).

Standard histological analysis of tumour samples

Tissue samples removed from Copenhagen rats were washed in PBS directly after sampling and immersed in 10% formalin during 24-48 hr depending on the size of the specimen. Samples were then processed following a standard tissue processing protocol and embedded in paraffin. Paraffin blocks were trimmed and once the whole sample was accessible section collection was started. 4-5 µm thick sections were cut from each sample. H&E staining was performed following a standard protocol. Sections were then examined on a Hamamatsu Nanozoomer Digital Pathology (NDP) scanner (Hamamatsu Photonics K.K., UK), which recorded whole section high resolution images.

Immunohistochemistry staining

Immunohistochemistry staining was performed by UCL Advanced Diagnostics. Briefly, for cleaved caspase-3 staining, a primary antibody was purchased from Cell Signaling Technology® (Cat. 9661). This is a rabbit polyclonal antibody which detects the endogenous fragment of activated caspase-3 enzyme, resulting from its cleavage adjacent to D175. Antigen retrieval was achieved at pH 6 during 30 minutes at 99°C. An epitope retrieval solution from Leica Biosystems (AR9961) was used. Staining was performed on a Leica Bond III automated immunostainer and detection was carried out using Leica Bond Polymer Refine DAB detection system (Leica DS9800) as follows: incubation with the primary antibody was allowed during 15 minutes at room

temperature (1/300 dilution). Slides were then blocked with hydrogen peroxide and an additional anti-mouse post-primary antibody was applied for 8 minutes. Finally, an 8-minute incubation with an anti-rabbit secondary antibody was completed.

Statistical analysis

Statistical analysis was performed using GraphPad Prism 6.

For tumour growth rate analysis, at least 3 animal subjects were used in each group ($n \geq 3$) but for light only controls and $AlPcS_{2a}$-PDT. In the latter group, 2 animals died during light treatment due to anaesthesia overdose. Therefore, $n = 2$ was used for these. A two-way ANOVA followed by Bonferroni *post hoc* multiple testing correction was used to in those cases where at least 3 animals were used ($n \geq 3$). In comparative analysis involving $n = 2$ groups, a one-way ANOVA between matched groups followed by Bonferroni *post hoc* was performed.

Significance level of $p < 0.05$ (*p = 0.05 to 0.01; **p = 0.01 to 0.001; ***p = 0.001 to 0.0001)

4.4 Results

4.4.1 Prostate tumours in Copenhagen rats

All PDT and PCI light treatments were performed on subcutaneous tumours due to the relatively easy generation and growth monitoring of this tumour model. Despite the greater accuracy and reliability in the evaluation of tumour treatment when tumour masses are found in their natural physiological environment (prostate in this specific project), the anatomical localisation of the prostatic gland hinders the accurate monitoring of tumour growth. Hence, reproducibility between animal subjects and assessment of tumour evolution can be hampered. In addition, tumour implantation in this case requires an additional surgical procedure (as described in the Materials & Methods section) with the associated risk and comorbidity in the animals this entails. Finally, the reduced size of rat prostate hampers the exclusive injection of cancer cells in this organ, jeopardising surrounding tissues, which may accommodate possible spillage of malignant cells. Consequently, the use of subcutaneous tumours in this case enables the faster generation of a larger number of tumours to perform studies on.

As reported in the *in vitro* study in Chapter 2, MatLyLu is a very metabolically active and rapidly growing cell line. Throughout the *in vivo* study, we observed that tumour growth was gradual up to around 0.8 cm diameter, from which point an exponential growth occurred. This would accelerate the period of time for animals to reach the humane pre-established endpoint based on tumour size and burden. Therefore, the aim during tumour generation was to determine an adequate cell number during implantation that would be large enough to result in tumour formation, yet in a controlled manner, since cells require a sufficient amount of time to form “organised” tumour masses. Additionally, this should be achieved within reasonable periods of time, which would suit our experimental timeline and enable reproducibility.

So as to determine this optimal cell number to generate tumours *in vivo*, different cell concentrations were tested. Initial experiments in tumour generation were performed using 10^6 cells/implantation, which resulted in 1 cm diameter tumours in 7 days. We then attempted $4x10^5$ cells, which lead to a delay of 1 day in tumour growth, reaching the 1 cm diameter after 8-9 days. The first interstitial-light treatments described below

were performed with 1 cm diameter tumours after a 10^6-cell implantation. Due to the sudden exponential tumour growth stated in the lines above, treatment was initiated on 0.5-0.7 cm tumours resulting from the implantation of $4x10^5$ cells.

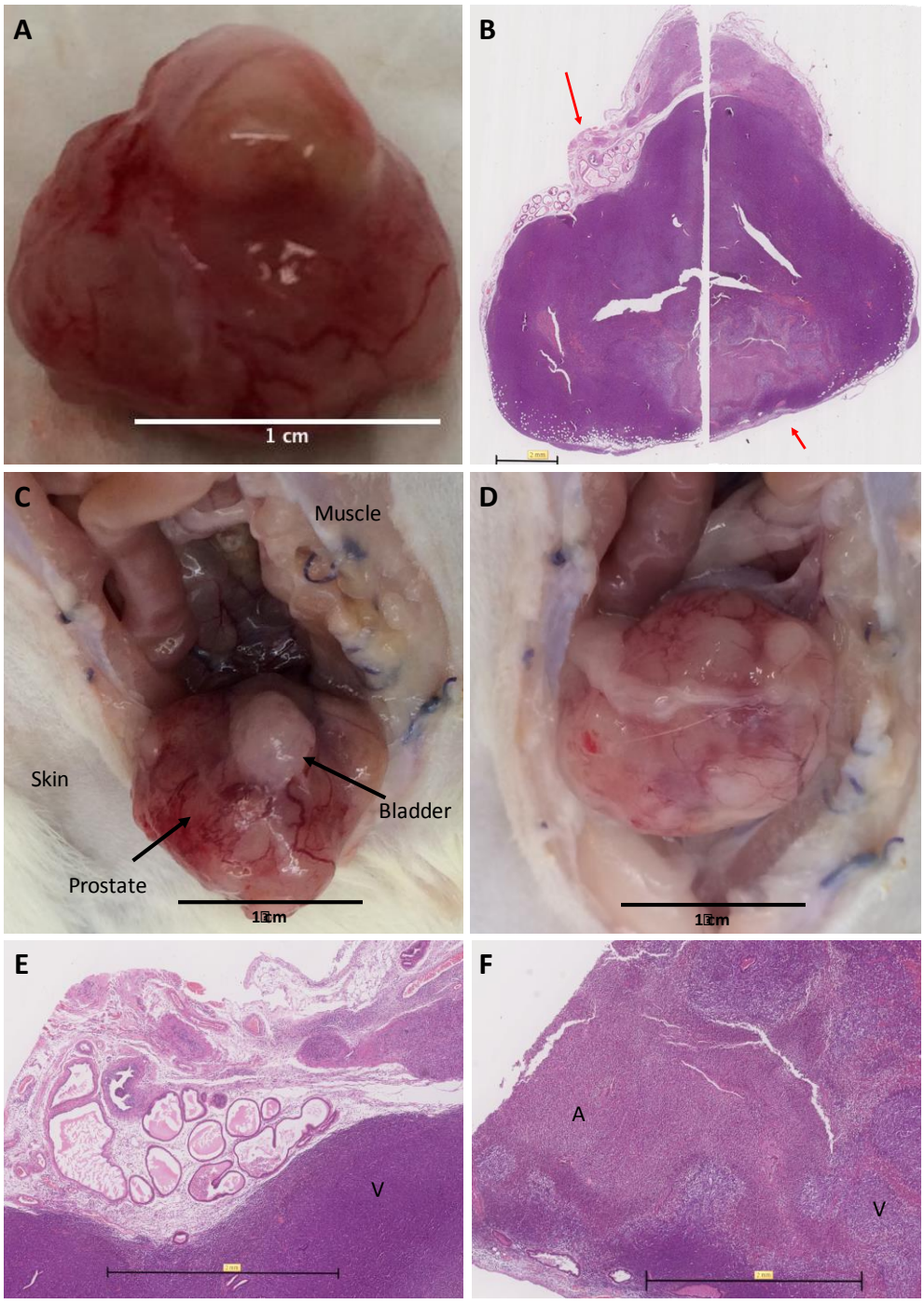

Figure 59. Orthotopic prostate tumour.

$5x10^4$ MatLyLu cells were implanted into the ventral lobe of the prostate in Copenhagen rats through surgical procedure. (A) tumour removed 8 days post implantation; (B) H&E staining, top red arrow indicates the remaining glandular prostate tissue, bottom red arrow indicates an affected tumour area; (C), (D) tumour prior to removal – both show highly vascularised tumours; (E), (F) detail of H&E staining at 2.5X magnification. Scale bars shown as 1 cm for tumour shown in (A), (C), (D); 2 mm for H&E tumour staining (B), (E), (F). "A" and "V" in (E), (F), indicate affected prostate tumour and viable tumour regions respectively.

Even though we did not perform treatment on orthotopic tumours for the reasons stated above, we attempted the orthotopic implantation of MatLyLu cells for potential future experiments. In this case, rats bearing tumours in the prostate gland were regularly monitored to assess tumour growth through abdominal palpitation. No tumour mass was detected by this mean; however, based on previous *in vitro* knowledge regarding the fast growth rate of MatLyLu cells, animal subjects were euthanised 8 days post surgery.

Only the rat that had been injected with the largest cell number ($5x10^4$ cells) developed a tumour of large dimensions - 1.4 cm^3 (Figure 59A, Figure 59C, Figure 59D). This tumour invaded the whole prostate (Figure 59A), which consequently lost its characteristic anatomical glandular structure, being detectable only in a small region of the periphery as indicated with a red arrow in Figure 59B. In addition, the highly vascularised nature of the tumour under investigation was observed in this specimen. Interestingly, despite this tumour had not received treatment, an affected area in the central region of the tumour was found (Figure 59D). This is a common feature of large tumours, generally spontaneous necrosis due to fast growth.

Briefly, we observed throughout our study that MatLyLu tumours were very fast growing and frequently resulted in multi-nodular tumours. This correlates with previous observations of cells cultured *in vitro* during the present project as well as in preceding studies, where doubling time was 19.7 hr, contact inhibition was lost and clumps were found even at low confluence (Wenger et al., 1984).

4.4.2 Amphinex PDT in rat subcutaneous prostate carcinoma

Amphinex® was the first photosensitiser to be employed in our *in vivo* study since it was being used at the same time in the first-in-man PCI clinical for cancer treatment trial at UCLH (University College London Hospital). As stated in the Introduction section above, the success of this study has been recently reported (Sultan et al., 2016).

In the present project, initial experiments involved the evaluation of pharmacokinetics and biodistribution in the rat model described, prior to the conduction of PDT and PCI light treatments. These investigations were carried out following two different techniques as will be reported in the sections below: quantification by chemical extraction and qualitative observation through fluorescence microscopy.

4.4.2.1 Quantitative biodistribution of $TPCS_{2a}$ (Amphinex) in Copenhagen rats – Chemical extraction

In order to evaluate pharmacokinetics of $TPCS_{2a}$ in our animal model as well as to determine the optimal drug light interval for light treatments, chemical extraction of certain organs was carried out. An optimal DLI is important to maximise the amount of photosensitiser present in the tumour mass whilst keeping levels in surrounding healthy tissues under certain limits to avoid undesired phototoxicity in the event of unavoidable normal tissue illumination.

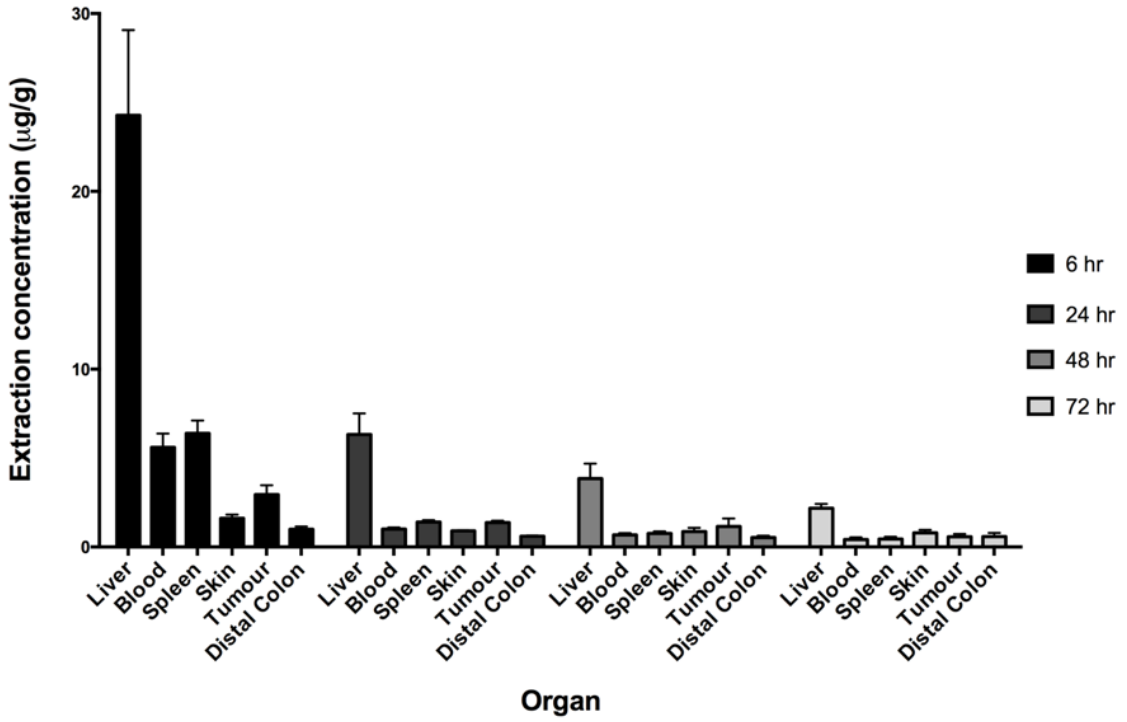

Figure 60. Biodistribution of $TPCS_{2a}$ in liver, blood, spleen, skin, tumour and distal colon.

2.5 mg/kg $TPCS_{2a}$ were administered i.v. via tail vein to 15 Copenhagen rats (n=3, including control). Samples were obtained 6 hr, 24 hr, 48 hr and 72 hr after injection. Solvable™ was used to dissolve tissue samples. Fluorescence of the samples was measured at 652 nm. To quantify, standard curves of known concentrations of $TPCS_{2a}$ were obtained for each of the studied organs. Concentration is shown as mean μg per gram of tissue ± SEM.

Liver and spleen were chosen due to their intrinsic nature as filtration organs. Blood is the vehicle responsible for the systemic distribution throughout the body and for this reason it was also investigated. As for skin, when using light-based therapies, it is important to consider side phototoxicity that might emerge as a consequence of the exposure to natural sunlight and visible light in the environment. Finally, it is also important to consider levels of PS in tissues located in the proximities of the prostate

such as bladder or distal colon. Therefore, the amount of $TPCS_{2a}$ in distal colon was quantified through chemical extraction; while levels in bladder and prostate, were assessed through fluorescence microscopy (reported in the following section) due to their reduced size.

As shown in Figure 60, the earliest time point (6 hr) resulted in the largest amount of photosensitiser in all organs sampled. Not surprisingly, liver was the organ exhibiting the greatest presence of $TPCS_{2a}$ at all time points evaluated. However, it was quickly cleared, being present at 24.3 µg/g, 6.3 µg/g and 2.3 µg/g at 6 hr, 24 hr or 72 hr respectively. In blood and spleen similar amounts were found 6 hr after administration, 5.6 µg/g and 6.4 µg/g correspondingly. Both of these tissues also exhibited analogous clearance of the photosensitive compound, being levels significantly lower at 24 hr and negligible at 72 hr. In distal colon $TPCS_{2a}$ was not retained at remarkable concentrations in any of the time points investigated (0.99 µg/g - 0.58 µg/g). Skin exhibited a similar accumulation and clearance profile as described for distal colon, with a slightly higher accumulation at the 6 hr time point (1.6 µg/g). Regarding the tumour tissue of interest, 6 hr was also the time point exhibiting the largest amount of $TPCS_{2a}$ (2.9 µg/g) and then gradually decreased, showing only insignificant traces 72 hr after administration (0.6 µg/g).

4.4.2.2 Qualitative biodistribution of Amphinex in Copenhagen rats – Fluorescence microscopy

Fluorescence microscopy was used to assess biodistribution in liver, spleen, skin, tumour, distal colon in a qualitative manner in addition to the quantification reported above. In addition, this was an additional verification of the accumulation of the photosensitiser under study and later clearance from the mentioned tissues. Prostate, urethra and bladder were not subject to chemical extraction given their reduced size (the amount of existing tissue would have been insufficient to follow the chemical extraction protocol as described in the Materials & Methods section). However, a qualitative assessment of the accumulation of TPCS2a in these tissues was carried out through fluorescence imaging 6 hr, 24 hr, 48 hr and 72 hr after injection of photosensitiser solution. These fluorescence images are dis played in Figure 61, Figure 62 and Figure 63.

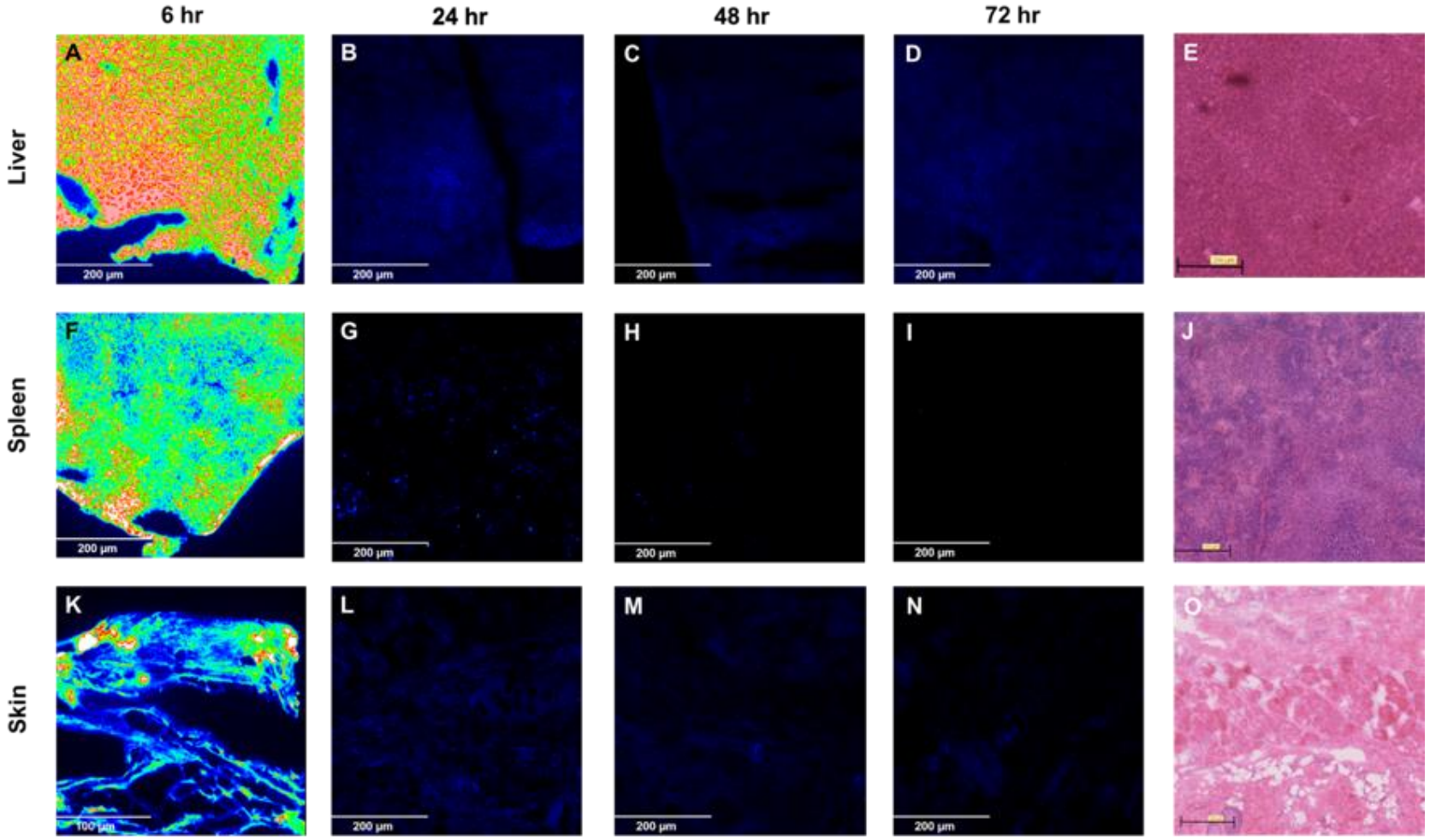

Figure 61. Distribution of $TPCS_{2a}$ in liver, spleen and skin.

2.5 mg/kg $TPCS_{2a}$ were administered i.v. via tail vein in 15 Copenhagen rats (n=3, including control). Fluorescence images were taken from liver (A, B, C, D); spleen (F, G, H, I); skin (K, L, M, N). Tissues were sampled 6 hr, 24 hr, 48 hr and 72 hr after injection of 2.5 mg/kg $TPCS_{2a}$. (E), (J), (O) H&E staining from each tissue shown at 10X magnification. Scale bars shown as 200 µm.

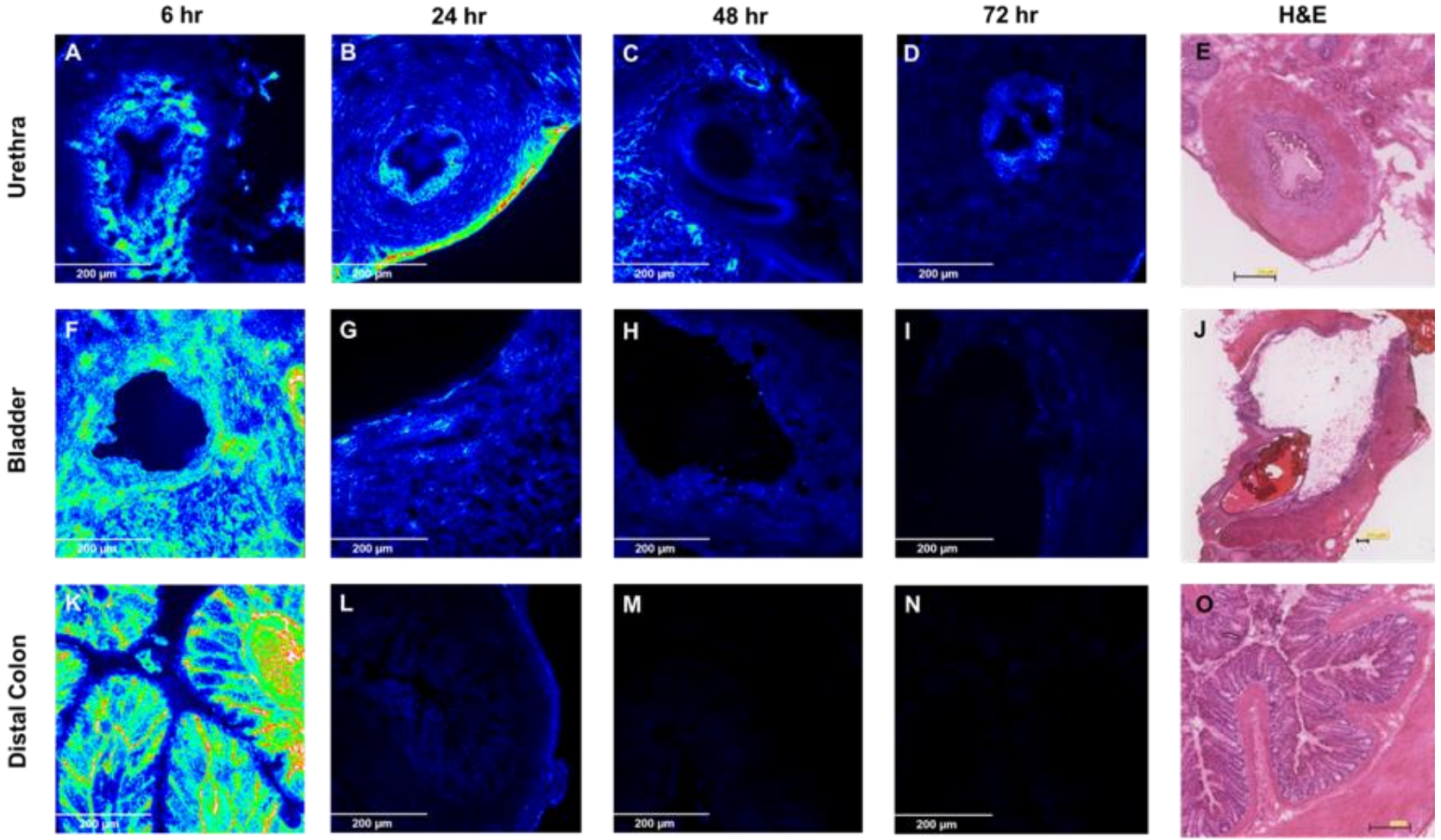

Figure 62. Distribution of $TPCS_{2a}$ in urethra, bladder and distal colon.

2.5 mg/kg $TPCS_{2a}$ were administered i.v. via tail vein in 15 Copenhagen rats (n=3, including control). Fluorescence images were taken from urethra (A, B, C, D); bladder (F, G, H, I); distal colon (K, L, M, N). Tissues were sampled 6 hr, 24 hr, 48 hr and 72 hr after injection of 2.5 mg/kg $TPCS_{2a}$. (E), (J), (O) H&E staining from each tissue shown at 10X magnification. Scale bars shown as 200 µm.

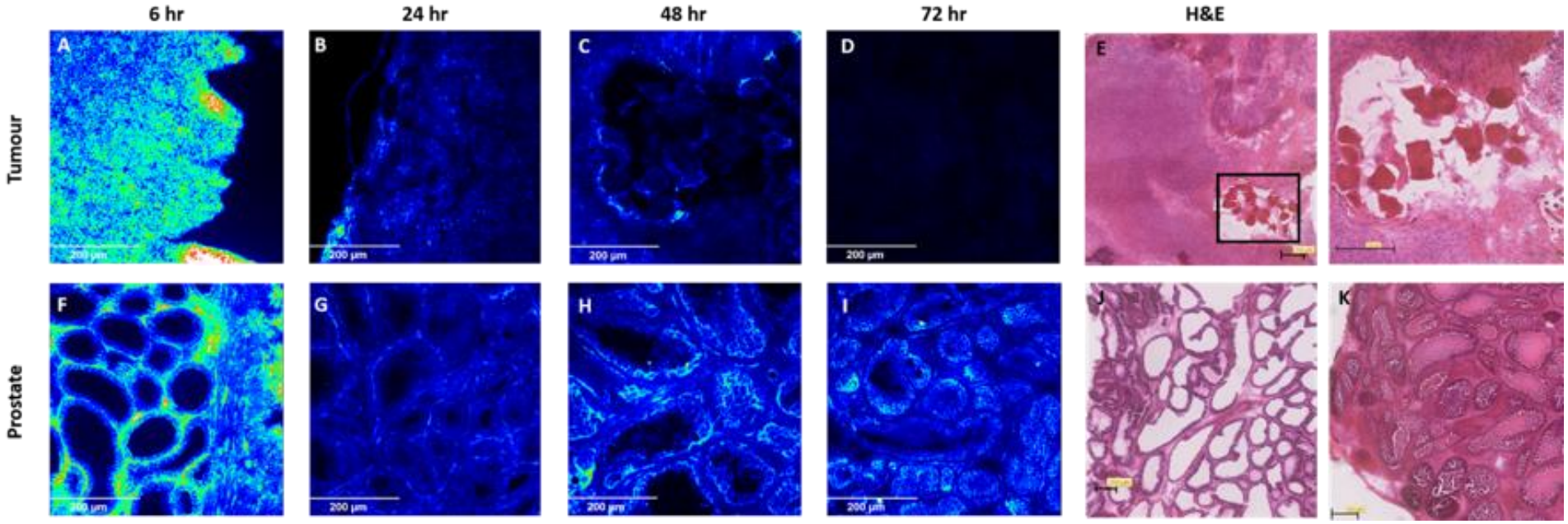

Figure 63. Distribution of $TPCS_{2a}$ in subcutaneous prostate tumour and prostate.

2.5 mg/kg $TPCS_{2a}$ were administered i.v. via tail vein in 15 Copenhagen rats (n=3, including control). Fluorescence images were taken from subcutaneously grown tumour (A, B, C, D); prostate (F, G, H, I). Tissues were sampled 6 hr, 24 hr, 48 hr and 72 hr after injection of 2.5 mg/kg $TPCS_{2a}$. (E), (J), (K) H&E staining from each tissue shown at 10X magnification. Scale bars shown as 200 µm.

Similarly to chemical extraction findings, images 6 hr after administration of photosensitiser resulted in the highest intensity of fluorescence, thus accumulation of TPCS2a in all tissues (Figure 61A, Figure 61F, Figure 61K, Figure 62A, Figure 62F, Figure 62K, Figure 63A, Figure 63F, Figure 63K), which was then significantly reduced by 24 hr (Figure 61B, Figure 61G, Figure 61L, Figure 62B, Figure 62G, Figure 62L, Figure 63B, Figure 63G, Figure 63L). Liver (Figure 61A) displayed the greatest emission of fluorescence out of all sampled tissues, followed by spleen (Figure 61F). Similar fluorescence levels were found between the rest of the tissues 6 hr after injection. 24 hr after injection negligible fluorescence was detected in liver (Figure 61B), spleen (Figure 61F), skin (Figure 61L) and distal colon (Figure 62L); which were kept constant hereafter up to micrographs taken at 72 hr (Figure 61B-Figure 61D; Figure 61G-Figure 61I; Figure 61L-Figure 61N; Figure 62L- Figure 62N respectively). Although emission of fluorescence at 24 hr was also reduced in urethra (Figure 62B), bladder (Figure 62G), tumour (Figure 63B) and prostate (Figure 63G) compared to 6 hr, this fall was not as drastic as in liver, spleen and skin.

Fluorescence in urethra seemed to be quite similar 6 hr – 48 hr after injection, as shown in Figure 62A-Figure 62C, being significantly reduced by 72 hr (Figure 62D). As for bladder, emission of fluorescence was reduced by 24 hr (Figure 62G), followed by similar levels 24 hr – 72 hr (Figure 62G- Figure 62I).

Tumour tissue seemed to retain $TPCS_{2a}$ up to 48 hr post administration (Figure 63B-Figure 63C), although a higher fluorescence resulted from micrographs taken at 6 hr (Figure 63A). Importantly, this fluorescence was uniformly distributed and located within cells, not restricted to vascular structures within the tumour mass, which is a particularly important observation regarding light treatment in PCI procedures. Healthy prostate exhibited a similar accumulation pattern of photosensitiser throughout the study, although levels were slightly higher at the earliest imaged time point (Figure 63F). No significant fluorescence was detected in control samples.

4.4.2.3 $TPCS_{2a}$ light treatment (PDT)

Although the earliest time point (6 hr) in the distribution and pharmacokinetic study (Figure 60) showed the greatest accumulation of $TPCS_{2a}$ (Amphinex®) in tumours, we started performing light treatments following a 24 hr drug light interval. This would

ensure a more subcellular effect as opposed to high dose PDT, enabling the comparison with PCI in further experiments.

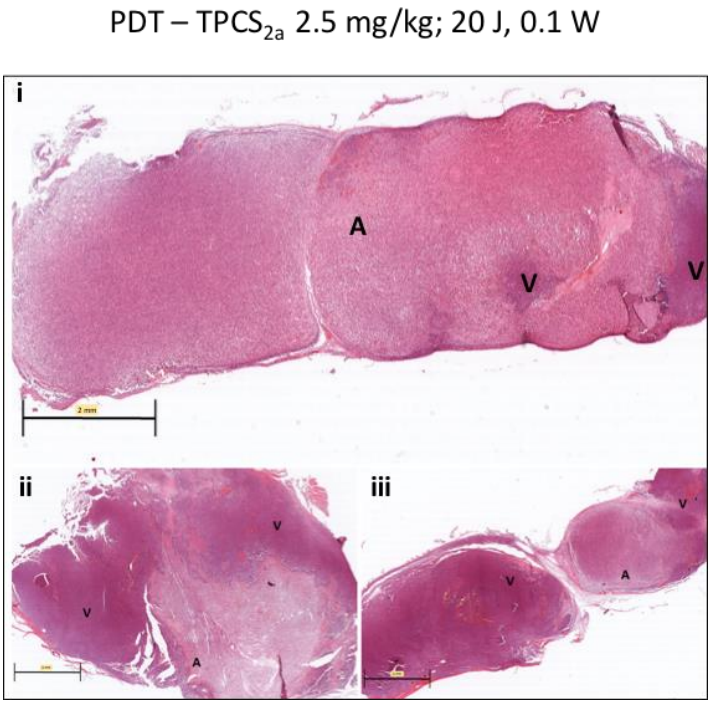

Figure 64. Evaluation of affected tumour area 24 hr after $TPCS_{2a}$-PDT interstitial light treatment to subcutaneous prostate tumours.

2.5 mg/kg $TPCS_{2a}$ was injected i.v. via tail vein to Copenhagen rats bearing subcutaneously grown prostate tumours (i, ii, iii). 24 hr after administration, light treatments were carried out at a fluence rate of 20 J and 0.1 W power and animals were euthanised 24 hr after light treatment. Once sampled, tumours were H&E stained and examined on a Hamamatsu Nanozoomer Digital Pathology (NDP) scanner, 1.25X magnification. A: affected tumour area; V: viable tumour area; scale bars shown as 2 mm.

We initiated PDT treatment to subcutaneous tumours using interstitial illumination. An early assessment of photooxidative damage was carried out 24 hr after a 20 J light treatment of tumours in animals previously injected with $TPCS_{2a}$. As indicated as “A” in Figure 64, the combination of $TPCS_{2a}$ and light resulted in large affected regions in these tumours. The additional staining against cleaved caspase-3, marker for apoptotic cell death, revealed a major participation of apoptosis resulting from PDT photooxidative damage, as observed in Figure 65, one of the tumour samples belonging to this first group of treated animal subjects also analysed through H&E staining in Figure 64i.

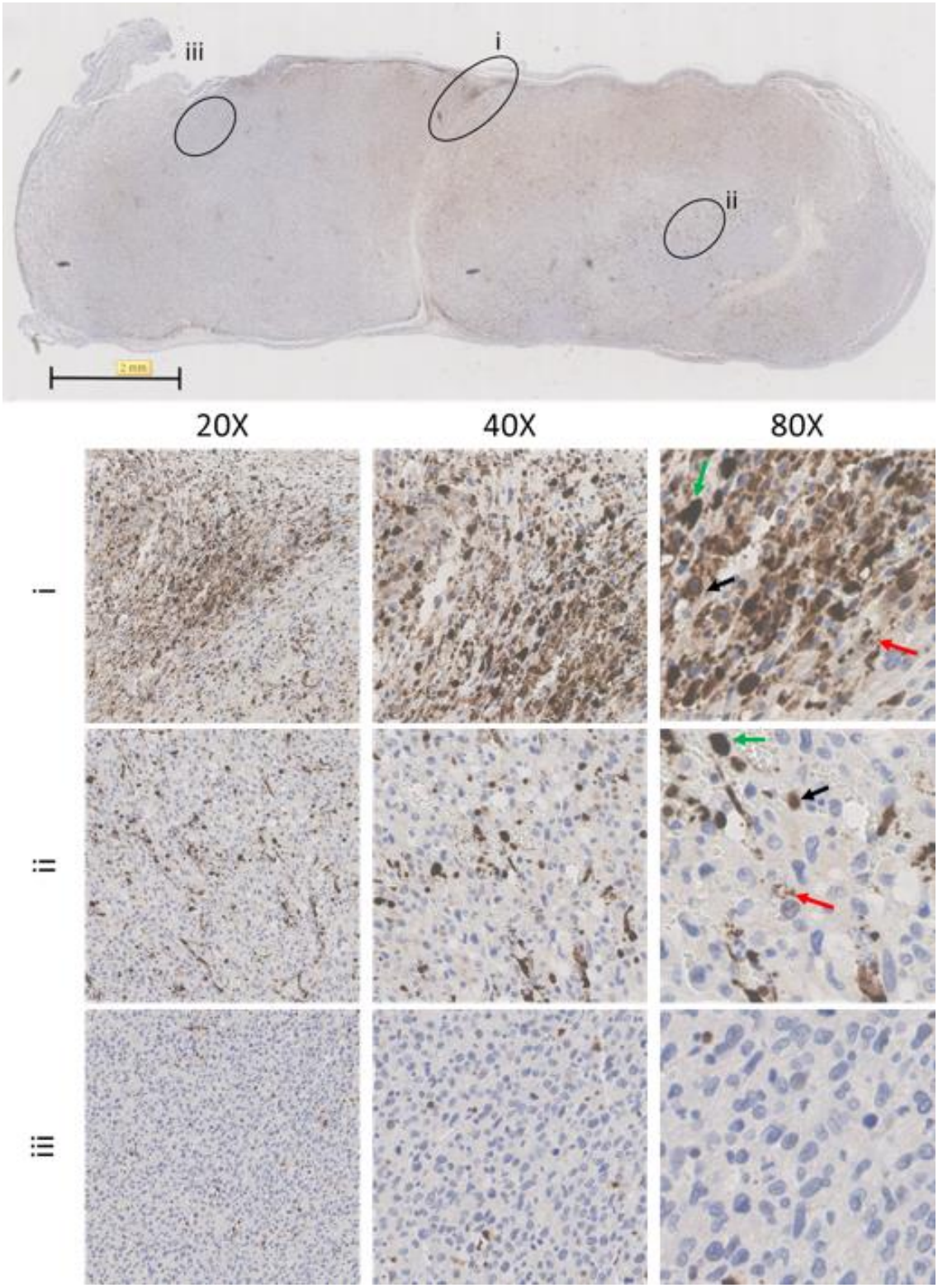

Figure 65. Evaluation of apoptosis 24 hr after $TPCS_{2a}$-PDT interstitial light treatment to subcutaneous prostate tumours.

2.5 mg/kg $TPCS_{2a}$ was injected i.v. via tail vein to Copenhagen rats bearing subcutaneously grown prostate tumours. 24 hr after administration, light treatments were carried out at a fluence rate of 20 J and 0.1 W power and animals were euthanised 24 hr after light treatment. Once sampled, tumours were stained with anti-cleaved caspase-3 (D175) and examined on a Hamamatsu Nanozoomer Digital Pathology (NDP) scanner. (i), (ii) and (iii) are different ROIs within the tumour sample; shown at 20X, 40X and 80X magnification. Same tumour sample as shown in Figure 64i. Different stages of the apoptotic process are indicated with black (earlier stages), green (later stages) and red (final stages) arrows. Scale bars shown as 2 mm.

During early stages of apoptosis thecleavage of pro-caspase-3 results in an active form of the enzyme in the cell cytosol, that then participates in the apoptotic pathway. In the tumour sample under investigation, this is indicated with black arrows in Figure 65, where a brown stain is consistent throughout the cell cytosol. As apoptosis occurs, nuclear chromatin is condensed in the nuclear fraction, specifically at the nuclear membrane, and the cytoplasm shrinks, hence the nucleus appears to occupy the totality of the cell structure. This is a significant observation during apoptotic cell death. In Figure 65, this stage is indicated with green arrows, pointing at dark brown-stained cells. Finally, the fragmentation of cells in late stages of apoptosis and appearance of apoptotic bodies is highlighted with red arrows. The three different ROIs indicated in Figure 65 show: largely affected areas based on the number of apoptotic cells (Figure 65i), areas affected to a lower extent (Figure 65ii), or negligible apoptosis (Figure 65iii). Staining of the tumour periphery was particularly noteworthy.

Interestingly, control untreated tumours (Figure 66) and tumours exposed to light alone in the absence of photosensitiser (Figure 68, Figure 71), also exhibited a large affected area, alike $TPCS_{2a}$ and 20 J-treated tumours (Figure 64). Nevertheless, distribution of these areas was different in control tumours and those treated shown above: $TPCS_{2a}$ and 20J light resulted in a more homogeneous and uniformly affected area while controls exhibited disorganised affected regions throughout the tumour tissue.

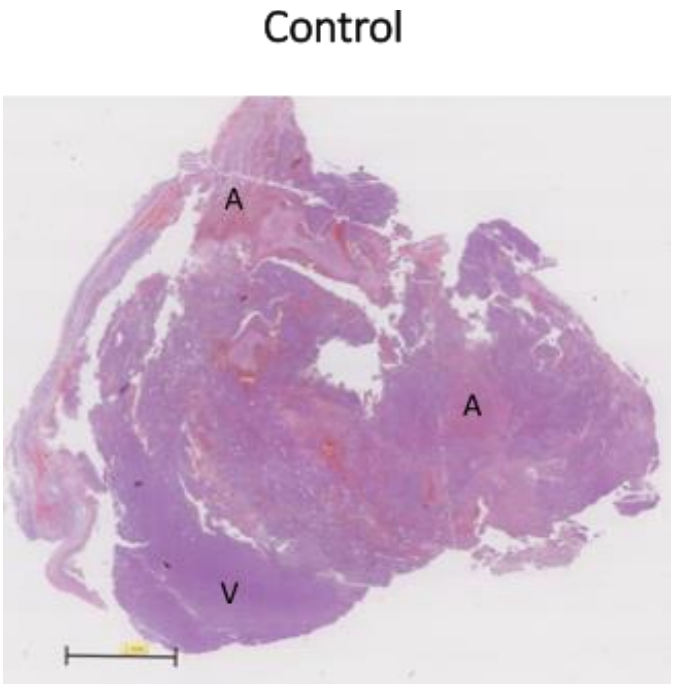

Figure 66. Control subcutaneous prostate tumour in Copenhagen rats.

6-7 days after implantation of tumour cells subcutaneously, a standard H&E staining was performed in untreated tumours and these were then examined on a Hamamatsu Nanozoomer Digital Pathology (NDP) scanner, 1.25X magnification. A: affected tumour area; V: viable tumour area; scale bars shown as 2 mm.

The observation of magnified H&E tumour images revealed clear differences in morphological features of cells in viable and affected ROIs. With the assistance of a pathologist's expertise, we became acquainted with different morphological features of infiltrating leucocytes and were able to identify these in the tumour samples H&E-stained in the present chapter. For instance, polymorphonuclear leucocytes (i.e. neutrophils) are small cells, with granular cytoplasm and highly lobed nuclei. These cells can be mistaken by apoptotic cells, which display large intracellular spaces (suggesting inexistent connexions between cells), enlarged nuclear compartment, more condensed chromatin and shrunk cytoplasm. For these reason, tumour samples were stained with anti-cleaved caspase-3, apoptotic marker.

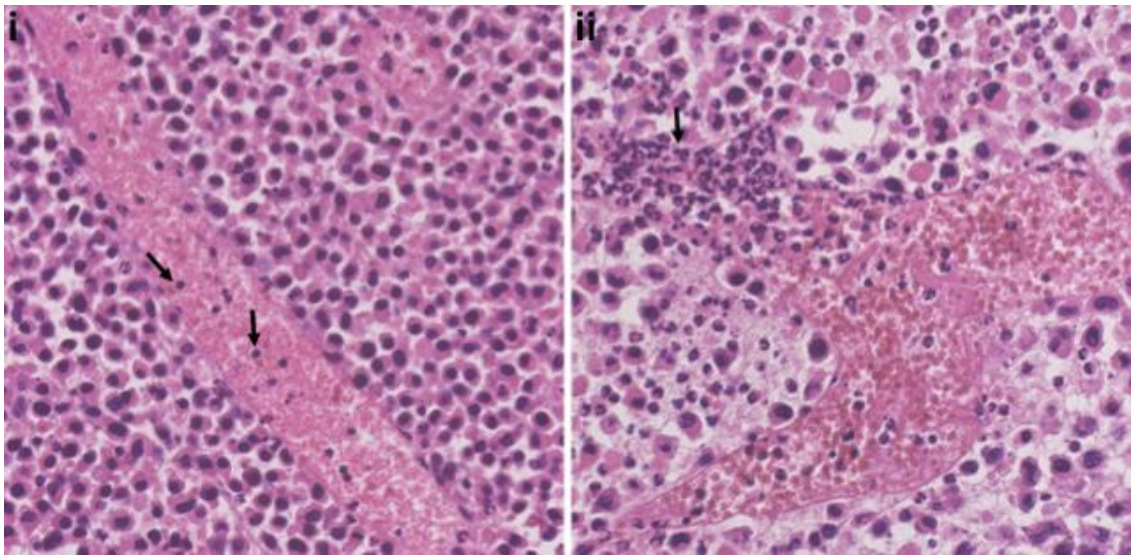

Figure 67. Extravasation of leucocytes and tumour infiltration.

Highlighted with black arrows: (i) circulating leucocytes shown inside a blood vessel in the tumour mass; (ii) leucocytes being release from circulating vessels due to possible endothelial cell damage resulting in leaky vasculature. Shown at 20X magnification.

Some of these infiltrating cells also exhibited disparities in their affinity for haematoxylin and eosin: a more eosinophilic cytoplasm is observed in cells within the affected area in the tumour sample, based on the pink shade acquired by these, as opposed to the purple-blue shade observed in the cytosol of cells within the viable tumour area. Along these lines, leucocytes being released from blood vessels and then infiltrating tumour tissue are shown in Figure 67. We also determined the presence of infiltrating leucocytes, indicated as IC and with red or green arrows in Figure 68i.

As opposed to the tumour sample displayed in Figure 65, apoptotic cells were found in interstitial light-control tumours to a significantly lesser extent, as indicated with black arrows in Figure 68ii. This was also applicable to images shown below (Figure 70,

Figure 73), observing no clear differences between treatment groups. In addition to apoptotic cells in Figure 68, observation of cells which appear to be losing their natural structure ("disintegrating"), suggest the presence of necrotic regions (circled in black in Figure 68i).

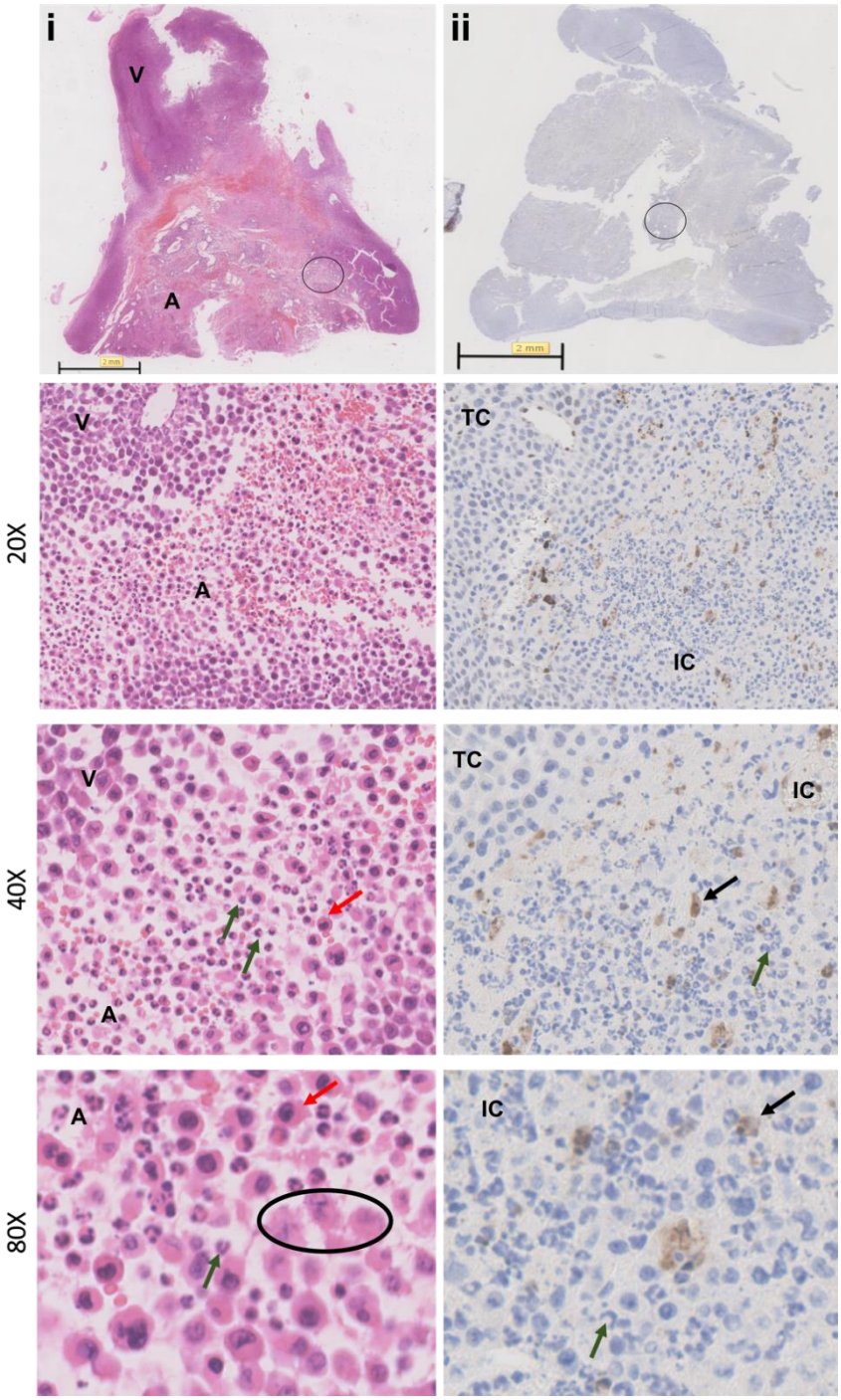

Figure 68. Interstitial light only-control tumour.

6-7 days after tumour cell implantation, tumours were exposed to light at a fluence rate of 20 J and 0.1 W power. Once sampled, tumours were stained and examined on a Hamamatsu Nanozoomer Digital Pathology (NDP) scanner. (i) H&E staining, (ii) cleaved caspase-3 (D175) staining. 20X, 40X and 80X magnification shown. A: affected tumour area; V: viable tumour area. TC: tumour cells; IC: infiltrating cells. Black arrows indicate apoptotic cells; red and green arrows indicate different infiltrating leucocytes; necrotic cells highlighted within a black circle. Scale bars shown as 2 mm.

Despite causing significant damage to tumours, the combination of 2.5 mg/kg of photosensitiser and 20 J light, would have been excessive for PCI approaches, in which therapeutic outcome does not only rely on the photooxidative component. Therefore, aiming to compare PDT and PCI in later experiments, light dose was reduced to 10 J (Figure 69i).

Nonetheless, a 10 J light fluence rate did not result in a sufficient photooxidative effect in tumours as observed after H&E staining (Figure 69i) and light dose was increased again to 20 J. Yet, to avoid an excessive photooxidation as shown earlier in Figure 64, the concentration of photosensitiser was reduced and two different doses of $TPCS_{2a}$ were assayed (see Figure 69ii and Figure 69iii).

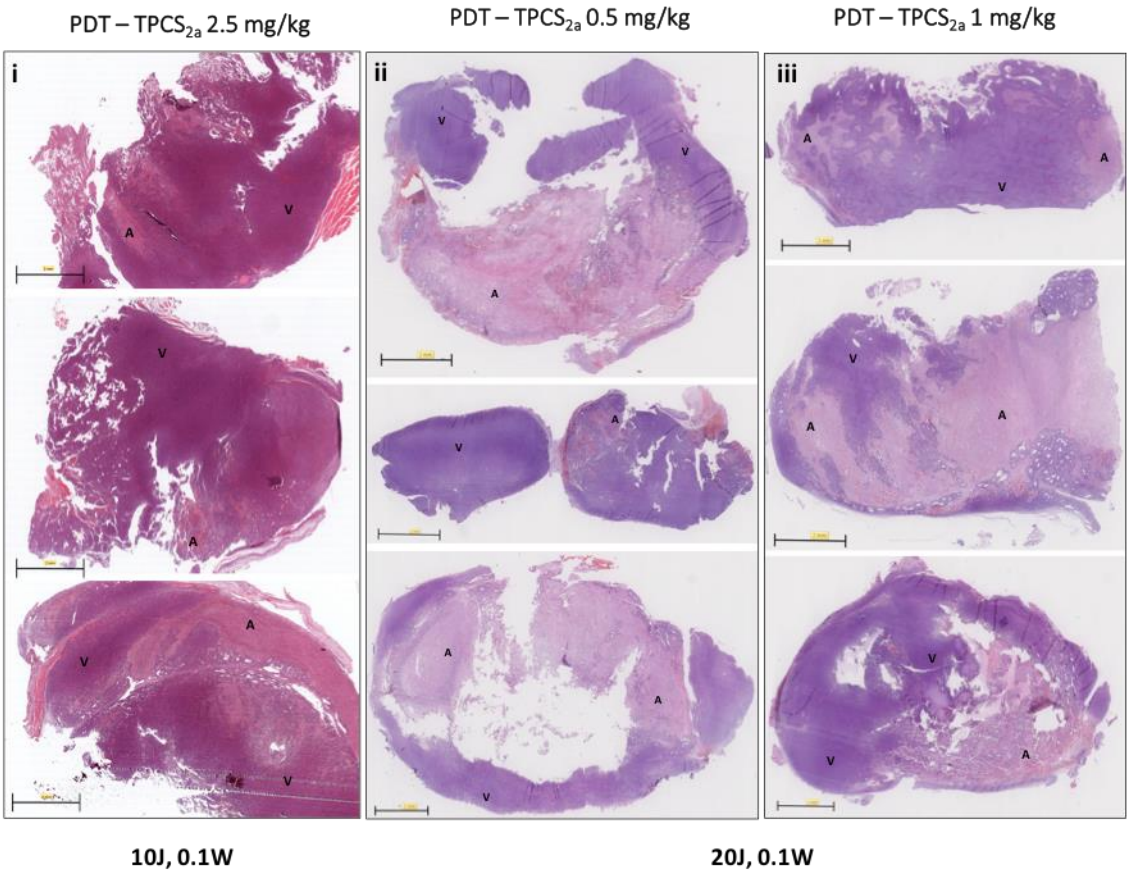

Figure 69. $TPCS_{2a}$-PDT interstitial light treatment to subcutaneous prostate tumours.

Different concentrations of $TPCS_{2a}$ [(i) 2.5 mg/kg; (ii) 0.5 mg/kg; (iii) 1 mg/kg)] was injected i.v. via tail vein to Copenhagen rats bearing subcutaneously grown prostate tumours. 24 hr after administration, light treatments were carried out at a fluence rate of 10 J or 20 J and 0.1 W power. Once sampled, tumours were H&E stained and examined on a Hamamatsu Nanozoomer Digital Pathology (NDP) scanner, at 1.25X magnification. A: affected tumour area; V: viable tumour area; scale bars shown as 2 mm.

Regardless of the $TPCS_{2a}$ concentration used, 20 J resulted in a greater phototoxicity compared to 10 J, Figure 69ii and Figure 69iii as opposed to Figure 69i. Despite

observing large affected areas in these tumour samples, growth rate was unaffected, rapidly reaching the endpoint and having to euthanise these animals only 5-7 days after light treatment as displayed in Figure 75. There was great disparity in the overall affected surface area between tumours within the same treatment group: the affected area on sections was not reproducible and presented significant variability (labelled as "A" in the figures). Consequently, no quantitative evaluation was performed on these damaged regions.

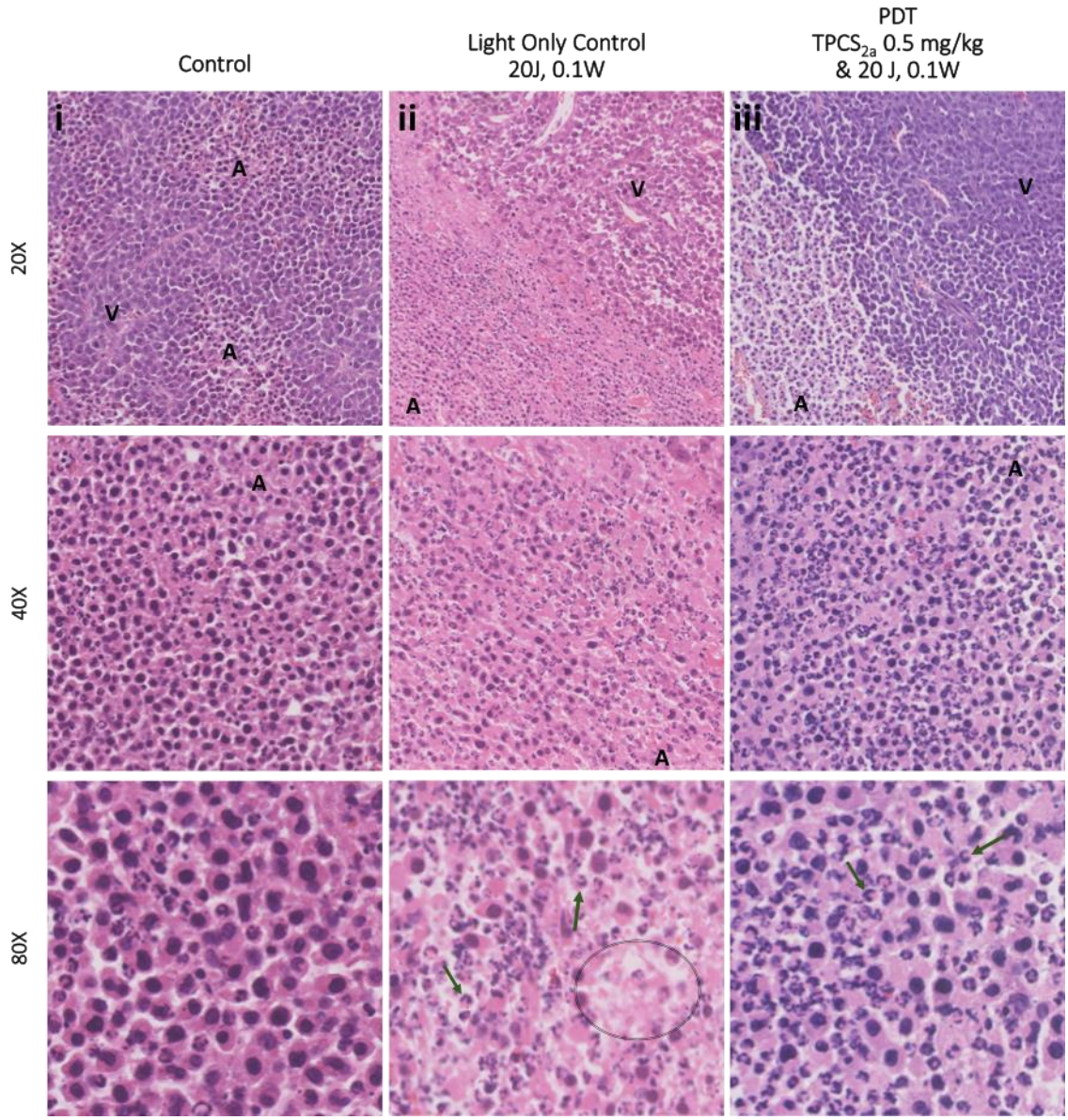

Figure 70. Detail of H&E staining of control and subcutaneous prostate tumours treated with $TPCS_{2a}$-PDT interstitial illumination.

Once sampled, tumours were H&E stained and examined on a Hamamatsu Nanozoomer Digital Pathology (NDP) scanner. 20X, 40X and 80X magnification shown. A: affected tumour area; V: viable tumour area. Green arrows indicate infiltrating leucocytes; necrotic cells highlighted within a black circle.

The investigation of these samples to a greater detail (Figure 70), also revealed morphological features of infiltrating leukocytes as described above. These are indicated with green arrows in the figure. In addition, some necrotic cells were also identified.

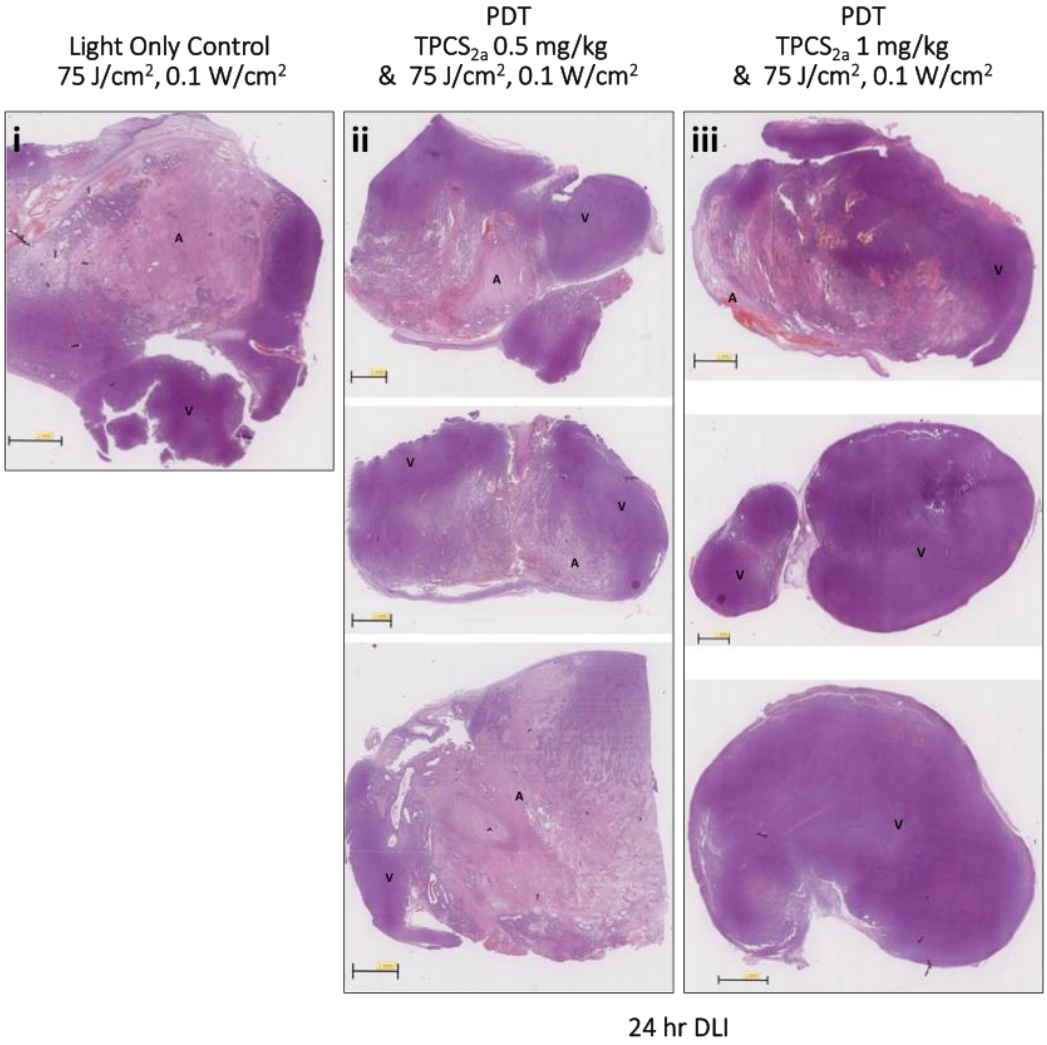

Figure 71. $TPCS_{2a}$-PDT surface-light treatment to subcutaneous prostate tumours (24 hr DLI).

(i) Surface light control. Different concentrations of $TPCS_{2a}$ [(ii) 0.5 mg/kg; (iii) 1 mg/kg] were injected i.v. via tail vein to Copenhagen rats bearing subcutaneously grown prostate tumours. 24 hr after administration, light treatments were carried out at a fluence rate of 75 J/cm² and 0.1 W power. Once sampled, tumours were H&E stained and examined on a Hamamatsu Nanozoomer Digital Pathology (NDP) scanner, at 1.25X magnification. A: affected tumour area; V: viable tumour area. Scale bars shown as 2 mm.

During interstitial treatments, we encountered an added challenge: difficulty in piercing the tumour capsule effectively due to the size of tumours before illumination, thereby the delivery of light throughout the entire structure of the tumour could be compromised. As a consequence, we then moved on to carry out surface instead of

interstitial light delivery so as to compare the outcome and assess whether this could result in an enhancement of light treatment.

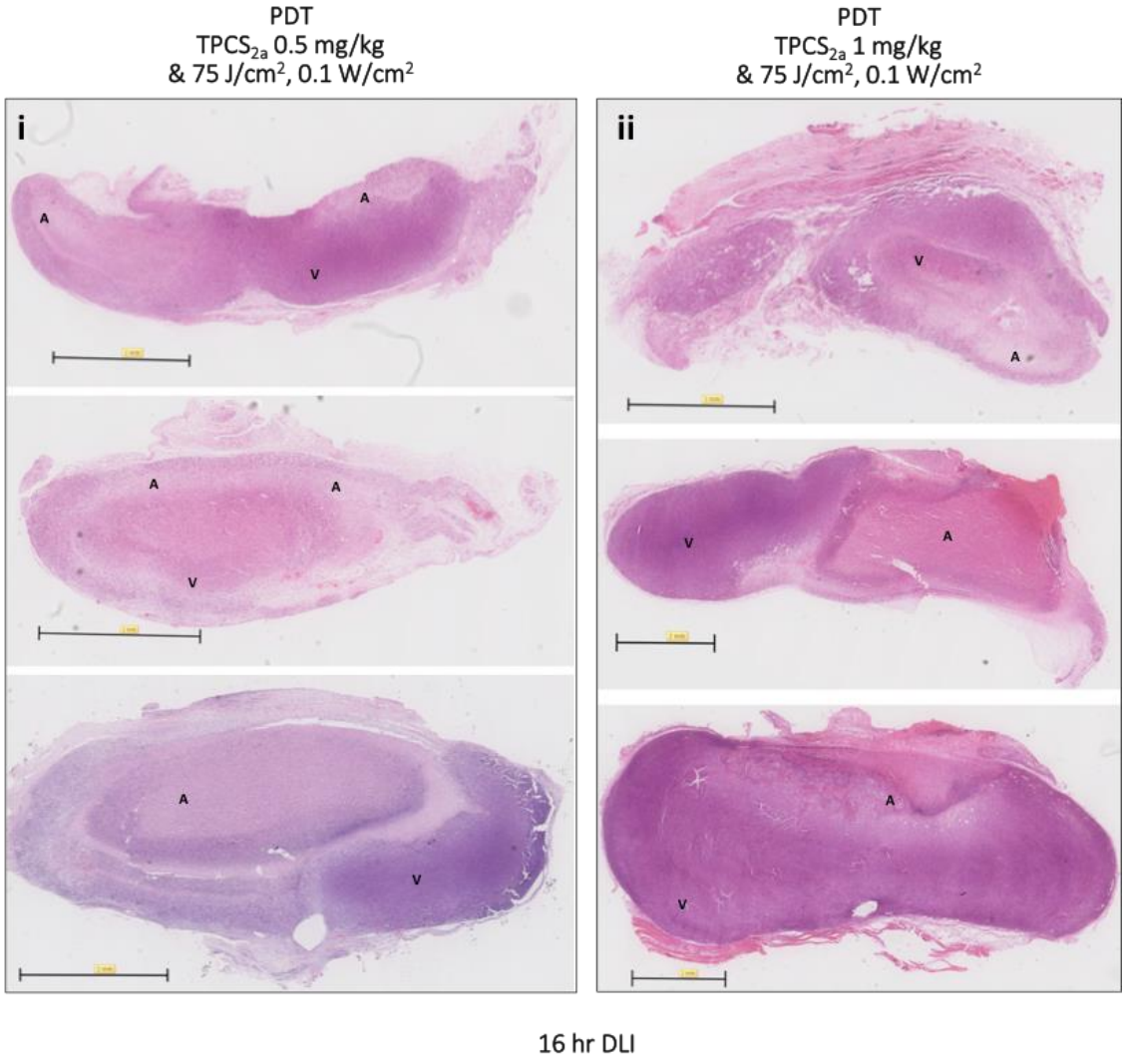

Figure 72. $TPCS_{2a}$-PDT surface-light treatment to subcutaneous prostate tumours (16 hr DLI).

Different concentrations of $TPCS_{2a}$ [(i) 0.5 mg/kg; (ii) 1 mg/kg - 3 different tumour samples for each group] were injected i.v. via tail vein to Copenhagen rats bearing subcutaneously grown prostate tumours. 16 hr after administration, light treatments were carried out at a fluence rate of 75 J/cm^2 and 0.1 W power. Once sampled, tumours were H&E stained and examined on a Hamamatsu Nanozoomer Digital Pathology (NDP) scanner, at 1.25X magnification. A: affected tumour area, V: viable tumour area; scale bars shown as 2 mm.

Similar findings to those stated after interstitial light delivery were observed in these surface-light groups of treatments (Figure 71). Briefly, no consistency was found within the same light/PS group. For example, no damaged areas were observed in some of the tumours treated with 1 mg/kg PS and light as opposed to large regions in a different sample belonging to the same group. In addition, the affected area of tumours treated with the highest photosensitiser dose (Figure 71iii) was smaller compared to the lowest PS dose (Figure 71ii). Moreover, similarly to the interstitial light control group (Figure

68), surface-light alone also resulted in largely affected tumours as shown in Figure 71i.

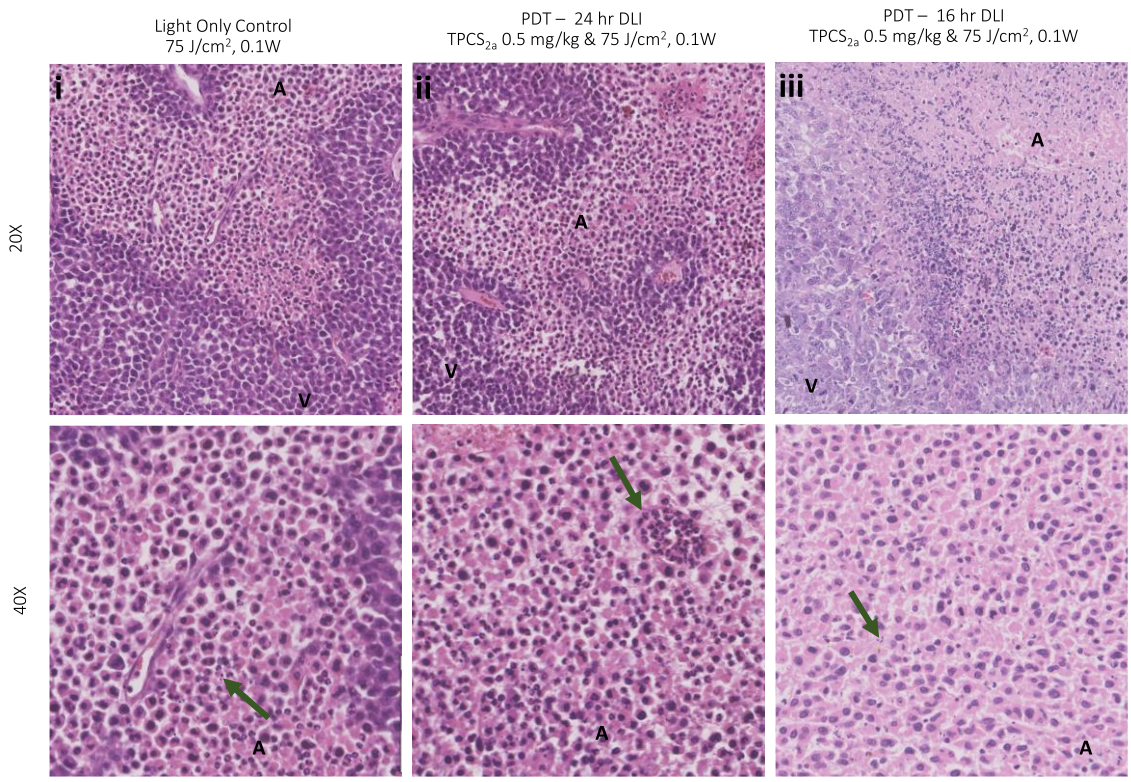

Figure 73. Detail of H&E staining of $TPCS_{2a}$-PDT surface illumination to subcutaneous prostate tumours.

Once sampled, tumours were H&E stained and examined on a Hamamatsu Nanozoomer Digital Pathology (NDP) scanner. (i) Surface light control. (ii, iii) 0.5 mg/kg $TPCS_{2a}$ was injected i.v. via tail vein to Copenhagen rats bearing subcutaneously grown prostate tumours. 16 hr (ii) or 24 hr (iii) after administration light treatments were carried out at a fluence rate of 75 J/cm² and 0.1 W power. Green arrows indicate infiltrating leucocytes. A: affected tumour area; V: viable tumour area.

Finally, we decided to carry out a last study shortening the drug light interval from 24 hr to 16 hr so as to take advantage of the increased amount of photosensitiser present in the tumour region during light treatment, as observed in 4.4.2.1 Quantitative biodistribution of $TPCS_{2a}$ (Amphinex) in Copenhagen rats – Chemical extraction. This group of light treatments, shown in Figure 72, resulted in a more uniformly affected area in the tumours, and samples also displayed greater similarity between them. In addition, growth rate of these was delayed by an average of 2 days (Figure 75).

As in the interstitial light delivery groups, similar observations resulted from the magnification of H&E surface light tumour samples (Figure 73).

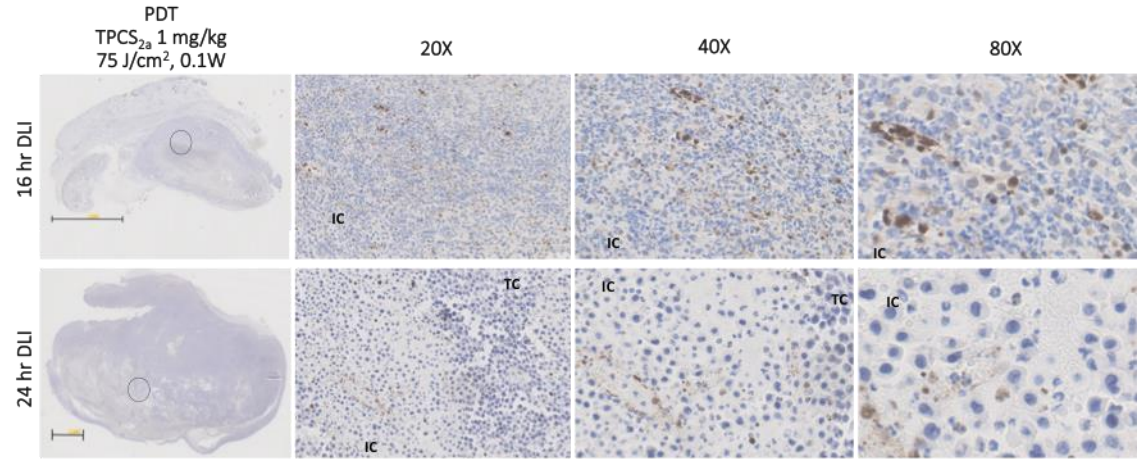

Figure 74. Evaluation of apoptosis 16 hr and 24 hr after $TPCS_{2a}$-PDT surface light treatment to subcutaneous prostate tumours.

1 mg/kg $TPCS_{2a}$ was injected i.v. via tail vein to Copenhagen rats bearing subcutaneously grown prostate tumours. 16 hr and 24 hr after administration, light treatments were carried out at a fluence rate of 75 J/cm^2 and 0.1 W power. Once sampled, tumours were stained with anti cleaved caspase-3 (D175) and examined on a Hamamatsu Nanozoomer Digital Pathology (NDP) scanner. 20X, 40X and 80X magnifications are shown. Same tumour samples as shown in Figure 71iii and Figure 72ii. TC: tumour cells; IC: infiltrating cells. Scale bars shown as 2 mm.

Surface-light tumour samples were also stained with anti cleaved caspase-3 (Figure 74). These were not as heavily stained as the interstitial light treated tumour sample removed 24 hours after illumination (Figure 65). Stained cells were found dispersed throughout the tumour tissue, being more relevant in the 16 hr DLI group. Morphological variations of cells within affected tumour areas reported in the H&E stained samples shown in Figure 71 and Figure 72, were also detected in the same ROIs in cleaved caspase-3 stained samples (Figure 74). Yet, cleaved caspase-3 staining was not particularly noteworthy in these cells with morphological features different to healthy tumour. Again, this took us to consider the presence of different cell types within tumour cells in Figure 74 - IC (infiltrating cells).

An evaluation of the delay of tumour growth after $TPCS_{2a}$-PDT is shown in Figure 75. No significant differences were found overall. Both light- and PS- alone controls showed no delay in tumour growth rate, these continued growing at the same pace and consequently animal subjects had to be euthanised 5-7 days after injection of photosenstiser in the PS-alone control or after light delivery in the light-alone controls (both interstitial and surface illumination). Similarly to these controls, PDT treatments 10 J / 2.5 mg/kg and 20 J / 0.5 mg/kg (both $TPCS_{2a}$ and interstitial light) did not affect tumour growth. When the photosensitiser dose was increased to 1 mg/kg a weak improvement was observed, being tumours removed 7 days after light. Similar observations resulted from all surface light treatments at a 24 hr DLI. However,

although still not significantly different to the above, growth of tumours treated through surface illumination after a 16 hr-DLI seemed to be slightly delayed and most subjects were euthanised 10 days after light (Figure 75).

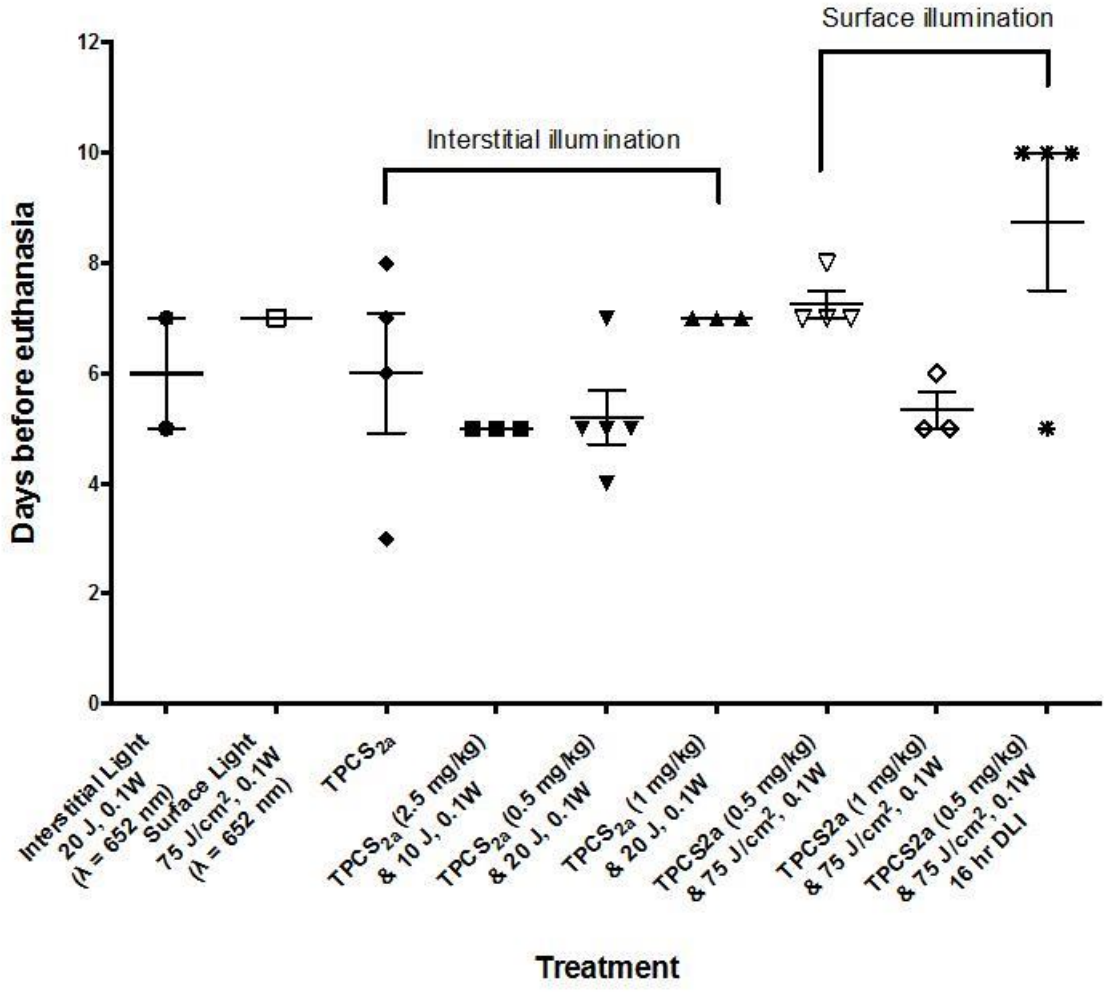

Figure 75. Tumour growth after $TPCS_{2a}$-based treatment until end point.

Scatterplot of days between light delivery to tumours and euthanasia of animal subjects based on tumour size/burden endpoint. Each symbol represents an independent animal subject. Data shown as mean ± SEM.

4.4.3 BPD-MA and $AlPcS_{2a}$ PDT in rat subcutaneous prostate carcinoma

As will be later reported in Chapter 5, BPD-MA and $AlPcS_{2a}$ were the photosensitisers used to evaluate the generation of an immune response after light-based therapies. Therefore, a preliminary assessment on the tumour eradication capacity of both was carried out.

4.4.3.1 Biodistribution of BPD-MA

BPD-MA is a widely used photosensitiser in PDT approaches, as reviewed in 4.1 Introduction. Due to its main vascular effect, shorter DLI are generally used.

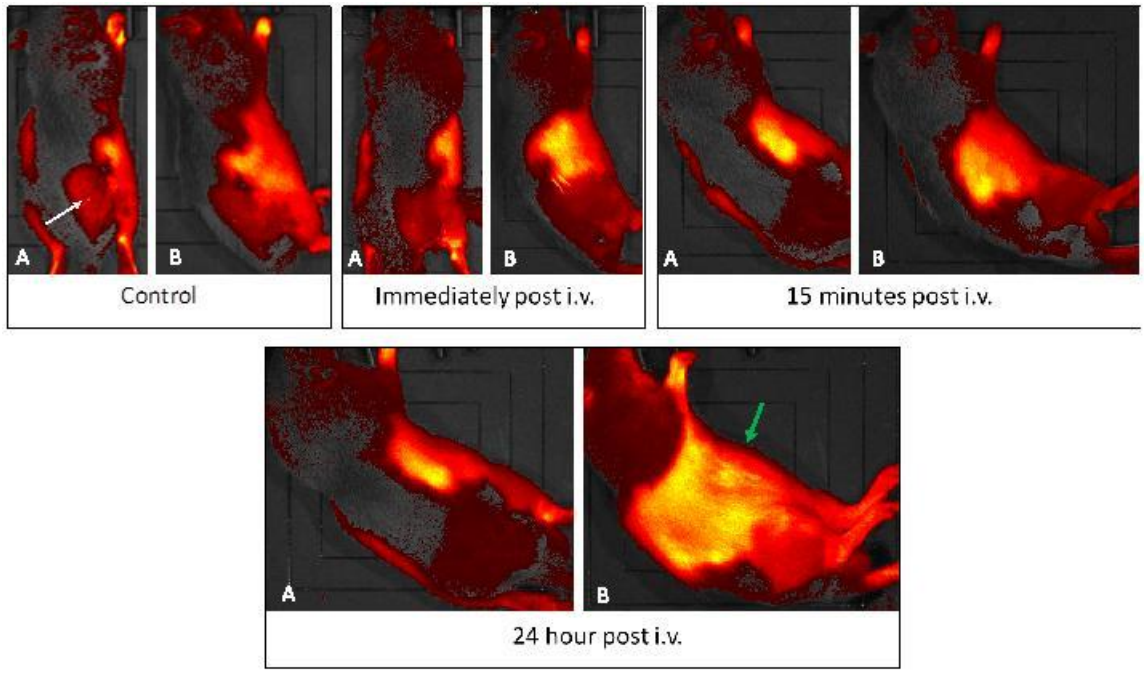

Figure 76. BPD-MA biodistribution in Copenhagen rats.

1 mg/kg BPD-MA was administered i.v. via tail vein. Fluorescence images were taken immediately after injection and 15 min, 24 hr post administration. (A) – Dorsal, (B) – Lateral view. White arrow indicates s.c. growing tumour, green arrows indicate the abdominal region where liver is located.

Before performing light treatments on tumour-bearing rats, we evaluated the distribution of this photosensitiser at different time points including 15 minutes, which was the drug light interval chosen for PDT procedures in our study. This was carried out by performing live imaging to anesthetised animal subjects using an *in vivo* imaging system (IVIS). Due to the limited sensitivity of the system through the skin and the intrinsic autofluorescence of tissues, this enabled only a qualitative evaluation, allowing the determination of particularly outstanding events, as displayed in Figure 76.

As with most exogenous substances entering an organism, the greatest accumulation of BPD-MA was found in liver from the earliest imaging time point, immediately after administration. This liver uptake increased over time as observed 24 hr after injection (indicated with green arrow). No significant fluorescence was detected around the tumour area, specified with a white arrow in Figure 76.

4.4.3.2 Biodistribution of $AlPcS_{2a}$

Alike above described for BPD-MA, distribution studies were also performed with $AlPcS_{2a}$ using the same imaging system, shown in Figure 77. Due to differences in photophysical properties between BPD-MA and $AlPcS_{2a}$, *in vivo* biodistribution was not compared between compounds in a quantitative manner.

As opposed to BPD-MA, $AlPcS_{2a}$'s amphiphilic properties make this photosensitiser suitable not just for PDT but more importantly for PCI. Therefore, longer DLI were considered before exposure to light and imaging was performed at later time points, i.e. 6 hr is the earliest imaging time point as opposed to the 15 minutes imaging conducted with BPD-MA. Regarding this phtalocyanine compound, accumulation in the abdominal region increased as soon as it was administered, suggesting presence in the liver. This further increased 6 hr later, and even more at the 24 hr time point (Figure 77). Importantly, an increase in fluorescence in the tumour-bearing region was found 24 hr after administration (indicated with a white arrow in Figure 77).

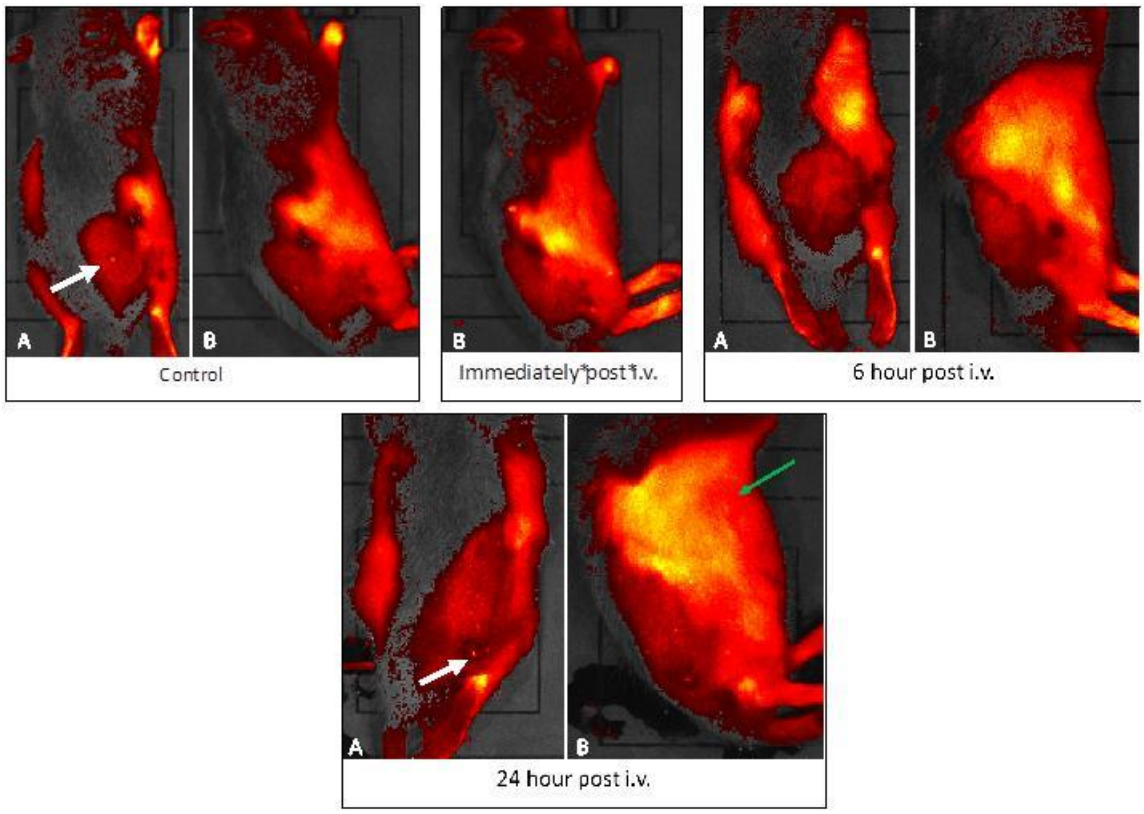

Figure 77. $AlPcS_{2a}$ biodistribution in Copenhagen rats.

2 mg/kg $AlPcS_{2a}$ was administered i.v. via tail vein. Fluorescence images were taken immediately after injection and 6 hr, 24 hr post administration. (A) – Dorsal, (B) – Lateral view. White arrow indicates s.c. growing tumour, green arrows indicate the abdominal region where liver is located.

4.4.3.3 BPD-MA-based light treatment (PDT)

As stated for $TPCS_{2a}$, 7 days after s.c. implantation of $4x10^5$ cells, BPD-MA was administered i.v. and tumours were surface-illuminated when they had reached a 0.5-0.7 cm diameter. Subcutaneously grown tumours were completely eradicated in 18% (4/22) of the animal subjects treated with BPD-MA following PDT procedures. An example of the evolution of these tumours after light treatment is displayed in Figure 78. Light treatment induced the formation of black eschars in the skin directly above tumours, sign of necrosis after PDT. It then became a scab with progressively reduced size and finally the wound was completely healed (i.e. 35 days after light).

Figure 78. Tumour evolution after treatment with BPD-MA following PDT procedures until complete eradication.

1 mg/kg BPD-MA was administered via tail vein to Copenhagen rats bearing subcutaneously grown prostate tumours. Light treatment was performed after a 15-minute drug light interval at a fluence rate of 120 J/cm^2 and 0.06-0.1 W power. Images shown 72 hr, 7 days, 11 days, 15 days, 22 days and 35 days after surface illumination of tumours.

Moreover, tumour growth in non-cured animals was delayed compared to the previously observed $TPCS_{2a}$-based PDT (Figure 75). Specifically, the endpoint was delayed from 7-10 days, as seen in $TPCS_{2a}$ groups, up to 13 days after light treatment on average (Figure 85).

As for the histological analysis of these tumour samples (Figure 79), observations were similar to those above described for $TPCS_{2a}$ PDT-treated (Figure 68 - Figure 73). Affected regions in tumour samples were large and more homogeneously distributed than above described, although there were still differences in the magnitude of these areas between samples within the same treatment group (Figure 79). Again, based on their morphological features, a mixture of different cell types was likewise found in these tumours, highlighted with red and green arrows in Figure 79.

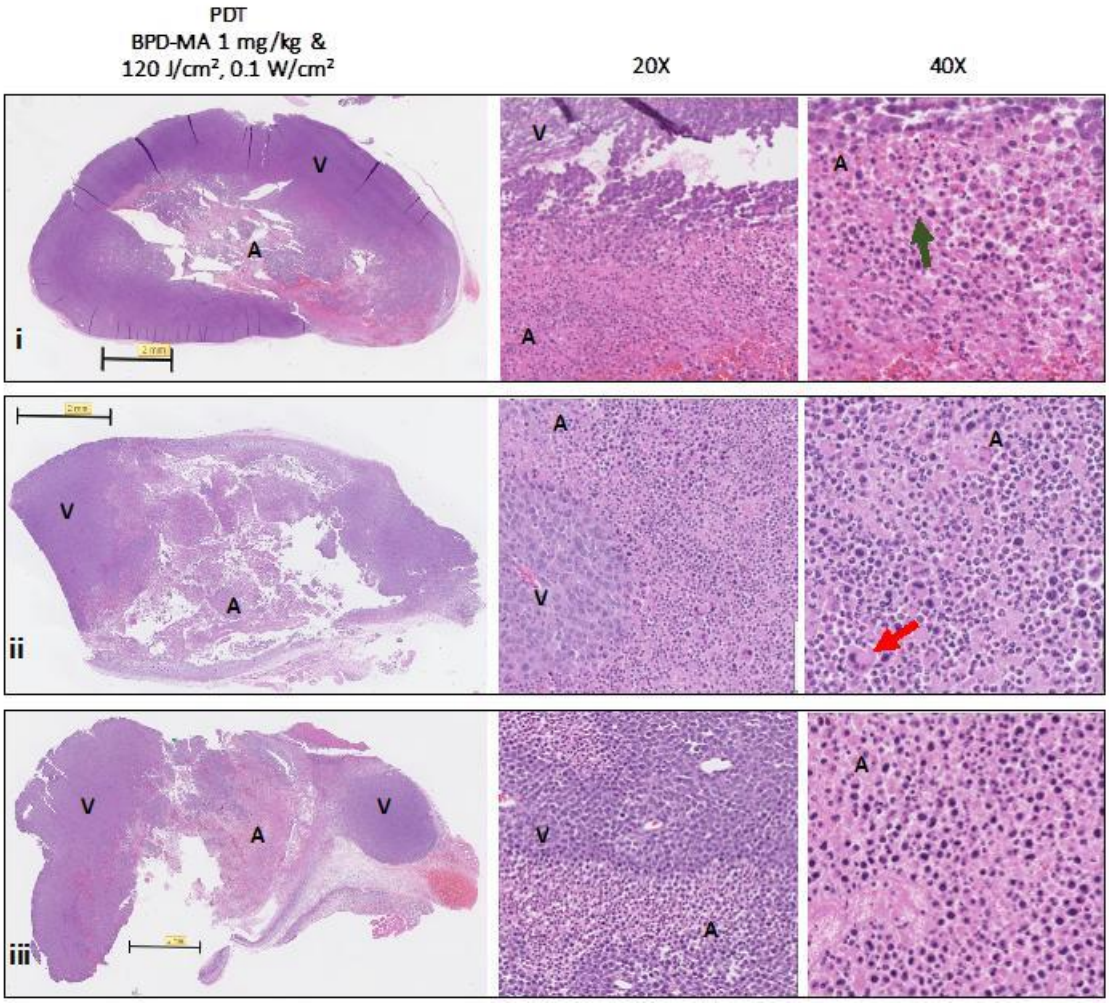

Figure 79. BPD-MA-PDT surface-light treatment to subcutaneous prostate tumours (15 min DLI) and detail of H&E staining.

1 mg/kg BPD-MA was injected i.v. via tail vein to Copenhagen rats bearing subcutaneously grown prostate tumours (i, ii, iii). 15 min after administration, light treatments were carried out at a fluence rate of 120 J/cm² and 0.06-0.1 W power. Once sampled, tumours were H&E stained and examined on a Hamamatsu Nanozoomer Digital Pathology (NDP) scanner. 20X and 40X magnifications are shown. A: affected tumour area, V: viable tumour area. Green and red arrows indicate different cell types among tumour cells. Scale bars shown as 2 mm.

The analysis of cleaved caspase-3 in these samples, revealed disperse apoptotic cells as occuring in the above-reported cases (Figure 74). In addition, affected areas shown in H&E also corresponded in this treatment group with lightly caspase-3-stained

regions. As described in Figure 74 for $TPCS_{2a}$-PDT, phenotipical features different to healthy tumour cells, were noteworthy. These regions were considered and indicated in magnified images in Figure 80 as infiltrating cells (IC).

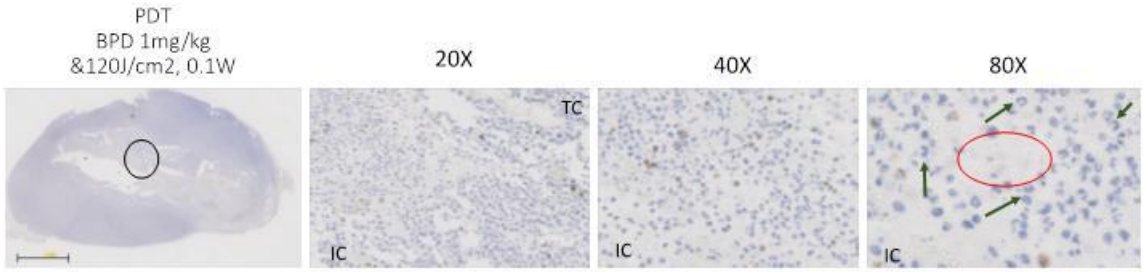

Figure 80. Evaluation of apoptosis after BPD-MA -PDT surface light treatment to subcutaneous prostate tumours.

1 mg/kg BPD-MA was injected i.v. via tail vein to Copenhagen rats bearing subcutaneously grown prostate tumours. 15 min after administration, light treatments were carried out at a fluence rate of 120 J/cm^2 and 0.06-0.1 W power. Once sampled, tumours were stained with anti cleaved caspase-3 (D175) and examined on a Hamamatsu Nanozoomer Digital Pathology (NDP) scanner. Same tumour sample as shown in Figure 79i. 20X, 40X and 80X magnifications are shown. TC: tumour cells; IC: infiltrating cells. Green arrows indicate infiltrating leucocytes, disintegrating necrotic tumour cells are circled in red. Scale bars shown as 2 mm.

4.4.3.4 $AlPcS_{2a}$-based light treatment (PDT & PCI)

Prior to combining $AlPcS_{2a}$ with saporin in PCI approaches, we evaluated the phototoxicity resulting from PDT.

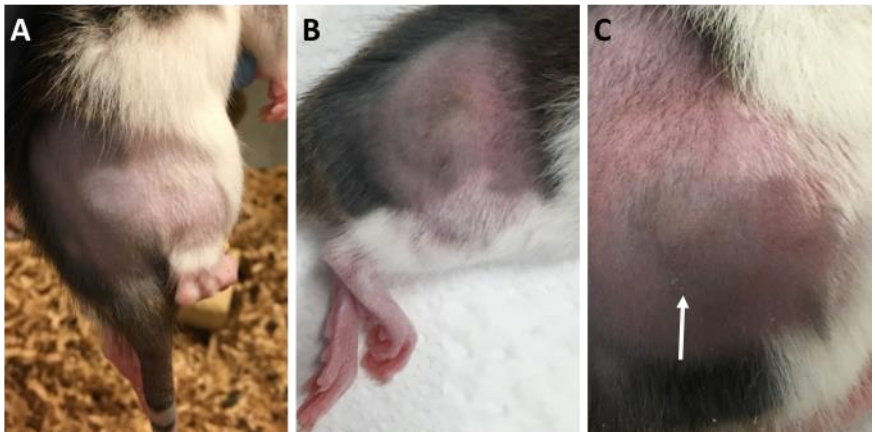

Figure 81. Damage to animal subjects' hind leg after surface light treatment with AlPcS2a-PDT (6 hr DLI).

2 mg/kg $AlPcS_{2a}$ was injected i.v. via tail vein to Copenhagen rats bearing subcutaneously grown prostate tumours. 6 hr after administration, light treatments were carried out at a fluence rate of 100 J/cm^2 and 0.06-0.1 W power. (A) Immediately after light and (B) 24 hr after light animals retracted and dragged the illuminated hind leg; (B), (C) 24 hr after light, the illuminated area of the skin appeared bruised (indicated with white arrow).

A 6 hr-DLI was used in the first PDT experiments of the study. However, this resulted in severe damage to the animal's legs (see Figure 81): the area above the tumour bruised and stiffened, animals then walked dragging their illuminated hind leg as soon as they woke up from anaesthesia. Despite some mobility being restored, they never recovered the full condition exhibited prior to light delivery. Furthermore, pain and distress symptoms were recognised in these subjects and only these received additional analgesics beyond the dose given before light treatment.

Therefore, so as to enable clearance of PS and reduce phototoxicity, DLI was increased from 6 hr to 24 hr. Following this light treatment, large damaged areas were seen in tumours, indicated as "A" in Figure 82.

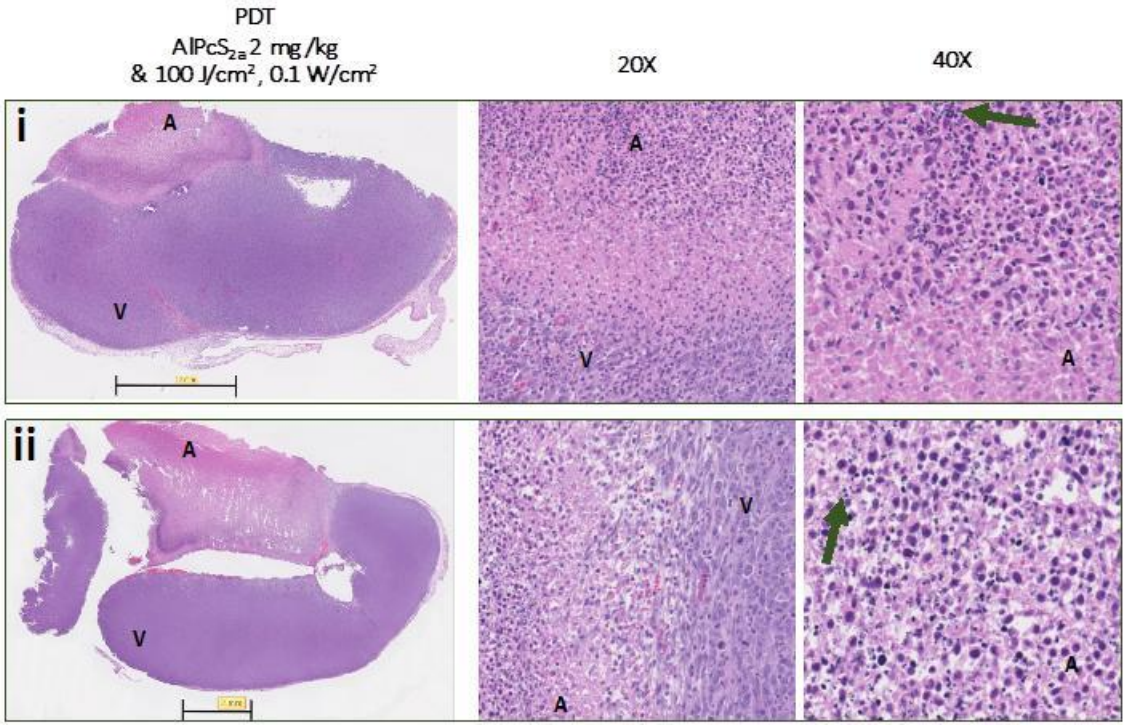

Figure 82. AlPcS$_{2a}$-PDT surface-light treatment to subcutaneous prostate tumours (24 hr DLI) and detail of H&E staining.

2 mg/kg AlPcS$_{2a}$ was injected i.v. via tail vein to Copenhagen rats bearing subcutaneously grown prostate tumours (i, ii). 24 hr after administration, light treatments were carried out at a fluence rate of 100 J/cm^2 and 0.06-0.1 W power. Once sampled, tumours were H&E stained and examined on a Hamamatsu Nanozoomer Digital Pathology (NDP) scanner. 20X and 40X magnifications are shown. A: affected tumour area, V: viable tumour area. Green arrows indicate infiltrating leucocytes, scale bars shown as 2 mm.

Similar findings resulted from staining PCI-treated samples, as shown below in Figure 83. Again, H&E revealed a similar observations to the above reported for TPCS$_{2a}$ (Figure 69-Figure 73) and BPD-MA (Figure 79) regarding cellular morphology. This is detailed with green and red arrows in Figure 82 and Figure 83.

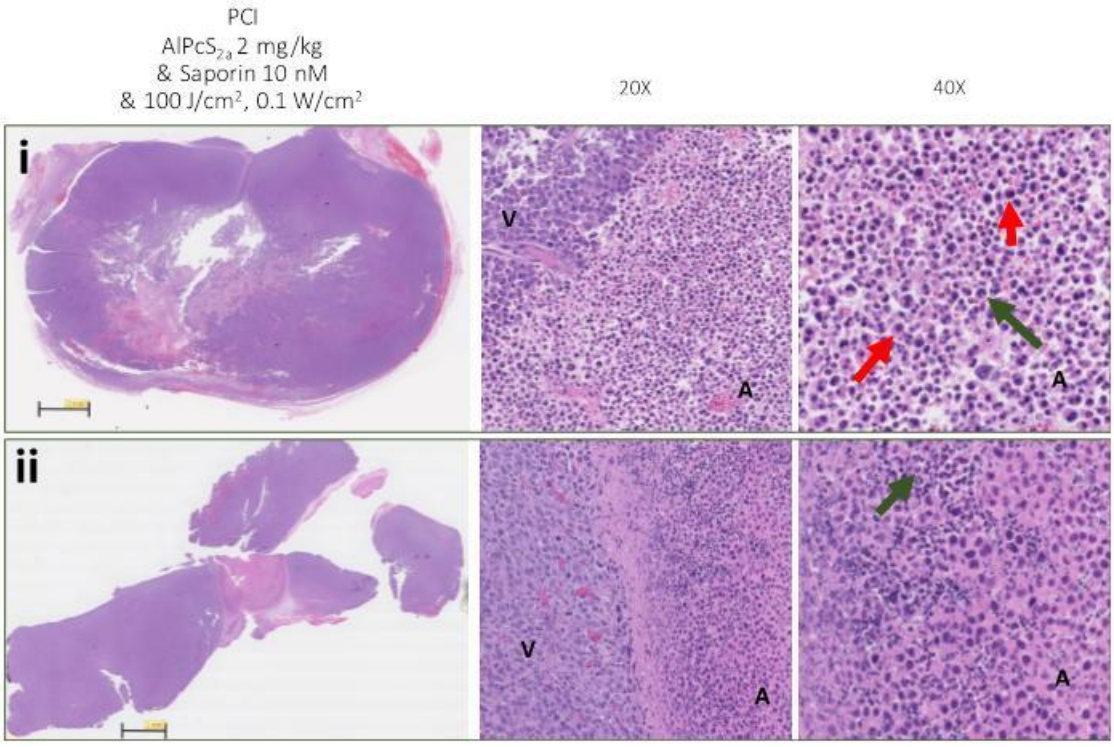

Figure 83. AlPcS$_{2a}$ & saporin-PCI surface-light treatment to subcutaneous prostate tumours (24 hr DLI) and detail of H&E staining.

2 mg/kg AlPcS$_{2a}$ was injected i.v. via tail vein to Copenhagen rats bearing subcutaneously grown prostate tumours (i, ii). 250 µg/kg saporin was injected i.v. via tail vein 1 hr prior to light delivery. 24 hr after administration of AlPcS$_{2a}$, light treatments were carried out at a fluence rate of 100 J/cm^2 and 0.06-0.1 W power. Once sampled, tumours were H&E stained and examined on a Hamamatsu Nanozoomer Digital Pathology (NDP) scanner. 20X and 40X magnifications are shown. A: affected tumour area, V: viable tumour area. Green and red arrows indicate different infiltrating cell types. Scale bars shown as 2 mm.

AlPcS$_{2a}$-based phototoxicity also led to apoptotic cell death based on the positively stained cells shown in Figure 84 in both PDT and PCI (indicated with black arrows). Again, as reported above for TPCS$_{2a}$ and BPD-MA (Figure 74 and Figure 80 respectively) those regions which appear differentially stained in H&E, indicated as “A” in Figure 82 and Figure 83, correspond to tumour areas with large infiltration of leucocytes. These cells exhibiting characteristic morphologies are pointed with red and green arrows in Figure 84.

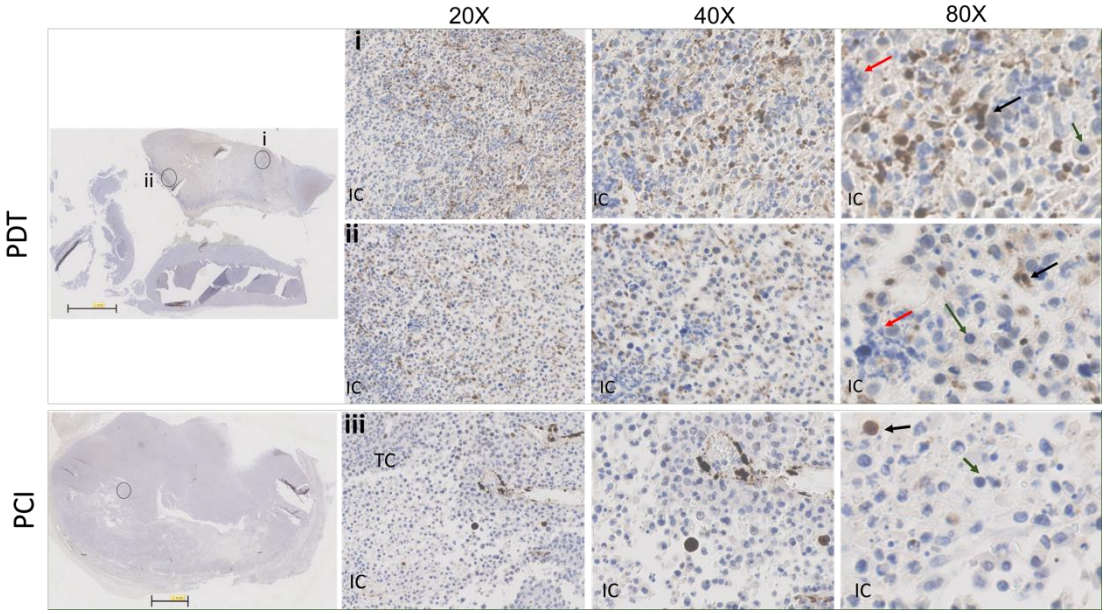

Figure 84. Evaluation of apoptosis after AlPcS$_{2a}$-PDT/PCI surface light treatment to subcutaneous prostate tumours.

(i,ii) PDT, (iii) PCI samples. 2 mg/kg AlPcS$_{2a}$ was injected i.v. via tail vein to Copenhagen rats bearing subcutaneously grown prostate tumours. 24 hr after administration, light treatments were carried out at a fluence rate of 100 J/cm^2 and 0.06-0.1 W power. In PCI groups 250 µg/kg saporin was injected i.v. via tail vein 1 hr prior to light delivery. Once sampled, tumours were stained with anti cleaved caspase-3 (D175) and examined on a Hamamatsu Nanozoomer Digital Pathology (NDP) scanner. Same tumour samples as shown in Figure 82ii and Figure 83i. 20X, 40X and 80X magnifications are shown. TC: tumour cells; IC: infiltrating cells. Green and red arrows indicate different infiltrating leucocytes; black arrows indicate apoptotic cells. Scale bars shown as 2 mm.

Combination of AlPcS$_{2a}$ with saporin did not result in different observations of that described for PDT with AlPcS$_{2a}$ or any other of the previously examined PS nor did it enhance delay in tumour growth as shown in Figure 85, which revealed the endpoint was reached at the same time for both group of treatments, around 10 days after light. No significant differences between treatment groups were detected. However, compared to TPCS$_{2a}$, there was a tendency to delay the end point by 3 days with AlPcS$_{2a}$ compared to the 24 hr-DLI observations after TPCS$_{2a}$-PDT shown in Figure 75. AlPcS$_{2a}$ also slightly improved the mean outcome after TPCS$_{2a}$-PDT in the 16 hr DLI group. As for BPD-MA, it surpassed the outcome shown by both AlPcS$_{2a}$ and TPCS$_{2a}$, delaying the endpoint at least 3 days, compared to AlPcS$_{2a}$ (Figure 85).

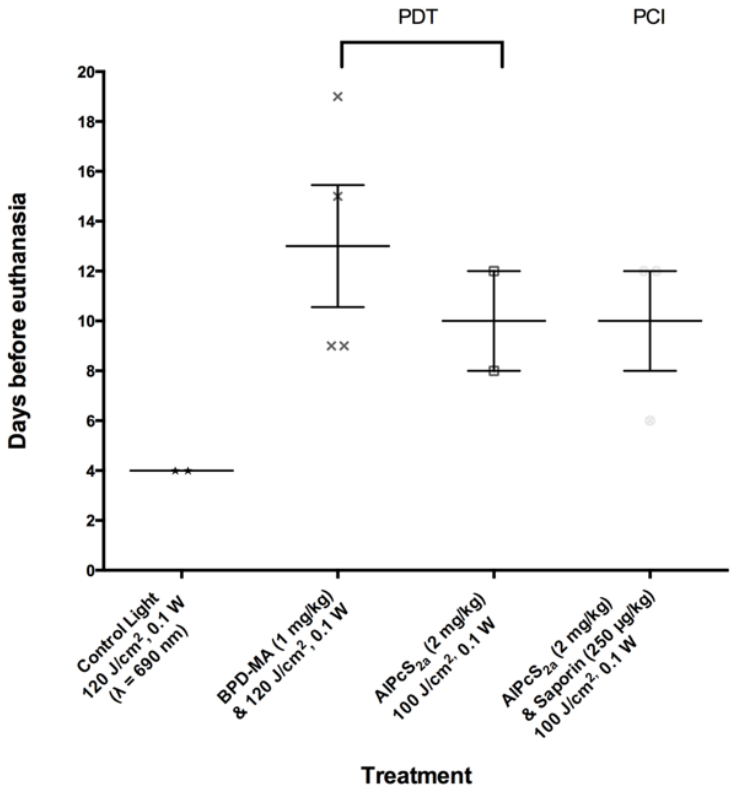

Figure 85. Tumour growth after BPD-MA or $AlPcS_{2a}$-based treatment until end point.

Scatterplot of days between PDT/PCI treatment to tumours and euthanasia of animal subjects based on tumour size endpoint. Data shown as mean ± SEM.

4.4.4 Survival curves after light treatment

Despite the overall comparison of all light treatments reported in the sections above concluded no significant variances as regards tumour growth, survival of animal subjects displayed in Kaplan-Maier curves, did result in significant differences after light treatment. As a matter of fact, increasing PS and light doses led to a general increase in survival, irrespective of whether light delivery was performed interstitially (Figure 86A) or superficially (Figure 86B, Figure 86C and Figure 86D).

The shortest survival resulted from interstitial-PDT using $TPCS_{2a}$ as photosentiser (1 week after treatment at best with the highest light dose assayed, 20 J and 1 mg/kg PS - Figure 86A). The maximum survival resulted from surface-PDT using BPD-MA (greatest survival of animals seen 19 days after post treatment at the highest concentration assayed, 1 mg/kg - Figure 86C). BPD-MA survival was followed by $AlPcS_{2a}$-PDT/PCI (both of which displayed the greatest survival of animal subjects up to 12 days post light - Figure 86D). $TPCS_{2a}$ surface-PDT following a 16-hr DLI was next in maximal survival of animals at 10 days post light at most Figure 86B, while the same

treatment following a 24-hr DLI only slightly improved survival to that displayed after interstitial-PDT of the same PS by 1 day (8 days after light as opposed to 7), although a lower PS dose was used (0.5 mg/kg rather than 1 mg/kg respectively).

Most of the animals treated with light alone survived 4-5 days after light at best and none of these exceeded survival over 1 week after illumination, displayed with black lines in Figure 86. Surprisingly, the surface light-alone group resulted in a better outcome than the $TPCS_{2a}$-based surface PDT group of animals (maximal survival of 7 and 6 days respectively - Figure 86B).

Overall, significant observations in survival curves were only found in BPD-MA – 4/22 (Figure 86C) and $AlPcS_{2a}$-PCI (Figure 86D) groups compared to untreated ($p = 0.0005$ and $p = 0.0455$ respectively). Conversely, the other two treatments exhibiting a noticeable delay in tumour endpoint, $AlPcS_{2a}$-PDT (Figure 86D) and $TPCS_{2a}$-surface light following a 16 hr DLI (Figure 86B), showed p values = 0.0833 and 0.256 respectively.

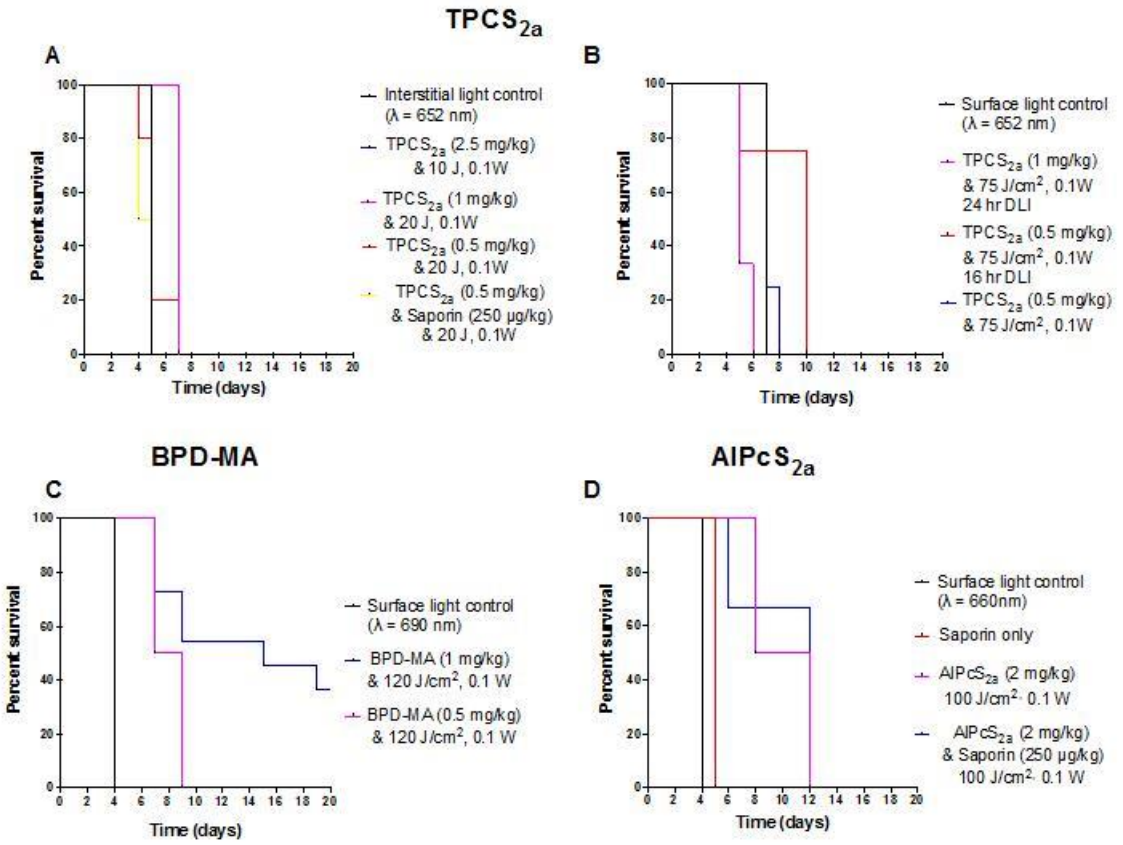

Figure 86. Summary of survival proportions for different light treatments performed with $TPCS_{2a}$, BPD-MA and $AlPcS_{2a}$.

Survival curves were plotted for the different light treatments reported in the sections above. (A) $TPCS_{2a}$-PDT following interstitial light treatment. (B) $TPCS_{2a}$-PDT following surface light treatment. (C) BPD-MA-PDT following surface light treatment. (D) $AlPcS_{2a}$-PDT/PCI following surface light treatment.

4.5 Discussion

Throughout the present chapter, we have reported the effect of light-based treatments in a highly aggressive prostate cancer tumour model. These tumours were generated implanting MatLyLu cells in syngeneic Copenhagen rats. As repeatedly commented, this cell line divides rapidly, which has shown evidence to lead to a disorganised tumour structure forming clumps *in vitro* and often resulting in multinodular tumours *in vivo*. In addition, MatLyLu tumours grew gradually up to a certain threshold, then growth became exponential. The above posed a difficulty during the generation of tumours of reproducible properties to compare treatment groups of PDT and PCI.

Cells were implanted subcutaneously in most cases, although an orthotopic tumour model was also developed for future experiments, since implantation of cells in the prostate preserves the natural host environment surrounding tumours, hence resulting in more realistic studies. This was performed following a protocol described in previous studies based on the same model (Momma et al., 1998). Out of all the cell concentrations we assayed, only the highest cell number ($5x10^4$) resulted in tumour formation. Moreover, despite we could not notice tumour formation by abdominal palpitation and no pain or unrecoverable loss weight were observed in the tumour-bearing rat, animal euthanasia revealed that the tumour formed had reached an excessive size in only 8 days after cell injection. The fact that lower cell concentrations did not form tumour could be due to an insufficient initial cell challenge or a possible human error during the injection of cells. This last hypothesis seems more likely based on the growth potential of MatLyLu cells experienced *in vitro* stated in Chapter 2. Regardless, we confirmed the potential to generate orthotopic prostate tumours surgically through mini-laparotomy. Importantly, this procedure did not cause major stress to animals and it was performed in a safe and aseptic manner: no deaths caused by the procedure itself nor infection in any of the animals were reported.

Other authors have concluded faster tumour growth rate in orthotopically as opposed to subcutaneously implanted tumours (Chen et al., 2005). Higher levels of endothelial-growth related proteins have been also observed in orthotopic tumours, which translated in a denser vasculature. This was important during the BPD-based light treatment performed, after which a greater photooxidative damage was reported in orthotopic tumours especially following a cellular-targeted rather than vascular-targeted PDT approach. Importantly, the effect of the tumour microenviroment in the overall

outcome of PDT was determined (Chen et al., 2005). Similarly, images shown in Figure 59 confirm that the orthotopic tumour model under investigation is highly vascularised.

In our examinations, light treatment was only performed on subcutaneous tumours using several photosensitisers of diverse nature and thereby photophysical properties, namely $TPCS_{2a}$, $AlPcS_{2a}$ and BPD-MA. PDT was the light-based treatment performed the most, while PCI was conducted on fewer occasions combining saporin exclusively with $AlPcS_{2a}$. An early assessment of pharmacokinetics and biodistribution of photosensitisers was conducted before performing PDT or PCI. This was measured quantitatively through chemical extraction in the case of $TPCS_{2a}$ (Figure 60), as well as qualitatively through fluorescence imaging of frozen tissue sections ($TPCS_{2a}$, Figure 61- Figure 63) or by live imaging using an "IVIS" system (BPD-MA or $AlPcS_{2a}$, Figure 76, Figure 77 respectively). In all cases, the liver resulted in the highest accumulation of all photosensitive compounds irrespective of the technique used (chemical extraction or fluorescence imaging) and whether the earliest time point was immediately after injection (IVIS images shown in Figure 76, Figure 77) or 6 hr after administration of PS solutions (chemical extraction displayed in Figure 60 or fluorescence imaging or cryosections shown in Figure 61- Figure 63). Regarding TPCS2a, observations upon quantification via chemical extraction (Figure 60) correlated with fluorescence imaging (Figure 61- Figure 63). The former revealed that 6 hr after administration most of the compound had already been cleared from circulation as concluded by the higher presence in liver (24.3 µg/g) and lower levels in blood (5.6 µg/g) (Figure 60). Not surprisingly and to a lesser degree, the spleen displayed a similar accumulation/clearance profile.

As reported above, accumulation in skin had an irrelevant impact overall (1.6 µg/g tissue at best), this would result in minimal skin phototoxicity if taken to a clinical context. In our studies, no side skin photosensitivity was reported in animals administered with $TPCS_{2a}$. However, animal subjects were never exposed to direct light and always kept under subdued light conditions and housed in amber-tinted cages, which reduce the overall penetration of light. In contrast, in the recently published clinical trial in humans using this same photosensitiser, greater sensitivity was reported. Precautionary measures were followed by patients to avoid skin phototoxicity as stated previously (Sultan et al., 2016).

Pharmacokinetics of $TPCS_{2a}$ in organs located in close proximity to the prostate (i.e. bladder, urethra, distal colon) revealed insignificant accumulation from 24 hr, despite some fluorescence being detected at 6 hr (Figure 62). This is important during light

treatment, since the welfare of healthy surrounding tissues could potentially be ensured with the optimal $TPCS_{2a}$ and light doses, as well as DLI.

In our subcutaneous prostate tumours, accumulation of $TPCS_{2a}$ was notable 6 hr after injection (2.9 µg/g), was then cleared and only traces were seen by 72 hr (Figure 60, Figure 63). The fact that fluorescence was located intracellularly rather than in extracellular compartments within tumours suggests this photosensitiser could potentially result in a valuable PCI effect. In addition, as suggested by the study performed by Chen et al., the denser vasculature in orthotopically implanted prostate tumours would have resulted in a larger accumulation of photosensitser than shown in subcutaneous findings (Chen et al., 2005).

Importantly, photosensitiser levels in the normal prostate were similar to those seen in subcutaneous tumours (Figure 63). In addition, it was the only tissue where fluorescence was reduced 6-24 hr but remained constant from then up to 72 hr (Figure 63). This could act as a "double-edged sword": on the one hand, presence of $TPCS_{2a}$ in the event of a prostate-located tumour would be ensured; on the other hand, this could result in side photooxidative damage to healthy areas of the prostate gland.

Distribution of BPD-MA and $AlPcS_{2a}$ was carried out exclusively in a qualitative manner using an *in vivo* imaging system. Differences in the intensity of fluorescence resulting between both photosensitisers could be due to differences in their quantum yields as well as the fact that excitation/emission settings were only optimal for BPD-MA, since we were limited by filters existing in the equipment. For all of the above, no comparison in accumulation and distribution between both compounds is possible, since the IVIS system cannot detect reliably internal fluorescence within the animal's body due to tissue autofluorescence, particularly in the overlying skin. Accordingly, it was used to determine significant events, such as abdominal accumulation in the case of both photosensitisers (Figure 76, Figure 77). Founded on the known accumulation of photosensitisers and other foreign bodies in the liver when entering an organism especially via intravenous administration, we concluded it is likely the organ responsible to a major extent for the accumulation of fluorescence in the abdominal region. Potentially, the spleen could have also resulted in some significant accumulation of both photosensitisers.

Previous investigations confirm the targeting of vascular structures soon after administration of BPD-MA (explained by its intrinsic hydrophobic structure) and determine that, transport rate from the vascular space into the parenchyma will define

the transition between vascular and cellular PDT (Zhou et al., 2004). Similarly, vasculature density was directly correlated with the intensity of fluorescence in tumours in a different study, also concluding differences between subcutaneous and orthotopic tumours (Zhou et al., 2006). Available published reports suggest an early accumulation of BPD-MA in vascular structures in tumours followed by transport to tumour parenchyma.

As for $AlPcS_{2a}$ (a more amphiphilic PS) Dietze et al. recognised the rapid elimination of PS from the blood stream as early as 24 hr, while presence in tumours was maintained 2-48 hr. However, while 2 hr after administration fluorescence was found within proximities of the tumour vasculature as well as stromal compartments, a higher emission of fluorescence was confirmed in tumour cells at the later 48 hr time point (Dietze et al., 2005). In this study, a large accumulation in the liver was also reported. Our own observations, as stated above, are supported by these previous findings, since we found a slight increase in fluorescence emission in the area bearing the subcutaneously grown tumour (Figure 77). This was not observed with BPD-MA (Figure 76). As a matter of fact, had there been more adequate excitation/emission settings IVIS available, we think this observation would have been more noticeable.

Once we had studied the *in vivo* distribution of photosensitisers, we moved on to evaluate the outcome of light treatment to tumours, as described in the Results section. The first set of light treatments were carried out in 1 cm diameter tumours, which were formed only 7 days after implantation of 10^6 cells. We considered that the exceedingly fast growth of these would be unrealistic *in vivo* in human patients and consequently reduced the cell burden during tumour implantation to $4x10^5$. In addition, to widen the available window of tumour progression prior to exponential tumour growth, tumours were treated at a smaller size hereafter (0.5-0.7 cm diameter).

All photosensitisers were assayed in PDT applications, aiming to optimise these as a base for later PCI experiments. In an attempt to replicate the conditions that would be applied in PCI in the clinic, Amphinex® ($TPCS_{2a}$) was the first photosensitiser used and light was delivered interstitially based on the current clinical prostate PDT: placing fibres in the gland within needles (Moore et al., 2009; Svanberg et al., 2010). Interstitial and surface illumination have been compared in their application for different PDT approaches. For instance, the former led to an enhancement in therapeutic outcome over the latter for intramuscular squamous cell carcinoma treatment (Sajisevi et al., 2015). 24 hr after PDT, necrotic cell death observed was more significant in interstitial-PDT than transcutaneous-PDT. During interstitial PDT, light distribution is a complex

process where intensity and dose are higher in areas immediately adjacent to the fibre, being the base of the tumour less exposed to light. Based on the heterogeneity and high vascularisation observed in MatLyLu tumours, added to difficulties encountered while piercing the tumour capsule to insert the fibre, light treatment was later on performed superficially on exposed tumours. In line with this, inserting the fibre in the centre of tumours could have caused bleeding and this might have affected light distribution.

Along these lines, the importance of a good PDT-planning in large-volume tumours regarding dosimetry of light was addressed in the study carried out by Davidson et al. (Davidson et al., 2009). This study describes the use of software to tailor light treatments to each specific prostate cancer patient in terms of number, position and length of fibres required as well as energy delivered. Generally, the use of interstitial illumination is accepted for deeper lesions (Svanberg et al., 2010). Likewise, the deeper penetration in PCI commented in the Background and Introduction, would further enhance the treatment of deeply located tumours.

A 24 hr DLI was selected for the first groups of treatments using $TPCS_{2a}$, based on previous investigations carried out by other members of the research group together with findings from the biodistribution study (1.37 µg/g tissue), verifying the presence of photosensitiser in tumour tissue at this specific time point. Following interstitial illumination, nearly the entire surface of the tumour sample resulted in PDT-based damage 24 hr after light when combining $TPCS_{2a}$ 2.5 mg/kg and 20 J interstitial light (Figure 64). As a matter of fact, apoptosis seemed to be the main cause of cell death as revealed upon staining against cleaved caspase-3 in Figure 65, finding a largely noteworthy caspase-3 positive area 1 day after light treatment. Briefly, the comparison of H&E and caspase-3 staining of the same tumour sample indicated that those regions with a healthy appearance in H&E staining only had a few apoptotic cells; whereas areas which were differentially H&E-stained, were heavily stained for caspase-3.

As reviewed in the Background and Introduction, apoptosis is the cell death mechanism reported in many studies previously as the most relevant induced by PDT (Agostinis et al., 2011). This may vary depending on the target cells, photosensitiser and light radiance used (Rodríguez et al., 2016). In an attempt to identify the optimal PDT conditions which maximise apoptotic cell death using Foslip as a photosensitiser in a squamous carcinoma mouse model, it was recently concluded that reduction of photosensitiser dose could successfully result in apoptosis *in vivo* under specific light conditions. In their study, probably assisted by the liposomal encapsulation of mTHPC,

a reduction of Foslip's dose to 40 mg/kg enabled the observation of apoptosis in tumours when illuminating at 100 mW/cm^2 (Haedicke et al., 2016). Detection of apoptotic cell death was achieved at early time points in their investigations. Moreover, the use of low PS doses would limit unwanted phototoxicity. The authors of the study made an additional important consideration regarding the outcome observed: available ground-state oxygen is essential to ensure the success of the treatment. As a matter of fact, the consumption of this oxygen in tumours during PDT is dependent on a combination of photosensitiser levels in the tumour area, absorption coefficient of such and light fluence employed (Foster and Gao, 1992).

Rather than euthanising animals 24 hr after light delivery, animal subjects treated hereafter were monitored regularly and tumours were not removed until these reached a pre-established end point (1.8 cm^3). Regardless of whether light delivery was performed interstitially or via surface illumination, no consistency was observed in any of the $TPCS_{2a}$-based light treatments and each tumour sample seemed to behave in a particular manner in terms of phootoxidative-induced affected tumour area (Figure 69, Figure 71). Uncured BPD-MA-based (Figure 79) and $AlPcS_{2a}$-based (Figure 82, Figure 83) light treatments on tumours, showed a similar pattern of affected areas. In relation to this, heterogeneity and irreproducibility reported in a different PDT study carried out on Dunning R3327-AT2 prostate carcinoma, were attributed to the intrinsic hypoxic characteristics of the model (Bozzini et al., 2013a). Other investigations combining PDT with agents such as misonidazole (cytotoxic to hypoxic cells), resulted in an enhancement over PDT alone in tumour eradication rate and growth delay (Gonzalez et al., 1986).

Based on our observations after interstitial illumination, we conclude that higher PS doses (2.5 mg/kg) combined with lower light irradiance (10 J) as shown in Figure 69i did not result in as much photooxidative damage as lower PS doses (0.5-1 mg/kg) combined with higher light irradiance (20 J). In the recent clinical application of PCI (Sultan et al., 2016), 0.25 mg/kg $TPCS_{2a}$ represented a dose threshold, above which no dose-response was noticed using the same light dose, hence concluding light dose was a limiting factor. This therefore supports our above-stated findings.

The use of a shorter DLI, such as 16 hr in surface illumination, showed an improvement over the treatments just stated (Figure 72). In this case, tumour size was controlled to some extent and affected areas were more homogeneous. This translated to a broader time frame between light treatment and sacrifice of the animals, as represented in Figure 75. Although 24 hr DLI successfully induced cell apoptosis

(Figure 65), a rapid breakdown of PS due to the extraordinarily fast growth of MatLyLu cells (as already suggested *in vitro*), could have been responsible for an insufficient PDT effect. *In vivo*, this translates in a greater photochemical damage when illuminating tumours earlier by ensuring larger accumulation of PS in tissue. Based on the above, we consider 16 hr DLI improves the therapeutic outcome exhibited after a 24 hr DLI and will further optimise PDT treatment so as to then conduct PCI experiments in combination with saporin in future work.

Untreated and light-only controls in the study also revealed affected areas, as shown in the H&E stained tumour samples in Figure 66, Figure 68, Figure 70 and Figure 71 (stained in a light pink colour, rather than the characteristic dark purple of healthy tumour cells). The fact that these were also shown in the untreated control indicate an intrinsic "source of damage". These regions were even more heterogeneous than in PDT-treated tumours, scattered throughout the tumour and appeared to emerge from central regions of the tumour. As a consequence, we hypothesise these are spontaneous necrotic regions induced by hypoxia in the centre of tumours, which probably became accentuated due to the fast growth and thereby oxygen consumption in these tumours. In addition to a rapid growth-related spontaneous necrosis, the surgical procedure itself could have caused distress during both orthotopic and subcutaneous implantation, as suggested by the histological evaluation of the orthotopic tumour in Figure 59, which also revealed an affected central region of the tumour-invaded prostate gland.

The above has been observed in previous studies, for example secretion of tumour necrosis factor β (TNF-β) by myeloma cells has been confirmed (Bataille et al., 1989) and an inversely proportional correlation between necrosis pre-treatment and prognosis has been reported in osteosarcomas (Björnsson et al., 1993). In this last publication, the authors concluded that tumours presenting a significant spontaneous necrosis were more likely to grow faster and displayed a more significant migratory phenotype. It is unlikely that there was any light-alone induced cell death in our investigations, founded on the previously conducted *in vitro* experiments (commented in Chapter 2 and Chapter 3), and supported by the fact that untreated control tumours also exhibited these affected areas.

Overall, we consider the enhancement of the therapeutic outcome and success rate of BPD-MA PDT in this investigation, that successfully eradicated tumours in 18% of the treated animals, was based on the vascular effect caused by this PS (Fingar et al., 1999; Kawczyk-Krupka et al., 2015b). Soon after light treatment, these tumours

developed a black eschar in the area of the skin which had been directly exposed to light, as shown in Figure 81. Described as tissue necrosis, this has been reported previously in BPD-MA vascular-PDT studies, for instance for the treatment of squamous cell carcinoma in mice (Marcus et al., 1994) or ovarian adenocarcinoma grown on a chorioallantoic membrane (Ismail et al., 1999). We have previously described a dense vascular structure and blood supply in MatLyLu tumours as indicated in Figure 59. Therefore, the use of short DLI (such as the followed 15 min) would ensure a vascular shutdown in these. This seems to have a major implication in the cure of animal subjects, observation additionally reinforced by the delayed endpoint found in the non-eradicated BPD-MA treated tumours compared to the outcome exhibited by the other light treatments (Figure 75, Figure 85).

As for $AlPcS_{2a}$, damage caused to tumour-bearing legs after light treatment following a 6 hr DLI (described in Figure 81) could be due to neurotoxicity induced by accumulation of PS in the peripheral nerves. Although there are no previous $AlPcS_{2a}$-related neurotoxicity reports in the literature, it has been observed with other PS, such as mTHPC, where cells of the peripheral nervous system were seen to be susceptible to mTHPC PDT-mediated necrosis (Wright et al., 2007). In contrast, nerve sparing was noted post PDT in neck cancer in human patients and *in vitro* cell death was reduced compared to satellite glia and cancer cells (Wright et al., 2009).

In our present investigation, no improvement of PCI over PDT was confirmed. Based on the preceding success of PCI *in vitro* and *in vivo* with different PS ($AlPcS_{2a}$ among others) (Berg et al., 2005; Martinez de Pinillos Bayona et al., 2016), we consider that the procedure we followed still requires further optimisation and will be addressed in future work.

The comparison of caspase-3 staining between tumours sampled 24 hr after light as commented above, and those removed at a later time point (i.e. from 5-10 days after light, based on the volume endpoint), concluded a drastic reduction of the number of apoptotic cells. These cells appeared disperse throughout the whole structure of tumours (including control), with a higher prevalence in peripheral regions and surrounded by infiltrating leukocytes (Figure 68, Figure 73, Figure 80 and Figure 84) This, together with the low cure rate achieved in of our animal subjects, could be explained as follows:

- PDT did cause apoptotic cell death after delivery of light, since the cytotoxic potential of all 3 photosensitisers used has been previously reported in

Chapter 2, and there is no evidence of lack of photooxidative-based cytotoxicity *in vivo*.

- By the time tumours were removed, infiltrating leukocytes had been released from circulation, as indicated in Figure 67 showing extravasation from vessels located in tumours. Hereafter, these infiltrating cells would have initiated their phagocytic activity, engulfing dying tumour cells.
- Likewise, infiltrating leukocytes could have been released in control tumours, engulfing spontaneous necrotic and apoptotic dying cells.
- In parallel, tumours cells remaining viable after light treatment would have surpassed the number of affected cells (based on the doubling rate of MatLyLu cells), overtaking the tumour mass and in the end leading to uncontrollable tumour growth. Had the samples been removed at an earlier time point, the number of dead tumour cells could have been larger.

On the whole, we conclude that light-based treatment for tumour eradication is largely dependent on features of each particular tumour and these should be considered while designing PDT or PCI procedures. Specifically, the tumour described in the present thesis, is fast growing and highly vascularised. Based on these, the complete cure of tumour-bearing subjects requires complete eradication of tumour cells: should viable cells be noted post treatment, tumour regrowth would be almost inevitable; on the other hand, vascular-targeted procedures are more likely to result in a beneficial therapeutic outcome (as seen with BPD-MA). Along this same line of thought, PCI could have a better chance of succeeding if vascular components were targeted. For instance exploiting the potential of vascular targeted toxins such as VEGF-saporin in a similar manner to performed with VEGF-gelonin for colorectal cancer treatment (Weyergang et al., 2014). In addition, as indicated in our *in vitro* findings, PCI is a challenging technique to optimise due to the number of different variables involved (PS dose, light irradiance, DLI, etc.). Therefore, taking the present investigations as a basis, further work is required in the optimisation of such for the currently investigated prostate cancer model.

Importantly, cell death resulting from these treatments trigger systemic processes which result in infiltrating circulating cells such as leukocytes, macrophages and neutrophils (associated with inflammation). This lays the foundation for investigations reported in the following chapter of the present thesis, regarding the activation of the immune system post PDT.

Chapter 5 Stimulation of the immune system following PDT and PCI in Prostate Cancer

5.1 Introduction

The importance of the immune system during cancer treatment dates back a long way, even though its importance has not been realised until recently. Already in Egyptian times it was noted that wound infection during surgical procedures leads to tumour regression due to the activation of the immune system (Castano et al., 2006; Mroz et al., 2011a). This was actively studied and pursued by Dr William Coley back in the nineteenth century. Dr Coley observed how a sarcoma tumour kept recurring in the left cheek of a patient until the extensive wound got severely infected by *S. pyogenes.* The patient then developed strong febrile reactions, identified as "key" in the treatment, in the end leading to tumour shrinkage (Hoption Cann et al., 2003). Dr. Coley developed a vaccine composed of *S. pyogenes* and *S. marcescens,* which he widely and successfully used not only for sarcoma treatment but also carcinoma, melanoma, lymphoma and myeloma, even when these had been considered inoperable and incurable (Hoption Cann et al., 2003). Overall, it was hypothesised back then that tumour regression depended on the generation of an innate immune response in a non-specific manner, observing regrowth in those cases where the febrile phase had disappeared. In the same way, regression was resumed if the infection was reintroduced, as concluded when injections were given on a regular basis.

Since then, the importance of significantly activating the immune response for cancer treatment is now firmly established, including focal therapies (Korbelik and Dougherty, 1999). However, some of the current gold standards for cancer treatment (chemotherapy or radiotherapy for example) can also induce an immunosuppressive effect which could negatively affect tumour regression (Hoption Cann et al., 2003). An effective cancer treatment nowadays should involve both, the elimination of tumour cells as well as the activation of the immune system. Moreover, this should not only enhance tumour regression triggering an innate immune response (as described in Dr. Coley's observations), but also induce systemic anti-tumour long-term protection that could potentially avoid formation of a distant secondary deposit of tumour cells or even individual circulating cancer cells. Accordingly, we will review previous reports on the use of light-based therapies combining these two "arms" of cancer treatment.

5.1.1 The immune response

The immune system has the potential of generating protection against exogenous molecules whilst avoiding damage to endogenous self-tissues. This is possible due to the existence of specific features present in foreign bodies, which enable the preservation of self-tolerance. This is a critical step based on the highly toxic mechanisms T cells can exert on strange infiltrating bodies (Chaplin, 2010).

The immune response is composed of two major arms:

- Innate immunity: these are the very primary protective mechanisms which a foreign body encounters upon entrance in the organism, encoded in germ-line genes. It comprises physical barriers (skin, mucosa, cell-cell interactions), soluble proteins and molecules constitutively present in biological fluids (for instance complement proteins), molecules released by cells during activation (i.e. cytokines, chemokines, lipid mediators, active amines and enzymes, etc.), surface receptors and cytosolic proteins capable of recognising motifs in the surface of the invading foreign body.
- Adaptive immunity: this is mainly based on the antigen-specificity displayed by T and B lymphocyte receptors. This specificity is generated by somatic rearrangement and reassembly of gene elements encoded by the germ-line (rather than being directly encoded by these genes without further processing). During this process, several many combinations of genes exhibiting different specificities towards the antigen of interest are assayed. By the end of the somatic rearrangement a unique receptor, displaying the highest specificity against a particular antigen, will be selected and will in turn lead to the clonal expansion of T and B lymphocytes. This process becomes outstanding 7 days after the immunological challenge. The antigens that are not selected for, will have their apoptotic pathway activated through the NFκB pathway.

These two parts of the immune response act in a synergistic manner to bring about an optimal response: the innate response will be the earliest line of defence activated in a host organism followed by the stimulation of an adaptive immune response (Chaplin, 2010). Based on the aim of the present chapter, namely to investigate the elucidation of tumour-specific immunoprotection in our prostate cancer tumour model, a greater

focus will be given to the cellular adaptive arm of the immune response, specifically T cells.

5.1.1.1 The role of NF-κB pathway in the immune response

Extracellular events during immune stimulation result in signal transduction, most of which involves the transcription factor Nuclear Factor (NF)-κB, in the end causing changes in gene expression. As a matter of fact, it has a wide range of crucial functions in the innate and adaptive immune response and we will comment hereupon the more relevant roles of NF-κB, to our present project (Hayden et al., 2006).

Five related transcription factors have been identified belonging to the NF-κB family of proteins, namely p50, p52, RelA/p65, c-Rel and RelB which shuttle between cytoplasm and nucleus and bind DNA sequences known as *K*B regulating changes in gene expression. While RelA, c-Rel and RelB can activate gene expression due to the presence of transcription activation domains in their C-terminal, p50 and p52 lack these regions and therefore will only be able to inhibit transcription. In order to achieve this however, they need to be released from their interaction with the protein Bcl-3 (Hayden et al., 2006).

This pathway tends to remain inactive under resting conditions, being all the constituents in the cytoplasm bound to their corresponding inhibitory from the IκB protein family (IκBα, IκBβ, IκBε, IκBγ, IκBNS, IκBη, IκBζ, Bcl-3, and precursors p105 and p100). During activation, these inhibitory proteins are phosphorylated by IκB kinases (IKK) and consequently degraded, then triggering the signalling cascade that will result in changes in gene expression within the nucleus. These IKK proteins are IKKα and IKKβ, which in addition require the regulatory scaffold NEMO. Two important routes for the activation of this pathway have been described, either canonical or non-canonical, and the requirement of each IKK will be different depending on which of both pathways is initiated.

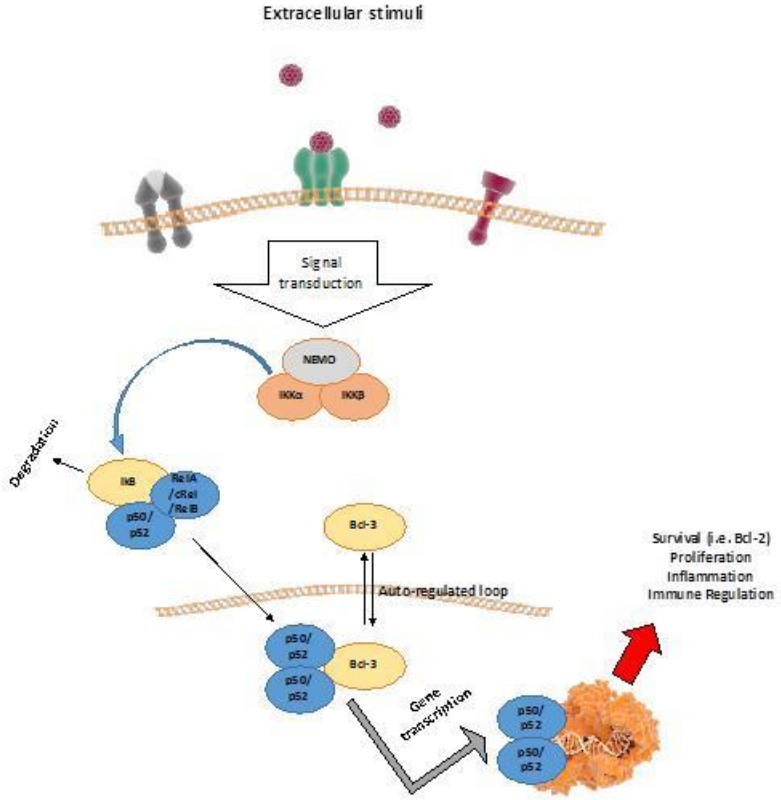

Figure 87. NF-κB pathway in the immune response.

Schematic representation of signalling transduction upon cellular stimulation in relation to the NF-κB pathway effectors. Under resting conditions, the five transcription factors identified to date (p50, p52, RelA, cRel, RelB) remain bound to their respective inhibitory proteins, known as IκB. These inhibitory proteins are phosphorylated by IKK proteins and degraded during activation, triggering the signalling cascade that will result in regulation of gene expression in the nucleus of the cell. Bcl-3 acts as an inhibitory protein of p50 and p52, regulating the transcription of a wide rage of genes involved in survival (i.e. Bcl-2), proliferation, inflammation or immune regulation.

Among IκB proteins, Bcl-3 (initially identified as a proto-oncogene) has been widely studied. It is known to interact with p50 and p52 regulating both canonical and non-canonical gene transcription. For instance, association between Bcl-3 and p50 or p52 in DNA promoters activates transcription of genes. Nonetheless, it can also have an inhibitory effect in gene transcription binding repressive p50 to DNA. Some studies have demonstrated the stabilisation of p50 binding to DNA, inhibiting its degradation or preventing other active transcription factors from exerting their activity. An example of this stabilisation occurs in response to TNF and TLR (toll like receptor signalling) (Carmody et al., 2007; Wessells et al., 2004), where Bcl-3 helps maintain homeostasis of the innate immune response by limiting the excessive activation of TLR. An excessive signalling could result in an overload and in the end lack of responding capacity in the presence of stimuli. Phosphorylation in Bcl-3 might be essential for its activity, for example limiting its capacity to promote the interaction between p50 and DNA binding sites. Bcl-3 is mainly found in the nuclear compartment although

cytoplasmic accumulation has also been seen in certain cells and localisation in either could have a major influence in its function.

Among genes regulated by Bcl-3, it promotes T cell survival inhibiting the activation of Bim protein (member of the pro-apoptotic Bcl-2 family) although the mechanism is not fully understood (Herrington and Nibbs, 2016). Bcl-2, was initially recognised as anti-apoptotic (even anti-necrotic in some cases), but several more proteins belonging to this family have been identified to date, exhibiting both anti- and pro- apoptotic functions (Tsujimoto, 1998). In fact, subcellular localisation of Bcl-2 has been related to opposite roles: its anti-apoptotic role has been associated to mitochondria, where it is transported from the default localisation in the ER- and nuclear- membrane assisted by chaperones, thereby blocking the apoptotic pathway (i.e. inhibiting pore formation, cytochrome c release or caspase cascade among others). Studies by Portier and Taglialatela showed that localisation of Bcl-2 in the nuclear compartment unavoidably ends in cell death (Portier and Taglialatela, 2006). As for its relation to NF-κB, as an example, during the clonal selection of B and T cells in the thymus and bone marrow there is a high apoptotic rate and NF-κB has important anti-apoptotic functions, via the anti-apoptotic Bcl-2 factor among others (Heckman et al., 2002).

5.1.1.2 Cellular constituents of the immune response

There are many different types of leukocytes involved in the cellular immune response, each subset being featured by the expression of specific surface markers, assigned as cluster of differentiation (CD). All cells described in the current section are generated from a single progenitor, “pluripotent hematopoietic stem cell” that will either lead to a lymphoid progenitor or myeloid progenitor, as displayed in Figure 88.

Relevant to our present study, granulocytes (also known as polymorphonuclear leukocytes) emerge from a common myeloid progenitor and have an important interface role between the innate and adaptive immune response. Some of these granulocytes have been identified in tumour samples described in Chapter 4. Briefly, neutrophils and macrophages have a key phagocytic role engulfing foreign “suspicious” bodies during the innate phase. Neutrophils are additionally involved in the secretion of cytokines in early stages of the immune response, while the latter can also act as APCs in an adaptive phase. Compared to neutrophils, macrophages persist longer in

the site of inflammation and are frequently associated with chronic inflammatory processes, acquiring different phenotypes based on the cytokines involved during their activation (i.e. pro-inflammatory as opposed to anti-inflammatory), and play an important role in tumour progression/regression. Immature dendritic cells exhibit a similar phagocytic function during the innate response and are the most relevant antigen presenting cells, interacting with T cells during the initiation of the adaptive response. The other granulocytes, namely eosinophils, basophils and mast cells will play an major role releasing the content in their cytoplasmic granules during the adaptive the immune response once they are activated by an antibody (Charles A Janeway et al., 2001).

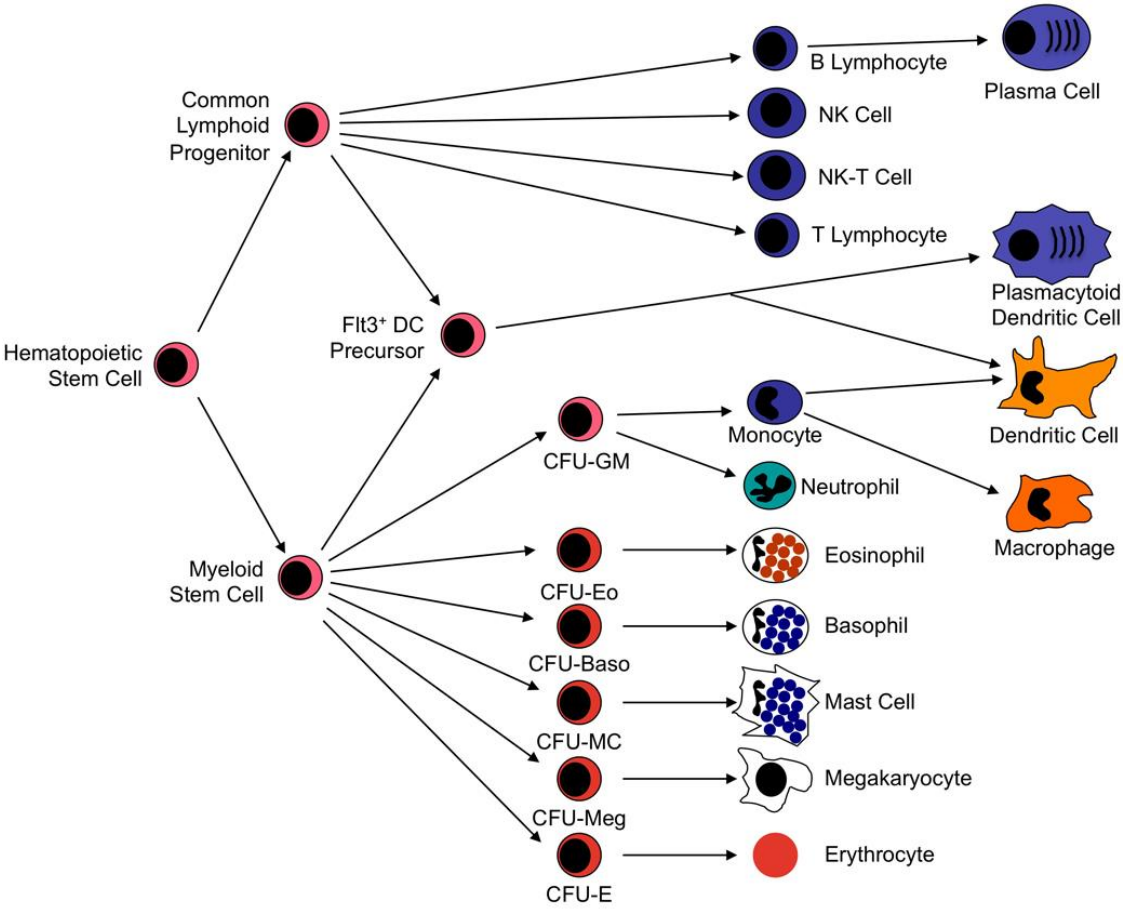

Figure 88. Differentiation of myeloid cells and lymphocytes from a common hematopoietic stem-cell progenitor.

Image taken from [(Chaplin, 2010)*]*

As for the lymphoid progenitor, it will differentiate into four major populations cells: B-cells, Natural killer cells (NK), T-cells and NK-T cells (sharing features present in both NK and T cells). Shortly, B-cells are defined by the presence of a surface B-cell receptor which will recognise antigens and produce antibodies accordingly (humoral

immune response). NK cells on their side can recognise tumour cells or virus infected cells via a complex variety of surface receptors, while T-cells are featured by the expression of a surface T cell receptor (TCR) that will interact with surface receptors in antigen presenting cells (APCs). The TCR is a transmembrane heterodimer protein complex with additional side chains involved in signal transduction, for example the CD3 complex (CD3ε among other constituents). As a matter of fact, different T cell subtypes exhibiting disparities in their phenotypical features have been described (see Table 9).

Name	Surface Receptors
Naïve	CD3, TCR, IL-7R, CD62L, CCR7
Cytotoxic	CD3, TCR, CD8
Exhausted	CD3,CD8, PD1, TIM3, 1B11, LAG3
Anergic	CD3, TCR, BTLA
Helper	CD3, TCR, Cytokine receptor, CD4, Chemokine receptor
Regulatory	CD3, TCR, CD4, GITR, CTL4, CD25, FoxP3
Memory	CD3, TCR, CD44, IL-7R, CCR7
NKT	TCR, NK1.1, SLAMF1, SLAMF6, TGFβR
γδ	CD3, γδTCR,
CD8αα	CD3, TCR, CD8αα, B220

Table 9. T cell subsets and their respective surface receptors.
Adapted from [(Dong and Martinez, 2015)*]*

5.1.1.3 Antigen presentation and generation of a T-cell specific immune response

Whether antigens are from pathogen- or tumour- origin, these will be recognised by APCs via cell surface glycoproteins known as major histocompatibility (MHC) molecules also called human leukocyte-associated (HLA) antigens. Two major MHC molecule types have been identified on the surface of APCs: class I presents antigens synthesised by the cell, while class II presents ingested and processed antigens. T cells will only be capable of antigen recognition when these have been incorporated in

MHC molecules on APCs' surface. Specifically, MHC I molecules will present antigens to $CD8^+$ T cells contrary to MHC II molecules, which present antigens to $CD4^+$ T cells. Upon recognition of MHC molecules by either the CD8 or CD4 domain in T cells, with the added participation of co-stimulatory molecules present on the surface of APCs (CD80, CD86) or T cells (CD28), the acquisition of a fully active phenotype in previously naïve T cells occurs. In fact, when antigens are taken up, the expression of MHC, CD80, CD86 is increased. Therefore, an effective T-cell immunotherapeutic pursues loading cytosolically processed antigens on MHC I molecules in order to exploit CD8 T cell responses.

Among all T cell subsets ($CD3^+$), we would like to highlight in our current study cytotoxic T cells and regulatory T cells.

- $CD3^+CD4^+$ - Helper T cells, participate mediating both the cellular and the humoral immune response. However, these will not be covered in the present chapter.
- $CD3^+CD4^-CD8^+$ - Cytotoxic T cells (Tcs), recognise specific antigens and directly kill pathogen-infected or mutated cells through the secretion of effector molecules such as perforin and granzyme, inducers of apoptosis in target cells. In addition, these cells can limit regulatory cells responsible for immunosuppression.
- $CD3^+CD4^+CD8^-$ - Regulatory T cells (Tregs), promote tolerance and immunosuppression.
    - $CD3^+CD4^+CD8^-FoxP3^+$ - Natural Regulatory T cells present a nuclear forkhead box P3 transcription factor key in their development. These cells mainly exert their regulatory function through secretion of anti-inflammatory cytokines: TGFβ and IL-10.
    - $CD3^+CD4^+CD8^-FoxP3^{+/-}$ - Induced/Adaptive T cells developed via antigen-specific stimulation, hence the variable expression of FoxP3 (often dependant on IL10). Rather than being developed in the thymus (as natural Treg), this Treg subset is induced in peripheral regions from naïve $CD4^+$ cells. As noted above in natural regulatory T cells, induced T cells also exert their regulatory function through secretion of anti-inflammatory TGFβ and IL-10.

Antigen presentation takes place in secondary lymphoid tissues, i.e. lymph nodes, which exhibit distinguishable regions characterised by B or T cell accumulation. In these, circulating antigen-loaded APC will interact with naïve cells undergoing somatic mutation to select the cell clone showing the highest affinity for a specific antigen.

Mature B and T cells then receive specific signals indicating their egress out of the lymph nodes and release into the blood stream (Chaplin, 2010).

5.1.1.4 Immune inhibitory checkpoints: PD1 and PD-L1

Antigen presentation is a regulated process whereby the interaction between T cell receptor and MHC molecules present in the surface of APCs involves additional molecules which in the end will determine whether a stimulatory or inhibitory signal is transduced. These are known as immune checkpoints.

CD28 present in the surface of T cells has a major role as stimulator of the immune response, enhancing the activation of T cells against a particular antigen. In contrast, immune checkpoint inhibitors which interfere with this activation process have been described: PD1 (programmed cell death protein 1) and CTLA-4 (cytotoxic T lymphocyte-associated antigen 4, which will be further commented below). Both of these are present on the surface of activated T cells and participate in the blockage of an anti-tumour response upon interaction with receptors in the surface of APCs or tumour cells, in the case of CTLA-4 and PD1 respectively. This has resulted in a great interest to develop therapeutic strategies that can overcome this inhibition, and hence favour potent anti-tumour protection as is the case of the antibodies ipilimumab (anti-CTLA-4) or Nivolumab (anti-PD-1) (Philips and Atkins, 2015).

Focusing on PD1, it is a transmembrane protein belonging to the CD28 family, expressed $CD4^+$ and $CD8^+$ T cells, B cells, NK cells, monocytes DCs; yet not present on resting T cells unless induced by prolonged exposure to antigens. Its expression was first identified as a consequence of the apoptotic pathway (Ishida et al., 1992). PD1 binds to two main ligands, PD-L1 or PD-L2, resulting in a down-regulation of effector-T cell activation: inhibiting proliferation, causing cytolysis, interfering in the expression of anti-apoptotic molecules, cytokines and other biochemical pathways (Philips and Atkins, 2015). In addition, it has been related to the promotion of Treg-development, assisting the maintenance of FoxP3 and their suppressive effect. In the anti-tumour context, expression of PD-L1 has been shown in many different tumour cases, reporting that binding of PD-L1 to PD1 facilitates immune evasion by tumours. Tumours exhibiting high PD-L1 levels have been associated to poor prognosis (Jin et al., 2010). Conversely a direct relationship between high expression of PD1 and a

favourable prognosis was noted in follicular lymphoma patients (Carreras et al., 2009). Interestingly, an alternative expression between PD1 and FoxP3 was found in this study, indicating that the suppressive tumour microenvironment could be determinant in the overall outcome of follicular lymphoma.

In line with this, cancer cells can avoid immune recognition and control through immunoediting: diseased cells that escape elimination by the immune system undergo an editing procedure after which they go unnoticed by immune system effectors, becoming stealth tumour cells.

5.1.1.5 The interplay between cytotoxic and regulatory T cells in cancer

As previously noted, $CD4^+CD8^-FoxP3^+$ are a highly immunosuppressive subtype of T cells, responsible for the maintenance of immune homeostasis. They play an essential role in immune tolerance to self-tissues which in fact appears to be deregulated in autoimmune diseases or allergic reactions (Takeuchi and Nishikawa, 2016). As briefly mentioned, these cells exert their suppressive role releasing inhibitory cytokines, consuming IL-2, degrading ATP, establishing direct contact through inhibitory receptors such as CTLA4 or else releasing cytotoxic enzymes such as granzyme-B or perforin (Alroqi and Chatila, 2016).

Treg-induced immunosuppression does not only affect the effector phase of the immune response, but in fact Tregs can also interfere during earlier phases, i.e. during antigen presentation affecting the generation of Tcs. Briefly, CTLA4 has an important role engaging with CD80 and CD86 molecules during this process and can transmit inhibitory signals to APCs, blocking the consequent maturation of cells, and thus impeding the establishment of an adaptive immune response (Walker and Sansom, 2011). Moreover, the role of IL-2 is crucial in “tipping” the balance in favour of Tc or Tregs, based on the potential to activate both cell subsets. Low IL-2 levels have been associated with an increase of Tregs; while higher concentration might assist the proliferation of Tcs (Boyman and Sprent, 2012).

Importantly, the secretion of Treg-recruiting cytokines has been described in tumour cells (Takeuchi and Nishikawa, 2016). In this regard, tumour associated macrophages (TAM) play a relevant role. These cells are a heterogeneous population in relation to

oxygen levels and tumour growth. Two main types have been identified, M1 and M2. It is the inflammatory microenvironment created during early stages of tumour development that will cause the infiltration of these TAM. In this specific context, M1-TAM release chemoatractants to bring NK cells among others into play (i.e. IL.6, IL-12, TNF-α). In addition, this pro-inflammatory environment will additionally help maintain the M1 phenotype. However, tumour progression or the appearance of hypoxic regions in the tumour mass, promote polarisation towards the M2 phenotype. This will result in the secretion of different cytokines such as IL-10 and TGFβ, which have been indicated above as inhibitors of the anti-tumour immune response (Zamarron and Chen, 2011) .

Therefore, within a tumour environment, the presence of antigen-specific Tcs can be compensated by infiltrating Tregs and it is this balance that will determine the efficiency of anti-tumour immunity.

5.1.1.6 Modulation of T cell response by cyclophosphamide

Based on the above summary, it is not surprising that tumours with large infiltration of $CD4^+CD25^+FoxP3^+$ Tregs exhibit poor prognosis. So as to balance the tumour microenvironment towards cytotoxic effector T cells rather than regulatory effector T cells, different strategies have been investigated. As concerns the present thesis, we will highlight the use of cyclophosphamide (CY). CY is a drug widely used as chemotherapeutic (Cytoxan®, Neosar®) for the treatment of different cancers as is the case of Burkitt's lymphoma, Hodgkin's and non-Hodgkin's lymphoma, t-cell lymphoma, neuroblastoma, etc. It induces cytotoxicity by introducing alkyl groups into DNA chains causing cross-linking and in the end impeding proliferation of cells. Importantly, a similar CY-induced cell damage has been reported in tumour and lymphocytes and has been used accordingly both for cancer and to treat immune-related diseases such as lupus or chronic transplant rejection (Abu Eid et al., 2016).

Interestingly, the administered cyclophosphamide dose regime (concentration, sequence of repeated administration, timing) will determine whether this drug has a direct cytotoxic effect or else it acts mediating the elucidated immune response. In line with this, low doses (administered in single doses or following a metronomic regime) have demonstrated potential to selectively deplete Tregs, opposite to high doses, which indiscriminately cause death to all cells. As an example, 200 mg/kg CY resulted

in cytotoxic effects, reducing cell number in all T cell subsets; whereas 20 mg/kg suppressed $CD4^+CD25^+$ cells whilst sparing $CD8^+$ (Motoyoshi et al., 2006). Further proof of this resulted from observations on immunocompetent and nude animal subjects: low doses only had a therapeutic effect in the former individuals, as opposed to high doses, which were effective irrespective of the immunological condition (Motoyoshi et al., 2006).

CY has been taken one step further in humans in several clinical trials. These have shown the potential of CY in the generation of antigen-specific effector T cells in cancer treatment, for example concluding an enhanced survival of patients when CY administration was conducted 3 days before vaccination of cancer patients (Walter et al., 2012); in a different study, depletion of Tregs as well an increased activity of NK and Tcs were confirmed after metronomic administration of CY (Ghiringhelli et al., 2007).

However, all these reductions of Tregs seem to be transient and consequently, normal levels are recovered overtime, suggesting repeated administration might improve overall results (Abu Eid et al., 2016).

5.1.2 PDT and the immune response

It has been hypothesised based on previous observations that the oxidative damage induced by Photodynamic Therapy can trigger what has been coined as “immunogenic cell death” (ICD). Tumour cells killed by PDT release molecules otherwise confined in cellular compartments such as the cytosol or nucleus, i.e. damage-associated molecular patterns (DAMPs) or tumour-associated antigens (TAAs) (Castano et al., 2006; Mroz et al., 2011a; Panzarini et al., 2013; Xiaojie Wang et al., 2015). These act in a similar way as pathogen-associated molecular patterns (PAMPs) during infection. Phagocytic cells, for example macrophages, are largely present in tumours and can recognise and phagocyte these molecules, as well as release chemoattractant cytokines. The acute inflammatory process induced by PDT will likewise further attract host leukocytes to infiltrate in the tumour (monocytes, neutrophils for example). In fact, the effect of PDT in the tumour microenvironment appears to be essential in the elucidation of an immune response. One example of this is based on the quick consumption of oxygen post-PDT in combination with induced vascular shutdown. This facilitates the production of hypoxia inducible factor (HIF), identified in several myeloid cell responses, i.e. secretion of inflammatory cytokines (TNF-α, nitric oxide, IL-1),

expression of toll-like receptors, expression of co-stimulatory molecules in DCs (Garg et al., 2010). The above insinuates a connection between the innate and adaptive response of the immune system. A summary of the inflammatory process found in the tumour microenvironment after light-based treatment is shown in Figure 89.

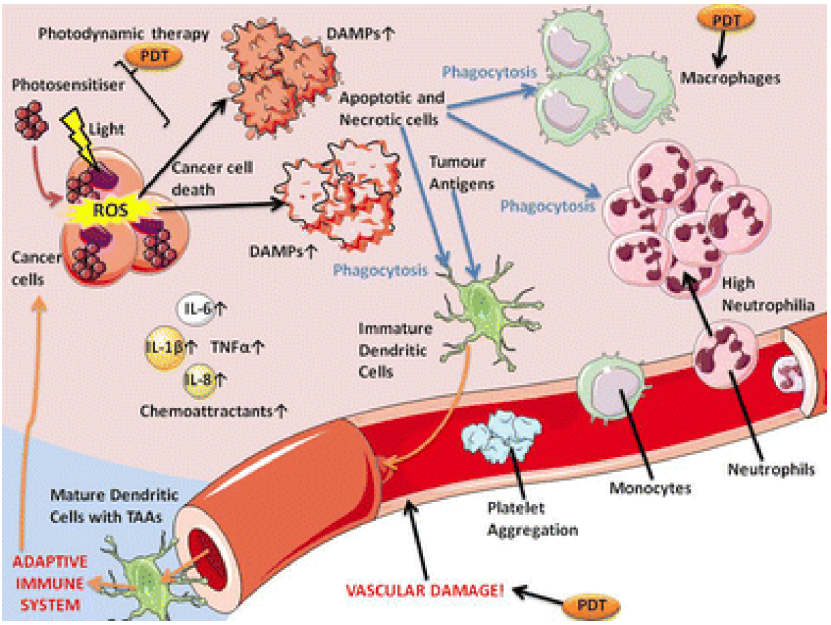

Figure 89. PDT-induced effects on tumour microenvironment, interaction with the immune system.

Image from (Garg et al., 2010) *illustrating the acute inflammation induced after PDT. The release and recognition of DAMPs by phagocytic cells after tumour cell death and later attraction of additional host immune-related cells is displayed. This involves the interaction between the innate and adaptive immune response.*

In this context, antigen presenting cells (APCs) such as circulating dendritic cells (DCs) will bind TAA via receptors present in their surface, then becoming mature and active DCs. Mature DCs will be released into in the blood stream reaching the lymph nodes, where antigen cross-presentation to naïve T-cells occurs, generating active T-cell formation as graphically displayed in Figure 90.

Despite DAMPs having been traditionally related to necrotic cells (widely considered to be pro-inflammatory and immunogenic), recent anti-cancer studies suggest the existence of additional forms of immune stimulation after specific forms of programed cell death such as apoptosis, necroptosis, etc. (Hernandez et al., 2016). In fact, the apoptotic pathway seems to have a more relevant role in the immunogenicity post PDT (Mroz et al., 2011a). Whether cell death occurs in an immunogenic manner or not seems to rely on the initiating lethal stimulus, which is not a mere correlation with cell death levels: not all anti-tumour therapies induce the release of immunogenic factors and those that do may act differently in different tumours (Kepp et al., 2009).

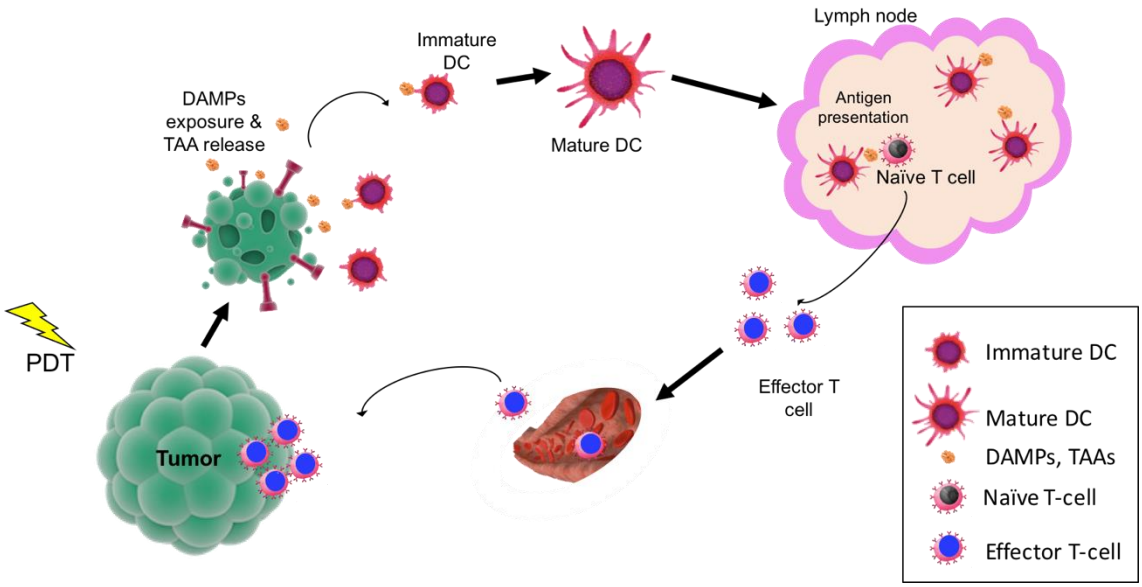

Figure 90. Release of DAMPs/TAAs by PDT-killed tumour cells, presentation of antigens and generation of effector T cells.

PDT-killed cells release intracellular DAMPs/TAAs that will be recognised by circulating dendritic cells. These migrate to the lymph nodes and stimulate naïve T-cells leading to the generation of different types of effector T-cells (i.e. helper, cytotoxic, regulatory, etc.). These cells will be released into the blood stream, reaching the tumour they are specific against, recognising it and potentially destroying it.

Among DAMPs, hydrophobicity has been suggested as a key signal capable of activating the immune system. Widely common DAMPs frequently contain hydrophobic regions, such as heat-shock proteins (HSP), High Mobility Group Box 1 (HMGB1), calreticulin, adenosine triphosphate, hyaluronan or S100 proteins. For instance, an early exposure of calreticulin in the surface of tumour treated cells has been noted before these even show apoptotic death features, which will be recognised by DCs as an “eat me” signal. Another case is the natural location of HMGB1 in the cell cytoplasm and its release into the cytosol under hypoxia in tumour cells (Hernandez et al., 2016). Especially notable is heat-shock protein 70 (HSP70), an intracellular chaperone that prevents aggregation of unfolded proteins, thereby inhibiting apoptosis. When released under cellular stress, it binds to DCs’ surface receptors, participating in their activation and maturation (Castano et al., 2006). This also reveals the double effect DAMPs may have in tumour “progression/regression”: if intracellular, these can sometimes avoid tumour cell death and even aggregate with tumour associated antigens located in the cytosol; when released they mediate T-cell response through the interaction with APCs.

There is evidence of several PDT strategies inducing a similar response as stated above. For instance, *in vitro* studies carried out on HeLa cells, proved the expression of the DAMPs calreticulin, HSP70 and HSP90 in a different manner depending on

whether cell death occurred via apoptosis or autophagy (larger release in the former) (Panzarini et al., 2014). In a similar manner, hypericin-PDT induced the release of calreticulin and HSP70 following a different pattern (Garg et al., 2012). *In vivo* studies have also verified the release of HSP70, calreticulin or HMBG1, as reported post ALA-PDT in a squamous cell carcinoma mouse model (Xiaojie Wang et al., 2015). This release of DAMPs and consequent antigen presentation are preliminary steps during the generation of immunological memory. Take as an example the observations reported back in 1999, in which the transfer of splenocytes from cured EMT6-bearing mice (previously PDT-treated) to immunocompromised mice subjects resulted in important cure rates (Korbelik and Dougherty, 1999). EMT6 mammary sarcomas are highly immunogenic and the generation of tumour-sensitised T lymphocytes has been confirmed before. For example after Photofrin-based PDT performed on immunocompetent mice, scid (these suffer from a genetic mutation that alters gene rearrangement and selection of clones, resulting in a lack of mature T and B cells in these animals) and nude (naturally thymus devoid). In this study, cures only resulted from the fully immunocompetent mice (Korbelik et al., 1996).

5.1.3 Enhancement of PDT-induced immunoprotection

The double-face or dual mechanism of the immune response noted above, has resulted in PDT combinatorial studies focusing on both: (i) an enhancement of tumour-immunogenicity to favour the increase of tumour-antigen release and (ii) recognition by antigen presenting cells (cytotoxic T cell response) and depletion of immunosuppression (regulatory T cell response) (Panzarini et al., 2013).

5.1.3.1 PDT-based vaccines

PDT has lately demonstrated the potential to exploit immunogenic cell death and therefore successfully generate protection against specific tumour antigens. For instance, DCs acquired an activated phenotype upon exposure *in vitro* to PDT-induced apoptotic tumour cells. This was concluded through the observation of characteristic morphological changes, e.g. enlarged dendrites, as well as the increased expression of surface markers CD80, CD86 and MHCII (Ji et al., 2016). Moreover, these DCs released stimulatory cytokines such as IL-2 and IFN-γ. Interestingly, in this same study control necrotic cells released the inhibitory cytokine IL-10. The *in vitro* generated DC

vaccine was used *in vivo*, showing immunoprotection to tumour challenge (Ji et al., 2016).

A different investigation generated antigen-specific $CD8^+$ cells in squamous cell carcinoma-bearing mice upon administration of *in vitro* PDT-treated cancer cells (Korbelik et al., 2007). Specifically, the expression and release of TAAs in *in vitro* PDT-treated cells was confirmed before vaccination of animal subject. In addition, post vaccination, these showed large number of cytotoxic T cells with degranulating capacity. Despite the fact that anti-tumour protection *in vivo* was systemic, the authors stated in their report a correlation concerning the therapeutic outcome and the distance between vaccination site and tumour. In fact a more efficient antigen presentation was suggested in secondary lymphoid organs located closer to the lesion. An important consideration about PDT vaccines was raised: tumour growth rate might be decisive in the generation of immunological protection post vaccination – a delay in TAA presentation after vaccination might a bad prognosis in faster growing tumours (Korbelik et al., 2007).

Overall, there are only a few examples among a wide range of studies proving the positive stimulation of APCs (namely DCs), by PDT-killed tumour cells, which in turn successfully generate fully effective cytotoxic T cells against tumours.

5.1.3.2 PDT and cyclophosphamide

In addition to enhancing antigen presentation, PDT strategies have been performed in combination with cyclophosphamide administration to tackle the impairment of T cell subsets present in the tumour microenvironment. Following this line of thought, Castano et al. performed cyclophosphamide administration before BPD-PDT to J774-bearing mice (alike EMT6 it is known to be a highly immunogenic cell line in which a specific antigen has been described) (Castano et al., 2008). Cures were only observed in animals treated with a combination of low dose CY and PDT (70%). No cures resulted from either low (50 mg/kg) or high CY (150 mg/kg) alone; yet, while the former resulted in depletion of Tregs, the latter showed a reduction in the number of all lymphocyte populations. In fact, low dose CY resulted in an enhanced survival compared to the control, as opposed to high dose CY. Furthermore, the authors confirmed the cytotoxic potential of lymphocytes removed from mice which had rejected the second challenge of tumour cells against specific tumour cells *ex vivo*

(Castano et al., 2008). Similar results were obtained from the treatment of CT26-tumour. This study also showed an PDT-induced increase in the number of Tregs measured in spleens and lymph nodes the first couple of days after light treatment (Reginato et al., 2013).

This immunoregulatory strategy has also been combined to generate PDT-vaccines. Accordingly, an *in vitro* generated vaccine was injected peritumourally in combination with cyclophosphamide in some subjects. These showed a significant improvement on the vaccine's therapeutic effect, resulting in permanent cures when injecting the immunomodulator twice. No improvement was found with CY alone, indicating it cannot be used as treatment alone. In addition to Tregs, this study also looked into the immunosuppressive effect caused by myeloid-derived suppressor cells (MDSC). It was also concluded that both cell types have an important influence before and after PDT-vaccination and should be taken into account for combinatorial therapies (Korbelik et al., 2015).

5.1.4 PCI and immunotherapy

PCI technology has also been used to develop cancer vaccines (Håkerud et al., 2015; Waeckerle-Men et al., 2013a). As opposed to PDT vaccines, in which it tumour treated cells themselves are used as vaccine, PCI vaccines benefit from PCI's intrinsic cytosolic delivery. Briefly, PCI is used to deliver tumour antigens into the cytosol of APCs (antigen presenting cells) and enhance the presentation of antigens via MHC I rather than MHC II (which does not require cytosolic processing of peptide-antigens). An example of this was the study conducted by Hakerud et al. (Håkerud et al., 2015), in which the exogenous antigen ovalbumin and the photosensitiser $TPCS_{2a}$ were coadministered *in vivo*, enabling a sufficient amount of time before illumination to ensure the uptake of the antigen in APCs. A successful generation of $CD8^+$ T cells was then concluded founded on the release of effector cytokines (IFN-γ). Besides, tumour samples revealed large infiltration of these specific cells, compared to the control tumours. Importantly, survival of these individuals was significantly enhanced compared to untreated subjects, resulting in complete tumour cures (Håkerud et al., 2015). Similar results had been previously reported by the same group in different tumour models (Håkerud et al., 2014; Waeckerle-Men et al., 2013b).

Moreover, the underlying mechanism of these PCI-vaccines was elucidated *in vitro* (Waeckerle-Men et al., 2013b). The successful entry of ovalbumin in the cytosol of

bone marrow-derived DCs was confirmed through the enhancement in the release of IFN-γ after incubating these with purified $CD8^+$ cells. High photosensitiser and light doses however seemed to be disadvantageous in the antigen-presentation process, suggesting harmful photosensitisation of DCs above a certain threshold. The expression of DC surface molecules relating to an activated DC phenotype (CD80, CD86, MHCI) was also observed after PCI photosensitisation of immature DCs (Waeckerle-Men et al., 2013b).

5.2 Aims

Based on previous reports regarding the elucidation of an immune response after PDT, the main aim of the present chapter was to assess such potential in aggressive prostate adenocarcinomas, such as the rat model investigated in the current thesis. With this main aim, several experimental objectives were addressed:

- Following the tumour eradication reported in Chapter 4 after BPD-MA-PDT, we evaluated whether light treatment had generated specific immunoprotection against MatLyLu cells in cured subjects. Accordingly, we observed the capacity of rejecting a second challenge of tumour cells in these animals, without giving any additional light treatment.
- Immunostimulants, specifically cyclophosphamide, were used as coadjuvants to light treatments so as to investigate the possible enhancement of tumour cure rates following these therapies.
- We conducted a molecular analysis of the immune response generated. Briefly, the PDT-induced immunoprotection was measured through quantification of the expression of relevant immune-related genes in formalin-fixed, paraffin-embedded (FFPE) tumour samples. In addition, immunohistochemical (IHC) observations were conducted on a subset of proteins.

The shared mechanism between PDT and PCI suggests that the immune stimulatory capacity described after light-induced photooxidation, would be likewise triggered by PCI. This, together with the larger therapeutic effect seen *in vitro* in Chapter 2 and Chapter 3 took us to consider whether PCI could lead to a possible enhancement of the stimulation of the immune system (should a PCI procedure be optimally established and followed). For these purposes, we used the same syngeneic rodent model used in Chapter 3, ensuring a fully competent immune system.

5.3 Materials & Methods

Animals and tumour models

Experiments were carried out using a subcutaneous syngeneic rat prostate adenocarcinoma tumour model (MatLyLu subline, Dunning R3327). Copenhagen rats were used throughout (100-300 g). All animal experiments were performed in compliance with the subcommittee on Research Animal Care (IACUC) of Massachusetts General Hospital in accordance with NIH guidelines (2015N000120).

As described in Chapter 4 for the generation of the primary subcutaneous tumour, $4x10^5$ MatLyLu cells prepared in 100 µl RPMI 1640 media were implanted into the right flank of syngeneic Copenhagen rats (approximately 100 g), previously shaved. A state of general anaesthesia was maintained using inhaled isoflurane throughout the procedure.

Tumour rechallenge in cured animal subjects

Animal subjects completely cured post BPD-MA PDT (as stated in Chapter 4) were given a second challenge of MatLyLu cells, as displayed in Figure 91.

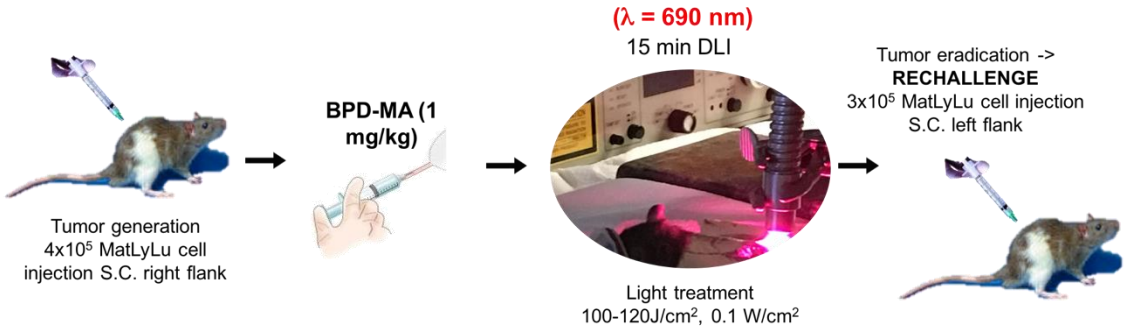

Figure 91. Timeline for tumour rechallenge in previously cured PDT-treated animals.

Tumours were generated in animal subjects around 7 days before light treatment injecting $4x10^5$ MatLyLu cells subcutaneously into the right flank of Copenhagen rats. Following a 15 minute DLI for BPD-PDT, rats were subjected to light treatment (λ = 690 nm) and tumour progression was evaluated regularly. Animal subjects showing complete tumour regression were given a second challenge of MatLyLu cells ($3x10^5$) subcutaneously into the left flank.

$3x10^5$ MatLyLu cells prepared in 100 µl RPMI 1640 media were implanted subcutaneously into the left flank of syngeneic Copenhagen rats, previously shaved. A

state of general anaesthesia was maintained using inhaled isoflurane throughout the procedure.

Chemicals and photosensitisers

$AlPcS_{2a}$ was purchased from Frontier Scientific. The stock solution was prepared by dissolving powder in sodium hydroxide, and neutralising with 0.1 M hydrochloric acid to a 1-2 mg/ml final concentration. Working $AlPcS_{2a}$ solutions were kept at 4°C and experimental concentrations were obtained diluting the stock solution in cell media to reach desirable concentrations.

Saporin (Sigma Aldrich, S9896) was dissolved in PBS to a final concentration of 0.25 mg/ml for intravenous (i.v.) injection and kept at 4ºC.

Cyclophosphamide (Sigma Aldrich, C7397) was dissolved in PBS to a final concentration of 10 mg/ml. Solutions were prepared fresh each time immediately before intraperitoneal (i.p.) injection.

Light source

LumaCare™ lamp LC-122 (LumaCare, USA) was used attached to a fibreoptic probe emitting in the spectral region 635-670 nm.

$AlPcS_{2a}$ PDT and PCI treatments in combination with cyclophosphamide

2 mg/kg of $AlPcS_{2a}$ was injected i.v. via tail vein 24 hr before light treatment. No surgical procedure was carried out during $AlPcS_{2a}$ PDT or PCI procedures. The fibreoptic attached to the lamp was placed above the skin covering the tumour, which had been previously shaved. Laser power was set to 0.1 W/cm^2 at a light irradiance of 100 J/cm^2. During light treatments a state of general anaesthesia was maintained using inhaled isoflurane throughout the procedure. Buprenex (0.05-0.1 mg/kg) was administered subcutaneously prior to the procedure and the days following if the animals were found in pain or distress.

In animals belonging to PCI groups, 250 µg/kg saporin was administered 1 hr prior to light.

Early investigations in Copenhagen rats concerning cyclophosphamide (CY) were carried out injecting 50 mg/kg CY intraperitoneally (i.p.) four times: twice before light

treatment and twice after light treatment. Due to excessive toxicity this was later on reduced to two injections: 24 hr and 48 hr before light treatment.

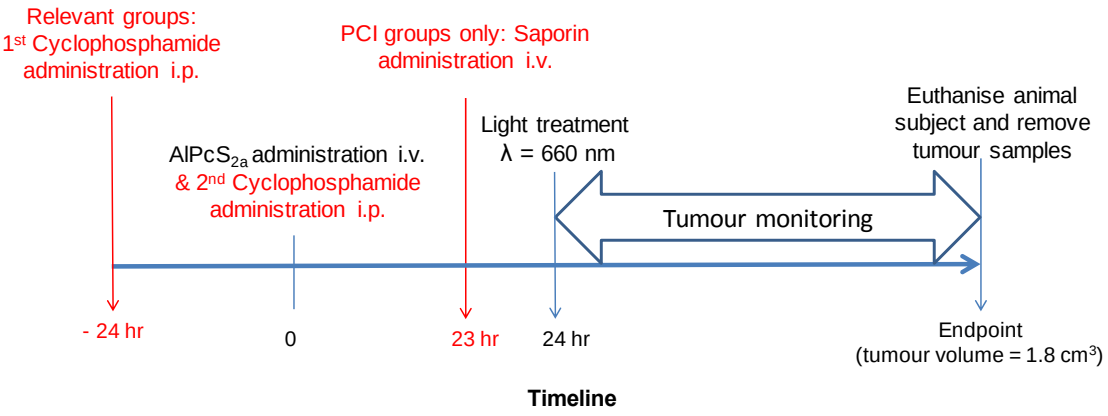

Figure 92. Timeline for $AlPcS_{2a}$ treatments combined with immunostimulants (CY) in vivo.

$AlPcS_{2a}$ solutions were injected i.v. via tail vein allowing a 24 hr DLI. Administration of cyclophosphamide was performed twice: 24 hr and 48 hr before light treatment. 1 hr before light treatment, 250 μg/kg saporin was administered i.v. via tail vein to animal subjects belonging to the PCI group. After light treatment, animals were monitored regularly and sacrificed when tumour volume reached a humane endpoint (volume = 1.8 cm^3)

Measurement of emission of fluorescence in animal subjects displaying "black" draining lymph nodes

A similar procedure to chemical extraction described in Chapter 4 was followed with control and black-appearing inguinal lymph nodes removed from rat subjects. Tissue was immersed in 3 ml Solvable™ (PerkinElmer) and placed in a water bath at 50°C until completely dissolved. Right before measuring fluorescence, samples were allowed to cool to room temperature and transferred to a quartz cuvette.

The emission of fluorescence from black and control lymph node-tissue were compared to an $AlPcS_{2a}$ solution of known concentration (all prepared in Solvable™). Fluorescence was measured 610-750 nm, setting excitation at 640 nm. Measurements were performed using a Horiba Jobin Yvon Fluoromax-3 Fluorescence Spectrometer (Horiba Scientific).

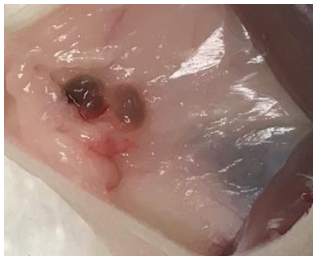

Figure 93. Example of inguinal lymph nodes upon co-administration of $AlPcS_{2a}$ and cyclophosphamide.

Animals exposed to $AlPcS_{2a}$ and cyclophosphamide presented blackened inguinal lymph nodes which were assessed through H&E and emission of fluorescence, compared to a control lymph node sampled from a non-treated animal.

Standard histological analysis of tumour samples

Tissue samples removed from Copenhagen rats were washed in PBS directly after sampling and immersed in 10% formalin during 24-48 hr depending on the size of the specimen. Samples were then processed following a standard tissue processing protocol and embedded in paraffin. Paraffin blocks were trimmed and started collecting sections once whole sample was accessible. 4-5 µm thickness sections were cut from each sample. H&E staining was performed following a standard protocol. Sections were then examined on a Hamamatsu Nanozoomer Digital Pathology (NDP) scanner (Hamamatsu Photonics K.K., UK), which recorded whole section high resolution images.

Immunohistochemistry staining

Immunohistochemistry staining was performed by UCL Advanced Diagnostics.

- Caspase-3 staining: see detailed description in Chapter 4, 4.3 Materials & Methods.
- CD3 staining: CD3 primary antibody was purchased from Dako (Cat. A0452). This is a rabbit polyclonal antibody which detects the CD3ε chain on surface T cell receptors. Antigen retrieval was achieved at pH 6 during 30 minutes at 99°C. An epitope retrieval solution from Leica Biosystems (AR9961) was used. Staining was performed on a Leica Bond III automated immunostainer and detection was carried out using Leica Bond Polymer Refine DAB detection system (Leica DS9800) as follows: incubation with the primary antibody was allowed during 15 minutes at room temperature (1/100 dilution) followed by an 8-minute incubation with an anti-rabbit secondary antibody.
- Bcl-3 staining: Bcl-3 primary antibody was purchased from Abcam (Cat. Ab49470). This is a mouse monoclonal antibody (1E8 clone) which detects A 200 amino acid truncate of Bcl-3. Antigen retrieval was achieved at pH 9 during 20 minutes at 99°C. An epitope retrieval solution from Leica Biosystems (AR9640) was used. Staining was performed on a Leica Bond III automated immunostainer and detection was carried out using Leica Bond Polymer Refine DAB detection system (Leica DS9800) as follows: incubation with the primary antibody was allowed during 15 minutes at room temperature (1/100 dilution). Slides were then blocked with peroxidase and an additional anti-mouse post-primary antibody was applied for 8 minutes. Finally, an 8-minute incubation with an anti-rabbit secondary antibody was completed.

- Bcl-2 staining: Bcl-2 primary antibody was purchased from Leica (Cat. NCL-L-bcl-2). This is a mouse monoclonal antibody (bcl-2/100/D5 clone) which detects Bcl-2 oncoprotein. Antigen retrieval was achieved at pH 9 during 30 minutes at 99°C. An epitope retrieval solution from Leica Biosystems (AR9640) was used. Staining was performed on a Leica Bond III automated immunostainer and detection was carried out using Leica Bond Polymer Refine DAB detection system (Leica DS9800) as follows: incubation with the primary antibody was allowed during 15 minutes at room temperature (1/50 dilution). Slides were then blocked with peroxidase and an additional anti-mouse post-primary antibody was applied for 8 minutes. Finally, an 8-minute incubation with an anti-rabbit secondary antibody was completed.
- PD-L1 staining: PD-L1 primary antibody was purchased from Cell Signaling Technology (Cat.13684). This is a rabbit monoclonal antibody (E1L3N clone) which detects endogenous levels of PD-LA protein. Antigen retrieval was achieved at pH 9 during 30 minutes at 99°C. An epitope retrieval solution from Leica Biosystems (AR9640) was used. Staining was performed on a Leica Bond III automated immunostainer and detection was carried out using Leica Bond Polymer Refine DAB detection system (Leica DS9800) as follows: incubation with the primary antibody was allowed during 15 minutes at room temperature (1/200 dilution). Slides were then blocked with peroxidase and an additional anti-mouse post-primary antibody was applied for 8 minutes. Finally, an 8-minute incubation with an anti-rabbit secondary antibody was completed.

Laser capture microdissection (LCM) of ROIs differentially stained with anti CD3

Samples were stained with an anti CD3 antibody as detailed above. Differentially CD3-stained regions were identified on each section and used as reference to dissect a sufficient amount of sections (4 - 5 µm) which would produce enough RNA. The size of each section would determine the number of sections required (4 – 8).

Before microdissection, Cresyl Violet staining was conducted so as to facilitate observation of slides under the microscope: a 0.1% solution of Cresyl Violet was prepared in distilled water and slides were immersed in a Coplin jar containing the dye solution for 2 minutes, then allowed to dry.

Cresyl violet-stained sections were delineated based on the ROIs established in CD3 staining so as to perform an independent analysis on the samples. This was performed on a Zeiss PALM MicroBeam Laser Capture microscope. Laser capturing of ROIs

however, was proved inefficient in our research group (resulting in insufficient RNA yields) and instead, laser cutting was used to delimit our ROIs by removing immediately adjacent unwanted areas and dissecting ROIs manually using a needle (see Figure 94).

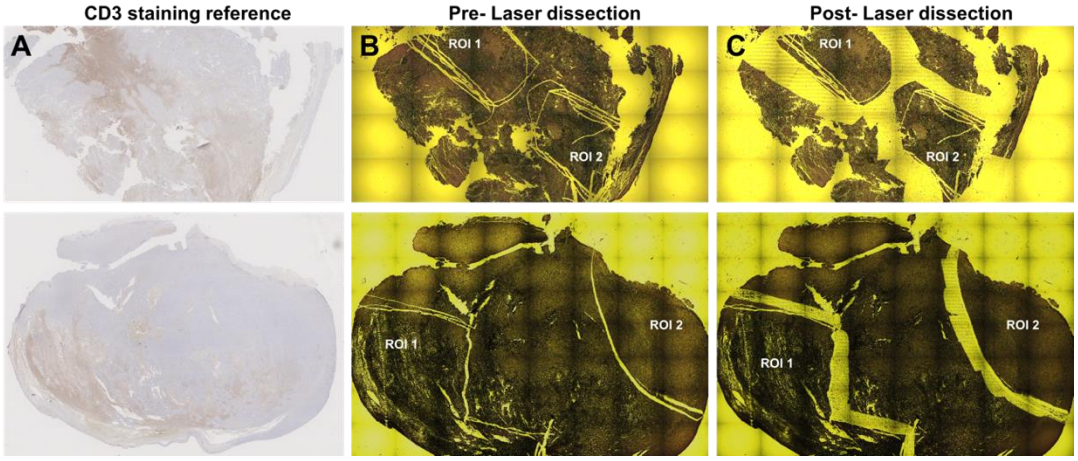

Figure 94. Microdissection of Cresyl Violet stained slides on a laser capture microscope.

(A)Tumour samples were stained with anti CD3, identifying on these differentially stained regions of interest (ROI). ROI 1 corresponds to areas of the tumour slide appearing with an overall brown stain; ROI 2 corresponds to areas of the tumour section presenting discretely stained cells. (B) Tumour samples were stained with Cresyl Violet and ROI were identified on a conventional visible light microscope. (C) Using a laser capture microscope, the areas adjacent to the ROIs identified on the CD3-stained slide, were removed to ensure no cross-contamination between differentially stained ROIs would occur during RNA extraction carried out next. Images shown at 1.25X magnification.

RNA extraction from FFPE samples

RNA extraction was conducted using a RecoverAll™ Total Nucleic Acid Isolation (Ambion, Life Technologies, AM1975) from 4-5 µm FFPE tumour sections previously microdissected. A modified protocol from Ambion RecoverAll™ kit was followed with addition of Turbo DNase step to the extracted RNA at the end.

Once the extraction had been completed, RNA concentration and purity were measured in a DS-11 FX nanodrop spectrophotometer/Fluorometer (DeNovix Inc.). Samples resuting in a 260/280 ratio 1.8 – 2.5 together with a 230/260 ratio above 1, were considered good enough quality to continue with cDNA synthesis.

An additional purification step was performed on samples exhibiting large organic contamination (not meeting the above 260/280, 230/260 ratio requirements) or insufficiently high RNA concentration using RNA Clean & Concentrator 5/25 (Zymo Research). A protocol provided by the manufacturer was followed.

cDNA synthesis from RNA template

Single stranded cDNA was synthesised from RNA previously extracted (detailed above) using a SuperScript first-strand Synthesis System for RT-PCR (Invitrogen, Cat. 11904-018). RNA samples were completely defrosted prior to use.

Two different approaches were followed for cDNA synthesis:

- Poly-A specific: poly-A tail present in all post transcriptional mRNA can be recognised by oligo (dT) primers, resulting in the non-gene specific reverse transcription of all mRNA.
- Gene-specific priming: FFPE samples can present highly degraded RNA due to fixation and processing of tissue samples, often resulting in the loss of poly-A tails. Therefore, reverse primers whose sequences had been designed to be complementary to specific genes were also used to reverse-transcript mRNA sequences containing our genes of interest (see Table 10 below for primer sequences)

A mix solution was prepared combining RNA (100 ng), oligo (dT) (50 pmol) or primers (1 pmol) in nuclease-free water (NFW), and dNTP (10 nmol).

Gene	Primers sequence	Biological Role
*18S ribosomal RNA (housekeeping)	AGCGAGGTGGTTGATTCTTG (F) TCGCTCCACCAACTAAGAAC (R)	18S ribosomal RNA.
Survivin	GTTCAGACCGAGCAAGAG (F) CAAGTCTGGCTCGTTCTC (R)	Member of the inhibitor of apoptosis family (IOA). It has multiple roles preventing apoptosis and promoting proliferation, for example inhibiting members or the caspase cascade.
CD3ε	AAGGTGCTGTCTGTCTTGAG (F) TTCCACGACAGACAGAACTC (R)	Component of the CD3 complex, part of the T cell receptor. It mediates processes occurring during T cell activation
Lysosomal Associated Membrane Protein 1 (LAMP1)	TGTCACCCCAAACACCCGTG (F) ACAGTGGGGTTTGTGGGCAC (R)	Transmembrane glycoprotein highly expressed in cytotoxic T cells. Involved in signalling transduction for several characteristic functions of this T cell subset.
Granzyme-A (GzmA)	CCCAGTATCGTACCTATCCC (F) GGGTCATAGCATGGATAGGG (R)	Highly abundant protease in the cytosol of effector T cells such as cytotoxic T cells and NK cells. When released during stimulation of the immune system, it promotes target cell death in an apoptosis-independent manner.
Perforin	TACTTCACCCACGGCATCAAC (F) ATGAAGTGGGTGCCGTAGTTG (R)	Highly abundant protease in the cytosol of effector lymphocytes. It is involved in granule-dependent cell death causing pore formation by integrating in target cell membranes. This promotes cytolysis and apoptosis via an enhancement in the uptake of granzymes.
Tumour Necrosis Factor Apoptosis-Inducing Ligand Receptor (TRAIL R)	ACTCGTTGCGTCTGAGCGACA (F) TGAGCAACGCAGACTCGCTGT (R)	Surface receptor containing an intracellular death domain. It can be activated by TNF-related pro-apoptotic ligands, then transducing an apoptotic signal.
B cell Lymphoma 3-encoded protein (Bcl-3)	TCGCCGATACAATAAGACCTG (F) AGCGGCTATGTTATTCTGGAC (R)	Transcriptional co-activator that activates associating to NF-κB homodimers. Its expression can be induced via an autoregulatory loop induced by NF-κB, mediated by the nuclear permanence of p50.

B cell CLL/ Lymphoma 2 (Bcl-2)	GTGTACTGGGGTGGCTTGAGTTTCT (F) CACATGACCCCACCGAACTCAAAGA (R)	Mitochondrial membrane protein involved in blockage of apoptosis.
Forkhead Box P3 (FOXP3)	CACCTTTGGAGTGAAGAACCAG (F) GTGGAAACCTCACTTCTTGGTC (R)	Transcriptional regulator with an essential role in suppression exerted by T regs. Assists the maintenance of homeostasis in the immune response.
Programmed Cell Death Protein 1 Receptor (PD1)	CAGGGATCTTCACGGGTTGT (F) GTCCCTAGAAGTGCCCAACA (R)	Immunoglobulin surface protein involved in the regulation of T cell function in tolerance and immunity. It can inhibit effector T cell functions binding to its ligand, possibly inducing cell death.
Programmed Cell Death Ligand 1 (PDL1)	TCGAAGAGGAGAGAGAACCT (F) AGCTTCTCCTCTCTCTTGGA (R)	Inhibitory ligand secreted by T or B cells among others, as well as several tumour cells. Interaction with its receptor inhibits activation and cytokine production of T cells, hence resulting in an escape to the immune response.
Tumour Necrosis Factor Receptor Superfamily (FAS)	CCACGTTCCCAGTGTCACAA (F) GGTGCAAGGGTCACAGTGTT (R)	Surface receptor involved in apoptotic-mediated cell death via the caspase cascade, initiated upon caspase-8 proteolytic activation. It has been related to immune peripheral tolerance, causing T cell suicide.
Tumour Necrosis Factor Receptor Superfamily Ligand (FASL)	GTCTCCAACCTGTCCCTTCTT (F) CAGAGGTTGGACAGGGAAGAA (R)	Cytokine binding to FAS. Possible participation in apoptosis and development of cytotoxic T cells.

Table 10. Sequences of primers used for cDNA synthesis and qRT-PCR.

(R) Reverse (anti-sense) primer sequence. (F) Forward (sense) primer sequence.

Control samples were prepared replacing RNA with NFW. Each RNA sample mix above prepared was incubated at 65 ºC for 5 minutes in a 2720 Thermal Cycler (Applied biosystems, Life Technologies) covered by a heated lid, and then placed on ice for 2 minutes. Meanwhile, a reaction mix was prepared containing: RT buffer (10X), MgCl2 (25 mM), DTT (0.1 mM), RnaseOUT and SuperScript retrotranscriptase enzyme, as provided by the manufacturer. This reaction mixture was added into each RNA sample mix the incubated at 50ºC for 50 minutes and at 85ºC for 15 minutes covered by the thermal cycler´s heated lid. Samples were then cooled on ice during 5 minutes. Finally, RNase H was added and tubes were incubated at 37ºC for 20 minutes covered by the thermal cycler´s heated lid. When finished, cDNA was kept at -20ºC until use.

Real time polymerase chain reaction (qRT PCR) for relative quantification of specific gene expression

iTaq™ Universal SYBR® Green Supermix (BioRad Cat. 1725121) was used to quantify the expression of specific genes in qRT PCR.

Reaction mixtures were prepared independently for each gene's set of primers (reverse and forward) in NFW combining: primers (5 pmol of each reverse/forward) for genes indicated in Table 10 and SYBR Green Supermix (1X). 1 µl of the previously synthesised cDNA solution (including controls) was plated in triplicate for each gene and then 9 µl of each primer reaction mixture were added.

A real time thermal cycler CFX Connect™ Real-Time PCR Detection System (Bio-Rad) was used to amplify and detect fluorescence emission from the SYBR® Green probe. SYBR® Green is a fluorescent dye binding to double-stranded DNA by intercalating between the bases. Fluorescence can be measured at the end of the amplification cycles to quantify the relative expression of genes compared to a constitutively expressed gene (housekeeping), 18S in our study. This resulted in ΔCt values for each gene assessed in every case.

NOTE: Ct is the threshold cycle or number of amplification cycles after which fluorescence emission passes a threshold cycle (SYBR® Green). This baseline was set up in our case within the exponential region of the amplification of our house keeping gene, 18S. ΔCt is the difference in the number of amplification cycles required to detect fluorescence emission between the house keeping gene and the gene of

interest. The larger ΔCt value is, the higher number of cycles are required to detect the gene of interest, concluding a lower expression in the cell and vice versa.

Statistical analysis

Statistical analysis was performed using GraphPad Prism 6.

For tumour growth rate analysis at least 3 animal subjects were used in each group ($n \geq 3$) but for $AlPcS_{2a}$-PDT (with and without cyclophosphamide). In these group, 2 animals died during light treatment due to anaesthesia overdose. Therefore, $n = 2$ was used for these. In RT-qPCR experiments, each data point was the result of experiments carried out in triplicate but for $AlPcS_{2a}$-PDT (with and without cyclophosphamide) tumour samples ($n = 2$ as stated above). Each of these repeats is the result of the quantification of gene expression in triplicate from each cDNA sample.

A two-way ANOVA followed by Bonferroni *post hoc* multiple testing correction was used to in those cases where at least 3 animals were used ($n \geq 3$). In comparative analysis involving $n = 2$ groups, a one-way ANOVA between matched groups followed by Bonferroni *post hoc* was performed.

Significance level of $p < 0.05$ (*p = 0.05 to 0.01; **p = 0.01 to 0.001; ***p = 0.001 to 0.0001)

5.4 Results

5.4.1 Cyclophosphamide as a co-adjuvant to AlPcS$_{2a}$-based therapies

During our early investigations with cyclophosphamide, animals received 4 injections of 50 mg/kg (i.p.): two were performed before light treatment and two post illumination. These resulted in excessive systemic toxicity in the animals. For instance a significant loss of weight was noted compared to the initial baseline, which animal subjects did not recover as displayed in Figure 95A. These subjects died 9 days after the first injection of CY.

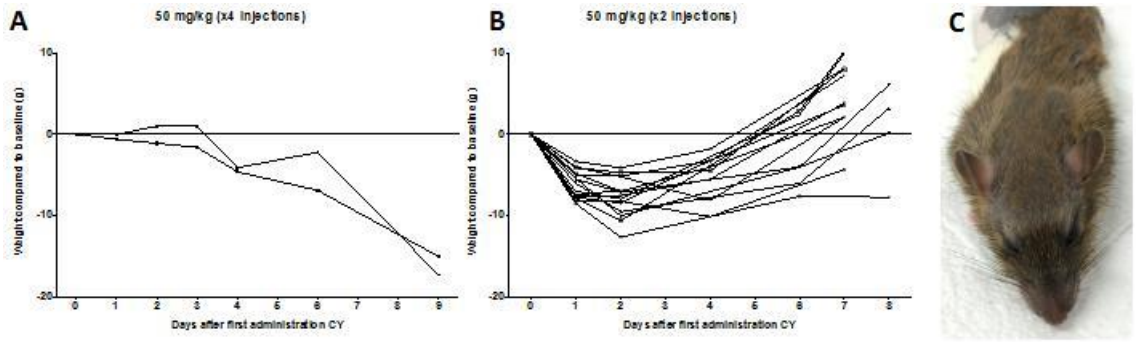

Figure 95. Effect of cyclophosphamide in Copenhagen rats' welfare.

(A) Weight loss observed in animal subjects after 4 i.p. injections of CY (50 mg/kg each), 2 before light treatment and 2 after light treatment (at 24 hr and 48 hr). (B) Weight loss observed in animal subjects after 2 i.p. injections of CY (50 mg/kg each) before light treatment (24 hr and 48 hr). Each data point in (A) and (B) corresponds to individual animal subjects' weight. (C) Change in fur colour and thickness in animal subjects after i.p. injections of CY (50 mg/kg).

Consequently, only 2 injections (50 mg/kg i.p.) of the immunoadjuvant (CY) were given in experiments carried out from then on. Although an initial weight loss was also seen in this group of animals soon after the first injection of CY (Figure 95B), this weight was recovered in all subjects (data only shown up to 8 days after the first injection). In addition, the fur in all animal subjects CY-injected became lighter in colour and thinner as can be noticed by the visibly evident differences in the rat's face shown in Figure 95C.

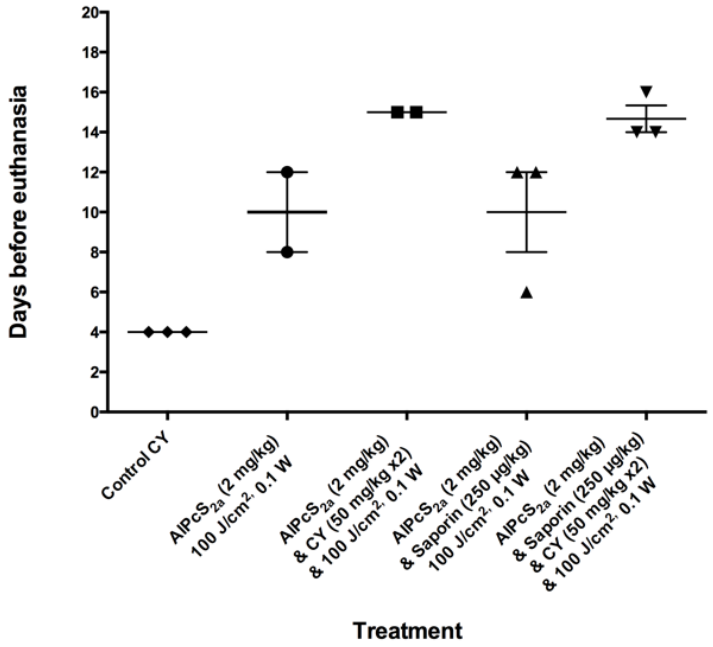

Figure 96. Tumour growth after $AlPcS_{2a}$-based treatment in combination with cyclophosphamide until end point.

Scatterplot of days between light delivery to tumours and euthanasia of animal subjects based on tumour size endpoint. Each symbol represents an independent animal subject. Data shown as mean ± SEM (n = 2 or 3).

Non-significant differences were found between groups with and without CY. However, the administration of cyclophosphamide in combination with $AlPcS_{2a}$-based light treatments (both PDT and PCI) resulted in a delayed tumour growth trend as indicated by the average 10-day endpoint after $AlPcS_{2a}$-PDT/PCI (also shown in Figure 85 in Chapter 4) as opposed to the average 15-day endpoint when CY was co-administered Figure 96). As noted in Chapter 4, the presence of saporin did not seem to alter tumour growth during PCI. In addition, animals subjected to cyclophosphamide injections alone did not experience delay in tumour growth and these were removed as soon as 4 days after the first CY injection. Again, this was not significantly different to tumour growth seen in any of the animals exposed to light-based treatments. Yet, there was a 6-day difference on average between tumour removal in CY control animals and the earliest euthanasia performed in animals belonging to any light-based treatment.

As described in Chapter 4 for $AlPcS_{2a}$-based treatments in the absence of CY, we analysed tumour samples removed from animals which had been also injected with CY, shown in Figure 97, Figure 99 and Figure 98. H&E staining did not reveal any particularly noteworthy events induced by CY neither in PDT (Figure 97) nor PCI (Figure 99) tumours. Similarly to previous tumour samples shown in Chapter 4, affected areas within viable regions were identified in the tumours we are describing now. These regions exhibited different properties (i.e. size and distribution) between

samples belonging to the same group, showing again the lack of reproducibility when analysing samples through standard H&E staining. Evaluating the magnification of affected regions, infiltrating leukocytes were also recognised alike reported in section 4.4.2.3 in Chapter 4. These cells with characteristic morphological features are highlighted with red and green arrows in Figure 97 and Figure 98. Necrosis was also detected in tumours as suggested by disintegrated cellular membranes and regions showing loss of structure in the tumour section. In addition, extended zones lacking an intense blue stain characteristic of the nuclear organelle, indicate the remnants of cytoplasmic compartments from previously existing cells.

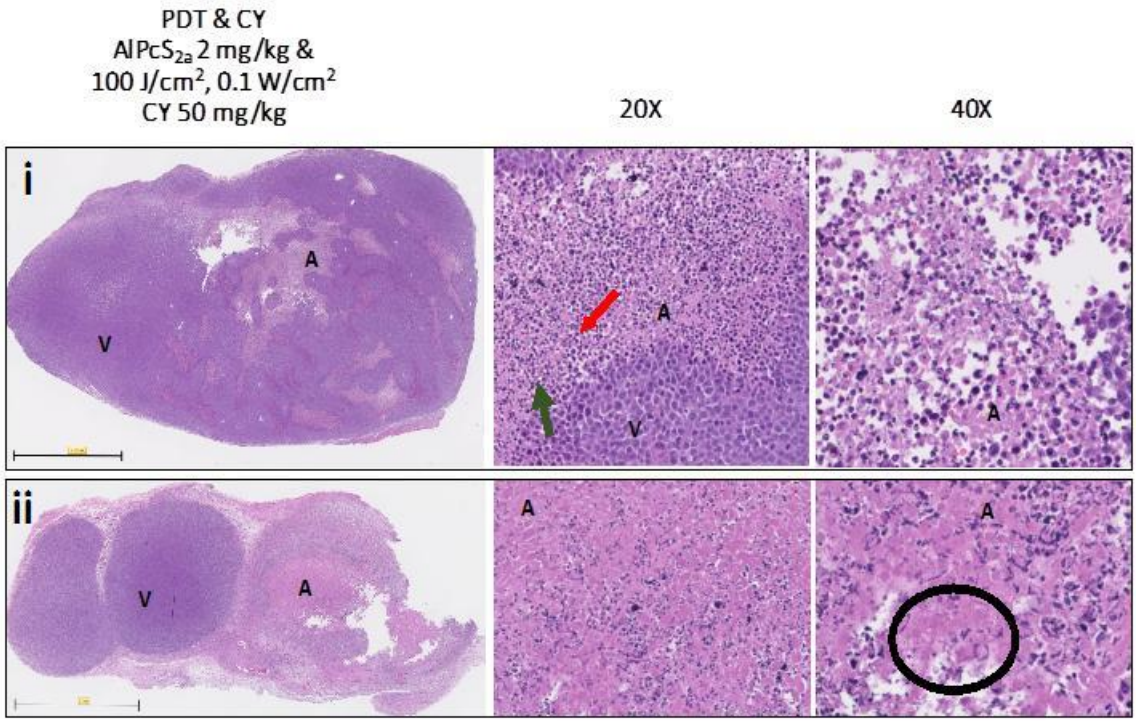

Figure 97. AlPcS$_{2a}$-PDT surface-light treatment (24 hr DLI) in combination with cyclophosphamide to subcutaneous prostate tumours and detail of H&E staining.

2 mg/kg AlPcS$_{2a}$ was injected i.v. via tail vein to Copenhagen rats bearing subcutaneously grown prostate tumours (i, ii). 50 mg/kg cyclophosphamide was injected i.p. 48 hr and 24 hr before light delivery. 24 hr after administration of AlPcS$_{2a}$, light treatments were carried out at a fluence rate of 100 J/cm^2 and 0.06-0.1 W power. Once sampled, tumours were H&E stained and examined on a Hamamatsu Nanozoomer Digital Pathology (NDP) scanner. 20X and 40X magnifications are shown. A: affected tumour area, V: viable tumour area. Green and red arrows indicate different infiltrating cell types; necrotic cells highlighted within a black circle. Scale bars shown as 2 mm.

An interesting observation was made from Figure 98ii. In this specific tumour sample, the affected area appeared in between 2 viable tumour regions in the slide: this area area might have been the most damaged region after exposure to light, experiencing tumour regrowth sidewise from viable cells located in the edges of the region.

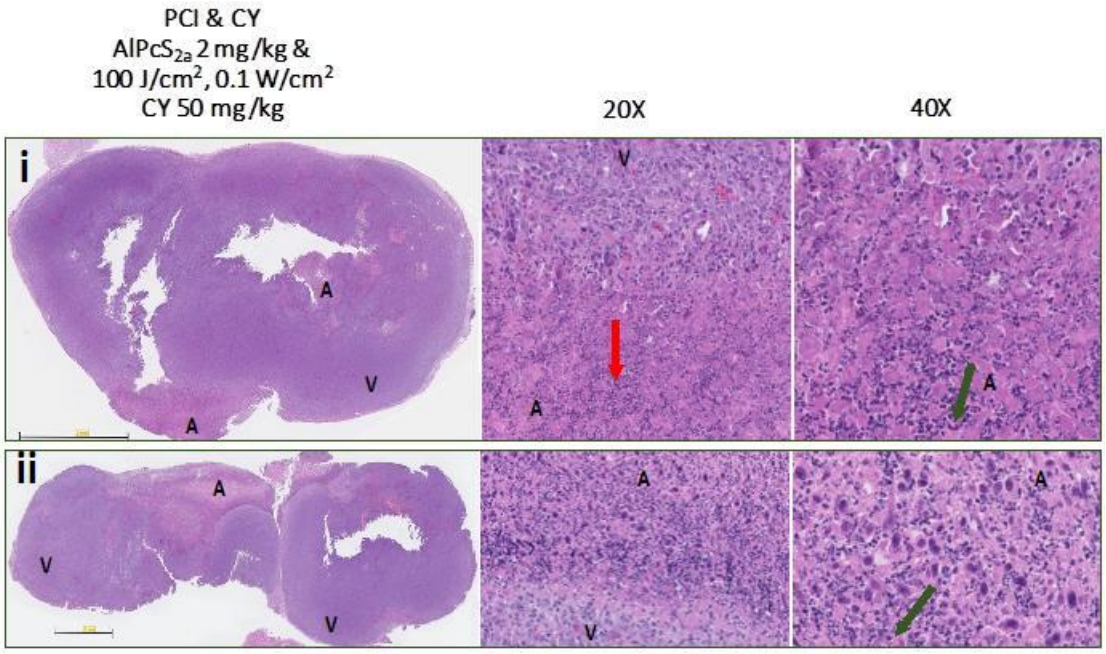

Figure 98. AlPcS$_{2a}$ & saporin -PCI surface-light treatment in combination with cyclophosphamide to subcutaneous prostate tumours (24 hr DLI) and detail of H&E staining.

2 mg/kg AlPcS$_{2a}$ was injected i.v. via tail vein to Copenhagen rats bearing subcutaneously grown prostate tumours (i, ii). 250 µg/kg saporin was injected i.v. via tail vein 1 hr prior to light delivery. 50 mg/kg cyclophosphamide was injected i.p. 48 hr and 24 hr before light delivery. 24 hr after administration of AlPcS$_{2a}$, light treatments were carried out at a fluence rate of 100 J/cm^2 and 0.06-0.1 W power. Once sampled, tumours were H&E stained and examined on a Hamamatsu Nanozoomer Digital Pathology (NDP) scanner. 20X and 40X magnifications are shown. A: affected tumour area, V: viable tumour area. Green and red arrows indicate different infiltrating cell types. Scale bars shown as 2 mm.

Again, like stated in sections in to previous chapters, apoptosis was assessed in representative samples of CY groups (see Figure 99). A larger number of apoptotic cells were found in these compared to the PDT or PCI alone samples shown in Figure 84 in Chapter 4. Clumps of dying cells are observed in Figure 99 upon co-administration of CY, revealed by caspase-3 staining. Infiltrating cells were also found in the two tumour samples shown.

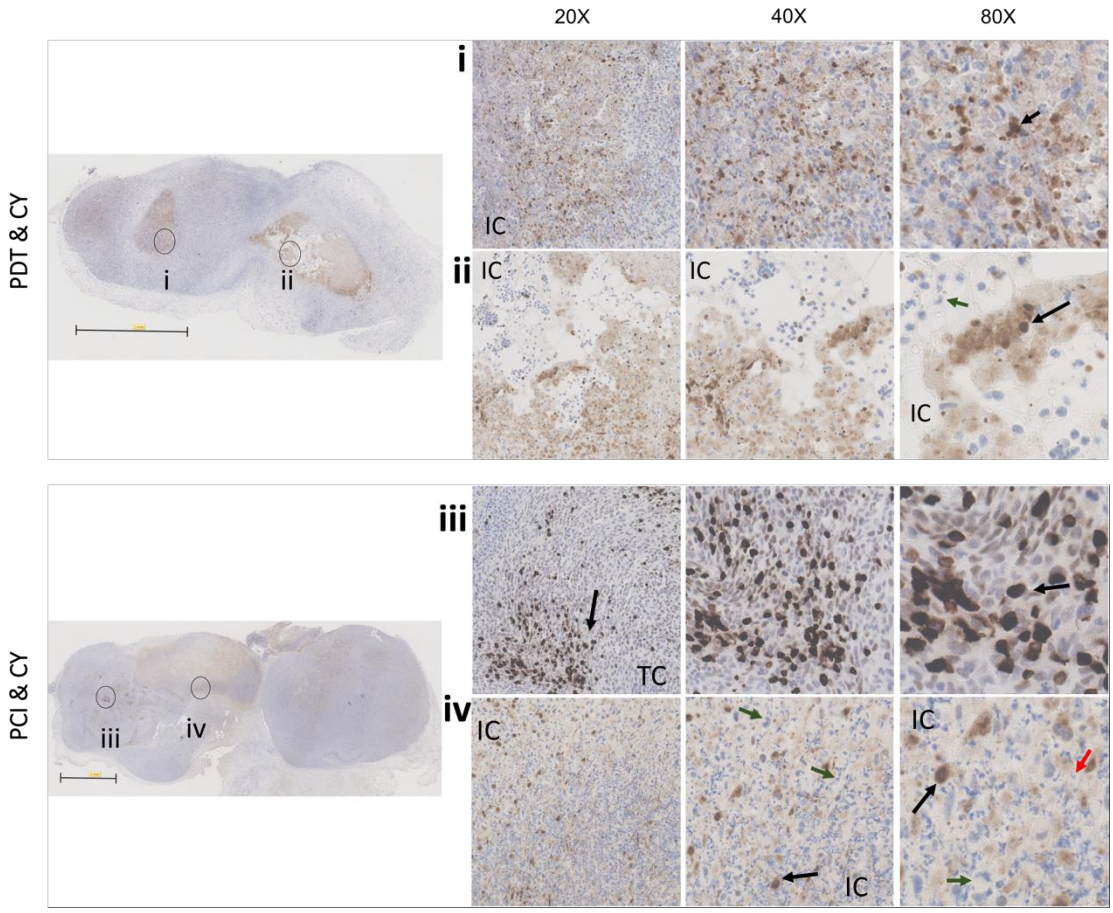

Figure 99. Evaluation of apoptosis after AlPcS$_{2a}$-PDT/PCI surface light treatment in combination with cyclophosphamide to subcutaneous prostate tumours.

(i, ii) PDT, (iii, iv) PCI combined with CY samples. 2 mg/kg AlPcS$_{2a}$ was injected i.v. via tail vein to Copenhagen rats bearing subcutaneously grown prostate tumours. 50 mg/kg cyclophosphamide was injected i.p. 48 hr and 24 hr before light delivery. 24 hr after administration, light treatments were carried out at a fluence rate of 100 J/cm^2 and 0.06-0.1 W power. In PCI groups 250 µg/kg saporin was injected i.v. via tail vein 1 hr prior to light delivery. Once sampled, tumours were stained with anti cleaved caspase-3 (D175) and examined on a Hamamatsu Nanozoomer Digital Pathology (NDP) scanner. Same tumour samples as shown in Figure 97ii and Figure 98ii. 20X, 40X and 80X magnifications are shown. TC: tumour cells; IC: infiltrating cells. Green and red arrows indicate different infiltrating leucocytes; black arrows indicate apoptotic cells. Scale bars shown as 2 mm.

5.4.1.1 Blackening of inguinal lymph nodes upon combination of AlPcS$_{2a}$ with cyclophosphamide

During the experiments carried out injecting CY as an immunostimulant to AlPcS$_{2a}$-based treatments, we found that draining lymph nodes removed from the inguinal chain of animal subjects, had acquired black pigmentation both in the contralateral and ipsilateral side to tumour implantation as shown in Figure 100A. This was consistent in all animals treated with both AlPcS$_{2a}$ and CY, regardless of the presence of saporin.

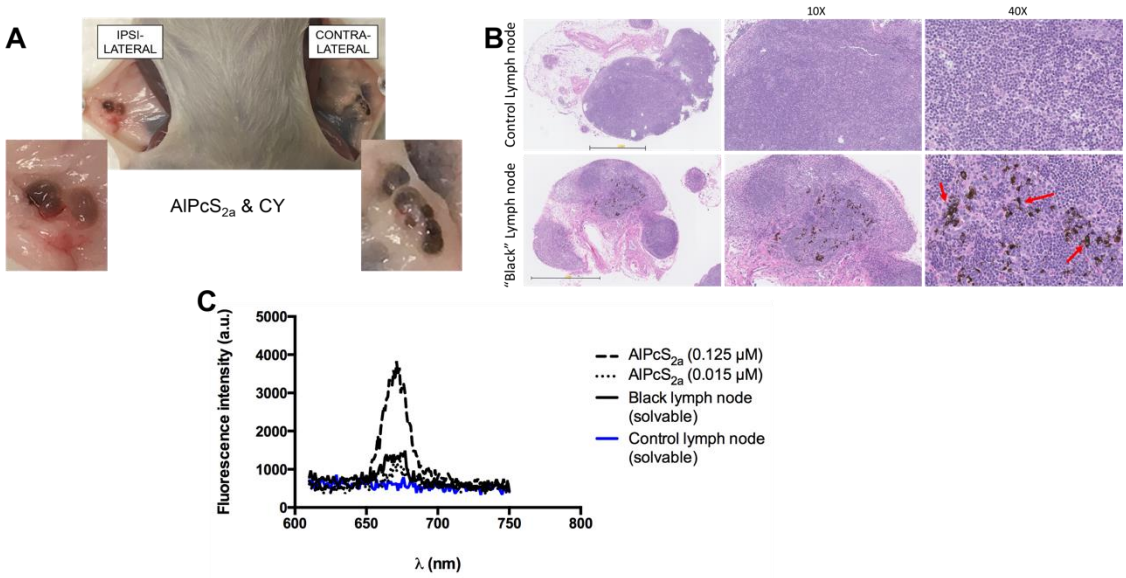

Figure 100. Blackening of inguinal lymph nodes upon coadministration of $AlPcS_{2a}$ and cyclophosphamide.

(A)Ipsilateral and contralateral draining inguinal lymph nodes in animals exposed to both $AlPcS_{2a}$ and cyclophosphamide. (B) Once sampled, black-appearing and control lymph nodes were H&E stained and examined on a Hamamatsu Nanozoomer Digital Pathology (NDP) scanner. 10X and 40X magnifications are shown. Red arrows indicate black aggregates within black-appearing lymph node tissue. Scale bars shown as 1 mm. (C) Emission of fluorescence of black lymph node sample compared to control lymph node sample and $AlPcS_{2a}$ solution of known concentration. Solvable™ was used to dissolve tissue samples as well as to prepare the $AlPcS_{2a}$ solution.

A standard H&E procedure on these lymph node samples revealed the presence of black aggregates as indicated with red arrows, which were inexistent in healthy lymph nodes removed from control individuals as displayed in Figure 100B.

In solution, $AlPcS_{2a}$ acquires a blue tonality. Therefore, suspecting that these could be $AlPcS_{2a}$-based aggregates, we dissolved the "blackened" and control lymph nodes in solvable and measured the emission of fluorescence of the solution, comparing it to $AlPcS_{2a}$ solutions of known concentration. As shown in Figure 100C, the emission of fluorescence of black lymph nodes in solution coincided with that exhibited by a solution of $AlPcS_{2a}$ of around 0.015 μM, exhibiting an excitation peak around 665 nm.

5.4.2 Second tumour challenge to BPD-MA-cured Copenhagen rats

As stated in Chapter 4, 18% (4/22) of the animal subjects treated with BPD-MA PDT were completely cured from the initial tumour challenge (4×10^5 MatLyLu cells) and were then given a second challenge of the same cells. So as to avoid an overwhelming

effect on the immune system and thus enable a successful rejection of these tumour cells, this second tumour challenge was slightly lower than initially performed (3 x 10^5 cells). However, none of the rechallenged individuals successfully rejected their 2nd injection of MatLyLu cells and tumour regrowth was noted in all individuals.

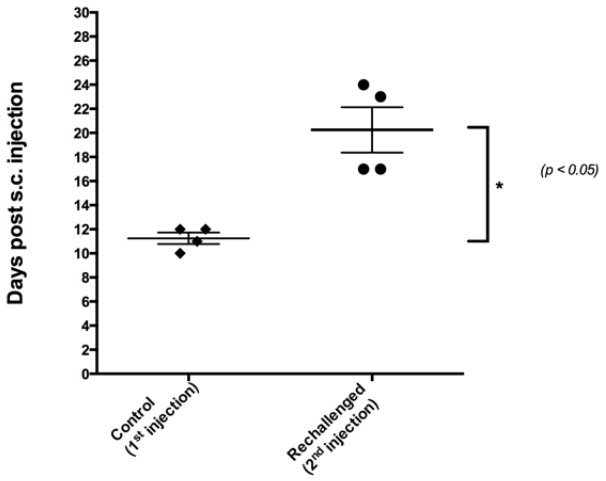

Figure 101. Tumour growth after initial tumour challenge or second challenge in cured animals, until end point.

Scatterplot of days between the first injection of tumour cells or the second injection of tumour cells in previously cured animal subjects, and euthanasia based on tumour size endpoint. Each symbol represents an independent animal subject. Data shown as mean ± SEM; significance p < 0.05

Figure 101 displays the endpoint delay experienced by rechallenged animal subjects compared to untreated controls exposed to the initial MatLyLu tumour challenge. Whereas tumours reached the volume endpoint an average of 11 days after injection, the implantation of cancer cells in cured animals experienced a delay in 11 days on average (22 days overall) to reach the volume endpoint (Figure 101), and this difference was significantly different.

Despite the fact that rechallenged tumours had not been directly exposed to light-based treatments, the histological analysis of these tumour samples revealed affected regions (Figure 102) akin to previous observations arising from light treated tumours (Figure 71, Figure 72, Figure 79 and Figure 84). This is especially noteworthy in Figure 102ii, in which a large surface area appears to be damaged compared to Figure 102i. These areas are also largely composed of infiltrating leukocytes, highlighted with arrows in the micrographs, as already described for other tumour samples (i.e. Figure 97 or Figure 98). Moreover, while the affected area seems to be localised in a central region in the latter sample, the former seems to be affected from the outside, expanding towards the inside of the tumour structure.

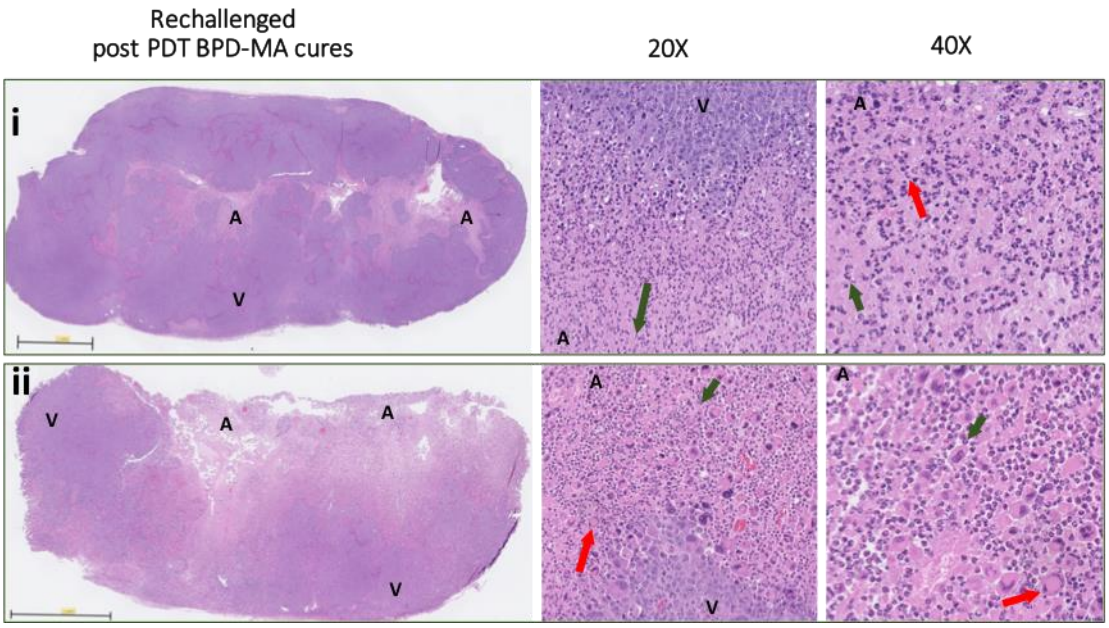

Figure 102. Non rejected secondary tumour in animals previously cured from the primary tumour after BPD-MA PDT treatment, and detail of H&E staining.

(i, ii) Rat subjects which had been completely cured from the primary MatLyLu subcutaneous tumour after light treatment (BPD-MA PDT) were given a second subcutaneous challenge of MatLyLu cells on the opposite flank (left side). Secondary tumours were non rejected and once sampled, these were H&E stained and examined on a Hamamatsu Nanozoomer Digital Pathology (NDP) scanner. 20X and 40X magnifications are shown. A: affected tumour area, V: viable tumour area. Green and red arrows indicate different infiltrating cell types. Scale bars shown as 2 mm.

As for the evaluation of apoptotic cell death displayed in Figure 103, large apoptotic tumour regions were found in this tumours in spite of the lack of direct treatment performed on these.

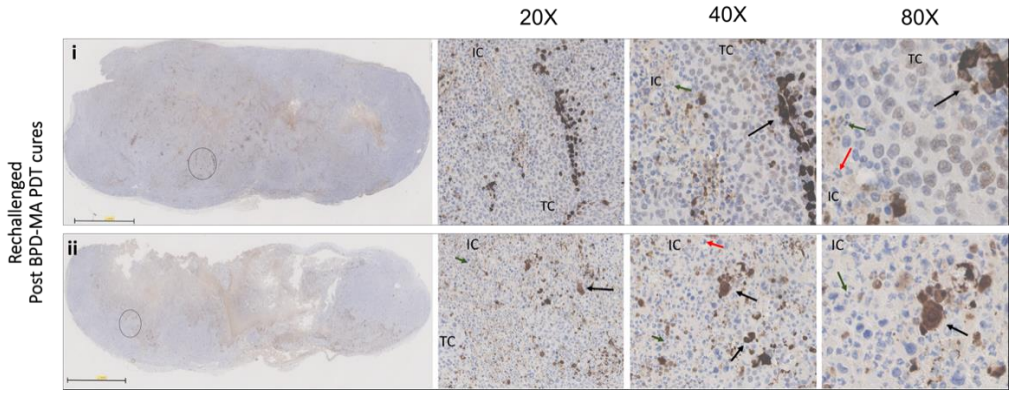

Figure 103. Evaluation of apoptosis in non rejected secondary subcutaneous tumours regrown in previously cured BPD-MA PDT-treated animal subjects.

Rat subjects which had been completely cured from the primary MatLyLu subcutaneous tumour after light treatment (BPD-MA PDT) were given a second subcutaneous challenge of MatLyLu cells on the opposite flank (left side). Secondary tumours were non rejected and once sampled, these were stained with anti cleaved caspase-3 (D175) and examined on a Hamamatsu Nanozoomer Digital Pathology (NDP) scanner. Same tumour samples as shown in Figure 102. 20X, 40X and 80X magnifications are shown. TC: tumour cells; IC: infiltrating cells. Green and red arrows indicate different infiltrating leucocytes; black arrows indicate apoptotic cells. Scale bars shown as 2 mm.

5.4.3 Evaluation of the *in vivo* activation of the immune system activation

As highlighted above, a major aim of this thesis, and specifically reported in the current chapter, was to assess whether light-based therapies are capable of eliciting an immune response during cancer treatment which would confer long term protection should formation of secondary tumour deposits occur. In line with this, we now address the presence of different immune-related molecules on tumour samples via immunohistochemical staining. Then we will comment on the quantification of the expression of relevant genes in different treatment groups.

5.4.3.1 Bcl-2/Bcl-3 in PDT-treated tumour samples

As briefly pointed out above, Bcl-2 and Bcl-3 have closely related biological roles in the immunological response through the NF-κB pathway. Staining of two tumour samples, untreated and PDT-treated respectively did not result in a particularly noteworthy staining against the apoptotic regulator Bcl-2 as displayed in Figure 104. A faint positive cytosolic staining was identified in a few disperse cells within the untreated control tumour samples (as indicated with a red arrow in Figure 104A), which we could not recognise in the treated specimen (Figure 104B).

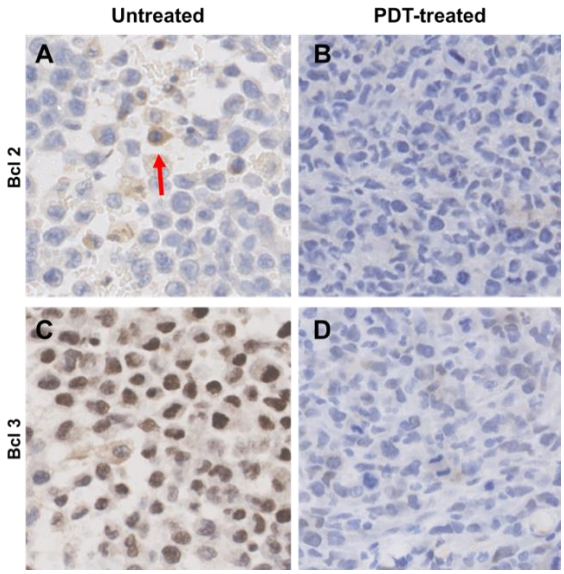

Figure 104. Evaluation of Bcl-2 and Bcl-3 staining in untreated and PDT-treated tumours.

Untreated and PDT-treated tumour samples were stained with anti Bcl-2 and Bcl-3 and examined on a Hamamatsu Nanozoomer Digital Pathology (NDP) scanner. 80X magnification shown. (A) Bcl-2 staining on untreated tumour. (B) Bcl-2 staining on PDT-treated tumour, red arrow highlights cytoplasmic staining. (C) Bcl-3 staining on untreated tumour. (D) Bcl-3 staining on PDT-treated tumour.

On the other hand, the transcriptional coactivator Bcl-3, displayed a strong nuclear presence in untreated tumours (Figure 104C), whilst no expression was detected in the PDT-treated sample (Figure 104D).

5.4.3.2 PD-L1 expression on rechallenged tumour samples

The great focus nowadays on immune checkpoint inhibitors and the use of immune checkpoint blockade strategies as therapeutic alternatives in cancer treatment, prompted us to evaluate the expression of the relevant programme cell death ligand 1 (PD-L1) in cured and rechallenged animals.

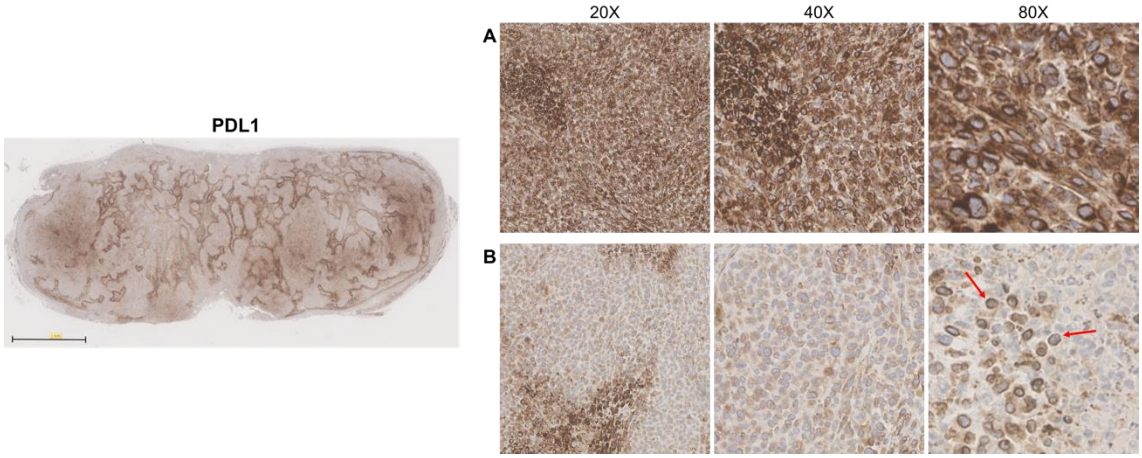

Figure 105. Evaluation of Programmed Cell Death-1 Ligand (PD-L1) in non rejected secondary subcutaneous tumours regrown in previously cured BPD-MA PDT-treated animal subjects.

Rat subjects which had been completely cured from the primary MatLyLu subcutaneous tumour after light treatment (BPD-MA PDT) were given a second subcutaneous challenge of MatLyLu cells on the opposite flank (left side). Secondary tumours were not rejected and once sampled, these were stained with anti PD-L1 and examined on a Hamamatsu Nanozoomer Digital Pathology (NDP) scanner. Same tumour samples as shown in Figure 102i and Figure 103i. 20X, 40X and 80X magnifications are shown. (A) Shows stronger stained regions. (B) Shows weaker stained regions. Red arrows highlight the stain in the external cell membrane. Scale bars shown as 2 mm.

It was found that nearly the whole surface of a tumour sample belonging to a rechallenged animal subject presented positive stain against PD-L1. Within the overall staining, lightly and strongly stained regions could be clearly differentiated. Figure 105A highlights stronger staining in the tumour sample, whereas Figure 105B shows a weaker, although still positive staining on the tumour. As indicated with red arrows in Figure 105B, PD-L1 was localised in the external cell membrane. Interestingly, the

expression of PD-L1 seemed to be higher in the centre of the tumour, while the periphery did not seem to exhibit as strong a signal.

It was also found that tumour areas where infiltrating leukocytes were spotted, as indicated with red arrows in Figure 106, did not show significant presence of the PD-L1 molecule based on the lack of staining seen in that specific tumour area.

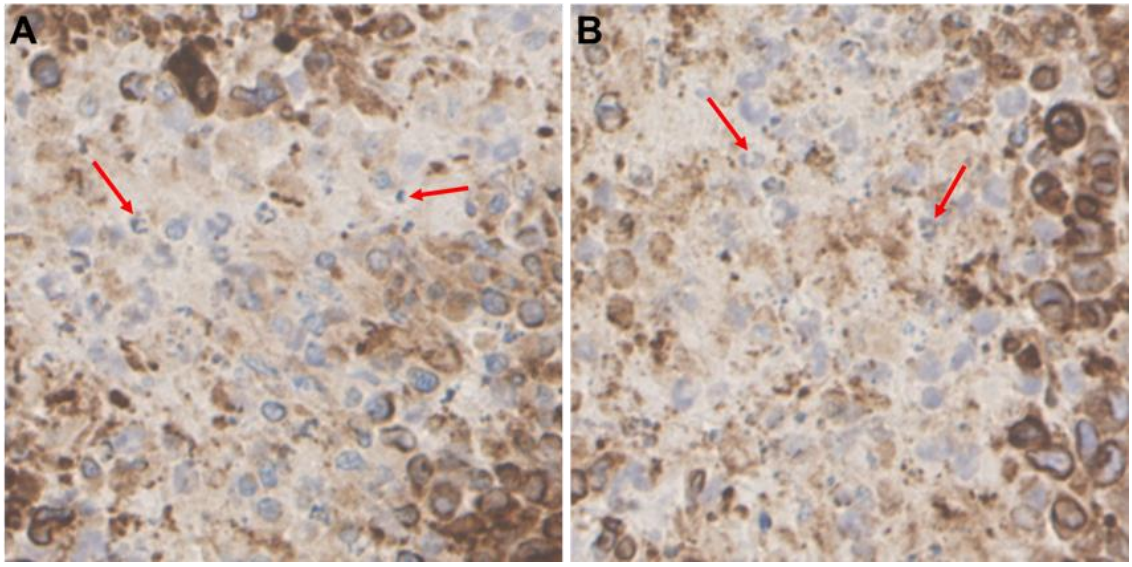

Figure 106. Detail of Programmed Cell Death-1 Ligand (PD-L1) in non rejected 2ary subcutaneous tumours regrown in previously cured BPD-MA PDT-treated animal subjects.

Rat subjects which had been completely cured from the primary MatLyLu subcutaneous tumour after light treatment (BPD-MA PDT) were given a second subcutaneous challenge of MatLyLu cells on the opposite flank (left side). Secondary tumours were not rejected and once sampled, these were stained with anti PD-L1and examined on a Hamamatsu Nanozoomer Digital Pathology (NDP) scanner. Same tumour samples as shown in Figure 102i and Figure 103i. (A) and (B) show details of different regions in the tumour at 80X magnification. Red arrows highlight the presence of infiltrating leukocytes.

5.4.3.3 CD3$^+$ Lymphocyte infiltration in tumours

Among the complexity of the immune response, we have mainly focused on the anti-tumour role exerted by T cells. As noted above, CD3 is a major surface marker on these and consequently its expression on tumour samples belonging to the different treatment groups described throughout Chapter 4 and Chapter 5 was evaluated.

After observing all tumours stained for CD3, we concluded that staining was more prominent in the peripheral area of tumours. For instance, in tumour samples that exhibited a lower number of infiltrating CD3$^+$ cells these were mainly found in the periphery whilst in tumours showing a greater infiltration, these cells were in addition

found dispersed throughout the tumour. Moreover, tumours composed of several nodules also showed greater infiltration in the interface between two nodules. A detail of these is shown in Figure 107B and Figure 107A respectively. In both cases localisation of CD3 in the external cell membrane was confirmed, highlighted in Figure 107 with red arrows.

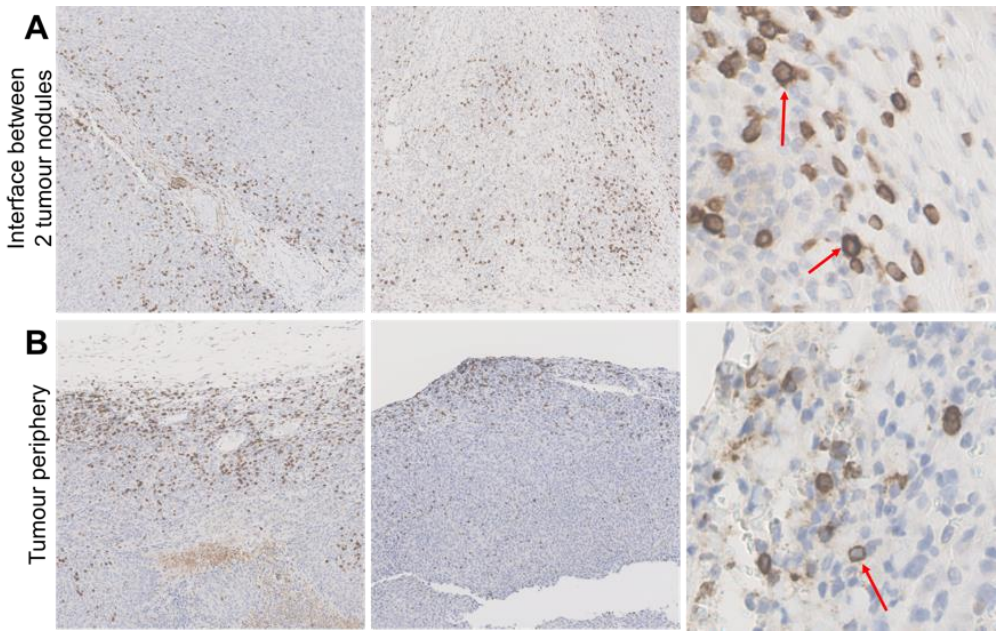

Figure 107. Detail of CD3-staining in tumour samples.

Representative tumour samples from each treatment group described throughout Chapter 4 and Chapter 5 were stained with anti CD3ε (chain on surface T cell receptors) and examined on a Hamamatsu Nanozoomer Digital Pathology (NDP) scanner. (A) Detail of the high density of positively stained cells in the interface between tumour nodules (multinodular samples). (B) Detail of the high density of positively stained cells in the tumour periphery. 10X and 80X magnifications are shown.

Interestingly, a comparison of PD-L1 and CD3 positively stained zones in the rechallenged tumour sample showed that both stains were complementary: $CD3^+$ regions were $PD\text{-}L1^-$ and conversely, $CD3^-$ were $PD\text{-}L1^+$. This is displayed in Figure 108, where circled areas represent the clear complementarity found between CD3 and PD-L1. For example, regions highlighted with red circles exhibit lack of CD3 staining yet a strong PD-L1 signal. In contrast, regions highlighted with green circles exhibit reduced PD-L1 staining yet a strong CD3 infiltration.

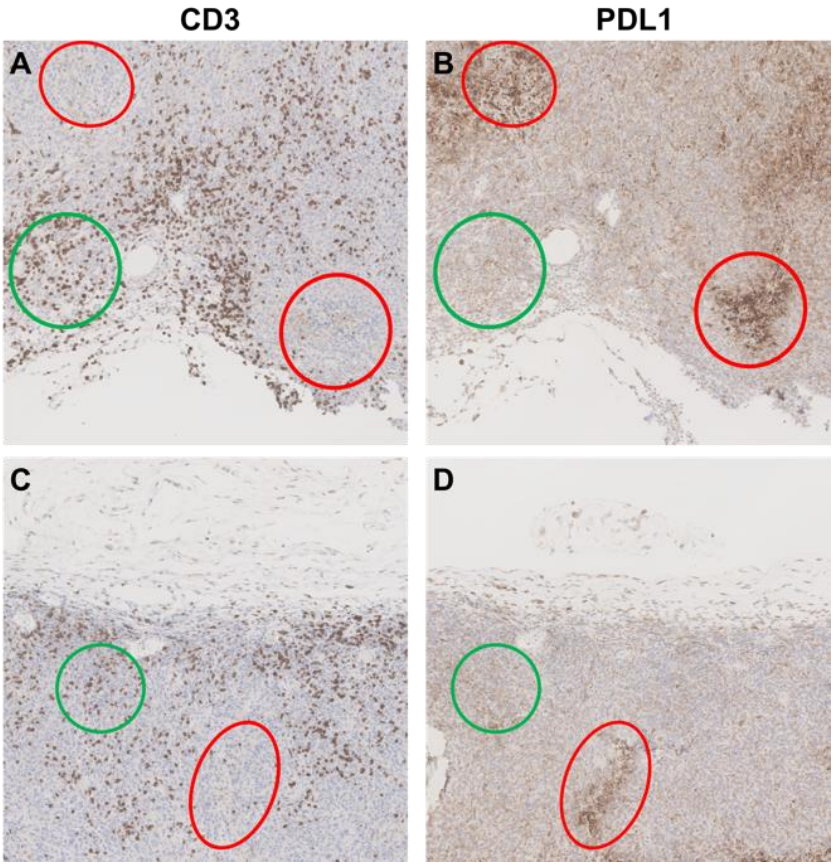

Figure 108. Comparison of CD3 and PD-L1 staining in rechallenged tumour samples.

Rat subjects which had been completely cured from the primary MatLyLu subcutaneous tumour after light treatment (BPD-MA PDT) were given a second subcutaneous challenge of MatLyLu cells on the opposite flank (left side). Secondary tumours were non rejected and once sampled, these were stained with anti CD3 and PD-L1 and examined on a Hamamatsu Nanozoomer Digital Pathology (NDP) scanner. Same tumour samples as shown in Figure 102i, Figure 103i and Figure 109E. (A) and (C) show details of CD3 staining. (B) and (D) show details of PD-L1 staining on the same area. 10X magnification is shown. Red and green circles indicate the same region in the tumour stained for the expression of either marker.

CD3 resulted in differentially stained regions on tumour samples. Two clearly visible regions were identified: defined regions displaying a generalised staining (ROI 1) and regions displaying discrete positively stained cells scattered throughout the tumour (ROI 2). Generally, ROI 1 corresponded to those areas identified as affected in the standard H&E staining in which the amount of infiltrating leukocytes was also larger. These identified ROIs were then used as a reference to perform an independent quantification of gene expression on either ROI through tissue microdissection, as explained in detail in 3.3 Materials & Methods.

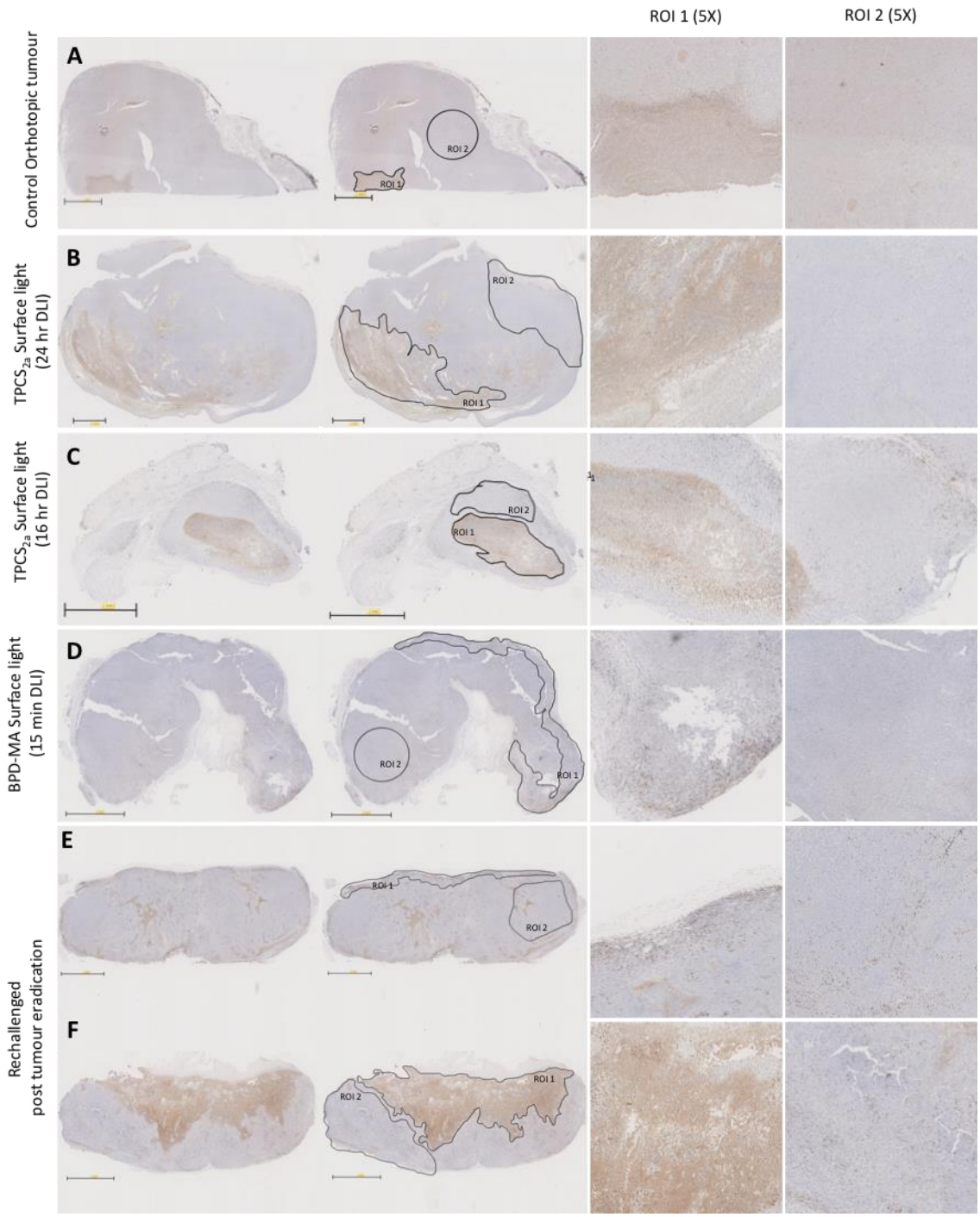
ROI 1 (5X)
ROI 2 (5X)
Control Orthotopic tumour
A
ROI 2
ROI 1
TPCS2a Surface light (24 hr DLI)
B
ROI 2
ROI 1
TPCS2a Surface light (16 hr DLI)
C
ROI 2
ROI 1
BPD-MA Surface light (15 min DLI)
D
ROI 2
ROI 1
Rechallenged post tumour eradication
E
ROI 1
ROI 2
F
ROI 1
ROI 2

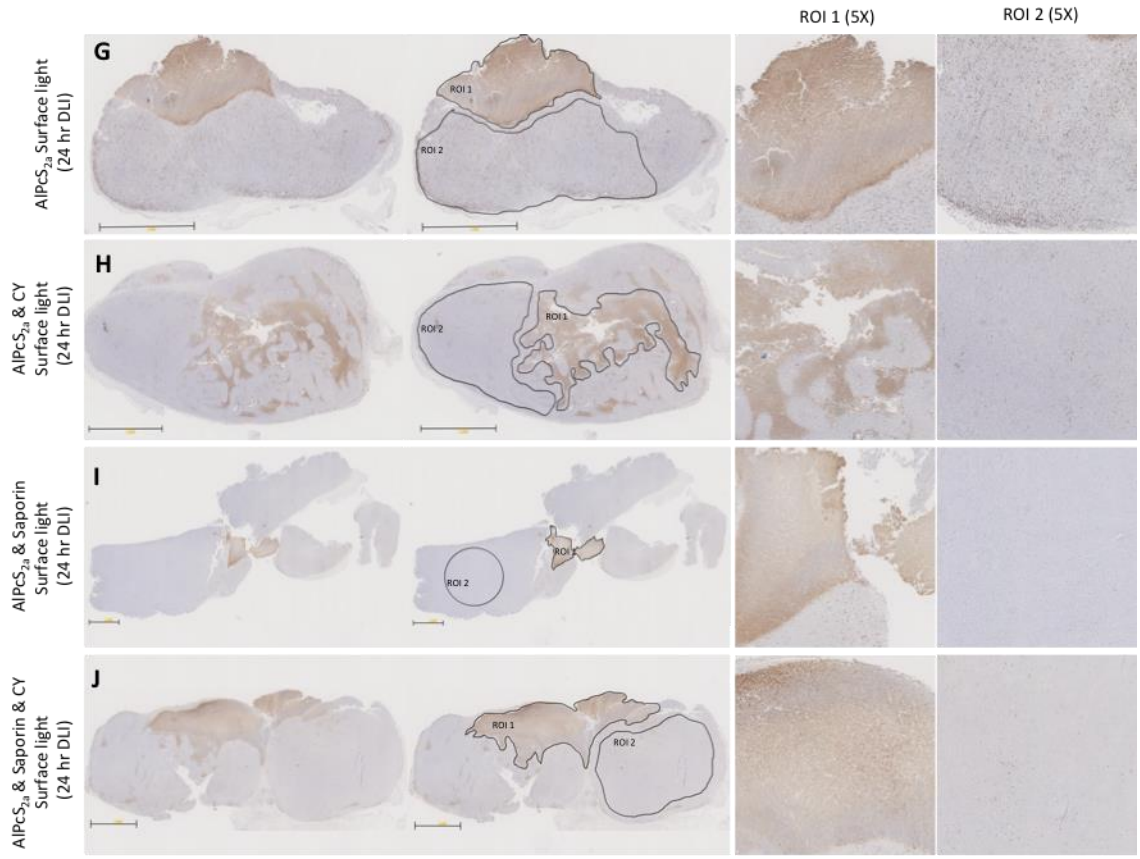

Figure 109. Tumour sample staining against CD3 and identification of differentially stained ROIs.

Representative tumour samples from each treatment group described throughout Chapter 4 and Chapter 5 were stained with anti CD3ε (chain on surface T cell receptors) and examined on a Hamamatsu Nanozoomer Digital Pathology (NDP) scanner. ROIs were identified on these slides based on whether an overall stained region was found (ROI1) or else positively stained cells were found disperse throughout the tumour structure (ROI2). 5X magnification of each ROI is shown. (A) Orthotopic untreated control tumour. (B) $TPCS_{2a}$ (PDT) surface light treated tumour (24 hr DLI). (C) $TPCS_{2a}$ (PDT) surface light treated tumour (16 hr DLI). (D) BPD-MA (PDT) surface light treated tumour (15 min DLI). (E, F) Regrown tumours after 2nd injection of tumour cells upon complete tumour regression post BPD-MA PDT. (G) $AlPcS_{2a}$ (PDT) surface light treated tumour (24 hr DLI). (H) $AlPcS_{2a}$ (PDT) & CY surface light treated tumour (24 hr DLI). (I) $AlPcS_{2a}$ & Saporin (PCI) surface light treated tumour (24 hr DLI). (J) $AlPcS_{2a}$ & Saporin (PCI) & CY surface light treated tumour (24 hr DLI). Scale bars shown as 2 mm.

A representative tumour sample from each treatment group is displayed in Figure 109, in which some of the ROIs used for gene expression quantification are defined. Features of ROIs in each tumour sample were different regarding both size and pattern of distribution. The lack of consistency determined in the differentially stained ROIs between tumour samples relates to observations from H&E staining, given the correlation between ROI 1 and the affected areas described in the latter along Chapter 4 and Chapter 5.

As mentioned above, in general all tumour samples exhibited infiltration of CD3 cells in the periphery regions rather than more central regions (Figure 109). We would like to highlight particularly the large infiltration of discretely stained $CD3^+$ cells noted in the

ROI 2 in rechallenged and $AlPcS_{2a}$-PDT samples (Figure 109E, Figure 109F and Figure 109G respectively).

5.4.3.4 Molecular analysis on tumour samples

Prior to the analysis of gene expression in ROIs as described above and represented in Figure 109, we assessed whether a poly(A)-specific retrotranscription of mRNA would result in an efficient recognition of mRNA sequences from FFPE samples, hence successfully quantify our genes of interest. We measured 5 genes of the whole panel of selected genes in 6 randomly chosen RNA samples from tumours as shown in Figure 110. Some of the genes measured showed large deviation between repeats in the same sample as indicated by the error bars. Bcl-3 was not recognised in any of the cases. Accordingly, despite the fact that cDNA resulting from non-poly(A) specific retrotranscription would only be used to assess the expression of specifically selected genes and therefore each cDNA sample would require a more time consuming process, we decided to follow a gene-specific retrotranscription for our samples of interest.

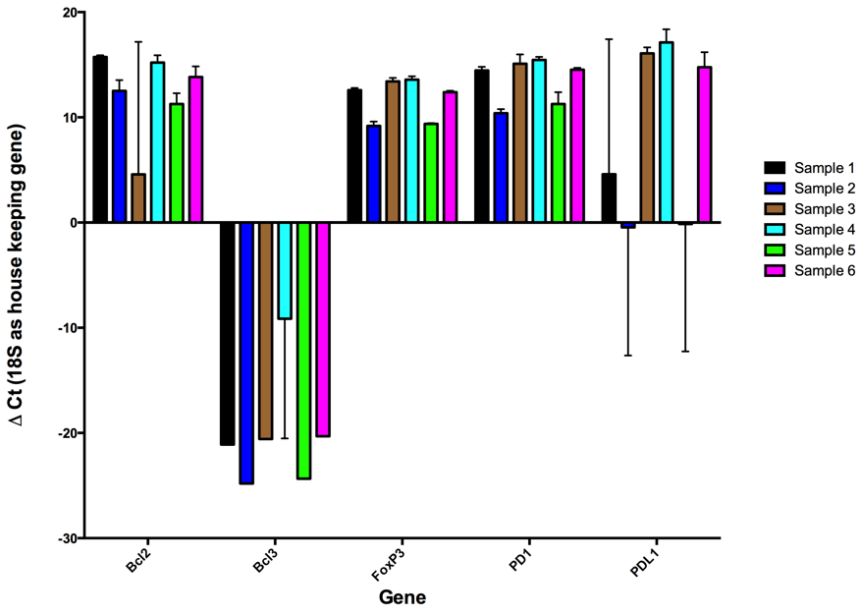

Figure 110. Gene expression based on cDNA reverse-transcribed using poly (A)-specific priming.

cDNA from 6 tumour samples was obtained using non specific primers, recognising poly(A) tails in mRNA. qRT-PCR was then used to quantify the expression of Bcl2, Bcl3, FoxP3, PD1 and PD-L1 genes. 18S was used as housekeeping gene to determine ΔCt values. Data shown as mean ΔCt ± SEM.

Among the wide range of genes involved in the immune response, selected CD3ε, Lamp1, FoxP3, Perforin, Granzyme-A, Bcl-2, Bcl-3, Survivin, TRAIL-R, FAS, FAS-L, PD1, PD-L1 based on their relevance in T cell-mediated response and possible cell death induced via the apoptotic pathway. This assessment of gene expression is displayed in Figure 111, Figure 112 and Figure 113, performed independently in each ROI and treatment group as noted above.

Regarding T cell markers (), CD3ε appeared to be significantly up-regulated mostly in the rechallenged yet non-rejected tumour samples ($p < 0.0001$) compared to the untreated tumour. Although not as significant, it also showed up-regulation in treatment groups such as BPD-MA PDT ($p = 0.0084$) and $AlPcS_2$-PDT ($p = 0.0056$) -both in ROI 2- and $AlPcS_2$-PCI ($p = 0.0157$) in ROI 1. Variations were also detected between treatment groups, predominantly an up-regulation in rechallenged compared to the rest of the treatment groups (see Table 11). No major differences were found in the expression of Lamp 1. Conversely, the comparison of FoxP3 between control and treated samples resulted in a down-regulation only in BPD-MA treated animals ($p = 0.0014$). Moreover, this down-regulation was also significantly different to other treatment groups. Briefly, in ROI 2 relevant differences were detected between BPD-MA treated tumours and those regrown post rechallenge ($p < 0.0001$), $TPCS_{2a}$-PDT (16 hr DLI, $p = 0.0408$), $AlPcS_{2a}$-PDT ($p = 0.0007$), $AlPcS_{2a}$-PDT & CY ($p = 0.0184$), and $AlPcS_{2a}$-PCI & CY ($p = 0.0065$). In ROI 1 differences were not that noticeable, concluding only a weak down-regulation in BPD-MA treated compared to rechallenged. Overall, these three genes were especially altered in rechallenged tumours and despite CD3ε seemed to be likewise altered between both ROIs defined, variations in FoxP3 were largely found in ROI 2.

Cytolytic effector molecules such as Perforin and Granzyme-A showed differential variations between ROIs. For instance, ROI 1 in untreated samples had significantly higher presence of the former compared to $TPCS_{2a}$-PDT (24 hr DLI), $AlPcS_{2a}$-PDT & CY, $AlPcS_{2a}$-PCI and $AlPcS_{2a}$-PCI & CY. As for ROI 2, Granzyme-A was considerably up-regulated only in rechallenged tumours, although these alterations were not as strong as those noted above for T cell markers (i.e. $p = 0.0012$ *vs.* $p < 0.0001$). Despite not many significant differences between groups were noted, again variations in Perforin seemed to be more present in ROI 1 and Granzyme-A in ROI 2. In line with this, an up-regulation of Perforin was observed in $AlPcS_{2a}$-PDT treated samples as opposed to $AlPcS_{2a}$-PDT & CY or $AlPcS_{2a}$-PCI. On the other hand, again it was only the rechallenged tumour showing an important increase in the expression of Granzyme-A compared to $AlPcS_{2a}$-PDT & CY.

With reference to apoptosis, while Bcl-2 was not particularly noticed in any case, expression of Bcl-3 was similarly altered in both ROIs (Figure 112). In detail, a significant up-regulation was detected in most treated tumours - $TPCS_{2a}$-PDT (16 hr DLI), rechallenged, $AlPcS_{2a}$-PDT, $AlPcS_{2a}$-PDT & CY, $AlPcS_{2a}$-PCI & CY. Particularly interesting are the observations from BPD-MA PDT treated and rechallenged samples in ROI 2. Compared to the rest of the treatments, a significant down-regulation resulted from the former compared to rechallenge ($p < 0.0001$), $AlPcS_{2a}$-PDT ($p < 0.0001$), $AlPcS_{2a}$-PDT & CY ($p < 0.0001$), $AlPcS_{2a}$-PCI ($p = 0.0017$) and $AlPcS_{2a}$-PCI & CY ($p < 0.0001$). Refer to further details in Table 11.

No major findings resulted from untreated and treated samples regarding PD1, PD-L1, TRAIL-R (Figure 112 and Figure 113). Survivin only showed changes in ROI 1, specifically a down-regulation in tumours after some of the conducted treatments. TRAIL-R was not altered in a major manner, only rechallenged samples showed some up-regulation against other treated tumours (see Table 11). Although no treatment showed significant variation of TRAIL-R and PD-L1 with the control group, rechallenged samples exhibited significantly higher expression levels than those treated using some other PS ($p = 0.0039$ at the most). Finally, a significant up-regulation of FAS and FAS-L in $AlPcS_{2a}$-PDT (ROI 1) and FAS-L in rechallenged (ROI 2) were detected. Further comparison between groups revealed that changes in FAS and FAS-L were restricted to ROI 1. Specifically, an up-regulation of both FAS and FAS-L was found again in $AlPcS_{2a}$-PDT over other treatment groups. The most significant down-regulation of FAS resulted from the combination of $AlPcS_{2a}$-PDT with CY ($p = 0.0008$).

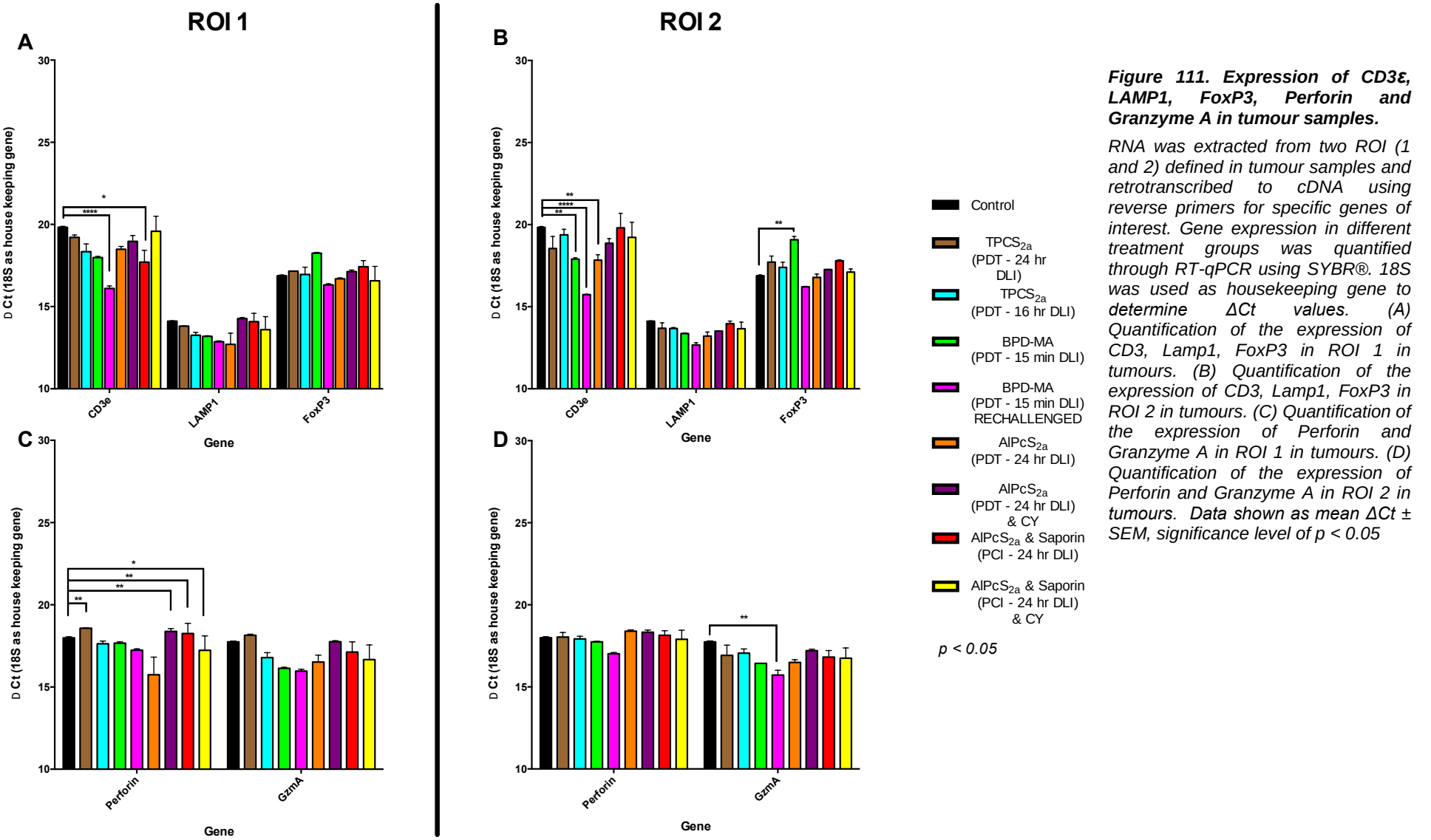

Figure 111. Expression of CD3ε, LAMP1, FoxP3, Perforin and Granzyme A in tumour samples.

RNA was extracted from two ROI (1 and 2) defined in tumour samples and retrotranscribed to cDNA using reverse primers for specific genes of interest. Gene expression in different treatment groups was quantified through RT-qPCR using SYBR®. 18S was used as housekeeping gene to determine ΔCt values. (A) Quantification of the expression of CD3, Lamp1, FoxP3 in ROI 1 in tumours. (B) Quantification of the expression of CD3, Lamp1, FoxP3 in ROI 2 in tumours. (C) Quantification of the expression of Perforin and Granzyme A in ROI 1 in tumours. (D) Quantification of the expression of Perforin and Granzyme A in ROI 2 in tumours. Data shown as mean ΔCt ± SEM, significance level of $p < 0.05$

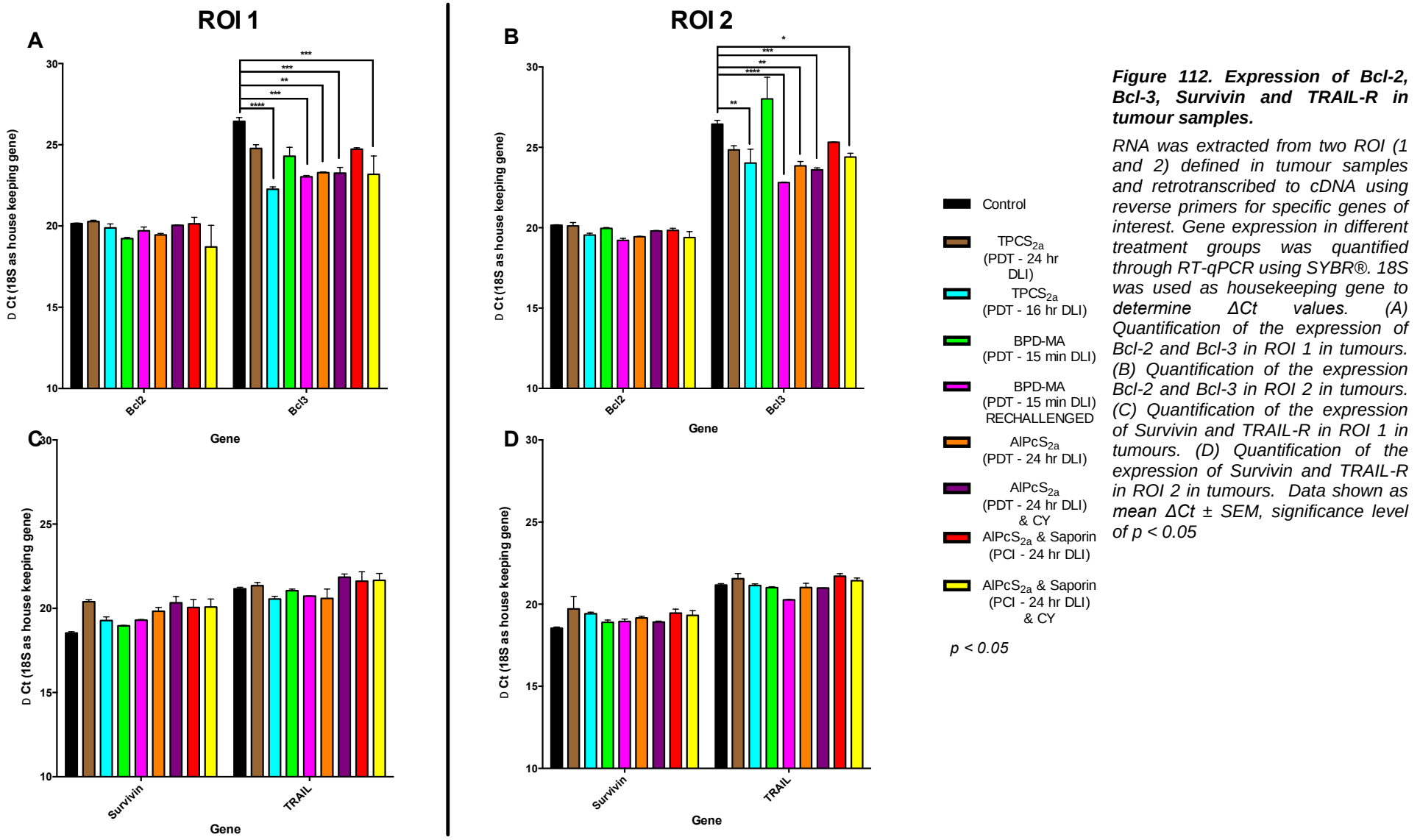

Figure 112. Expression of Bcl-2, Bcl-3, Survivin and TRAIL-R in tumour samples.

RNA was extracted from two ROI (1 and 2) defined in tumour samples and retrotranscribed to cDNA using reverse primers for specific genes of interest. Gene expression in different treatment groups was quantified through RT-qPCR using SYBR®. 18S was used as housekeeping gene to determine ΔCt values. (A) Quantification of the expression of Bcl-2 and Bcl-3 in ROI 1 in tumours. (B) Quantification of the expression Bcl-2 and Bcl-3 in ROI 2 in tumours. (C) Quantification of the expression of Survivin and TRAIL-R in ROI 1 in tumours. (D) Quantification of the expression of Survivin and TRAIL-R in ROI 2 in tumours. Data shown as mean ΔCt ± SEM, significance level of $p < 0.05$

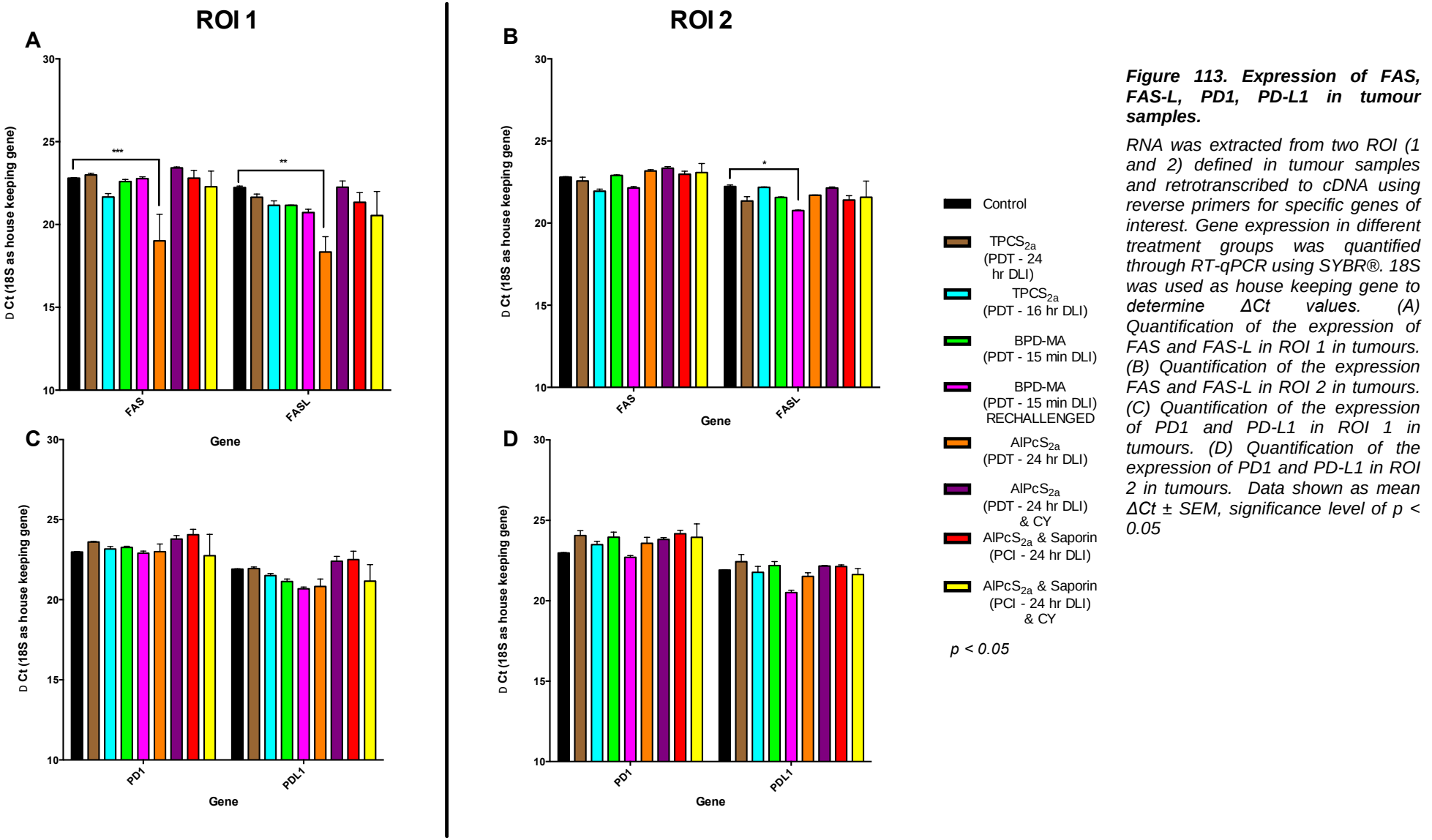

Figure 113. Expression of FAS, FAS-L, PD1, PD-L1 in tumour samples.

RNA was extracted from two ROI (1 and 2) defined in tumour samples and retrotranscribed to cDNA using reverse primers for specific genes of interest. Gene expression in different treatment groups was quantified through RT-qPCR using SYBR®. 18S was used as house keeping gene to determine ΔCt values. (A) Quantification of the expression of FAS and FAS-L in ROI 1 in tumours. (B) Quantification of the expression FAS and FAS-L in ROI 2 in tumours. (C) Quantification of the expression of PD1 and PD-L1 in ROI 1 in tumours. (D) Quantification of the expression of PD1 and PD-L1 in ROI 2 in tumours. Data shown as mean ΔCt ± SEM, significance level of p < 0.05

		ROI 2								
	(p < 0.05)	**Control**	**TPCS$_{2a}$-PDT Surface Light (24 hr DLI)**	**TPCS$_{2a}$-PDT Surface Light (16 hr DLI)**	**BPD-MA-PDT Surface Light (15 min DLI)**	**BPD-MA-PDT Surface Light (15 min DLI) RECHALLENGED**	**AlPcS$_{2a}$-PDT Surface Light (24 hr DLI)**	**AlPcS$_{2a}$-PDT Surface Light (24 hr DLI) & CY**	**AlPcS$_{2a}$& Saporin (PCI) Surface Light (24 hr DLI)**	**AlPcS$_{2a}$& Saporin (PCI) Surface Light (24 hr DLI) & CY**
	Control			Bcl3 - ** (↑)	CD3e - ** (↑) FoxP3 - ** (↓)	CD3e - **** (↑) Bcl3 - **** (↑) FASL - * (↑) GzmA - ** (↑)	CD3e - ** (↑) Bcl3 - ** (↑)	Bcl3 - *** (↑)		Bcl3 - * (↑)
	TPCS$_{2a}$-PDT Surface Light (24 hr DLI)	Survivin - ** (↓)			Bcl3 - *** (↓)	CD3e - **** (↑) Bcl3 - * (↑) PDL1 - ** (↑) TRAIL - * (↑)				
	TPCS$_{2a}$-PDT Surface Light (16 hr DLI)	Bcl3 - **** (↑)	Bcl3 - * (↑)		FoxP3 - * (↓) Bcl3 - **** (↑)	CD3e - **** (↑)				
	BPD-MA-PDT Surface Light (15 min DLI)					CD3e - ** (↑) FoxP3 - **** (↑) Bcl3 - **** (↑) PDL1 - * (↑)	FoxP3 - *** (↑) Bcl3 - **** (↑)	FoxP3 - * (↑) Bcl3 - **** (↑)	CD3e - * (↑) Bcl3 - ** (↑)	FoxP3 -** (↑) Bcl3 - **** (↑)
ROI 1	**BPD-MA-PDT Surface Light (15 min DLI) RECHALLENGED**	CD3e - **** (↑) Bcl3 - *** (↑)	CD3e - **** (↑)	CD3e - ** (↑)	FOXP3 - * (↑)		CD3e - ** (↓)	CD3e - **** (↑) PDL1 - * (↓) GzmA - * (↓)	CD3e - **** (↑) Bcl3 - ** (↓) PDL1 - * (↓) TRAIL - ** (↓)	CD3e - **** (↑)
	AlPcS$_{2a}$-PDT Surface Light (24 hr DLI)	Bcl3 - ** (↑) FAS - ** (↑) FASL - ** (↑)	FAS - ** (↑) FASL - * (↑) Perforin - ** (↑)		FAS - * (↑)	CD3e - ** (↑) FAS - ** (↑)			CD3e - ** (↑)	
	AlPcS$_{2a}$-PDT Surface Light (24 hr DLI) & CY	Bcl3 - *** (↑) Survivin - ** (↓)				CD3e - *** (↑)	FAS - *** (↓) FASL - ** (↓) Perforin - * (↓)			
	AlPcS$_{2a}$& Saporin (PCI) Surface Light (24 hr DLI)	CD3e - * (↑) Survivin - * (↓)		Bcl3 - * (↓)			FAS - ** (↓) Perforin - * (↓)			
	AlPcS$_{2a}$& Saporin (PCI) Surface Light (24 hr DLI) & CY	Bcl3 - *** (↑) Survivin - * (↓)				CD3e - **** (↑)	FAS - * (↓)			

Table 11. Multiple comparison of the expression of CD3ε, Lamp1, FoxP3, Perforin, Granzyme-A, Bcl-2, Bcl-3, Survivin, TRAIL-R, FAS, FAS-L, PD1, PD-L1 in tumour samples.

*Summary of significant differences between treatment groups displayed in , **Error! Reference source not found.** and **Error! Reference source not found.**. (↑) Indicates gene up-regulation in the corresponding treatment group; (↓) indicates gene down-regulation in the corresponding treatment group. Significance level of $p < 0.05$*

5.5 Discussion

In the present chapter, we have evaluated the potential anti-tumour protection exerted by PDT and PCI using different photosensitiers. We have also co-administered light treatments with cyclophosphamide, as an immune-adjuvant based on its known capacity to eliminate regulatory T cells at low doses (described in detail in 5.1Introduction).

Existing MSDS information on cyclophosphamide monohydrate (Cytoxan®, Bristol-Myers Squibb Company) claim an LD50 (lethal dose 50) in rat of 94 mg/kg and 121 mg/kg when administered orally or intraperitoneally respectively. Besides, the oral LOAEL (lowest observed adverse effect level) stated was 50 mg/kg, resulting in 80-90% bioavailability and showing an excretion half-life 4-6 hours after administration. Based on these, as well as available scientific reports claiming 50 mg/kg to be within the low-dose range of the agent, we initiated experiments conducting four i.p. injections (daily): two before light treatment and the remaining two in the days following delivery of light. The unexpected death of these individuals made us consider whether the combination of both treatments (light-based and cyclophosphamide) could have had an additive effect and thus resulted in excessive toxicity. We therefore then reduced the number of injections of the immune-adjuvant to two 50 mg/kg as has been studied before in combination with light therapies (Castano et al., 2008; Reginato et al., 2013). Hair loss, skin discoloration and loss weight are some of the reported side effects of cytoxan® as chemotherapeutic in humans, which were also experienced by all our animals (Figure 95). However, non-recovered weight loss after four injections reflects the extreme toxicity caused, opposite to the recovery and even weight gain of animals subjected to only two injections. In spite of the side effects reported, cyclophosphamide alone did not affect tumour growth, and tumour-bearing animals subjected to this treatment were euthanised only 4 days after the first injection of the immunoadjuvant was performed as they reached the end point of tumour burden at this point (Figure 96).

Based on the hypothesis that a potent immune response would have only been elicited after the complete eradication of tumours in 18% of the animal subjects following BPD-MA PDT (reported in Figure 78 in Chapter 4), we limited the administration of CY to $AlPcS_{2a}$-treated animals either following PDT or PCI to assess whether CY could result

in an improved outcome. As a matter of fact, although this combination did not result in any complete tumour eradication, the delay in tumour growth suggests that optimisation of the treatment procedure could potentially result in complete cures. Previous studies have already reported the benefits of combining cyclophosphamide with PDT, although in these cases complete survival of animals was observed when using low doses – 50 mg/kg (Castano et al., 2008; Reginato et al., 2013). For instance, 66% of the animals survived more than 90 days after BPD-PDT (2 mg/kg, 150 J/cm^2, 0.1 W/cm^2) with CY, contrary to the lack of cures in any case belonging to the BPD-PDT alone group (Castano et al., 2008). In addition, in their study, CY alone resulted in an improved survival, similar to the BPD-PDT only group.

Regarding the pathological analysis of these $AlPcS_{2a}$ & CY-treated tumours, H&E staining did not reveal any significant differences resulting from the co-administration of the immunoadjuvant, neither in the absence nor presence of saporin. This indicates that no further interaction between these two drugs might be occurring. Again, as described in previous tumour samples, the heterogeneity in the resulting affected areas was not different when CY was co-administered. An interesting observation was found during the evaluation of apoptosis in these samples: there was a larger number of apoptotic cells despite the longer period of time existing between light treatment and euthanasia (due to the delay in tumour growth). In a previous chapter of the thesis we have hypothesised that despite PDT-based treatments induce apoptosis in tumours (seen in samples 24 hr after light, Figure 65), should there be any fast-growing MatLyLu surviving tumour cells, apoptotic-dead cells would be overtaken by the viable tumour. Accordingly, the greater apoptosis shown in Figure 99 leads us to think that CY might be contributing to the apoptotic death PDT/PCI- induced, thereby decreasing the amount of remaining MatLyLu viable cells and in the end delay being overtaken by viable tumour cells. As a matter of fact, it has been previously confirmed that when used as chemotherapeutic rather that immune co-adjuvant, CY triggers apoptosis in a caspase cascade- dependent manner in different types of tumours (Schwartz and Waxman, 2001; Tsai-Turton et al., 2007). Furthermore, CY could have induced apoptosis not only in tumour cells but in infiltrating cells to some extent, given the caspase-3$^+$ stain present in regions where large infiltration of leukocytes was found (Figure 99). This correlates with the effect CY has specifically on immune-related cells.

Regarding the blackening of the inguinal lymph nodes in rats where co-administration of $AlPcS_{2a}$ and CY had been conducted (shown in Figure 100), the coinciding emission

of fluorescence between a solution of $AlPcS_{2a}$-alone and a dissolved “black”-lymph node solution, took us to conclude that the abnormal colour exhibited by these nodes was due to the formation of aggregates of this specific PS. This accumulation of $AlPcS_{2a}$ could be the result of an enhanced phagocytic activity induced by CY. $AlPcS_{2a}$ is a stable compound that tends to dimerise forming aggregates in a pH-dependent manner which can be disrupted by 0.1 M NaOH (Chen et al., 2014). If under our experimental conditions $AlPcS_{2a}$ aggregates, the increased phagocytic activity induced by CY could result in the increased uptake of these aggregates by the lymph nodes. Although we did not assess any additional lymph nodes, owing to the proximity to CY’s injection site (peritoneum), the inguinal chain of lymph nodes would have been the most affected location.

In line with the hypothesis of an enhanced phagocytosis, a similar conclusion was drawn in a recent study investigating how to overcome resistance to antibody-based in cancer treatment (Pallasch et al., 2014). Specifically, the authors confirmed that cyclophosphamide triggered the secretion of a series of factors by tumour cells (i.e. CCL4, IL8, among others) and this would lead to an enhanced macrophage infiltration and phagocytosis.

Moreover, this PS aggregation would lead to a self-quenching effect, hence a reduction in $AlPcS_{2a}$’s photooxidative capacity, giving an additional possible explanation on the lesser therapeutic success observed with this PS.

Parallel to the investigation concerning cyclophosphamide, animals that had been completely cured from the first tumour challenge post BPD-MA-PDT treatment (as already described in Chapter 4) were given a second challenge of tumour cells. This was conducted to evaluate whether the initial curative PDT had provided the animals with anti-tumour protection, should an additional exposure to relevant tumour cells occur. We aimed to follow an immune response-mounting strategy. In short, we gave a second tumour challenge using a lower amount of tumour cells than initially used, yet known to cause tumour formation in naïve animal subjects. Had the initial PDT treatment elicited an immune response in cured individuals, this injection of MatLyLu cells would have been rejected and we would have consequently performed an additional, higher-dose, tumour challenge and so on. Rechallenged animals were not subjected to any additional treatment after the second challenge of tumour cells. Despite no rejection of the second MatLyLu cell injection was observed, these

secondary tumours grew at a significantly slower pace than the initially implanted tumours in untreated animals (Figure 101). It could be argued whether this significant difference in tumour growth is “real” or else it is due to the lower amount of cells used for the second implantation. Throughout the present thesis, several tumour cell numbers have resulted in tumour formation such as 5×10^4 in the orthotopic tumour, $4x10^5$ or 10^6 in subcutaneous tumour. Irrespective of differences in cell number used, these only occasioned growth differences of 1 or 2 days. Therefore, we consider the 11-day delay observed in the rechallenged rats is not a mere cell number effect.

Studies in J774 and CT26 tumours combining BPD-MA and CY, resulted in complete tumour regression and even rejection of tumour rechallenge on cured subjects (Castano et al., 2008; Reginato et al., 2013). Importantly, specific antigens in both of these tumours have been identified. In the study carried out in 2008, successful rejection of the second tumour injection was antigen-specific, as indicated by the non-rejection of alternative tumour cells - EMT6, also immunogenic (Castano et al., 2008). Additionally, in the 2013 study tumour rejection was exclusively observed provided an additional injection of CY was performed before rechallenge (Reginato et al., 2013). In this last case, the authors hypothesised that the antigen expressed by CT26 cells (gp 70) could have been behaved like a self-antigen causing reactivation of Tregs, thus requiring an additional depletion of these cells so as to achieve a successful tumour rejection (Reginato et al., 2013).

MatLyLu cells have not been reported to be particularly immunogenic and tumour-specific antigens have not been described to date. Other researchers have conducted studies aiming to enhance the immunogenicity of these cells by down-regulating the production of TGFβ (Matthews et al., 2000). TGFβ is known to stimulate development of Tregs, having an important role in immune suppression (Liu et al., 2008). This, together with the known Treg-induced immunosuppression (both during antigen presentation and the effector phase) leads us to consider whether if we had administered CY before BPD-MA-PDT treatment and tumour rechallenge, the rejection of secondary tumour deposits would have occurred. Even more, BPD-MA-PDT treatment (as indicated in Chapter 4) could have also resulted in a more successful survival rate.

The large affected tumour areas observed after performing H&E staining as well as the presence of apoptotic cells on these regrown tumours (Figure 102 and Figure 103),

indicate that even if PDT had not generated complete protection against further tumour formation, it would have triggered immune-protection to some extent. Comparing damaged areas in the two rechallenged tumour samples displayed, the differences recognised (size and location) could be due to intrinsic disparities in the immunological potential of the two animal subjects they belong to. However, these disparities might not be that significant based on the similar expression of genes measured next.

We then performed an evaluation on how the immune response was being stimulated through IHC and quantification of gene expression in defined ROIs independently. We would like to comment briefly that through the initial analysis of gene expression we performed using a poly(A)-specific retro-transcription method (Figure 110), we confirm previous reports regarding the low quality of RNA in FFPE samples due to the degradation of mRNA poly-(A) tails during tissue processing and embedding (Evers et al., 2011). For this reason the remaining investigations, were conducted using gene-specific priming in the reverse transcription step (Figure 111, Figure 112 and Figure 113).

Starting with the NF-κB inducible genes Bcl-2 and Bcl-3, light treatment seems to be affecting the expression of Bcl-3 in the nucleus as shown in Figure 104. Perhaps, the inflammatory process elicited after PDT signals the degradation of this protein in order to maintain homeostasis in response to a large stimuli (Figure 104D). Contrary, a significant expression of Bcl-3 was found localised in the nucleus in the untreated control (Figure 104C).

As for the downstream effect in Bcl-2 expression regulated by Bcl-3, a very weak positive cytoplasmic staining was only observed in the untreated control tumour (Figure 104A). This indicates that in malignancies with no damaging stimuli, the integrity of Bcl-3 remains, possibly activating (although weakly observed) the expression of Bcl-2, hence implying a slim anti-apoptotic signal occurring in the natural environment of viable non-treated tumours. On the other hand, the PDT-treated tumour sample displayed did not show any presence of Bcl-2, which we could consider as slight pro-apoptotic signalling after treatment (Figure 104B). However, throughout Chapter 4 and Chapter 5, although some apoptotic cells could be distinguished upon caspase-3 staining in PDT-exposed tumours, overall we did not make significant observations compared to controls. One possible explanation is as already discussed previously:

owing to the removal of tumours several days after light treatment, apoptosis was no longer as significant as immediately after PDT.

Besides, other studies have previously concluded a PDT-induced damage to Bcl-2 protein based on the mitochondrial damage exerted after photooxidation (Usuda et al., 2003; Xue et al., 2001). In general, the Bcl-2 signal observed in our samples not only in treated but also in control tumours does not completely correlate with this PDT-based damage.

As regards to findings in the qRT-PCR experiments a correlation with the above discussed IHC results was seen: no major changes were detected in either ROI. Conversely, the molecular analysis revealed opposite results to IHC staining in Bcl-3. The latter displayed down-regulation in PDT-treated samples compared to a positive nuclear stain in untreated tumours (Figure 104); while a significant up-regulation in the expression of Bcl-3 was measured in nearly all treatments, but for BPD-MA treated (Figure 112). This last observation is especially interesting, since BPD-MA has been the only PDT treatment resulting in an efficient tumour regression. Although this single down-regulation was not significantly different to control samples ($p = 0.3890$), it suggests that degradation/down-regulation of Bcl-3 might only occur in tumours subjected to a sufficient damage capable of affecting the downstream repression of anti-apoptotic signalling. Furthermore, successful cell death induced in tumours may be dependent on a certain threshold under which no tumour eradication is obtained. On the other hand, regrown secondary tumours have not received a direct exogenous damaging stimuli and thus alterations in the expression of Bcl-3 will rely on immune response effectors present in the tumour microenvironment. In line with this, should there be immunosuppressive effectors, the transduction of pro-apoptotic signals might be surpassed by the pro-survival counterpart.

Regarding PD-L1, the large positively stained section in rechallenged tumours (Figure 105), suggests the secretion of this ligand by tumour cells might have had a major role in tumour progression and lack of rejection of secondary tumours. This is related to the poor prognosis noted in previous studies (Jin et al., 2010). In our study, T cells generated post PDT would recognise the existence of a newly formed tumour and accordingly, infiltration would commence in the periphery of these tumours, as confirmed in Figure 107. However, it is possible that tumour cells receiving “danger signals” from infiltrating cells might have undergone an immunoediting process

following which the release of PD-L1 occurs, conferring protection against immune cells by inducing cell death in PD-1 expressing cells. This correlates with the opposing staining found between infiltrating $CD3^+$ cells and the commented PD-L1 (Figure 108): regions expressing PD-L1 cause cell death in T cells, resulting in no CD3 staining; while no PD-L1 release enables survival and intervention of effector T cells.

Despite the noticeable positive staining found in immunohistochemistry in the rechallenged sample stained with anti PD-L1 (Figure 105), qRT-PCR did not show a significant difference in the expression of PD-L1 between control and rechallenged tumour. However, an up-regulation trend was found in these particular specimens as reflected in the p values: $p = 0.1135$ (control against rechallenged) as opposed to $p > 0.999$ in the rest of the cases. Based on the discrete regions expressing PD-L1, as noted in the antagonistic staining between CD3 and such ligand, a more specific microdissection might be needed to obtain comparable findings in IHC and qRT-PCR.

TRAIL-induced apoptosis does not seem to be particularly relevant in the analysed tumour specimens. Likewise, at most it appeared to be altered among treatment groups but not compared to untreated samples. Briefly, the up-regulation in rechallenged samples suggests a major presence of cells susceptible to this induced cell death are detected after complete tumour regression, as a result of immunological changes arising from the previous light treatment.

As for CD3-stained tumours, further study with the assistance of a pathologist revealed that the repeated generalised brown staining, appearing in regions identified as ROI 1 could be due to non-specific staining frequently found in infiltrating polymorphonuclear cells such as neutrophils (possibly because of their cytoplasmic content reacting with the detection system used). This links to the correlation observed between affected areas in H&E stained slides and this ROIs 1. These affected areas exhibiting a heavy load of infiltrating leukocytes might be the reflection of a focus of inflammation. On the other hand, ROI 2 is featured by discrete intense-brown stained cells, and a lack of the overall staining as detected in ROI 1. Due to the general stain in ROI 1, these discretely stained cells are not as evident as in ROI 2, although still present (Figure 109).

Significant alterations in gene expression, especially in the rechallenged samples, reveal the previously noted argument that even if no rechallenge was rejected, the

immune system had been stimulated to some extent post PDT. As a matter of fact the most significant up-regulation of CD3ε ($p < 0.0001$) was found in ROI 2 in the rechallenged tumour, not only against the control, but also against other treatment groups (see Table 11). This suggests that a non-rejected secondary tumour grown after the eradication of a primary tumour elicits a greater infiltration of CD3 leukocytes than non-cured tumours. In addition, CD3 expression in ROI 2 seemed to be higher than that found in ROI 1 within each treatment group. We think this is based on the major infiltration of other cell types in the former as opposed to a more exclusive T cell infiltration in ROI 2. Overall, expression of CD3 in tumour samples could be summarised as follows: ROI 2 in rechallenged > ROI 1 in rechallenged > ROI 2 in remaining treatments > ROI 1 in remaining treatments > control.

The measurement of CD3ε through molecular analysis correlates with the observations made in IHC staining. In the latter, rechallenged samples were among the ones showing the greatest infiltration of positively stained cells, especially in ROI 2 (Figure 109E and Figure 109F), alike observations in qRT-PCR analysis (). This can be applied for other light-based treatments such as that seen after $AlPcS_{2a}$-PDT (Figure 109G) .

The lack of major alterations in the expression of Lamp 1 indicates that the infiltrating T cells recognised above, correspond to a T cell subset different from $CD8^+$ cytotoxic T cells and further investigations are required. As for T regs, characterised by FoxP3 expression, again the greater changes in gene expression found in ROI 2 correlate with the larger infiltration of T cells in these region rather ROI 1, where other infiltrating leukocytes have been mainly described. BPD-MA treated animals showed the greatest down-regulation in this marker, which could be indicating that this PDT treatment results in a reduction of the immunosuppression naturally present in the tumour microenvironment. The later increase in these T regs during the rechallenge stage suggests that in the absence of PDT, this subset of cells regrows and is present as normal, requiring an additional threat to face the new tumour challenge and assist anti-tumour effector T cells.

A similar argument can be applied for non-cured tumours subjected to the other PDT/PCI regimes described (i.e. $TPCS_{2a}$ and $AlPcS_{2a}$), which may not be potent enough to confront the immunosuppressive tumour MatLyLu. Accordingly, this also suggests that the co-administration of cyclophosphamide during tumour rechallenging

would enhance the survival rate and possibly secondary tumour rejection in MatLyLu-based tumours as shown in other tumours (Castano et al., 2008; Reginato et al., 2013).

Not surprisingly, the significant down-regulation in the expression of perforin was observed in ROI 1 in some treatment groups (which appears to be poorer in T cells than ROI 2), given that this particular cytolytic protein is found in cytotoxic lymphocytes and NK cells. Importantly, this also correlates with the up-regulation of granzyme A in ROI 2 in the rechallenged sample ($p = 0.0012$). Together with the large presence of CD3 cells found in this sample in particular, this indicates that infiltrated T cells are responsible for the secretion of cytolytic proteases such as granzyme A, regardless of the specific subset present. Besides, having in mind the hypothesis noted previously which relates ROI 1 to large inflammation and leukocyte infiltration occurring during this stage of the innate immune response, it is possible that the lack of attenuation of the inflammatory process observed (even 7 days after light treatment) could have been occasioned due to the reduced presence of perforin. Following this line of thought, previous studies have confirmed the regulatory role of DCs by observing that a deficiency in the release of perforin by these cells resulted in a pro-inflammatory effect as well as a higher presence of T helper cells (Zlotnikov-Klionsky et al., 2015). As a matter of fact, perforin has been previously claimed to exert a role in prevention of inflammation and autoimmune disorders through the control of DCs (Mossu et al., 2016) and eosinophilic-inflammation (Enomoto et al., 2012), release which was assigned to $CD8^+$ cytotoxic T cells.

Additionally, the down-regulation in the expression of perforin observed in $AlPcS_{2a}$-treated tumours when combined with CY or saporin (as opposed to PDT alone), could be due to the cytotoxic effect exerted by these agents to perforin-secreting cells.

In relation to the up-regulation of both FAS and FAS-L, in $AlPcS_{2a}$-PDT tumours, the fact that it was observed in ROI 1 rather than ROI 2 indicates a relationship with the inflammatory process taking place in the former region of interest (Figure 113). As a matter of fact, FAS ligand has been associated to the promotion of neutrophil infiltration, blockage of degranulation and pro-inflammatory signalling (Dupont and Warrens, 2007). This correlates with the non rejection of secondary tumours: these showed an up-regulation of FASL (even higher in ROI 2), which could have been responsible for inducing cell death in infiltrating T cells.

In conclusion, an activation of the immune response following light-based treatment to highly immunosuppressive and aggressive MatLyLu tumours was found. This was especially noteworthy in tumours that had not been rejected after the second implantation of tumour cells in previously cured animals. In addition, this serves as proof that a complete elimination of tumours is necessary prior to achieving a protective effect to some extent. Based on these results, we hypothesise that a strong enough anti-cancer therapy will affect the intrinsic immunosuppression induced by tumour cells, for instance reflected in the down-regulation of regulatory T cells and the blockage of the inflammatory process elicited by PDT. In relation to inflammation, the NF-κB seems to be having an important role through Bcl-3, which in this case will attenuate inflammation and possibly result in the reduction of anti-apoptotic signalling (i.e. Bcl-2). If the treatment results in the elimination of the initial tumour, should a distant tumour deposit occur, it will be recognised by previously generated T cells exhibiting a degranulating capacity as indicated by the presence of both granzyme-A and perforin. Unfortunately, the lack of an additional detrimental anti-tumour treatment impedes the elimination of components of the immune response with an important suppressive role (for example seen in the up-regulation of T regs). Consequently, despite tumour growth is delayed owing to the role of cytotoxic effector T cells, these will be overwhelmed by suppressive effector cells and tumours will in the end regrow. Following this line, we hypothesise that immunoadjuvants acting on the elimination of immunosuppression such as cyclophosphamide enhance the therapeutic outcome. Such is the case of $AlPcS_{2a}$-based treatment regardless of the presence of saporin, where retardation of tumour growth was observed.

Conversely, in those cases where the initial light-based treatment was not strong enough, a prolonged inflammation was detected, even more evident in tumour areas showing large infiltration of inflammatory cells. The lack of attenuation of this inflammatory stage may result in an inefficient protection against tumours, i.e. reduced $CD3^+$ infiltration via down-regulation of perforin or Bcl-3 and up-regulation of FAS-L.

Although we have not proved the existence of specific antigens in MatLyLu cells, we postulate that there is an efficient antigen presentation and effector T cell maturation, which does not exert its maximum potential due to immunosuppression. Such findings are intriguing and worth testing on human prostate tissue.

Overall, these results give an idea of how complex the immune response is, featured by its compensatory potential whereby blockage of a specific pathway might have an effect in a wide range of other routes. Further analysis is required to shed light on cytokines and effectors present in the different tumour microenvironments, which might provide a key in an effective therapy against prostate cancer.

Conclusions and Future Work

This study on PDT/PCI for prostate cancer treatment focused on the hypothetical improvement of the therapeutic outcome PCI would offer as opposed to PDT. Interestingly, the course of this PhD project evolved towards a more immunological perspective of energy-based therapeutic alternatives, as reflected in the structure of this thesis.

As a starting point, *in vitro* investigations are always recommended to determine events occurring in more complex organisms. In line with this, although findings in the experiments we performed *in vitro* were not directly translatable in the *in vivo* study, we actually found correlations between both. For instance, even though we could not determine the optimal DLI for *in vivo* treatments from those established *in vitro*, we did find that the fast growth and potentially accelerated metabolism of MatLyLu cells observed *in vitro* (thus expected *in vivo*), would benefit from shorter DLI to ensure the sufficient presence of PS in these tumour cells. Moreover, we also conclude from these early *in vitro* investigations that in optimised PCI protocols, higher light/drug doses are not necessarily better that lower doses. For example, 96 hr after light, the combination of saporin with 0.2 µg/ml PS and 1.26 J light resulted in a similar or even increase of cell death over 0.4 µg/ml PS and 2.1 J. Accordingly, we conclude that the application of such low doses of PS in PCI to human individuals would further minimise side effects (skin photosensitivity and damage to healthy tissue) observed with PDT.

In vitro investigations also confirmed the impact of physico-chemical properties of photosensitisers regarding the design of light therapy protocols and the interaction of photosensitive compounds with cells. Briefly, each cell type's physiological features (i.e. growth rate, metabolism, intracellular pathways, location, etc.), will determine the fate and photooxidative damage caused by PS. Taking this into consideration, we evaluated the benefits of different PS in our prostate cancer cells (namely $TPCS_{2a}$, $TPPS_{2a}$, $AlPcS_{2a}$ and BPD-MA). Although *in vitro* the behaviour of PS (at a cellular or subcellular level) is mainly dependent on DLI, *in vivo* bioavailability, hence photooxidative damage, is more a complex process that does not only depend on DLI. For instance, determining if a better outcome is achieved with PDT or PCI, whether DLIs should be directed to induce vascular shutdown or directly affect tumour cells, etc. Importantly, in a clinical setting, this implies differences between each cancer type and the necessity to know how different tumour cells respond to treatment in order to adapt

therapies to each individual case and maximise the therapeutic outcome, thereby ensuring success. In our results, despite PCI was successfully optimised in PC3 human cells, further optimisation will be carried out in the rat cell line MatLyLu.

Accordingly, in our future work we will conduct this optimisation of light treatment on MatLyLu cells in 3D models, where a more controllable environment is created. This will potentially facilitate the translation to rodent models and potentially human subjects. Moreover, we will investigate the even more biomimetic context described in "tumoroids", 3D models composed of two differentiated collagen matrices: one bearing tumour cells, representing the "stroma" of tumours, and a second scaffold seeded with non-tumour cells such as fibroblasts or endothelial cells, mimicking the parenchyma of tumours (Ricketts et al., 2014). Furthermore, patient-derived xenografts can be used to test whether the cellular effects found in the MatLyLu 3D model play similar role in patients (Kohli et al., 2015).

Overall, the determination of an optimised PCI protocol in the fast growing, aggressive and metastatic MatLyLu cells could serve as basis for tumours exhibiting similar properties, shedding light on how we could improve the outcome of these. Perhaps in our project, optimised PCI *in vivo*, could improve the limited successful tumour regression found after PDT – only 18% overall cures with one BPD-MA PDT. Therefore regarding future work to optimise light treatment *in vivo*, we would like to test $TPCS_{2a}$ (given the clinical relevance), at shorter DLI, i.e. 6 hr after i.v. administration. In our studies, since shorter DLI (15 minutes for vascular PDT and 16 hr for $TPCS_{2a}$-PDT) have shown a greater therapeutic outcome. Moreover, in addition to saporin, we aim to assess the delivery of additional chemotherapeutics already approved for prostate cancer, such as docetaxel or cabazitaxel. This would significantly facilitate the translation of an optimised PCI procedure to human patients in a prospective clinical trial.

On the other hand, benefits concluded after PCI *in vitro* led us to consider whether further design of treatments could (i) increase the uptake of PS through CPPs, hence intracellular concentrations, and (ii) limit the uptake of PS to tumour cells via targeting moieties, thereby improving site-specificity of light-based therapies. Following this second objective of the project, we found that CPPs do improve the uptake of PS conjugates in human cancer cells, and this results in an increased cytotoxicity with even lower doses of photosensitive drugs compared to PS alone. Consequently, we

aim to further test this *in vivo*, comparing the accumulation of such compounds in both malignant and normal cells when administered systemically.

In Chapter 3 we have also reported the use of targeting strategies with PS-conjugates potentially recognising CXCR4, although we did not confirm specificity against such receptor, based on the study with the inhibitor AMD3100. Consequently, we will further look into the interaction between CPPs and CXCR4. In line with this, in collaboration with the group synthesising the peptide conjugates in University of Bath, we will carry out investigations on the spatial structure of vMIP-II-TAT-TPP. This will determine whether the association between the targeting moiety (vMIP-II against CXCR4) and TPP could be causing steric hindrance that impedes the interaction between CXCR4 receptor and ligand in prostate cancer cells. Furthermore, we will verify the expression of such receptor in our PC3 cells to reject the hypothetical loss of this receptor in our cell stock. These studies will clarify the scenarios described in 3.5.

Should we resolve this in our future experiments, CXCR4 targeting could result in a successful active targeting of PS to diseased prostate cancer cells. Undoubtedly, the focal treatment of prostate cancer would benefit from an increased site-specificity and the consequent reduction of co-morbidity. However, future studies are needed to determine whether more focalised treatments render as good a therapeutic outcome as more radical approaches in highly aggressive and rapidly proliferating tumours. Briefly, the treatment of highly aggressive tumours might be more beneficial through the latter to ensure the complete eradication of tumour cells by treating larger regions (guaranteeing tumour edges are also “clean”), thus compromising specificity. Again, this indicates the importance of becoming aware of each particular tumour’s features.

Tumour illumination performed superficially (i.e. conducted with BPD-MA, $TPCS_{2a}$, $AlPcS_{2a}$) as opposed to interstitially (only conducted with $TPCS_{2a}$) resulted in a greater delay of tumour growth, possibly related to difficulties in fibre placement with the interstitial approach in small tumours, causing inconsistencies in homogeneous light delivery to the whole tumour. Further experiments would have to be carried out to determine the optimum light delivery approach for this subcutaneous tumour model. From these experiments, evidence suggests that the tumour periphery, if treated insufficiently, is highly proliferative resulting in recurrence of tumour growth. It also supports the argument above in relation to the treatment of aggressive tumours: compromising site-specificity (where treatment extends beyond the tumour boundary)

could favour complete tumour cell-killing, hence preventing tumour regression. Moreover, even though we have not concluded any improvement in tumour cure combining PS and saporin in PCI strategies, the enhanced cytotoxicity found *in vitro* leads us to think that the procedure followed *in vivo* with the different amphiphilic PS needs further optimisation (as challenging as it is for PCI). We consider that optimising PCI in the future could have an important effect in this peripheral region as proved previously as the main treatment or adjuvant to an alternative therapeutic approach (Norum et al., 2009c).

Overall, vascular-directed PDT resulted in the most successful therapeutic outcome, as concluded by the complete tumour regression after BPD-MA. In line with this, a major aim for future work is to determine how to increase tumour cure rate, i.e. enhancing tumour apoptosis and necrosis after light in a way that would result in the complete elimination of tumours in animal subjects. It is possible that the measurement of tumour cell death (i.e. apoptosis/necrosis) at earlier time point after light (for example 24 hr post treatment) will give us an idea on the success of each therapeutic approach, as opposed to euthanising animals once tumour regrowth has already commenced. In addition, based on the important vascular component determined in the studied model together with the above-mentioned targeting approaches, it would be interesting in the future to assess the outcome of PS/drug-conjugates targeted against vascular endothelial cells within the tumour. This has been successfully proved in PCI approaches previously using VEGF-conjugates (Weyergang et al., 2014).

Through the investigations presented herein a large inflammatory response triggered after light treatment of tumours was confirmed. The significant infiltration of innate-immune response cells, mainly neutrophils, was verified regardless of the PS or light conditions used. It seems that resolution of the inflammatory process will be determinant in the progression of the disease after light, and the additional generation of a more destructive adaptive response. In fact, the NF-κB pathway could be playing an important role in the interaction between innate and adaptive response in these energy-based therapies. For example, upon exposure of tumours to PDT, a reduction of Bcl-3 expression was shown through IHC, subsequent down-regulation of Bcl-2 (hence pro-apoptotic signalling) and importantly, resolution of inflammation. We aim to further investigate this so as to determine an adequate light-based regime which favours this scenario.

With reference to the involvement of the immune system in light-based therapies, important findings in our investigations came accompanied by the complete eradication of tumours. This is suggested by differences at the molecular level observed between rechallenged animals (which had been cured from the primary tumour) and the rest of the treated tumour samples. The most significant finding was noted by the up-regulation of the T cell marker CD3 in tumours grown in the rechallenged animals. Moreover, in the future we will conduct the evaluation of the tumour bed left behind in the cured animals, where the primary tumour was located. Through this examination, we aim to determine whether there are any viable tumour cells left as well as immunological components, which will further help understand tumour progression.

First, through this molecular analysis we have identified a great immunosuppressive factor in MatLyLu tumours, as suggested by the up-regulation of inducers of Tcell death such as PD-L1, or the enhanced infiltration of Tregs (FoxP3). An efficient light treatment seemed to involve an initial reduction of the expression of FoxP3. However, if this down-regulation is not sufficient, light treatment will not result in tumour eradication (e.g. non cured BPD-treated primary tumours). In the future, the aim is consequently to search for strategies through which this depletion would be achieved. For example, we could combine light treatment with PD-L1 inhibitors, as has been conducted in metastatic colorectal tumours previously using nanoparticles combining oxaliplatin (chemotherapeutic) and pyropheophorphide (PS) (He et al., 2016). In this study, a strong specific immune response was concluded against irradiated primary and distant secondary tumours.

Similarly, Treg depletion induced by cyclophosphamide could result in a beneficial outcome. Although it did not result in any tumour cure when combined with $AlPcS_{2a}$-PDT or PCI in our experiments, we consider that if combined with a treatment showing intrinsic capacity to affect tumours integrity and immunosuppressive environment (i.e. BPD-MA), CY could further enhance the therapeutic outcome. Based on this argument, in the future, we would like to administer CY prior to and during light treatment to assist Treg depletion both during antigen presentation and effector stages. In a similar way, we think the administration of such agent before rechallenging would also improve tumour rejection, based on the up-regulation of Tregs found in these regrown tumour samples. Potentially, we could also investigate the use of other immunoadjuvants, i.e. CpG, which instead of reducing immunosuppression, interact with TLR inducing innate

immune responses, for example stimulating monocytes, DCs or macrophages (Anzengruber et al., 2015; Xia et al., 2014).

Additionally, a reduced cytotoxic response was determined in the majority of tumours, probably influenced by the described immunosuppression. For instance, this is suggested by the alternative expression of CD3 and PD-L1 on rechallenged tumours. The presence of tumour-destructive T cells seemed to be being controlled by tumour cells via PD-L1 secretion. Furthermore, it would be interesting to examine in future work whether PD-L1 could also have an effect in B cell response using Omics technology.

Rechallenged tumours also exhibited an increased expression of cytolytic enzymes: Granzyme A and Perforin. Given the relation of Perforin with inflammation and antigen presentation to dendritic cells (described in Chapter 5), in the future we will further investigate the presence of $CD4^+$ T cells / T helper cells in our tumour samples. Similarly, we would like to assess in the future whether $CD8^+$ are present in the different tumour samples, given the association of these Tcells with specific cell recognition and an effector response.

Overall, the above-stated future investigations will enable a clearer elucidation on how the immune response evolves in the event of an inflammatory response (caused by light treatments in this case), what triggers the transition from an innate to an adaptive immune response, shed additional light on how B and T cell interaction occurs and how we could then attempt to direct these to a specific response, e.g. towards the increased/reduced presence of specific cell subtypes, etc. In relation to this, in future work, we will also perform whole-transcriptome analysis that will clarify alterations in the expression of every gene between different groups: untreated tumour cells, infiltrating $CD3^+$ cells in rechallenged tumours, PD-L1 secreting tumour cells in rechallenged tumours, FoxP3 expressing cells, etc. We think this will provide extremely valuable information as regards what causes the infiltration of each immune-related cell subtype.

Regarding the use of CY as immune-adjuvant, we would like to further investigate the increased phagocytic activity induced in lymph nodes, which we identified through the accumulation of $AlPcS_{2a}$ aggregates. Again following whole-transcriptome sequencing,

we will compare the expression of genes in normal lymph nodes and those exhibiting an altered activity.

Throughout our investigations, the molecular characterisation of tumour samples has proved to be an essential tool in the elucidation of the effect of light treatment induced in our treated tumours and how such treatment influences the resolution of tumour progression. It is particularly relevant to determine how we could exploit these alterations at the molecular level, to direct light treatments aiming to achieve an optimal molecular response in tumours. For example, we could use these discoveries to identify molecular “bio-markers” directly associated with positive prognosis so that therapies could be designed to pursue the activation of such bio-markers and vice versa. This way, prior to light-based therapies, tumour cells could be sensitised through adjuvant therapies so that fully successful PDT/PCI could be later performed. Importantly, based on the conclusions of the effect of PDT/PCI on the immune response, we can decipher the molecular immunological pathways that play a major role in autoimmune diseases, age-related autoimmunity (i.e. rheumatoid arthritis) and possibly understanding some of the allergies. In contrast to tumour-induced immunosuppression, in these cases there is hyper-activated immune response.

Finally, in prospective work, we would also like to carry out an evaluation using the orthotopic tumour model described in Chapter 4, thereby maintaining the gland’s microenvironment.

Appendix

Detailed preparation of TPP conjugates

- **General Procedure for the preparation of peptides by solid phase peptide synthesis**

The peptides were assembled according to the Fmoc strategy on Rink Amide MBHA Resin (Novabiochem, 200-400 mesh, 0.60 mmol/g loading) using an Activo P11 automated synthesiser fitted with a reactor heating jacket. The synthesis was performed on 250 mg of resin (0.15 mmol scale). Removal of the Fmoc group from the resin was performed with 20% piperidine/DMF (2.5 mL, 4 x 3 minutes). The first residue attachment for peptides starting with a glycine or an arginine was performed using 4 eq. of the amino acid, 4 eq. of DIC and 6 eq. of DIPEA (5 min preactivation then 1 h coupling), and was followed by an acetylation step (Ac_2O/DIPEA/DMF = 1/1/8, 2.5 mL, 1 x 10 minutes). Subsequent Fmoc deprotection steps were performed using 25% piperidine/DMF (3 mL, 1x5 minutes, 1x10 minutes), with the chain elongation steps being performed using 3 eq. of Fmoc-protected amino acid (Fmoc-Arg(Pmc)-OH, Fmoc-Gln(Trt)-OH), Fmoc-Lys(Boc)-OH, or Fmoc-Gly-OH) 3 eq. of PyBOP, and 6 eq. of DIPEA in 4.3 mL of DMF (35 minutes, 60°C). The peptide resin was washed thoroughly with DMF, DCM and then dried *in vacuo*.

For the cleavage and deprotection of the clickable peptides, the acylated peptidyl resin was swollen in DCM for 20 minutes, then it was treated with TFA/TIS/H_2O (95/2.5/2.5) for 4 hours. The resin beads were filtered off, washed with TFA, and the combined filtrates were evaporated to a small volume then anhydrous Et_2O was added. The resulting precipitate was collected by centrifugation and was washed twice more with Et_2O. The precipitated material was dissolved in 1% aq. TFA, filtered using a 0.2 µm syringe filter and the resulting solution was directly purified by semi-preparative HPLC. The purified peptides were then freeze-dried.

- **General procedure for the click chemistry of peptides**

A solution of peptide (1 µmol) and TPP-DBCO (2 µmol) in DMSO (4000 µL) was treated with pyridine (200 µL) and stirred at room temperature overnight, shielded from light. The mixture was diluted with 1% aq. TFA and directly purified by semi-preparative. The purified conjugate was freeze-dried to give a dark green solid.

Publications and Presentations

- **Published articles**

Martinez de Pinillos Bayona, A. et al., 2016. Enhancing the efficacy of cytotoxic agents for cancer therapy using photochemical internalisation. International Journal of Cancer, 138(5), pp.1049–1057.

- **Papers in preparation for publication**

Martinez de Pinillos Bayona, A.; Mroz P.; Thunshelle C.; Hamblin M. “Design features for optimization of tetrapyrrole macrocycles as antimicrobial and anticancer photosensitizers”. Submitted for publication in Chemical Biology & Drug Design.

Tarassoli, S; Martinez De Pinillos Bayona, A.; Pye, H.; Mosse, A., Callan, J.; MacRobert, A; McHale, A.; Nomikou, N. “Cathepsin B-degradable, NIR-responsive nanoparticulate platform for target-specific cancer therapy". Submitted for publication in Nanotechnology.

Martinez de Pinillos Bayona, A.; Woodhams J.; Hamoudi R.; Moore C.; MacRobert A. “Efficacy of photochemical internalisation using disulfonated chlorin and porphyrin photosensitisers: an *in vitro* study in 2D and 3D prostate cancer models”. Submitted for publication in Cancer Letters.

- **Conference Presentations**

2nd International Conference on Nanotechnology in Medicine (NANOMED); February 2014, London, UK. Martinez de Pinillos Bayona, A.; Moore, C.; MacRobert, A. “Photochemical Internalisation (PCI) as a potential prostate cancer treatment”

15th International Photodynamic Association (IPA) World Congress; May 2015, Rio de Janeiro, Brazil. Martinez de Pinillos Bayona, A.; Dondi, R.; Wang, L.; Yaghini, E.; Woodhams, J.; Moore, C.; Eggleston, I.; MacRobert, A. “Photochemical Internalisation for the local delivery of chemotherapy”

16th European Society for Photobiology (ESP) Congress; September 2015, Aveiro, Portugal. Dondi, R.; Yaghini, E.; Wang, L.; Martinez de Pinillos Bayona, A.; Tewari,

K.M.; MacRobert, A; Eggleston, I. “Clickable photosensitisers and peptides – efficient routes to targeted agents for PDT and photobiology”

106th American Association for Cancer Research (AACR) annual meeting; November 2015, Boston, USA. Martinez de Pinillos Bayona, A.; Dondi, R.; Wang, L.; Yaghini, E.; Woodhams, J.; Moore, C.; Eggleston, I.; MacRobert, A. “Photochemical Internalisation for the local delivery of chemotherapy in prostate cancer”

36th American Society for Laser Medicine & Surgery (ASLMS) annual conference; April 2016, Boston, USA. Martinez de Pinillos Bayona, A.; MacRobert, A.; Hamblin, M. “Stimulation of dendritic cells after Photochemical Internalisation (PCI), implications in cancer treatment”

United Kingdom & Ireland Controlled Release Society annual workshop & symposium; April 2016, Cardiff, UK. Tarassoli, S.; Martinez de Pinillos Bayona, A.; Reinert, H.; Pye, H.; Mosse, A.; Callan, J.; MacRobert, A; McHale, A.; Nomikou, N. “Novel polyglutamate-based indocyanine green nanoparticles for photothermal cancer therapy”

Photodynamic Therapy and Photodiagnosis Update; October 2016, Nancy, France. Martinez de Pinillos Bayona, A.; MacRobert, A.; Hamblin, M; Hamoudi, R. “Immune system stimulation in tumours treated with light-based therapies”

Bibliography

Abels, C., 2004. Targeting of the vascular system of solid tumours by photodynamic therapy (PDT). Photochem. Photobiol. Sci. 3, 765–71.

Abu Eid, R., Razavi, G.S.E., Mkrtichyan, M., Janik, J., Khleif, S.N., 2016. Old-School Chemotherapy in Immunotherapeutic Combination in Cancer, A Low-cost Drug Repurposed. Cancer Immunol. Res. 4, 377–82.

Adigbli, D.K., MacRobert, A.J., 2012. Photochemical internalisation: the journey from basic scientific concept to the threshold of clinical application. Curr. Opin. Pharmacol. 12, 434–8.

Adigbli, D.K., Wilson, D.G.G., Farooqui, N., Sousi, E., Risley, P., Taylor, I., Macrobert, a J., Loizidou, M., 2007. Photochemical internalisation of chemotherapy potentiates killing of multidrug-resistant breast and bladder cancer cells. Br. J. Cancer 97, 502–12.

Agostinis, P., Berg, K., Cengel, K.A., Foster, T.H., Girotti, A.W., Gollnick, S.O., Hahn, S.M., Hamblin, M.R., Juzeniene, A., Kessel, D., Korbelik, M., Moan, J., Mroz, P., Nowis, D., Piette, J., Wilson, B.C., Golab, J., 2011. Photodynamic therapy of cancer: an update. CA. Cancer J. Clin. 61, 250–81.

Allison, R.R., Sibata, C.H., 2010. Oncologic photodynamic therapy photosensitizers: a clinical review. Photodiagnosis Photodyn. Ther. 7, 61–75.

Alroqi, F.J., Chatila, T.A., 2016. T Regulatory Cell Biology in Health and Disease. Curr. Allergy Asthma Rep. 16, 27.

Altan, N., Chen, Y., Schindler, M., Simon, S.M., 1998. Defective Acidification in Human Breast Tumor Cells and Implications for Chemotherapy. J. Exp. Med. 187, 1583–1598.

Andrews, D.L., Scholes, G.D., Wiederrecht, G.P., 2010. Comprehensive Nanoscience and Nanotechnology. Academic Press.

Antoni, D., Burckel, H., Josset, E., Noel, G., 2015. Three-dimensional cell culture: a breakthrough in vivo. Int. J. Mol. Sci. 16, 5517–27.

Anzengruber, F., Avci, P., de Freitas, L.F., Hamblin, M.R., 2015. T-cell mediated anti-tumor immunity after photodynamic therapy: why does it not always work and how can we improve it? Photochem. Photobiol. Sci. 14, 1492–509.

Arentsen, H.C., Falke, J., Høgset, A., Oosterwijk, E., Alfred Witjes, J., 2014. The effect of photochemical internalization of bleomycin in the treatment of urothelial carcinoma of the bladder: An in vitro study. Urol. Oncol. 32, 49.e1-6.

Arumainayagam, N., Moore, C.M., Ahmed, H.U., Emberton, M., 2010. Photodynamic therapy for focal ablation of the prostate. World J. Urol. 28, 571–6.

Ayaru, L., Wittmann, J., Macrobert, A.J., Novelli, M., Bown, S.G., Pereira, S.P., 2007. Photodynamic therapy using verteporfin photosensitization in the pancreas and surrounding tissues in the Syrian golden hamster. Pancreatol. Off. J. Int. Assoc. Pancreatol. 7, 20–7.

Azzouzi, A.-R., Barret, E., Moore, C.M., Villers, A., Allen, C., Scherz, A., Muir, G., de Wildt, M., Barber, N.J., Lebdai, S., Emberton, M., 2013. TOOKAD(®) Soluble vascular-targeted photodynamic (VTP) therapy: determination of optimal treatment conditions and assessment of effects in patients with localised prostate cancer.

BJU Int. 112, 766–74.

Azzouzi, A.R., Barret, E., Bennet, J., Moore, C., Taneja, S., Muir, G., Villers, A., Coleman, J., Allen, C., Scherz, A., Emberton, M., 2015. TOOKAD® Soluble focal therapy: pooled analysis of three phase II studies assessing the minimally invasive ablation of localized prostate cancer. World J. Urol. 33, 945–53.

Bagga, S., Hosur, M.., Batra, J.K., 2003. Cytotoxicity of ribosome-inactivating protein saporin is not mediated through α 2 -macroglobulin receptor. FEBS Lett. 541, 16–20.

Bataille, R., Klein, B., Jourdan, M., Rossi, J.F., Durie, B.G., 1989. Spontaneous secretion of tumor necrosis factor-beta by human myeloma cell lines. Cancer 63, 877–80.

Battaglia Parodi, M., La Spina, C., Berchicci, L., Petruzzi, G., Bandello, F., 2016. Photosensitizers and Photodynamic Therapy: Verteporfin. Dev. Ophthalmol. 55, 330–6.

Battelli, M.G., Montacuti, V., Stirpe, F., 1992. High sensitivity of cultured human trophoblasts to ribosome-inactivating proteins. Exp. Cell Res. 201, 109–112.

Bayer, P., Kraft, M., Ejchart, A., Westendorp, M., Frank, R., Rösch, P., 1995. Structural studies of HIV-1 Tat protein. J. Mol. Biol. 247, 529–35. doi:10.1006/jmbi.1995.0158

Benov, L., 2015. Photodynamic therapy: current status and future directions. Med. Princ. Pract. 24 Suppl 1, 14–28.

Berg, K., Dietze, A., Kaalhus, O., Høgset, A., 2005. Site-specific drug delivery by photochemical internalization enhances the antitumor effect of bleomycin. Clin. Cancer Res. 11, 8476–85.

Berg, K., Høgset, A., Prasmickaite, L., Weyergang, A., Bonsted, A., Dietze, A., Lou, P.-J., Bown, S., Norum, O.-J., Møllergård, H.M.T., Selbo, P.K., 2006. Photochemical internalization (PCI): A novel technology for activation of endocytosed therapeutic agents. Med. Laser Appl. 21, 239–250.

Berg, K., Moan, J., 1994. Lysosomes as photochemical targets. Int. J. cancer J. Int. du cancer 59, 814–822.

Berg, K., Nordstrand, S., Selbo, P.K., Tran, D.T.T., Angell-Petersen, E., Høgset, A., 2011. Disulfonated tetraphenyl chlorin (TPCS2a), a novel photosensitizer developed for clinical utilization of photochemical internalization. Photochem. Photobiol. Sci. 10, 1637–51.

Berg, K., Selbo, P.K., Prasmickaite, L., Tjelle, T.E., Sandvig, K., Moan, J., Gaudernack, G., Fodstad, O., Kjølsrud, S., Anholt, H., Rodal, G.H., Rodal, S.K., Høgset, A., Fodstad, Ø., 1999. Photochemical Internalization : A Novel Technology for Delivery of Macromolecules into Cytosol. Cancer Res. 59, 1180–1183.

Berstad, M.B., Weyergang, A., Berg, K., 2012. Photochemical internalization (PCI) of HER2-targeted toxins: synergy is dependent on the treatment sequence. Biochim. Biophys. Acta 1820, 1849–58.

Bie, V., 1899. Remarks on Finsen's Phototherapy. Br. Med. J. 2, 825–30.

Björnsson, J., Inwards, C.Y., Wold, L.E., Sim, F.H., Taylor, W.F., 1993. Prognostic significance of spontaneous tumour necrosis in osteosarcoma. Virchows Arch. A Pathol. Anat. Histopathol. 423, 195–199.

Bolognesi, A., Polito, L., Scicchitano, V., Orrico, C., Pasquinelli, G., Musiani, S., Santi,

S., Riccio, M., Bortolotti, M., Battelli, M.G., 2012. Endocytosis and intracellular localisation of type 1 ribosome-inactivating protein saporin-s6. J. Biol. Regul. Homeost. Agents 26, 97–109.

Bono, N., Pezzoli, D., Levesque, L., Loy, C., Candiani, G., Fiore, G.B., Mantovani, D., 2016. Unraveling the role of mechanical stimulation on smooth muscle cells: A comparative study between 2D and 3D models. Biotechnol. Bioeng. 113, 2254–2263.

Bostad, M., Berg, K., Høgset, A., Skarpen, E., Stenmark, H., Selbo, P.K., 2013. Photochemical internalization (PCI) of immunotoxins targeting CD133 is specific and highly potent at femtomolar levels in cells with cancer stem cell properties. J. Control. Release 168, 317–26.

Boyle, R.W., Dolphin, D., 1996. Structure and biodistribution relationships of photodynamic sensitizers. Photochem. Photobiol. 64, 469–85.

Boyman, O., Sprent, J., 2012. The role of interleukin-2 during homeostasis and activation of the immune system. Nat. Rev. Immunol. 12, 180–90.

Bozzini, G., Colin, P., Betrouni, N., Maurage, C., Leroy, X., Simonin, S., Martin-Schmitt, C., Villers, A., Mordon, S., 2013a. Efficiency of 5-ALA mediated photodynamic therapy on hypoxic prostate cancer: a preclinical study on the Dunning R3327-AT2 rat tumor model. Photodiagnosis Photodyn Ther. 10, 296–303.

Bozzini, G., Colin, P., Betrouni, N., Nevoux, P., Ouzzane, a, Puech, P., Villers, a, Mordon, S., 2012. Photodynamic therapy in urology: what can we do now and where are we heading? Photodiagnosis Photodyn. Ther. 9, 261–73.

Bozzini, G., D, M., Colin, P., Nevoux, P., Villers, A., Ph, D., Mordon, S., Betrouni, N., 2013b. Focal therapy of prostate cancer: energies and procedures. Urol. Oncol. 31, 155–67.

Brücher, B.L.D.M., Jamall, I.S., 2014. Cell-cell communication in the tumor microenvironment, carcinogenesis, and anticancer treatment. Cell. Physiol. Biochem. 34, 213–43.

Bull-Hansen, B., Cao, Y., Berg, K., Skarpen, E., Rosenblum, M.G., Weyergang, A., 2014. Photochemical activation of the recombinant HER2-targeted fusion toxin MH3-B1/rGel; Impact of HER2 expression on treatment outcome. J. Control. Release 182, 58–66.

Burtey, A., Wagner, M., Hodneland, E., Skaftnesmo, K.O., Schoelermann, J., Mondragon, I.R., Espedal, H., Golebiewska, A., Niclou, S.P., Bjerkvig, R., Kögel, T., Gerdes, H.-H., 2015. Intercellular transfer of transferrin receptor by a contact-, Rab8-dependent mechanism involving tunneling nanotubes. FASEB J. 29, 4695–712.

Butzbach, K., Rasse-Suriani, F.A.O., Gonzalez, M.M., Cabrerizo, F.M., Epe, B., 2016. Albumin-folate-conjugates for Drug-targeting in Photodynamic Therapy. Photochem. Photobiol.

Carmody, R.J., Ruan, Q., Palmer, S., Hilliard, B., Chen, Y.H., 2007. Negative regulation of toll-like receptor signaling by NF-kappaB p50 ubiquitination blockade. Science 317, 675–678.

Carreras, J., Lopez-Guillermo, A., Roncador, G., Villamor, N., Colomo, L., Martinez, A., Hamoudi, R., Howat, W.J., Montserrat, E., Campo, E., 2009. High numbers of tumor-infiltrating programmed cell death 1-positive regulatory lymphocytes are associated with improved overall survival in follicular lymphoma. J. Clin. Oncol. 27, 1470–6.

Castano, A.P., Demidova, T.N., Hamblin, M.R., 2005. Mechanisms in photodynamic therapy: part two-cellular signaling, cell metabolism and modes of cell death. Photodiagnosis Photodyn. Ther. 2, 1–23.

Castano, A.P., Demidova, T.N., Hamblin, M.R., 2004. Mechanisms in photodynamic therapy: part one-photosensitizers, photochemistry and cellular localization. Photodiagnosis Photodyn. Ther. 1, 279–93.

Castano, A.P., Mroz, P., Hamblin, M.R., 2006. Photodynamic therapy and anti-tumour immunity. Nat. Rev. Cancer 6, 535–45.

Castano, A.P., Mroz, P., Wu, M.X., Hamblin, M.R., 2008. Photodynamic therapy plus low-dose cyclophosphamide generates antitumor immunity in a mouse model. Proc. Natl. Acad. Sci. U. S. A. 105, 5495–500.

Castiñeiras Fernandez, J., 2007. Libro del Residente de Urologia. Graficas Marte.

Cavallaro, U., Nykjaer, A., Nielsen, M., Soria, M.R., 1995. α2-Macroglobulin Receptor Mediates Binding and Cytotoxicity of Plant Ribosome-Inactivating Proteins. Eur. J. Biochem. 232, 165–171.

Chaplin, D.D., 2010. Overview of the immune response. J. Allergy Clin. Immunol. 125, S3-23.

Chapple, C.R., Steers, W.D. (Eds.), 2011. Practical Urology: Essential Principles and Practice. Springer.

Charles A Janeway, J., Travers, P., Walport, M., Shlomchik, M.J., 2001. The components of the immune system.

Chen, B., Pogue, B.W., Zhou, X., O'Hara, J.A., Solban, N., Demidenko, E., Hoopes, P.J., Hasan, T., 2005. Effect of tumor host microenvironment on photodynamic therapy in a rat prostate tumor model. Clin. Cancer Res. 11, 720–7.

Chen, H., Xiao, L., Anraku, Y., Mi, P., Liu, X., Cabral, H., Inoue, A., Nomoto, T., Kishimura, A., Nishiyama, N., Kataoka, K., 2014. Polyion complex vesicles for photoinduced intracellular delivery of amphiphilic photosensitizer. J. Am. Chem. Soc. 136, 157–63.

Cheng, L., Montironi, R., Bostwick, D.G., Lopez-Beltran, A., Berney, D.M., 2012. Staging of prostate cancer. Histopathology 60, 87–117.

Copolovici, D.M., Langel, K., Eriste, E., Langel, Ü., 2014. Cell-penetrating peptides: design, synthesis, and applications. ACS Nano 8, 1972–94.

CRUK, 2016. Cancer Research UK Facts and Figures.

Cunderlíková, B., Bjørklund, E.G., Pettersen, E.O., Moan, J., 2001. pH-dependent spectral properties of HpIX, TPPS2a, mTHPP and mTHPC. Photochem. Photobiol. 74, 246–252.

Cunningham, D., You, Z., 2015. In vitro and in vivo model systems used in prostate cancer research. J. Biol. methods 2.

Daniels, T.R., Bernabeu, E., Rodríguez, J.A., Patel, S., Kozman, M., Chiappetta, D.A., Holler, E., Ljubimova, J.Y., Helguera, G., Penichet, M.L., 2012. The transferrin receptor and the targeted delivery of therapeutic agents against cancer. Biochim. Biophys. Acta 1820, 291–317.

Davidson, S.R.H., Weersink, R.A., Haider, M.A., Gertner, M.R., Bogaards, A., Giewercer, D., Scherz, A., Sherar, M.D., Elhilali, M., Chin, J.L., Trachtenberg, J., Wilson, B.C., 2009. Treatment planning and dose analysis for interstitial photodynamic therapy of prostate cancer. Phys. Med. Biol. 54, 2293–313.

Derossi, D., Joliot, A.H., Chassaing, G., Prochiantz, A., 1994. The third helix of the Antennapedia homeodomain translocates through biological membranes. J. Biol. Chem. 269, 10444–50.

Dietze, A., Bonsted, A., Høgset, A., Berg, K., 2003. Photochemical internalization enhances the cytotoxic effect of the protein toxin gelonin and transgene expression in sarcoma cells. Photochem. Photobiol. 78, 283–9.

Dietze, A., Peng, Q., Selbo, P.K., Kaalhus, O., Müller, C., Bown, S., Berg, K., 2005. Enhanced photodynamic destruction of a transplantable fibrosarcoma using photochemical internalisation of gelonin. Br. J. Cancer 92, 2004–9.

Dixon, M.J., Bourré, L., MacRobert, A.J., Eggleston, I.M., 2007. Novel prodrug approach to photodynamic therapy: Fmoc solid-phase synthesis of a cell permeable peptide incorporating 5-aminolaevulinic acid. Bioorg. Med. Chem. Lett. 17, 4518–22.

Domanska, U.M., Timmer-Bosscha, H., Nagengast, W.B., Oude Munnink, T.H., Kruizinga, R.C., Ananias, H.J.K., Kliphuis, N.M., Huls, G., De Vries, E.G.E., de Jong, I.J., Walenkamp, A.M.E., 2012. CXCR4 inhibition with AMD3100 sensitizes prostate cancer to docetaxel chemotherapy. Neoplasia 14, 709–18.

Dong, C., Martinez, G.J., 2015. T cells: the usual subsets.

Dougherty, T.J., Kaufman, J.E., Goldfarb, A., 1978. Photoradiation therapy for the treatment of malignant tumors. Cancer Res. 38, 2628–2635.

Dougherty, T.J., Lawrence, G., Kaufman, J.H., Boyle, D., Weishaupt, K.R., Goldfarb, A., 1979. Photoradiation in the treatment of recurrent breast carcinoma. J. Natl. Cancer Inst. 62, 231–7.

Downes, A., Blunt, T.P., 1877. Researches on the effect of light upon bacteria and other organisms. Proc. R. Soc. London 26, 488–500.

Dubrovska, A., Elliott, J., Salamone, R.J., Telegeev, G.D., Stakhovsky, A.E., Schepotin, I.B., Yan, F., Wang, Y., Bouchez, L.C., Kularatne, S.A., Watson, J., Trussell, C., Reddy, V.A., Cho, C.Y., Schultz, P.G., Debes, J., Tindall, D., Arnold, J., Isaacs, J., Vishnu, P., Tan, W., Dalerba, P., Cho, R., Clarke, M., Dubrovska, A., Kim, S., Salamone, R., Walker, J., Maira, S., Maitland, N., Collins, A., Patrawala, L., Calhoun, T., Schneider-Broussard, R., Li, H., Bhatia, B., Neal, D., Maitland, N., Collins, A., Griend, D. Vander, Karthaus, W., Dalrymple, S., Meeker, A., DeMarzo, A., Miki, J., Furusato, B., Li, H., Gu, Y., Takahashi, H., Tang, D., Patrawala, L., Calhoun, T., Bhatia, B., Choy, G., Dubrovska, A., Elliott, J., Salamone, R., Kim, S., Aimone, L., Darash-Yahana, M., Pikarsky, E., Abramovitch, R., Zeira, E., Pal, B., Engl, T., Relja, B., Marian, D., Blumenberg, C., Müller, I., Singh, S., Singh, U., Grizzle, W., Jr, J.L., Burger, J., Burger, M., Kipps, T., Barretina, J., Juncà, J., Llano, A., Gutiérrez, A., Flores, A., Vandercappellen, J., Damme, J. Van, Struyf, S., Zlotnik, A., Furusato, B., Mohamed, A., Uhlén, M., Rhim, J., Ehtesham, M., Mapara, K., Stevenson, C., Thompson, R., Pan, J., Mestas, J., Burdick, M., Phillips, R., Thomas, G., Lawson, D., Zong, Y., Memarzadeh, S., Xin, L., Huang, J., Mulholland, D., Xin, L., Morin, A., Lawson, D., Witte, O., Goldstein, A., Huang, J., Guo, C., Garraway, I., Witte, O., Chinni, S., Sivalogan, S., Dong, Z., Filho, J., Deng, X., Huang, H., Tindall, D., Miyamoto, K., Araki, K., Naka, K., Arai, F., Takubo, K., Zhu, S., Evans, S., Yan, B., Povsic, T., Tapson, V., Wu, Y., Peng, H., Cui, M., Whitney, N., Huang, Y., Caruz, A., Samsom, M., Alonso, J., Alcami, J., Baleux, F., Gomis, R., Alarcón, C., He, W., Wang, Q., Seoane, J., Hermann, P., Huber, S., Herrler, T., Aicher, A., Ellwart, J., Sun, Y., Fang, M., Wang, J., Cooper, C., Pienta, K., Goel, H., Li, J., Kogan, S., Languino, L., Struckhoff, A., Vitko, J., Rana, M., Davis, C., Foderingham, K., Zeng, Z., Samudio, I., Munsell, M., An, J.,

Huang, Z., Taichman, R., Cooper, C., Keller, E., Pienta, K., Taichman, N., Cooper, C., Chay, C., Pienta, K., Zheng, D.-Q., Woodward, A., Fornaro, M., Tallini, G., Languino, L., Porvasnik, S., Sakamoto, N., Kusmartsev, S., Eruslanov, E., Kim, W., Hwang-Verslues, W., Kuo, W., Chang, P., Pan, C., Wang, H., Passegué, E., Wagner, E., Weissman, I., Jamieson, C., Ailles, L., Dylla, S., Muijtjens, M., Jones, C., 2012. CXCR4 Expression in Prostate Cancer Progenitor Cells. PLoS One 7, e31226.

Duchardt, F., Fotin-Mleczek, M., Schwarz, H., Fischer, R., Brock, R., 2007. A comprehensive model for the cellular uptake of cationic cell-penetrating peptides. Traffic 8, 848–66.

Dupont, E., Prochiantz, A., Joliot, A., 2011. Penetratin story: an overview. Methods Mol. Biol. 683, 21–9.

Dupont, P.J., Warrens, A.N., 2007. Fas ligand exerts its pro-inflammatory effects via neutrophil recruitment but not activation. Immunology 120, 133–9.

Edinger, A.L., Thompson, C.B., 2004. Death by design: apoptosis, necrosis and autophagy. Curr. Opin. Cell Biol. 16, 663–9.

Elisabeth Olsen, C., Berg, K., Kristian Selbo, P., Weyergang, A., 2013. Circumvention of resistance to photodynamic therapy in doxorubicin-resistant sarcoma by photochemical internalization of gelonin. Free Radic. Biol. Med.

Enomoto, N., Hyde, E., Ma, J.Z.-I., Yang, J., Forbes-Blom, E., Delahunt, B., Le Gros, G., Ronchese, F., 2012. Allergen-specific CTL require perforin expression to suppress allergic airway inflammation. J. Immunol. 188, 1734–41.

Evers, D.L., He, J., Kim, Y.H., Mason, J.T., O'Leary, T.J., 2011. Paraffin embedding contributes to RNA aggregation, reduced RNA yield, and low RNA quality. J. Mol. Diagnostics 13, 687–694.

Fales, A.M., Yuan, H., Vo-Dinh, T., 2013. Cell-penetrating peptide enhanced intracellular Raman imaging and photodynamic therapy. Mol. Pharm. 10, 2291–8.

Fingar, V.H., Kik, P.K., Haydon, P.S., Cerrito, P.B., Tseng, M., Abang, E., Wieman, T.J., 1999. Analysis of acute vascular damage after photodynamic therapy using benzoporphyrin derivative (BPD). Br. J. Cancer 79, 1702–8.

Fitzpatrick, T.B., Pathak, M.A., 1959. Historical aspects of methoxsalen and other furocoumarins. J. Invest. Dermatol. 32, 229–31.

Foster, T.H., Gao, L., 1992. Dosimetry in photodynamic therapy: oxygen and the critical importance of capillary density. Radiat. Res. 130, 379–83.

Fretz, M.M., Høgset, A., Koning, G.A., Jiskoot, W., Storm, G., 2007. Cytosolic delivery of liposomally targeted proteins induced by photochemical internalization. Pharm. Res. 24, 2040–7.

Friberg, E.G., Cunderlíková, B., Pettersen, E.O., Moan, J., 2003. pH effects on the cellular uptake of four photosensitizing drugs evaluated for use in photodynamic therapy of cancer. Cancer Lett. 195, 73–80.

Furusato, B., Mohamed, A., Uhlén, M., Rhim, J.S., 2010. CXCR4 and cancer. Pathol. Int. 60, 497–505.

Gallagher-Colombo, S.M., Miller, J., Cengel, K.A., Putt, M.E., Vinogradov, S.A., Busch, T.M., 2015. Erlotinib Pretreatment Improves Photodynamic Therapy of Non-Small Cell Lung Carcinoma Xenografts via Multiple Mechanisms. Cancer Res. 75, 3118–26.

Gao, Y., Zhang, X.-C., Wang, W.-S., Yang, Y., Wang, H.-L., Lu, Y.-G., Fan, D.-L., 2015. Efficacy and safety of topical ALA-PDT in the treatment of EMPD. Photodiagnosis Photodyn. Ther. 12, 92–7.

Garg, A.D., Krysko, D. V, Vandenabeele, P., Agostinis, P., 2012. Hypericin-based photodynamic therapy induces surface exposure of damage-associated molecular patterns like HSP70 and calreticulin. Cancer Immunol. Immunother. 61, 215–21.

Garg, A.D., Nowis, D., Golab, J., Agostinis, P., 2010. Photodynamic therapy: illuminating the road from cell death towards anti-tumour immunity. Apoptosis 15, 1050–71.

Ghiringhelli, F., Menard, C., Puig, P.E., Ladoire, S., Roux, S., Martin, F., Solary, E., Le Cesne, A., Zitvogel, L., Chauffert, B., 2007. Metronomic cyclophosphamide regimen selectively depletes CD4 +CD25+ regulatory T cells and restores T and NK effector functions in end stage cancer patients. Cancer Immunol. Immunother. 56, 641–648.

Giese, A., 1964. Historical Introduction. Photophysiology 1–18.

Gleason, D.F., 1992. Histologic grading of prostate cancer: A perspective. Hum. Pathol. 23, 273–279.

Glowa, C., Peschke, P., Karger, C.P., Hahn, E.W., Huber, P.E., Debus, J., Ehemann, V., 2013. Flow cytometric characterization of tumor subpopulations in three sublines of the Dunning R3327 rat prostate tumor model. Prostate 73, 1710–20.

Gonzalez, S., Arnfield, M.R., Meeker, B.E., Tulip, J., Lakey, W.H., Chapman, J.D., McPhee, M.S., 1986. Treatment of Dunning R3327-AT rat prostate tumors with photodynamic therapy in combination with misonidazole. Cancer Res. 46, 2858–62.

Gottesman, M.M., 2002. Mechanism of Cancer Drug Resistance. Annu. Rev. Med. 53, 615–27.

Gray, H., 1918. Anatomy of the human body, Philadelphia: Lea & Febiger, 1918.

Greish, K., 2010. Enhanced permeability and retention (EPR) effect for anticancer nanomedicine drug targeting. Methods Mol. Biol. 624, 25–37.

Grignon, D.J., 2004. Unusual subtypes of prostate cancer. Mod. Pathol. 17, 316–327.

Haak, C.S., Togsverd-Bo, K., Thaysen-Petersen, D., Wulf, H.C., Paasch, U., Anderson, R.R., Haedersdal, M., 2015. Fractional laser-mediated photodynamic therapy of high-risk basal cell carcinomas--a randomized clinical trial. Br. J. Dermatol. 172, 215–22.

Haedicke, K., Graefe, S., Teichgraeber, U., Hilger, I., 2016. Lowering photosensitizer doses and increasing fluences induce apoptosis in tumor bearing mice. Biomed. Opt. Express 7, 2641–9.

Håkerud, M., Selbo, P.K., Waeckerle-Men, Y., Contassot, E., Dziunycz, P., K??ndig, T.M., H??gset, A., Johansen, P., 2015. Photosensitisation facilitates cross-priming of adjuvant-free protein vaccines and stimulation of tumour-suppressing CD8 T cells. J. Control. Release 198, 10–17.

Håkerud, M., Waeckerle-Men, Y., Selbo, P.K., Kündig, T.M., Høgset, A., Johansen, P., 2014. Intradermal photosensitisation facilitates stimulation of MHC class-I restricted CD8 T-cell responses of co-administered antigen. J. Control. Release 174, 143–50.

Hällbrink, M., Florén, A., Elmquist, A., Pooga, M., Bartfai, T., Langel, Ü., 2001. Cargo

delivery kinetics of cell-penetrating peptides. Biochim. Biophys. Acta - Biomembr. 1515, 101–109.

Hamoudi, R.A., Appert, A., Ye, H., Ruskone-Fourmestraux, A., Streubel, B., Chott, A., Raderer, M., Gong, L., Wlodarska, I., De Wolf-Peeters, C., MacLennan, K.A., de Leval, L., Isaacson, P.G., Du, M.-Q., 2010. Differential expression of NF-kappaB target genes in MALT lymphoma with and without chromosome translocation: insights into molecular mechanism. Leukemia 24, 1487–97.

Harmer, M., Denoix, P., Hamperl, H., 1970. The TNM-system. Aktuelle Probl. Chir. 14, 25–36.

Hatse, S., Princen, K., Bridger, G., De Clercq, E., Schols, D., 2002. Chemokine receptor inhibition by AMD3100 is strictly confined to CXCR4. FEBS Lett. 527, 255–62.

Hayden, M.S., West, A.P., Ghosh, S., 2006. NF-kappaB and the immune response. Oncogene 25, 6758–80.

He, C., Duan, X., Guo, N., Chan, C., Poon, C., Weichselbaum, R.R., Lin, W., 2016. Core-shell nanoscale coordination polymers combine chemotherapy and photodynamic therapy to potentiate checkpoint blockade cancer immunotherapy. Nat. Commun. 7, 12499.

Heckman, C.A., Mehew, J.W., Boxer, L.M., 2002. NF-kB activates Bcl-2 expression in t(14;18) lymphoma cells. Oncogene 21, 3898–3908.

Hedgecock, E.M., Sulston, J.E., Thomson, J.N., 1983. Mutations affecting programmed cell deaths in the nematode Caenorhabditis elegans. Science (80-.). 220, 1277–1279.

Hernandez, C., Huebener, P., Schwabe, R.F., 2016. Damage-associated molecular patterns in cancer: a double-edged sword. Oncogene.

Herrington, F.D., Nibbs, R.J.B., 2016. Regulation of the Adaptive Immune Response by the IκB Family Protein Bcl-3. Cells 5.

Høgset, A., Prasmickaite, L., Selbo, P.K., Hellum, M., Engesaeter, B.Ø., Bonsted, A., Berg, K., 2004. Photochemical internalisation in drug and gene delivery. Adv. Drug Deliv. Rev. 56, 95–115.

Hoption Cann, S.A., van Netten, J.P., van Netten, C., 2003. Dr William Coley and tumour regression: a place in history or in the future. Postgrad. Med. J. 79, 672–80.

Huang, P.S., Oliff, A., 2001. Drug-targeting strategies in cancer therapy. Curr. Opin. Genet. Dev. 11, 104–110.

Huang, Y., Hamblin, M.R., 2014. Handbook of Photomedicine. Taylor and Francis.

Huang, Z., 2005. A review of progress in clinical photodynamic therapy. Technol. Cancer Res. Treat. 4, 283–93.

Huang, Z., Xu, H., Meyers, A.D., Musani, A.I., Wang, L., Tagg, R., Barqawi, A.B., Chen, Y.K., 2008. Photodynamic therapy for treatment of solid tumors--potential and technical challenges. Technol. Cancer Res. Treat. 7, 309–20.

Isaacs, J.T., Heston, W.D., Weissman, R.M., Coffey, D.S., 1978. Animal models of the hormone-sensitive and -insensitive prostatic adenocarcinomas, Dunning R-3327-H, R-3327-HI, and R-3327-AT. Cancer Res. 38, 4353–9.

Isaacs, J.T., Isaacs, W.B., Feitz, W.F.J., Scheres, J., 1986. Establishment and characterization of seven dunning rat prostatic cancer cell lines and their use in

developing methods for predicting metastatic abilities of prostatic cancers. Prostate 9, 261–281.

Isaacs, J.T., Yu, G.W., Coffey, D.S., 1981. The characterization of a newly identified, highly metastatic variety of Dunning R 3327 rat prostatic adenocarcinoma system: the MAT LyLu tumor. Invest. Urol. 19, 20–3.

Ishida, Y., Agata, Y., Shibahara, K., Honjo, T., 1992. Induced expression of PD-1, a novel member of the immunoglobulin gene superfamily, upon programmed cell death. EMBO J. 11, 3887–95.

Ismail, M.S., Torsten, U., Dressler, C., Diederichs, J.E., Hüske, S., Weitzel, H., Berlien, H.P., 1999. Photodynamic Therapy of Malignant Ovarian Tumours Cultivated on CAM. Lasers Med. Sci. 14, 91–6.

Ji, J., Zhang, Y., Chen, W.R., Wang, X., 2016. DC vaccine generated by ALA-PDT-induced immunogenic apoptotic cells for skin squamous cell carcinoma. Oncoimmunology 5, e1072674.

Jin, H.-T., Ahmed, R., Okazaki, T., 2010. Role of PD-1 in Regulating T-Cell Immunity, in: Negative Co-Receptors and Ligands. p. 151.

Jori, G., 1996. Tumour photosensitizers: approaches to enhance the selectivity and efficiency of photodynamic therapy. J. Photochem. Photobiol. B. 36, 87–93.

Jung, Y., Kim, J.K., Shiozawa, Y., Wang, J., Mishra, A., Joseph, J., Berry, J.E., McGee, S., Lee, E., Sun, H., Wang, J., Jin, T., Zhang, H., Dai, J., Krebsbach, P.H., Keller, E.T., Pienta, K.J., Taichman, R.S., 2013. Recruitment of mesenchymal stem cells into prostate tumours promotes metastasis. Nat. Commun. 4, 1795.

Juzeniene, A., Nielsen, K.P., Moan, J., 2006. Biophysical aspects of photodynamic therapy. J. Environ. Pathol. Toxicol. Oncol. 25, 7–28.

Kager, M., Spruβ, T., Schneider, M.R., Angerer, E., 1992. Dunning R3327-G prostate carcinoma of the rat: an appropriate model for drug evaluation. J. Cancer Res. Clin. Oncol. 118, 334–338.

Kawczyk-Krupka, A., Bugaj, A., Potempa, M., Wasilewska, K., Latos, W., Sieroń, A., 2015a. Vascular-targeted photodynamic therapy in the treatment of neovascular age-related macular degeneration: Clinical perspectives. Photodiagnosis Photodyn Ther. 12, 161–75.

Kawczyk-Krupka, A., Wawrzyniec, K., Musiol, S.K., Potempa, M., Bugaj, A.M., Sieroń, A., 2015b. Treatment of localized prostate cancer using WST-09 and WST-11 mediated vascular targeted photodynamic therapy-A review. Photodiagnosis Photodyn. Ther. 12, 567–74.

Kempa, M., Kozub, P., Kimball, J., Rojkiewicz, M., Kuś, P., Gryczyński, Z., Ratuszna, A., 2015. Physicochemical properties of potential porphyrin photosensitizers for photodynamic therapy. Spectrochim. Acta Part A Mol. Biomol. Spectrosc. 146, 249–254.

Kepp, O., Tesniere, A., Schlemmer, F., Michaud, M., Senovilla, L., Zitvogel, L., Kroemer, G., 2009. Immunogenic cell death modalities and their impact on cancer treatment. Apoptosis 14, 364–75.

Kerr, J.F.R., Wyllie, A.H., Currie, A.R., 1972. Apoptosis - Basic Biological Phenomenon With Wide-Ranging Implications in Tissue Kinetics. Br. J. Cancer 26, 239-.

Kharkwal, G.B., Sharma, S.K., Huang, Y.-Y., Dai, T., Hamblin, M.R., 2011. Photodynamic therapy for infections: clinical applications. Lasers Surg. Med. 43, 755–67.

Kim, M.M., Liu, B., Miller, J., Busch, T.M., Zhu, T.C., 2014. Parameter determination for BPD mediated vascularPDT. Proc. SPIE--the Int. Soc. Opt. Eng. 8931.

Kimura, M., Miyajima, K., Kojika, M., Kono, T., Kato, H., 2015. Photodynamic Therapy (PDT) with Chemotherapy for Advanced Lung Cancer with Airway Stenosis. Int. J. Mol. Sci. 16, 25466–75.

Kohli, M., Wang, L., Xie, F., Sicotte, H., Yin, P., Dehm, S.M., Hart, S.N., Vedell, P.T., Barman, P., Qin, R., Mahoney, D.W., Carlson, R.E., Eckel-Passow, J.E., Atwell, T.D., Eiken, P.W., Mcmenomy, B.P., Wieben, E.D., Jha, G., Jimenez, R.E., Weinshilboum, R., Wang, L., 2015. Mutational landscapes of sequential prostate metastases and matched patient derived xenografts during enzalutamide therapy. PLoS One 10.

Korbelik, M., Banath, J., Saw, K.M., 2015. Immunoregulatory cell depletion improves the efficacy of photodynamic therapy-generated cancer vaccines. Int. J. Mol. Sci. 16, 27005–27014.

Korbelik, M., Dougherty, G.J., 1999. Photodynamic therapy-mediated immune response against subcutaneous mouse tumors. Cancer Res. 59, 1941–6.

Korbelik, M., Krosl, G., Krosl, J., Dougherty, G.J., 1996. The role of host lymphoid populations in the response of mouse EMT6 tumor to photodynamic therapy. Cancer Res. 56, 5647–52.

Korbelik, M., Stott, B., Sun, J., 2007. Photodynamic therapy-generated vaccines: relevance of tumour cell death expression. Br. J. Cancer 97, 1381–7.

Kouvroukoglou, S., Lakkis, C.L., Wallace, J.D., Zygourakis, K., Epner, D.E., 1998. Bioenergetics of rat prostate cancer cell migration. Prostate 34, 137–44.

Lai, P.-S., Lou, P.-J., Peng, C.-L., Pai, C.-L., Yen, W.-N., Huang, M.-Y., Young, T.-H., Shieh, M.-J., 2007. Doxorubicin delivery by polyamidoamine dendrimer conjugation and photochemical internalization for cancer therapy. J. Control. Release 122, 39–46.

Laptev, R., Nisnevitch, M., Siboni, G., Malik, Z., Firer, M.A., 2006. Intracellular chemiluminescence activates targeted photodynamic destruction of leukaemic cells. Br. J. Cancer 95, 189–96.

Lee, L.K., Whitehurst, C., Pantelides, M.L., Vernon, D.I., Moore, J. V., 1996. Interstitial photodynamic therapy in the Dunning R3327-AT6 prostatic carcinoma. Lasers Med. Sci. 11, 155–161.

Li, J., Tao, R., Wu, W., Cao, H., Xin, J., Li, J., Guo, J., Jiang, L., Gao, C., Demetriou, A.A., Farkas, D.L., Li, L., 2010. 3D PLGA scaffolds improve differentiation and function of bone marrow mesenchymal stem cell-derived hepatocytes. Stem Cells Dev. 19, 1427–36.

Light treatment in surgery. By Dr. O. Bernhard (St. Moritz). Translated by R. King Brown, B.A., M.D., D.Ph., Medical Officer of Health, Bermondsey: Lecturer in Public Health, Guy's Hospital Medical School. Medium 8vo. Pp. 307, illustrated. 1926. London: E, 1927. . Br. J. Surg. 14, 693–694.

Lilletvedt, M., Tønnesen, H.H., Høgset, A., Nardo, L., Kristensen, S., 2010. Physicochemical characterization of the photosensitizers TPCS2a and TPPS2a 1. Spectroscopic evaluation of drug--solvent interactions. Pharmazie 65, 588–95.

Lilletvedt, M., Tønnesen, H.H.H., Høgset, A., Sande, S.A.A., Kristensen, S., 2011. Evaluation of physicochemical properties and aggregation of the photosensitizers TPCS2a and TPPS2a in aqueous media. Die Pharm. - An Int. J. Pharm. Sci. 66,

9.

Lim, C.-K., Heo, J., Shin, S., Jeong, K., Seo, Y.H., Jang, W.-D., Park, C.R., Park, S.Y., Kim, S., Kwon, I.C., 2012. Nanophotosensitizers toward advanced photodynamic therapy of Cancer. Cancer Lett. 334, 176–87.

Lin, M.-W., Huang, Y.-B., Chen, C.-L., Wu, P.-C., Chou, C.-Y., Wu, P.-C., Hung, S.-Y., 2016. A Formulation Study of 5-Aminolevulinic Encapsulated in DPPC Liposomes in Melanoma Treatment. Int. J. Med. Sci. 13, 483–9.

Lindner, U., Trachtenberg, J., Lawrentschuk, N., 2010. Focal therapy in prostate cancer: modalities, findings and future considerations. Nat. Rev. Urol. 7, 562–71.

Liou, G.-Y., Storz, P., 2010. Reactive oxygen species in cancer. Free Radic. Res. 44, 479–96.

Liu, Y., Zhang, P., Li, J., Kulkarni, A.B., Perruche, S., Chen, W., 2008. A critical function for TGF-β signaling in the development of natural CD4+CD25+Foxp3+ regulatory T cells. Nat. Immunol. 9, 632–640.

LiWang, A.C., Cao, J.J., Zheng, H., Lu, Z., Peiper, S.C., LiWang, P.J., 1999. Dynamics study on the anti-human immunodeficiency virus chemokine viral macrophage-inflammatory protein-II (VMIP-II) reveals a fully monomeric protein. Biochemistry 38, 442–53.

Lou, P.-J., Lai, P.-S., Shieh, M.-J., Macrobert, A.J., Berg, K., Bown, S.G., 2006. Reversal of doxorubicin resistance in breast cancer cells by photochemical internalization. Int. J. Cancer 119, 2692–8.

Luo, Z., Fan, X., Zhou, N., Hiraoka, M., Luo, J., Kaji, H., Huang, Z., 2000. Structure-function study and anti-HIV activity of synthetic peptide analogues derived from viral chemokine vMIP-II. Biochemistry 39, 13545–50.

Madani, F., Lindberg, S., Langel, Ü., Futaki, S., Gräslund, A., Gr&#228, slund, A., Madani, F., Lindberg, S., Langel, &#220, lo, Futaki, S., Gr&#228, slund, A., 2011. Mechanisms of Cellular Uptake of Cell-Penetrating Peptides. J. Biophys. 2011, 1–10.

Malik, Z., Lugaci, H., 1987. Destruction of erythroleukaemic cells by photoactivation of endogenous porphyrins. Br. J. Cancer 56, 589–95.

Marcus, J., Glassberg, E., Dimino-Emme, L., Yamamoto, R., Moy, R.L., Vari, S.G., Papaioannou, T., Pergadia, V.R., Snyder, W.J., Grundfest, W.S., 1994. Photodynamic therapy for the treatment of squamous cell carcinoma using benzoporphyrin derivative. J. Dermatol. Surg. Oncol. 20, 375–82.

Martinez de Pinillos Bayona, A., Moore, C.M., Loizidou, M., MacRobert, A.J., Woodhams, J.H., 2016. Enhancing the efficacy of cytotoxic agents for cancer therapy using photochemical internalisation. Int. J. Cancer 138, 1049–1057.

Master, A., Livingston, M., Sen Gupta, A., 2013. Photodynamic nanomedicine in the treatment of solid tumors: perspectives and challenges. J. Control. Release 168, 88–102.

Master, A.M., Livingston, M., Oleinick, N.L., Sen Gupta, A., 2012. Optimization of a nanomedicine-based silicon phthalocyanine 4 photodynamic therapy (Pc 4-PDT) strategy for targeted treatment of EGFR-overexpressing cancers. Mol. Pharm. 9, 2331–8.

Mathews, M.S., Blickenstaff, J.W., Shih, E.-C., Zamora, G., Vo, V., Sun, C.-H., Hirschberg, H., Madsen, S.J., 2012. Photochemical internalization of bleomycin for glioma treatment. J. Biomed. Opt. 17, 58001.

Mathews, M.S., Chighvinadze, D., Gach, H.M., Uzal, F.A., Madsen, S.J., Hirschberg, H., 2011. Cerebral edema following photodynamic therapy using endogenous and exogenous photosensitizers in normal brain. Lasers Surg. Med. 43, 892–900.

Matoso, A., Epstein, J.I., 2016. Grading of Prostate Cancer: Past, Present, and Future. Curr. Urol. Rep. 17, 25.

Matthews, E., Yang, T., Janulis, L., Goodwin, S., Kundu, S.D., Karpus, W.J., Lee, C., 2000. Down-regulation of TGF-beta1 production restores immunogenicity in prostate cancer cells. Br. J. Cancer 83, 519–25.

McLaughlin, P.M.J., Trzpis, M., Kroesen, B.-J., Helfrich, W., Terpstra, P., Dokter, W.H.A., Ruiters, M.H.J., de Leij, L.F.M.H., Harmsen, M.C., 2004. Use of the EGP-2/Ep-CAM promoter for targeted expression of heterologous genes in carcinoma derived cell lines. Cancer Gene Ther. 11, 603–12.

Mester, E., Ludány, G., Sellyei, M., Szende, B., Tota, J., 1968a. The stimulating effect of low power laser rays on biological systems. Laser Rev 1:3.

Mester, E., Spiry, T., Szende, B., Tota, J., 1971. Effect or laser rays on wound healing. Am J Surg 122, 532–535.

Mester, E., Szende, B., Gartner, P., 1968b. The effect of laser beams on the growth of hair in mice. Radiobiol Radiother (Berl) 9, 621–626.

Momma, T., Hamblin, M.R., Wu, H.C., Hasan, T., 1998. Photodynamic therapy of orthotopic prostate cancer with benzoporphyrin derivative: local control and distant metastasis. Cancer Res. 58, 5425–31.

Moore, C.M., Emberton, M., Bown, S.G., 2011. Photodynamic therapy for prostate cancer--an emerging approach for organ-confined disease. Lasers Surg. Med. 43, 768–75.

Moore, C.M., Nathan, T.R., Lees, W.R., Mosse, C.A., Freeman, A., Emberton, M., Bown, S.G., 2006. Photodynamic therapy using meso tetra hydroxy phenyl chlorin (mTHPC) in early prostate cancer. Lasers Surg. Med. 38, 356–63.

Moore, C.M., Pendse, D., Emberton, M., 2009. Photodynamic therapy for prostate cancer--a review of current status and future promise. Nat. Clin. Pract. Urol. 6, 18–30.

Morrison, S.A., Hill, S.L., Rogers, G.S., Graham, R.A., 2014. Efficacy and safety of continuous low-irradiance photodynamic therapy in the treatment of chest wall progression of breast cancer. J. Surg. Res. 192, 235–41.

Mossu, A., Daoui, A., Bonnefoy, F., Aubergeon, L., Saas, P., Perruche, S., 2016. Plasmacytoid Dendritic Cells Die by the CD8 T Cell-Dependent Perforin Pathway during Acute Nonviral Inflammation. J. Immunol. 197, 1672–1682.

Motoyoshi, Y., Kaminoda, K., Saitoh, O., Hamasaki, K., Nakao, K., Ishii, N., Nagayama, Y., Eguchi, K., 2006. Different mechanisms for anti-tumor effects of low- and high-dose cyclophosphamide. Oncol. Rep. 16, 141–146.

Mroz, P., Hashmi, J.T., Huang, Y.-Y., Lange, N., Hamblin, M.R., 2011a. Stimulation of anti-tumor immunity by photodynamic therapy. Expert Rev. Clin. Immunol. 7, 75–91.

Mroz, P., Yaroslavsky, A., Kharkwal, G.B., Hamblin, M.R., 2011b. Cell death pathways in photodynamic therapy of cancer. Cancers (Basel). 3, 2516–39.

Muragaki, Y., Akimoto, J., Maruyama, T., Iseki, H., Ikuta, S., Nitta, M., Maebayashi, K., Saito, T., Okada, Y., Kaneko, S., Matsumura, A., Kuroiwa, T., Karasawa, K.,

Nakazato, Y., Kayama, T., 2013. Phase II clinical study on intraoperative photodynamic therapy with talaporfin sodium and semiconductor laser in patients with malignant brain tumors. J. Neurosurg. 119, 845–52.

National Cancer Institute, (U.S.A.), 2016. Cancer of the Prostate - SEER Stat Fact Sheets

Ndoye, A., Merlin, J.L., Leroux, A., Dolivet, G., Erbacher, P., Behr, J.P., Berg, K., Guillemin, F., 2004. Enhanced gene transfer and cell death following p53 gene transfer using photochemical internalisation of glucosylated PEI-DNA complexes. J. Gene Med. 6, 884–894.

Neumann, E., Frei, E., Funk, D., Becker, M.D., Schrenk, H.-H., Müller-Ladner, U., Fiehn, C., 2010. Native albumin for targeted drug delivery. Expert Opin. Drug Deliv. 7, 915–25.

Norum, O.-J., Bruland, Ø.S., Gorunova, L., Berg, K., 2009a. Photochemical internalization of bleomycin before external-beam radiotherapy improves locoregional control in a human sarcoma model. Int. J. Radiat. Oncol. Biol. Phys. 75, 878–85.

Norum, O.-J., Gaustad, J.-V., Angell-Petersen, E., Rofstad, E.K., Peng, Q., Giercksky, K.-E., Berg, K., 2009b. Photochemical internalization of bleomycin is superior to photodynamic therapy due to the therapeutic effect in the tumor periphery. Photochem. Photobiol. 85, 740–9.

Norum, O.-J., Giercksky, K.-E., Berg, K., 2009c. Photochemical internalization as an adjunct to marginal surgery in a human sarcoma model. Photochem. Photobiol. Sci. 8, 758–62.

Norum, O.-J., Selbo, P.K., Weyergang, A., Giercksky, K.-E., Berg, K., 2009d. Photochemical internalization (PCI) in cancer therapy: From bench towards bedside medicine. J. Photochem. Photobiol. B Biol. 96, 83–92.

Nyga, A., Cheema, U., Loizidou, M., 2011. 3D tumour models: novel in vitro approaches to cancer studies. J. Cell Commun. Signal. 5, 239–48.

Okon, I.S., Zou, M.-H., 2015. Mitochondrial ROS and cancer drug resistance: Implications for therapy. Pharmacol. Res. 100, 170–4.

Pallasch, C.P., Leskov, I., Braun, C.J., Vorholt, D., Drake, A., Soto-Feliciano, Y.M., Bent, E.H., Schwamb, J., Iliopoulou, B., Kutsch, N., van Rooijen, N., Frenzel, L.P., Wendtner, C.M., Heukamp, L., Kreuzer, K.A., Hallek, M., Chen, J., Hemann, M.T., 2014. Sensitizing protective tumor microenvironments to antibody-mediated therapy. Cell 156, 590–602.

Palm, T.A., 1890. The geographic distribution and etiology of rickets. Practitioner 45, 270–279.

Palm, T.A., 1888. Letter to the editor. Br. Med. J. 2, 1247.

Panzarini, E., Inguscio, V., Dini, L., Panzarini, E., Inguscio, V., Dini, L., 2013. Immunogenic Cell Death: Can It Be Exploited in PhotoDynamic Therapy for Cancer? Biomed Res. Int. 2013, 1–18.

Panzarini, E., Inguscio, V., Fimia, G.M., Dini, L., 2014. Rose Bengal Acetate PhotoDynamic Therapy (RBAc-PDT) Induces Exposure and Release of Damage-Associated Molecular Patterns (DAMPs) in Human HeLa Cells. PLoS One 9, e105778.

Parker, N., Turk, M.J., Westrick, E., Lewis, J.D., Low, P.S., Leamon, C.P., 2005. Folate receptor expression in carcinomas and normal tissues determined by a

quantitative radioligand binding assay. Anal. Biochem. 338, 284–293.

Parrish, J.A., Fitzpatrick, T.B., Shea, C., Pathak, M.A., 1976. Photochemotherapy of vitiligo. Use of orally administered psoralens and a high-intensity long-wave ultraviolet light system. Arch. Dermatol. 112, 1531–4.

Parrish, J.A., Fitzpatrick, T.B., Tanenbaum, L., Pathak, M.A., 1974. Photochemotherapy of Psoriasis with Oral Methoxsalen and Longwave Ultraviolet Light. N. Engl. J. Med. 291, 1207–1211.

Pass, H.I., 1993. Photodynamic Therapy in Oncology : Mechanisms and Clinical Use 85, 443–456.

Paszko, E., Vaz, G.M.F., Ehrhardt, C., Senge, M.O., 2013. Transferrin conjugation does not increase the efficiency of liposomal Foscan during in vitro photodynamic therapy of oesophageal cancer. Eur. J. Pharm. Sci. 48, 202–10.

PCUK, 2016. Prostate Cancer UK Facts and Figures.

Penjweini, R., Smisdom, N., Deville, S., Ameloot, M., 2014. Transport and accumulation of PVP-Hypericin in cancer and normal cells characterized by image correlation spectroscopy techniques. Biochim. Biophys. Acta 1843, 855–65.

Pereira, P.M.R., Korsak, B., Sarmento, B., Schneider, R.J., Fernandes, R., Tomé, J.P.C., 2015. Antibodies armed with photosensitizers: from chemical synthesis to photobiological applications. Org. Biomol. Chem. 13, 2518–29.

Philips, G.K., Atkins, M., 2015. Therapeutic uses of anti-PD-1 and anti-PD-L1 antibodies. Int. Immunol. 27, 39–46.

Pizova, K., Tomankova, K., Daskova, A., Binder, S., Bajgar, R., Kolarova, H., 2012. Photodynamic therapy for enhancing antitumour immunity. Biomed. Pap. Med. Fac. Univ. Palacky. Olomouc. Czech. Repub. 156, 93–102.

Policard, A., 1924. Etude sur les aspects offerts par des tumeurs experimentales examinees a la lumiere de Wood. C R Soc Biol 91, 1423–1428.

Polito, L., Bortolotti, M., Mercatelli, D., Battelli, M., Bolognesi, A., 2013. Saporin-S6: A Useful Tool in Cancer Therapy. Toxins (Basel). 5, 1698–1722.

Portier, B.P., Taglialatela, G., 2006. Bcl-2 Localized at the Nuclear Compartment Induces Apoptosis after Transient Overexpression. J. Biol. Chem. 281, 40493–40502.

Prasmickaite, L., Høgset, A., Selbo, P.K., Engesæter, B.Ø., Hellum, M., Berg, K., 2002. Photochemical disruption of endocytic vesicles before delivery of drugs : a new strategy for cancer therapy. Br. J. Cancer 652–657.

Prime, J., 1900. Des accidents toxiques produits par l'éosinate de sodium. Jouve et Boyer.

Provencio Pulla, M., 2011. Oncologia para Estudiantes de Medicina. Aran Ediciones, Madrid.

Puri, M., Kaur, I., Perugini, M.A., Gupta, R.C., 2012. Ribosome-inactivating proteins: current status and biomedical applications. Drug Discov. Today 17, 774–783.

Pye, H., Butt, M.A., Reinert, H.W., Maruani, A., Nunes, J.P.M., Marklew, J.S., Qurashi, M., Funnell, L., May, A., Stamati, I., Hamoudi, R., Baker, J.R., Smith, M.E.B., Caddick, S., Deonarain, M.P., Yahioglu, G., Chudasama, V., Lovat, L.B., Hynes, N.E., Lane, H.A., Slamon, D.J., Godolphin, W., Jones, L.A., Holt, J.A., Wong, S.G., Keith, D.E., Levin, W.J., Stuart, S.G., Udove, J., Ullrich, A., Ménard, S., Casalini, P., Campiglio, M., Pupa, S., Agresti, R., Tagliabue, E., Schoppmann,

S.F., Jesch, B., Friedrich, J., Wrba, F., Schultheis, A., Pluschnig, U., Maresch, J., Zacherl, J., Hejna, M., Birner, P., Gravalos, C., Jimeno, A., Butt, M.A., Gandy, M., Haidry, R.J., Bloom, E.S., Mackie, S., Khan, M.S., Louis-Auguste, J., Oukrif, D., Khan, S.-U.-R., Saraswati, R., Banks, M.R., Rodriguez-Justo, M., Lovat, L.B., Novelli, M., Chua, T.C., Merrett, N.D., Yoon, H.H., Shi, Q., Sukov, W.R., Wiktor, A.E., Khan, M., Sattler, C.A., Grothey, A., Wu, T.-T., Diasio, R.B., Jenkins, R.B., Sinicrope, F.A., Janjigian, Y.Y., Werner, D., Pauligk, C., Steinmetz, K., Kelsen, D.P., Jäger, E., Altmannsberger, H.-M., Robinson, E., Tafe, L.J., Tang, L.H., Shah, M.A., Al-Batran, S.-E., Yoon, H.H., Shi, Q., Sukov, W.R., Lewis, M.A., Sattler, C.A., Wiktor, A.E., Wu, T.-T., Diasio, R.B., Jenkins, R.B., Sinicrope, F.A., Stahl, P., Seeschaaf, C., Lebok, P., Kutup, A., Bockhorn, M., Izbicki, J.R., Bokemeyer, C., Simon, R., Sauter, G., Marx, A.H., Arteaga, C.L., Sliwkowski, M.X., Osborne, C.K., Perez, E.A., Puglisi, F., Gianni, L., Yarden, Y., Pines, G., Bang, Y.-J., Cutsem, E. Van, Feyereislova, A., Chung, H.C., Shen, L., Sawaki, A., Lordick, F., Ohtsu, A., Omuro, Y., Satoh, T., Aprile, G., Kulikov, E., Hill, J., Lehle, M., Rüschoff, J., Kang, Y.-K., Bailey, T.A., Luan, H., Clubb, R.J., Naramura, M., Band, V., Raja, S.M., Band, H., Krop, I.E., Kim, S.-B., González-Martín, A., LoRusso, P.M., Ferrero, J.-M., Smitt, M., Yu, R., Leung, A.C.F., Wildiers, H., Litvak-Greenfeld, D., Benhar, I., Dennis, M.S., Jin, H., Dugger, D., Yang, R., McFarland, L., Ogasawara, A., Williams, S., Cole, M.J., Ross, S., Schwall, R., Kenanova, V., Wu, A.M., Deyev, S.M., Lebedenko, E.N., Deonarain, M.P., Yahioglu, G., Stamati, I., Marklew, J., Agarwal, P., Bertozzi, C.R., Chudasama, V., Maruani, A., Caddick, S., Behrens, C.R., Ha, E.H., Chinn, L.L., Bowers, S., Probst, G., Fitch-Bruhns, M., Monteon, J., Valdiosera, A., Bermudez, A., Liao-Chan, S., Wong, T., Melnick, J., Theunissen, J.-W., Flory, M.R., Houser, D., Venstrom, K., Levashova, Z., Sauer, P., Migone, T.-S., Horst, E.H. van der, Halcomb, R.L., Jackson, D.Y., Maruani, A., Alom, S., Canavelli, P., Lee, M.T.W., Morgan, R.E., Chudasama, V., Caddick, S., Lee, M.T.W., Maruani, A., Baker, J., Caddick, S., Chudasama, V., Chudasama, V., Smith, M.E.B., Schumacher, F.F., Papaioannou, D., Waksman, G., Baker, J.R., Caddick, S., Smith, M.E.B., Caspersen, M.B., Robinson, E., Morais, M., Maruani, A., Nunes, J.P.M., Nicholls, K., Saxton, M.J., Caddick, S., Baker, J.R., Chudasama, V., Moody, P., Smith, M.E.B., Ryan, C.P., Chudasama, V., Baker, J.R., Molloy, J., Caddick, S., Ryan, C.P., Smith, M.E.B., Schumacher, F.F., Grohmann, D., Papaioannou, D., Waksman, G., Werner, F., Baker, J.R., Caddick, S., Castañeda, L., Maruani, A., Schumacher, F.F., Miranda, E., Chudasama, V., Chester, K.A., Baker, J.R., Smith, M.E.B., Caddick, S., Nunes, J.P.M., Morais, M., Vassileva, V., Robinson, E., Rajkumar, V.S., Smith, M.E.B., Pedley, R.B., Caddick, S., Baker, J.R., Chudasama, V., Bryden, F., Maruani, A., Savoie, H., Chudasama, V., Smith, M.E.B., Caddick, S., Boyle, R.W., Maruani, A., Smith, M.E.B., Miranda, E., Chester, K.A., Chudasama, V., Caddick, S., Maruani, A., Richards, D.A., Chudasama, V., Maruani, A., Savoie, H., Bryden, F., Caddick, S., Boyle, R., Chudasama, V., Castano, A.P., Demidova, T.N., Hamblin, M.R., Castano, A.P., Demidova, T.N., Hamblin, M.R., Castano, A.P., Demidova, T.N., Hamblin, M.R., Bastianpillai, C., Petrides, N., Shah, T., Guillaumier, S., Ahmed, H.U., Arya, M., Reginato, E., Wolf, P., Hamblin, M.R., Korbelik, M., Castano, A.P., Mroz, P., Hamblin, M.R., Overholt, B.F., Wang, K.K., Burdick, J.S., Lightdale, C.J., Kimmey, M., Nava, H.R., Sivak, M. V., Nishioka, N., Barr, H., Marcon, N., Pedrosa, M., Bronner, M.P., Grace, M., Depot, M., Mitsunaga, M., Ogawa, M., Kosaka, N., Rosenblum, L.T., Choyke, P.L., Kobayashi, H., Bhatti, M., Yahioglu, G., Milgrom, L.R., Garcia-Maya, M., Chester, K.A., Deonarain, M.P., Palumbo, A., Hauler, F., Dziunycz, P., Schwager, K., Soltermann, A., Pretto, F., Alonso, C., Hofbauer, G.F., Boyle, R.W., Neri, D., Pye, H., Stamati, I., Yahioglu, G., Butt, M., Deonarain, M., Redmond, R.W., Gamlin, J.N., Damen, C.W.N., Chen, W., Chakraborty, A.B., Oosterhout, M. van, Mazzeo, J.R., Gebler, J.C., Schellens,

J.H.M., Rosing, H., Beijnen, J.H., Castañeda, L., Wright, Z.V.F., Marculescu, C., Tran, T.M., Chudasama, V., Maruani, A., Hull, E.A., Nunes, J.P.M., Fitzmaurice, R.J., Smith, M.E.B., Jones, L.H., Caddick, S., Baker, J.R., Rockett, J.C., Larkin, K., Darnton, S.J., Morris, A.G., Matthews, H.R., Boonstra, J.J., Marion, R. van, Beer, D.G., Lin, L., Chaves, P., Ribeiro, C., Pereira, A.D., Roque, L., Darnton, S.J., Altorki, N.K., Schrump, D.S., Klimstra, D.S., Tang, L.H., Eshleman, J.R., Alvarez, H., Shimada, Y., Dekken, H. van, Tilanus, H.W., Dinjens, W.N.M., Pontén, J., Macintyre, E.H., Hong, V., Presolski, S.I., Ma, C., Finn, M.G., Kuimova, M.K., Bhatti, M., Deonarain, M., Yahioglu, G., Levitt, J.A., Stamati, I., Suhling, K., Phillips, D., Hargus, J.A., Fronczek, F.R., Vicente, M.G.H., Smith, K.M., Moreau, M., Raguin, O., Vrigneaud, J.-M., Collin, B., Bernhard, C., Tizon, X., Boschetti, F., Duchamp, O., Brunotte, F., Denat, F., Wakankar, A., Chen, Y., Gokarn, Y., Jacobson, F.S., Sapra, P., Shor, B., Wang, L., Amphlett, G., Blättler, W.A., Lambert, J.M., Zhang, W., Lazar, A.C., Wang, L., Blättler, W.A., Amphlett, G., Lambert, J.M., Zhang, W., Marcoux, J., Champion, T., Colas, O., Wagner-Rousset, E., Corvaïa, N., Dorsselaer, A. Van, Beck, A., Cianférani, S., Girish, S., Gupta, M., Wang, B., Lu, D., Krop, I.E., Vogel, C.L., Iii, H.A.B., LoRusso, P.M., Yi, J.-H., Saad, O., Tong, B., Chu, Y.-W., Holden, S., Joshi, A., Cleves, M.A., Savellano, M.D., Owusu-Brackett, N., Son, J., Ganga, T., Leung, N.L., Savellano, D.H., 2016. A HER2 selective theranostic agent for surgical resection guidance and photodynamic therapy. Photochem. Photobiol. Sci. 5, 341–354.

Raab, O., 1900. The effect of fluorescent agents on infusoria (in German). Z. Biol 39.

Reginato, E., Mroz, P., Chung, H., Kawakubo, M., Wolf, P., Hamblin, M.R., 2013. Photodynamic therapy plus regulatory T-cell depletion produces immunity against a mouse tumour that expresses a self-antigen. Br. J. Cancer 109, 2167–74.

Ren, F., Sheng, W.-Q., Du, X., 2013. CD133: a cancer stem cells marker, is used in colorectal cancers. World J. Gastroenterol. 19, 2603–11.

Ricketts, K.P.M., Cheema, U., Nyga, A., Castoldi, A., Guazzoni, C., Magdeldin, T., Emberton, M., Gibson, A.P., Royle, G.J., Loizidou, M., 2014. A 3D in Vitro Cancer Model as a Platform for Nanoparticle Uptake and Imaging Investigations. Small 10, 3954–3961.

Rizvi, I., Anbil, S., Alagic, N., Celli, J., Celli, J.P., Zheng, L.Z., Palanisami, A., Glidden, M.D., Pogue, B.W., Hasan, T., 2013. PDT dose parameters impact tumoricidal durability and cell death pathways in a 3D ovarian cancer model. Photochem. Photobiol. 89, 942–52.

Rodríguez, M.E., Cogno, I.S., Milla Sanabria, L.S., Morán, Y.S., Rivarola, V.A., 2016. Heat shock proteins in the context of photodynamic therapy: autophagy, apoptosis and immunogenic cell death. Photochem. Photobiol. Sci.

Rollier, A., 1927. Heliotherapy, with special consideration of surgical tuberculosis. London, Oxford Univ. Press.

Rosenkilde, M.M., Gerlach, L.-O., Jakobsen, J.S., Skerlj, R.T., Bridger, G.J., Schwartz, T.W., 2004. Molecular Mechanism of AMD3100 Antagonism in the CXCR4 Receptor. J. Biol. Chem. 279, 3033–3041.

Russell, E.H., Russell, W.K., 1927. Ultra-Violet Radiation and Actinotherapy.

Sajisevi, M., Rigual, N.R., Bellnier, D.A., Seshadri, M., 2015. Image-guided Interstitial Photodynamic Therapy for Squamous Cell Carcinomas: Preclinical investigation. J. oral Maxillofac. surgery, Med. Pathol. 27, 159–165.

Schmidt, M.H., Reichert, K.W., Ozker, K., Meyer, G.A., Donohoe, D.L., Bajic, D.M., Whelan, N.T., Whelan, H.T., 1999. Preclinical evaluation of benzoporphyrin

derivative combined with a light-emitting diode array for photodynamic therapy of brain tumors. Pediatr. Neurosurg. 30, 225–31.

Schrot, J., Weng, A., Melzig, M.F., 2015. Ribosome-inactivating and related proteins. Toxins (Basel). 7, 1556–615.

Schwartz, P.S., Waxman, D.J., 2001. Cyclophosphamide induces caspase 9-dependent apoptosis in 9L tumor cells. Mol. Pharmacol. 60, 1268–79.

Schwarze, S.R., Hruska, K.A., Dowdy, S.F., 2000. Protein transduction: unrestricted delivery into all cells? Trends Cell Biol. 10, 290–295.

Sehgal, I., Sibrian-Vazquez, M., Vicente, M.G.H., 2008. Photoinduced cytotoxicity and biodistribution of prostate cancer cell-targeted porphyrins. J. Med. Chem. 51, 6014–20.

Selbo, P.K., Høgset, A., Prasmickaite, L., Berg, K., 2002. Photochemical internalisation: a novel drug delivery system. Tumour Biol. 23, 103–12.

Selbo, P.K., Sandvig, K., Kirveliene, V., Berg, K., 2000a. Release of gelonin from endosomes and lysosomes to cytosol by photochemical internalization. Biochim. Biophys. Acta 1475, 307–13.

Selbo, P.K., Sivam, G., Fodstad, O., Sandvig, K., Berg, K., 2001. In vivo documentation of photochemical internalization, a novel approach to site specific cancer therapy. Int. J. Cancer 92, 761–766.

Selbo, P.K., Sivam, G., Fodstad, O., Sandvig, K., Berg, K., 2000b. Photochemical internalisation increases the cytotoxic effect of the immunotoxin MOC31-gelonin. Int. J. Cancer 87, 853–9.

Selbo, P.K., Weyergang, A., Eng, M.S., Bostad, M., Mælandsmo, G.M., Høgset, A., Berg, K., 2012. Strongly amphiphilic photosensitizers are not substrates of the cancer stem cell marker ABCG2 and provides specific and efficient light-triggered drug delivery of an EGFR-targeted cytotoxic drug. J. Control. Release 159, 197–203.

Selbo, P.K., Weyergang, A., Høgset, A., Norum, O.-J., Berstad, M.B., Vikdal, M., Berg, K., 2010. Photochemical internalization provides time- and space-controlled endolysosomal escape of therapeutic molecules. J. Control. Release 148, 2–12.

Sibata, C.H., Colussi, V.C., Oleinick, N.L., Kinsella, T.J., 2001. Photodynamic therapy in oncology. Expert Opin. Pharmacother. 2, 917–27.

Singh, S., Singh, U.P., Grizzle, W.E., Lillard, J.W., 2004. CXCL12-CXCR4 interactions modulate prostate cancer cell migration, metalloproteinase expression and invasion. Lab. Invest. 84, 1666–76.

Srinivasan, D., Muthukrishnan, N., Johnson, G.A., Erazo-Oliveras, A., Lim, J., Simanek, E.E., Pellois, J.-P., 2011. Conjugation to the cell-penetrating peptide TAT potentiates the photodynamic effect of carboxytetramethylrhodamine. PLoS One 6, e17732.

Sulston, J.E., Schierenberg, E., White, J.G., Thomson, J.N., 1983. The embryonic cell lineage of the nematode Caenorhabditis elegans. Dev. Biol.

Sultan, A.A., Jerjes, W., Berg, K., Høgset, A., Mosse, C.A., Hamoudi, R., Hamdoon, Z., Simeon, C., Carnell, D., Forster, M., Hopper, C., 2016. Disulfonated tetraphenyl chlorin (TPCS2a)-induced photochemical internalisation of bleomycin in patients with solid malignancies: a phase 1, dose-escalation, first-in-man trial. Lancet Oncol. 17, 1171–1334.

Svanberg, K., Bendsoe, N., Axelsson, J., Andersson-Engels, S., Svanberg, S., 2010. Photodynamic therapy: superficial and interstitial illumination. J. Biomed. Opt. 15, 41502.

Szpakowska, M., Chevigne, A., 2016. vCCL2/vMIP-II, the viral master KEYmokine. J. Leukoc. Biol. 99, 893–900.

Tai, W., Mahato, R., Cheng, K., 2010. The role of HER2 in cancer therapy and targeted drug delivery. J. Control. Release 146, 264–75.

Takeuchi, Y., Nishikawa, H., 2016. Roles of regulatory T cells in cancer immunity. Int. Immunol. 28, 401–9.

Taneja, S.S., Bennett, J., Coleman, J., Grubb, R., Andriole, G., Reiter, R.E., Marks, L., Azzouzi, A.-R., Emberton, M., 2016. Final Results of a Phase I/II Multicenter Trial of WST11 Vascular Targeted Photodynamic Therapy for Hemi-Ablation of the Prostate in Men with Unilateral Low Risk Prostate Cancer Performed in the United States. J. Urol. 196, 1096–1104.

Tangutoori, S., Spring, B., Mai, Z., Palanisami, A., Mensah, L., Hasan, 2016. Simultaneous delivery of cytotoxic and biologic therapeutics using nanophotoactivatable liposomes enhances treatment efficacy in a mouse model of pancreatic cancer. Nanomedicine 12, 223–34.

Tanielian, C., Wolff, C., 1995. Porphyrin-Sensitized Generation of Singlet Molecular Oxygen: Comparison of Steady-State and Time-Resolved Methods. J. Phys. Chem. 99, 9825–9830.

Taub, A.F., 2007. Photodynamic therapy: other uses. Dermatol. Clin. 25, 101–9.

Toivonen, S.C., Malinen, M., Küblbeck, J., Petsalo, A., Urtti, A., Honkakoski, P., Otonkoski, T., 2016. Regulation of human pluripotent stem cell derived hepatic cell phenotype by 3D hydrogel models. Tissue Eng. Part A.

Tosoian, J.J., Carter, H.B., Lepor, A., Loeb, S., 2016. Active surveillance for prostate cancer: current evidence and contemporary state of practice. Nat. Rev. Urol. 13, 205–15.

Tsai-Turton, M., Luong, B.T., Tan, Y., Luderer, U., 2007. Cyclophosphamide-Induced Apoptosis in COV434 Human Granulosa Cells Involves Oxidative Stress and Glutathione Depletion. Toxicol. Sci. 98, 216–230.

Tsujimoto, Y., 1998. Role of Bcl-2 family proteins in apoptosis: apoptosomes or mitochondria? Genes Cells 3, 697–707.

Usuda, J., Azizuddin, K., Chiu, S., Oleinick, N.L., 2003. Association between the photodynamic loss of Bcl-2 and the sensitivity to apoptosis caused by phthalocyanine photodynamic therapy. Photochem. Photobiol. 78, 1–8.

Vago, R., Marsden, C.J., Lord, J.M., Ippoliti, R., Flavell, D.J., Flavell, S.-U., Ceriotti, A., Fabbrini, M.S., 2005. Saporin and ricin A chain follow different intracellular routes to enter the cytosol of intoxicated cells. FEBS J. 272, 4983–4995.

van Driel, P.B.A.A., Boonstra, M.C., Slooter, M.D., Heukers, R., Stammes, M.A., Snoeks, T.J.A., de Bruijn, H.S., van Diest, P.J., Vahrmeijer, A.L., van Bergen En Henegouwen, P.M.P., van de Velde, C.J.H., Löwik, C.W.G.M., Robinson, D.J., Oliveira, S., 2016. EGFR targeted nanobody-photosensitizer conjugates for photodynamic therapy in a pre-clinical model of head and neck cancer. J. Control. Release 229, 93–105.

Verigos, K., Stripp, D.C.H., Mick, R., Zhu, T.C., Whittington, R., Smith, D., Dimofte, A., Finlay, J., Busch, T.M., Tochner, Z.A., Malkowicz, S., Glatstein, E., Hahn, S.M.,

2006. Updated results of a phase I trial of motexafin lutetium-mediated interstitial photodynamic therapy in patients with locally recurrent prostate cancer. J. Environ. Pathol. Toxicol. Oncol. 25, 373–87.

Vikdal, M., Weyergang, A., Selbo, P.K., Berg, K., 2013. Vascular endothelial cells as targets for photochemical internalization (PCI). Photochem. Photobiol. 89, 1185–92.

Villers, A., Puech, P., Flamand, V., Haber, G., Desai, M., Crouzet, S., Leroy, X., Chopra, S., Lemaitre, L., Ouzzane, A., Gill, I., 2016. Partial Prostatectomy for Anterior Cancer: Short-term Oncologic and Functional Outcomes. Eur Urol. S0302-2838, 30530–9.

von Scherer, J.J., 1841. Chemisch-physiologische Untersuchungen. Liebs Ann Chem Pharm 40, 1–64.

von Tappeiner, H., Jesionek, A., 1903. Therapeutische versuche mit fluoreszierenden stoffen. Munch Med Wochenschr 47, 2042–2044.

von Tappeiner, H., Jodlbauer, A., 1907. Die sensibilisierende wirkung fluoreszierender substanzer: gesamte Untersuchungen ber die photodynamische erscheinung. Leipzig: FCW Vogel.

von Tappeiner, H., Jodlbauer, A., 1904. Uber die wirkung der photodynamischen (fluorescierenden) stoffe auf protozoen und enzyme. Dtsch Arch Klin Med 80, 427–487.

Waeckerle-Men, Y., Mauracher, A., Håkerud, M., Mohanan, D., Kündig, T.M., Høgset, A., Johansen, P., 2013a. Photochemical targeting of antigens to the cytosol for stimulation of MHC class-I-restricted T-cell responses. Eur. J. Pharm. Biopharm. 85, 34–41.

Waeckerle-Men, Y., Mauracher, A., Håkerud, M., Mohanan, D., Kündig, T.M., Høgset, A., Johansen, P., 2013b. Photochemical targeting of antigens to the cytosol for stimulation of MHC class-I-restricted T-cell responses. Eur. J. Pharm. Biopharm. 85, 34–41.

Walker, L.S.K., Sansom, D.M., 2011. The emerging role of CTLA4 as a cell-extrinsic regulator of T cell responses. Nat. Rev. Immunol. 11, 852–63.

Walsh, M.J., Dodd, J.E., Hautbergue, G.M., 2013. Ribosome-inactivating proteins: potent poisons and molecular tools. Virulence 4, 774–84.

Walter, S., Weinschenk, T., Stenzl, A., Zdrojowy, R., Pluzanska, A., Szczylik, C., Staehler, M., Brugger, W., Dietrich, P.-Y., Mendrzyk, R., Hilf, N., Schoor, O., Fritsche, J., Mahr, A., Maurer, D., Vass, V., Trautwein, C., Lewandrowski, P., Flohr, C., Pohla, H., Stanczak, J.J., Bronte, V., Mandruzzato, S., Biedermann, T., Pawelec, G., Derhovanessian, E., Yamagishi, H., Miki, T., Hongo, F., Takaha, N., Hirakawa, K., Tanaka, H., Stevanovic, S., Frisch, J., Mayer-Mokler, A., Kirner, A., Rammensee, H.-G., Reinhardt, C., Singh-Jasuja, H., 2012. Multipeptide immune response to cancer vaccine IMA901 after single-dose cyclophosphamide associates with longer patient survival. Nat. Med. 18, 1254–61.

Wang, H., Li, L., Wang, P., Wang, X., Zhang, K., Liu, Q., 2016. Comparison of photodynamic treatment produced cell damage between human breast cancer cell MCF-7 and its multidrug resistance cell. Photodiagnosis Photodyn. Ther.

Wang, J.T.-W., Berg, K., Høgset, A., Bown, S.G., MacRobert, A.J., 2013. Photophysical and photobiological properties of a sulfonated chlorin photosensitiser TPCS(2a) for photochemical internalisation (PCI). Photochem. Photobiol. Sci. 12, 519–26.

Wang, J.T.-W., Giuntini, F., Eggleston, I.M., Bown, S.G., MacRobert, A.J., 2012. Photochemical internalisation of a macromolecular protein toxin using a cell penetrating peptide-photosensitiser conjugate. J. Control. Release 157, 305–13.

Wang, X., Hu, J., Wang, P., Zhang, S., Liu, Y., Xiong, W., Liu, Q., 2015. Analysis of the in vivo and in vitro effects of photodynamic therapy on breast cancer by using a sensitizer, sinoporphyrin sodium. Theranostics 5, 772–86.

Wang, X., Ji, J., Zhang, H., Fan, Z., Zhang, L., Shi, L., Zhou, F., Chen, W.R., Wang, H., Wang, X., Wang, X., Ji, J., Zhang, H., Fan, Z., Zhang, L., Shi, L., Zhou, F., Chen, W.R., Wang, H., Wang, X., Xiaojie Wang, J.J.H.Z.Z.F.L.Z.L.S.F.Z.W.R.C.H.W.X.W., 2015. Stimulation of dendritic cells by DAMPs in ALA-PDT treated SCC tumor cells. Oncotarget 6, 44688–44702.

Wang, X., Tsui, B., Ramamurthy, G., Zhang, P., Meyers, J., Kenney, M.E., Kiechle, J., Ponsky, L., Basilion, J.P., 2016. Theranostic Agents for Photodynamic Therapy of Prostate Cancer by Targeting Prostate-Specific Membrane Antigen. Mol. Cancer Ther. 15, 1834–44.

Watson, K., Edwards, R.J., 1999. HIV-1 trans-activating (Tat) protein: Both a target and a tool in therapeutic approaches. Biochem. Pharmacol. 58, 1521–1528.

Wein, A.J., Kavoussi, L.R., Novick, A.C., Partin, A.W., Peters, C. a., 2012. Campbell-Walsh Urology 10th Edition, Campbell-Walsh Urology.

Weishaupt, K.R., Gomer, C.J., Dougherty, T.J., 1976. Identification of singlet oxygen as the cytotoxic agent in photoinactivation of a murine tumor. Cancer Res. 36, 2326–9.

Wenger, A.S., Mickey, D.D., Hall, M., Silverman, L.M., Mickey, G.H., Fried, F.A., 1984. In vitro characterization of MAT LyLu: a Dunning rat prostate adenocarcinoma tumor subline. J. Urol. 131, 1232–6.

Wessells, J., Baer, M., Young, H.A., Claudio, E., Brown, K., Siebenlist, U., Johnson, P.F., 2004. BCL-3 and NF-kB p50 attenuate lipopolysaccharide-induced inflammatory responses in macrophages. J. Biol. Chem. 279, 49995–50003.

Weyergang, A., Cheung, L.H., Rosenblum, M.G., Mohamedali, K.A., Peng, Q., Waltenberger, J., Berg, K., 2014. Photochemical internalization augments tumor vascular cytotoxicity and specificity of VEGF121/rGel fusion toxin. J. Control. Release 180C, 1–9.

Weyergang, A., Selbo, P.K., Berg, K., 2006. Photochemically stimulated drug delivery increases the cytotoxicity and specificity of EGF–saporin. J. Control. Release 111, 165–173.

Weyergang, A., Selbo, P.K., Berstad, M.E.B., Bostad, M., Berg, K., 2011. Photochemical internalization of tumor-targeted protein toxins. Lasers Surg. Med. 43, 721–33.

White, B., Rossi, V., Baugher, P.J., 2016. Aminolevulinic Acid-Mediated Photodynamic Therapy Causes Cell Death in MG-63 Human Osteosarcoma Cells. Photomed. Laser Surg.

WHO, W.H.O.-, 2012. GLOBOCAN 2012 - International Agency for Research on Cancer

Wright, K.E., Liniker, E., Loizidou, M., Moore, C., Macrobert, A.J., Phillips, J.B., 2009. Peripheral neural cell sensitivity to mTHPC-mediated photodynamic therapy in a 3D in vitro model. Br. J. Cancer 101, 658–65.

Wright, K.E., MacRobert, A.J., Phillips, J.B., 2007. Intracellular localisation of mTHPC

and effect of photodynamic therapy in cells of the mammalian peripheral nervous system.

Xia, Y., Gupta, G.K., Castano, A.P., Mroz, P., Avci, P., Hamblin, M.R., 2014. CpG oligodeoxynucleotide as immune adjuvant enhances photodynamic therapy response in murine metastatic breast cancer. J. Biophotonics 7, 897–905.

Xiao, H., Neuveut, C., Tiffany, H.L., Benkirane, M., Rich, E.A., Murphy, P.M., Jeang, K.T., 2000. Selective CXCR4 antagonism by Tat: implications for in vivo expansion of coreceptor use by HIV-1. Proc. Natl. Acad. Sci. U. S. A. 97, 11466–71.

Xu, L., Li, Y., Sun, H., Li, D., Hou, T., 2013. Structural basis of the interactions between CXCR4 and CXCL12/SDF-1 revealed by theoretical approaches. Mol. Biosyst. 9, 2107–17.

Xue, L., Chiu, S., Oleinick, N.L., 2001. Photochemical destruction of the Bcl-2 oncoprotein during photodynamic therapy with the phthalocyanine photosensitizer Pc 4. Oncogene 20, 3420–3427.

Yang, Y., Zhang, Q., Gao, M., Yang, X., Huang, Z., An, J., 2014. A novel CXCR4-selective high-affinity fluorescent probe and its application in competitive binding assays. Biochemistry 53, 4881–4883.

Yavari, N., Andersson-Engels, S., Segersten, U., Malmstrom, P.-U., 2011. An overview on preclinical and clinical experiences with photodynamic therapy for bladder cancer. Can. J. Urol. 18, 5778–86.

Yewale, C., Baradia, D., Vhora, I., Patil, S., Misra, A., 2013. Epidermal growth factor receptor targeting in cancer: a review of trends and strategies. Biomaterials 34, 8690–707.

Yip, W.L., Weyergang, A., Berg, K., Tønnesen, H.H., Selbo, P.K., 2006. Targeted delivery and enhanced cytotoxicity of cetuximab-saporin by photochemical internalization in EGFR-positive cancer cells. Mol. Pharm. 4, 241–51.

Yuan, A., Hu, Y., Ming, X., 2015. Dendrimer Conjugates for Light-activated Delivery of Antisense Oligonucleotides. RSC Adv. 5, 35195–35200. doi:10.1039/C5RA04091D

Zahreddine, H., Borden, K.L.B., 2013. Mechanisms and insights into drug resistance in cancer. Front. Pharmacol. 4, 28.

Zamarron, B.F., Chen, W., 2011. Dual roles of immune cells and their factors in cancer development and progression. Int. J. Biol. Sci. 7, 651–8.

Zhang, L.-J., Yan, Y.-J., Liao, P.-Y., Margetic, D., Wang, L., Chen, Z.-L., 2015. Synthesis and antitumor activity evaluation of a novel porphyrin derivative for photodynamic therapy in vitro and in vivo. Tumour Biol.

Zhang, S., Qi, L., Li, M., Zhang, D., Xu, S., Wang, N., Sun, B., Vrielinck, L., Ostyn, F., Damme, B. van, Bogaert, W. van den, Fossion, E., Taille, A. de la, Katz, A., Bagiella, E., Olsson, C., O, K., Ayala, G., Wheeler, T., Shine, H., Schmelz, M., Frolov, A., Chakraborty, S., Rowley, D., Balkwill, F., Zlotnik, A., Scotton, C., Wilson, J., Scott, K., Stamp, G., Wilbanks, G., Fricker, S., Bridger, G., Balkwill, F., Fricker, S., Anastassov, V., Cox, J., Darkes, M., Grujic, O., Idzan, S., Labrecque, J., Lau, G., Mosi, R., Nelson, K., Qin, L., Santucci, Z., Wong, R., Greenlee, R., Hill-Harmon, M., Murray, T., Thun, M., Zlotnik, A., Balkwill, F., Kato, M., Kitayama, J., Kazama, S., Nagawa, H., McNeal, J., Shirozu, M., Nakano, T., Inazawa, J., Tashiro, K., Tada, H., Shinohara, T., Honjo, T., Rossi, D., Zlotnik, A., Taichman, R., Cooper, C., Keller, E., Pienta, K., Taichman, N., McCauley, L., Burger, M.,

Glodek, A., Hartmann, T., Schmitt-Graff, A., Silberstein, L., Fujii, N., Kipps, T., Burger, J., Altundag, K., Morandi, P., Altundag, O., Gunduz, M., Sutton, A., Friand, V., Brulé-Donneger, S., Chaigneau, T., Ziol, M., Sainte-Catherine, O., Poiré, A., Saffar, L., Kraemer, M., Vassy, J., Nahon, P., Salzmann, J., Gattegno, L., Charnaux, N., Perissinotto, E., Cavalloni, G., Leone, F., Fonsato, V., Mitola, S., Grignani, G., Surrenti, N., Sangiolo, D., Bussolino, F., Piacibello, W., Aglietta, M., Muller, A., Homey, B., Soto, H., Ge, N., Catron, D., Buchanan, M., Vaday, G., Hua, S., Peehl, D., Pauling, M., Lin, Y., Zhu, L., Lawrence, D., Foda, H., Zucker, S., Dang, C., Zhang, Y., Ma, Q., Shimahara, Y., Oelmann, E., Sreter, L., Schuller, I., Serve, H., Koenigsmann, M., Wiedenmann, B., Oberberg, D., Reufi, B., Thiel, E., Berdel, W., Zhu, Z., Friess, H., Wang, L., Bogardus, T., Korc, M., Kleeff, J., Büchler, M., 2008. Chemokine CXCL12 and its receptor CXCR4 expression are associated with perineural invasion of prostate cancer. J. Exp. Clin. Cancer Res. 27, 62.

Zhao, J.-F., Chen, J.-Y., Mi, L., Wang, P.-N., Peng, Q., 2011. Enhancement of Intracellular Delivery of Anti-cancer Drugs by the Tat Peptide. Ultrastruct. Pathol. 35, 119–123.

Zhou, N., Luo, Z., Luo, J., Hall, J.W., Huang, Z., 2000. A novel peptide antagonist of CXCR4 derived from the N-terminus of viral chemokine vMIP-II. Biochemistry 39, 3782–3787.

Zhou, X., Chen, B., Hoopes, P.J., Hasan, T., Pogue, B.W., 2006. Tumor vascular area correlates with photosensitizer uptake: analysis of verteporfin microvascular delivery in the Dunning rat prostate tumor. Photochem. Photobiol. 82, 1348–57.

Zhou, X., Pogue, B.W., Chen, B., Hasan, T., 2004. Analysis of Effective Molecular Diffusion Rates for Verteporfin in Subcutaneous Versus Orthotopic Dunning Prostate Tumors ¶. Photochem. Photobiol. 79, 323–331.

Zhu, T.C., Dimofte, A., Finlay, J.C., Stripp, D., Busch, T., Miles, J., Whittington, R., Malkowicz, S.B., Tochner, Z., Glatstein, E., Hahn, S.M., 2005a. Optical properties of human prostate at 732 nm measured in mediated photodynamic therapy. Photochem. Photobiol. 81, 96–105.

Zhu, T.C., Finlay, J.C., Hahn, S.M., 2005b. Determination of the distribution of light, optical properties, drug concentration, and tissue oxygenation in-vivo in human prostate during motexafin lutetium-mediated photodynamic therapy. J. Photochem. Photobiol. B. 79, 231–41.

Zlotnikov-Klionsky, Y., Nathansohn-Levi, B., Shezen, E., Rosen, C., Kagan, S., Bar-On, L., Jung, S., Shifrut, E., Reich-Zeliger, S., Friedman, N., Aharoni, R., Arnon, R., Yifa, O., Aronovich, A., Reisner, Y., Aharoni, R., Bar-On, L., Jung, S., Birnberg, T., Bar-On, L., Sapoznikov, A., Caton, M.L., Cervantes-Barragán, L., Makia, D., Krauthgamer, R., Brenner, O., Ludewig, B., Brockschnieder, D., al., et, Blasius, A.L., Barchet, W., Cella, M., Colonna, M., Brake, D.K., Smith, E.O., Mersmann, H., Smith, C.W., Robker, R.L., Chan, C.W., Crafton, E., Fan, H.N., Flook, J., Yoshimura, K., Skarica, M., Brockstedt, D., Dubensky, T.W., Stins, M.F., Lanier, L.L., al., et, Chawla, A., Nguyen, K.D., Goh, Y.P., Cildir, G., Akıncılar, S.C., Tergaonkar, V., Souza, C.T. De, Araujo, E.P., Bordin, S., Ashimine, R., Zollner, R.L., Boschero, A.C., Saad, M.J., Velloso, L.A., Dhodapkar, M.V., Steinman, R.M., Krasovsky, J., Munz, C., Bhardwaj, N., Elgazar-Carmon, V., Rudich, A., Hadad, N., Levy, R., Eller, K., Kirsch, A., Wolf, A.M., Sopper, S., Tagwerker, A., Stanzl, U., Wolf, D., Patsch, W., Rosenkranz, A.R., Eller, P., Feuerer, M., Herrero, L., Cipolletta, D., Naaz, A., Wong, J., Nayer, A., Lee, J., Goldfine, A.B., Benoist, C., Shoelson, S., Mathis, D., Fu, F., Li, Y., Qian, S., Lu, L., Chambers, F., Starzl, T.E., Fung, J.J., Thomson, A.W., Guilherme, A., Virbasius, J.V., Puri, V., Czech, M.P.,

Hotamisligil, G.S., Shargill, N.S., Spiegelman, B.M., Ilan, Y., Maron, R., Tukpah, A.M., Maioli, T.U., Murugaiyan, G., Yang, K., Wu, H.Y., Weiner, H.L., Jonuleit, H., Schmitt, E., Schuler, G., Knop, J., Enk, A.H., Kägi, D., Ledermann, B., Bürki, K., Seiler, P., Odermatt, B., Olsen, K.J., Podack, E.R., Zinkernagel, R.M., Hengartner, H., Kang, K., Reilly, S.M., Karabacak, V., Gangl, M.R., Fitzgerald, K., Hatano, B., Lee, C.H., Liu, J., Divoux, A., Sun, J., Zhang, J., Clément, K., Glickman, J.N., Sukhova, G.K., Wolters, P.J., Du, J., Gorgun, C.Z., al., et, Lu, L., Qian, S., Hershberger, P.A., Rudert, W.A., Lynch, D.H., Thomson, A.W., Lumeng, C.N., Bodzin, J.L., Saltiel, A.R., Lumeng, C.N., Deyoung, S.M., Bodzin, J.L., Saltiel, A.R., Lutz, M.B., Kukutsch, N.A., Menges, M., Rössner, S., Schuler, G., Ndifon, W., Gal, H., Shifrut, E., Aharoni, R., Yissachar, N., Waysbort, N., Reich-Zeliger, S., Arnon, R., Friedman, N., Nguyen, M.T.A., Favelyukis, S., Nguyen, A.K., Reichart, D., Scott, P.A., Jenn, A., Liu-Bryan, R., Glass, C.K., Neels, J.G., Olefsky, J.M., Nishimura, S., Manabe, I., Nagasaki, M., Eto, K., Yamashita, H., Ohsugi, M., Otsu, M., Hara, K., Ueki, K., Sugiura, S., al., et, Nishimura, S., Manabe, I., Takaki, S., Nagasaki, M., Otsu, M., Yamashita, H., Sugita, J., Yoshimura, K., Eto, K., Komuro, I., al., et, Odegaard, J.I., Ricardo-Gonzalez, R.R., Goforth, M.H., Morel, C.R., Subramanian, V., Mukundan, L., Eagle, A.R., Vats, D., Brombacher, F., Ferrante, A.W., Chawla, A., Osborn, O., Olefsky, J.M., Ouchi, N., Parker, J.L., Lugus, J.J., Walsh, K., Pillarisetty, V.G., Katz, S.C., Bleier, J.I., Shah, A.B., Dematteo, R.P., Rausch, M.E., Weisberg, S., Vardhana, P., Tortoriello, D.V., Revelo, X.S., Tsai, S., Lei, H., Luck, H., Ghazarian, M., Tsui, H., Shi, S.Y., Schroer, S., Luk, C.T., Lin, G.H., al., et, Rocha, V.Z., Folco, E.J., Sukhova, G., Shimizu, K., Gotsman, I., Vernon, A.H., Libby, P., Sadyś, M., Strzelczak, A., Grinn-Gofroń, A., Kennedy, R., Sakaguchi, S., Schipper, H.S., Prakken, B., Kalkhoven, E., Boes, M., Stary, G., Bangert, C., Tauber, M., Strohal, R., Kopp, T., Stingl, G., Sun, K., Kusminski, C.M., Scherer, P.E., Süss, G., Shortman, K., Taieb, J., Chaput, N., Ménard, C., Apetoh, L., Ullrich, E., Bonmort, M., Péquignot, M., Casares, N., Terme, M., Flament, C., al., et, Talukdar, S., Oh, Y., Bandyopadhyay, G., Li, D., Xu, J., McNelis, J., Lu, M., Li, P., Yan, Q., Zhu, Y., al., et, Tiao, M.M., Lu, L., Tao, R., Wang, L., Fung, J.J., Qian, S., Trinité, B., Chauvin, C., Pêche, H., Voisine, C., Heslan, M., Josien, R., Vosshenrich, C.A.J., Lesjean-Pottier, S., Hasan, M., Goff, O.R.-L., Corcuff, E., Mandelboim, O., Santo, J.P. Di, Waithman, J., Allan, R.S., Kosaka, H., Azukizawa, H., Shortman, K., Lutz, M.B., Heath, W.R., Carbone, F.R., Belz, G.T., Weisberg, S.P., McCann, D., Desai, M., Rosenbaum, M., Leibel, R.L., Ferrante, A.W., Winer, S., Chan, Y., Paltser, G., Truong, D., Tsui, H., Bahrami, J., Dorfman, R., Wang, Y., Zielenski, J., Mastronardi, F., al., et, Wu, D., Molofsky, A.B., Liang, H.E., Ricardo-Gonzalez, R.R., Jouihan, H.A., Bando, J.K., Chawla, A., Locksley, R.M., Xu, H., Barnes, G.T., Yang, Q., Tan, G., Yang, D., Chou, C.J., Sole, J., Nichols, A., Ross, J.S., Tartaglia, L.A., Chen, H., Yang, H., Youm, Y.H., Vandanmagsar, B., Ravussin, A., Gimble, J.M., Greenway, F., Stephens, J.M., Mynatt, R.L., Dixit, V.D., Yeung, K.Y., Ruzzo, W.L., Yu, P., Xiong, S., He, Q., Chu, Y., Lu, C., Ramlogan, C.A., Steel, J.C., Zangi, L., Klionsky, Y.Z., Yarimi, L., Bachar-Lustig, E., Eidelstein, Y., Shezen, E., Hagin, D., Ito, Y., Takai, T., Reich-Zeliger, S., al., et, 2015. Perforin-Positive Dendritic Cells Exhibit an Immuno-regulatory Role in Metabolic Syndrome and Autoimmunity. Immunity 43, 776–787.

Zwicke, G.L., Mansoori, G.A., Jeffery, C.J., 2012. Utilizing the folate receptor for active targeting of cancer nanotherapeutics. Nano Rev. 3.